SILICON FOR THE CHEMICAL AND SOLAR INDUSTRY XIII

Kristiansand, Norway

June 13 – 16, 2016

Editors: L. Nygård, B. Pachaly, I. G. Page, H. Rong, M. Tangstad, H. Tveit,

The Norwegian University of Science and Technology

N-7491 Trondheim, Norway

Front page illustration: Transformed charcoal and coal SiC particles in a molten SiO^2 matrix. Photo: Merete Tangstad

SILICON FOR THE CHEMICAL AND SOLAR INDUSTRY XIII

Kristiansand, Norway

June 13 – 16, 2016

Editors: Lars Nygård, Fesil AS
Bernd Pachaly, Wacker Chemie
Harry Rong, Elkem AS
Merete Tangstad, NTNU
Halvard Tveit, NTNU
Ingrid Gamst Page

The Norwegian University of Science and Technology

N-7491 Trondheim, Norway

Preface

June 2016 has finally arrived, and we are all looking forward to three interesting days of presentations, discussions and learning here in Kristiansand.

Even more important is the networking, where we can meet former partners and colleagues, and start new relationships with future business and research colleagues. This is an excellent opportunity for fruitful and constructive co-operation. The most serious matter is, of course, that this is business, and that a business must continuously improve to stay at the forefront of developments and remain successful.

Over time, there has been a large increase in the volume of usage and sales of silicon and silicon-products, and there are many participants eager to take part in this development. In order to remain successful in this business, we must all increase our levels of efficiency, competence, safety and environmental standards. This conference aims to contribute to the sharing of knowledge within these areas in the hope of achieving increased sustainable production.

The organizing committee is proud to publish a number of interesting papers within silicon production and silicon for chemical and solar industry. The organizing committee has changed since the last conference, and the committee now consists of Harry Rong and Halvard Tveit from Elkem, Lars Nygård from Fesil and Bernd Pachaly from Wacker as well as myself. This conference would not be possible without their valuable contributions. In addition, a large thank-you goes to our secretary, Ingrid Gamst Page.

Enjoy the conference.

Prof. Merete Tangstad
Department of Material Science and Engineering
Norwegian University of Science and Technology
June, 2016

CONTENTS

Silicon for the Chemical and Solar Industry XIII
Kristiansand, Norway, June 13 – 16, 2016

Carbon Neutral Metal Production – a new environmental friendly method for production of silicon

Alf Tore Haug[1)], Espen Dahl[1)], Therese Videm Buø[1)], Håvard Moe[1)], Per Carlsson[2)], Trond Andresen[2)], Judit Sandquist[2)], Per Eilif Wahl[2)]

1) Elkem AS
2) SINTEF Energy Research AS

Abstract

In this work pyrolysis of biomass is investigated experimentally in order to determine a complete mass and chemical energy balance for the main components; charcoal, gas and condensate. The motivation for this work is to provide relevant data, which later will be used in system studies for the next generation of Elkem silicon production processes called Carbon Neutral Metal Production. The integrated concept, have a potential to not only mitigate CO_2 by substituting fossil coal to charcoal but also generate new streams of income from bio-oil products. In this initial study the results indicate that roughly 50 % of the chemical energy in the wood log can be recovered as bio-oil. This under conditions which result in 25 % of charcoal with a fixed carbon content of 83 %.

Introduction

Increasing global consumption and the threat of anthropogenic climate change put pressure on the global society to increase resource efficiency and reduce CO_2 emissions. Current production of primary silicon and ferrosilicon alloys are characterized by high energy requirements and significant emission of climate gases. Elkem consumes roughly 12 TWh of energy (electricity and carbon based reductants combined) and emits an estimated 1.3 MT of CO_2 annually. In an effort to dramatically improve on these numbers, Elkem has proclaimed its ambitions to develop a novel silicon and ferrosilicon production process with the prospect of major reductions in overall energy consumption and close to zero CO_2 emissions from fossil carbon sources.

The novelty of the process lies in the direct integration between the silicon production process and a charcoal production facility, thereby enabling an additional reduction in energy consumption and CO_2 emissions. In combination with an energy recovery facility, the energy recovery factor of the total system will far outweigh that of conventional silicon-furnace heat recovery systems. The integrated charcoal, metal and energy recovery process has been termed *Carbon Neutral Metal Production* (CNMP for short). The integration with charcoal production introduces by-products that are novel to the conventional silicon production process; gases and condensate from pyrolysis, bark, and fines from biomass and charcoal handling. Consequently, this requires a new heat recovery system, boilers, handling, and more. There are also uncertainties coupled to the charcoal production, such as identifying process conditions for charcoal production in order to fulfil satisfactory specifications, as well as understanding how process conditions affect mass and energy distribution between the two by-products (gas and condensate).

Charcoal production is a subject that has been studied for centuries or millennia and several reviews are available on the topic [1-6]. The distinction between fast and slow pyrolysis refers to the heating rate of the fuel. Slow pyrolysis, is typically conducted at heating rates ranging from 1-5 °C/min, whilst during fast pyrolysis the heating rates are in the 100-1000 °C/s range. The heating rate is the most important factor influencing the yield of liquids; increased heating rate results in increased yield of liquids. The upper liquid yield limit is around 75 % on mass basis [7]. In order to obtain such high yields, a short vapour residence time (in the literature a vapour residence time of less than 2 s seems to be the generally agreed upon number) is necessary since the pyrolysis vapours react through secondary reactions and form gases and additional char through polymerization. If charcoal is of interest, prolonging the vapour residence time has showed to be positive in regards of charcoal yield since this promotes secondary, char forming reactions. This can be accomplished by limiting the amount of purge gas or by using large particles or thick beds thus introducing a mass transfer limitation from the biomass to the gas phase. The coupling to soak time (hold time) at maximum process temperature here becomes analogous; i.e. if the pyrolysis vapours are allowed to react with the charcoal for longer period of time more will be converted through secondary reaction to gas and additional charcoal [8, 9]. Fixed carbon content increases rapidly and roughly linearly with pyrolysis temperature from 300 to 400 °C (fixed carbon content 20-70 %) and then slows down reaching a maximum value at around 90 % at 800 °C [10] provided that sufficient residence time is given for the fuel particles.

In preceding work, it was identified early on that the carbonization technology needs to be integrated with existing infrastructure used in the silicon production process in order

to be energy efficient. Here, integration refers to both energy integration and mass integration. Energy integration can be to use heat from the silicon process and auxiliary equipment as a source of energy for charcoal production (and vice versa). Mass integration denotes recovering gas, fines, and condensate from the pyrolysis process and integrating them into either energy production units such as boilers or gas turbines, upgrading units or recovery units.

Taking this into consideration, the main objective with this paper is to perform a detailed characterization of the main products from pyrolysis at conditions relevant for a future Elkem process. The goal is that these and similar results can be used to conduct a system study of the complete process; where charcoal production is integrated into the silicon production process.

Method

Small scale pyrolysis experiments were performed in order to obtain a complete mass and chemical energy balance including the elemental balance for a feedstock relevant to the CNMP concept. Pine wood chips were selected as a reference feedstock since it is currently used in the existing silicon production process. Although the main product of interest is the charcoal, there may be economical incentives to optimize the recovery of condensates. Hence the experimental setup was designed to maximize the recovery (but not the production) of condensate. The experimental setup is schematically described in Figure 1, and consists of the following parts. A 40 mm pipe furnace approximately 500 mm long, a propylene-glycol cooled condenser operating at a set temperature of 0 °C, a glass wool filter designed to trap aerosols and a Tedlar bag for gas collection. The experiment was started by filling the inner pipe of the pipe furnace with wood chips and the pipe was then weighed and installed in the furnace. The biomass was then dried at 120 °C using a nitrogen purge of 5 l/min for about 60 minutes. During the drying process the condenser was by-passed and the steam was vented directly to the fume hood. After the drying process, the nitrogen and vent valves were closed and the valves to the condenser and gas bag were opened. Thereafter, the sample was heated with a heating rate of roughly 13 °C/min to 400-600 °C depending on which final temperature was investigated. After the maximum temperature was obtained the samples was kept there for 30-180 minutes depending on the chosen soak time. Consequently, during the pyrolysis experiment no purge gas was used and the pressure in the system was in practice "regulated" with the expansion of the Tedlar bag (i.e. atmospheric conditions). After the required soak time had been obtained the valve to the condenser and gas bag was closed, the furnace switched off and the samples were allowed to cool overnight with a small N_2 purge to prevent the charcoal samples from catching fire. Once the furnace had cooled off, the gas and condensate collection systems and the amount of charcoal were weighed and the yield was determined. The feedstock and products, condensate and charcoal, were analysed to determine the elemental composition and the heating value. The collected gas was analysed using a Varian CP-4900 micro-GC. Finally, a complete mass and

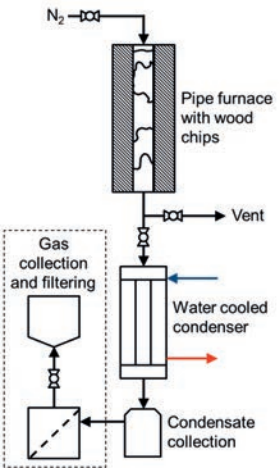

Figure 1. Schematics of the experimental setup

chemical energy balance was determined including the distribution of the major elements (C, H, O). In total, 19 different experiments were performed. The interpretation and evaluation of all the experimental results are reserved for an upcoming publication by the authors and this work focuses on the mass and chemical energy balance from one of these experiments. The conditions for the chosen experiment were as follows: heating rate of 13 °C/min, 500 °C final temperature, and a soak time of 3 hours.

Results and discussion

The composition and heating values for all the products including the original feedstock used in the pyrolysis experiment are displayed in Table 1. Notice that the standard proximate analysis was not performed for the condensate, since it was not regarded as applicative. The biomass analysis reveals no surprises and falls within similar values which can be found in tables and databases (for example [11]) for biomass. For the charcoal; since the entire proximate analysis is normalized and the moisture content is low; the corresponding fixed carbon content is quite high. However, if the moisture content is adjusted to 15%, which is the upper limit for an Elkem charcoal the fixed carbon content is reduced to roughly 72%, which is still well within the given process requirements (>60%). It is also worth mentioning that the 2% moisture content in the charcoal from the experimental campaign is more than likely absorbed humidity (from surrounding air) from when the sample was handled. The obtained condensate contains 33% moisture which is slightly higher than typical values reported for fast pyrolysis oils which are around 25% using different types of fast pyrolysis technologies [12].

Table 1. Proximate and ultimate analysis and heating value of the original feedstock used in the pyrolysis experiments together with the analysis of the obtained charcoal, condensate and gas.

Proximate analysis (as received wt-%)				
	Pine wood chips	Charcoal	Condensate	Gas
Moisture	25.4	2.0	33	-
Ash	0.2	0.8	0.002	-
Volatiles	61.2	14.5	-	-
Fixed carbon	13.2	82.8	-	-
Ultimate analysis (wt-%, solids as dry)				
C	53.4	86.9	35.5	36.7
H	6.4	2.8	8.5	2.0
O	39.9	10.2	55.9	61.3
N	0.2	0.1	nd.	-
S (mg/kg)	67.7	172.0	nd.	na.
Cl (mg/kg)	37.9	43.0	nd.	na.
Higher heating value (MJ/kg)				
HHV	17.4	32.6	15.3	7.9

It must be noted that fast pyrolysis is different from the pyrolysis process applied in this work and is used to maximize the yield and quality of the condensate. Hence, the obtained pyrolysis oil in this work is expected to have somewhat lower quality than that of the fast pyrolysis oils. This is also reflected on the heating value of 15.3 MJ/kg, which is lower compared to about 17 MJ/kg reported for fast pyrolysis oils. However, when calculated back on dry basis the heating values are on par with each other at around 22.8 MJ/kg. The pH for the condensate is similar as for fast pyrolysis oil at 2.5 but the total acid number (TAN) is almost twice as high at 205 mg KOH/g. Hence, from a combustion point of view, the condensate can be regarded as a "high" moisture content pyrolysis oil. From an upgrading point of view (to chemicals or engine fuels), larger challenges can be expected mainly due to the high TAN and high oxygen content.

In Table 2 the mass and chemical energy balance for the experiment is showed together with the elemental balance. The overall mass yield have been normalized whilst the others are showed as measured and calculated, hence they do not sum to unity and the difference can be interpreted is a reflection of the experimental uncertainty. The largest uncertainty here lays with the oxygen balance at +10.8%. Three different methods have been used to determine the composition of the different fractions and there is also an inherent uncertainty whilst weighing the different samples. However, current efforts are focused towards reducing the experimental uncertainties.

Table 2. The overall mass and chemical energy balance including the balance for the major elements C, H and O. Notice that the amount of gas in the overall mass balance was calculated by difference.

Mass balance (wt-%)				
	Charcoal	Condensate	Gas	Sum
Yield	25.7	64.3	10.0[a]	100
C	42.7	42.8	6.9	92.4
H	11.2	85.3	3.1	99.6
O	5.4	90.1	15.3	110.8
Energy balance (%)				
Yield	47.0	55.4	4.4	106.8

a) gas calculted by differnce

On mass basis; 25.7% of the dry biomass is converted into charcoal with the composition showed in Table 1. However, close to 45% of the chemical energy is found in the charcoal, around 55% is found in the condensate and the remaining 4.4% in the gas. It should be emphasized that in a larger scale pyrolyser less condensate and more gas is expected since the pyrolysis vapours can be given longer residence time. Typically longer vapour residence time results in secondary reactions which again results in a small increase in charcoal production but a significant increase in gas production and a consequential decrease in condensate production. However, since the condensate may have a larger outside-gate value then the inside-gate value of the gas this needs to be taken into account when different full scale pyrolysis technologies are considered. The carbon content of the biomass feedstock is more or less equally distributed between the charcoal and the condensate with a remainder of 6.9 % found in the gas. For hydrogen and oxygen the condensate dominates; claiming 85% and 90% of the available atoms, respectively.

Upgrading of condensate

Applying the fast pyrolysis process, the bio-oil liquid product, depending on the quality, can be sold and applied as a burner fuel directly. The process is well demonstrated and several stakeholders exist globally [13]. Standards for bio-oil burner fuel exist as well, even though bio-oil is currently not a well-established market product. Standardization for other purposes is ongoing [14]. Catalytic bio-oil upgrading processes have not yet been sufficiently demonstrated, and their technology readiness level (TRL) is low. The catalysts used are mainly commercial refinery catalysts; new catalyst development is ongoing at research stage. The commercial catalysts as well as the process itself are facing several critical bottlenecks that are hindering successful demonstration and commercialization. The short catalyst lifetime and the occurring deactivating/poisoning mechanisms are the main challenges. The catalyst deactivation is caused by the coke formation on the catalyst surface, temporarily blocking the active sites, while mineral deposition can irreversibly deactivate the active sites (poisoning). Although the catalytic pyrolysis oil upgrading processes are not commercial and critical challenges remain, there are considerable efforts made towards demonstration. The efforts made in the catalytic upgrading processes are expected to increase, hence the TRL, mainly due to several reasons: (i) current techno-economic calculations show great viability potential of liquefaction processes (pyrolysis and hydrothermal liquefaction) in production of biofuels and (ii) finding new ways to utilize existing oil refineries, infrastructure and know-how will be essential.

System perspective

There are several possible configurations for an integrated charcoal-silicon process and the one showed in Figure 2 is just given as an example, different configurations will be investigated in future case studies. However, already at this stage some aspects and consequences of an integrated process can be discussed.

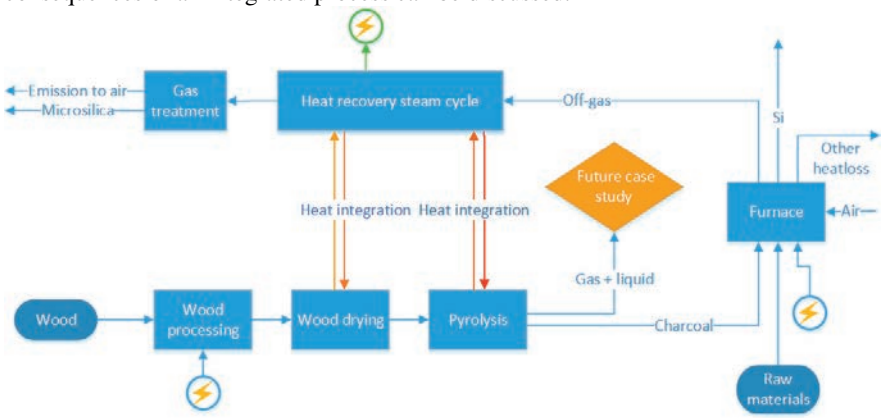

Figure 2. Simplified block flow diagram of a potential CNMP concept.

From a given biomass specification and operation parameters such as temperature and residence time, the pyrolysis unit/carbonizer will require different heat demand, which will influence output flow rates, composition/element balance, and energy content of charcoal, gases, and condensate. In addition, the integrated process is strongly governed by specified furnace operation. Upstream; the furnace load and composition of raw materials determine the necessary charcoal feed, which again affects pyrolysis load and required wood input, as well as several related processing stages; wood input, de-

barking, chipping and drying energy; the pyrolysis energy requirement, and output and distribution of by-products (condensate). Downstream, furnace operation affects the flow rate, temperature, and composition of the off-gas. The off-gas heat recovery and re–integration to wood drying and pyrolysis introduce some feedback, and thus an implicit problem formulation. The combustible gas and liquid by-products from the pyrolysis introduce possibilities for either export of condensate (as a bio-oil), or extended electrical energy recovery through gas turbine/motor combustion, additional steam cycle, or a combined cycle (CC).

This publication represents the first step towards a much larger case study were experimental results are integrated through mathematical models in a system model describing the entire silicon process. Consequently, several aspects remains to be investigated, for example; how will an integrated charcoal production affect the transfer of unwanted elements such as Na, P and B to the final silicon and micro silica products. How will process economy be influenced by fluctuations in prices for raw material and new products. The authors are well aware of these challenges but also recognize that this initial study shows some very promising results.

Conclusions

Under the pyrolysis conditions and experimental setup used in this study a significant amount (more than 50%) of the original chemical energy in the biomass feedstock can be recovered as condensate/bio-oil. At these conditions a charcoal with a fixed carbon content of roughly 80 % can be produced and 25 % on mass basis of the original dry wood log can be turned into charcoal. In the continuation of this work the economic viability of the integrated process together with other configurations will be investigated to determine an optimum integration in terms of energy and mass together with an evaluation of upgrading strategies and market and technological maturity for high value products from the bio-oil.

References

1. Antal, M.J., et al., *Review of methods for improving the yield of charcoal from biomass.* Energy & Fuels, 1990. **4**(3): p. 221-225.
2. Babu, B.V., *Biomass pyrolysis: A state-of-the-art review.* Biofuels, Bioproducts and Biorefining, 2008. **2**(5): p. 393-414.
3. Manyà, J.J., *Pyrolysis for biochar purposes: A review to establish current knowledge gaps and research needs.* Environmental Science and Technology, 2012. **46**(15): p. 7939-7954.
4. Meyer, S., B. Glaser, and P. Quicker, *Technical, economical, and climate-related aspects of biochar production technologies: A literature review.* Environmental Science and Technology, 2011. **45**(22): p. 9473-9483.
5. Mohan, D., C.U. Pittman Jr, and P.H. Steele, *Pyrolysis of wood/biomass for bio-oil: A critical review.* Energy and Fuels, 2006. **20**(3): p. 848-889.
6. Shen, D., et al., *The pyrolytic behavior of cellulose in lignocellulosic biomass: a review.* RSC Advances, 2011. **1**(9): p. 1641-1660.
7. Bridgwater, A.V., D. Meier, and D. Radlein, *An overview of fast pyrolysis of biomass.* Organic Geochemistry, 1999. **30**(12): p. 1479-1493.
8. Gaston, K.R., et al., *Biomass Pyrolysis and Gasification of Varying Particle Sizes in a Fluidized-Bed Reactor.* Energy & Fuels, 2011. **25**(8): p. 3747-3757.
9. Demirbas, A., *Effects of temperature and particle size on bio-char yield from pyrolysis of agricultural residues.* Journal of Analytical and Applied Pyrolysis, 2004. **72**(2): p. 243-248.
10. Antal Jr, M.J. and M. Grønli, *The art, science, and technology of charcoal production.* Industrial and Engineering Chemistry Research, 2003. **42**(8): p. 1619-1640.
11. ECN, *Phyllis2, database for biomass and waste*.
12. Bridgwater, A.V., *Review of fast pyrolysis of biomass and product upgrading.* Biomass and Bioenergy, 2012. **38**: p. 68-94.
13. *PyNe database*.
14. Lehto, J., et al., *Fuel oil quality and combustion of fast pyrolysis bio-oils*. 2013, VTT Technology p. 79.

Silicon for the Chemical and Solar Industry XIII
Kristiansand, Norway, June 13 - 16, 2016

Metallurgically purified silicon for photovoltaics – current development routes at Silicor Materials

M. Heuer[1)]*, M. Kaes[1)], T. Bartel[1)], A. Turenne[2)], T. Jester[2)]
1) Calisolar GmbH, Magnusstrasse 11, 12489 Berlin, Germany
2) Silicor Materials, Inc., P.O. Box 610220, San Jose, CA 95161, USA
*E-mail: Matthias.Heuer@silicormaterials.com

Introduction

The most common feedstock material for photovoltaics is polysilicon produced by Chemical Vapor Deposition (CVD) of silanes via the classical Siemens technology and similar processes. An alternative route of producing solar grade silicon is the purification of raw silicon using metallurgical processes without converting it into silanes. The general challenge of the metallurgical route to Solar Grade (SoG) silicon is to establish an impurity control along the metallurgical processes and to ensure a silicon product ready to be used in photovoltaic applications.
At Silicor Materials this is achieved using enhanced segregation during a solvent growth of silicon from a Si-Al melt solution at temperatures significantly lower than the melting point of Si [1].
The process can be described as a liquid to solid refining process comprising a number of refining steps, whereby, metallurgical grade silicon (MG-Si) with a purity level of 99.5% Si is refined up to the levels needed for solar application. The four principal refining steps are:

- Solvent Growth Refining – A molten, hypereutectic aluminum-silicon alloy is allowed to cool, leading to a growth of a network of pure silicon crystals, from which the remaining liquid eutectic can be decanted.
- Wet-Chemical Aluminum Removal – The remaining eutectic on the silicon crystals is dissolved in hydrochloric acid forming poly aluminum chloride (PAC).
- Directional Solidification – Clean silicon crystals are re-melted and directionally solidified resulting in fully refined silicon ingots.
- Final Preparation – Purified silicon ingots are cleaned, cut, chunked and blended to eliminate residual chemical variation.

In addition to the primary output of SoG-Si, the process route has two by-products of added commercial value, i.e. an Al-Si master alloy for use in the aluminum casting industry and poly aluminum chloride, used as a coagulant for waste-water treatment applications.
Silicor's purification process has the advantage that the solvent growth refining takes care of all impurities except aluminum and can be carried out at relatively low temperatures in simple equipment that is well established in the metallurgical industry.
Naturally, the final removal of aluminum is most essential and takes place in a directional solidification which is assisted by a pure liquid glass-flux on top of the melt [2]. Accordingly the research and development at Silicor Materials is focused on further improvements of the solvent growth refinement and the final removal of Al.

Current development of the Solvent Growth Refinement

At the present state a counter current system is used to achieve purification over a number of solvent growth passes like shown in Figure 1, which involve the melting and solidification of the Al-Si alloy at ever increasing purity. In effect the incoming pure aluminum acts to dilute the impurity levels and the solidification at each pass acts to segregate these impurities so that they end up in the master aluminum alloy.

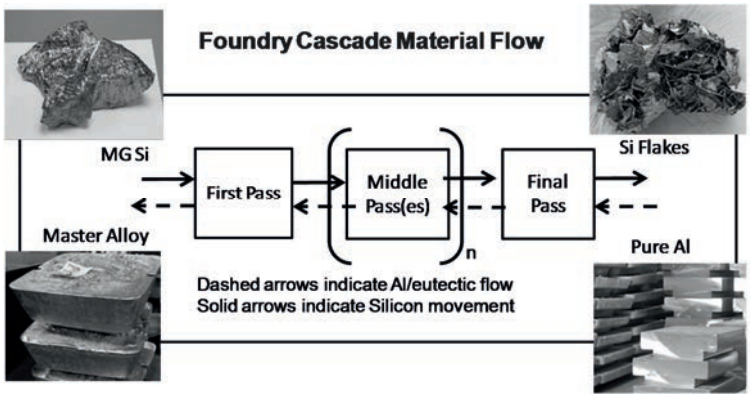

Figure 1: Material flow during the solvent refining.

In such process the clean silicon, which already has seen several passes of purification, can only get in contact with the most pure aluminum making sure there is no cross contamination between different levels of the purification steps. The number of passes can be varied according to the quality of the incoming material and the target specification of the process [3].

A further significant improvement of the process can be achieved when the spent eutectic is purified and recycled. This reduces the amount of fresh aluminum needed in the process, makes the control of impurities simpler and enhances the reduction of boron and phosphorus in the silicon. The purification of the eutectic can be carried out at low temperature in liquid state and using the same simple equipment. Therefore a current R&D focus is on purification of Si-Al melts.

Figure 2 shows some examples for the B- and P- contents of commercially available high purity aluminum and the resulting B- and P- contents of purified eutectics. Since the purification result of the eutectic is based on a chemical equilibrium and doesn't depend on the input quality, lower quality and lower-cost aluminum can be used and the impurities do not accumulate during the recycling. If purified Al-Si is used during the solvent growth step, the B- and P- removal is improved in contrast to the current state process as shown in Figure 3. To make both versions of the process comparable purification factors $X_{B \text{ or } P} = [B \text{ or } P]_{single\ sample}/[B \text{ or } P]_{median,\ MG\text{-}Si}$ are shown.

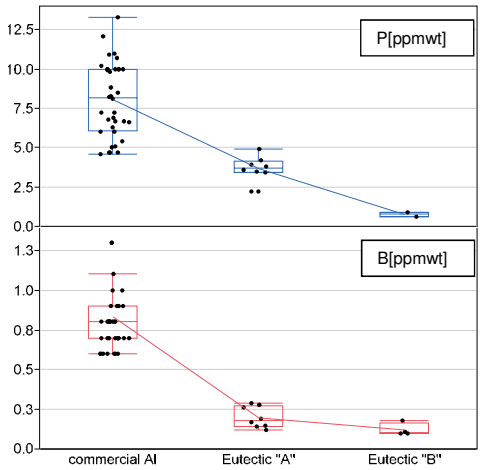

Figure 2: B- and P- contents of commercially available high purity aluminum and purified eutectics of process “A” and “B” measured by GDMS.

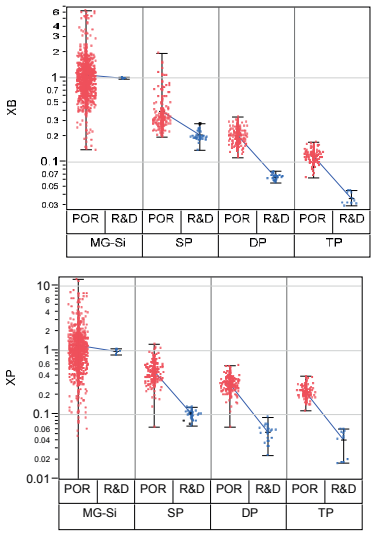

Figure 3: B- and P- removal factors with (R&D) and without purification of the eutectic (POR) from ICP-OES measurements. To compare both processes the data points were normalized by the median of the input MG-Si. Data are grouped into MG-Si (input), SP (Single Pass in Al-Si), DP (Double Pass) and TP (Triple Pass).

The data show that after three passes in a solvent growth refinement 96.6% of the Boron and 95.5% of the Phosphorus of the input MG-Si are removed. The removal of all other impurities (e.g. transition metals) during the solvent growth happens simultaneously and at a much higher removal rate than B and P. According to the actual specification Silicor guarantees B≤0.3ppmwt and P≤0.74ppmwt. With the purification and recycling of eutectics a significant reduction of these values is expected.

Developments on Al removal and final material quality

As already mentioned before, the solvent growth refining removes all impurities except aluminum and the final removal of aluminum is most essential and takes place in a directional solidification. This process step was engineered to be carried out with large quantities in simple molds and is assisted by pure liquid glass-flux on top of the silicon melt [2]. In Figure 4 SIMS measurements of the final Al content in finished good is compared for directional solidification with and without the use of a glass-flux. Using the flux allows a control of the Al at levels equal and below 0.2ppmwt which is a concentration that doesn't degrade the performance of a solar cell made from the material [4].

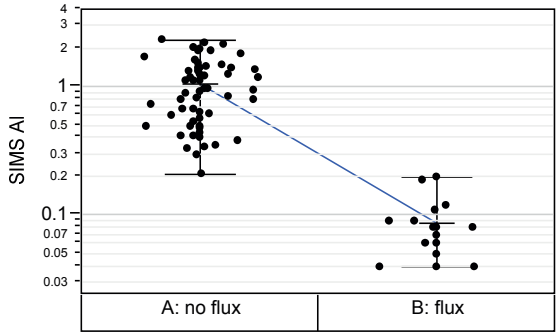

Figure 4: SIMS measurements of the final Al content in finished good is compared for directional solidification with and without the use of a glass-flux.

Table 1 presents some ICPMS measurements on transition metals in finished good solar grade silicon from Silicor's purification process.

Table 1: ICP-MS measurements of transition metals

Element	Concen-tration [ppba]	N Purity
Ti	3.091	>8N
Cr	0.025	>10N
Fe	1.664	>8N
Ni	1.133	>8N

Cu	0.155	>9N
Zn	2.034	>8N
Mo	0.053	>10N
Mn	0.047	>10N
Co	0.027	>10N
Zr	0.002	>11N
Nb	0.003	>11N
Ta	0.072	>10N
W	0.003	>10N
V	0.002	>11N
sum	8.3	SEMI PV17 Class I

The data presented in table 1 are close to the detection limit of the lab and confirm that the material in regards of transition metals fulfills the SEMI PV17 criteria for class one solar grade silicon.
This is also in good accordance with the cell efficiencies obtained at various customers which are presented in Figure 5.

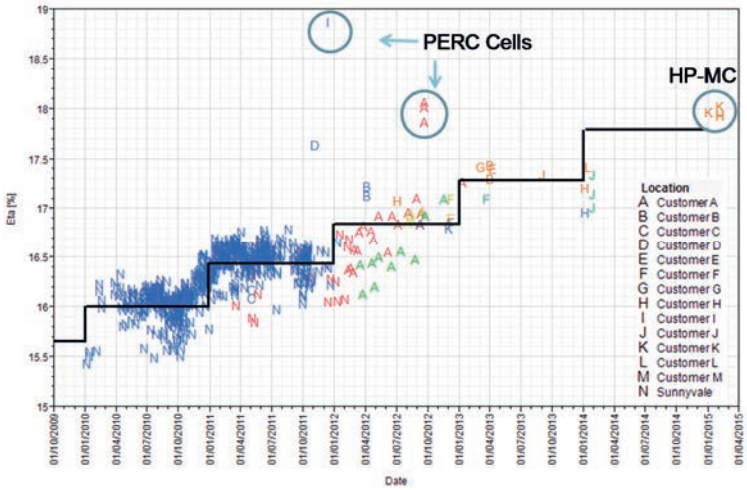

Figure 5: Cell efficiencies obtained with solar-silicon purified by Silicor's technology.

Data points represent average efficiency of single solar ingots. A maximum Eta of 18.9% has been reached on PERC cells with 100% Silicor solar Si and standard BSF-cells after HP-mc-crystallization reach the baseline of the customer. This suggests that the silicon purified using Silicor's process is not a limiting factor for solar cell efficiency.

References

1. Morita, K., Yoshikawa, T., (2011), Thermodynamic evaluation of new metallurgical refining processes for SOG-silicon production, Trans. Nonferrous Met. Soc. China, 21, 685−690.
2. Turenne et al. “Cover flux and method for silicon purification”, Patent application WO 2014118630 A1, 2013.
3. Turenne et al. “Method of purifying silicon utilizing cascading process”, US Patent 8,580,218; 2012
4. Bartel, T., Lauer, K., Heuer, M., Kaes, M., Walerysiak, M., Gibaja, F., Lich, J., Bauer, J., Kirscht, F., The Effect of Al and Fe Doping on Solar Cells Made from Compensated Silicon, (2012), Energy Procedia Vol. 27 pp. 45-52, Doi 10.1016/j.egypro.2012.07.027.

New and future applications of different metallurgical silicon qualities: how could we produce them?

Míguez JM[1)], Pérez A[1)], Souto A[1)], Diéguez J[1)] and Ordás R[1)]

1) FerroGlobe, Spain

Abstract

Each year we could find new applications for silicon and most of them are related with the most dynamic sectors of the economy. Silicon is today not only a raw material but also a vector of development in the new economy (3D printing, batteries, biomedicine…). Some years ago there were only two main markets for metallurgical silicon: aluminum and silicone market. In fact, in 2002, Aluminum and Silicone market represented nearly 96% of the market. In 2015, the irruption of PV applications with 20% of the market share have changed the picture. In that period production companies adapted their structures to those relevant changes. Are we now ready for the changes the new economy are introducing in our markets? In this paper we will try to summarize some new applications we see coming in the horizon and the response we can offer from FerroGlobe to these changes in the end markets of silicon.

Introduction

During the development of the production process for Solar Grade Silicon, Silicio FerroSolar has tested several technologies. This technologies for silicon purification are suitable for the production of any special quality between 3N to 6N purities. We could choose one or some of them to fulfill the customer's requirements. We can even develop tailored solutions adjusting the levels of certain impurities by doping or obtaining certain granulometries by clean grinding and milling techniques. Some new applications for Silicon and some of our technologies are shown below.

Metallic heat transfer fluids

Silicon and some of its alloys are ideal candidates to build massive storage solutions owing to its low cost and abundance on earth. In the case of silicon, other advantages of are the high latent heat (1,8 MJ/kg) and the high melting temperature (1410ºC).

Datas et al. proposes a new TES (Thermal energy storage) concept that has the potential to achieve one of the highest energy densities among the existing energy storage solutions and uses silicon, an abundant, cheap and safe material. In this system, energy is stored as latent heat in the phase change of silicon and the energy is released in the form of electricity by means of thermophotovoltaic (TPV) cells (Fig 1). The energy not converted in electricity by the TPV cells is delivered in the form of heat (e.g. hot water).

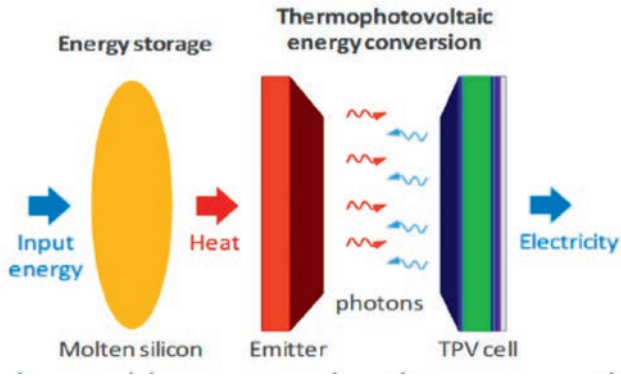

Figure 1. TES concept

In other study, Kotzé et al. identifies the AlSi12 alloy as the best PCM (Phase Change Material) for a TES system.

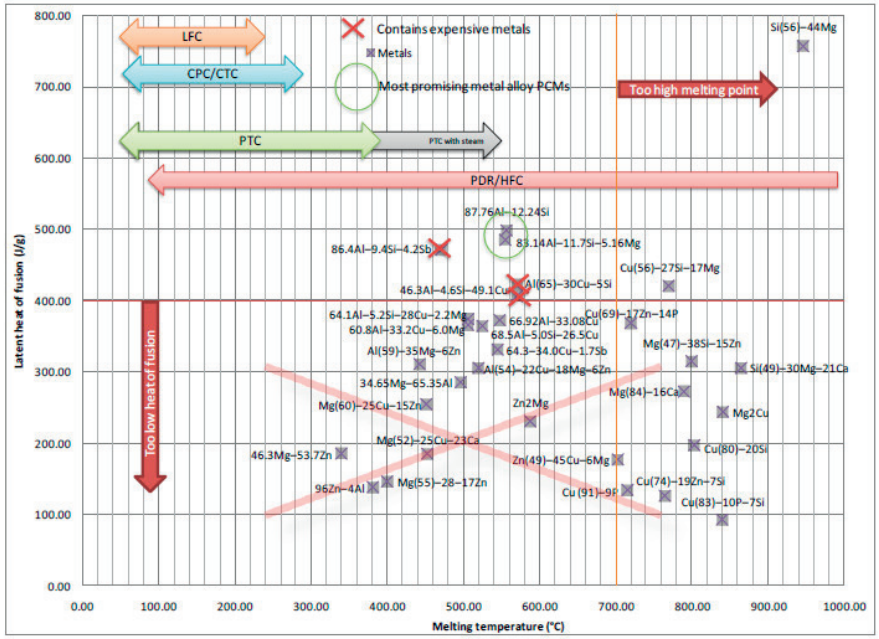

Figure 1. Metallic Phase Change materials with details in the selection thereof.

They complete a simulation of a Solar Thermal Power Generation plant with 100 MWe that should operate 24 hours. For a storage system of 15 h, it is required 23.593 t of AlSi12 and that would mean approximately 3.000 t of silicon for this plant.

New silicones

There are new silicone applications that could represent a frog-leap in the consumption of metallurgical silicon. The one we expect that will be the most important is its use for 3D printing to manufacture prototypes, spare parts and much more. 3D Printing is based on materials such as thermoplastics (which are melted before applying), metals and ceramics. In 2015, the German company Wacker revealed that the have developed a new silicone suitable to be used for 3D printing machines. This is a first step because for the moment the main application will be prototyping although there are plenty of opportunities, as long as the technique is developed, there will be more applications in the Health sector and Medicine, Automotive and Transport and Other Industries.

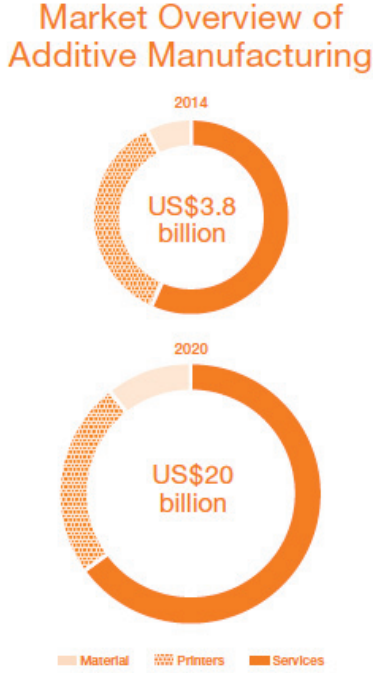

Figure 1. Market evolution of 3D printing sector (source: Wacker Chemie AG Q2 2015 report)

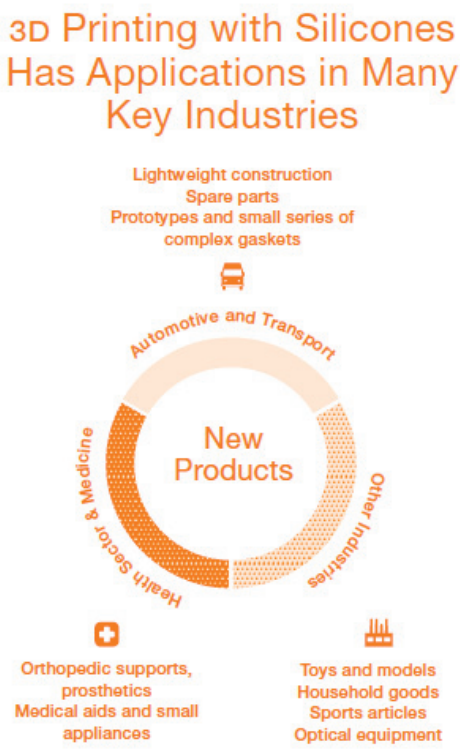

Figure 1. New applications for 3D printing with silicones (source: Wacker Chemie AG Q2 2015 report)

In general, the silicone market is diversified across industries and applications such as Performance Additives and Functional Ingredients, Construction, Consumer Care, Coatings and so on. This is a growing market because it has a CARG 2005-2015 of 5% and it represents a 11,5 billion euro industry. The 3D printing industry is growing at a much faster pace of 30% annually so that in 2023 this sector could be one of the most important within the silicone market.

Batteries

One of the major focuses of Li-ion batteries over the last two decades has been in the development and discovery of novel anode architectures with enhanced properties such as increased capacity, cycle life and rate performance, together with consideration of production cost and environmental impact. Silicon has been considered the best choice for a number of important theoretical considerations.

Firstly, silicon forms a stable alloy with lithium of up to 4.4 Li^+ per formula unit Si, leading to a vast theoretical capacity of $4212mA \cdot h \cdot g^{-1}$, which is considerably higher than that of graphite ($372mA \cdot h \cdot g^{-1}$). Secondly, Si anodes display long voltage plateaus at approximately 370 mV vs Li/Li^+, thereby providing stable operating voltages when coupled with positive electrodes such as $LiCoO_2$. Lastly, Si is the second most abundant element in the Earth's crust and is thus considered a candidate for reasons of viable production cost and availability. However, silicon has a drawback that it is fact that Si suffers from a large volume change (±400%) during (de)alloying process, the strain of which potentially leads to pulverization of the local structure.

In order to avoid the latter problem, one approach mixes small quantities of silicon particles in a flexible polymer binder, adding carbon to the mix to conduct electricity. Tesla, for example, is increasing the capacity of his car batteries by adding little by little increasing amounts of silicon in the anode. They have set the goal of increasing the capacity of its batteries by 5% per year (although not all this increases will solely due to adding more silicon).

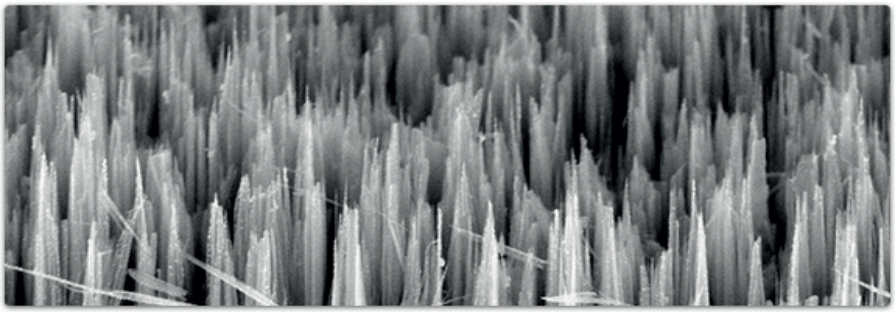

Figure 1. Pillared silicon particle produce by assisted etching

A novel approach by Nexeon has been to form nanoscale Si pillar arrays on micron scale (2-25 microns) by metal assisted etching (Fig. 1), the resulting structure is treated with binder and additives to form a composite electrode.

Independently of the approach, it is required micronized silicon with a purity between 99,99% to 99,999%.

SiOx nanoparticles (spherical silica)

One of the manufacturing methods for obtaining spherical silica is using metallurgical silicon, grinding it to very small particles and then oxidizing these particles to obtain superfine spherical SiOx particules. There are many applications for this product:

- Additive to increase fluidity and reduce flash in various resins (epoxy resins, etc), such as semiconductor sealants.
- Toner external additive materials.
- Silicone filler.
- Sintering material and sintering agent.
- Filler for liquid type sealants.
- Abrasive powder.

Optical applications

Meseguer et al. introduced the Silicon Colloids which are almost spherical silicon micro and nanoparticles with a very smooth surface, able to scatter and also trap light very efficiently in a large-span frequency range, covering from the visible to the far infrared regions.

This material has potential application in the fields of biomedicine, cosmetics, infrared protective paints for cars and buildings, thermal and UV resistant plastics, thermal insulation clothes and thermal insulating creams for winter sports.

Ceramics

Silicon Nitride

Silicon nitride offers solutions to problems faced in industries that require high-temperature, high-strength materials and very small allowable tolerances. Direct nitridation is the most well understood Si3N4 synthesis process. The reaction is as follows:

$$3Si + 2N \rightarrow Si_3N_4 + Heat \text{ (at } \sim 1400^\circ C)$$

Direct nitridation results in a theoretical weight gain of 66.67% of the weight of silicon metal; however, empirical evidence shows the weight gain of a fully nitrided part to be approximately 60% due to volatilization of silicon during the process. The kinetics of the direct nitridation reaction can be improved through the use of catalysts but not every producer uses catalysts to avoid contamination.

There are mainly two qualities, Industrial quality (3-4N material) and PV quality. The former is used as additive for the manufacture of special ceramics as reaction bonded silicon nitride or SiAlON. Silicon nitride with PV Quality is used as coating on the quartz crucibles for multicrystalline silicon technology. The needed quality for this silicon is quite high because the silicon nitride will be in direct contact with liquid silicon.

Figure 1. Silicon Nitride Powder for ceramics applications

Silicon Carbide composites

Carbon ceramic discs are infused with silicon to obtain silicon carbide, one of the hardest substances on earth. As a result, superior braking performance can be exhibited and an attractive mirrored finish is achieved. The advantages of this new brakes are that they are extremely durable, they have better appearance and above all they withstand higher temperatures.

Molybdenum Disilicide

This ceramic material is mainly used for heating elements in industrial or laboratory furnaces. Elements fabricated of this unique material support high power densities on their surface, can be cycled rapidly and could be used in high temperature in air. There is also a great development in the use of this material in turbine blades.

Other applications

Gillette™ has patented a new method for producing silicon blades for shaving razors using monocrystalline silicon (US20150360376A1).

Silicio FerroSolar's Technologies

Some of the technologies for silicon refining developed at Silicio FerroSolar are the following ones:

EMCC Furnace: In this furnace, silicon is charged in a cold crucible with an induction coil which melts silicon creating a silicon bath which is vigorously stirred by the electromagnetic forces. Then the silicon bath is fed continuously and the pulling begins. It is a very clean process, because there is not hot crucible and the stirring effect could help to remove inclusions, including silicon carbide inclusions.

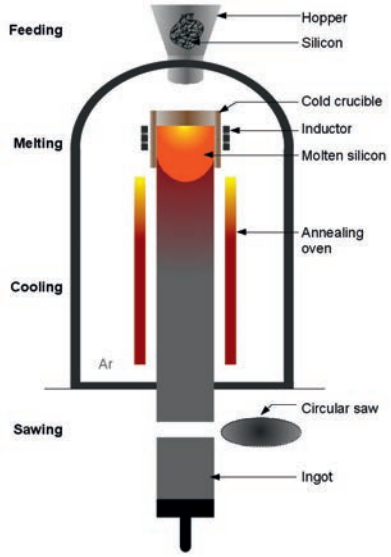

Figure 1. EMCC technnology

For this reason, is a very suitable technology for recycling top cuts from PV Industry

Segregation Furnaces: we have developed segregation furnaces that allow us to reduce the metallic impurities content and to produce 3N-6N silicon quality.

Induction Furnaces: in the Induction Furnaces we carry out slagging processes to reduce all the impurities whose oxides are more stable than silicon, namely Boron, Aluminum, Calcium, etc. This is especially useful for the Boron reduction for the production of 3N to 6N material. In these furnaces we could also remelt silicon fines, e.g. kerf from wafer slicing.

Vacuum furnaces: by refining silicon in vacuum atmosphere we are able to remove phosphorus, aluminum, calcium and oxygen. The main application of this furnace is for 6N material and when it is required silicon without oxygen.

Crushing and grinding: we work with state of the art materials to avoid the silicon pollution during crushing and grinding. We are capable to obtain also smaller particles (less than 100 microns) without contamination of silicon during processing.

CONCLUSION

During the development of the project for the production of Solar Grade Silicon, Silicio FerroSolar has tested several technologies for silicon purification that allow the company to develop new products which could enhance the growth of the new silicon markets. We could offer tailored solutions for almost any new application of silicon.

REFERENCES

1. Linde, Jorn de (ed): *CRU Silicon Metal Market Outlook*, March 2016
2. Lokke-Øwre, Erik, Gunna Halvorsen: *The future of the Silicon Industry*, Silicon for Chemical Industry VI, 2002
3. Kotzé, J. P., von Backström, T. W., & Erens, P. J.: *A combined latent thermal energy storage and steam generator concept using metallic phase change materials and metallic heat transfer fluids for concentrated solar power*. SolarPACES, 2011, Granada.
4. *Wacker Chemie Quarterly Report Q2 2015* http://www.wacker.com/cms/media/en/documents/investor-relations/quarterly_report_1502.pdf (PDF | 1.4 MB)
5. Nexeon Technology Overview Url: http://www.nexeon.co.uk/technology-2/ (last visit April 28, 2016)
6. Rodriguez, I; Fenollosa, R. and Meseguer F.: *Light control, an enormous new Market for silicon?* Silicon For Chemical and Solar Industry, XI, 2012
7. Datas, A. Martí, C. del Cañizo and A. Luque: *All-Silicon Energy Storage (ASES),* 31st European Photovoltaic Solar Energy Conference and Exhibition, pp 80-83
8. Armstrong, Mark J, O'Dwyer, Jim, Macklin, WJ, Holmes, Justin D.: *Evaluating the performance of nanostructured materials as lithium-ion battery electrodes,* Nano Research January 2014, Volume 7, Issue 1, pp 1-62
9. Ruoff, Christian: *Tesla tweaks its battery chemistry: a closer look at silicon anode development*, posted September 23, 2015 Url: https://chargedevs.com/features/tesla-tweaks-its-battery-chemistry-a-closer-look-at-silicon-anode-development/ (last visit april 28, 2016)
10. Simms, Graham John; Leussink Peter Johannus and Sonnenberg, Neville: *Methods of manufacturing silicon blades for shaving razors*, US Patent 2015/0360376, December 2015
11. Miguez, JM; Pourade, N; Boulle, Florine; Varela, Gonzalo; Ordás, Ramón: *Scrap recycling in an electromagnetic cold crucible furnace*. EU PVESEC International Congress Center Munich, Germany, 20-24 June, 2016

High purity silicon sizing by high voltage pulse power technology

Johannes Kaeppeler, Marion Morach
SELFRAG AG, Switzerland

Abstract

Size reduction of solid high purity silicon by pneumatic hammer or by jaw crusher requires manual operation steps which are costly and difficult to reproduce, it leads to unwanted losses and contamination, and particles shapes which are not suitable for an efficient and dense filling of crucibles. The presented method aims to improve the crushing process by using High Voltage Pulse Power technology. Pulses with energy of up to 750 Joule/pulse at 170-200kV are introduced into the silicon to achieve a controlled size reduction of the silicon. The energy is introduced by 2 electrodes and reaching the Si rod or pieces through de-ionized water. Beside the good control of particle shape and size, the lowest contamination levels are reached due to no physical contact of the crushing unit with the silicon. This supports a more efficient silicon sizing process and decreases the volume of potentially environmentally-hazardous chemicals required as less etching is required. The controllable and accurate size distribution reduces waste and off-spec material.

Purpose of the work

Key purpose of the work is to introduce and develop a state of the art process to the Si- industry to increase production yield, save costs and produce higher quality final products. To develop an environmental friendly process is taken into consideration with the recycling possibility of off-spec material as well as the required low energy consumption of the overall process. The technological implementation of the achieved specifications are used for the design of continuous operating plants at customer sites.

1 Background and Selfrag principle

SELFRAG plants are based on high voltage (HV) pulse power technology. Its principle is based on the introduction of energy via electrical discharges into solids immersed in water and situated between or near two electrodes. To achieve that, SELFRAG reduces the voltage pulse rise time to below 500 ns (Figure 1). At such situations water has a higher breakdown voltage than the solid (1). A discharge enters the material and interacts with the solid by polarisation and field distortion effects. If the discharge interconnects to the counter-electrode the track is filled with energy to produce shock waves with local pressures of 10^9 [Pa]. Following fragmentation occurs in a tensile dominated stress regime.

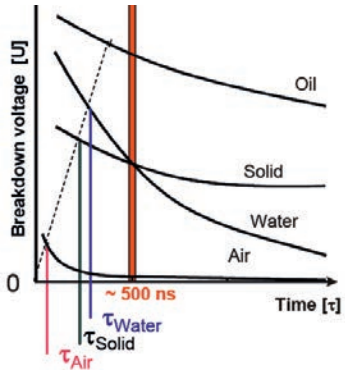

Figure 1: Physical principle of the SELFRAG process.

Selfrag principle for silicon crushing

The strength of the discharge and shock wave depends on the generator setup and can be closely controlled in exact ranges. The energy depends on the available capacitors and chosen voltage. Therefore the generator can be customized for any application. To achieve fragmentation the introduced energy per surface must be high enough to overcome elastic behaviour of the material.
For the crushing of silicon a Marx-generator with the following process setup has been chosen to perform tests on pilot plant level:

Table 1: Parameter of Marx-generator and pilot plant

Voltage (kV)	**90-200**
Pulse energy (J)	150-750
Electrode gap (mm)	10-60
Feed size (mm)	50-500
Processing mode	Batch
Max throughput (kg/h)	600

To ensure that high purity silicon has no mechanical contact with the electrodes, the two electrodes are mounted angular. The crushing process can be defined in 3 phases (Figure 2):

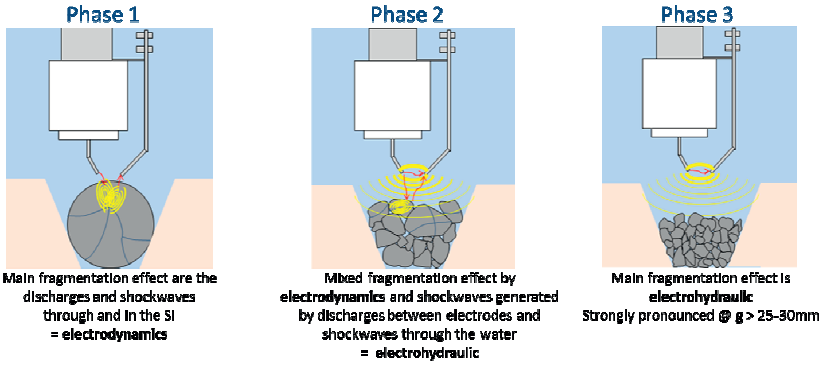

Figure 2: Principle of the Si-crushing steps

2 Main parameter definition and tests

The Selfrag plant for silicon applications (patent pending) consist of the high voltage generator with angular electrode configuration (Figure 3) and a multi- purpose process vessel of 1m length placed on a conveyor. Adjustable parameters are the electrode gap, water gap, speed of the conveyor, frequency and voltage. These parameters are mainly defining the size distribution achieved.
As key parameters the following have been defined and tested:

- Minimum voltage required to achieve reliable discharges
- Distance **g** between electrode pair and rod
- Gap e between electrodes
- Conveyor speed : v → defines throughput

Additional variation is added by the product:

- Rod size & quality
- Diameter d; D, Diameter variation on length D-d
- Surface quality of the rod ('popcorn') level

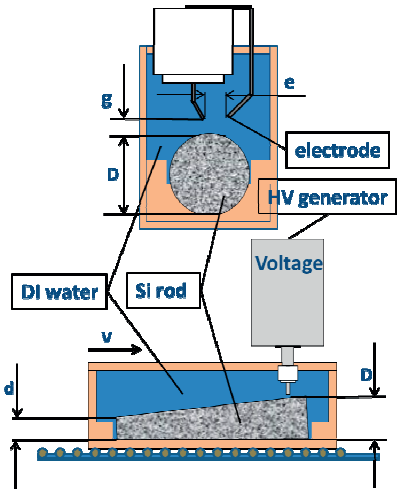

Figure 3: Parameters influencing the size reduction process

Parameter Tests

The previously described parameters had been tested to clarify the influence on the overall process. A process yield of 2-30mm has been defined to produce chip size material. To achieve stable discharges for all tests the min. voltage of 170kV has been chosen.

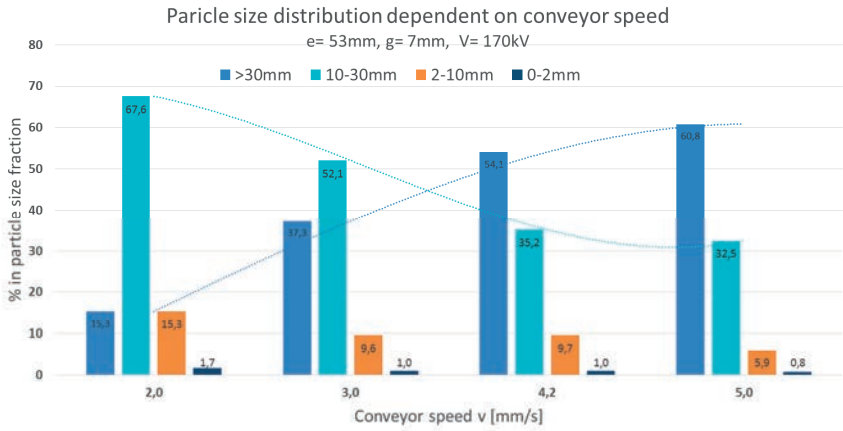

Figure 4: Parameter 1 - Conveyor speed influence on the throughput

Increased conveyor speed leads to bigger particles sizes and increased throughput.

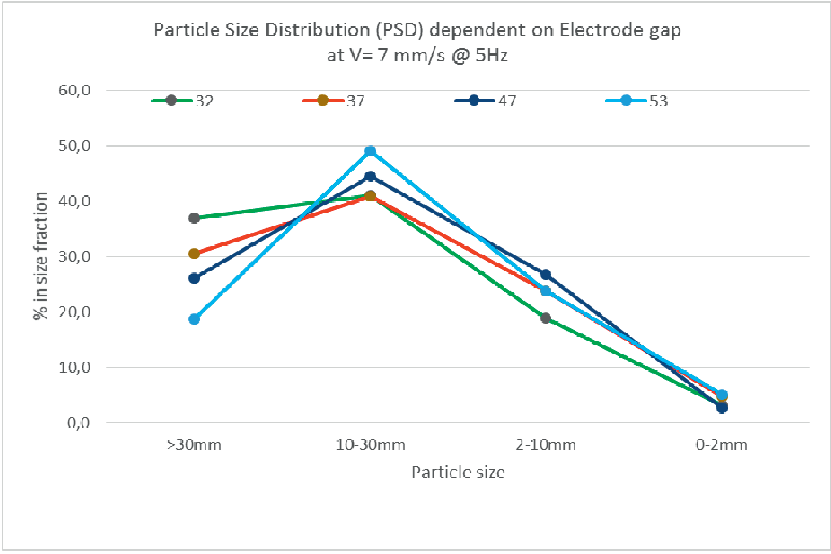

Figure 5: Parameter 2 - electrode gap

2-30mm was the target particle size fraction.

A larger electrode gap, means the distance between the two electrodes, shows increasing yield. The maximum electrode gap to reach stable discharges is defined by the Marx-Generator setup. Larger electrode gap will decrease the discharge probability.

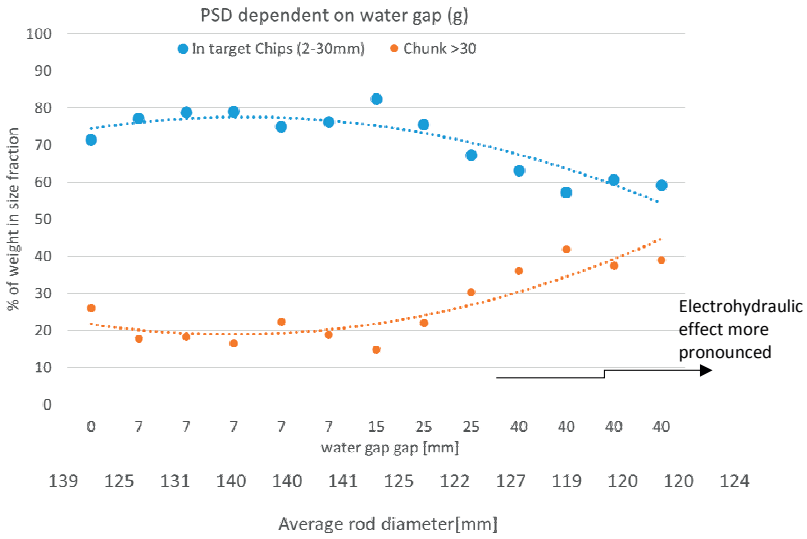

Figure 6: Parameter 3 - water gap influence on yield

The water gap is defined by the distance of the electrodes to the rod.

The process shows relatively low sensitivity to a water gap of up to 25mm, with increasing water gap the electrohydraulic effect is more pronounced. This leads to coarser products and less fragmentation effect.

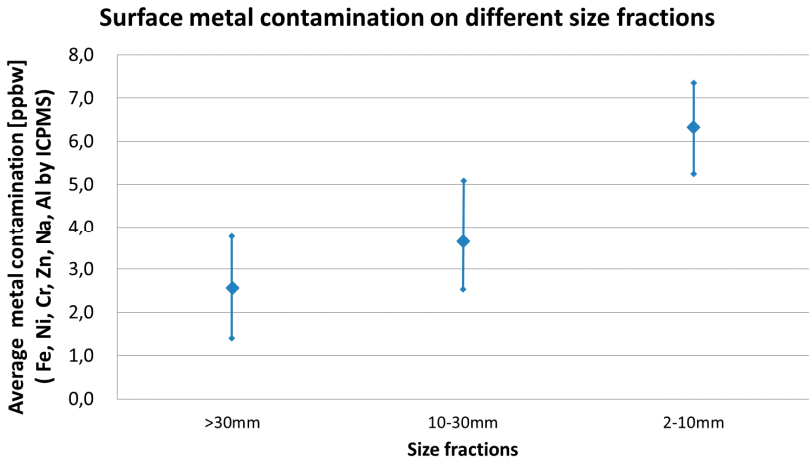

Figure 7: Parameter 4 - metal contamination level after process

The surface metal impurities for the different size classes after the process had been measured. Impurities were tested for Fe, Ni, Cr, Zn, Na, Al, by ICP-MS, total over 170 single samples.

Due to no direct contact of the Si with the electrodes lowest surface contamination could be measured on average below 9ppb/w over all measured size classes. Coarser products show due to the better surface/weight ratio lower impurities. A chemical treatment step (etching) is not required for solar grade materials.

3 Industry implementation and key factors

For the Si-producers key factors can be defined which justify an implementation of the described process into manufacturing lines.

1. Product yield
2. Product shape
3. Low metal impurities
4. Total cost of ownership

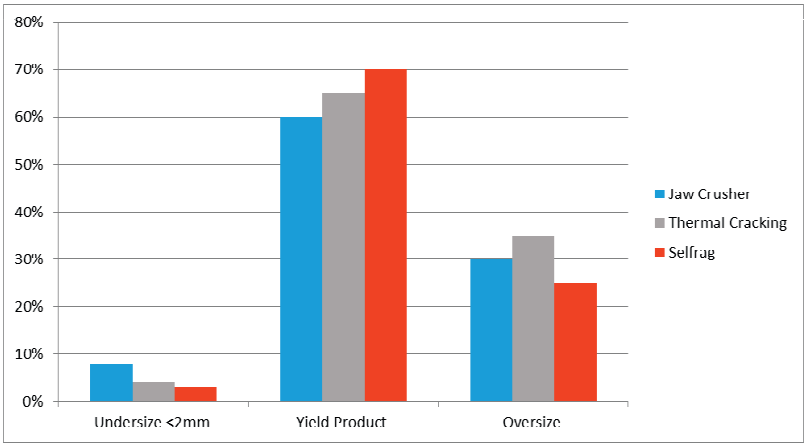

Figure 8: Product yield - Comparison of different crushing methods

For a yield product of 2-30mm size different Si- rods with average weight of 15kg and 450mm length had been crushed and compared with results of competing methods.

The size distribution with the HV-process is more accurate and up to 5% more yield product can be achieved while the under-and oversized material can be reduced. Furthermore the HV-process can treat full rods and would not require a pre-crushing step as the other two methods do- this may avoid additionally material losses.

Product shape
To achieve highest filling grades of the crucibles, facilitate packaging and transportation, a roundish and flowable product could improve these processes.

Figure 9: L: HV-crushed product R: Jaw crusher product

Metal impurities
To avoid metal impurities is a key goal of any Si-handling or crushing process. Results have been shown in chapter 2.
A process which reduces handling steps and is fully automated can provide more security on the appearing impurities.
An important factor which is not fully considered by the industry yet is the surface/volume ratio, to minimize the natural oxygen layer whereas with the roundish particles of the HV-process less surface is generated compared to standard crushing methods.

Total cost of ownership

Less automation leads consequently to higher labor cost. With increasing labor cost worldwide, even in former low cost countries and constantly low Si-market prices, a production cost reduction could improve the revenues of the producers. Furthermore a smaller product size is difficult to achieve with mechanical methods.

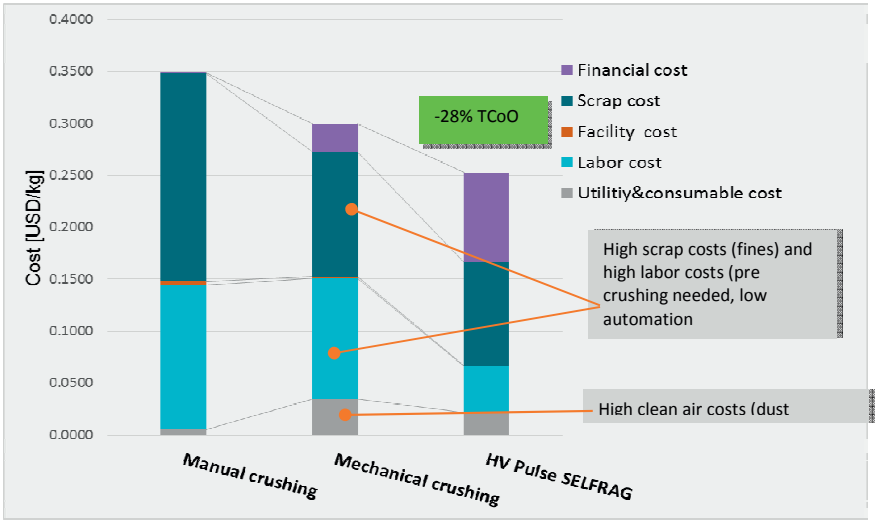

Assumptions:

Labor costs:	5 USD/hour	Yield loss manual crushing:	2 %
Silicon costs (added value):	10 USD/kg	Yield loss mechanical crushing:	1.2 %
Electric power costs:	0.06 USD/kWh	Yield loss HV pulse SELFRAG:	1 %
Throughput per worker @manual crushing:	88.8 tons/year	Production yield	2-30mm

Figure 10: Cost comparison of 3 different processes: Mechanical crushing (jaw crusher), manual crushing (pneumatic hammer) and HV-crushing:

In comparison minus 28% in the total cost of ownership per kg can be calculated.

Conclusion

By minimising mechanical contact for breaking the silicon with up to 200 000 Volt, the high voltage fragmentation provides less contamination for higher and more consistent quality silicon. The lower risk of contamination means that less or no etching of the silicon is required to remove any compromised surface material. This helps to speed up the silicon sizing process but also decreases the volume of potentially environmentally-hazardous chemicals required. The controllable and accurate size distribution reduces waste and off-spec material.

The implementation of the HV-crushing process to the industry has already started with installations at key market players during 2015. Under current development is the recycling process of off-spec monocrystalline silicon material.

Literature

1. Bluhm, H., Frey, W., Giese, H., Hoppé, P., Schultheiß, C. and Sträßner, R. 2000. Application of Pulses HV Discharges to Material Fragmentation and Recycling. IEEE Transactions on Dielectrics and Electrical Insulation 7 (5), 625 –636

Five furnaces five different stories

M. Ksiazek[1], M. Tangstad[2], E. Ringdalen[1]
1) SINTEF Material and Chemistry, Norway
2) *NTNU, Department of Material Science and Engineering, Trondheim, Norway*

Abstract

Since 2008 five excavation of submerged arc furnaces (SAF) was carried out in Norwegian ferroalloy industry. The paper presents comparison of observation and data from excavations of two ferrosilicon furnaces and three silicon furnaces. In this paper similar type of zones have been given the same terminology in order to compare the different excavations, Some of the main differences between the different excavations is the extent of slag in the furnaces as well as the extend of SiC crust. The high temperature zone varies from cokebed to large cavities.

Introduction and background

In principle, the production process for high silicon ferrosilicon and silicon are very similar. Both processes involve carbothermic reduction of SiO_2 in a submerged arc furnaces. However, in the ferrosilicon process the iron ore or other source of iron is added. In the Si production, quartz and carbon materials in the form of charcoal, coal and coke are added as raw materials. Woodchips are added to increase the permeability of the charge as it descends in the furnace. The Si-production process requires temperature above 1800 °C hence electrical energy consumption in the order of 11-13 MWh per ton of produced metal [1]. The main literature today, describing the Si process is the work by Schei [l1] where the interior of the furnace is summarized in **Error! Reference source not found.**.

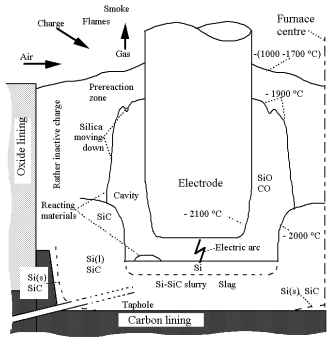

Figure 1: Zone and interior of Si furnace [1].

In the lower part of the furnace the electrical energy is provided through an arc. Here the Si producing reaction are taking place, (1) as well as the SiO(g) forming reactions (2) and (3):

$$SiO(g) + SiC = 2Si + CO(g) \quad (1)$$
$$2SiO_2 + SiC = 3SiO(g) + CO(g) \quad (2)$$
$$Si + SiO_2 = 2SiO(g) \quad (3)$$

In the cavity, there will hence be a mixture of SiO and CO gas in addition to other high temperature gas species. The cavity is formed due to the condensate (Si, SiO_2, SiC) sticking the charge together, creating a void below as the raw materials are consumed. As the SiO_2 starts to melt, in the condensate and in the raw materials, the mechanical strength of the roof top will decrease, and hence the roof top temperature is in the area of 1650-1800 ºC [2]. The arc is not necessarily a single arc. It can be multiple arcs as well. The arc will mainly go towards the Si bath or the SiC crust and as calculated, the arc could be maximum 10-15cm, based on the electrical parameters. It hence shows that **Error! Reference source not found.** is an illustration, and not showing the accurate scale.

As the gas species are ascending into the charge at lower temperatures, the major part of SiO gas will react. The gas can react on the surface of the raw materials according to reversing reaction (2) and (3), producing a condensate of SiO_2, Si and/or SiC, or with the carbon added according to reaction (4).

$$SiO(g) + 2C = SiC + CO(g) \quad (4)$$

The back reaction of (2) and (3) and reaction (4) will of course be very important regarding obtaining a high Si yield and low energy consumption. For FeSi process the reduction of iron oxides to metallic iron takes place in the upper zone of furnace.
By the term "metallurgical excavation" it is hence defined as: using personal only dealing with the metallurgy in the furnace, taking and analysing samples and reporting their findings. Generally, the metallurgical excavations of industrial furnaces are commonly carried out in addition to the rapid reconstruction of furnaces (Si furnace in Elkem Thamshavn, FeSi furnace in Elkem Bjølvefossen, Wecker Si-furnace no.4). This meant that the excavation and sampling was also done as fast as possible. Hence, the geometry of the zones in the furnace was based on visual estimation from the outside of the furnace and samples were picked as they were removed from the furnace. There are a number of actions that is traditionally taken during shut down in the belief that it will ease the mechanical excavation-especially when fast re-building is the priority. One is to move the electrodes in the manner of "pushing" the metal and slag out as well as freeing the electrodes. Another is to melt the charge down before shut-down, meaning stopping the charging some time before shutdown in the belief that less material will be easier to remove. As excavations of industrial and pilot scale furnaces are quite seldom and in addition have a high cost, there is not a multitude of reported information. Though there have been some reports from industrial excavations, the descriptions of zones in the furnace have not been focused to big extend. However, publication by Tranell et al. [2] reported the various zones in a FeSi furnace and the summary of this work is used in this paper. Tangstad et al. also distinguished and described several zones in Si furnace after the excavation in Elkem Thamshavn [3]. Recent three metallurgical furnace excavations give the possibility to compare obtained data with the data published previously. The geometry of the zones in a Si furnace is dependent on the operation history, and hence it can be a number of different geometries, sizes and composition of the various parts of the furnace.

The Furnaces, furnaces operation and shot-downs.

Finnfjord furnace no. 1 produced FeSi75 alloy was operated at 17.5 MW. The furnace is about 5 m in inner diameter and 2.5m high and it was stopped with normal operation with the electrodes down in operating position due to scheduled maintenance. After the furnace was stopped the charge materials at the top were stoked to get even surface. The surface in the

center of the furnace caved down approximately 0.5m during the cooling process. Excavation took place, 5 months after shut down.

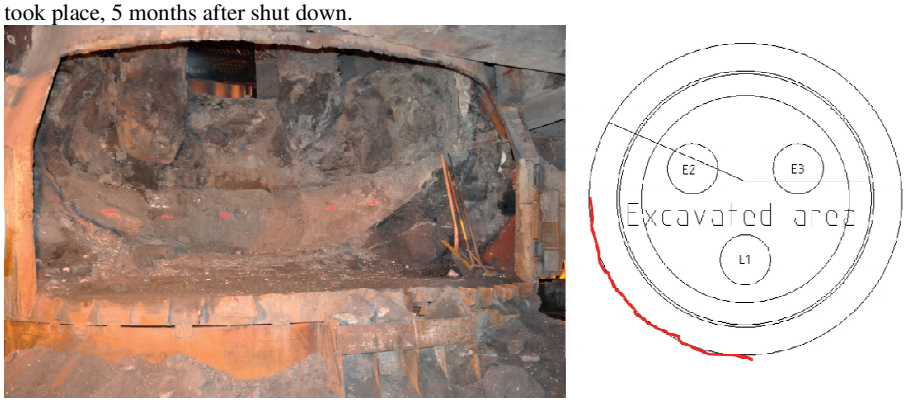

Figure 2: Pictures of furnace 75 FeSi in Finnfjord with marked excavation front.

Elkem Thamshavn. Due to the detection of temperature rise in the bottom lining, the Si producing furnace was stopped in the beginning of March 2013. The furnace was shut down without any special considerations, as it was believed that it was only a temporarily shut down. The furnace was operated at about 40 MW and the total size is 11.3 m and about 4.5 m high from the shell to the top of the charge. Electrodes were cut before the excavation began, which made it impossible to observe. The furnace was relined and then restarted as fast as possible.

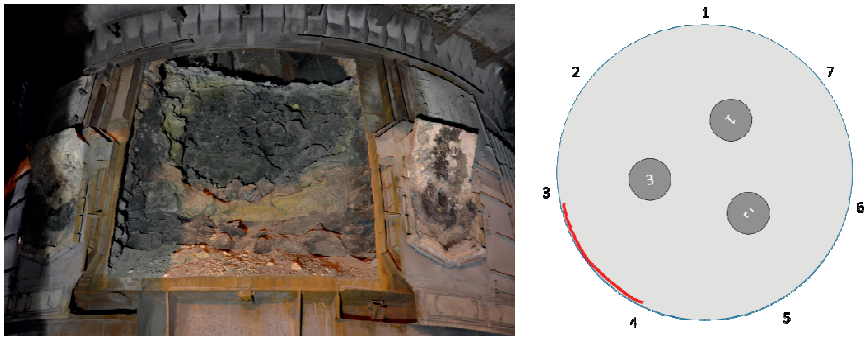

Figure 3: Pictures of furnace in Elkem Thamshavn with marked excavation front.

Elkem Bjølvefosen.The interior of the furnace 1 producing 50% FeSi. Dimension were about 6-7m in inner diameter and 2.8m high. The electrodes were moved after shutdown. This means first of all, that it was not possible to see if cavities are present or not below the electrodes. Secondly, it also means that mass from above could be found in the lower part of the furnace than originally positioned. The charge was hot-glowing (Figure 4) as the excavation started and this will of course limit the extent of the excavation, in the manner that samples cannot be exactly positioned.

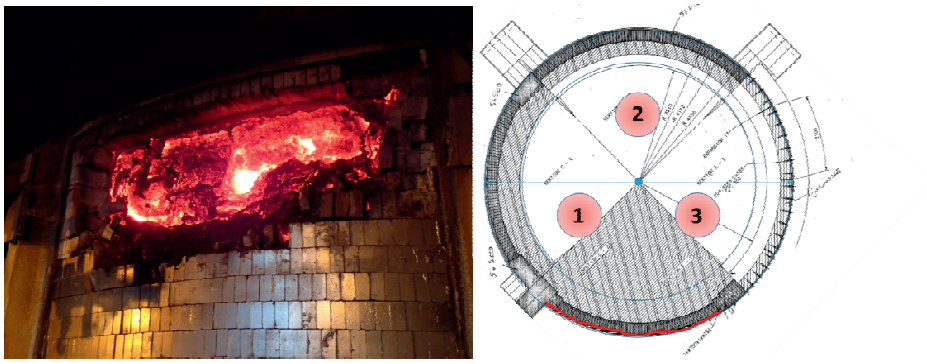

Figure 4: Pictures of 50FeSi furnace in Elkem Bjølvefosen with marked excavation front.

Wacker Chemicals. In August 2015, 33MW Si-furnace no 4 was shut down due to total renovation project. Excavation started one day after the furnace was stopped. Furnace was about 4m high and about 8.5m in inner diameter. Electrodes were cut before the excavation began. In April 2016 a 13 MW Si-furnace no. 1 was also shut down. Furnace was about 3 m high and about 5 m in inner diameter. Furnace was stopped with the electrodes down in operating position. Excavation started one week after the production was ended. Despite of small size of the furnace and relatively long period between shut down and excavation, interior of the reactor was very hot.

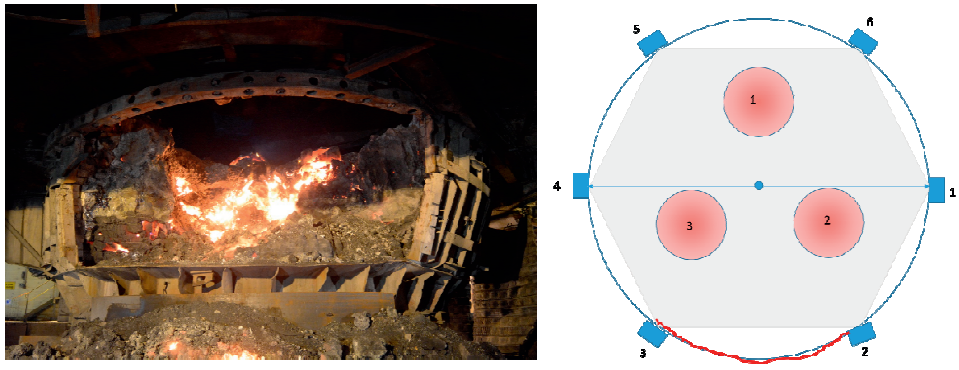

Figure 5: Pictures of furnace no.4 in Wacker with marked excavation front.

Figure 6: Pictures of furnace no.1 in Wacker with marked excavation front.

Excavations observation and discussion

From visual observation and classification of collected samples, it was possible to distinguish a few main zones in industrial furnaces. As previously reported, only considering the horizontal crossed section, zones in Si furnace can be divided to [3]:

1) Inactive zone, located around walls of the furnace, mostly consist of deposited slag and pre-melted raw materials. This zone was observed in all excavation.
2) Electrode track zone, as the furnace shell is rotating
3) Inner zone, area located in central part of the furnace towards the electrodes.

However, this description does not give completed overview about reaction zones in the furnace. Figures 6 and figure 7 present overview of reaction zones of 5 furnaces. Sketches presents whole internal part of the furnaces parts including the zones close to electrode where Si production occurs but also upper part of the furnace where condensation reactions take place.

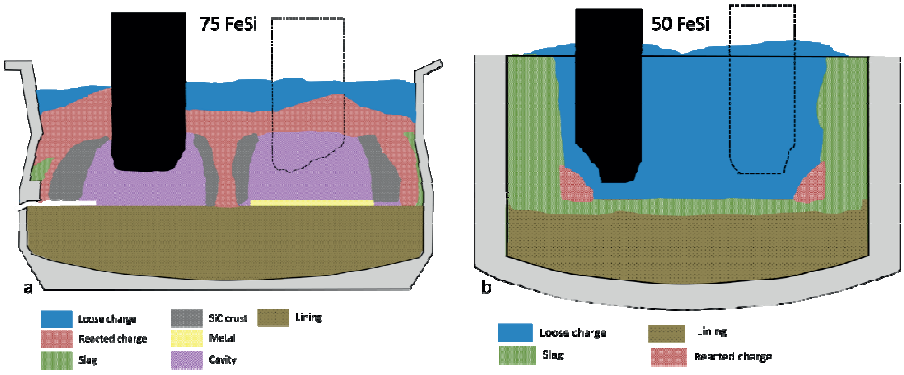

Figure 7: Overview of zones in two FeSi furnaces: a) 75 FeSi in Finfjord, b) 50 FeSi in Elkem Bjølvefosen.

As figure 7 shows that the zones found in two FeSi furnaces, differ significantly. For high Si operation (75FeSi), loose materials were found on the top of the charge. Below this layer, reacted charge was observed. The term "reacted charge" can be defined as raw materials including smelted quartz with possible condensate deposition and SiC from carbon materials. Picture of sample showing reacted charge is presented in figure 8a . Moreover, visible cavities were found around the electrodes tip surrounded by the SiC crust with gas channels. Picture of SiC crust is presented on figure 8b. Under the electrodes, a mixture of melted quartz, SiC and alloy was seen. The production of silicon in this zone is assumed to be the main reaction

due reaction between SiO and SiC. Small amount of slag was noticed on the outer part of the furnace, in the co-called inactive zone.
In 50 FeSi furnace one zone of loose charge material from the charge top and down to the electrode tip position was seen. On the outside of the electrodes, from bottom to the top of the charge was massive slag layer. In addition, a more than 1m high slag layer was present covering the entire bottom. In some areas, slag layer was deposited 0.5 higher than electrode tip. This slag layer contained Ca-Al-silicates but was also spiced with small SiC particles. All slag samples investigated contained quite some carbon from the SiC. Presence of condensates layer in the upper part of the furnace or SiC crust around electrode tip was not observed. Furnace charge was very easy to remove, it was running out of the furnace and the material looked more like a coal bed, than a cavity operation.

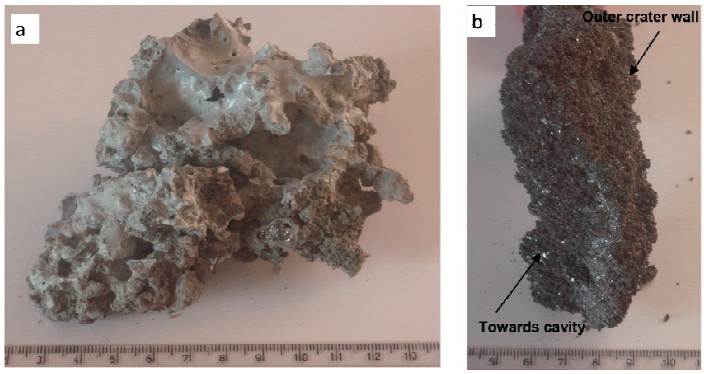

Figure 8: Materials found in 75FeSi: a) reacted charge, b) SiC crust.[2]

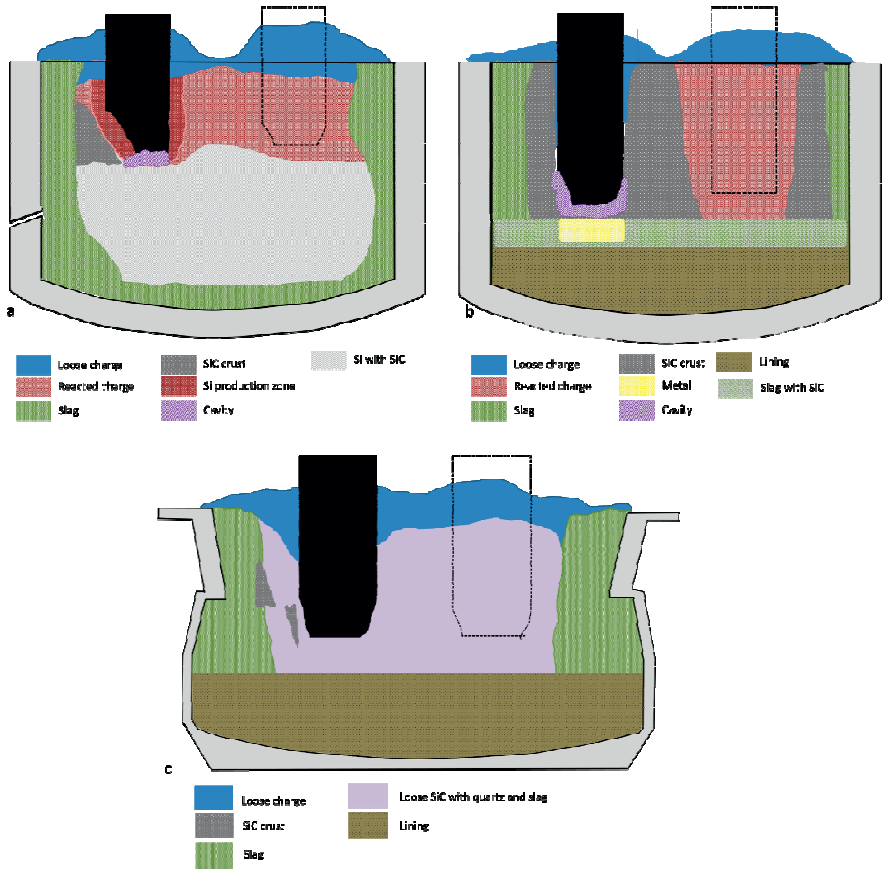

Figure 9: Overview of zones in Si furnaces: a) Wacker furnace no.1, b) Elkem Thamshavn, c) Wacker furnace no.4

An overview of the zones found in Si furnaces is shown in figure 9. On the top of the furnaces raw materials were loosely packed. Due to its loose structure this layer is always removed firs as dig out progresses That can lead to misinterpretation about findings for example of unreacted quartz particles in the bottom part of the furnace. Below the loose charge layer, reacted charge, held together with smelted quartz/condensates was observed. In Elkem Thanshavn and Wacker furnace 1, the reacted charge looks relatively similar, which can be seen in figure 10. However in furnace no. 4 in Wacker this area of furnace consist mostly of particle of SiC mixed with melted quartz and white slag. Samples collected from this area are presented in figure 11. This layer was soft and easy to dig out of the furnace. Loose SiC with quartz and slag was tightly surrounding all three electrodes without any empty space between electrodes and charge.

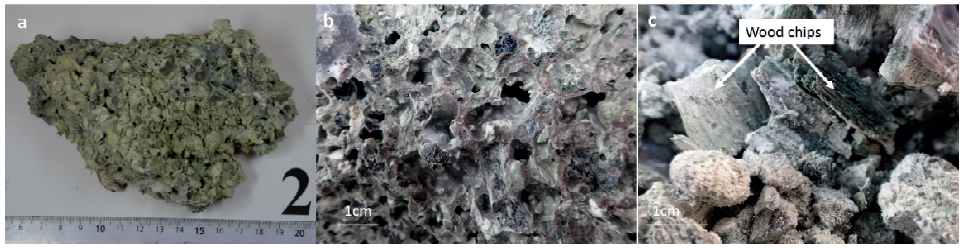

Figure 10: Reacted charge found in: a) Elkem Thamshavn, b) and c) Wacker furnace no.1.

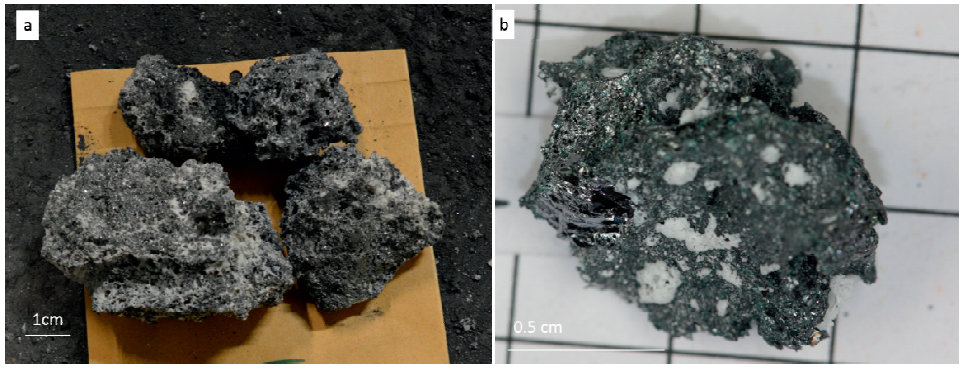

Figure 11: Loose SiC with quartz and slag found in Wacker furnace no. 4.

The main common zone for all three furnaces is about 1-1.5 m thick inactive zone located around the furnace wall. Slag deposited from the bottom lining to the very top of the furnace. In the bottom, layer consist mostly of green slag. Upwards, mixture of slag and some quartz particle was found. Photo of slag deposition inside the furnace and its scanning electron microscope image (SEM) is presented in the figure 12.

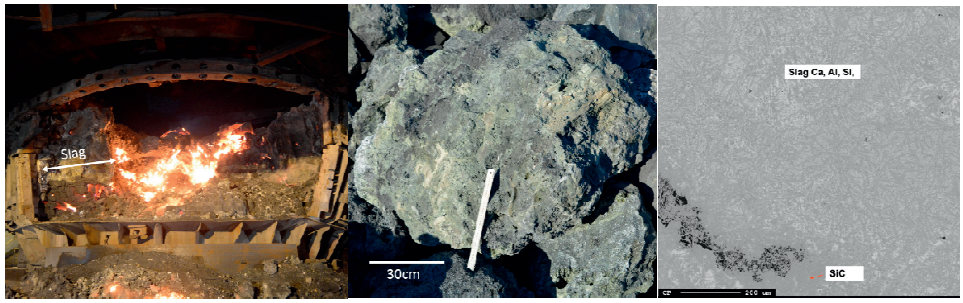

Figure 12. Slag deposition inside the furnace (Wacker no. 4) and its SEM image.

SiC crust found in Elkem Thamshavn was filling up almost half of the interior of the furnace, from the bottom up to the top. There are large gas channels in the size of 5-10 cm, as can be seen in figure13. The figure show two large pieces removed. The gas channels were also seen in the previous FeSi excavation in Finfjord. Formation of SiC crust was aslo observed during Wacker excavations. In both cases, it was found on the outside of the electrode track zone in the height close to the electrode tip.

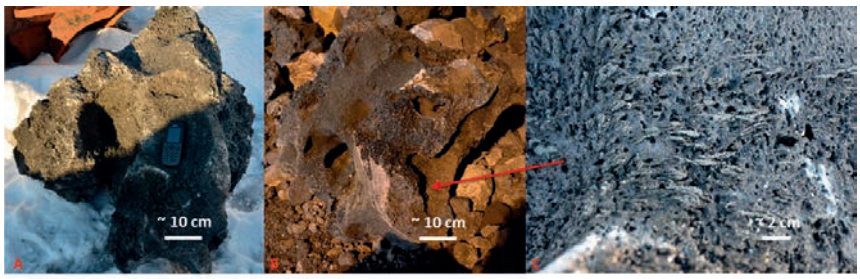

Figure 13: SiC deposit with gas channels (A, B), SiC crystals on the channel wall (C). [3]

During the excavation of furnace no. 1 at Wacker it was possible to have close look and pick up the sample directly from area around the electrode tip. Electrodes were still in their working positions; they were not cut off before start of excavation, as it was in case of other Si furnaces. Around the electrode tip there was area filled with the mixture of SiC, Si and melted quartz. It is believed that the production of silicon in this zone is to be preliminary, thus it was marked on the figure 9a as Si production zone. Additionally on the figure 9a, below electrode the cavity was marked. It is believed that it was filled with melted materials from Si production zone, as furnace was stopped. It is expected that in this area the electric arc will go towards Si bath or the SiC crust. Similar cavity was observed during the excavation in Elkem Thamshavn, however there was only SiC crust surrounding the electrode tip. Below the electrode small region with metal bath was identified, however the major zone in the bottom was mixture of green slag and SiC.
Some very small areas of metal bath was observed in Wacker furnace no. 1 below electrodes. However, the main phase was mixture of SiC and Si, which was about 2m thick. In case of furnace no. 4 the liquid metal leaked out during the dig out, thus was very difficult to estimate area where it was cumulated.

Conclusion

- Five industrial scale furnaces (two FeSi and three Si) were excavated for the purpose of finding reaction zones.
- Excavation of two FeSi furnaces indicate that during 50FeSi production process heat to the system is delivered via coke bed. While 75FeSi production process seems to be cavity operation as Si production process.
- Inactive zone, consisting mostly of thick slag layer seems to be significant zone in the furnace. Thus, it limits the space for "active" zones, for example hinder the flow of the charge material but also can cause the problems with the tapping a furnace.
- Distribution of the zones, and appearance of different zones it self can firstly be determined by furnace operation strategy, not by used raw materials. Wacker furnaces used similar raw materials-however, zones and they distributions in those furnaces differ significantly.

Acknowledgement

The authors wish to thank the staff in Finfjord, Elkem Bjølvefosen, Elkem Thamshavn and Wacker Holla for great support and hospitality during the excavation.

Additionally special thanks to Liv Rasmussen (Elkem) and Siri Marie Bø (NTNU) for help during the excavation. Financial support from SFI for excavation projects is gratefully acknowledged.

References

1. A. Schei, J. Kr. Tuset, and H. Tveit, *Production of High Silicon Alloys*, Tapir, Trondheim, Norway, 1998, 89-91.
2. G. Tranell, M. Andersson, E. Ringdalen, O. Ostrovski, J.J. Steimo, *Reaction zones in a FeSi75 Furnace-Results from Industrial Excavation*. Infacon XII, Helsinki, Finland.
3. M. Tangstad, M. Ksiazek, and B. Faaness, *Zones and materials in the Si furnace*, Silicon for the Chemical and Solar Industry XII, Trondheim, Norway.

Silicon for the Chemical and Solar Industry XIII
Kristiansand, Norway, June 13 – 16, 2016

Recycling silicon from kerf and grinding processes - the lost PV potential of silicon wastes

Dipl. Eng. Lou Parous[1], Dr. Frank Weber[1], M.Sc. Eng. Valdiney Domingos de Oliveira[1], Dr. Wolfgang Herbst[1].
Viridis.iQ GmbH, Konstanz, Germany

1) Viridis.iQ GmbH - Von-Emmich-Str. 4, 78467 – Konstanz - Germany

Abstract

Every year the Photovoltaic sector expands as the cost benefits of solar are disseminated worldwide with projections now for solar to reach the 100 GW per year installed capacity in a very short time. With each GW of silicon based solar demand, more and more metallurgical silicon is needed to support the polysilicon sector, which is now on the verge of recovery after the last crisis in that industrial segment.

For all silicon based solar technologies, the processes required to provide polysilicon for those technologies mandate the need for a ground metallurgical silicon powder as a feedstock for this industrial segment. The silicones industry also requires the same ground silicon, but the process of grinding silicon generates an off size material that cannot be used by either industry. In fact, every year more than 100 000 tons of silicon off spec waste is generated from this process that fall out of the value chain for which they were originally produced.

Additionally, further down the process of making solar devices, the manufacturing of solar wafers generates an additional more than 100 000 tons of silicon contaminated with SiC from the FAS[1] and LAS[2] process steps that is not used to make solar energy. The potential solar power from these wastes is forever lost and represents over 45 GW annually given today's PV market.

The authors are developing and planning a waste silicon recycling factory to convert this waste from kerf and grinding processes back into the value chain as a feedstock for polysilicon production, thereby reducing the lost potential of this waste and providing a low cost feedstock for polysilicon producers. The authors are currently developing a factory project to capture the lost opportunity of waste silicon by combining proven technology advancements in solid-liquid separation techniques with modern gas atomization of silicon fines, resulting in chemically superior silicon with low impurities and homogenous physical characteristics for polysilicon production and Methylchorosilane production.

[1] Fixed abrasive slurry

[2] Loose abrasive slurry

Solar's new future

It is clear that the world's photovoltaic sails have been filled with a new wind of opportunity as the technology moves into the mainstream with a more healthy and sustainable y-o-y growth. Additionally, the emergence of new markets like India with aggressive installation and manufacturing aspirations makes the future of solar energy quite bright indeed.

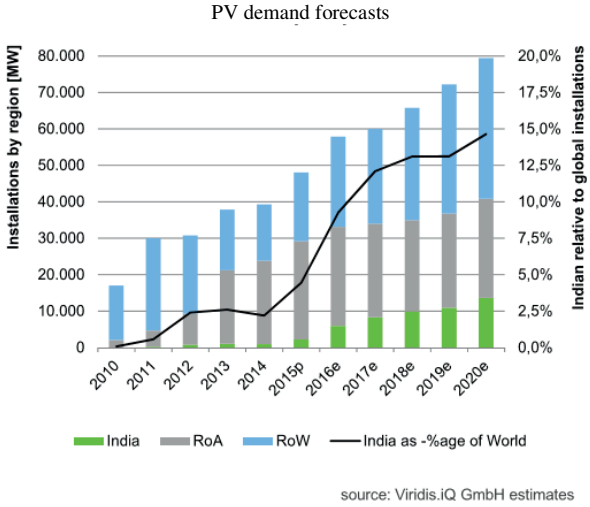

Figure 1 PV market growth forecasts

The prospect of an 80 GW solar market in 2020 from only 18 GW in 2010 is a testament to the mainstream spread of Photovoltaics and has led to an enormous supply chain infrastructure build up as suppliers and equipment providers expanded their businesses to support the growth. When the solar market was in its infancy the volumes of materials, and consequently wastes from the processes for those materials, was very low. As the market has continued to grow the industry has had to deal not only the increasing material streams that are needed to sustain the growth, but also the wastes.

Aside from the overall demand growth of the solar segment, the changes in the actual production costs have been equally as dramatic. Polysilicon production costs have seen huge reductions due in part to economies of scale that have pushed producer costs to the mid $10's per kg levels with further reductions in sight.

Unseen wastes

The name "waste" implies a material that has no value, however in most modern industrial factories, almost all "wastes" have some value, even if that value is negative

in the sense that the wastes must be disposed off. In the current work, the term "waste" means off grade material that is not or cannot be used for its intended purposes. In the metallurgical silicon world, this "waste" is off grade silicon dust that is generated from the grinding processes that cannot be sold or used as a feedstock in the polysilicon or chemical markets. In the world of solar wafer manufacturing, this "waste" is kerf loss from the wafering process that also cannot be reused in the Photovoltaic value chain.

The amount of waste built into the Photovoltaic value chain is growing with each GW of installed solar capacity yet an outsider looking in will find these wastes somewhat obscure. As the solar industry transitions from subsidized to free market dynamics the growth of these wastes are seen equally as persistent.

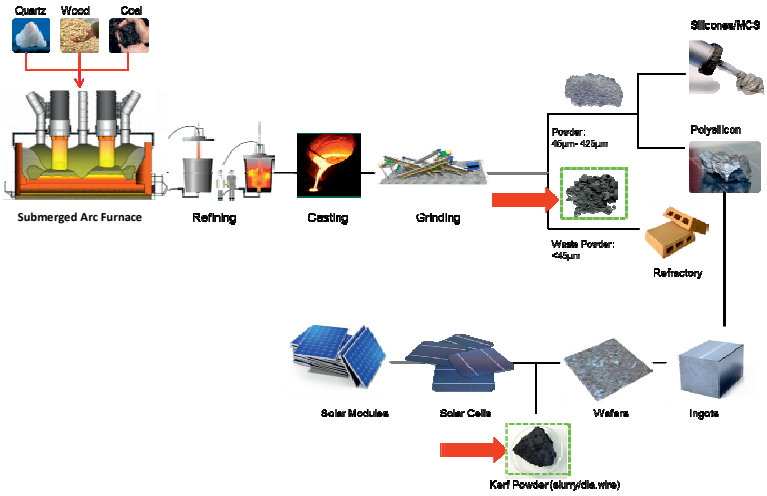

Figure 2 MG silicon and PV value chain

It is clear that there are wastes in every industrial process and almost all industries attempt to reduce or mitigate these wastes and convert them into valuable products. In the case of energy intensive industries, the recycling of waste, for which energy was expended to produce, become valuable low hanging fruits to reduce costs and disburse fixed costs. In the case of silicon wastes there are two main sources of wastes in the PV value chain. These are

(i) Silicon grinding fines
Grinding wastes occur as the off size produced during the grinding operations of metallurgical silicon to produce on spec silicon powder feedstock for the Trichlorosilane and Methylchorosilane processes. These wastes are generated from the milling and grinding process steps and vary in quantity as a function of the technology used, equipment age and wear, process parameters and size and characteristics of the material processed. The material is generally lower

than 45 microns in size and cannot easily be used in the processes for which the ground material is intended. Generally, the wastes vary from 5% - 10% of the volume of material processed. In 2015, the volume of this wastes is estimated to be 70 000 to 140 000 tons per year[3]. Fine grain silicon wastes are replete with practical challenges relating not only to handling but also to contamination and environmental impact. In standard casting of silicon metal, slow cooling of the moulds create areas of macro and micro grain structures, the latter containing high levels of metallic impurities which are prone to fracture easiest during standard milling/grinding of silicon to small PSDs (Particle Size Distribution). Standard customer specifications of silicon metal for the polysilicon industry generally (with exceptions) require a lower limit of approx. 45µm in diameter, below which the material is not conducive to efficient fluidization in the TCS reactor. Some debate exists as to whether the solution to improving the utilization of this material is equipment related, i.e. re-designs of the specific reactors, or improved techniques in sizing of silicon. In this case, the authors are convinced the solution is the latter due to lower processing costs of resizing this material via atomization versus high capital costs of equipment reconstruction or upgrades.

(ii) Kerf from LAS and FAS wafering processes
Silicon ingots made from high purity polysilicon are sliced into wafers and generate a loss of silicon ("kerf") equal to the thickness of the wire used in the cutting process. This silicon, which is of equally high purity as polysilicon, is mixed with the cutting fluid and remnants of the wire used, which usually is coated with silicon carbide (LAS based) or Nickel (FAS based). The material is very fine in nature and can reach sizes of less than 5 microns. The waste from this process varies according to the thickness of the wire and other factors but generally is estimated to be 40%-45% of the original polysilicon processed. In 2015, the wastes from this source are estimated to be 150,000 tons.

In total, the waste generation of silicon from the PV and Chemical sector in 2015 exceeded 200 000 tons. This amount of wastes will only increase as the PV sector grows.

Wasted energy

A real accounting of the cost of the wastes in question in terms of energy expended is astounding, but this can be ignored because the energy spent to produce the primary metallurgical silicon and polysilicon will be consumed with or without the wastes. A more relevant perspective is the amount of potential energy lost from these wastes because the silicon could not be transformed to a solar device that can generate electricity.

The total lost potential solar energy from the aforementioned wastes can easily be calculated by taking the total silicon and estimating the annual electricity output this silicon would have generated had it been used to make solar devices. Assuming 150

[3] Based on estimates of the total demand of metallurgical silicon required by the photovoltaic and chemical sectors

000[4] tons of grinding wastes and 150 000 tons of kerf wastes or a total of 300 000 tons of wastes silicon and a conversion of 6 grams of silicon per watt, the total lost potential solar power of this waste exceeds 45 GW per year. To put this in perspective, by the end of 2015, Germany had cumulative installed PV capacity of just under 40GW[5]. Therefore, every year more potential solar electricity is lost due to silicon wastes than the entire cumulated PV output capacity of Germany.

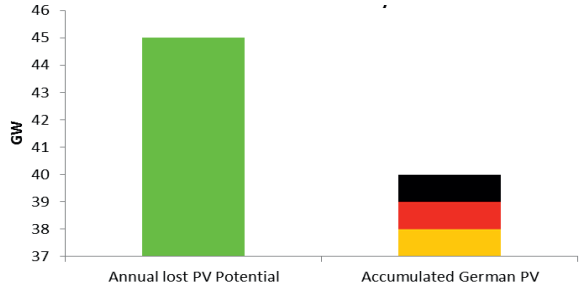

Figure 3 Annual lost potential solar electricity vs. the accumulated solar installations in Germany

Can the silicon wastes in the industry be recycled?

As previously mentioned, the wastes from the PV sector consist of two main sources: undersize wastes from metallurgical silicon grinding and silicon containing kerf wastes from wafer slicing operations. It should be noted that previous work on the subject of kerf recycling has been focused on recycling kerf wastes, due to the high purity of the silicon in this material, into a substitute for polysilicon, from which it originates.

The dream of many during the time of high polysilicon prices was to take this waste, separate it from the silicon carbide and PEG into which is was intricately mixed and reuse it in ingot furnaces to make new ingots.

Below is a cursory review of previously published projects including one current project, which follows or has followed the approach as described above, along with some comments on each:

[4] Which is then converted to polysilicon

[5] https://www.energy-charts.de/power_inst.htm

(i) Project RE-Si- CLE, “Recycling of Silicon Waste from PV Production Cycle” (EU funded, 2002 to 2004): No industrial realization, difficulties related to small SiC particles

(ii) Projekt „SICAREC“ (Deutsche Bundesstiftung Umwelt, 2009 bis 2013): „Recyclingverfahren für Siliziumwafer-Sägeabfälle mit Wiederverwertung des Siliziums in der Solarzellenfertigung“: No industrial realization.

(iii) J Air Waste Manag Assoc. 2013 May; 63(5):521-7. Tsai TH, Shih YP, Wu YF, „Recycling silicon wire-saw slurries“: The separation of Si and SiC has been found as a major challenge

(iv) Yen-Chih Lin, Teng-Yu Wang, Chung-Wen Lan, Clifford Y. Tai, „Recovery of silicon powder from kerf loss slurry by centrifugation“, Powder Technology 200 (2010) 216–223: Centrifugation results up to around 91% at a yield of 74.1% have been seen as realistic, however not sufficient for industrial implementation.

(v) Project SIKELOR „Silicon kerf loss recycling“ (EU funded, 2014 - 2016), Garbo (IT), University of Greenwich (GB), University of Padua (IT), EAAT (D), HZDR (Helmholtz- Zentrum Dresden-Rossendorf, D): currently running research project, also targeting solar grade material

In conclusion, an industrial application of these approaches has not been reached so far either a) due to the immense challenges of getting polysilicon purity levels and/or b) due to the significantly fallen polysilicon prices.

The current approach of recycling wastes by Viridis.iQ GmbH does not follow the same logic as those listed above. The idea of recycling wastes firstly has to take into account that the wastes themselves are of lower purity and likely can only be reused at places in the value chain where this purity is accepted by the process. In the current case, the recycling of grinding and kerf wastes can only realistically be reused at the beginning of the PV value chain where the strongest and most rigorous purification step is used, i.e. the conversion of solid silicon to gaseous trichlorosilane or Methylchorosilane and its subsequent distillation.

The recycling process planned by Viridis.iQ is based on a three step approach in which the various waste sources are homogenized and treated with a wet chemical, thermal and shaping step.

The wet chemical process step results in a dry powder that is then melted in a specially designed melting furnace, from which the liquid silicon is then atomized in a modified inert gas atomizer.

The input material to the process is micron size silicon waste from grinding processes and dried kerf, containing silicon and silicon carbide which has already gone through a separation process. The material is loaded into a specially designed thermal treatment furnace for melting and then tapped into ladles for pouring into the atomizer.

The resulting material is a customized silicon bead of average diameter 100 – 300 microns depending on customer requirements. The chemical purity of the material is improved due to the standard refining technique applied in the melting step with slagging and gas injection.

Depending on the mix of incoming raw materials, the resulting final product can be tailored by increasing the mix of kerf (which has low metal content) and/or modifying the refining steps. The integrated design of the factory allows for a small footprint and can be implemented into existing industrial infrastructure.

Margin Improvements

Currently polysilicon producers are pushing cost reductions through economies of scale, improved processes and upgrades or installation of new technologies. With global top Tier 1 average cash costs for polysilicon being approximately $14.5/kg[6], the overall cost structure of polysilicon becomes increasingly dependent on metallurgical silicon. Current metallurgical silicon prices are seeing a slump but generally are still on the rise as average producer costs are rising.

Notwithstanding an intermediate drop in prices as new capacity comes on stream in Iceland and other possible locations, the increase in demand for metallurgical Silicon, even if only from the solar sector, will more than compensate for these incremental capacity additions. A comparison of the evolution of the PV demand on metallurgical silicon sheds light on the overall impact that this industry is having on the silicon market.

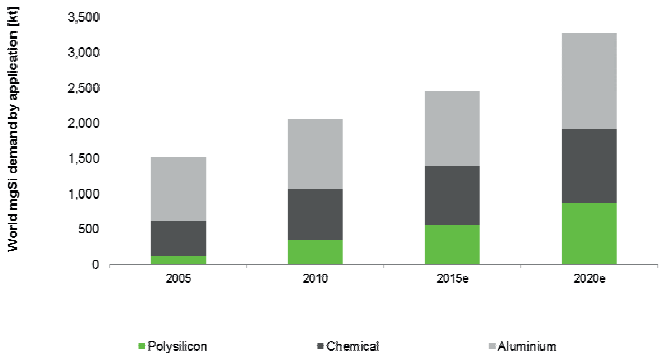

Source: CRU, Viridis.iQ estimates

Figure 4 Growth of MG silicon segments

[6] Viridis.iQ internal modelling

The figure shows that the PV sector in 2015 is larger in terms of its demand of mgSilicon, than the entire Chemicals market was in 2005. In 5 more years the

Photovoltaics market will be nearly 85% the size of the Chemicals market, in terms of volume of silicon that is required.

The metallurgical silicon industry is becoming increasingly dependent on the solar sector to diversify it from the Aluminum sector.

The purpose of the above figure is to demonstrate the impact the solar market has on the metallurgical silicon industry. But this impact is not one sided as the metallurgical silicon industry also has growing importance on the polysilicon sector in terms of costs. Metallurgical silicon costs today represent nearly 20% of production costs some Tier 1 polysilicon and chemical producers[7] and this is only from one single raw material.

Therefore, a polysilicon producer who grinds its own metallurgical Silicon and sells its current waste stream from grinding for low value to the refractory sector is motived to recycle these wastes and use them in their polysilicon plant.

In fact, there are already concerted efforts to increase the usage of higher and higher portions of fines from the grinding process in the polysilicon and chemical processes, but these efforts also have a high costs in terms of increased slurry handling and lower energy efficiency, not to mention that the grinding fines carry in more impurities to the system due to their nature.

Improving metallurgical silicon performance in the polysilicon and chemical processes also are a focus of many producers, as with polysilicon prices in the mid $10's per kilogram, every effort must be made to squeeze higher efficiencies from the process.

Metallurgical silicon producers also are increasingly focused on cost reductions as their has long been a cost driven business. A review of the possible benefits to a metallurgical silicon producer who grinds their own silicon if they were to recycle their wastes, based on the Viridis.iQ approach, has been undertaken based on hypothetical parameters.

The result of the exercise shows possible increase in gross margins of 1%. This exercise assumes estimated premiums and costs for ground silicon powder as well as conversion costs of the wastes based on the proposed technology.

A polysilicon producer who owns and operates its own metallurgical silicon production facility might also benefit from translated cost savings from recycling of grinding wastes under various conditions. These financial benefits are estimated to be on the order of 90 – 160 basis points based on internal modelling.

[7] Wacker Chemie Q1 2016 conference call note – April 28th 2016

Technical Solution

The proposed technology concept utilizes in-house developed process steps along with inert gas atomization technology.

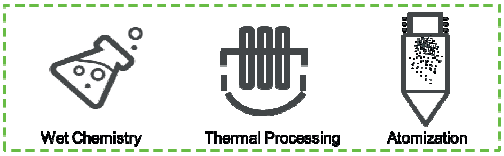

The wet and thermal steps will not be disclosed herein but the atomization process step brings distinct advantages including improved handling from uniform particle shape and size; increased reaction rate due to evenly distributed intermetallic phases formation of binary, ternary and even multicomponent silicides at the grain boundaries (some beneficial to the MCS reaction).

Of the many benefits of atomized silicon to the polysilicon process[8], one of the main ones is the ability of doping the material with a selected catalyst that can aid in the reaction kinetics of both the Direct Chlorination and Hydrochlorination processes. The cooling rate of silicon, when atomized, is on the order of 10^5 – 10^6 K/second which prohibits metallic impurities in the silicon from quickly segregating, as can easily happen in traditional casting of silicon and slow cooling of ingots. Additionally, the physically restricted shape of the particle creates barriers to segregation from one particle to another. Rapid cooling of the silicon during atomization also creates surface points on the particle at which the intermetallic phases are present. When low temperature catalysts are used, these "last to freeze" elements tend to also be present on the surface.

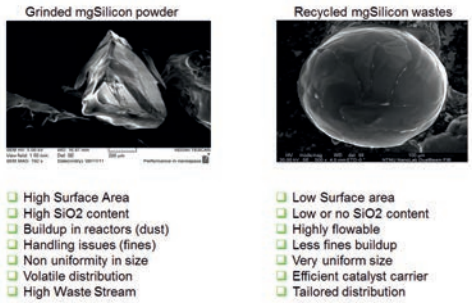

Figure 5 Comparison of grinded MG silicon versus recycling MG silicon wastes

[8] Uniform size and shape, flowability, lower segregation of impurities, usage of fine grain feedstock, low surface area, catalyst addition, etc.

Initial planned production

Viridis.iQ is planning to build and operate an initial recycling production factory for the recycling of kerf and grinding fines wastes. This factory will be designed to handle both waste streams to maximize cost benefits and to capitalize on availability of waste streams. The initial location of the factory is planned in Europe at the existing site of an operating partner in order to reduce CAPEX and infrastructure costs and to utilize existing procurement channels. Currently Viridis.iQ is raising capital for the project with a planned start up in 2017 and a capacity of 3000 tons per year of metallurgical silicon powder meeting the specifications of polysilicon and chemical customers.

Conclusion

The photovoltaic market continues to grow and is expected to reach 80 GW of installed capacity per year by 2020, which represents a growing dependency on the metallurgical silicon for which it uses as a feedstock. The solar industry value chain currently loses nearly 200 000 ton of usable silicon per year due to process restrictions that force this material to drop out of the sector. This lost potential of silicon represents nearly 45 GW of annual power production, which is more than the accumulated installed solar capacity of Germany.

The recycling of waste silicon is not a new development and many efforts have been tried but mainly based on using the wastes from kerf as a substitute for polysilicon. The authors have developed a different approach that instead considers the wastes as a substitute for metallurgical silicon feedstock and not polysilicon. This approach is more industrially and economically viable and technically possible with the development of the process done by Viridis.iQ.

The process steps developed include a wet chemical, thermal treatment and gas atomization step; the latter of which brings added benefits to the material via superior homogeneous physical properties and the ability to add specialized catalysts to improve reactivity in polysilicon production.

Tapping Si furnaces using advanced oxygen lances

Peter Sylvén
Envicom AB, Sweden, peter.sylven@envicomab.com

Abstract

Tapping a large Submerged Arc Furnace efficiently, safe and causing a minimum of damages to the taphole refractories is an art. When mechanically tapping a large Silicon furnace producing high purity grade Silicon, the challenges are even greater. When you survey the methods used around the world today, you will find operators using either drills, shotguns, graphite stinger rods, oxygen steel pipes, aluminium pipes, oxygen pipes with ceramic coating, pieces of wood or all of the above.

Good taphole management is crucial for a safe and profitable furnace operation. In addition, the capability to keep the taphole in as good condition as possible will reduce the gas blowing from the furnace through the taphole. This in turn will improve the environmental impact and more importantly, the working conditions for the operators.

This paper will show the proven advantages using the new carbon steel oxygen thermal lances from Trefimet, with a computed design of the inserted steel profiles, for this operation. Once developed for the copper smelters, this patented invention is now successfully used by leading Silicon producers, both for refreshing a taphole where the flow of silicon has dropped due to the precipitation of SiC or the opening up of a new taphole.

Keywords: Taphole, Oxygen lance, Thermal lance, Silicon Metal.

Plain steel pipes vs. advanced lances

Furnace tapping using oxygen steel pipes has not seen a significant change in over 100 years. Until now. Well-known problems related to the use of standard pipes as well as wire filled lances in a Silicon furnace, include, but are not limited to:

- Inaccurate tool: pipe bends and flame is not focused, causing damages & shortening the life of the taphole refractories, which adds cost and loss of production.
- Increased Fe contamination of the Silicon produced, resulting in reduced revenue.
- Physically hard and unsafe to operate, as you need to push the pipe against the taphole to keep it ignited.
- Safety: slow getting the job done, results in extended exposure to the operator in an unsafe area of the furnace.
- Cost: high oxygen consumption & high lance consumption. Ceramic coating needed to protect pipes from high tapping temperature.
- Time consuming and frustrating to connect one lance to another; increased waste and cost. Screw joints many times result in labor injuries to arms and joints.
- Deteriorating taphole conditions resulting in gas blowing, with an impact on the environment as well as operator health.

Many of these drawbacks are related to the use of primitive steel pipe oxygen lances. One of these consequences appears when the lance has to be pressed against its attack point. The pipe bends and more importantly, that pressure generates an undesired radial combustion, speeds up lance consumption and generates an irregular perforation. Thus, this effect lowers the lance's capability to concentrate all its energy at the attack point, wasting energy on its own consumption and tearing up undesired zones of taphole refractories.

The basic concept of any thermal lance is that it generates a thermal energy flow from Fe combustion contained in the steel of the lance itself. In order for this combustion to take place, the Fe's ignition temperature must be reached and it must also be in contact with high purity oxygen at the right pressure and flow rate. The flame at the tip of the lance has a temperature of about 3 000C (5 400F). The kinetic energy of the oxygen drags the combustion forward leaving only the tip of the lance lit; its effective attack edge.

The plain steel pipe lance is a hollow tube, without inserts resulting in the steel coming into contact with oxygen only in the internal wall of the tube. The thicker the walls "the better", as you are adding more Fe to the combustion. The new advanced thermal lances on the other hand, have several specially designed internal ducts which allow the oxygen to get in contact with both sides of its steel internal profiles. The result is a significantly increased steel/oxygen contact surface in the important combustion zone compared to the standard oxygen pipes. In addition, it cools the section of the pipe not burning, extending its longevity in a taphole environment.

The oxygen pipe is ignited by heating its tip with a solid combustible mass already ignited (i.e. burning coal), the pure oxygen increases the combustion, so that heat and oxygen bounce against the outer wall of the oxygen pipe (see Figure 1).

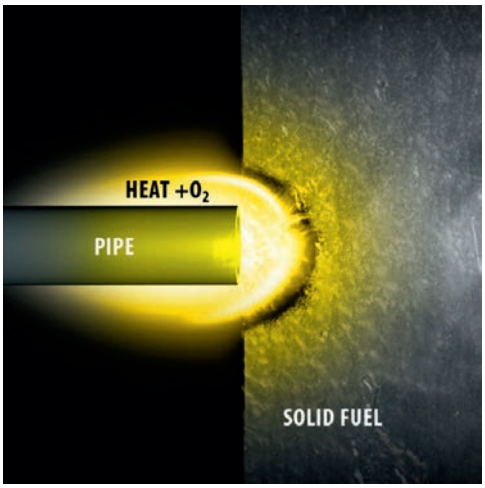

Figure 1. Oxygen lance tip combustion

Under this condition, any steel portion of the oxygen pipe, at Fe ignition temperature and in contact with oxygen, will react in combustion. However, as soon as the oxygen pipe is pulled back, the heat and oxygen bounce will end; extinguishing the Fe combustion and usually just a few sparks will remain. Many times it is hard to keep these sparks ignited until they reach the attack point, leaving the operator with a difficult, non-standard, and many times unsafe procedure to ignite the oxygen pipe (see Figure 2).

Figure 2. Remaining sparks when standard lance is removed from surface

The new advanced lance ignites just like a standard steel oxygen pipe, by heating its tip and letting oxygen pass through. However, when the tip's combustion starts it will

continue burning, even after the lance is pulled back from the burning mass. No matter the amount of oxygen, the lance will remain ignited thanks to its internal oxygen ducts that always keep enough Fe at ignition temperature and in contact with oxygen. This gives the operator an easy, safe and standard procedure to ignite the lance and to keep it ignited (see Figure 3).

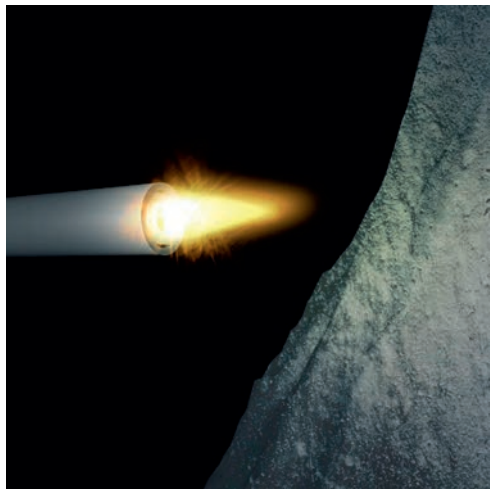

Figure 3. Advanced oxygen lance self-sustained ignition

Since the standard oxygen pipe cannot keep being ignited by itself, it will only generate energy when the oxygen conducted through the pipe is bouncing against a surface. The bouncing oxygen ignites the external wall of the pipe, generating energy fluxes back around the pipe tip (usually the target material is in front), making it very inefficient (see Figure 4).

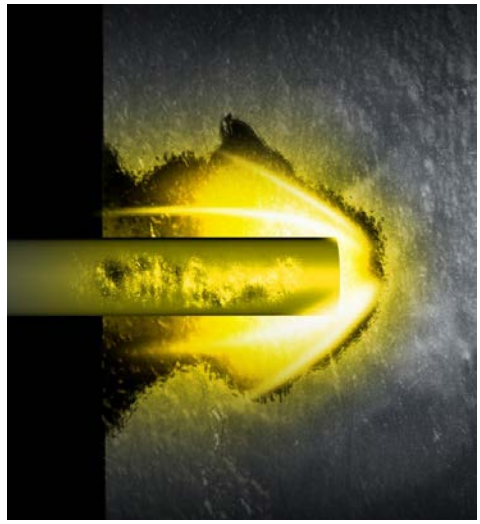

Figure 4. Inefficient cutting using standard lance

In contrast, thanks to their close to perfect steel/oxygen balance, the new advanced lances can keep being ignited without the need to bounce the oxygen through the lance against a surface. This will focus the energy forward and coaxially to the lance, concentrating the lance power against the target material (see Figure 5).

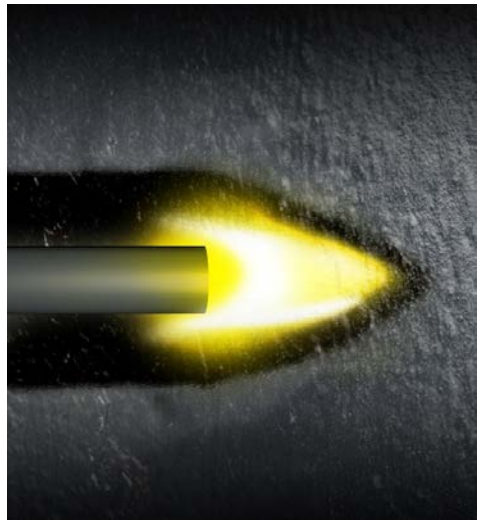

Figure 5. Efficient cutting using advanced lance

As previously stated, the standard oxygen pipe works only when the oxygen bounces, and it will ignite at random points behind the tip, sometimes several inches back. This random and unstable pipe burning causes energy loss, since a great deal of energy is

used to heat and cut the pipe itself, focusing some of the energy backward and around the lance, lowering the effectiveness of the oxygen pipe energy generation.

Since the new advanced lance generates its energy forward, no points behind the tip of the lance are exposed to ignition temperatures. This fact dramatically lowers the energy wasted on heating and cutting the lance itself. This allows most of the energy to attack the target material (Figure 5 above). The increased effectiveness of the energy generation of the new lances therefor makes them significantly faster and more efficient than the standard oxygen pipes.

The new lances are each specifically designed for different applications and conditions. Therefore, most of the oxygen is burned during the combustion process, and none of the oxygen excess will reach critical lining areas. In addition, since these lances operate faster, they will use oxygen during a much shorter time compared to the standard oxygen pipe. This results in a significant saving in the oxygen consumption in order to get the same job done.

These lance has several oxygen ducts configured between their inserts offering a total passage way along the whole length of the lance, no strangulation is required to maintain the inserts in place. The result is that the oxygen can "run freely" through the lance. That is the explanation to the fact that these new lances operates well even with lower oxygen pressure, utilizing existing oxygen supply and plant equipment.

The new advanced oxygen lance

Chilean based lance manufacturer Trefimet has over the last 15 years, together with the local copper industry, developed and patented an advanced thermal lance design and lance-to-lance connection system. These new lances provide an outstanding performance for a faster, more efficient, and more cost-effective furnace tapping operation. The lances are supplied in several different models, each adapted to the exact application and conditions where it will be used.

Figure 6 shows one model with square and rounded steel inserts and an outside diameter of 13,7mm; the TR25.

Figure 6. The TR25 advanced oxygen lance

The company has developed a perfect balance between speed and the available mass for the combustion process, creating the right exothermic reaction for each furnace taphole demand.

These advanced oxygen lances offer an almost perfect combustion, resulting in an operation with minimum emissions of fugitive gaseous and pollutants. In addition, it completes the operation in less time than what is required by a standard lance. Therefore, it emits much less fugitive gases during operation. The reduced number of lances required, lower oxygen consumption and no left-overs (thanks to the special lance-to-lance quick connector system EasyClick™) are some of the benefits taphole operators enjoy using these new lances.

Increased accuracy and speed

These new lances are very accurate tools that enable the operator to perform a more controlled operation; resulting in longer taphole life, fewer repairs and less down-time Moreover, a lower projection of particles reduces the wear of PPE (personal protective equipment.) Increased safety is also an important consideration. Trefimet lances generate a more efficient and accurate energy which does not require pressing the lance against the target; it lowers the projection of incandescent particles and gas generation, giving greater control over the operation. The reduced operation time required decreases the time of exposure for the operator at high temperatures. Less stress, heat and sparks, coupled with greater cutting control, improve operations safety, cutting accuracy and working conditions.

The Trefimet SuperOxibar, UltraOxibar and the TR models were developed specially for Si metal furnace tapping operations.

Benefits for silicon tapping operations

Most of the thermal energy flow, due to the modus operandi of a standard oxygen steel pipe (it needs something in front on which to bounce the oxygen, and heat in order to combust), takes a perpendicular direction from the pipe, breaking by fusion everything within a radius of 5 or more times the diameter of the pipe. Figure 7, shows the consequential damages that a standard pipe could cause to the tapping channel refractories.

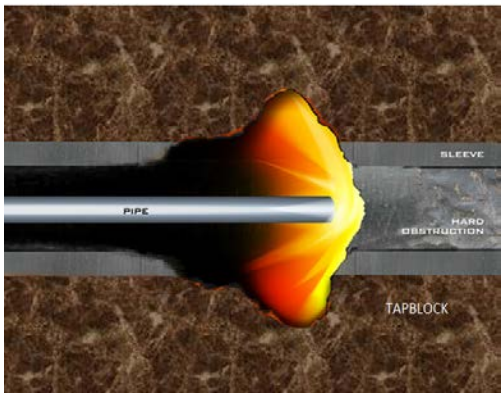

Figure 7. Standard pipe in taphole

Damage to the refractories is significant, which ultimately requires frequent taphole maintenance. Needless to say, this maintenance has financial consequences for the furnace operations.

Since the new advanced Trefimet lance generates its energy forward, no points behind the tip of the lance are exposed to ignition temperatures. This fact dramatically lowers the energy wasted on heating and cutting the lance itself and allows for most of the energy to attack the target material. The increased effectiveness of the energy generation of the new Trefimet lances makes them faster and more efficient than the standard oxygen pipes.

Once ignited, these lances do not need material in front on which to bounce the heat and oxygen; it will remain ignited under all conditions. This allows the operator to direct the lance in any direction he deems necessary. In Figure 8, a typical controlled taphole opening is illustrated, causing no refractory damage.

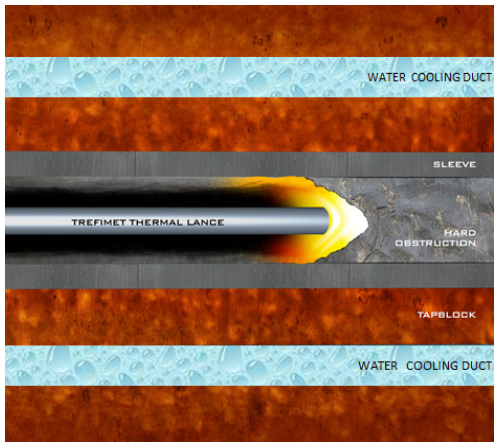

Figure 8. Trefimet lance in a taphole

Longer lasting lances due to “self-cooling” effect”

The many advantages operating a Trefimet lance in a Silicon furnace taphole has been described in detail above. This reduces or at some furnaces, eliminates the need for alternative taphole opening methods, many which are inefficient as well as unsafe.

In addition, the low temperature oxygen that flows through the many ducts of a Trefimet lance, keeps the lance cooler, resulting in the lance better resisting the high ambient temperature in front of the taphole. Historically, Si metal furnace operators have been using ordinary steel oxygen pipes with ceramic coating, but as the lances are operating slow, many lances are lost before they actually get the job done. This also results in increased Fe contamination to the product. This is why the Trefimet lance operates cooler than a plain steel pipe;

Part of this is due to the fact that the *convective heat transfer* of oxygen is a function of the *velocity of the gas* through the pipe/lance. The ducts in the Trefimet lance will result in increased gas velocity as the flow is the same (oxygen can be regarded as incompressible at the speeds in question, as the differences in density is negligible). One can show that for a TR38 lance, this results in an increased cooling effect with approximately 25%.

The more significant part of the decreased temperature of the Trefimet lance is due to the increased heat transfer area caused by the steel ducts inside the lance vs. a plain pipe. Using Newton's Law of Cooling:

$$Q = k \times A \times \Delta T$$

where we are interested in concluding how the cooling effect (Q) changes with the change in heat transfer area (A). k is the convective heat transfer coefficient for steel (~50 W/m2K) and ΔT the temperature difference.

One can then show that the increase in cooling area between a standard steel pipe and the TR38 lance results in an increased cooling effect of 500%. Looking at the TR75, the increase will be even larger (Figure 9, The TR75 thermal lance)

The added cooling effect will result in less lance consumption, faster operation and therefore significantly less Fe contamination to the Silicon.

Figure 9. Showing the internal duct design of one very powerfull Trefimet model

Conclusion

Trefimet has managed to develop a patented and advanced oxygen lance design that offers the following advantages to Silicon furnace operators:

- It focuses its energy on the attack point, resulting in more accurate perforations – faster to operate and less damage to taphole. Less labor injuries inflicted.

- Faster operation results in significantly reduced Fe contamination to the Silicon.
- Faster operations also results in decreased exposure time and therefore increased safety.
- Offers lower oxygen and lance consumption.
- No need to push lance forward. Keeps ignited. Easier to operate, lance bends less.
- Very easy to connect lances with the EasyClick™ system– faster, less labor injuries, and less wasted pipes.
- It generates less fumes and particles – easier to operate and your target is more visible.
- Improved taphole condition reduces gas blowing, reducing the environmental impact and increasing operator safety.
- Oxygen flow cools the critical part of the lance exposed to flowing Silicon; results in extended lance life in a tough environment, thus faster operation and less Fe contamination.

As stated at the beginning of this paper, an important tool for many Silicon tapping operations has for many decades been the oxygen steel pipe. But this has not been considered an operation that brings added value, and, therefore, there has been practically no product development during all these years.

Furnaces have been made more efficient and computer controlled, electrode systems have been modernized; moving from carbon electrodes to composite electrodes, taphole clays are today environmentally friendly as well as great for the tapping process, cooling systems have been improved, lance holders with built in safety valves are almost standard, refractory concepts and materials have been refined to offer improved furnace life and safety, just to mention a few developments that have taken place in recent years. And now, finally, the oxygen lance technology has reached a new level. This is truly a step change. These new lances are very accurate tools that enable the operator to perform a more controlled operation; resulting in longer taphole life, fewer repairs, increased safety, less down-time and increased revenue.

Operational Aspects of the Metallurgical Silicon Process

Birger Andresen
FESIL RANA Metall AS,Vikelvfaret 4, N-7054 Ranheim, Norway

Abstract

The carbothermic metallurgical silicon process is briefly described and selected operational aspects are discussed.

Process overview and furnace equipment

Silicon is produced in a carbothermic process in submerged arc furnaces with three alternate current electrodes as shown in Figure 1.

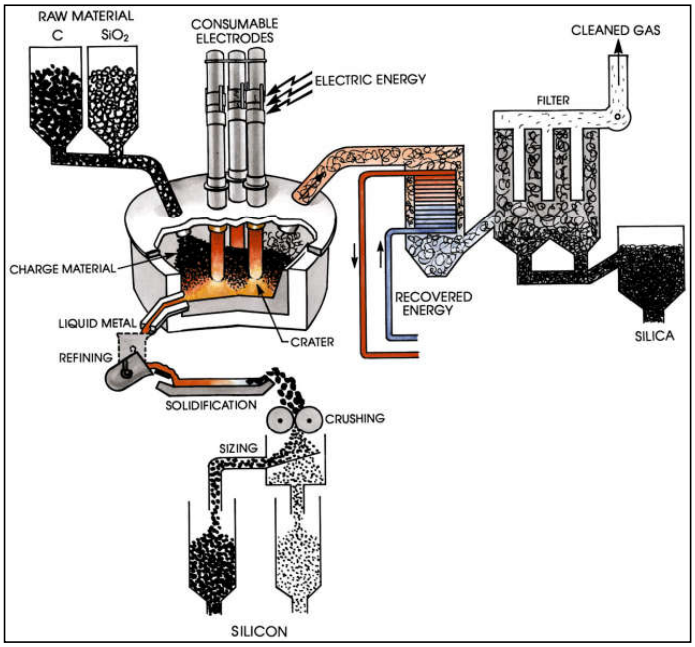

Figure 1: A typical modern plant for production of silicon including the most important raw materials, off-gas handling and post tap hole treatment as illustrated by Schei, Tuset & Tveit [1]. The refining step is optional. Solidification may be done in several different ways, including water granulation.

Furnace size

Carbothermic silicon furnaces range from very small units in the order of 5 MW to about 45 MW. The process is run 24 hours a day week in and week out unless there are problems with the operation or maintenance is required.

Energy consumption and raw material demand

A well operated medium or large furnace uses about 10.5 MWh per metric ton tapped silicon and upwards depending on the electrical efficiency of the furnace and the silicon recovery. A 35 MW furnace hence produces just over 3 ton silicon and 1 ton silica an hour. This requires that about 7500 kg quartz and 2800 kg fix-C (reactive carbon) are fed to the furnace every hour. The actual amount of carbon materials is in the same order as the quartz, but varies with the ratio of coal, coke, charcoal and wood chips since these materials have significantly different contents of water, volatiles and ash. Tapping is continuous unless there are problems with the furnace operation, the tapping area or with critical equipment.

The furnace pot

The diameter of the steel furnace pot for a large furnace is over ten meters while the height from the bottom steel plate to the top of the charge may be six-seven meters. The height of the charge may be three-four meters. The furnace pot can be stationary for small furnaces, but it rotates slowly for most medium sized and large furnaces, typically with a speed corresponding to one full turn in about a month. The rotation is partly to protect the lining below the electrodes and partly to help break up crusts that might otherwise form in the charge. Too fast rotation may cause electrode breakages.

The electrodes

The process requires a lot of electric energy which is delivered by three consumable carbon electrodes at a relative low voltage and high currents. Typical values are 150-300V and 50-100 kA.

The electrode diameter for large furnaces is in the order of 1.5 meters. The electrodes are going through sealed openings in the smoke hood. They are lifted and lowered automatically in combination with changing transformer settings in response to changes in the furnace resistance, furnace conditions and electric strategy.

Many silicon furnaces use approximately 2.5 meter long full sized prebaked electrode elements which are screwed together with carbon nipples to compensate for an electrode consumption in the range 50-100 kg/ton tapped silicon. Other furnaces use a relatively small graphite core in the centre of a steel cylinder filled with Søderberg electrode paste known from production of ferrosilicon [2]. The Søderberg paste is baked to solid electrode in the electrode holder region. This so-called compound electrode is then extruded from the steel casing to keep the contamination of iron from the steel casing at an acceptable level. Such electrodes are less expensive than prebaked electrodes, but require more complex electrode equipment. They also have some additional functional challenges compared to prebaked electrodes, but may have some metallurgical advantages due to the high conductivity of the graphite core.

Feeding raw materials

The raw materials are mixed after weighing and then fed to the top of the furnace either through several tubes like the one shown on Figure 1 or by special trucks delivering batches through gates in the side walls of the smoke hood, or both. These gates are also used for inspection of the furnace top and for stoking and tasks like

moving raw materials around and removing large blocks from broken electrodes. Feeding only by truck is not suited for large furnaces.

Charge tubes give the possibility to feed much of the materials automatically. It is then possible to feed little material quite often rather than large batches less often by truck. This is referred to as semi-continuous feeding, which has proven to be favourable both for the process as such, for reducing the wear on the furnace hood and for reducing emission of for example NO_X in the off-gas. The main reason is that the variations in gas production are reduced and the gas distribution becomes more even so that the temperature peaks are smaller and shorter. The combustion of CO(g), SiO(g) and volatiles above the charge then becomes more steady and favourable for low production of NO_X. The details are complex and not fully understood yet.

Tapping and refining

Liquid silicon is tapped into ladles or moulds through one out of several tap holes in the side close to the bottom of the furnace. These are repaired on a semi-regular basis. A lot of hard work in very warm, dusty and tough conditions including splashing of liquid silicon and intense welding torch like gas flames is required in this area to keep the tap hole open. Otherwise slag will clog the channel or freezing silicon may cause problems. The operators use rods of wood, oxygen through hollow rods of aluminium or iron (beware of iron contamination) or shoots with coarse calibre zink bullets to keep the tap hole open.

A poorly drained furnace will not perform well. It is essential that a new tap hole is opened in the correct height and with the correct angel so it meets the silicon inside the furnace at the right place. It is also essential that the skilful operators manage to preserve optimal conditions in the tapping area until a new tap hole is opened. Tapping is continuous, at least for medium size and large furnaces, unless furnace operation or maintenance requires otherwise.

Figure 2: Operator working in the tapping area.

The silica fume in the tapping area is collected as good as possible and routed into the main off-gas channel from the smoke hood to be recovered in the fume filter. Some furnaces have separate fume filters for the gas from the tapping area.

The typical tapping time for large furnaces is 1 1/2 to 2 hours. The silicon is normally refined during tapping by purging oxygen and air through it via a porous plug in the bottom of the ladle while fluxes are added at the top to adjust the refining slag. The goal is to reduce the aluminium and calcium content to the desired levels,

which will vary from one customer to the other. Further refining may be done after tapping, if needed. This is normally decided upon receiving the analysis of samples taken shortly before the ladle is full. Stable furnace operation and tapping makes the refining much easier.

Suggested literature on tapping is [1] and [3] and on refining of silicon [1] and [4].

Process gases, silica fumes and energy recovery

Almost all free carbon that is added in the raw materials will leave the furnace as CO(g). Only a small amount of it will be dissolved in the liquid silicon. A small fraction of the CO(g) will come out of the tap hole, but most of it will leave through the charge top together with some SiO(g) produced in the hot zone and water vapour, volatiles and other gases driven off from the carbon materials as they are heated. These very hot gases mix with air sucked in through the charging gates above the charge and they will burn to CO_2(g) and fine SiO_2-particles called silica fume or silica dust as they are sucked into the filter unit where the silica is collected. The silica is sold, mostly to producers of concrete. Typically 10-20% of the quartz ends up as silica, depending on the furnace operation.

Modern furnaces normally have energy recovery from the hot process gases before filtering out the silica. Producing hot water for district heating is more energy efficient than producing electric energy, but not all plants have a demand for district heating nearby.

Basic overall chemical reactions

In the carbothermic silicon process we use carbon at high temperatures, in the order of 2000 C, to remove the two strongly bonded oxygen atoms from the silicon in quartz (SiO_2) according to Eq. 1.

$$SiO_2(l) + 2C(s) = Si(l) + 2CO(g) \qquad (1)$$

If we have exactly 2 moles of chemically active carbon (fix-C) for every mole of quartz, we say that the *carbon balance* is 100%.

However, several other chemical species are present at these high temperatures, most notably SiO(g), CO(g) and SiC(s), giving the more realistic Eq. 2 which is discussed in much more detail for example in [1] than it is here.

$$a\ SiO_2(l) + b\ SiC(s) + c\ C(s) = x\ Si(l) + y\ SiO(g) + z\ CO(g) + u\ SiC(s) \qquad (2)$$

This equation allows both for net production of silicon carbide in periods where we add more carbon that we should have done (overcoked process, u>0 and b=0) or net consumption of SiC that has been deposited earlier if we add less carbon than we should have done (undercoked process, b>0, u=0).

The special case b=0 and u=0 means a process where SiC is neither consumed nor produced overall. Eq. 2 then transforms to Eq. 2.a when the parameter 'a' in Eq. 2 is assigned the value 1 and x is the silicon yield (the fraction of Si in the quartz in the raw materials that comes out of the tap hole as liquid silicon).

$$SiO_2(l) + (1+x)\ C(s) = x\ Si(l) + (1-x)\ SiO(g) + (1+x)\ CO(g) \qquad (2.a)$$

This is the situation we are aiming for where the carbon balance is optimal and good furnace operation may prevail for a long time if everything else is also optimal.

Eq. 2.a shows that a carbon balance given by Eq. 3 is needed in the raw material mix at a silicon yield of x if there are no losses during transportation of raw materials and if there are no other carbon consuming reactions taking place in the process.

$$\text{Fix-C} = 100\% \bullet (1+x)/2 \qquad (3)$$

Eq. 3 shows that we need a carbon balance of 100% • (1+1)/2 = 100% if we have no carbon losses for a silicon yield of 100%. At a silicon yield of 85%, the optimal carbon balance is 100% • (1+0.85)/2 = 92.5%, while a silicon yield of 0% (producing only silica according to Eq. 4 or Eq. 2.a with x=0) requires a carbon balance of 100% • (1+0.00)/2 = 50.0%.

$$SiO_2(l) + C(s) = SiO(g) + CO(g) \qquad (4)$$

The important observation is that the amount of carbon required increases with 1.0% for every 2.0% increased silicon yield. This means that more carbon must be added in periods with high silicon yield and that the amount of carbon must be reduced if the silicon yield drops.

Even Eq. 2 is still a simplified approach since a lot of other elements and compounds, of which Al, Ca, Ti, S, water and volatiles are perhaps most important, enters the process through the raw materials. However, for a discussion of the operational aspects, Eq. 2 is just fine.

Chemical reactions in different zones

It is common to split the furnace in an upper/outer zone with mostly moderate temperatures and a high temperature inner/lower zone surrounding the gas filled cavity around the electrode tips. Figure 3 illustrates the conditions around one electrode, including the most important chemical compounds and reactions in various parts of the furnace.

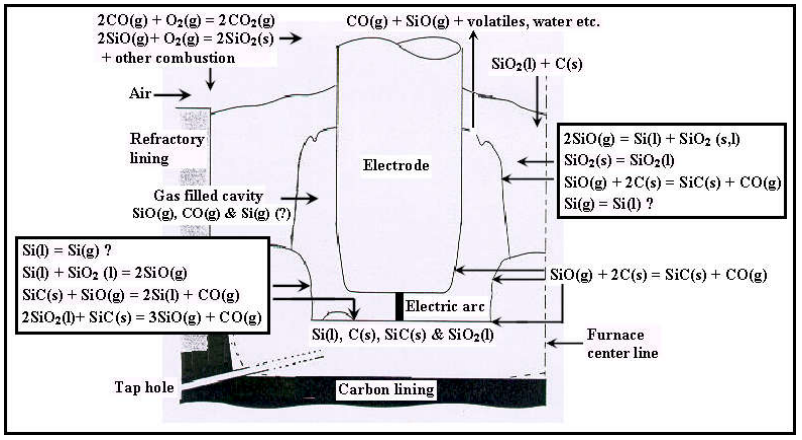

Figure 3: Schematic sketch of the area around one electrode. The figure is based on a drawing by Schei, Tveit and Tuset [1].

High temperatures are required to produce silicon, at least 1812 C. In practice, it is believed that the temperature around the electrode tip is in the order of 2000 C. These

high temperatures are reached by an alternate current electric arc burning preferably from the tip of the electrode to the metal pool below it.

A large gas filled cavity forms around the lower part of the electrode because the raw materials do not always move easily downwards on their own for reasons to be explained later. The high energy density clears the area around the electrode tip to create a cavity in which the electric arc can burn and deliver high enough temperatures for silicon production.

The electric arc can also burn from the flank of the electrode to the cavity wall and passes through the hot electrically conducting materials there, most importantly C and SiC, and continue all the way to the other electrodes. On its way, energy is released in the cavity walls and wherever the current goes by ohmic heating and by small electric arcs from one conducting particle to the next. Calculations show that the core of the electric arc can exceed 25 000K. Hence radiation is important for heat transfer in this zone.

Silicon is primarily produced in the hot zone by Eq. 5, but also in the upper zone by Eq. 6.

$$SiC(s) + SiO_2(l) = 2\,Si(l) + CO(g) \quad (5)$$

$$2SiO(g) = Si(l) + SiO_2(l) \quad (6)$$

SiO(g) produced by several reactions in the hot zone will react with carbon in the upper part of the furnaces according to Eq. 7.

$$SiO(g) + 2C(s) = SiC(g) + CO(g) \quad (7)$$

Eqs. 6 and 7 are the most important reactions to prevent SiO(g) from being lost from the charge top.

Selected operational aspects

A comprehensive description of all important operational aspects will take all to long to give. Only a few selected aspcets are described below.

In the upper zone, the quartz is heated as it descends and meets hot gas emerging from the lower/inner zone. The quartz melts in the lower part of this zone and flows down under the electrode as a highly viscous fluid. Little else happens to the quartz in the upper zone, expect that it may start reacting when it gets to the cavity wall and becomes exposed to high temperature gases and radiation from the electric arc.

Too large quartz lumps will reach the hot zone without being properly heated in the center. This will lower the temperature in the hot zone, which is bad since the ratio of SiO(g) to CO(g) then increases, bringing more SiO(g) out of the zone together with the CO(g). Recovery of SiO(g) then becomes more difficult and the losses increase.

Too small quartz fractions, on the other hand, may also cause problems since the gas distribution may then suffer. Mechanically and thermally weak quartz will add to the fines fractions and is in general unwanted.

The carbon materials will also be heated in the upper part of the furnace. Preferably they react completely to silicon carbide according to Eq. 7 in the upper part.

Even gas distribution, small enough carbon particles and good intrinsic SiO-reactivity promotes this reaction which is extremely important for two reasons:

1. If all carbon reacts according to Eq. 7 in the upper zone, then half of the carbon exits the furnace as CO(g) without ever reaching the hot zone. This minimizes the amount of CO(g) produced in the hot zone, and hence also minimizes the amount of SiO(g) that leaves with it since the SiO(g)/CO(g) ratio in the hot zone is defined by the temperature there and kinetics. Less carbon in the hot zone therefore implies that less SiO(g) must be captured in the upper zone, and the silicon yield increases.
2. Eq. 7 captures SiO(g) before it leaves the furnace. This is obviously good for the silicon yield.

Eq. 7 provides one out of two reactions to capture SiO(g) on its way out. The other is the so-called condensation reaction (see Eq. 6) which occurs when hot SiO(g) is cooled as it meets colder raw materials. The reaction product from Eq. 6 is an intimate mixture of glassy silica and silicon. This substance will gather on particles and in-between them as a glassy, glue like substance. The reaction is highly exothermic, and it will therefore heat the charge. Three major problems occur if we have enhanced SiO(g) concentrations in the upper zone, for example if Eq. 7 fails:

1. The charge may become so hot that the condensation reaction can no longer continue.
2. The desired even gas distribution is ruined since the glassy condensate forms a fairly compact lid inside the charge where the gas cannot pass. The gas then forces its way through narrow channels and we get concentrated welding torch like flames emerging from small areas at the charge top, often close to the electrodes. We say that the furnace is blowing when this happens. Obviously, most of the gas, including the SiO(g), then passes through a very small fraction of the raw materials. This means that a smaller amount of the carbon in the raw materials will be exposed to SiO(g). Carbon conversion to SiC by Eq. 7 then suffers and things get even worse.
3. The condensate lid that prevents even gas distribution also prevents the raw materials from descending easily in the furnace. We say that the raw materials are hanging in the furnace. Stoking may then be necessary to help the materials move downwards. The operator will notice that the charge top grows higher in areas where this happens if the raw material system continues to feed the furnace at the normal rate. The area underneath the electrode then runs out of charge and the cavity wall moves upwards since the material flow has decreased or even stopped. This continues until the cavity wall has moved so high up in the furnace that it collapses and large amounts of charge rushes down to the hot zone. This is usually accompanied with violent outburst of gas and dust that can rush out of the furnace through the charging gates. This can be very dangerous in extreme situations.

Large amounts of SiO(g) may arise from various problems. Poor conversion of carbon to SiC according to Eq. 7 is one. Another is a temperature drop in the hot zone since the SiO/CO gas ratio in the hot zone increases with falling temperatures. A third is if we have too little carbon in the raw materials (undercoked furnace), which means that less quartz molecules will find two carbon atoms to form silicon. Instead they find only one and therefore ends up as SiO(g) rather than silicon.

A temperature drop in the hot zone can for example occur if raw materials suddenly rush down to the hot zone as described above. It can also result from too

coarse quartz lumps that do not have time to heat properly all the way to the center before entering the hot zone. A third reason is if the set point for the current is too low, corresponding to a low value of the Westly constant, also known as C_3 (see Eq. 8, where I is the current in kA and P is the furnace load in MW).

$$C_3 = I / P^{2/3} \quad (8)$$

Typical values of C_3 for medium sized furnaces are in the range 8,5 – 9,5. Lower values of C_3 means that a higher fraction of the furnace load is delivered to the upper part of the furnace. This increases the melting of quartz, which in turn increases the amount of charge that is supplied to the hot zone. At the same time, there is less energy available in the hot zone and the chemical conversion rate there decreases. A too low C_3 value therefore results in more raw materials being supplied to the hot zone than can be consumed by the endothermic reactions. Raw materials can then build up below the electrode. Three main problems then occur:

1. The molten quartz does not conduct electricity. Too large amounts of it below the electrode can thus prevent the electric arc from burning down towards the metal pool. Instead it may be forced to burn from the electrode flank to the side of the cavity wall. This means that even more of the energy will be delivered to the upper part of the furnace and the problem may escalate.
2. A surplus of molten quartz may gather in the tapping channel or in its inlet and cause problems in tapping the furnace.
3. The temperature may decrease in the hot zone because more energy is delivered high up in the gas-filled cavity and less further down. This will increase the SiO/CO ratio of the gas leaving the hot zone, which is unfavorable as described earlier.

Good furnace operation requires that the C_3 value is chosen such that the material transport to the hot zone matches the chemical consumption there. The energy balance is then correct.

Situation 1 above normally changes the dynamic behavior of the electrode. An electric arc that burns downwards against the metal pool with no major obstructions will usually move only short distances up and down, typically less than 15 cm, in response to relatively small dynamic changes in the furnace resistance. However, a major change in resistance occurs once insulating quartz blocks the electric arc so that it suddenly jumps over to a highly conducting area of the cavity wall. The current then increases abruptly and the electrode regulator responds by lifting the electrode to lower the current as it expects to increase the length of the electric arc by this. However, since the electric arc now all of a sudden burns high up on the electrode flank, there will be little, if any, increase in the length of the electric arc as the electrode moves up. Instead the root of the electric arc just slides along the electrode flank until the tip of the electrode reaches up to where the electric arc burns. Then the resistance starts to increase and the electrode lifting stops. We typically see an electrode that moves up 30-50 cm in a few minutes as it connects to the side of the cavity wall in this way.

Once the electrode tip is lifted this far up, there is no easy way for it down again, at least if the cavity wall has not become a narrow cylinder around the electrode. Instead it must work its way gradually down again by reacting or melting away parts of the cavity wall so that the electric arc length increases or the electric conductivity of the

cavity wall increases. By my experience, it often takes in the order of 20-50 minutes before the electrode tip returns to the original position.

While it was burning up in the cavity wall, the electric arc delivered much energy there and less than usual underneath the electrode. More than usual quartz melted down and less was consumed below the electrode during this cycle, and there is likely a lot of molten quartz under the electrode as it returns to its original level. It would be no big surprise if the electrode now jumps over to the cavity wall again and repeats the cycle as shown in Figure 4.

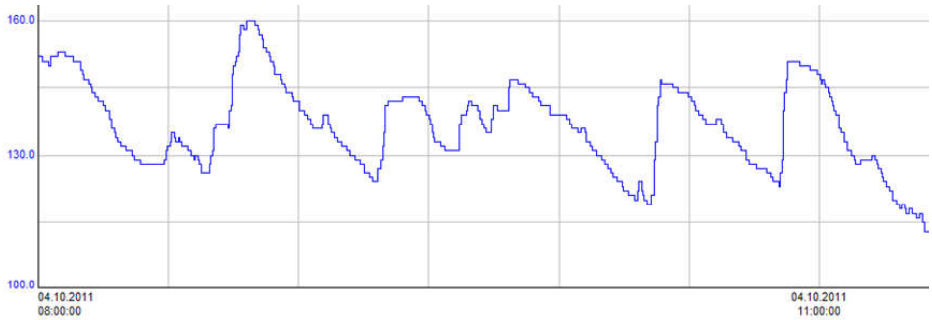

Figure 4: Example of an electric arc that repeatedly jumps over to the cavity wall about 30 cm up on the electrode flank and gradually works its way down again in about half an hour.

If this continues, it would be a good idea to consider increasing the set point for the current for a while to add more energy below the electrode and by that "clean up the area" removing surplus charge. As soon as the electrode dynamics return to normal, you should return to the normal C_3 value as this is by experience the value at which the furnace performs best over time.

I would recommend considering a slightly higher carbon balance for the raw material mix in the charge if the temporary increase in the C_3 value does not work within some hours since the problem may instead be caused by too little carbon in the charge.

Significant wear of the electrode flank is a likely result if this is allowed to continue for long periods. The lower part of the electrode may then become very thin, which would cause severe problems to the furnace operation. At some point the thin tip of the electrode may suddenly break off. This is a larger problem in the ferrosilicon process than it is for the silicon process as the iron in the charge increases the electric conductivity of the cavity wall significantly.

Problematic electrode erosion may also occur if there are too much carbon in the center of the furnace compared to the outside. The electric arc may then have a tendency to burn towards the center of the furnace, eroding away the lower part of the electrode on the flank facing the center.

The carbon balance

Undercoked furnace

The case $b > 0$ in Eq. 2 means that SiC already present in the furnace is consumed and serves as an additional carbon source for the reduction of quartz. It also serves as a silicon source adding to the silicon from the quartz. The value of u is then zero. This technically corresponds to an *undercoked process* where we have too little carbon in the raw material mix. However, if enough SiC is available, the process may not be

undercoked in practice. The silicon yield may even be better than normal in this case since extra silicon is produced from the SiC while the silicon yield is calculated based on the silicon charged as quartz via the raw materials only. However, the silica production will normally also be higher than usual in this situation since there is then less carbon than usual in the raw materials to catch ascending SiO(g) according to Eq. 7 before it leaves the furnace top.

If the charge is undercoked and there is no more (or too little) SiC available, the process becomes truly undercoked. Then the silicon yield drops as we do not have enough carbon to remove both oxygen atoms from as much quartz as during optimal furnace operation. This means that some of the quartz that would normally react according to Eq. 1 and produce silicon, instead must react according to the gross reaction Eq. 4 and produce SiO(g).

The consequence is that more silica is produced and the silicon yield drops accordingly. The top of the charge will then often become very hot, the gas distributing becomes very uneven and the downwards material flow of the charge will often suffer for reasons already discussed.

Overcoked furnace

$u > 0$ in Eq. 2, on the other hand, there is more carbon in the raw materials than what is needed with the current silicon yield. This extra carbon will form SiC that builds up in the furnace as it does not find enough oxygen in the quartz to leave as CO(g). The value of b in Eq. 2 is then zero. This corresponds to an overcoked situation.

If you enter an overcoked situation from a period with good furnace operation, the silicon yield is expected to be almost unchanged, perhaps even somewhat better than normal since you have more than usual carbon to catch ascending SiO(g) with. More silicon is then returned to the hot zone where some of it may add to the silicon yield.

The increased capture of SiO(g) also means that less SiO(g) leaves the furnace. The operators are likely to see a nice and calm furnace top, good tapping conditions and good production, and they will have a tendency to be happy with a nice day at work while they should instead start to worry because SiC will gradually build up and eventually cause major problems if it is allowed to continue long.

The basic problem in the tapping area will be that the SiC after a while will make it harder for the silicon to drain out from the tap hole. In the charge, the SiC will form crusts that can prevent a good downwards material flow. Over time, these crusts are likely to change the geometry of the cavity around the lower part of the electrodes from wide and well functioning cavities to narrow cylindric cavities where the electric arc easily jumps over to the cavity wall from somewhere up on the electrode flank as described above.

Again, the electrode will move fast upwards several tens of cm, but this time it will have a tendency to rush fast down again as the SiC-cylinder may have almost the same diameter far up along the electrode so that it does not matter so much for the current whether the arc burns high up in the cavity or further down.

So if you observe an electrode that rushes fast up and fast down again, you are welcome to suspect an overcoked furnaces. To remove the SiC, you have to run the furnace slightly undercoked, with the unpleasant side effects of undercoked operation.

Uncertainties in the carbon balance

As stated earlier, we need too add 1% more carbon in the raw material mix for every 2% increase in the silicon yield. This means that the carbon balance is a dynamic quantity that the metallurgist must pay much attention to.

There are three major difficulties in reaching a perfect carbon control if we skip discussing stupid errors in the weighing system or in other basic measurement- and control systems.

The first is that we do not know exactly how much carbon we lose from the weighing system until the carbon enters the production zones down in the furnace. Materials may fall off the transport band or stick to it if wet. This can be checked and estimated by frequent inspections of the transport route.

The second is that we have variations in the moisture of the carbon materials that are difficult to estimate, especially if carbon materials are stored outside. Then a heavy rain fall will give soaking wet materials close to the surface of the big pile of raw materials while the interior may preserve its former moisture level. The water content will then vary dramatically depending on from where in the pile the materials are taken from day to day. The obvious solution is to store all carbon materials in a building so that rain, snow or sun make no difference to the moisture levels. In any case, the water content of the carbon materials must be measured on a regular basis since variations will be found even for materials stored indoors. The frequency will, however, be much higher for materials stored outside.

The third difficulty is that we do not know exactly what the silicon yield really is at any given point in time. There are several reasons for this. One is that you cannot blindly trust the amount of silicon that is tapped during a day since there may be much more or much less silicon left inside the furnace now than it was 24 hours ago. And you have no way to know what that difference is. Also, even though the silicon process is often "promoted" as a slag free process, this is not really the case. The raw materials have significant amounts of calcium and aluminium that partly leave the furnace dissolved in the silicon and partly as a (mostly) Al_2O_3, CaO and SiO_2 containing tapping slag. The amount of tapping can vary very much from one tapping to the next and from one day to the next. It is not practical to measure the amount of tapping slag with high precision.

This means that there are considerable errors both in the actual amount of carbon that ends up inside the furnaces over a day and in the amount of liquid silicon produced in the same period. This means that we need to trend the estimated carbon addition and the silicon production over several days, and consider adjusting the carbon balance if we observe that significantly too much (or little) carbon seems to be added during the last 2-5 days or so.

Neither do we know how much SiC that has been produced or consumed in the report period. To estimate this, it is wise to calculate a total silicon balance and see how silicon units accumulate or is consumed over weeks and months.

The problem with finding a good estimate for the true silicon yield based on the amount of tapped silicon means that many metallurgists use the silica production for estimating the silicon yield.

Finally it is noted that all metallurgists know that a high content of calcium in the tapped silicon indicates that the temperature in the production zone is high provided that no significant changes are done to the raw material mix. It is then reason to believe that the electric arc is burning towards the metal pool. A low calcium content will indicate either (a) that the electrode tip is too high up in the furnace or (b) that the electric arc burns high up on the electrode flank or (c) that the process is undercoked or (d) that the C_3 value is too low or (e) that considerable amounts of silicon is stored inside the furnace. Who said that the silicon process was easy to understand?

.

Conclusion

Increased conversion of carbon in the raw materials to SiC before they enter the hot zone around the electrode tip increases the silicon yield. High SiO reactivity combined with small enough particles and a fairly even gas distribution are important with respect to this. High temperature in the hot zone is important for the silicon yield because the SiO/CO ratio of the gas here decreases with temperature. It is believed that this is achieved by selecting electrical set points that give an energy distribution between the charge and the metal pool that results in a chemical conversion in the hot zone that equals the material transport from the cavity walls around the electrode tip. The optimal electrical set points change with the raw material mix and state of the furnace. The problems in measuring basic process parameters and changes in the raw materials are among the most challenging aspects of the process control. Long time constants for some important sub processes are also very demanding to handle.

There are large amounts of measurements and observations that can be used to help the operators and metallurgists in understanding what is happening inside the furnace. Some of these are described here. The more complex ones, often found by combining several trend curves and observations, are those that really make the process interesting and provide improved operations. The different producers wisely keep these tools and knowledge within their own company.

References

1. Schei A., J. Kr. Tuset & H. Tveit, Production of High Silicon Alloys, Tapir Forlag, Trondheim, Norway 1998, ISBN 82-519-1317-9.
2. Bullón J., M. Lage, A. Bermudez & F. Pena, The New Compound Electrode: Current Situation and Thermoelectric Studies, Infacon 8, Bejing, China, 1998.
3. Tveit H., T. Halland, K-I Landrø, S. T. Johansen & B. Ravary, The Tapping Process in Silicon Production, Silicon for the Chemical Industry VI, Loen, Norway, 2002.
4. Nygaard L. & B. Andresen, Refining of Silicon Metal, Silicon for the Chemical Industry VI, Loen, Norway, 2002.

Sistruc: A microstructure model for optimization of silicon materials

S. Gouttebroze[1)], Q. Du[1)], M. M'Hamdi[1)]
1) SINTEF Materials and Chemistry, Pb.124 Blindern, 0314 Oslo, Norway

Abstract

Silicon is a key material in various markets such as silicones, photovoltaics, or aluminium castings. Each market segment has its own requirements in term of composition, particle shapes, intermetallic phases and more. It is therefore essential to control and tailor the amounts of major elements to achieve highest downstream performance, for example reactivity between silicon and methyl chloride to produce methylchlorosilanes precursors for silicone. Sistruc is a microstructure model developed by SINTEF in collaboration with Elkem. The model predicts the micro-segregation and formation of intermetallic phases during the solidification of metallurgical-grade silicon alloys. The model includes the four major elements Al, Ca, Fe and Ti in addition to B and P. As an industrial tool, Sistruc is designed to be extremely fast and user-friendly. In the present paper, an efficient algorithm to solve the solidification of metallurgical-grade silicon based on simplified phase diagram is presented. The calibration of the model is explained and the quality of the predictions is assessed. Finally, an example illustrates the use of Sistruc to optimize the quality of silicon material in terms of intermetallic content for an industrial case.

Introduction

Liquid metallurgical silicon is produced by reduction of quartz. Impurities are present from the raw materials used in the production process. During solidification, metallic impurities will segregate and form intermetallic phases mostly at the grain boundaries. Depending on the solidification process (especially the cooling rate) and melt quality, different particles can nucleate and grow. The amount and type of particles present will affect subsequent processing steps. Indeed metallurgical silicon is not used as a finished product but as raw material for other processes (for example: i) as an alloying element for aluminium, ii) as a raw material for chemical industry (e.g. production of silicones), iii) as a raw material for production of solar and electronic grade silicon. For each market, the quality and specifications for the solidified silicon are of high importance. For example, as illustrated by Anglezio [1], the intermetallic compounds affects the

selectivity (ratio of dichlorodimethylsilane over total chlorosilanes) and reactivity (quantity of chlorosilane produced per hour and kg of Si) of the chlorosilane synthesis in the fluidized bed reactor.

Iron, aluminium, calcium and titanium are usually the main elements in metallurgical grade silicon. Other elements are referred to as trace elements. Previous studies have provided a description of the intermetallic phases found in MG-Si material produced with standard process route [1, 2, 3, 4, 5]. The main intermetallic phases are FeSi2, Al3FeSi2, FeSi2Ti, Al2CaSi2, Al6CaFe4Si8, CaSi2, Al6Fe4Si6 and TiSi2. Some studies have been carried out to assess the effect of composition and cooling rate on the type and amount of particles.

Nevertheless, this empirical knowledge has not yet been fully systematized into an efficient and practical tool. The purpose of this paper is to present such a tool under development by SINTEF in collaboration with Elkem. The model is currently based on gathered literature data covering the major binary and ternary systems. The main challenge is in integrating it into a predictive microstructure model covering a large range of compositions and various solidification conditions. This paper will describe the microstructure model, its calibration and a simple application to illustrate the potential use in industrial product/process design. Please note that unless otherwise stated all alloy composition are given in wt%.

Microstructure model

The microstructure model, hereafter referred to as Sistruc, has been initially developed in 2009 by A.L. Dons following a similar approach as for the Alstruc model [6]. The main objective of this tool is to be predictive, fast and user-friendly which implies that one has to balance complexity with some simplifications and approximations. In the following sections, we will present the main aspects of the current version. One essential aspect of the current model is that it solves equilibrium phase formation during solidification. At any step during solidification, the solid-liquid interface is assumed to be at equilibrium and the phases form accordingly. Possible solid state phase transformations are not accounted for in the model.

Model equations

Two main values have to be computed by the model to determine the phase formation path: i) the concentration dependence of the liquidus temperature and ii) the solubility of the different phases. In addition, for some particles, the model also computes the particle composition based on the current liquid composition. The generic formula to compute the liquidus temperature is given by:

$$T_{liq} = 1414 + \sum_i \sum_{k=1}^{3} \alpha_i^k {C_i}^k + \sum_i \sum_{j \neq i} \beta_{ij} C_i C_j \quad (1)$$

where *i* denotes the solute element (Al, Ca, Fe, Ti, B and P are considered in the model) and C the concentration in the liquid, α_i^k are the coefficients of the third order polynomials.

The solubility limit for the solute elements is given by:

$$C_i^* = A_i e^{-\frac{B_i}{T}} \quad (2)$$

where T is the temperature in Kelvin.

The formation of the intermetallic compounds is generally defined by a combination of the previous information and the particle composition. For example for Al_3FeSi_2 phase, precipitation occurs when:

$$\frac{C_{Fe}}{C_{Fe}^*} \cdot \left(\frac{C_{Al}}{C_{Al}^*}\right)^3 > 1 \quad (3)$$

The value on the right hand side is adjusted to better fit the literature data. In some cases, the simple combination of concentration over solubility limit is not sufficient and another formula is used as for Al_2CaSi_2:

$$C_{Ca} \cdot C_{Al}^2 > A_{Al2CaSi2} e^{-\frac{B_{Al2CaSi2}}{T}} \quad (4)$$

For the quaternary phase $Al_6CaFe_4Si_8$, the lack of data has led to ignore the temperature dependence. Nevertheless, it was checked that the transformation occurs in the proper temperature range as described by Anglezio [2].

In addition, one has to compute the composition of the particles. The composition of the particles can be:

- fixed (usually stoichiometric, e.g. Al_2CaSi_2)
- temperature dependent (e.g. SiB_3 vs. SiB_6)
- liquid composition dependent (e.g. FeSi2 that is actually (Al, Ca)-$FeSi_{2.4}$)

The solidification of Si and liquid enrichment is, in the current version, simply computed assuming no diffusion in the solid phase and infinite diffusion in the liquid phase. The implementation of a more realistic model accounting for finite diffusion is planned for later releases.
At the solidification of cell *n*, for all elements *i*, the mass balance is according to:

$$f_l^{n-1} C_i^{n-1} = f_l^n C_i^n + \sum_j \varphi_j^n \varphi_j^{i,n} \quad (5)$$

where f_l^n is the liquid fraction remaining in the whole domain when step *n* is solidified, C_i^n is the "averaged" concentration of specie *i* in the remaining liquid at step *n*, φ_j^n is the mass fraction of phase j in the cell n, and $\varphi_j^{i,n}$ the composition of the phase *j*.

Algorithm

The solidifying grain is discretized into 200 cells (with geometric progression).The calculation starts by initializing the concentration and the solid fraction. The liquidus

temperature is computed from the initial concentration. Then at each solidification step (except last step), the following algorithm is employed:

1. Store the starting concentration
2. LOOP to find the appropriate amount of Si phase (sub-step is set at 1% of the current cell size)
    a. Compute the liquid concentration assuming a partial solidification of the cell without any precipitation based on the starting concentration
    b. LOOPs for precipitation
        i. Test if precipitation occurs for each particle based on this "trial" liquid concentration
        ii. If precipitation occurs, compute the composition and amount of precipitate that forms (applying the mass balance) until the solubility limit is reached
        iii. Update the "trial" liquid concentration with the new liquid concentration for that solubility limit
        iv. Go to the next particle type
    c. Test if the total amount of phases formed (including Si) is close to the mass of the cell, and if not go back to Step 2 and increase the amount of solidifying Si
3. From the previous steps we have now a list of particles that precipitate with their compositions and the precipitated amount. This amount corresponds almost to the mass of cell (>90%), therefore only a limited scaling is required.

User interface

Sistruc model is programmed in Free Pascal to allow easy build-up of user interfaces. The code structure is divided between handling user interaction and a mathematical core where the equations are solved. A modular approach has been used to enable further development of the code and introduction of more advanced models.
The user interface, as illustrated in Figure 1, is extremely simple when using the default options. The user needs only to enter the alloy composition and run the calculation. The program will then generate the history of temperature, liquid concentration, amount of phases, etc., to be plotted directly in the graphical user interface. Moreover, text files are generated for visualization and post-processing in a spreadsheet.

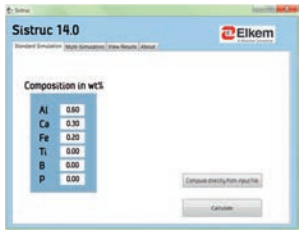

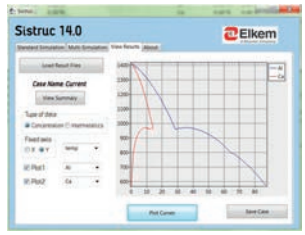

*** Initial composition in wt%
Element Alloy1
Al 0.600%
Ca 0.300%
Fe 0.200%
*** Average phases amount in the grain in wt% ***
Si-solid 98.337%
Al-eutectic 0.087%
Al3FeSi2 0.028%
Al2CaSi2 0.992%
Al6CaFe4Si8 0.556%

Figure 1. User-interface and microstructure summary output.

Additional options can be enabled through the addition of specific keywords in the input file. A tool is also available to run simultaneously a set of batch simulations for direct comparison of ranges of compositions. This interface will be extended to include

additional parameters such as solidification rate or ingot thickness to compute through thickness variations.

Model calibration

The current version of Sistruc is mainly calibrated by comparison with phase diagram data published in the literature. The parameters α_i^k from Equation (1) and A_i and B_i from Equation (2) are obtained by fitting the following binary phase diagrams: Al-Si, Ca-Si, Fe-Si, Si-Ti, B-Si and P-Si. Newly reassessed data [7] are used for some phase diagrams (e.g. Ca-Si and Si-Ti). Based on this first set of parameters, the calibration procedure is continued by dealing with ternary phase diagram: Al-Fe-Si [8, 9], Al-Ca-Si [10], Ca-Fe-Si [11], Al-Si-Ti [12] and Fe-Si-Ti [13]. The main focus is put on liquidus projections and how the model will predict critical points (e.g. eutectoid Al2CaSi2-CaSi2-Si). In addition when temperature curves are available, β_{ij} parameter in Equation (1) is determined. The equation for the formation of $Al_6CaFe_4Si_8$ has been previously established and is only slightly adjusted to take into account the change in predicted liquidus temperature.

Predicted solidification path for three systems are presented in Figure 2 to Figure 4 including the type of phase formed. The results are consistent with published liquidus projection. For example, eutectoid Al_2CaSi_2-$CaSi_2$-Si is predicted at 958 °C for a concentration of 24%Al and 25%Ca while the published data indicates 921 °C for a concentration of 22%Al and 28%Ca. This discrepancy results from two sources. First the fitting with the limited set of parameters for Equation (1) does not allow a very accurate description. At the critical point, the predicted temperature is 941 °C instead of 921 °C. Second, Sistruc algorithm induces some numerical approximations (for example in the successive treatment of the particle instead of simultaneous formation) that leads to a displacement of the critical point. Nevertheless the error amplitude seems acceptable for the objective of this microstructure model.

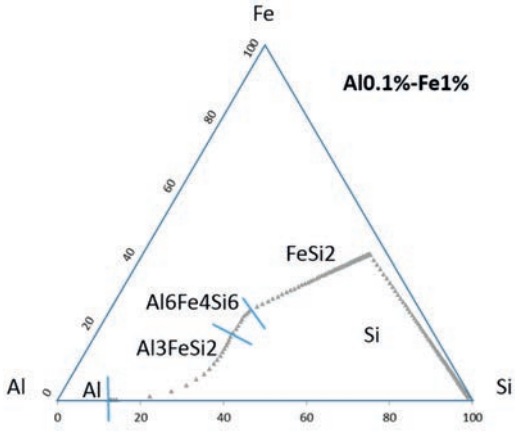

Figure 2. Computed solidification path for a silicon alloy with 0.1%Al-1%Fe

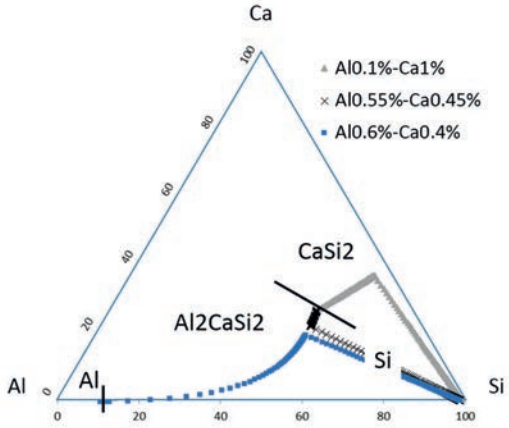

Figure 3. Computed solidification path for three silicon alloys with 0.1%Al-1%Ca, 0.55%Al-0.45%Ca and 0.6%Al-0.4%Ca

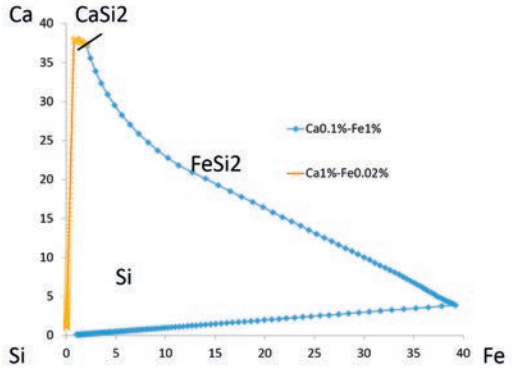

Figure 4. Computed solidification path for a silicon alloy with 0.1%Ca-1%Fe and 1%Ca-0.02%Fe

Additional work is planned to assess the predictive power of the model by comparison with solidification experiments and DTA measurements.

Application

In order to illustrate the potential of this new tool, one case study is presented. The study analyses the effect of alloy composition on the amount of the different precipitated phases.

Sistruc is used to here to tailor the composition in order to obtain desired intermetallic compounds for specific downstream process. The range of studied alloys is presented in Table 1. The results show that the model is able to reproduce the well-known effect of inverting the Al/Ca ratio between alloy 1 and 2 which leads to the disappearance of $CaSi_2$. Comparison of alloy 2 and 3 illustrates the effect of Fe content on the amount of

$Al_6CaFe_4Si_8$. Increasing again the amount of Al, leads to the formation of Al_3FeSi_2 instead of $FeSi_2$ which is beneficial for the reaction between silicon and methyl chloride. The presence of Ti will not only forms $TiSi_2$ (and usually $FeSi_2Ti$ but the model seems not very accurate for this compound) but also significantly increase the formation of Al_3FeSi_2 (+20% from alloy 5 to 6). Alloy 7 shows the effect of Fe on the different compounds in the presence of Ti.

Table 1. Effect of the alloy composition on the amount and type of intermetallic compounds

Element	Alloy 1	Alloy 2	Alloy 3	Alloy 4	Alloy 5	Alloy 6	Alloy7
Al	0.40 %	0.60 %	0.550 %	0.70 %	0.80 %	0.80 %	0.80 %
Ca	0.60 %	0.40 %	0.340 %	0.29 %	0.30 %	0.30 %	0.30 %
Fe	0.30 %	0.30 %	0.40 %	0.30 %	0.30 %	0.30 %	0.49 %
Ti						0.02 %	0.02 %
				Phases			
Si	97.54 %	97.85 %	97.85 %	98.08 %	97.96 %	97.91 %	97.58 %
FeSi2	0.67 %	0.41 %	0.49 %				
CaSi2	0.77 %						
Al2CaSi2	1.02 %	1.41 %	1.14 %	0.89 %	0.93 %	0.94 %	0.80 %
Al3FeSi2				0.05 %	0.07 %	0.09 %	0.06 %
Al-eutectic				0.15 %	0.23 %	0.22 %	0.14 %
TiSi2						0.05 %	0.05 %
Al6CaFe4Si8	0.00 %	0.34 %	0.52 %	0.83 %	0.81 %	0.80 %	1.37 %

The presented analysis illustrates how Sistruc can be used to quickly test different compositions, predict trends and also provides quantitative estimations.

Conclusion

A user-friendly microstructure model, Sistruc, has been developed to predict the formation of intermetallic compounds in metallurgical silicon during solidification. The model has been recently upgraded, calibrated and further developed. The model is based on a simplified approach. The model parameters have been calibrated with literature data for binary and ternary systems. The model has been applied to study the effect of the alloy composition on the appearance of specific phases.
As a conclusion, the current version of Sistruc is a good tool for industrial optimization of metallurgical silicon composition to reach specific requirements. While the calibration through literature phase diagram data is a good starting point, validation by comparison with solidification experiments is a necessary step to assess the predictive power of the model. Further improvements of the model are underway and will focus on the effect of solidification rate by accounting for finite diffusion in combination with a grain size prediction model.

Acknowledgments

The funding of Elkem and the Norwegian Research Council through the CORSICA project is greatly acknowledge.

References

[1] T. Margaria et al., "Intermetallic compounds in metallurgical silicon," in *INFACON 6*, 1992.

[2] J. C. Anglezio et al., "A study of the Si-rich domain of the Al-Ca-Fe-Si quaternary system," *Calphad,* vol. 18, no. 3, p. 311, 1994.

[3] T. Margaria, "Influence of cooling on silicon structure," in *Silicon for the Chemical Industry III*, Trondheim, 1996.

[4] G. C. Vogelaar, "Analysis of intermetallic phases in silicon ingots of different thickness," in *Silicon for the Chemical Industry III*, Trondheim, 1996.

[5] M. F. Møll, "Solidification of silicon - Macro- and microstructure as functions of thermal history and composition," PhD thesis, NTNU, 2014.

[6] A. L. Dons et al., "The alstruc microstructure solidification model for industrial aluminum alloys," *Met. Mat. Trans. A,* vol. 30, no. 8, p. 2135, 1999.

[7] J. Safarian et al., "Liquidus of silicon binary systems," *Met. Mat. Trans. BB,* vol. 42, p. 852, 2011.

[8] N. Krendelsberger et al., "On the reaction scheme and liquidus surface in the ternary system Al-Fe-Si," *Met. Mat. Trans. A,* vol. 38, 2007.

[9] V. Raghavan, "Al-Fe-Si (Aluminum-Iron-Silicon)," *J. Phase Equilibria,* vol. 23, no. 4, 2002.

[10] FactStage, [Online]. Available: http://www.crct.polymtl.ca/fact/facthelp/FS61new.htm.

[11] S. Ciu et al., "Thermodynamic optimization of Ca-Fe-Si system and its application to metallurgical grade Si-refining process," *Met. Mat. Trans. E,* vol. 1, p. 67, 2014.

[12] V. Raghavan, "Al-Si-Ti (Aluminum-Silicon-Titanium)," *J. Phase Equilibria,* vol. 30, no. 1, 2009.

[13] V. Raghavan, "Fe-Si-Ti (Iron-Silicon-Titanium)," *J. Phase Equilibria,* vol. 30, no. 4, 2009.

Growth of impurity phases below the melting point of silicon and consequences on fluidized bed reactor efficiency

A. Broggi, H. Tveit
Norwegian University of Science and Technology, Faculty of Natural Sciences and Technology, Trondheim (Norway)

Abstract

One of the challenges with silicones production is the accumulation of impurities from metallurgical grade silicon (MG-Si) in the fluidized bed reactor (FBR). Previous studies have demonstrated that the amount of intermetallic impurities is dependent on the thermal history of silicon. Two different thermal histories were chosen to investigate compositional changes. XRF chemical analysis in different areas of the cast confirm the effects of oxidation refining and segregation. The software SiStruc® calculated the expected contents of phases based only on thermodynamics. EPMA and BSE-SEM image analysis estimated the phase composition of an untreated and on the treated samples. A comparison between expectations from SiStruc® and EPMA-BSE combined analysis is also presented. It can be stated that there could be reactions between intermetallic phases. The effects of the annealing and refining on the composition are compared to the expected change on reactivity and selectivity in the silicones production.

1. Introduction

Silicones production is the most valuable application of silicon in chemical industry. Composition, concentration and shape of the intermetallics in MG-Si are key aspects in silicones production. The composition of the intermetallics is affected by the purity of the raw material, as well as by the refining and casting processes [1]. The composition of both the raw material and the furnace electrode sets the quantities of Fe and Ti, whereas Ca and Al contents can be corrected through ladle refining [2]. The casting technique influences the intermetallics' shape and size. The shape of the intermetallics can be characterized by controlling the thermal history of the solidification of silicon [3]. The aim is the best size and shape distribution, as well as low accumulation of particles in the fluidized bed reactor. When this occurs, the reactor is damaged and the reaction is more difficult to control [4].

Changes in shape and composition of the intermetallic compounds occur during solidification. The driving forces of these transformations are mainly diffusion and surface energy reduction [5-7]. Studies have been performed concerning the characterization of the intermetallics in MG-Si, by controlling the thermal history.

The distribution of intermetallic phases is influenced by the cooling rate and grain size of the starting material [8].

The annealing after solidification can have effects on microstructure. Rong [3] melted a silicon sample and solidified it at known cooling rate. A second sample was melted and held at 1200°C for 12 hours. Only the intermetallic particles were still in liquid state at this temperature, whereas the silicon matrix was solid. The shapes of the intermetallic phases changed and the grain size was not affected. In the starting sample the inclusions are found as elongated bands on the grain boundary. After annealing they appear as round particles. It seems that the elongated particles have split due to a decrease in surface energy. The temperature required to get an annealing effect is estimated to be above the melting point of the intermetallics, between 900°C and 1200°C.

Iron, aluminium, calcium and titanium are the most common impurities in MG-Si and make up to 4% of the total weight percentage. High amounts of $FeSi_2$ are expected to be found in MG-Si. The $FeSi_2$-phase will have two different microstructures according to the temperature of MG-Si. They are respectively called high temperature $FeSi_2$ (HT-$FeSi_2$ or $FeSi_{2.3}$) and low temperature $FeSi_2$, (LT-$FeSi_2$ or $FeSi_2$). If the cooling rate to room temperature is fast enough, the HT-$FeSi_2$ structure can be obtained at low temperatures. The cooling rate is fast enough in industrial solidification to avoid a complete transition from HT to LT-structure. It has been shown by a previous work that this transformation takes 3 hours at 700°C in order to be complete [9]. Besides, Anglezio et al. [10] have reported that the HT-$FeSi_2$ is stabilized by aluminium substitution in the lattice. According to Margaria [11] the maximum content of Al can be up to 8% at. in order to improve the stability in a efficient way. Boomgard [12], Tveit [13] and Bjorndal [14] state that the transformation occurs in two steps:

- *Step 1*: *HT-$FeSi_2$ → LT-$FeSi_2$(Si)*: The transformation occurs with a change in volume, and starts at defects such as cracks or grain boundaries. If these are not present, the reaction will be hindered.

- *Step 2: LT-$FeSi_2$(Si) → LT-$FeSi_2$(Si) + Si*: As soon as Step 1 has started, an interface will begin to move through the material. Behind the interface there will be a supersaturated LT-phase where silicon precipitates. As a matter of fact, the HT-phase structure has a high vacancy concentration in the Fe lattice. Therefore silicon precipitates can be noticed during this transition, especially at the grain boundaries. The lattice increases its dimension. Stresses and cracks are therefore generated because of silicon precipitation.

Margaria et al. [15] have analysed the variation in relative amounts of intermetallic phases after annealing at different temperatures. They identified the compounds by X-ray analysis and Scanning Electron Microscopy. Five annealings were performed at five different temperatures. It was noticed that the amount of quaternary phase $Al_6CaFe_4Si_8$ increased while the amounts of $CaAl_2Si_2$ and $FeSi_2$ decreased. The peak of this transformation is reached at about 925°C. An equilibrium reaction was written to explain this phenomenon. The reaction between intermetallic compounds could be a possible mechanism, but it was not proved in that work.

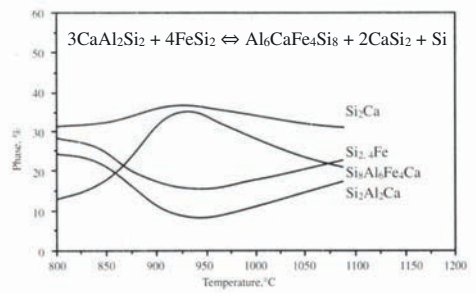

Figure 1: Effect of annealing on the relative fractions of intermetallic compounds [15]

Softwares have been developed to forecast the composition and amount of the intermetallic at a given impurity level. The PC-program SiStruc® was developed in 2009 [16]. Its main purpose consists of calculating the composition, amount and melting ranges of intermetallic phases in silicon, given the weight percentages of Fe, Ca, Al, Ti, B and P. The calculation developed in the program are based on directional solidification laws, such as Scheil equation. These conditions are not very close to the industrial solidification, but they can at least give a good expectation.

Forecasting the composition of silicon is important for a high final product quality. Silicon undergoes a reaction with methyl-chloride during the Direct process to produce dimethyl-dichlorosilane. There have been several attempts to describe the effect on the Direct process of the different intermetallic compounds, but there is no complete consensus about it so far. Many parameters interfere with reactivity and selectivity of the reaction. For this reason, experiments are difficult to reproduce, and results between different authors are difficult to compare. The results from these works have been gathered in Table 1.

Table 1: Effect on reactivity and selectivity of the intermetallic phases. Legenda: + = Positive effect; ÷ = Negative effect; n.p. = Analysis not performed

Phase	Reference	Reactivity		Selectivity	
		Reference	Sørheim [17]	Reference	Sørheim [17]
$FeSi_2$	[15]	÷	0	÷	0
$CaSi_2$	[15]	+	0	÷	÷÷
$FeSi_2Ti$	[15]	÷	0	÷	0
$Al_8Fe_5Si_7$	[18]	+	++	÷	÷
Al_2CaSi_2	[15,18]	++	+++	÷÷	÷÷
$Al_6CaFe_4Si_8$	[15,18]	0	÷	+	++
Al_3FeSi_2	[19]	++	n.p.	0	n.p.
$Al_4CaFe_4Si_6$	[19]	÷	n.p.	+	n.p.

In this case of study, samples from a MG-Si thin cast will undergo different thermal histories and casting conditions to investigate the effect on the phase composition. A relation between the variation in phase composition and expected effects on MCS production for each phase will be presented. The software SiStruc® will predict the phases present and confirm that industrial solidification is not happening at equilibrium conditions. An hypothesis about the mechanisms of the transformation can be made by looking at literature and results from previous works.

2. Experimental

2.1 Thermal history experiments

Three MG-Si samples were collected from a thin cast produced at the Elkem silicon production plant in Salten (Norway). The dimensions of each sample were of 10x10xτ mm, with τ varying between 30 and 45 mm and being the thin cast thickness. The first one was not treated at all, in order to be kept as reference. The second one shared a surface with the first sample. It was heated up to 600°C in the LHT 04/18 furnace, available at the department of Materials science and Engineering at NTNU. The temperature was kept for 17 hours, then the sample was cooled down to room temperature. These two samples will be respectively called untreated and treated samples from now on.

The third sample underwent a different thermal history. The annealing consisted of three steps, as shown in Figure 2. About 250 g of silicon from the original cast were crushed manually to a lump size of 2-3 cm diameter. They were heated up to 1450°C at a rate of 30°C/min in a cylindrical carbon mold exposed to air. The carbon crucible dimensions were respectively 10 cm diameter and 12 cm in height. The bottom of the mold is spherical-dome-shaped, with height of 5 cm. This temperature was maintained for 2 hours, in order to melt the material. Afterwards the lid of the furnace was opened and the sample was cooled down to 1200°C for annealing. The cooling rate for this step was measured to be 30°C/min. Once the annealing temperature had been reached steadily in the furnace, the lid was closed again and the temperature was maintained for 17 hours. In the end, the furnace lid was opened to cool down the mold as fast as possible to room temperature. A cooling rate of 20°C/min has been reached in this way. The sample with this thermal history has been called annealed.

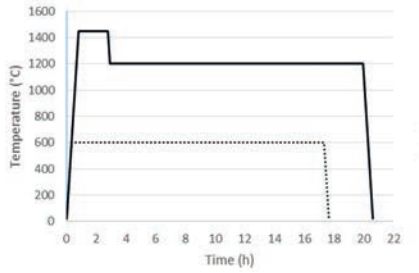

Figure 2: Schematic representation of the two thermal histories chosen. The continuous and dashed lines correspond respectively to the annealed and the treated sample.

2.2 XRF analysis

A XRF chemical analysis has been carried on the untreated material and the annealed sample. The material as cast was analysed by Henning Kjønli and the annealed material's analysis were carried out by Ingvill Vikan Myhre. Both the analysis have been performed at Elkem Thamshavn (Norway).

The composition of a piece of material as cast was obtained to represent the untreated sample. The annealed sample underwent a different analysis. Once a specimen for metallographic analysis had been extracted, the remaining material was sliced in the horizontal direction. The cut was performed manually by using a 2 mm thick diamond blade disc. Five slabs were obtained from this procedure. Each layer

had a thickness of approximately 5 mm. The external layers of carbides and oxides have been removed by grinding with SiC-paper.

2.3 EPMA, EDS and BSE analysis

EPMA (Electron Probe Micro-Analysis) has been performed on the treated and the annealed samples by using a JEOL JXA-8500F. The work has been performed together with Morten Raanes at the Department of Material Science and Engineering at NTNU. Points showing different contrast were selected to detect the relative mass percentage of Fe, Al, Si, Ca, Ti, Ba and Cu. It was possible to spot the correct phase thanks to the information collected from literature [3,17].

BSE images were chosen to analyse further the three samples. A Hitachi SU-6000 FE-SEM was used. Each image has a different scale according to the size of the intermetallic, but a resolution of 2560x1920 pixel was kept. The EDS-spectra detected the elements present in the phase in chosen single points. The phase percentage in the intermetallics was calculated by using the software ImageJ®. Extension of areas with different contrast have been measured. Table 2 resumes the number of intermetallics analysed with each method for each sample.

Table 2: Number of particles analysed and sum of their extension

Sample	EPMA	EDS	Total intermetallic area per sample (μm^2)
Untreated	0	54	113 633
600°C 17h Treated	29	31	166 507
1200°C 17h Annealed	21	33	171 761

3. Results

3.1 XRF and SiStruc® analysis

Table 3 gathers the percentages of impurities in the three cases. The values for the sample annealed at 1200°C for 17 hours are the average of the five slabs. An approximate composition of the untreated material is presented due to industry's restrictions. The relative variation is expressed by the following formula:

$$Relative\ variation = \frac{\%X_{annealed} - \%X_{untreated}}{\%X_{untreated}} \quad (1)$$

Table 3: Average value of the %wt. of Fe, Al, Ca, Ti found after XRF analysis

Element	Untreated	1200°C 17h Annealed	Relative variation
Fe	0.40	0.27	-20%
Ca	0.05	0.04	-35%
Al	0.15	0.12	-10%
Ti	0.05	0.02	-25%

Inserting these data in SiStruc® gave expectations about the content and the composition of the phases present in each sample. Table 4 resumes the results of the SiStruc® analysis and the relative variation between the two samples. The percentage in brackets next to the %wt expresses the mass fraction of the phase if only the intermetallic phases were considered. The relative variation is expressed by Eq. (1).

Table 4: SiStruc analysis performed on the untreated and the treated sample

Phase	%wt. untreated	%wt. annealed	Relative variation
$FeSi_2$	0.458 (47%)	0.361 (48%)	-21%
$Al_6CaFe_4Si_8$	0.190 (20%)	0.104 (14%)	-45%
$CaAl_2Si_2$	0.184 (19%)	0.118 (16%)	-36%
$TiFeSi_2$	0.093 (10%)	0.067 (9%)	-28%
$Al_8Fe_5Si_7$	0.023 (2%)	0.075 (10%)	+226%
$TiSi_2$	0.009 (1%)	0.009 (1%)	0%
Al_3FeSi_2	0.009 (1%)	0.015 (2%)	+67%
TOTAL	0.966 (100%)	0.749 (100%)	-22%

The total quantity of intermetallics decreases after the annealing. $FeSi_2$ is the most expected compound in both samples. The quaternary phase and $CaAl_2Si_2$ follow, but in the annealed sample their quantities decrease. $TiFeSi_2$ is present in the same relative mass fraction for each sample. $Al_8Fe_5Si_7$ is expected to increase after the annealing with respect to other phases. $TiSi_2$ and Al_3FeSi_2 might be found in low amounts.

3.2 EPMA and BSE-SEM analysis

3.2.1 Untreated and treated sample at 600°C

Figure 4 show two complex intermetallic particles from the untreated sample and the sample treated at 600°C. These two samples have been compared in the same paragraph since the microstructure was very similar. The particles come from the solidification fronts meeting point. This position in the cast lies in slightly below the centre of the thin cast. The material solidifies last in this section. All the phases predicted by SiStruc® can be seen in the two figures. $FeSi_2$ is both present at its high temperature (HT) and low temperature (LT) structure. They could be recognised from their stoichiometry, as well as by the presence of cracks and Si precipitates in the LT-$FeSi_2$. $Al_6CaFe_4Si_8$ and $Al_8Fe_5Si_7$ do not show peculiar shapes and are detected all over the sample. $CaAl_2Si_2$ is mostly present in the centre of the cast, especially at the edges of elongated intermetallics. $TiFeSi_2$ comes either as large particles at the borders of the intermetallics, or as rectangular precipitates in the intermetallics' cores. Eventual cracks formed go through $FeSi_2$ without crossing $TiFeSi_2$ particles in the majority of the cases. Other dissolved elements form compounds in minor quantity.

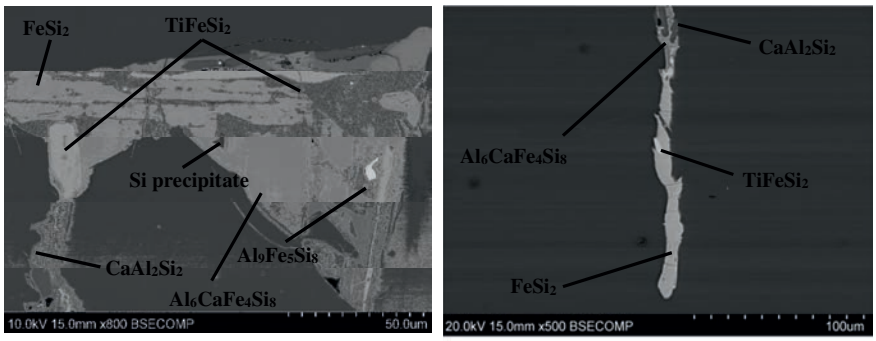

Figure 4: Two particles coming respectively from the solidification fronts meeting point of the untreated sample (a) and from the bottom of the treated sample at 600°C (b)

3.2.2 Sample annealed at 1200°C

Figure 5 shows two intermetallics found in the annealed sample. $FeSi_2$ is still the main compound present in the particles. HT-$FeSi_2$ was not found. Si precipitates and cracks are more frequent in this sample rather than in the other two. Their quantity increases where LT-$FeSi_2$ is detected. $Al_6CaFe_4Si_8$ was reduced in quantity, as predicted by SiStruc®. This causes $TiFeSi_2$ to be the second most common intermetallic in the annealed sample. $CaAl_2Si_2$ was not found in any particle chosen, even if it was expected by SiStruc® to be the second most present phase. $Al_8Fe_5Si_7$ occupies larger areas compared to what was seen in the untreated material. $TiFeSi_2$ changes its features about the particle size distribution. It is more common to find high number of $TiFeSi_2$ particles, with irregular shapes and small areas. Some particles kept the rectangular microstructure anyway.

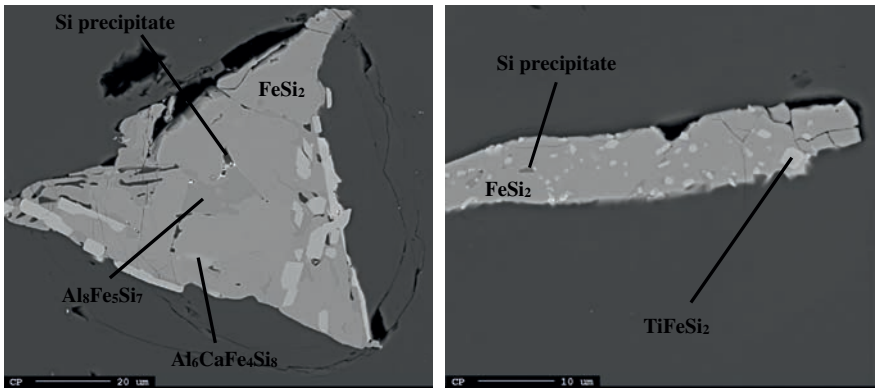

Figure 5: BSE images coming from the center (a) and bottom (b) of the sample annealed at 1200°C.

4. Discussion

4.1 Non-equilibrium effects: untreated sample

SiStruc® is a software merely based on thermodynamics. Solidification is far from equilibrium in this case. Data about %wt of different elements have to be handled carefully. Non-equilibrium conditions might have caused deviations from the previsions calculated by SiStruc®. $TiSi_2$ and Al_3FeSi_2 were expected to be found at least in low quantities in the untreated sample, whereas none of them was found. Besides, $Al_6CaFe_4Si_8$ is found in higher quantity than $CaAl_2Si_2$.

Having a look at the cooling ranges can explain these differences. Figure 6 shows the cooling ranges calculated by SiStruc® for the composition of the untreated sample. $FeSi_2$ will be the first compound which solidifies. It will be the most present because of the high content of Fe in the material. $TiSi_2$ and $TiFeSi_2$ will form at the same point, but previous works have verified that $TiSi_2$-formation reaction is hindered when there is a high presence of Fe [3,17]. $CaAl_2Si_2$ forms at a lower temperature compared to $Al_6CaFe_4Si_8$. Ca will be involved in the quaternary phase transformation first. What is left will start reacting with Al and Si to form $CaAl_2Si_2$. It can be hypothesized that the formation of $Al_6CaFe_4Si_8$ has a faster kinetics than the formation of $CaAl_2Si_2$.

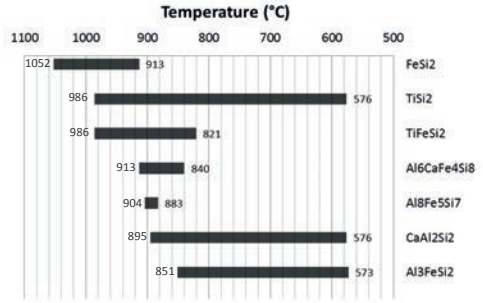

Figure 6: Cooling ranges of intermetallic phases calculated by SiStruc®. The temperatures delimiting the melting range are written on the side of each bar

It is not true that the longer the melting range, the more phase will be present. The amount of some elements in the material will be the determining factor. Ca and Ti are present in a lower extent compared to Fe and Al. Ca is limiting the quantity of Ca-containing phases, and Ti does the same for the $TiFeSi_2$ phase.

4.2 Refining and segregation effects in the annealed sample

Changes in composition were expected in the annealed sample. Silicon was molten in air. A white layer was noticed on the top of the cast, once the sample was extracted from the furnace. This layer is generated by the oxidation of the material during the melting step. Elements diffused to a slag phase from MG-Si. The slag will contain mainly Si, Al and Ca oxides. All these elements have negative $\Delta G°$ at 1450°C [20], which is the highest temperature reached during the treatment. Ca also starts to evaporate at temperatures slightly above 1450°C. This transformation could have happened as well, thus further reducing the content of calcium.

Minor oxidation effects could have altered the quantity of Fe and Ti. However, their ΔG for the oxidation reaction is less negative than silicon. Once Si becomes solid, elements are not able to diffuse rapidly to the slag, hence the lower distribution coefficients for Ti and Fe compared to Al and Ca [21]. The segregation effect becomes the most plausible hypothesis for Fe and Ti decrease and displacement in the sample (Figure 7). The material for the chemical analysis was taken from the sides of the cast and not from the center. The segregation is controlled by the heat exchange coming from the lateral sides of the mold, as well as from vertical solidification. A solidification front is developing from the bottom with a slower velocity compared to the solidification velocity from the sides and from the top. This can be said since the sample was standing on a warm surface. The temperature gradient developed from the bottom was therefore small.

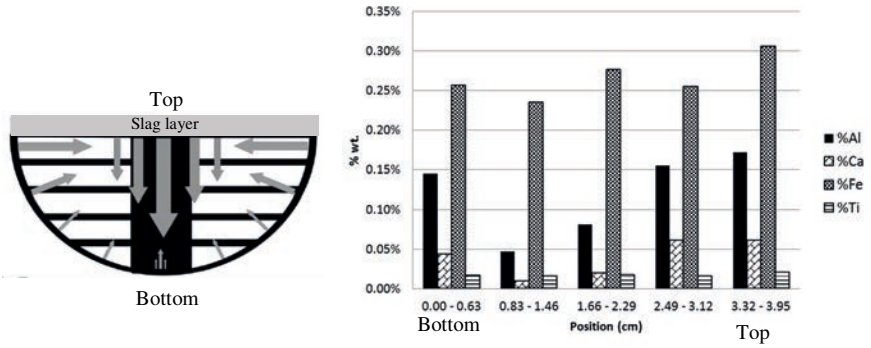

Figure 7: (a) Segregation and solidification sketch compared to the material extracted for chemical analysis (white areas) and the material collected for metallographic analysis, or discarded by cutting (black areas). The horizontal and the inclined arrows show the movement of impurities caused by segregation effects, whereas the vertical arrows show the effects of directional solidification. (b) Concentration profiles of impurity elements: results from XRF analysis of the annealed sample at 1200°C.

4.3 Chemical reactions: annealing effect

4.3.1 Reaction between intermetallics

The first one is a proposed mechanism by Margaria [8] which involves several intermetallic phases in MG-Si. The second is a structural transition from a metastable to a stable lattice structure of the $FeSi_2$ phase. This mechanism was confirmed by several experiments and previous works [9-13]. According to Margaria [8], an annealing at 900°C decreases the quantity of $CaAl_2Si_2$ and increases the amount of $Al_6CaFe_4Si_8$ according to the equilibrium:

$$3CaAl_2Si_2 + 4FeSi_2 = Al_6CaFe_4Si_8 + 2CaSi_2 + Si \quad (2)$$

Unfortunately the present work cannot prove that this reaction is happening. The equilibrium reaction should increase the content of quaternary phase after an annealing. However, the quantity of Ca lost during the melting step was higher than expected. Therefore the quaternary phase is noticed in lower amounts in the annealed sample. $CaAl_2Si_2$ might have not formed. If it did, the annealing would start the reaction until the total consumption of $CaAl_2Si_2$. $CaSi_2$ was not found in the annealed sample. The chemical composition of the analysed silicon does not fall in the $CaSi_2$ existing range in the graph traced by Margaria [15].

4.3.2 $FeSi_2$ transition

Si precipitates are formed in areas close to the $FeSi_2$ phase. This compound undergoes a transition from $FeSi_{2.4}$ (high-temperature structure) to $FeSi_2$ (low-temperature structure) according to the equilibrium:

$$FeSi_{2.4} = FeSi_2 + 0.4Si \quad (3)$$

This reaction increases the lattice parameters of this compound. Dilatation of lattice induces stresses in the phase and causes cracks. Cracks created pass through the silicon matrix and all the common intermetallic phases except $TiFeSi_2$, as shown

from a similar work performed by Jo [22]. The silicon matrix absorbs part of the stress caused by this dilatation. This material is universally known for its very low ductility. However, it seems it has enough to absorb this stress. If the ductility of silicon had not been high enough, cracks would have widely branched all over the surface with high speed. The transformation has partially occurred in the untreated sample during its solidification in the industrial mould. Annealing can enhance the formation of LT-$FeSi_2$ and the precipitation of silicon. Cracks will be larger and more common in an annealed sample. Figure 8 shows cracks in intermetallics from the annealed sample. A comparison with the untreated sample can be referred to Figure 4.

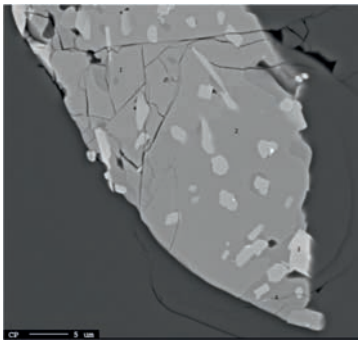

Figure 8*:* Cracks due to $FeSi_2$ phase transformation in a particle of the annealed sample

4.4 Phase characterization

Figure 9 reports the relative phase content predicted by SiStruc® compared to the amount measured with ImageJ® in the three samples. $CaAl_2Si_2$ is present in lower amounts, since it is the last Ca-containing phase which solidifies. Ca would have already reacted to form $Al_6CaFe_4Si_8$. $FeSi_2$ has a similar relative percentage between the untreated sample and SiStruc®. Fe will rather form $FeSi_2$ or $TiFeSi_2$ in the annealed sample, since the Ca content is reduced by the oxidative refining effect. Ti is affected only by segregation, therefore $TiFeSi_2$ will be relatively more present in the annealed sample. $Al_8Fe_5Si_7$ increases relevantly, but its relative percentage is still very low. In the end, the similarity between the sample treated at 600°C and the untreated sample shows that at this temperature no changes in phase composition are happening.

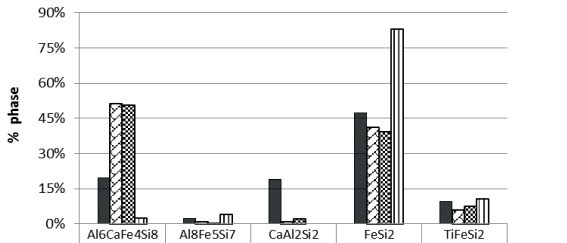

	Al6CaFe4Si8	Al8Fe5Si7	CaAl2Si2	FeSi2	TiFeSi2
SiStruc - Untreated	20%	2%	19%	47%	10%
Untreated	51%	1%	1%	41%	6%
600°C 17h Treated	51%	0%	2%	39%	7%
1200°C 17h Annealed	3%	4%	0%	83%	11%

Figure 9: Comparison between SiStruc® calculation and image analysis

5. Conclusions

Three MG-Si samples underwent three different thermal histories. The first one was untreated, the second one was treated at 600°C without a melting step and the last one was melted at 1450°C for 2 hours, then annealed at 1200°C. Both the treatments lasted for 17 hours. XRF chemical analysis and EPMA detected chemical and phase composition. It was demonstrated that the first two samples have the same microstructure. This implies that at 600°C no change occurs in the material.

Oxidation, segregation and chemical reactions are the mechanisms of the changes in impurity level and displacement in the samples. The first acts as a slag refining treatment. Segregation moves Fe and Ti to the center and the top of the mold. The reactions are of two kinds. The first reaction consumes $CaAl_2Si_2$ and $FeSi_2$. $Al_6CaFe_4Si_8$, $CaSi_2$ and Si are supposed to increase, but the oxidation step did not allow the creation of Ca-containing phases. In the second reaction, $FeSi_2$ undergoes a transition from HT- to LT-structure. This decreases the percentage of $FeSi_2$ and creates silicon precipitates. Experiments could have been carried on in an inert atmosphere to limit compositional changes. Refining and segregation effects needed to be discussed together for the annealed sample.

Final considerations about the effects of the annealing and refining on the production of MCS are resumed in Table 5 and 6. Table 5 regards the impurity level change for each intermetallic phase's relative percentage. Table 6 has been formulated by a comparison with Table 1. The conclusions are that refining effects decrease both reactivity and selectivity, whereas annealing increases selectivity but decreases reactivity.

Table 5: Variation in relative phase percentage after refining at 1450°C for 2 hours, followed by annealing at 1200°C for 17 hours. Legenda: + = increase; 0 = unvaried; ÷ = decrease

Effect	$FeSi_2$	$TiFeSi_2$	$Al_8Fe_5Si_7$	$CaAl_2Si_2$	$Al_6CaFe_4Si_8$
Annealing	÷	0	0	÷	+
Refining	+	+	+	÷	÷

Table 6: Expected effects on MCS production after a melting step of 2 hours at 1450°C and an annealing at 1200°C for 17 hours. Legenda: 0 = unvaried; P = moving towards +; N = moving towards ÷

Effect	Phase	Reactivity change	Selectivity change
Annealing • Ca-ternary phase to Ca-quaternary phase • Reduced $FeSi_2$	$FeSi_2$	P	P
	$TiFeSi_2$	0	0
	$Al_8Fe_5Si_7$	0	0
	$CaAl_2Si_2$	N	P
	$Al_6CaFe_4Si_8$	N	P
	OVERALL	**N**	**P**
Refining • Reduced Al and Ca content in MG-Si	$FeSi_2$	N	N
	$TiFeSi_2$	N	N
	$Al_8Fe_5Si_7$	P	N
	$CaAl_2Si_2$	N	P
	$Al_6CaFe_4Si_8$	P	N
	OVERALL	**N**	**N**

Acknowledgements

This work was supported by Elkem AS (Norway). The authors thank Vegar Andersen, Kjell Håkon Berget, Tobjørn Røe and Harry Rong from Elkem AS (Norway) for comments that greatly improved the manuscript and for the great interest shown for this work.

References

1. S. Bernardis, *Engineering impurity behaviour on the micron-scale in metallurgical-grade silicon production,* Doctoral thesis at Massachusetts Institute of Technology, Cambridge, USA, 2012
2. A. Schei, H. Tveit, *Production of silicon alloys*, Trondheim: Tapir Forlag, 1998
3. H. Rong. *Silicon for the direct process to methyl-chlorosilanes*, Doctoral thesis at Institute for inorganic chemistry, NTH Norge tekniske Høgskole, Trondheim, Norway,1992.
4. J.O. Hoel. *Fluidized bed reactor presentation (private communication)*, Trondheim, Norway, 2014
5. E.D. Hondros, *Interfacial and surface thermochemistry*, North-Holland: Cahn R.W. and Haasen P.Eds. , 1983
6. P.Shewmon, *Diffusion in solids*, The mineral, metals & materials society, 1983
7. A.P. Sutton*, Interfaces in crystalline materials*, University of Michigan, USA: Clarendon press, 1995
8. T. Margaria, *Identification and Control of the Characteristics of Silicon used in Direct Synthesis*, in "Silicon for the chemical industry", 1994, pp. 69– 80
9. J.A. deHuff, *The structure of ferrosilicon*, Electrical furnace proceeding, 1969, pp.167–174.
10. J.C. Anglezio et al., *Characterization of Metallurgical Grade Silicon*, Journal of Materials Research, **5**, 1990, pp.1894–1899
11. T. Margaria. et al., 1996. *Silicon Refining: Experimental Studies and Industrial Means to Control Silicon Quality*, in "Silicon for the chemical industry", 1996, pp.21–31
12. J. van den Boomgaard, *Stability of the high-temperature phase $FeSi_2$*. Journal of the iron and steel institute, 1994
13. H. Tveit, 1988. *Størkning av 75% Ferrosilisium: Forløp. struktur og styrke*. Doctoral thesis at NTH Norge tekniske Høgskole, Trondheim, Norway 1988
14. M. Bjorndal, *Studier av en faseovergang i 58% ferrosilisium ved hjelp av elektronmikroskopi*, Master thesis in Physics of Materials, NTH Norge tekniske Høgskole, Trondheim, Norway 1990
15. T. Margaria et al., *Intermetallic compounds in metallurgical grade Silicon*, in "INFACON", Cape Town, 1992, pp. 209–214.
16. A.L. Dons, Final report Si-struc-SINTEF F9400, 2009
17. H. Sørheim, *The influence of intermetallilc phases on the production of methylchlorosilanes,* Doctoral thesis at NTH Norge tekniske Høgskole, Trondheim, Norway 1994
18. G. Laroze et al., *Proceedings of the Silicon for the chemical industry*, in "Silicon for the chemical industry", Geiranger, Norway, 1992, pp. 151–163.
19. G. Schüssler,. NO Patent 169831.
20. D. Gaskell, D, *Introduction to the thermodynamics 5th ed*., New York (USA): Taylor and Francis, 2008
21. K. Morita et al., *Thermodynamics of solar-grade-silicon refining,* Intermetallics, **11**, 2003 pp.1111–1117.
22. M.R. Jo et al., *A nano-Si/FeSi 2 Ti heterostructure with structural stability for highly reversible lithium storage*, Nanoscale, 6(**2**), 2014, pp.1005–1010.

A new and fast method for determination of boron, phosphorus and other trace elements in metallurgical grade silicon

A. Rietig, J. Acker
Brandenburg University of Technology Cottbus-Senftenberg, Faculty 2 - Department of Physical Chemistry, 01968 Senftenberg, Germany

Abstract

A new method for accurate and precise determination of non-metallic and metallic impurities in silicon was developed and statistically validated. The first step is the fast dissolution of silicon in a microwave-assisted high pressure system to minimize a loss of phosphorus. The essential innovation is the use of the concentrated digestion solution for ICP-OES measurements. This approach avoids the common removal of the silicon and acid matrix by volatilization, which can cause considerable losses of boron. Finally, for the ICP-OES measurements in such high-silicon matrices the optimum measuring conditions were determined and a careful selection of emission lines with respect to selectivity, spectral and non-spectral inferences and matrix effects was performed. The method of matrix matched calibration (MMC) is used for quantification of the impurities' contents. For Al, Mg, Ca, Ti, Cr, Mn, Fe, Ni, Cu, Zr and P the validation was performed against certified reference materials (IPT134, IPT135, NIST57b). To validate the determination of boron 9 silicon samples of different boron contents from three interlaboratory comparisons were used. The new procedure allows the determination of impurities of 4N-silicon (12 elements) with high precision and accuracy.

Introduction

Metallurgical silicon (MG-Si) is an important raw material in silicon industry. Both metallic and non-metallic impurities significantly influence the reaction behaviour of silicon as known from the hydrochlorination or the Müller-Rochow reaction. All industries that use silicon need to determine the amount of impurities with high precision and high accuracy in the shortest possible time.

Most crucial for the chemical analysis are the digestion and the subsequent sample preparation. After the dissolution of MG-Si in a mixture of HF/HNO_3 the matrix components, i.e. the high amount of dissolved silicon (H_2SiF_6) and the excess of the acids HF and HNO_3, have to be removed by evaporation since they produce massive interferences during the measurements by ICP-OES (optical emission spectrometry

with inductively coupled plasma). Both steps bear an enormous potential to lose boron and phosphorus which are known to form several volatile compounds.

How can these losses be explained? According to the model of silicon dissolution in HF/HNO_3 mixtures by Robbins and Schwarz the reaction products are only H_2SiF_6, NO and H_2O [2,3]. However, this model turned out to be insufficient: The reduction of nitric acid yields to various nitrous oxides, such as NO_2 [4], NO, N_2O [7] and N_2O_3 [4,5] and proceeds finally to the ammonium ion [6]. Besides the nitric acid other reactive species have been identified that are involved in the reaction again [4]. Kooij et al. detected hydrogen as reaction product [7], which was later quantified as function of the etching mixture composition and temperature [8]. The material balance by Acker et al. reports the formation up to 0.33 mol H_2 per mol of dissolved silicon in a mixture of 90% HF / 10% HNO_3 (v/v) [9]. So it is reasonable to assume that the massive liberation of nitrogen oxides and hydrogen favours losses of volatile boron and phosphorus compounds throughout the dissolution of silicon.

At first the volatile phosphorus compounds should be discussed. It is known that phosphine is formed from phosphidic intermetallic compounds by hydrolysis in water. During the dissolution of highly doped silicon in alkaline medium already the formation of gaseous PH_3 is indicated by its characteristic smell [10]. Once formed, PH_3 is lost for the chemical analysis since it practically not hydrolyzes in aqueous solution. [11] Furthermore, it is reasonable to assume, that PF_3 and PF_5 are formed in the dissolution of Si. PF_3 hydrolyzes very slowly in aquerous solution to phosphorous acid and HF (Eq. 1) [11].

$$PF_3 + 3\,H_2O \longrightarrow HPO(OH)_2 + 3\,HF \tag{1}$$

H_3PO_3 is a strong reducing agent that is oxidized [11] to phosphoric acid (Eq. 2).

$$HPO(OH)_2 + H_2O \rightleftharpoons PO(OH)_3 + 2\,H^+ + 2e^- \tag{2}$$

In aqueous solution PF_5 hydrolyses slowly and stepwise via phosphoryl fluoride to phosphoric acid [11] according to Eq. 3.

$$PF_5 \underset{-2HF}{\overset{+H_2O}{\rightleftharpoons}} POF_3 \underset{-HF}{\overset{+H_2O}{\rightleftharpoons}} PO(OH)F_2 \underset{-HF}{\overset{+H_2O}{\rightleftharpoons}} PO(OH)_2F \underset{-HF}{\overset{+H_2O}{\rightleftharpoons}} PO(OH)_3 \tag{3}$$

Whichever gaseous phosphorus compound is formed, extensive studies by ICP-OES and ion chromatography proved that the dissolved phosphorus is entirely present as phosphate. This implies that the major loss of phosphorus primarily occurs during Si dissolution [10].

BF_3 was identified as the major volatile boron compound in the HF/HNO_3 dissolution of silicon [8]. It was furthermore shown, that boron losses up to 30% can be achieved if silicon is dissolved under harsh conditions and high dissoluion rates [10]. Under moderate conditions most of the BF_3 seems to react with water to give boric and hydrofluoric acid (Eq. 4).

$$4\,BF_3 + 3\,H_2O \longrightarrow B(OH)_3 + 3\,HF \tag{4}$$

BF_3 reacts with hydrofluoric acid subsequently to tetrafluoroboric acid (Eq. 5) [11]:

$$BF_3 + HF \longrightarrow 3\,HBF_4 \tag{5}$$

HBF_4 and boric acid are in equilibrium to each other and linked by several intermediates, which is determined by HF/F^- concentration and pH [13]:

$$HBF_4 \underset{\mp HF}{\overset{\pm H_2O}{\rightleftharpoons}} HBF_3(OH) \underset{\mp HF}{\overset{\pm H_2O}{\rightleftharpoons}} HBF_2(OH)_2 \underset{\mp HF}{\overset{\pm H_2O}{\rightleftharpoons}} HBF(OH)_3 \underset{\mp HF}{\overset{\pm H_2O}{\rightleftharpoons}} HB(OH)_4 \tag{6}$$

In contrast to phosphorus, boron has the potential to evaporate during the evaporation of the silicon and acid matrix. The volatility of BO_x species from HF-free

neutral and acidic aqueous solutions was intensively studied [14,15]. To avoid such losses the complexation of boron with mannitol was proposed [16-20]. Volatilization procedures at moderate temperatures stopped before drying showed identical recoveries of boron regardless mannitol was added or not [19]. Gaillardet et al. were not able to confirm a complexation of boric acid with mannitol at a pH lower than 7 [16]. In contradiction to the volatile BO_x species, an evaporation of volatile BF_3 from HBF_4 during the removal of the silicon and acid matrix components according to Eq. 7 had not been detected yet [10].

$$HBF_4 \xrightarrow[\text{[HF containing solution]}]{\Delta T} HF_{(g)} + BF_{3(g)} \quad (7)$$

In summary, the digestion of Si and the evaporation of the silicon and acid matrix are the most sensitive steps in the analysis of MG-Si. Both can cause serious losses of phosphorus and boron. The aim of this work is the development of a new procedure, which minimizes the losses of boron and phosphorus during the digestion and which completely renounces the critical step of matrix evaporation. Because of the high-silicon and acid matrix ICP OES was the method of choice to quantify the impurity concentrations. The new method was applied for the analysis of the SRM's NIST57b, IPT134, IPT135, as well as in three interlaboratory comparisons. A detailed statistical assessment of the method including Gaussian error propagation over the whole method is applied to demonstrate their accuracy and precision.

Experimental

Materials and reagents

Solid silicon samples were dissolved in mixtures of deionized water (18 MΩ cm^{-1}, Milli-Q), 65% (w/w) HNO_3 (suprapur, Merck Millipore) and 40% (w/w) HF (suprapur, Merck Millipure). The following silicon samples were used: Electronic-grade p-type silicon (Silchem GmbH Freiberg, Germany: 10.5 Ω cm) with a particle size ≥ 2 mm, the standard reference materials SRM 57b (National Institute of Standards and Technology), IPT 134 and IPT 135 (Instituto de Pesquisas Tecnológicas, Sáo Paulo, Brazil), as well as a total of 9 MG-Si samples from interlaboratory comparisons (FerróPem) [25-27] with a particle size < 250 µm.

For preparation of calibration standards and sample dilutions a mixture of 1% (v/v) HNO_3 / 1% (v/v) HF (each suprapur, Merck Millipore) is used. Multi-element calibration standards are prepared from stock solutions with a concentration of 1 g L^{-1} (Merck, Roth).

Microwave assisted digestion procedure

500 ± 5 mg of silicon samples were directly weighed into the microwave vessel. For silicon samples with an average particle size < 2 mm, 28 mL of an acid mixture of 5.65 mol L^{-1} HF / 0.85 mol L^{-1} HNO_3 were added. Before sealing the vessel the total mass of the sample mixture was noted. For samples having an average grain size > 2 mm, 18 mL of an acid mixture of 8.6 mol L^{-1} HF/ 1.35 mol L^{-1} HNO_3 were added. After a successful digestion 10 mL of water (18 MΩ cm^{-1}, Milli-Q) were added to obtain a comparable acid matrix for any digestion solutions.

Adapted from about 50 variations in acid mixture compositions and temperature-time programs for the high-pressure microwave digestion system (MLS Ethos Start, 100 mL PTFE vessels, ϑ_{max}=120°C), the following procedure was found to be optimum. The temperature was first raised from room temperature to 50°C within 3 min, and then held at that temperature for 20 min. Next, the temperature was

increased to 80°C within 3 min and held for 20 min. Finally, the vessels were linearly heated over 5 min to 120°C, with a holding time of 30 min. After cooling the sample the total mass of the sample mixture was noted again in order to determine the mass loss caused by escaping reaction gases during digestion. The digestion solution was directly used without further treatment to prepare sample solutions for measurements. A digestion solution of electronic-grade silicon (eg-Si) acts as method blank.

Sample preparation and ICP-OES measuring conditions

At first the sample was scanned using ICP-OES to determine the approximate element contents. For this procedure the digestion solution was diluted with a mixture of HF/HNO_3 (each 1% (v/v)) so that the content of the dissolved sample is approximately 2 mg g^{-1}. The method blank solution was used to prepare the scan standard which was diluted to the same content of dissolved silicon and spiked with a multi-element standard with typical element concentrations.

With the knowledge of the approximate element contents the sample solution was diluted with HF / HNO_3 (1% (v / v)) to match the contents of the dissolved sample between 1 mg g^{-1} and 4 mg g^{-1} depending on the scanned element contents. A multi-element standard stock solution was prepared in such a way that the element concentrations matched to the ratios of the impurity element concentration obtained by the ICP-OES scan. Aliquots of this standard stock solution were added to a constant aliquot of the method blank solution with a silicon content comparable to the sample solutions. A 6-point calibration was made at equidistant intervals so that the middle of the calibration ranges represents the element concentrations of the sample.

To determine the 12 major impurity elements (B, Mg, Al, P, Ca, Ti, Cr, Mn, Fe, Ni, Cu, Zr) an (ICP-OES) with duo-view option (iCap 6500 DUO, Thermo Scientific, Germany) was used. The HF-resistant sample introduction system was equipped with a parallel path nebulizer made of PEEK (MiraMist, Burgener Inc.), a cyclonic PTFE spray chamber (Glass Expansion) and a ceramic injection tube (ibid.). The plasma and integration parameters are listed in Table 1.

Table 1: Instrumental and integration conditions of the ICP-OES

RF incident power [W]	1150	Plasma viewing mode	axial or axial and radial
Plasma argon flow rate [L min^{-1}]	12	Maximum averaging time [s]	
Auxiliary argon flow rate [L min^{-1}]	0.5	UV (axial / radial)	20 / 15
Nebulizer argon flow rate [L min^{-1}]	0.5	Vis (axial / radial)	10 / 5
Sample uptake rate [U min^{-1}]	50	Subarry readout	
Inner diameter of the torch injector [mm]	2	width	20

Selection of element characteristic emission lines for ICP-OES analysis was carried out after detailed checks of interferences with other analyte elements and with silicon as the major matrix component. Finally, the selection was made according to the criteria of low interferences, high intensities and low signal-to-background ratios. In order to uncover unexpected spectral and non-spectral interferences, at least 3 emission lines are measured for each element. The most suitable analytical emission wavelengths for the measurement in high silicon matrices are summarized in Table 2. The Ar emission at 404.442 nm is used for monitoring the plasma stability, and the Si emission at 390.552 nm to check the consistency of the matrix.

Table 2: Selected analytical emission wavelength for ICP-OES, (I): atom emission, (II): ion emission

element	analytical wavelength / nm				
B	182.591 (I)	/ 182.641 (I)	/ 208.893 (I)	/ 208.959 (I)	/ 249.678 (I)
Mg	279.553 (II)	/ 280.270 (II)	/ 285.213 (I)		
Al	237.312 (I)	/ 308.215 (I)	/ 309.271 (I)	/ 394.401 (I)	/ 396.152 (I)
P	177.495 (I)	/ 178.284 (I)	/ 178.766 (I)	/ 185.942 (I)	/ 213.618 (I)
Ca	315.887 (II)	/ 317.933 (II)	/ 393.366 (II)		
Ti	334.941 (II)	/ 336.121 (II)	/ 337.280 (II)	/ 338.376 (II)	
Cr	205.552 (II)	/ 206.149 (II)	/ 267.716 (II)	/ 283.563 (II)	
Mn	257.610 (II)	/ 260.569 (II)	/ 279.482 (I)	/ 293.930 (II)	
Fe	238.204 (II)	/ 239.562 (II)	/ 259.837 (II)	/ 259.940 (II)	/ 261.187 (II)
Ni	216.556 (II)	/ 231.604 (II)	/ 341.476 (I)	/ 352.454 (I)	
Cu	204.379 (II)	/ 213.598 (II)	/ 224.700 (II)	/ 324.754 (I)	/ 327.396 (I)
Zr	327.305 (II)	/ 343.823 (II)	/ 349.621 (II)		
Si	390.552 (I)	*to control matrix stability*			
Ar	404.442 (I)	*to control plasma stability*			

Results and discussion

ICP-OES performance and selection of analytical emission lines

The ICP-OES analysis in high-silicon and acidic matrices requires a reselection and critical assessment of the analytical emission lines. To identify possible spectral and non-spectral interferences originated by such matrices the silicon/acid concentration in a multi-element standard solution (cf. Table 3) was increased gradually from 0 to 5 mg g^{-1} with the help of a method blank solution. With increasing silicon and acid concentrations, a dramatic decrease of the signal-to-background ratio was found for all emissions in the UV range, while the emissions in the visible range are not significantly affected by the matrix.

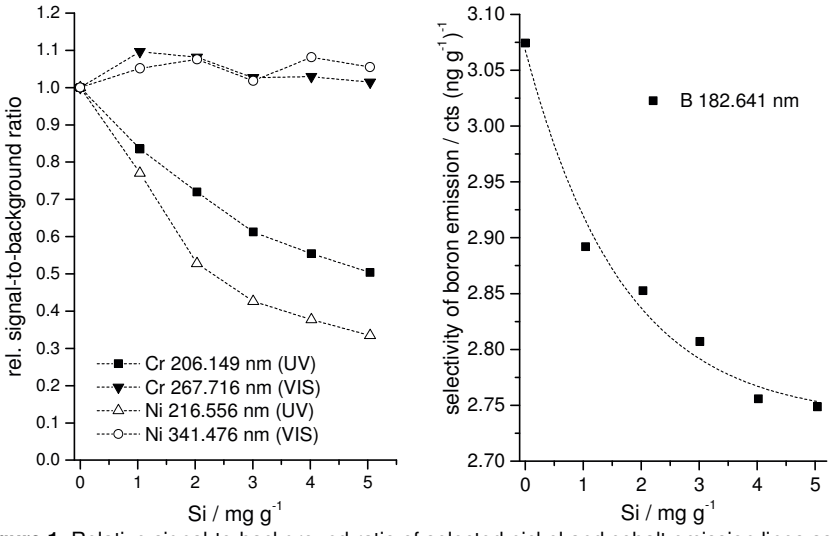

Figure 1: Relative signal-to-background ratio of selected nickel and cobalt emission lines as a function of silicon matrix concentration for standard solutions of 67 ng g^{-1} Ni and 67 ng g^{-1} Co (left) and selectivity (given as slope of calibration function) of boron emission at 182.641 nm as a function of silicon concentration, determined by calibrations from Table 3 (right).

Fig. 1 left, illustrates this in the case of selected nickel and cobalt emissions; the signal-to-background ratio is represented relatively to that of a silicon-free solution. In particular for the non-metals boron and phosphorus, which exclusively show atomic emissions with sufficient intensity in the UV range, a decrease in selectivity with increasing silicon and acid matrix was found. (Fig.1, right)

Additionally, the high-silicon content complicated the determination of phosphorus in the analysis solutions by spectral interferences as shown in Fig. 2. Apart from the interference of copper with the most intensive phosphorus emission lines 177.495 nm and 213.618 nm, an additional direct interference with silicon at 213.618 nm was observed (Fig. 2). A determination of phosphorus in the required concentration range is not possible solely by matrix matching of the calibration standards.

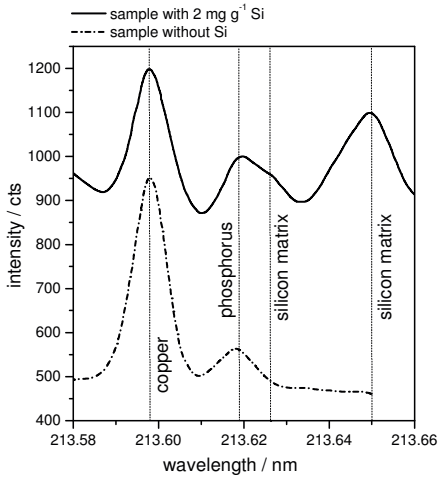

Figure 2: Comparison of spectra between a silicon-free calibration solution (50 ppb Cu, 80 ppb P) and a real sample matrix with 2 mg g^{-1} silicon matrix (25 ppb Cu, 60 ppb P).

After careful assessment regarding spectral and non-spectral interferences between the matrix and the analyte element emission lines, the most suitable emission lines for the analytical determination of metals and non-metals in high-silicon and acid matrices are summarized in Table 2.

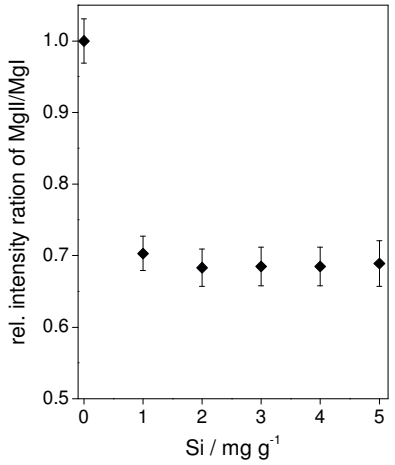

Figure 3: Relative intensity ratio between Mg ion emission at 280.270 nm and Mg atom emission at 285.213 nm of magnesium normalized to the MgII/MgI intensity ratio of the silicon free solution

Another important contribution to the quality of the analytical measurements in such high-silicon and acid matrices is plasma stability. The stability control was performed by means of the scattering of the measured Ar emission intensities [21] both as short-term stability (internal measurement replications) as well as long-term stability (series of measurements). Furthermore, there was a permanent monitoring of the intensity ratio MgII /MgI, which indicates changes in the excitation conditions with increasing silicon and acid matrix. [21-23] Fig. 3 shows that the characteristic value of the robust plasma decreased by adding a silicon content of 1 mg g^{-1} by approximately 30%, whereas with further increasing silicon content in the analyte solution (1 mg g^{-1} to 5 mg g^{-1} Si) the intensity ratio MgII/MgI remained constant, so that identical excitation conditions prevailed over a variable range of the Si contents. A stable analytical plasma could be approved in measurements with 2 mg g^{-1} silicon matrix over a time of 6 hours.

Limits of quantification

For the assessment of the method, the detection and quantification limits were calculated using the calibration method according to DIN 32 645 [29]. Compared to the blank value method the calibration function method provides not the smallest limits, but it provides the more realistic picture of actually determinable concentrations. The limitations of the calibration method depended on the selected range of operation. For their determination under varying silicon matrix concentrations an 8-point multi-element calibration with identical concentrations in equidistant intervals was performed for each. The average concentrations of the calibration functions are shown in Table 3.

Table 3 Average concentrations of calibration functions to determine LOQ

element	**B**	**Mg**	**Al**	**P**	**Ca**	**Ti**	**Cr**	**Mn**	**Fe**	**Ni**	**Cu**	**Zr**
$\overline{w}$ **/ ng g^{-1}**	70	35	140	35	140	70	35	35	140	35	35	35

Consequently, the limit of quantification of the method is co-determined by the quality of each performed calibration by means of the residual standard deviation. All limits were calculated for the significance level $\alpha = 0.01$. To calculate limits of quantification an uncertainty of 10% (k = 10) was chosen.

Due to the decreasing signal-to-background ratio of the emissions in the UV range with increasing silicon concentration a minimum limit of quantification at a silicon concentration of 4 mg g^{-1} in analytical solution was obtained. With further increasing silicon content the limit of quantification increased again due to the non-spectral interference.

In consequence, the lowest limits of quantification for the multi-element analysis of 12 elements shall be determined in solution of 4 mg g^{-1} silicon. A further increase of the matrix would lead only for a few emission lines to a slight, but not significant improvement in detection capability. Table 4 shows the minimally achievable limits of quantification by measuring a solution with a matrix of 4 mg g^{-1} Si.

Assuming a similar distribution of elements, a maximum purity level of silicon of 99.996% can be definitely analysed by measuring against a correspondingly matrix-matched calibration. In comparison the classical method, including the time-consuming volatilization of the high-silicon and acid matrix, allows the determination of silicon with a purity of 99.998% for identical conditions. [10]

Table 4 Minima of LOQ (k = 10) calculated from calibration functions of multi-element standard solutions with 4 mg g^{-1} Si, all analytical wavelengths measured in axial viewing

element	*wavelength / nm*	w_{LOQ} / µg g^{-1}	element	*wavelength / nm*	w_{LOQ} / µg g^{-1}	element	*wavelength / nm*	w_{LOQ} / µg g^{-1}
B	*182.641*	2.96	**Ca**	*317.933*	15.2	**Fe**	*239.556*	4.13
Mg	*285.213*	1.20	**Ti**	*334.941*	0.71	**Ni**	*216.556*	1.47
Al	*308.215*	3.92	**Cr**	*205.552*	1.79	**Cu**	*324.754*	1.83
P	*185.942*	5.00	**Mn**	*257.610*	0.31	**Zr**	*349.621*	0.46

Comparison with certified reference materials

Table 5 compares the values of the certified reference materials (SRM 57b IPT134, IPT135) with the analytical results obtained by the new microwave-assisted digestion procedure with ICP-OES measurements against a matrix matched calibration (MMC).

Table 5: Comparison between impurity contents in certified reference materials and results obtained by the new developed microwave-assisted procedure measured in high-silicon matrix and quantified by MMC; n = 5; all units are µg g^{-1}

	NIST SRM 57b		**IPT 134**		**IPT 135**	
element	**certified value**	**found value**	**certified value**	**found value**	**certified value**	**found value**
B	(12.5 ± 2.1)*	13.4 ± 0.6	*not certified*	6.6 ± 0.8	*not certified*	7.4 ± 0.5
Mg	*not certified*	2.4 ± 0.2	48 ± 3	49.9 ± 0.9	12 ± 1	11.9 ± 0.2
Al	1690 ± 220	1551 ± 53	850 ± 30	842 ± 23	450 ± 30	377 ± 16
P	16.3 ± 1.5	15.6 ± 1.2	33 ± 2	31.0 ± 2.3	27 ± 1	24.3 ± 2.1
Ca	22.2 ± 4.5	21.0 ± 6.9	1020 ± 30	1026 ± 21	110 ± 10	113 ± 7
Ti	346 ± 49	329 ± 7	97 ± 4	100 ± 2	113 ± 4	119 ± 2
Cr	17.3 ± 3.3	14.7 ± 0.4	11 ± 1	9.0 ± 0.4	6 ± 1	4.9 ± 0.1
Mn	78.2 ± 7.2	70.0 ± 1.5	113 ± 5	101 ± 1	70 ± 3	65.5 ± 0.4
Fe	3400 ± 60	3294 ± 45	2900 ± 100	2828 ± 26	1250 ± 30	1280 ± 16
Ni	15.3 ± 1.7	15.6 ± 0.7	6 ± 1	4.9 ± 0.6	5 ± 1	3.6 ± 0.3
Cu	17.2 ± 5.8	22.8 ± 0.5	14 ± 2	15.8 ± 2.3	8 ± 1	8.6 ± 0.4
Zr	17.8 ± 0.6	17.5 ± 0.4	*not certified*	5.8 ± 0.1	*not certified*	4.4 ± 0.1

* in 2015 a new certified value for boron was published from NIST: (14.43 ± 0.27) ppm

According to the International Conference of Harmonization [24] two analytical values are in agreement if their distance does not exceed ± 10%. However, this approach was considered as impractical in the present case since the confidence intervals for some of the certified element contents are well above 20%. Therefore, the assessment of conformity between the found and certified values, including their confidence intervals, was done in accordance to the t-Student test. The precision is interpreted as repeatability that should be significantly less than 5% for $n \geq 3$ analyses.

For all investigated silicon samples the determination of metal impurities in the high-silicon and acid matrices turned out to be uncomplicated. Only for low-calcium concentrations (NIST 57b) a reduced repeatability was found, which was already indicated in the broad confidence interval of the certified value. In previous studies, it was found that the decreased repeatability due to low calcium levels can be traced back to a blank value problem [10].

Special attention was given to the validation of the boron contents. The certified boron content of SRM 57b was derived from measurements using two different methods. While the solid analysis by PGAA provided a boron content of

(14.3 ± 0.2) ppm, the determination by ICP-OES only provided (10.6 ± 0.4) ppm boron. Information about the sample preparation prior to the ICP-OES analysis was not given. [1] As can be seen from Table 5 the boron concentration that was determined exceeds the average certified value, while there is a match with the content determined by PGAA. In 2015 a new certified value for boron of (14.43 ± 0.27) ppm was published. This new value is based on a new PGAA measurement and on a recent ICP-OES determination by Galler et al. [1], who obtained a value of (15 ± 0.7) ppm by PGAA and (14.2 ± 0.6) ppm by ICP-OES. The found boron contents for the IPT materials are not further discussed because there is no certified value for the boron content.

The determined phosphorus contents match with the certified values. They show absolute deviations from the certified contents of 5-10%, which is not least because of the complex spectral and non-spectral background interferences in ICP-OES analysis (see. Fig. 2) so that the obtained confidence intervals (include precision and accuracy) are partly significantly above 5%.

Interlaboratory comparisons

Due to the described complex problems for a correct determination of boron in silicon and the absence of certified or verified reference values round robin tests for analysis of boron in silicon samples were initiated by Dr. Gilles Humbert from FerróPem (France). Between 17-22 laboratories participated in each test [25-27]. Each round robin test included four silicon samples with different concentrations of boron, wherein each one of the samples had a boron content < 1 ppm, which is below the detection capability of the proposed method (cf. LOQ). The evaluation of the laboratory comparisons was carried out in accordance with DIN-ISO 5725-2 [28].

First, the three silicon samples with different boron concentrations of the first round robin test were analysed by the new method and the results validated against the values obtained in the first interlaboratory comparison [25]. Table 6 compares the numerical results of the first interlaboratory comparison [25] with results obtained by the new method.

Table 6: Reference values of boron an phosphorus determination as result of laboratory comparison after critical assessment [25] according to results obtained in high-silicon and acid matrix and quantified by matrix matched calibration, n = 4

	reference values results of lab comparison			**found values** by MMC		**reference values** results of lab comparison			**found values** by MMC	
	boron contents					phosphorus contents				
	p'	n'	$\overline{w}'$ / µg g^{-1}	$\overline{w}$ / µg g^{-1}		p'	n'	$\overline{w}'$ / µg g^{-1}	$\overline{w}$ / µg g^{-1}	
Ref. 1A	16*	64	**12.4** ± 1.3	**13.5**	± 0.4	9*	36	**68.4** ± 5.7	**69.7**	± 3.7
Ref. 1C	17	68	**41.4** ± 2.7	**43.8**	± 0.7	10	40	**29.8** ± 2.9	**31.1**	± 2.2
Ref. 1D	17	68	**38.0** ± 4.1	**41.1**	± 0.6	10	40	**17.3** ± 2.1	**15.9**	± 1.0

Additionally, all individual results of boron contents obtained in the interlaboratory comparisons are shown as frequency diagrams in Fig. 4. The distance between the minimum and the maximum boron content of each sample was divided into 15 equidistant classes.

Particularly for boron (Fig. 4) it becomes apparent that only the single results in the low-boron-doped sample reference 1A show a pattern that is fairly similar to that of a t-distribution. Significantly different are the scattering patterns of the samples with levels around 40 ppm of boron, which are not t-distributed and therefore are not

subject of exclusively random variations. Keeping the potential pathways for boron losses in mind, the distribution of the individual results and the absence of a significant peak of individual values in the range of the averaged reference value indicated systematically inferior results.

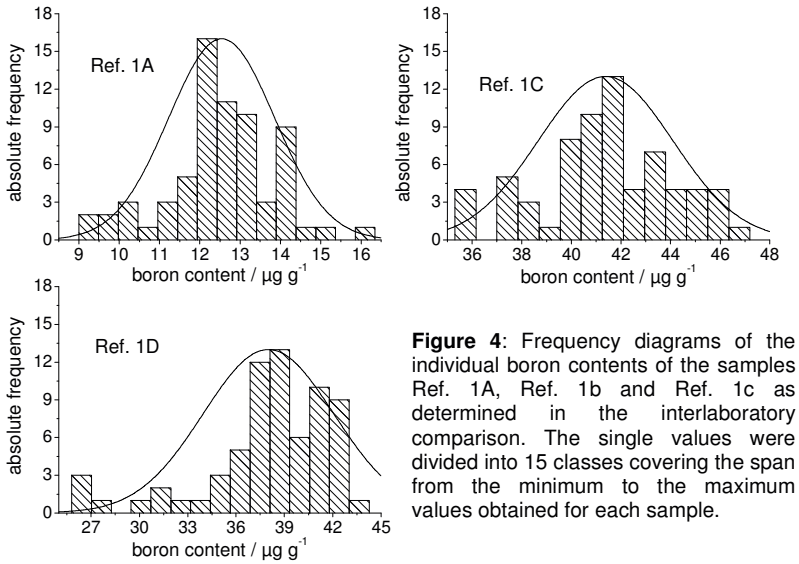

Figure 4: Frequency diagrams of the individual boron contents of the samples Ref. 1A, Ref. 1b and Ref. 1c as determined in the interlaboratory comparison. The single values were divided into 15 classes covering the span from the minimum to the maximum values obtained for each sample.

The boron contents determined in high-silicon and acid matrices are nearly 10% higher than the average reference values from the interlaboratory comparison, however, with a higher precision and accuracy at the same time. The slight deviations is explained by the enormous scatter of the reference values as shown in Fig, 4. In spite of these slight deviations, the t-Student test leads to a formal match between the reference values and the found values.

The phosphorus contents found with the new method (Table 6) are in good agreement with the averaged reference values of interlaboratory comparisons. Nevertheless, with decreasing phosphorus content a decrease in the accuracy and precision of analytical results was observed, as already found in the reference materials.

Our lab participated in the two following interlaboratory comparisons [26, 27] consisting of each three silicon samples of different boron and phosphorus concentrations with the newly developed method. The results of the interlaboratory comparisons after eliminating the outliers are compared in Table 7 with the results of the analysis by ICP-OES measurements in high-silicon and acid matrices. All measurements were quantified against a matrix matched calibration. With the exception of phosphorus contents in Table 7 the n = 4 determined results are part of the reference value of the interlaboratory comparisons on their own. The uncertainties of the values reported in Table 7 are calculated by Gaussian error propagation over the whole method.

Table 7: Reference values of boron an phosphorus determination as result of laboratory comparison after critical assessment [26,27] according to results of new microwave assisted procedure quantified by MMC, standard deviations include the error propagation over the whole method, n = 4

	reference values results of lab comparison			**found values** by MMC		**reference values** results of lab comparison			**found values** by MMC	
	boron contents					phosphorus contents				
	p'	n'	$\overline{w}'$ / µg g^{-1}	$\overline{w}$ / µg g^{-1}		p'	n'	$\overline{w}'$ / µg g^{-1}	$\overline{w}$ / µg g^{-1}	
Ref. 2A	15	60	**53.0** ± 2.6	**53.2** ± 0.9		13	52	**22.6** ± 2.1	**22.0** ± 2.9	
Ref. 2B	14	56	**42.7** ± 2.6	**41.5** ± 0.2		14	56	**34.2** ± 2.6	**34.0** ± 1.6	
Ref. 2C	14	56	**71.7** ± 4.2	**71.1** ± 1.4		13	52	**25.6** ± 2.4	**26.3** ± 1.2	
Ref. 3A	19	76	**31.4** ± 6.1	**33.0** ± 0.4		15	60	**23.1** ± 2.0	**23.6** ± 0.9	
Ref. 3B	18	72	**53.1** ± 5.4	**53.6** ± 1.1		15	60	**14.0** ± 1.6	**14.6** ± 0.5	
Ref. 3C	19	76	**11.0** ± 1.5	**10.7** ± 0.4		14	56	**42.0** ± 4.8	**44.5** ± 1.4	

Table 7 shows an excellent agreement between our values and the reference values obtained in the interlaboratory comparisons. It demonstrates that this new method provides highly accurate and precise analytical results. The fact of slightly higher boron contents found in Table 6 is not confirmed by the results in Table 7. The higher contents of boron of the silicon samples and the lower uncertainty of the reference values contribute to the better agreement with our found values.

In addition to B and P all interlaboratory comparisons tested several other trace element impurities, which substantially coincides with the scope of testing (cf. Table 3). None of the element contents determined by the new method had been identified as an outlier in the interlaboratory comparisons. Our analytical values passed all statistical tests and therefore represent partial results of the reference values.

Conclusion

The present paper describes a new and fast method for the determination of trace elements in MG-Si. The silicon samples are digested in a microwave-assisted high-pressure system and then analyzed without prior removal of matrix components directly by ICP-OES. Digestion in a closed vessel system minimizes losses of phosphorous during the dissolution of silicon. The avoidance of the time-consuming critical step of matrix evaporation prevents significant losses of volatile boron species. The newly developed method is statistically validated, whereby its proof of practicality for the determination of trace elements in silicon, particularly boron and phosphorus, is demonstrated. All analytical results are supplied with an uncertainty that is calculated by a consequent application of the Gaussian error propagation including uncertainty contributions that include the weighing errors for each dilution step and the initial sample masses, the confidence intervals of calculated concentrations for each selected emission line and the average concentration per element over the selected emission lines with their individual confidence intervals. The new method allows a precise and accurate determination of impurities in silicon with a purity of 99.996%.

Acknowledgement

The authors thanks especially Dr. Gilles Humbert from FerróPem (France) for the initiation of the interlaboratory comparisons for determining boron and other trace elements in silicon, as well as all participants of the round robin tests for the permission to share their results.

References

1. P. Galler, A. Raab, S. Freitag, K. Blandhol, J. Feldmann, J. Anal. At. Spectrom., **29**, 2014, 614 – 622
2. H. Robbins, B. Schwartz, J. Electrochem. Soc., **106**, 1959, 505–508
3. H. Robbins, B. Schwartz, J. Electrochem. Soc., **123**, 1970, 1903–1909
4. M. Steinert, J. Acker, A. Henßge, K. Wetzig, J. Electrochem. Soc., **152**, 2005, C843-C850
5. M. Steinert, J. Acker, M. Krause, S. Oswald, K. Wetzig, J. Phys. Chem. B, **110**, 2006, 11377-11382
6. M. Steinert, J. Acker, K. Wetzig, J. Phys. Chem. C, **112**, 2008, 14139-14144
7. E.S. Kooij, K. Butter, J.J. Kelly, Electrochem. Solid State, **2/4**,(1999, 178–180
8. V. Hoffmann, M. Steinert, J. Acker, J. Anal. At. Spectrom., **26**, 2011, 1990–1996
9. J. Acker, A. Rietig, M. Steinert, V. Hoffmann, J. Phys. Chem. C, **116**, 2012, 20380–20388
10. A. Rietig, Staatsexamensarbeit, Friedrich-Schiller-Universität Jena, 2014
11. A.F. Holleman, E. Wiberg: Lehrbuch der anorganischen Chemie, 102. Aufl., Walter de Gryter, 2007
12. Gmelin: Handbook of inorganic and oranometallic chemistry, 8th Edition, Band Phosphorous, supplement volume C1, Springer Verlag, 1993
13. J. Fucskó, S. H. Tan, H. La, M. K. Balazs, Applied Spectroscopy, **47**, 1993, 150–155
14. S. Böhlke, Dissertation, Technische Universität Dresden, 2010
15. S. Böhlke, H. Ohlmeyer, C. Schuster, Annual Meeting on Nuclear Technology 2007, May 22 - 24, 2007, Karlsruhe, 2007
16. J. Gaillardet, D. Lemarchand, C. Göpel, G. Manhès, J. Geostandards Geoanalysis, **25**, 2001, 67-75
17. C. Feldmann, Anal. Chem., **33**, 1961, 1916–1920
18. T. Ishikawa, E. Nakamura, Proc. Japan Acad. B, **66**, 1990, 91–95
19. J. Takahashi, American Laboratory, **41**, 2009, 28
20. M. Balski, F. Emmerling, H. Kipphardt, U. Panne, Anal. Methods, **6**, 2014, 4003 – 4008
21. E. Poussel, J.M. Mermet, Spectrochim. Acta B, **48**, 1993, 734-755
22. J. M. Mermet, Anal. Chim. Acta, **250**, 1991, 85-94
23. J. Nölte: ICP Emissionsspektrometrie für Praktiker, Wiley-VCH Weinheim, 2002
24. ICH, 1996. In: International Conference on Harmonization (ICH) of Technical Requirements for the Registration of Pharmaceuticals for Human Use, Validation of analytical procedures: Methodology, ICH-Q2B, Geneva, 1996
25. G. Humbert: Interlaboratory Comparison, Silicon Samples, Circuit #1, 2013
26. G. Humbert: Interlaboratory Comparison, Silicon Samples, Circuit #2, 2014
27. G. Humbert: Interlaboratory Comparison, Silicon Samples, Circuit #3, 2015
28. DIN-ISO 5725-2, 2002
29. DIN 32 645, 1994

Pyrogenic Silica - A High-Tech Material from Products of Silicon Processing

Torsten Gottschalk-Gaudig[1)] and Erwin-Peter Mayer[1)]
1) Wacker Chemie AG, Burghausen, Germany

Abstract

Side products of the silicon processing during chlorosilane and methyl chlorosilane production can be used for pyrogenic silica production. Pyrogenic silica is a nanostructured particulate material with aggregate sizes in the range of ca. 100 – 250 nm. The material reveals unique structural properties due to the fractal character of the aggregates. The publication describes the production process and elucidates the influence of the process and specific process conditions on the morphology of pyrogenic silica. Selected physico-chemical characteristics of pyrogenic silica are discussed and the interplay between pyrogenic silica morphology and its main industrial applications is demonstrated.

Introduction

Pyrogenic silica is a typical example for synthetic amorphous silica (SAS). Other examples for this class of materials are precipitated silica and silica gels. The latter are produced in a so called wet process by controlled precipitation of silica, whereas pyrogenic silica is obtained in a gas-borne high temperature hydrolysis/oxidation of chlorosilanes..

Pyrogenic silica is characterized by large specific surface area of ca. 50 – 400 m^2/g and a highly structured aggregated morphology. Typical industrial applications of pyrogenic silica like active fillers for plastics and elastomers, rheology control additive, and thermal insulation are making use of these characteristics.

Production Process

Raw materials for production of pyrogenic silica are chlorosilanes obtained in the production of photovoltaic or semiconductor silicon and methyl chlorosilanes from Müller-Rochow process.

In case of chlorosilanes, tetrachlorosilane, $SiCl_4$, is mainly used for pyrogenic silica production [1]. However, also other chlorosilanes such as trichlorosilane, $HSiCl_3$ or dichlorosilane. H_2SiCl_2, can be used. The use of chlorosilanes in the production of value added pyrogenic silica is an attractive alternative to silane conversion, which is very demanding in terms of energy.

Target product of the Müller-Rochow methylchlorosilane process is dimethyldichlorosilane, Me_2SiCl_2. However, an important side product is methyltrichlorosilane, $MeSiCl_3$, of 3 – 15% relative yield, which is also often used as a raw material in pyrogenic silica production [2].

The formation of pyrogenic silica from $SiCl_4$ is a high temperature hydrolysis in a hydrogen-oxygen flame according to Eqs. 1 and 2.

$$2\,H_2 + O_2 \longrightarrow 2\,H_2O \quad (1)$$

$$SiCl_4 + 2\,H_2O \longrightarrow SiO_2 + 4\,HCl \quad (2)$$

From thermodynamic data of Eq. 1 and 2, an adiabatic flame temperature of ca. 1700 K can be calculated.

The corresponding reaction of $(CH_3)SiCl_3$ is a high temperature hydrolysis/oxidation (Eqs. 3 and 4).

$$2\,H_2 + O_2 \longrightarrow 2\,H_2O \quad (3)$$

$$CH_3SiCl_3 + 2\,O_2 \longrightarrow SiO_2 + CO_2 + 3\,HCl \quad (4)$$

The oxidation of the methyl group results in a higher adiabatic flame temperature of approximately1900 K. Based on the stoichiometry of eq. 4, no additional water is needed for the hydrolysis of the Si-Cl bonds. However, the hydrogen-oxygen flame reaction (eq. 3) is still needed to provide enough energy for the particle formation as discussed below.

The particle formation is assumed to be a complex process of chemical reactions combined with different particle growth processes. Fig. 1 schematically depicts this process. Main parameters to control the particle growth are the absolute temperature and the residence time of particles in a certain temperature range [3].

The notion is that in the very early stage of the process cascade SiO_2 molecules form, which instantaneously fuse to so-called proto-particles of ca. 1nm in size (range 1 in Fig. 1) [4]. This happens close to the hottest part of the flame. Due to the high temperature, which is far above the melting temperature of amorphous SiO_2 (T_m^{SiO2}), proto-particles are in fact droplets of liquid SiO_2. Collision of proto-particles results in particle growth by coalescence (s. range 2). Finally, primary particles of 5 – 50 nm in diameter result. Their size primarily depends on temperature and residence time. The viscosity of molten SiO_2 strongly depends on temperature and water content [5]. Hence, with decreasing temperature the viscosity heavily increases and below a certain temperature complete coalescence of particles upon collision is no longer possible. As a consequence, particle-particle collision in this cooler part of the flame (range 3) causes aggregation [6]. The primary particles within the aggregates are fused by sinter bridges. When the temperature drops below the melting temperature of SiO_2, agglomeration starts. Within the agglomerates the aggregates hold together due to strong surface forces like London, Keesom, and van der Waals forces [3].

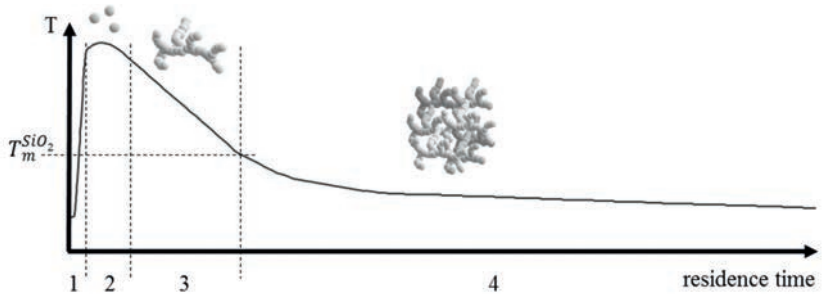

Figure 1: Particle growths scheme of pyrogenic silica.

Several grades of pyrogenic silica are commercially available, which mainly differ in their specific surface area. Typically, silica grades in a range of 50 – 400 m^2/g are available. The specific surface area is determined by the size of the primary particles. By increasing the size of primary particles, the specific surface area drops. The primary particles size can be precisely controlled by the flame temperature and/or residence time of the primary particles in range 2 of the particle growth scheme.

Fig. 2 shows a schematic illustration of the net process of pyrogenic silica production.

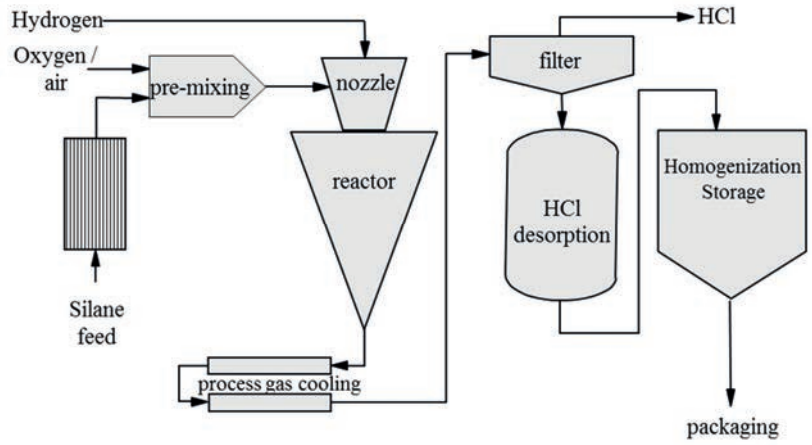

Figure 2: Illustration of the net process of pyrogenic silica production.

After pre-mixing of air and silane feed, all components are introduced by means of a nozzle into a reactor, where combustion and subsequent particle formation occurs. The particle fraction is separated after cooling from the main gas volume. A very important step is the desorption of HCl traces from the silica surface. The pyrogenic silica is collected in silos for final homogenization to guarantee constant product properties and finally packed into bags.

Properties of Pyrogenic Silica

Main characteristics of pyrogenic silica are a large specific surface area and a complex hierarchical morphology consisting of primary particles, aggregates, and agglomerates.

Pyrogenic silicas are available in a specific surface range of 50 – 400 m^2/g. The surface area is measured by nitrogen gas adsorption and calculated from the adsorption isotherm by means of the Brunauer-Emmett-Teller equation, resulting in the so-called BET surface area [7]. In fig. 3, a typical gas adsorption isotherm of pyrogenic silica is depicted.

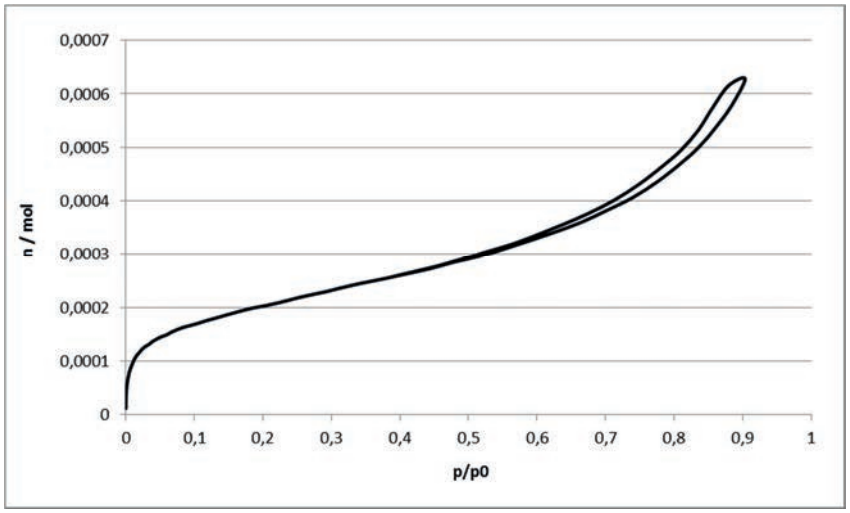

Figure 3: Nitrogen gas adsorption isotherm of pyrogenic silica.

The gas adsorption isotherm of fig. 3 belongs to the type IV isotherms according to the classification of Brunauer, Deming, Deming and Teller and is characterized by a hysteresis loop in the large relative pressure p/p_0 range. The hysteresis loop is due to capillary condensation of nitrogen in silica mesopores [8].

The surface structure of pyrogenic silica is complex and still a matter of research. The sharp upturn of the gas adsorption isotherm in the low p/p_0 range indicates high surface energy. From the BET analysis a non-specific silica surface energy γ_s^d of 134 mJ/m^2 has been calculated[9]. However, this value is probably too high and biased by specific interaction resulting from surface silanol groups (Si-OH) with nitrogen molecules. Using Inverse Gas Chromatography (IGC) in infinite dilution mode a γ_s^d of ca. 60 mJ/m^2 for a pyrogenic silica with a specific surface area (SSA) of 200 m^2/g was found[10], which is a more reasonable number for pure non-specific interactions. The energetic heterogeneity of the pyrogenic silica surface is corroborated by IGC experiments in finite dilution mode. Fig. 4 shows the adsorption energy distribution calculated for the abovementioned 200 m^2/g silica and hexylamine as the IGC probe. The distribution function shows two modes, one low-energy peak at ca. 23 kJ/mol and a peak at ca. 35 kJ/mol for the high-energy sites.

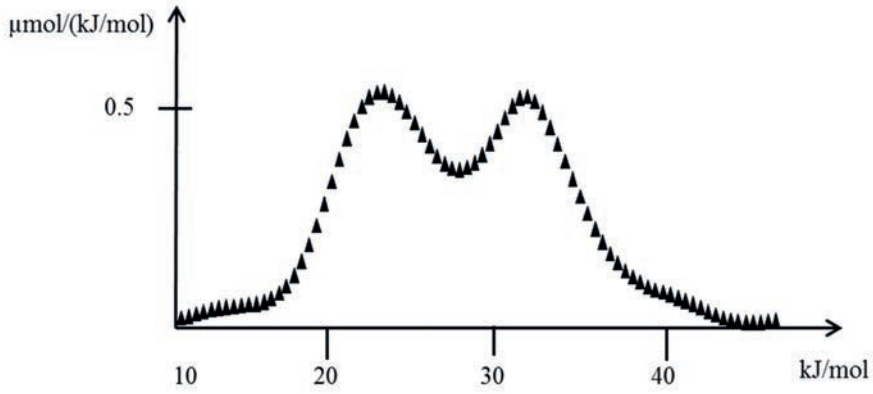

Figure 4: Adsorption energy distribution calculated for a 200 m^2/g silica and hexylamine as IGC probe.

The high-energy peak can be assigned to the specific interaction of hexylamine with silanol groups.

The existence of silanol groups at the silica surface have been proven by IR and NMR spectroscopy, respectively [11, 12]. Fig. 5 reveals a typical DRIFT spectrum of pyrogenic silica.

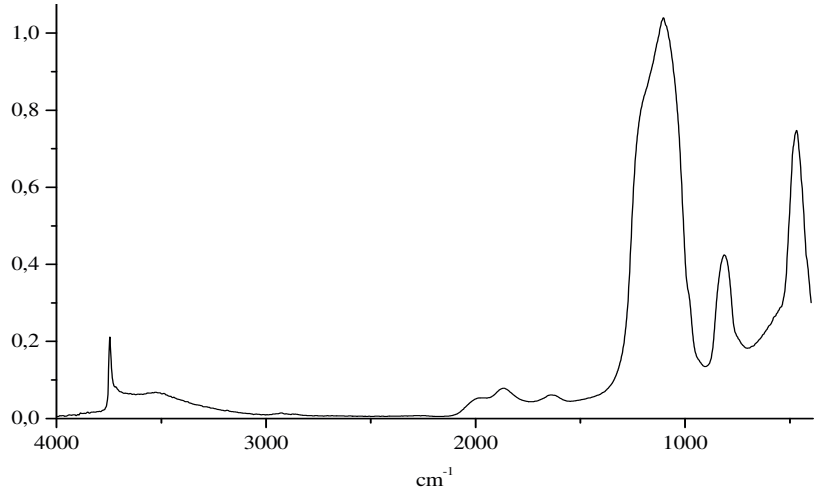

Figure 5: DRIFT spectrum of pyrogenic silica in KBr.

The sharp peak at 3745 cm^{-1} can be assign to isolated SiOH groups. The broad resonance from ca. 3740 to ca. 3100 cm^{-1} is caused by hydrogen bond coupled silanols. The hydrogen bond can be formed between silanol and water molecules or between two silanol groups close to each other, respectively, as depicted in fig.6.

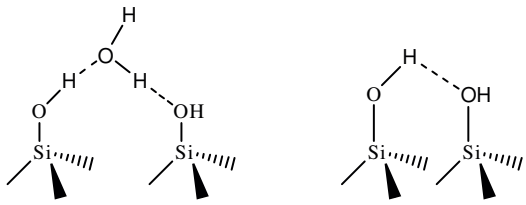

Figure 6: Hydrogen bonds at silanol groups.

More details about different silanol structures on silica surface can be obtained from solid state NMR spectroscopy [13-15]. Fig. 7 shows a solid state ^{29}Si CPMAS spectrum of pyrogenic silica of 200 m^2/g specific surface area.

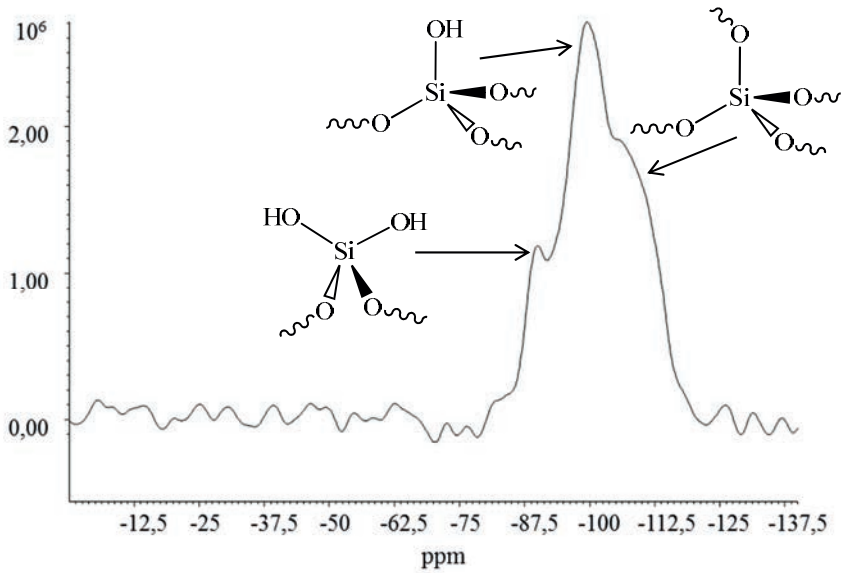

Figure 7: ^{29}Si CPMAS spectrum of pyrogenic silica of 200 m^2/g specific surface area.

The spectrum shows 3 signals at -90 ppm, -100 ppm, and a shoulder at -110 ppm, respectively. The first signal can be assigned to geminal silanol groups (Q2 groups), the second peak to isolated or vincinal silanol groups (Q3 groups) and the shoulder can be assigned to the Q4 backbone ($SiO_{4/2}$)[16]. NMR spectroscopy in CPMAS mode is a non-quantitative method. Hence, the intensities of the signals do not reflect the real molar fraction of the corresponding silicon atoms and silanol group density of the silica surface cannot be calculated from these data.

However, the silanol group density is an important parameter affecting several fundamental properties of pyrogenic silica, for example: i) colloidal stability of aqueous pyrogenic silica dispersions, ii) polymer adsorption due to specific interactions, or iii) grafting density of surface modified silica. Determination of silanol group density is a delicate analytical challenge. Different methods such as spectroscopy (IR, NMR), thermogravimetry [17], mass spectrometry [18], acid-base titration [19], gas volumetry using $LiAlH_4$ or organometallic compounds (MeLi)[20], or chemical modification

techniques with alcohols [21] or silanes like hexamethyldisilazane have been employed [22]. Silanol group densities in the range of ca. 2 – 4.5 silanol/nm^2 have been reported for pyrogenic silica. One factor which hampers the accurate determination of silanol numbers is the highly reactive nature of the silica surface, analytical results are easily biased by strong coordination of water molecules to silanols. In order to completely remove adsorbed water, elevated temperature and reduced pressure is needed, which can finally result in silanol condensation yielding strained siloxane bridges at the silica surface according to eq. 5 [23].

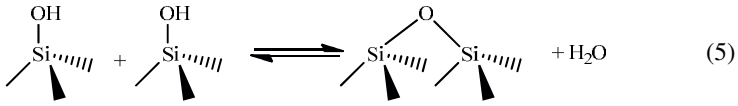

(5)

Formation of strained siloxane bridges from silanol condensation also has been postulated to occur during the high-temperature production process [24]. As a consequence, pyrogenic silica isolated immediately after the flame reactor should reveal a low silanol group density and high reactivity toward water according to reverse reaction of eq. 5. This is corroborated by the observations that pyrogenic silica collected directly after the HCl desorption unit and immediately stored under dry argon exhibits a silanol group density of only 1.3 – 1.4 silanol/nm^2 and undergoes a rapid increase of silanol group density when stored at 94 % rel. humidity. The development of silanol numbers over time is shown below in fig. 8 were determined by means of $LiAlH_4$ titration of samples that have been dynamically dried in a stream of dry nitrogen.

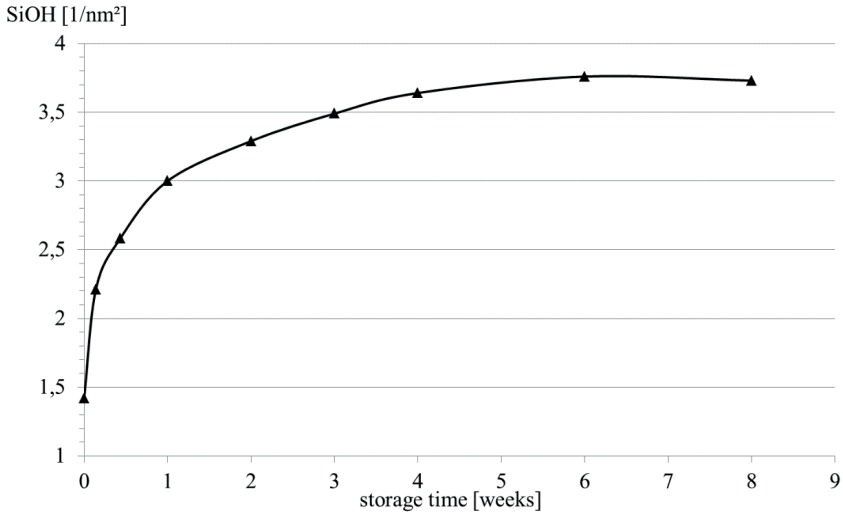

Figure 8: Evolution of silanol group density of pyrogenic silica stored at 94 % rel. humidity.

The rapid increase in silanol groups levels with time and approaches an upper limit of ca. 3.8 SiOH/nm^2. The same behavior was found independently in systematic studies of silica aging under controlled humidity conditions [25, 26].

The three dimensional morphology of pyrogenic silica is a direct consequence of the production temperature above melting temperature of silica and the strong influence of temperature on melt viscosity of silica. In certain temperature range only partly fusion of silica particles after collision is possible due to high viscosity of molten SiO_2. This results in hard, permanent sintered aggregates which are the ultimate particle form of pyrogenic silica. In contrast to colloidal silica which forms in a low temperature precipitation process in aqueous solution, isolated primary particles have never been observed for pyrogenic silica.
Fig. 9 depicts TEM micrographs showing pyrogenic silica aggregates without (left) and with (right) application of intense shear force during sample preparation.

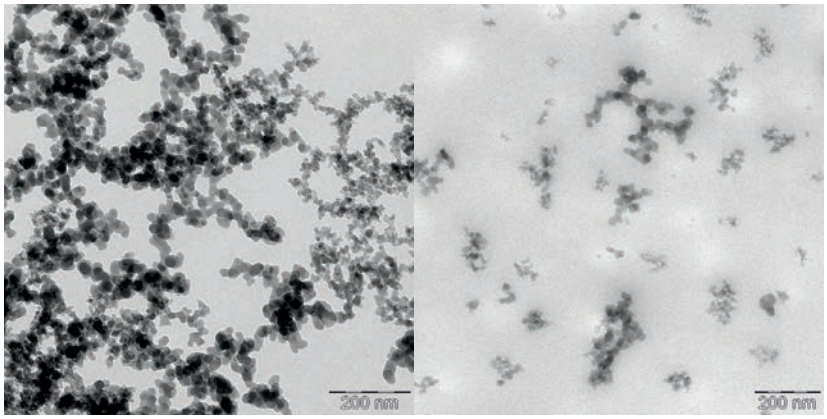

Figure 9: TEM micrographs of silica aggregates without application of shear (left; dry powder on TEM grid) and with application of shear (right; embedded in cured epoxy resin).

In order to describe the irregular structure of pyrogenic silica aggregates the concept of fractals and self-similarity is often used. Fractal systems follow the fundamental relation 6 [27].

$$M(l) \sim l^D \qquad (6)$$

The relation states that the mass of a fractal object within a set of concentric spheres decreases with decreasing radius l of the spheres according to l^D. Exponent D of the power law is called the fractal dimension of mass. Scattering methods like small angle X-ray scattering (SAXS) are often used to study the structure of fractal objects. Parameters like the fractal dimension D_m can be extracted from a $I(q^{-1})$ vs. q^{-1} scattering plot where I is the scattering intensity and q is the magnitude of wave vector, where $q = 4\pi/\lambda \sin(\theta/2)$, θ is the scattering angle, and λ the wave length. Fig. 10 displays scattering data for pyrogenic silica of 200 m^2/g specific surface area. The plot reveals two power-law regimes. The low q-regime reflects scattering from fractal aggregates. The fractal dimension can be directly extracted from the power-law slope, which is 2.13 for the example shown. The high q-regime is due to scattering at the primary particle surface. From the power-law slope here a so-called surface fractal dimension D_s can be calculated using the relation $I \sim q^{(-P)}$ where $P = 6 - D_s$, which in this case results in a surface fractal dimension of 1.93. D_s of close to 2 is indicative of a essentially flat

surface without surface porosity. The mass fractal dimension of 2.13 indicates an open, very space filling structure. However, in literature even lower fractal dimensions in the range of 1.5 – 1.9 have been reported for pyrogenic silica [28, 29]. The differences might be due to different conditions within production processes of the pyrogenic silica producers. The space-filling properties of pyrogenic silica aggregates are an important feature which directly leads to the use to pyrogenic silica as rheological control additive, thermal insulation material, and reinforcing filler [30]. The different application will be discussed later.

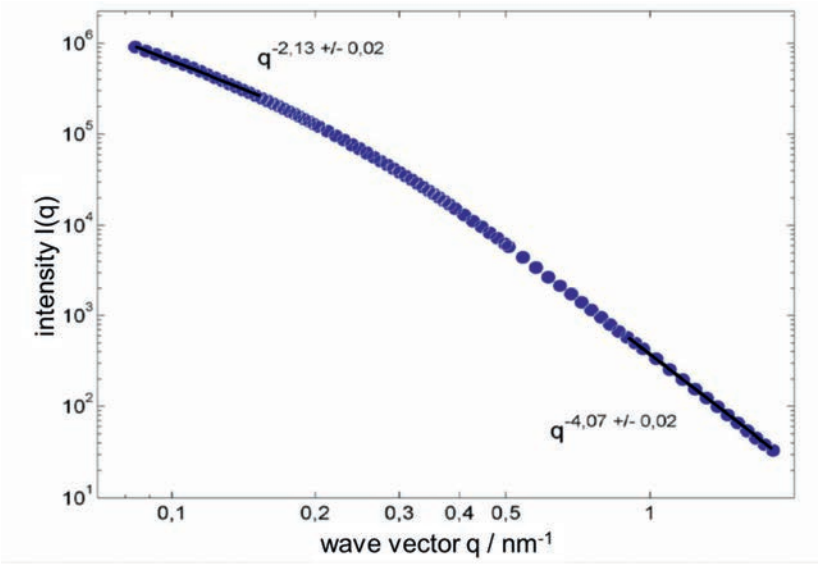

Figure 10: Scattering date for pyrogenic silica of 200 m^2/g specific surface area.

Particle size and particle size distribution are important parameters to characterize powders [31]. However, particle size of hierarchical systems like pyrogenic silica is an ill-defined feature. The values strongly depend on the measuring technique and conditions of sample preparation. Depending on the size range of the hierarchical system, different techniques are employed. Particle size of primary particles within the sintered aggregates can be determined by TEM analysis or from the specific surface area according to eq. 7 which results in the Sauter diameter D_{pp} of primary particles.

$$D_{pp} = \frac{6}{SSA \cdot \rho_{SiO_2}} \qquad (7)$$

The Sauter diameter of primary particles of silica with 200 m^2/g specific surface area is ca. 14 nm. The Sauter diameter of pyrogenic silica is often cited in scientific literature but this is somehow misleading since it implies that isolated primary particles are accessible.

For most applications, the aggregate size is the relevant parameter. An established method to determine the particle size of sub-micron particles is photon correlation

spectroscopy (PCS) [32]. PCS measures the diffusion coefficient, which is subsequently recalculated into the particle size of a solid sphere using the well-known Stokes-Einstein-Equation. Hence, for irregular pyrogenic silica aggregates a diffusion-equivalent hydrodynamic solid sphere diameter is obtained. In Fig. 11 the evolution of hydrodynamic equivalent diameter of pyrogenic silica with increasing specific surface area is depicted. A clear decrease of aggregates size with increasing specific surface area can be observed.

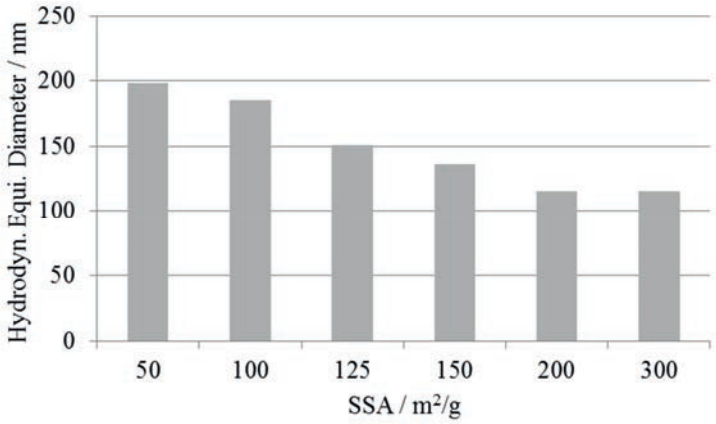

Figure 11: Evolution of hydrodynamic equivalent diameter of pyrogenic silica with increasing specific surface area. Measurement was performed in epoxy resins RIM 135 at 80 °C.

Pyrogenic silica agglomerates are situated in a size range > 1 µm. A FE-SEM micrograph of a pyrogenic silica agglomerate is depicted in Fig. 12.

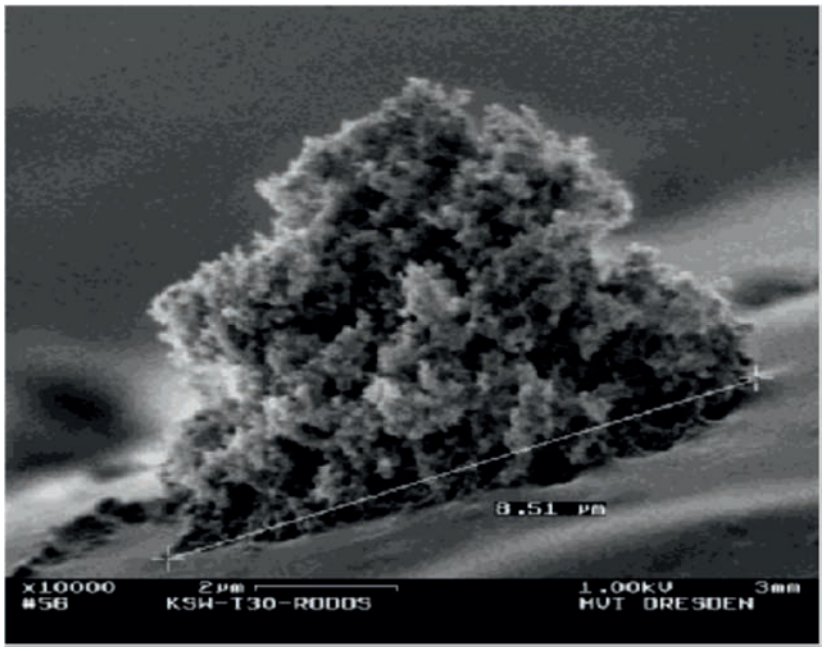

Figure 12: Field emission SEM micrograph of pyrogenic silica agglomerate.

Accurate particle sizing of pyrogenic silica agglomerates is challenging due to shear sensitivity of the internal structure of the agglomerates. The aggregates within the agglomerate structure interact by relatively weak dispersion forces. Application of mechanical shear during sample preparation and measurement are able to overcome the dispersion forces and will therefore affect the resulting particle size and particle size distribution [31]. The effect of shear on pyrogenic silica particle size is illustrated in Fig. 13, which shows the maximum readings of the nm-mode and µm-mode of the particle size distribution of a laser light diffraction experiment of an aqueous pyrogenic silica dispersion containing 1 wt% of pyrogenic silica of 300 m^2/g SSA with increasing stirring time.

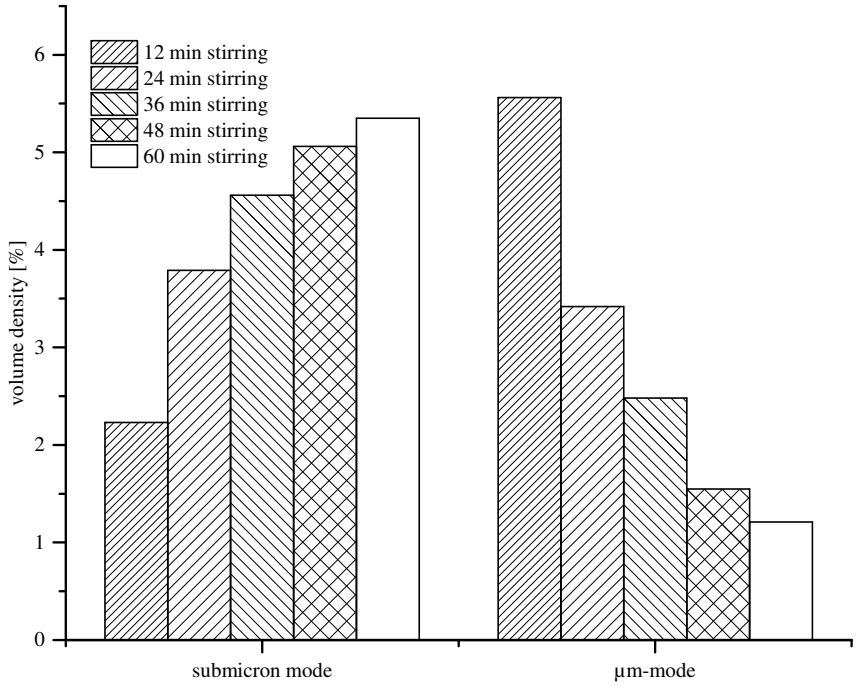

Figure 13: Laser light diffraction data of an aqueous dispersion of pyrogenic silica of 300 m^2/g SSA stirred at 3000 rpm (internal stirrer of Mastersizer 3000) for different periods of time.

Under these mild shear conditions, the particle size distribution shows a bimodal distribution with one mode in the nm-range and a second mode in the µm-range. With increasing stirring time, the sub-micron mode increases in intensity. The intensity of the coarse particle peak (µm-mode) strongly decreases.

Applications of pyrogenic silica

Main industrial applications of pyrogenic silica are summarized in table 1.

Table 1: Main industrial applications of pyrogenic silica.

Application	desired effect	dosage / wt%
reinforcing filler	Improving mechanical properties of silicone elastomers	ca. 30
rheological additive	Flow control of sealants, adhesives, and coatings	1 – 10
thermal insulation	High and low temperature insulation	ca. 80
anti-blocking additive	Free flow of adhesive powders	0.05 – 1
charge regulation additive	Charge regulation of toner particles	ca. 0.5 – 1
pharmaceutical excipient	Improved powder handling, tabletting, and tablet disintegration	ca. 1

The different applications finally reflect the properties of pyrogenic silica, i.e. large surface area and fractal-like structure of the sub-micron sinter aggregates. In the following section, some applications are discussed in more detail.

Reinforcement of Silicone Elastomers

Silicone elastomers are widely used in automotive, food and household, energy transportation and distribution, medical, etc. [33].
Silicone elastomers consist of chemically cross-linked siloxane polymers and ca. 30 wt% of silica. The silica particles act as reinforcing fillers, i.e. they increase strength (moduli) and improve the ultimate properties (deformation and stress at break) of silicone elastomers. Fig. 14 schematically depicts the stress-strain behaviour of silicone elastomers with and without reinforcing silica.

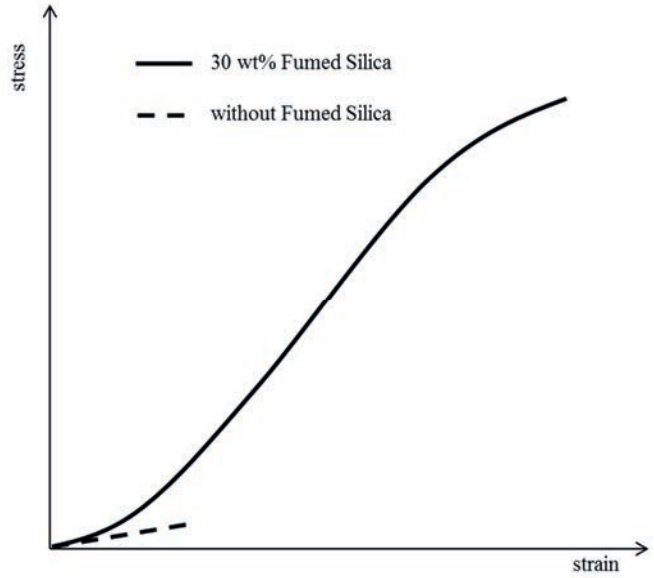

Figure 14: Schematic stress-strain behaviour of silicone elastomers with and without reinforcing silica.

By using pyrogenic silica, modulus, deformation at break, and stress at break can be increased by at least ca. one order of magnitude [2]. Despite the maturity of these materials, the exact mechanisms of silica reinforcement are still not fully understood. However, it is generally accepted that the inclusion of particles with a high modulus, as well as particle-polymer interactions and particle-particle interactions are important factors to improve the mechanical properties of elastomers [34-36]. In order to improve particle dispersion and modulate particle interactions the silica surface is often chemically modified, i.e. the surface silanol groups are reacted with reactive silanes or siloxanes to form stable Si-O-Si bonds. This can be achieved by in-situ silane treatment during compounding of silica into the gum base. An widely used silane modifier is hexamethyldisilazane ($(CH_3)_3Si\text{-}N(H)\text{-}Si(CH_3)_3$)[2].

Rheology Control

Mixing pyrogenic silica into fluid causes a strong increase in viscosity and can result even in gel formation, depending on the silica loading. This effect is used to control the flow properties of sealants, adhesives, and coatings [30]. The silica improves application properties like extrusion rate, sag resistance, prevention of pigment sedimentation, and paintability. The increase in viscosity comes along with a non-Newtonian behaviour such as shear thinning and thixotropy. This property is depicted in Fig. 15, which shows a thixotropy experiment simulating storage (low shear rate; a), application (high shear rate; b), and structure recovery (low shear rate; c).

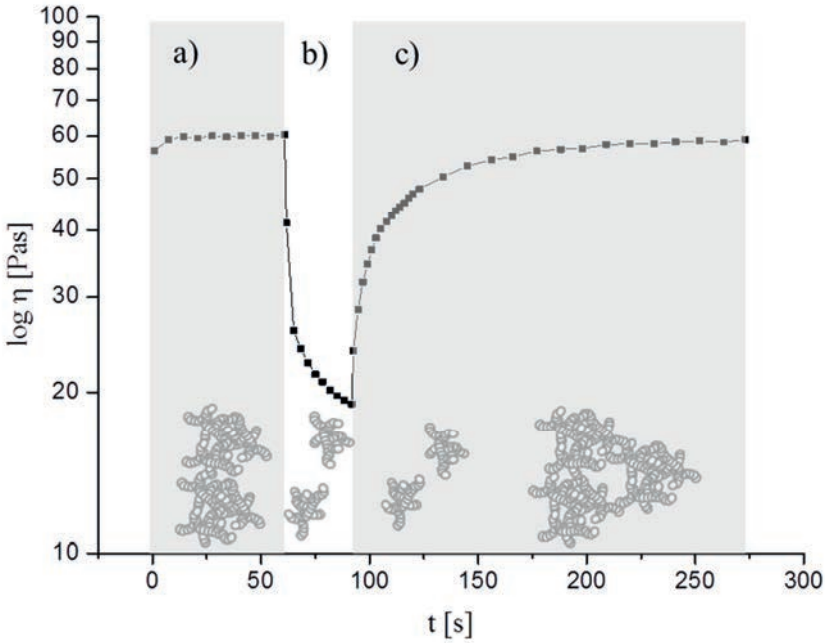

Figure 15: Thixotropy experiment of Epikote 828 containing 5 wt% pyrogenic silica (SSA 200 m^2/g); block a): 0.5 s^{-1}, block b) 500 s^{-1}, block c) 0.5 s^{-1} and an illustration of the evolution of the internal silica network structure.

In block a) of the thixotropy test, a low shear rate of 0.5 s^{-1} is applied. This simulates a situation of low mechanical impact like storage where the internal rest structure is only slightly disturbed. The high viscosity is a result of a percolating particle network which effectively immobilizes the fluid within the network. Instantaneous increase of the shear rate to 500 s^{-1} (block b) induces degradation of the network structure and reduces the immobilized fluid volume. The network degradation is reflected by strong shear thinning. The high shear rate phase is intended to simulate the application of a formulation like pumping, spraying, or painting. In the subsequent low-shear phase (0.5 s^{-1}; block c) the structure recovery of the particulate network is monitored. Proper choice of the silica grade and adaption of the silica loading allows tailoring of the degree shear thinning and the rate of structure recovery according to the requirements of the corresponding application.

Thermal Insulation

Pyrogenic silica is the most effective thermal insulation material, which is readily available in large quantities [37]. Table 2 summarizes the thermal conductivity of selected insulating materials.

Table 2: Thermal conductivity of selected insulating materials at 293 K.

Material	λ_{tot} [$mWm^{-1}K^{-1}$]	test specimen
pyrogenic silica	ca. 20	fiber inforced panel
silica aerogel	ca. 15	monolith
mineral wool	ca. 40	fiber mat
extruded polystyrene (XPS)	ca. 35	panel
expanded polystyrene (EPS)	ca. 40	panel

According to eq. 8, the total thermal conductivity λ_{tot} is a combination of gas-borne thermal conductivity λ_g, solid body thermal conductivity λ_s, and radiation thermal conductivity λ_r.

$$\lambda_{tot} = \lambda_g + \lambda_s + \lambda_r \qquad (8)$$

For non-compacted pyrogenic silica powder at 300 K λ_g of ca. 20 $mWm^{-1}K^{-1}$, λ_r of ca. 2 $mWm^{-1}K^{-1}$, and λ_s of ca. 5 $mWm^{-1}K^{-1}$ was obtained which results in total thermal conductivity λ_{tot} of ca. 27 $mWm^{-1}K^{-1}$. The radiation thermal conductivity is a consequence of IR radiation passing through the silica. This contribution is of minor importance at ambient temperature and can be significantly reduced by means of IR radiation opacifiers like carbon black or magnetite. Solid body thermal conductivity results from thermal vibrations transmitted through the silica. This contribution is also relatively weak due to the fractal structure of pyrogenic silica aggregates. Their fractal nature gives rise to a distinct tortuosity of the silica chains within the aggregates and a large number of dead chain ends. Even the gas-borne thermal conductivity, although being the main contributor for pyrogenic silica, shows quite low numbers compared to other insulation materials. The magnitude of gas-borne thermal conductivity is directly related to the porosity and the mean pore size of the insulating material according to eq.9 [38].

$$\lambda_g = \frac{\Pi \cdot \lambda_{g,0}(T)}{1+2\beta\frac{l_m}{D}} \qquad (9)$$

Π is the porosity of the thermal insulator, which is for pyrogenic silica ca. 0.98, λ_{g0} is the thermal conductivity of the gas, β is a gas-specific co-factor, I_m is the mean free path length of the gas, and D is the mean pore size of the insulator.
Pyrogenic silica is a mesoporous material (s. above) with pore sizes smaller than the mean free path length of air at standard conditions (ca. 70 nm). The combination of all factors discussed above is reason for the outstanding insulation properties of pyrogenic silica. Reduction of λ_g is an efficient way to further improve the insulation properties of pyrogenic silica. This concept is successfully applied in case of so called vacuum insulation panels where a foil-wrapped pyrogenic silica panel is evacuated. A total thermal conductivity of ca. 5 $mWm^{-1}K^{-1}$ can be achieved.

References

1. H. Barthel, L. Roesch and J. Weis, *Pyrogenic silica - production, properties, and applications*, Organosilicon Chem. II, Vol. 1996, VCH Weinheim, p761
2. B. Pachaly, F. Achenbach, C. Herzig and K. Mautner, *Silicone*, Winnacker/Küchler, Chemische Technik: Prozesse und Produkte, Vol. 5, 2005, Wiley-VCH, Weinheim, p1095
3. S. Tsantilis and S.E. Pratsinis, *Soft- and Hard-Agglomerate Aerosols Made at High Temperatures*, Langmuir, **20**, 2004, p5933
4. G.D. Ulrich, *Flame synthesis of fine particles*, Chemical & Engineering News, **62**, 1984, p22
5. G. Urbain, *The effect of differing water contents on the viscosity of liquid silica*, Revue Internationale Des Hautes Temperatures Et Des Refractaires, **26**, 1990, p193
6. G.D. Ulrich and N.S. Subramanian, *III. Coalescence as a Rate-Controlling Process*, Combustion Science and Technology, **17**, 1977, p119
7. S. Brunauer, P.H. Emmett and E. Teller, *Adsorption of Gases in Multimolecular Layers*, Journal of the American Chemical Society, **60**, 1938, p309
8. S.J. Gregg and K.S.W. Sing, *Adsorption, Surface Area and Porosity,* Second Edition, 1982, Academis Press Inc., London
9. H. Barthel, *Gas adsorption on silylated silica*, 4th Symp. on Chemically Modified Surfaces, 1992, p243
10. B. Hamdi, T. Gottschalk-Gaudig, H. Balard, E. Brendlé, N. Nedjari and J.B. Donnet, *Aging process of some pyrogenic silica samples exposed to controlled relative humidities: Part II: Evolution of their surface properties studied using inverse gas chromatography*, Colloids and Surfaces A: Physicochemical and Engineering Aspects, **488**, 2016, p46
11. A.P. Legrand, *The Surface Properties of Silicas,* 1998, John Wiley & Sons, Chichester
12. E.F. Vansant, P. Van Der Voort and K.C. Vrancken, *Charakterization and Chemical Modification of the Silica Surface,* 1997, Elesevier Science B.V., Amsterdam
13. H.C. Marsmann, *29Si-Kernresonanzuntersuchungen an wäßrigen Silicatlösungen*, Z. Naturforsch., **29b**, 1974, p495
14. G.E. Maciel and D.W. Sindorf, *Silicon-29 NMR study of the surface of silica gel by cross polarization and magic-angle spinning*, Journal of the American Chemical Society, **102**, 1980, p7606
15. D.W. Sindorf and G.E. Maciel, *Silicon-29 NMR study of dehydrated/rehydrated silica gel using cross polarization and magic-angle spinning*, Journal of the American Chemical Society, **105**, 1983, p1487
16. C.C. Liu and G.E. Maciel, *The Pyrogenic Silica Surface: A Study by NMR*, Journal of the American Chemical Society, **118**, 1996, p5103
17. R. Mueller, H.K. Kammler, K. Wegner and S.E. Pratsinis, *OH Surface Density of SiO2 and TiO2 by Thermogravimetric Analysis*, Langmuir, **19**, 2003, p160
18. L.T. Zhuravlev, *Concentration of hydroxyl groups on the surface of amorphous silicas*, Langmuir, **3**, 1987, p316
19. G.W. Sears, *Determination of specific surface area of colloidal silica by titration with sodium hydroxide*, Analytical Chemistry, **28**, 1956, p1981
20. J. Mathias and G. Wannemacher, *Basic characteristics and applications of aerosil. 30. The chemistry and physics of the aerosil surface*, Journal of Colloid and Interface Science, **125**, 1988, p61

21. A. Vidal, E. Papirer, W.M. Jiao and J.B. Donnet, *Modification of silica surfaces by grafting of alkyl chains. I - characterization of silica surfaces by inverse gas-solid chromatography at zero surface coverage*, Chromatographia, **23**, 1987, p121
22. S. Haukka and A. Root, *The reaction of hexamethyldisilazane and subsequent oxidation of trimethylsilyl groups on silica studied by solid-state NMR and FTIR*, Journal of Physical Chemistry, **98**, 1994, p1695
23. C.J. Brinker, R.J. Kirkpatrick, D.R. Tallant, B.C. Bunker and B. Montez, *NMR confirmation of strained "defects" in amorphous silica*, J. Non Cryst. Solids, **99**, 1988, p418
24. A.P. Legrand, H. Taibi, H. Hommel, P. Tougne and S. Leonardelli, *Silicon functionality distribution on the surface of amorphous silicas by silicon-29 solid-state NMR*, J. Non Cryst. Solids, **155**, 1993, p122
25. H. Balard, J.B. Donnet, H. Oulanti, T. Gottschalk-Gaudig and H. Barthel, *Study of aging of pyrogenic silicas by gravimetry and microcalorimetry*, Colloids and Surfaces A: Physicochemical and Engineering Aspects, **378**, 2011, p38
26. B. Hamdi, T. Gottschalk-Gaudig, H. Balard, E. Brendlé, N. Nedjari and J.B. Donnet, *Ageing process of some pyrogenic silica samples exposed to controlled relative humidities: Part I: Kinetic of water sorption and evolution of the surface silanol density*, Colloids and Surfaces A: Physicochemical and Engineering Aspects, **491**, 2016, p62
27. P. Pfeifer, *Catalyst surfaces, macromolecules, and colloidal aggregates: fractal dimension as concealed symmetry of irregular structures*, Chimia, **39**, 1985, p120
28. A.J. Hurd and W.L. Flower, *In situ growth and structure of fractal silica aggregates in a flame*, Journal of Colloid and Interface Science, **122**, 1988, p178
29. D.W. Schaefer and A.J. Hurd, *Growth and structure of combustion aerosols. Pyrogenic silica*, Aerosol Science and Technology, **12**, 1990, p876
30. H. Barthel, M. Dreyer, T. Gottschalk-Gaudig, V. Litvinov and E. Nikitina, *Pyrogenic silica - Rheological Additive for Adhesives, Resins, and Paints*, Organosilicon Chem. V, Vol. 2001, VCH, Weinheim, p752
31. H. Barthel, M. Heinemann, M. Stintz and B. Wessely, *Particle sizes of pyrogenic silica*, Chem. Eng. Technol., **21**, 1998, p745
32. U. Kätzel, R. Bedrich, M. Stintz, R. Ketzmerick, T. Gottschalk-Gaudig and H. Barthel, *Dynamic Light Scattering for the Characterization of Polydisperse Fractal Systems: I. Simulation of the Diffusional Behavior*, Particle & Particle Systems Characterization, **25**, 2008, p9
33. A. Tomanek, *Silicone & Technik,* 1990, Carl-Hanser Verlag, München
34. L. Bokobza, *New developments in rubber reinforcement*, KGK, Kautschuk Gummi Kunststoffe, **62**, 2009, p23
35. G. Heinrich, M. Klüppel and T.A. Vilgis, *Reinforcement of elastomers*, Current Opinion in Solid State and Materials Science, **6**, 2002, p195
36. L. Bokobza, *The Reinforcement of Elastomeric Networks by Fillers*, Macromolecular Materials and Engineering, **289**, 2004, p607
37. H. Katzer and J. Weis, *Microporous Thermal Insulation: Theory, Properties, Applications*, Organosilicon Chemistry III, Vol. 1998, Wiley-VCH, Weinheim, p682
38. M.G. Kaganer, *Thermal Insulation in Cryogenic Engineering,* 1969, Israel Program for Scientific Translations,

Copper transport in the methylchlorosilane fluidized bed reactor

Cécile ROSIER[1)], Maxime RISS[1)], and Michel HUET[1)]

[1]*BLUESTAR SILICONES - 55 av Frères Perret 69190 SAINT FONS – France*

Abstract

In the continuous methylchlorosilane process, the fresh silicon fed to the fluidized bed reactor has to be activated in an efficient way in order to provide high and stable performances in term of productivity and selectivity. Fresh silicon particles are activated both by reaction with fresh catalyst and by transfer of catalyst from already activated particles.
A specific experimental lab procedure was developed to get information on catalyst transport from activated to fresh silicon particles. The effect of temperature, cocatalyst concentration and addition of aluminium on copper transport in the methylchlorosilane reactor and reaction performances of the catalytic sites resulting from this transport were investigated.

It was observed that the amount of copper transported from activated to unactivated silicon was only slightly affected by experimental conditions.

Cocatalysts transfer seemed more affected by experimental conditions: High concentration of tin on added silicon fraction seemed correlated with transfer at high temperature; high concentration of tin and zinc were obtained when the cocatalysts – or zinc alone – were added during the transfer step.

The reactivity of the catalytic sites obtained by transfer was significantly higher than the reactivity of the catalytic site obtained by reaction between silicon and fresh catalyst. Best reactivities were achieved at relatively low concentrations of cocatalysts.

Introduction

The synthesis of methylchlorosilanes is the first step of production in the silicone industry [1, 2]. Direct process, discovered by Eugene Rochow in 1939 [3], involves a heterogeneous catalytic reaction between silicon and methyl chloride. Copper is the catalyst of direct synthesis. Zinc and tin are also used as promoters, as they improve reaction performances when present in optimal proportions. Dimethyldichlorosilane

(Me_2SiCl_2) is the main product of the reaction but it is produced together with many by-products.

$$Si_{(s)} + MeCl_{(g)} \xrightarrow{Cu,Zn,Sn} MCS_{(g)} + lowboiling_{(g)} + highboiling_{(g)}$$
$$MCS = Me_2SiCl_2, MeSiCl_3, Me_3SiCl, MeHSiCl_2, Me_2HSiCl...$$

Industrially, this heterogeneous and highly exothermic reaction (ΔHr = -284.1 KJ/mol if we take only Me_2SiCl_2 into account), takes place in a fluidized bed reactor (FBR) under a pressure of between 2.5 and 4 bars and a temperature around 300°C. Common objective of the MCS producers is to perform the reaction with a high level of productivity, a high selectivity of Me_2SiCl_2 and good silicon utilization.
Despite numerous studies and publications, today the mechanism of the direct synthesis of MCS has not been fully understood. Particularly for this reaction, is that the catalyst and promoters are supported on silicon, which is a reactant [4].
The performances of the reaction will depend on the initiation step (active sites formation though reaction between silicon and copper), on the evolution of the contact mass (silicon surface is constantly changing due to silicon consumption by the reaction) and on the ability of the system to regenerate. Copper transport from activated particles to fresh silicon is key to maintain stable performances.

Bibliographic review

In a batch mode, performances of the direct synthesis will depend on the initiation step. This step has been extensively studied at lab scale since the fifties [5-8]. In this step, chemistry and hydrodynamics are strongly interlinked. Main drivers for the initial performances are silicon chemical quality and particle size distribution (PSD), catalysts and cocatalysts chemical quality and PSD, pressure, temperature, quality of the mixing. At the end of the initiation, stable performances in term of productivity and selectivity are obtained in the reactor.

In batch mode, deactivation of the mass can be observed at lab scale: after consumption of a part of the silicon, the performances start decreasing as represented in the graph below.

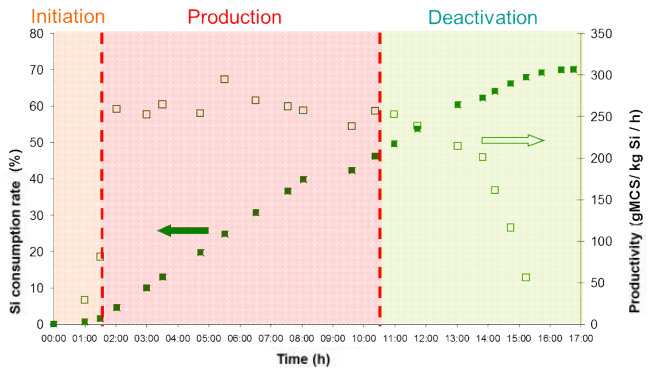

Figure 1 : Silicon conversion and productivity evolution in MCS batch reaction

Previous work [9] has shown that the deactivation occurred together with the formation of a thick catalyst coating layer at the surface of silicon particles, the layer preventing contact between methyl chloride gas and silicon surface.

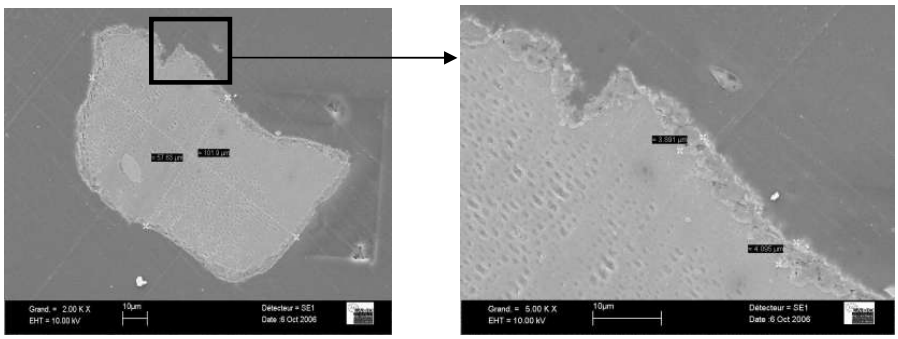

Figure 2 : SEM picture of silicon particle coated with catalyst, sampled during deactivation phase

Some studies describe the deactivation phenomenon. MCS reaction performed at different Cu amounts in lab stirred bed reactor [10] indicated higher productivity and lower initiation time with higher amount of copper, but quicker deactivation and lower Me_2SiCl_2 selectivity. SEM-EDX analyses indicated a rough textured surface for deactivated masses with copper only in a shallow surface layer. Deactivation was explained as a limited diffusion of copper into the unreacted Si surface, due to contact between Cu discrete areas at the surface. In another study [11], main factor for the deactivation is the enrichment of free copper. Observation of high level of carbon deposit and high level of chlorine in the reactor containing deactivated masses could be explained by MeCl decomposition at the surface of free copper. A mechanism was proposed by Weber et al [12] to explain deactivation due to too high copper amounts.

In the industrial reactor, after the initiation stage, silicon is added continuously into the FBR together with a certain amount of catalyst.

Fresh silicon particles are initiated by reaction with copper coming either from fresh catalyst addition (same mechanism as during initiation phase) or from activated silicon particles. This transfer of catalyst from an “old” already activated particle to a new one will activate the fresh particle and reduce accumulation of catalyst at the surface of the old one limiting the deactivation phenomenon described above. This concept can be illustrated by the following scheme :

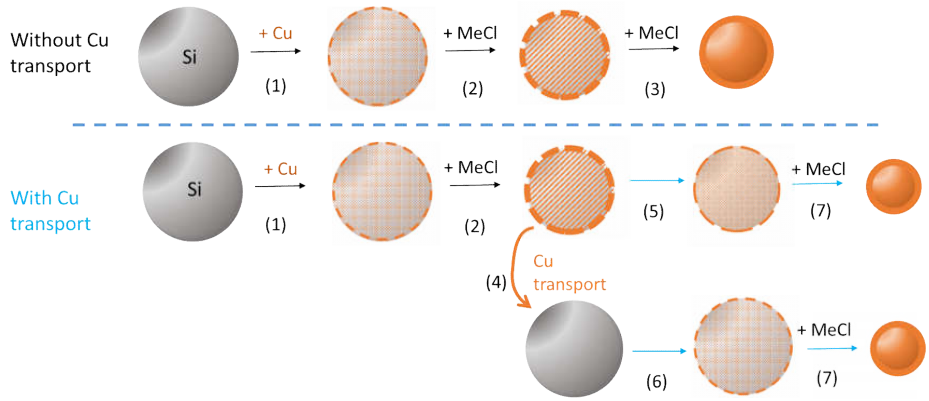

Figure 3 : Silicon particle evolution with or without copper transport

After initiation (1), activated silicon particles is consumed by reaction with methyl chloride (2) until the catalyst layer at the silicon surface is too thick and prevent methyl chloride and silicon contact. If copper is transported from an activated to a fresh silicon particle (4) catalyst concentration is decrease at the initial particle surface (5) enable further conversion of the silicon particle (7). In the same time a new silicon particle is activated (6). The mechanism can be continuously repeated.

Very few documents describe the transport phenomenon in the MCS reactor.

Some work concerning catalysts movement in the FBR was done to understand poor performances obtained at industrial scale with low aluminium silicon [13-14]. Hypothesis to explain the bad performances was the lack of catalyst movement in the FBR, in relation with low Al content. Experiments performed at lab scale consisted in vaporizing CuCl, $ZnCl_2$, and mix of them together with $AlCl_3$ or not. $AlCl_3$ was proved to favour vaporization of copper and zinc chlorides, by forming $ZnCl_2$-$AlCl_3$ or CuCl-$AlCl_3$ adducts with low boiling temperature.

In order to maintain stable performances in the industrial FBR and avoid particle deactivation, it seems necessary to have homogeneous and low copper concentration at the silicon particles surface. Good catalyst transport from activated to fresh silicon particles should contribute to establish these conditions. The objectives of the study is to better understand parameters influencing the catalyst transport from activated to non activated silicon particles and the performances of the catalytic sites resulting from this transport. Specific experiments were designed for this purpose.

Experimental procedure

Experiments will consist in producing reactive mass at lab scale and studying the transfer of catalyst from the reactive mass to fresh silicon.

The indicators for the study will be the amount of copper on added fresh silicon after the transfer and the productivity of fresh silicon activated by copper transport.

The parameters studied will be the experimental conditions during the transfer step: temperature and addition of tin, zinc and aluminium.

Lab reactor :

Experiments are carried out in a glass stirred bed reactor of a capacity of 0.8 liters. The schematic drawing of the experimental set- up is shown in Figure 4.

The reactor is heated by an electric oven coupled with a regulating system PID. The temperature setting is fixed between 250 and 300°C. Methyl chloride (MeCl) is continuously distributed through a porous plate at a mass flow rate of 60g/h. Methylchlorosilanes (MCS) are condensed, at the column outlet, by a water cooler. Unreacted methyl chloride is trapped in an acetone and dry ice mix.

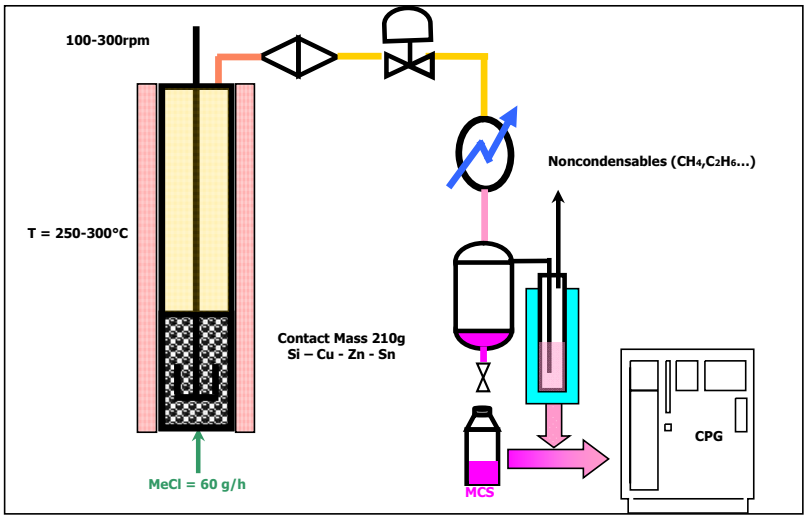

Figure 4 : Scheme of experimental set-up of MCS synthesis in laboratory stirred bed.

Specific procedure

The reaction proceeds over 2 days.

On the first day, contact mass of 210g of silicon (0-100µm), and the catalytic species copper (as CuCl) , zinc and tin (as bronze) added as solid powders are mixed for 20 minutes. The contact mass is loaded into the reactor and maintained under the experimental procedure described above over a period of 7 hours. During runs, condensed MCS are collected every hour and analysed by gas chromatography. After 7 hours, the temperature is decreased and the reactive mass is maintained over night at room temperature under nitrogen.

Day 1 procedure is the same for all the experimental study. The same silicon powder (same impurities and size distribution 0-100 µm) and the same catalyst quality were used for all experiments. Around 50g of silicon is converted during day 1.

On the second day, 50g of silicon (125-160µm) are loaded to the reactor. Specific conditions are used for a period of 2 hours before the reaction is restarted under the same conditions as in day 1. After 7h reaction with sampling as in day 1, the reaction is stopped and the mass is cooled under nitrogen. The two fractions – the one from day one and the one from day 2 - are separated by sieving and characterized.

Day 2 conditions will change for each experiment: contact mass from day 1 and fresh silicon will be mixed in specific conditions of temperature, cocatalyst addition…

The experimental procedure can be summarized as follows :

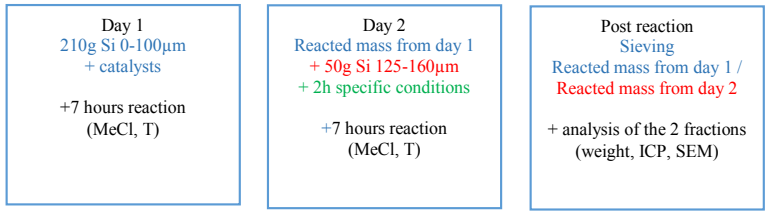

Characterization methods

Liquid samples are collected at every hour and analysed by gas chromatography**.** From GC analysis and mass balance, we can define the following criteria:

Silicon consumption rate: quantity of silicon converted during the reaction. It is determined from mass balance on silicon in the outlet condensed gas, analyzed by GC. It is expressed in weight percent.

Productivity: Is the methylchlorosilanes mass flow-rate produced per kilo of silicon initially loaded in the reactor (g MCS/(kg.h)).

Dimethyldichlorosilane selectivity: Is the weight percentage of dimethyldichlorosilane in the total sample of methylchlorosilanes produced.

Remaining Solid particles are collected at the end of the experiment. For each batch the solids are separated using a 100 micron screen. The two fractions (-100µm and +100µm) are weighed and characterised by elemental analysis (ICP) and SEM.

From these analyses, we can define the following criteria:

Silicon consumption rate (Si utilization) of the fractions from the first and second day.

Catalyst content in each of the fractions from the first and second day, which will give the amount of catalyst and cocatalyst transport from activated to non-activated silicon.

In this study, performances of the reactions in term of productivity and selectivity is similar for all the experiments in day 1 (same experimental conditions), and is the result of the two fractions and additives performances for day 2. Productivity and selectivity from the very different situations of day 2 will not be systematically commented.

The study will focus on analysis done on solids samples, and more specifically on the fraction +100µm representative silicon activated by catalyst transfer.

Experimental Results

Impact of temperature on copper transport

In first series of experiments, fresh silicon added to the reactor on day 2 was mixed with reacted contact mass at a fixed temperature under nitrogen over a period of 2h. After 2 hours period, methyl chloride was fed to the reactor and temperature was adjusted to standard MCS reaction conditions.

At the end of the experiment, the contact mass was sieved at 100µm; Upper and lower fraction were weighed and analysed by ICP.

Table 1: Mixing silicon and contact mass under nitrogen at fixed temperature before MCS reaction : analysis of fractions from day 1 and from day 2

					Catalyst content			Catalyst transfer		
Exp	Temp (°C)	Si Fraction (day)	Weight (g)	Si utiliz. (wt%)	Cu (wt%)	Sn (ppm)	Zn (ppm)	Cu (%)	Sn (%)	Zn (%)
1	25°C	-100µm (d1)	106g	49%	3,3	170	1410			
1	25°C	+100µm (d2)	32g	**36%**	0,8	70	490	3%	6%	2%
2	200°C	-100µm (d1)	107g	49%	2,7	160	1340			
2	200°C	+100µm (d2)	43g	**14%**	1.0	250	510	6%	28%	3%
3	300°C	-100µm (d1)	114g	46%	2,9	190	1080			
3	300°C	+100µm (d2)	46g	**9%**	0,7	240	370	4%	28%	2%

We can observe that silicon utilization of the fraction +100µm is significantly different from an experiment to the other. It seems that the thermal treatment under nitrogen has a negative impact on the silicon consumption rate. The higher temperature the treatment is, the lower is the silicon consumption rate.

Qualitative SEM analysis illustrate this assumption: the silicon surface of fraction +100µm is less consumed for treatment at higher temperature:

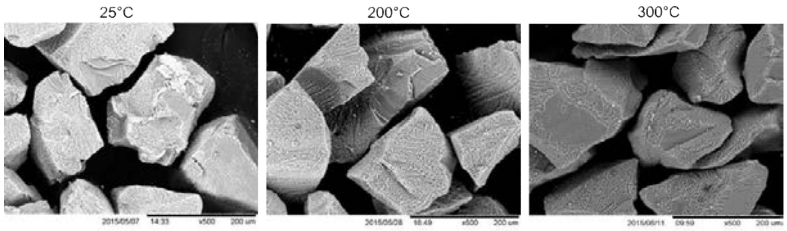

Figure 5: SEM analysis of fraction +100µm after experiments with treatments under nitrogen at 25, 200 and 300°C

Elemental analysis performed on each contact mass fraction give the concentration of each element of the catalytic system. As no catalyst or cocatalyst was added together with fresh silicon on day 2, catalysts measured on fraction + 100µm is exclusively from transfer from activated particles from day 1 to fresh silicon. The transfer could occur either during the treatment period (2 hours at fixed temperature under nitrogen) or during the 7 hour reaction under methyl chloride.

Elemental analysis indicate that a low quantity of copper was transferred in the three experiments. At the end of the second day, only 3 to 6 wt% of the copper initially introduced in the reactor was present at the surface of the silicon particles from fraction + 100µm.

Percentage of zinc transferred was also very small. On the contrary, the percentage on tin transferred is significant and very different depending on the treatment temperature under nitrogen.

It seems that tin can be transferred under nitrogen from activated particles to a fresh silicon particles, the transfer being favoured by higher temperature: 4 to 5 times more tin has been transferred during the treatment at 200 or 300°C. Amount of tin in the +100µm fraction at the end of the reaction varies between 70 and 250ppm.

Impact of temperature and cocatalyst addition on copper transport

In this experimental section, cocatalysts tin and zinc were added together with fresh silicon on day 2. As before, the mix of contact mass and silicon was stirred under nitrogen at a fixed temperature.

The quantity of cocatalyst added is calculated based on the quantity of fresh silicon added on day 2. The ratio (added cocatalyst / added fresh silicon) is the same as the initial ratio loaded on day 1.
As tin and zinc are added to the reactor, only copper transfer can be estimated.

Table 2: Mixing silicon and contact mass with cocatalyst under nitrogen at fixed temperature before MCS reaction : analysis of fractions from day 1 and from day 2

						Catalyst content			Cu transfer
Exp	Temp (°C)	Cocatalyst added	Si Fraction (day)	Weight (g)	Si utiliz. (wt%)	Cu (wt%)	Sn (ppm)	Zn (ppm)	Cu (%)
4	25°C	Sn + Zn	-100µm (d1)	113g	46%	2,8	190	2090	
4	25°C	Sn + Zn	+100µm (d2)	44g	**11%**	0,8	210	800	6.5%
5	200°C	Sn + Zn	-100µm (d1)	120g	43%	2,3	100	2170	
5	200°C	Sn + Zn	+100µm (d2)	48g	**4%**	1,0	260	770	4.8%
6	300°C	Sn + Zn	-100µm (d1)	100g	52%	3	200	2200	
6	300°C	Sn + Zn	+100µm (d2)	47g	**6%**	0,7	210	910	4.5%

Catalyst and cocatalyst content on the fraction +100ppm, is nearly the same for the 3 experiments, and does not vary based on the treatment temperature.

The composition of the fraction +100µm is significantly affected by cocatalyst addition: compared to experiments 1-3 without cocatalyst addition, the amount of zinc was doubled (from 400-500ppm to 800-900ppm), the amount of tin was the same as in experiments 2 and 3 (no cocatalyst addition, T = 200-300°C). However, copper transport was not significantly improved by cocatalyst addition (from 3-6% to 5-6% of Cu transferred).

The decrease in silicon utilization seems mainly related to cocatalyst composition of the fraction: it seems that higher amount of cocatalyst in this fraction is detrimental to the productivity of the transferred catalytic site.

Impact of cocatalyst and additive on copper transport at room temperature

In these experiments, the mixing between contact mass and fresh silicon is performed at room temperature for 2 hours. Quantity of zinc added together with fresh silicon was identical as in the previous experiments: Aluminium was added (as Si_2Al_3Fe) in equimolar amount to Zn.

In these experiments, Al content in the two fractions was also measured.

Table 3 : Mixing silicon and contact mass with cocatalyst under nitrogen at fixed temperature before MCS reaction : analysis of fractions from day 1 and from day 2

						Catalyst content				Cu transfer
Exp	Temp (°C)	Cocatalyst added	Si Fraction (day)	Weight (g)	Si consump. rate (wt%)	Cu (wt%)	Sn (ppm)	Zn (ppm)	Al (ppm)	Cu (%)
1	25°C	/	-100µm (d1)	106g	49%	3,3	170	1405	2400	
1	25°C	/	+100µm (d2)	32g	**36%**	0,8	70	490	1950	3.0%
4	25°C	Sn/Zn	-100µm (d1)	113g	46%	2,8	190	2090	1690	
4	25°C	Sn/ Zn	+100µm (d2)	44g	**11%**	0,8	210	800	1070	6.5%
7	25°C	Zn	-100µm (d1)	100g	52%	3,3	210	3370	1970	
7	25°C	Zn	+100µm (d2)	46g	**8%**	0,8	140	1360	1170	5.0%
8	25°C	Al	-100µm (d1)	128g	39%	2,3	170	1390	1860	
8	25°C	Al	+100µm (d2)	34g	**32%**	0,6	100	490	1130	2.8%

The two experiments giving the highest silicon reactivity are the one without any addition and the one with Al addition. In both cases, a low percentage of Cu was transferred to the fraction +100µm and the amount of tin and zinc on this fraction was low.

Zn addition led to a high Zn concentration in both fractions, much higher than when added together with tin. The activity for this experiment was significantly increased and Me_2SiCl_2 selectivity decreased.

The addition of Al does not increase the concentration of Al in either fraction, indicating that it does not react with the surface or that it is evaporated from the silicon. The concentration of other elements seems to decrease in the contact mass as well. A mass balance of the different element for the 4 experiments above is given in the table below :

Table 4 : Mass balance on catalytic species in the lab reactor

	% of loaded catal in -100µm			% of loaded catal in +100µm			% of loaded catal in reactor		
Exp	Cu	Sn	Zn	Cu	Sn	Zn	Cu	Sn	Zn
1	50%	48%	21%	4%	6%	2%	54%	54%	24%
4	46%	47%	28%	5%	19%	4%	51%	66%	32%
7	48%	56%	39%	5%	16%	7%	53%	72%	47%
8	42%	56%	26%	3%	9%	2%	45%	66%	28%

Based on these results, it seems that zinc addition to the reactor make species less volatile / more accumulated in the reactor, and that aluminium make zinc and copper more mobile. Tin seems not being affected by aluminium addition.

Discussion

In any tested conditions, a low quantity of copper (3% to 7%) was transported from activated particles to fresh silicon in the lab reactor conditions. The amount of transported copper was not highly affected by the conditions evaluated.

On the contrary, tin and zinc content in the fraction above 100µm (silicon added on day 2) varied a lot with the experimental conditions. Tin transport under nitrogen seemed significantly favoured by temperature.

Zinc addition seemed to increase catalyst retention in the lab reactor, whereas aluminium seemed to make catalytic species more mobile

Calculation of surface concentration of catalyst on fraction +100µm after transfer indicated quite stable concentration in copper, systematically lower (2 to 4 times) than copper concentration in the initial composition. Tin surface concentration are in most of the cases significantly higher than in the initial composition whereas zinc surface concentration is systematically lower.

Table 5 : Surface molar concentration of catalyst

				Surface Catalyst concentration			Cu transfer
Exp	Temp (°C)	Cocatalyst added	Si Fraction (day)	Cu (mmol/m²)	Sn (µmol/m²)	Zn (µmol/m²)	Cu (%)
Initial		/	-100µm (d1)	28,3	78	2607	
1	25°C	/	+100µm (d2)	9,0	44	533	3
2	200°C	/	+100µm (d2)	15,0	198	747	6
3	300°C	/	+100µm (d2)	11,1	200	579	4
4	25°C	Sn+Zn	+100µm (d2)	12,5	171	1223	7
5	200°C	Sn+Zn	+100µm (d2)	16,8	236	1269	5
6	300°C	Sn+Zn	+100µm (d2)	11,5	183	1464	5
7	25°C	Zn	+100µm (d2)	12,9	116	2142	5
8	25°C	Al	+100µm (d2)	7,1	66	564	3

Reactivity of copper transferred to fresh silicon was strongly affected by transfer conditions and was systematically higher than the reactivity of the initial contact mass (day 1). Reactivity of transferred catalyst could be up to 10 times higher than initial reactivity.

The graph below represent the catalyst turnover (mol Si converted /(mol Cu.h)) for some of the experiments.

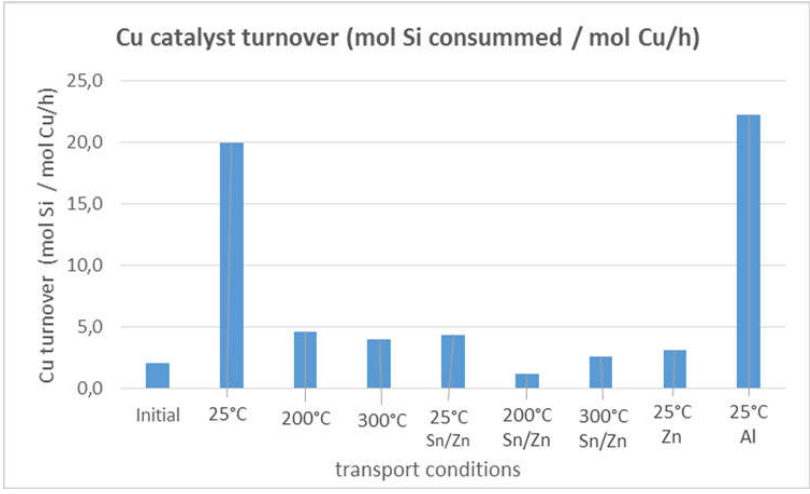

Figure 6: Copper catalyst turnover for different transfer conditions

Highest levels of reactivity were obtained mainly in the experiment at room temperature without any addition and in the one with Al addition. In both cases, copper and promoters were at low level in the fraction from day 2.

As reactivity seems to be more correlated with the level of cocatalyst we tried to establish simple correlations between cocatalyst amount in the fraction + 100µm and the silicon consumption rate of this fraction.

Inverse correlation could be found between silicon consumption rate of the fraction +100µm and the product of tin and zinc molar content in this fraction, indicating that high concentrations of cocatalysts seems detrimental for the reactivity of the fraction +100µm.

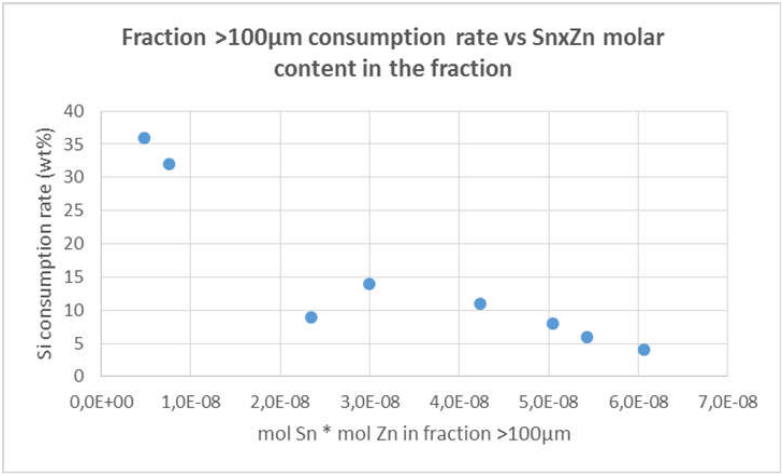

Figure 7: Fraction +100µm consumption rate versus (Sn*Zn) molar content in this fraction

If tin and zinc are necessary to initiate the reaction between silicon and catalyst, their role in catalyst transfer is less clear. It seems that the transfer of copper is not correlated to the transport of cocatalyst; Cocatalyst do not seem to contribute to copper transport.

Cocatalysts in the fraction + 100µm seem to act as a poison for the direct synthesis reaction. Surface concentration of tin and zinc in this fraction are much higher than standard conditions and the ratio Sn / Cu and Zn / Cu are much higher as well. Poisonous effect of cocatalysts used at too high concentration is described in the literature [15].

Conclusions

A specific experimental lab procedure was developed to get information on catalyst transport from activated to fresh silicon particles. Parameters influencing copper transport in the methylchlorosilane reactor and reaction performances of the catalytic sites resulting from this transport were investigated.
It was observed that the amount of copper transported from activated to unactivated silicon was quite low and was only slightly affected by experimental conditions. In any conditions, copper was distributed quite evenly at the silicon surface.

Cocatalysts transfer seemed more affected by experimental conditions: High concentration of tin on added silicon fraction seemed correlated with transfer at high temperature; high concentration of tin and zinc were obtained when the cocatalysts – or zinc alone – were added during the transfer step.

The reactivity of the catalytic sites obtained by transfer was significantly higher – up to 10 times higher - than the reactivity of the catalytic site obtained by reaction between silicon and fresh catalyst.

Best reactivities were achieved at relatively low concentrations of cocatalysts.

High concentrations of cocatalysts is suspected of being the main factor degrading the reactivity of fresh silicon.

References

1. Clarke M. P., Journal of organometallic chemistry, 376, 1989, p165
2. Seyferth D, Organometallics, 20 (24), 2001, p4978
3. Rochow E. G., Journal of American Chemical Society, 67: 1945, p963
4. Kim J. P., Rethwisch D. G, The direct synthesis of methylchlorosilanes, 134 : 1991, p168
5. Banholzer W. F., Lewis N., and Ward W., Journal of catalysis, 101, 1986, p405
6. Frank T. C., Kester K. B., and Falconer J. L., Journal of catalysis, 95:, 1985, 396-405
7. Tamhankar SS et al – Chem Eng. Sci. 36, 1981, p1365
8. Acker J – Silicon Chemistry 2, 2003, p195
9. N. Morin, PhD Thesis, 2008
10. Luo W, Zhang G, Wang G, Wang J – Tsinghua Sci. & technol. Vol11/2, 2006, p252
11. Luo W, Wang G, Wang J – Chem. Eng. Commun. 193, 2006, p754
12. Weber G et al. – CR Acad Sci Paris, t307, série II, 1988, p1155
13. Bablin JM, Crawford AC, DeMoulpied DC, Lewis LN – Ind Eng. Chem. Res. 42, 2003, p3555
14. Hoel J O, Frank R, Rong HM, Oye HA, Silicon Chemical Industry IV, 1998, p201
15. Wang C, Liu T, Huang Y, Wang G, Wang J, Ind. Eng. Chem. Res., 52 (15), 2013, p5282

Aluminum Species in Methylchlorosilanes Production: From Identification to Sequestering or Removal

J. Mohsseni, A. Bockholt, Wacker Chemie AG, Germany

Abstract

Aluminum chloride originating from aluminum impurities in metallurgical silicon is a constant contaminant in the product mixture of the Müller-Rochow direct synthesis. It causes several problems in the later stages of the silane distillation and purification process by reaction with other components of the product mixture. For example, these reactions account for the precipitation of solids which block filters and evaporator pipes, thus causing high maintenance costs. Tetrachloroaluminates were found to be major constituents of the precipitated solids. Strategies could be devised to avoid precipitation or to remove the aluminum compounds from the product mixture.

Introduction

The Müller-Rochow direct synthesis is a well-established process for the large scale production of methylchlorosilanes. The reaction of silicon with chloromethane affords a mixture of the desired methylchlorosilanes contaminated with undesired side products. Side products are alkanes, alkenes, chloroalkanes and aluminum chloride originating from the reaction of aluminum contaminations of silicon with chloromethane. This mixture is separated and the products are purified by distillation processes where under certain conditions for example in evaporators precipitation of solids is observed. These solids often block filters as well as pipes and tubing (Figure 1), thus causing high maintenance costs.

Figure 1: *Blocked evaporator pipes*

The nature of these solid compounds is relatively unknown, though. So investigations were started to identify the main constituents and to devise methods to prevent their precipitation.

Results and Discussion

Generally, all samples of the precipitates were taken in air directly after disassembly of evaporators or filters. They were introduced into an argon filled glove box where they were washed with n-hexane and dried to remove all silane and soluble organic residues. The precipitates found in the filters consisted of brown moisture sensitive powders. In pipes and tubing these powders were compacted and had to be milled before washing and subsequent analysis.

Elemental analysis of the solid precipitates by inductively coupled plasma atomic emission spectroscopy (ICP-AES) showed that the main constituents with mass fractions > 10 % are chlorine, carbon and aluminum. Iron and silicon were identified as secondary constituents with mass fractions from 1 - 5 %. The actual percentages were found to be varying slightly from sample to sample depending on the origin, but chlorine is always the element with the highest mass fraction, followed by carbon and aluminum. A typical result of the elemental analysis of a press cake sample is shown in figure 2.

Element	Mass Fraction [%]	Element	Mass Fraction [%]
Cl	37.70	P	0.32
C	27.00	Zr	0.10
Al	10.00	Ti	0.03
Fe	4.80	S	0.03
H	3.50	Na	0.03
Cu	3.20	Ca	0.02
Si	3.00	K	0.01
Sn	1.20	Mn	0.01
Zn	0.72	B	0.01

Figure 2: *Results of ICP-AES elemental analysis of solid precipitates from filters, percent by weight*

The solids were further characterized by scanning electron microscopy (SEM) in combination with energy dispersive x-ray (EDX) analysis. The SEM images show very homogeneous samples with particle sizes from 1 to 20 μm (Figure 3). The EDX spectra are in very good agreement with the ICP-AES results.

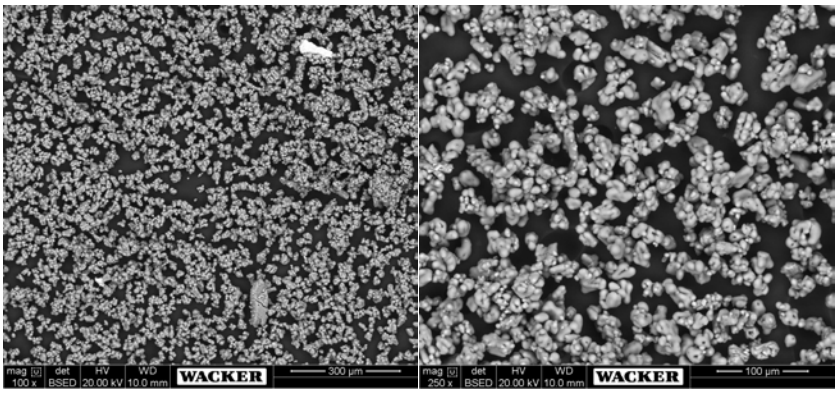

Figure 3: *Survey (left) and close-up SEM images of solid precipitates from filters, survey scan showing rust particle (white)*

Scattered in the samples a few rust particles were found accounting for a fraction of the iron contents of the solids as found in ICP-AES. The rust particles show very different morphologies and compositions compared to the rest of the sample and are therefore easily identified (Figure 4).

Since aluminum is a major constituent of the precipitates, solid state ^{27}Al-NMR was employed to identify the actual aluminum species present. For this, only rust-free samples were used. The peaks in the spectra were assigned by reference measurements. Samples from filters early in the distillation process contain two different aluminum species which could be identified as tetrachloroaluminate and aluminum chloride. Later in the process, only tetrachloroaluminate was found in samples from filters and evaporators (Figure 5).

There are a few metals that can act as possible cations for the tetrachloroaluminate anion, with copper and iron being the most abundant in the precipitates. Generally, all tetrachloroaluminate salts are scarcely soluble in the product mixture of the Müller-Rochow direct synthesis, so precipitation of the identified compounds is not surprising. Rather unexpectedly, the precipitates comprise a high carbon content. The nature of the carbon species in the precipitates could not be elucidated; thermogravimetric analysis in combination with mass spectrometry (TGA-MS) shows the elimination of chloroalkanes and alkanes at elevated temperatures (> 175°C). Since the precipitates are solids, the carbon species must be of high molar masses or polymeric or both. Since no evidence for elemental carbon was found and the hydrogen content of the precipitates suggests a saturated linear organic compound of high molar mass, polymers are most likely. They have to originate from reactions of the alkanes, alkenes and chloroalkanes in the product mixture. Such reactions could be those of chloroalkanes with the Lewis-acidic aluminum chloride to form tetrachloroaluminate and carbocations which then further react with alkenes to form polymers via cationic polymerization.

The silicon species present were found to be mainly highly crosslinked siloxanes probably resulting from the reaction of silane residues with moisture which occurred while taking the samples from filters or evaporators in air.

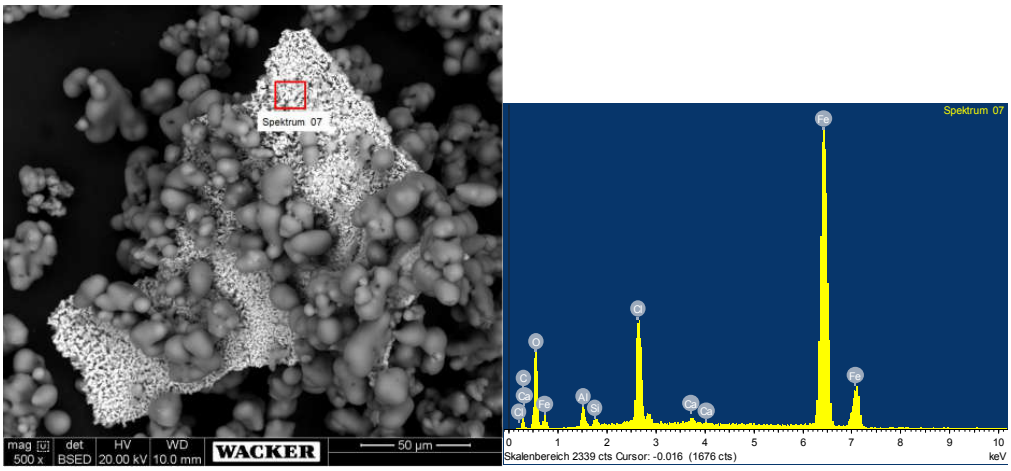

Figure 4: *SEM image of a rust particle covered by precipitate particles (top) and corresponding EDX spectrum*

The aluminum species in the solids have to originate from the product mixture of the direct synthesis. ICP-AES analysis showed that the mixture contains 150 – 250 ppm aluminum when it enters the distillation process. A ^{27}Al-NMR-investigation of several samples of that mixture found two different aluminum species (Figure 6). The broad signal/shoulder at approximately 90 ppm could be assigned to $AlCl_3$ by reference measurements while the species generating the sharp signal at 102 ppm remained obscure. In the first stages of the distillation process the aluminum concentration in the high boilers of the distillation range rises to 1700 ppm and a third aluminum species appears at 117 ppm, again showing a broad signal (Figure 7).

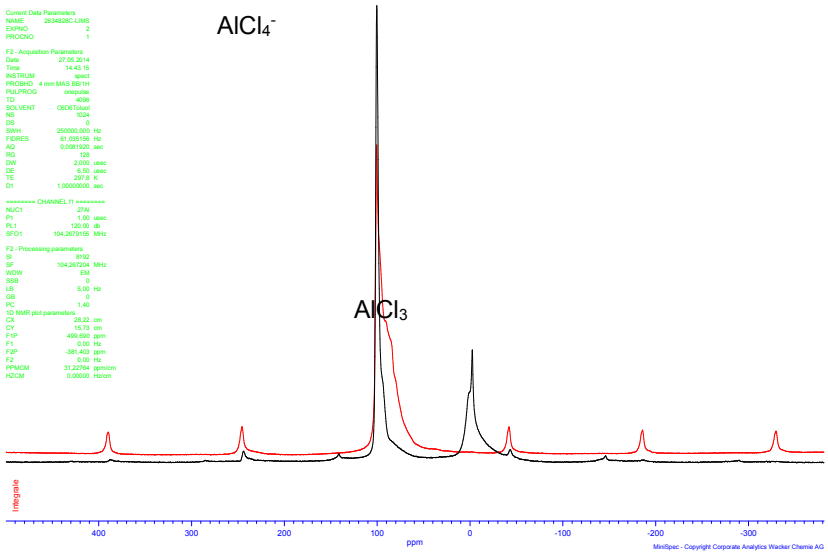

Figure 5: *^{27}Al-MAS-NMR (15 kHz) of solids from the filters of the first silanes distillation column (black) and from the disilanes distillation column (red)*

It was not possible to quantify the ratio of the three species in the spectrum because integration of the signals is made inaccurate by the quadrupole moment of the aluminum nucleus but it is

obvious that $AlCl_3$ is the dominant species in the high boilers. Broad signals in ^{27}Al-NMR indicate low symmetry and broad signals were found for both the species at 117 ppm and $AlCl_3$. Furthermore, reference measurements of methylaluminum chlorides showed that no such compound is present in the mixture. So the species causing the signal at 117 ppm remained unidentified, but since it has to be formed by reaction of the two aluminum species present in the product mixture, it most probably is closely related to $AlCl_3$, possibly $Al_2Cl_7^-$.
In the disilane columns of the distillation the concentration of aluminum in the high boiling residues which are discharged as waste from the last distillation columns rises further to about 4500 ppm. Two more aluminum species at 40 ppm and 96 ppm can be found in NMR spectra of the residue (Figure 8). As can be seen, a major fraction of the aluminum species in the mixture still consists of $AlCl_3$.

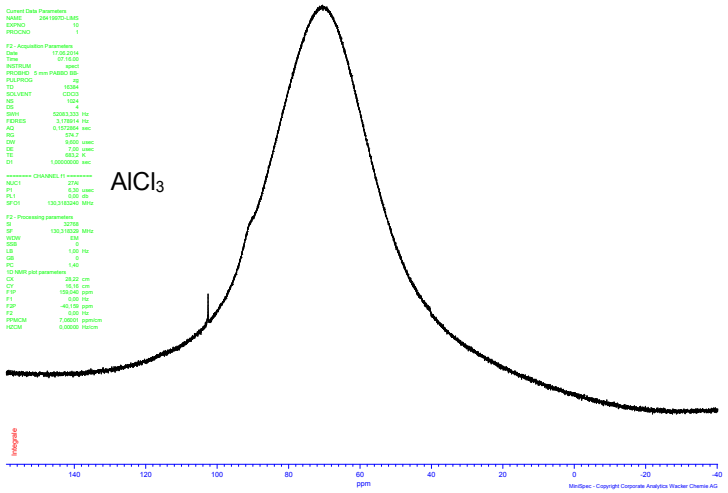

Figure 6: *^{27}Al-NMR of the direct synthesis product mixture (Al concentration ~200 ppm, broad hump from 20 – 120 ppm caused by probe and cavity of the NMR spectrometer*

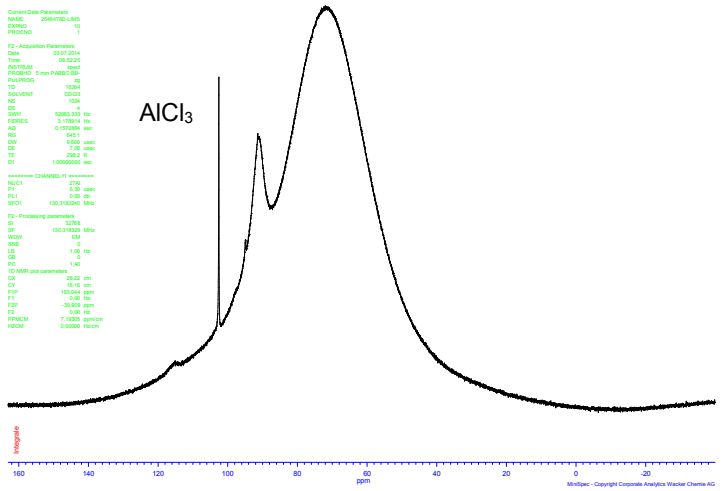

Figure 7: *^{27}Al-NMR of the high boilings of the distillation process (Al concentration ~1700 ppm), broad hump from 20 – 120 ppm caused by probe and cavity of the NMR spectrometer*

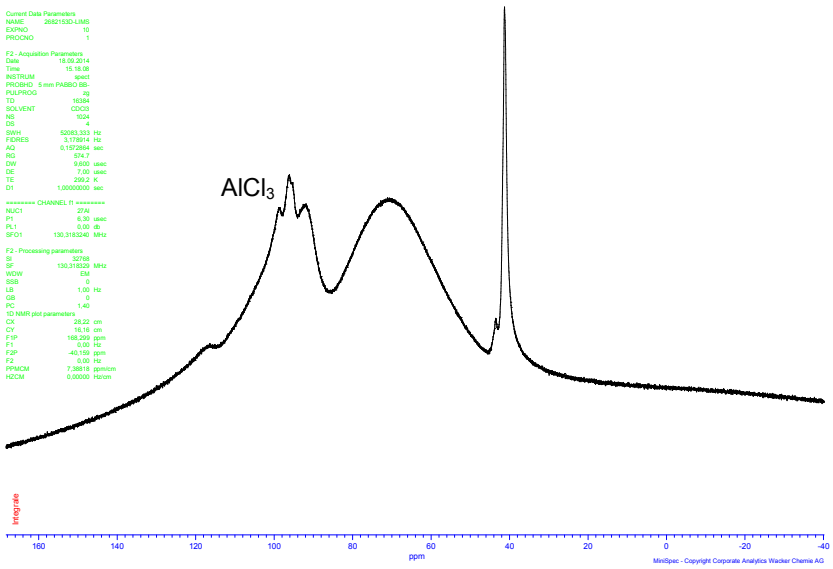

Figure 8: *^{27}Al-NMR of the high boilings discharged from the distillation process as waste (Al concentration ~4500 ppm), broad hump from 20 – 120 ppm caused by probe and cavity of the NMR spectrometer*

Thus, the results of the NMR investigations strongly suggest that $AlCl_3$ is the main cause of the precipitation of solids in the distillation process. It is present in the primary product of the direct synthesis and is present in all stages of the distillation process. It therefore most likely is the reactant to form several undesired products. The most problematic products are tetrachloroaluminate salts which are scarcely soluble in silanes and in the high boiling residues of the silane purification process. Together with carbon compounds they form solid precipitates to be found in filters and on the walls of evaporator pipes.

After identification of the main cause for the precipitates there are several methods conceivable to avoid processes leading to the formation of solids. The most obvious method would be the removal of $AlCl_3$ from the silane product mixture of the direct synthesis. Since it has a considerable solubility in this mixture it can´t be filtered off.

Published are several procedures to bond dissolved $AlCl_3$ to solids in packed bed columns. For this, reactions with Lewis-basic functional resins, clays or sodium chloride (NaCl) to give sodium tetrachloroaluminate ($NaAlCl_4$) are described in the patent literature [1]. The problem of packed bed columns is the limited mass flow which can be realized with this kind of equipment if the mobile phase is a liquid and the complexity of the regeneration or renewal of the column material. Thus, a high volume production can usually not be achieved if the purification of the product mixture involves passing it over a packed bed. Furthermore, the reaction with NaCl works best in the gas phase and at elevated (> 180°C) temperatures to remove the then molten $NaAlCl_4$ from the packed bed, but this causes high process costs and may result in changes in the product mixture due to undesired side reactions.

More suitable for mass production would be processes which generate an insoluble aluminum compound directly after synthesis by addition of an agent to the product mixture. The resulting compound could then be removed by separation processes like filtration or phase separation. These conversions should be fast and complete at or near room temperature to remove all or most of the aluminum in a short time and with low costs. The strong Lewis-acidic nature of $AlCl_3$ is very helpful in this respect.

The reaction of $AlCl_3$ with NaCl to yield $NaAlCl_4$ can be carried out by adding NaCl to the product mixture and stirring the resulting slurry. But this is a very slow process since the

reaction only takes place at the surface of NaCl crystals and the resulting $NaAlCl_4$ sticks to the surface, thus leaving it unreactive. This results in long process times and a huge excess of NaCl is needed.

Faster are reactions with organic compounds like urea[2] or imidazolium salts[3] which yield ionic liquids. We found them to be scarcely soluble in the silane mixture and they can be easily separated from it by phase separation techniques[4]. Quenching of $AlCl_3$ can be monitored by NMR in these cases (Figure 9). In one experiment, the aluminum concentration dropped from 160 ppm to 20 ppm in about 5 minutes when the product mixture of the direct synthesis was stirred with 2,5 wt-% of methylimidazolium chloride. The remaining aluminum concentration of 20 ppm was shown to correspond to the solubility of the resulting methylimidazolium tetrachloroaluminate in the silane mixture. The signal at 102 ppm in the aluminum NMR could therefore be assigned to tetrachloroaluminate.

Another way of preventing precipitation is blocking the reactions yielding tetrachloroaluminate. This can be achieved by adding a strong aprotic Lewis base to the silane mixture which bonds to the $AlCl_3$ firmly, thus preventing it from abstracting chlorine from chloroalkanes or other compounds. Best suited for this are nitriles with high boiling points which are cheap and readily available, like adiponitrile (Figure 10)[5]. It is sufficient to add these compounds to the silane mixture at low concentrations of 150 - 2500 ppm because their reaction with $AlCl_3$ is fast and complete. The formed complexes are considerably stable at all temperatures of the distillation process and the high boiling point of any excess nitriles prevents them from contaminating product fractions of the silane separation. The complexes and the nitriles remain in the high boiling residue and are discarded.

Since tetrachloroaluminates are soluble in polar organic solvents, solids that have already formed can be dissolved in aprotic high polarity solvents like tertiary amines and nitriles with high boiling points, thus cleaning the metal surfaces of pipes and tubing[6]. This can be achieved by pumping the solvent through the evaporators and tubing of the distillation equipment or after disassembly of the same. Pumping it through a closed system prevents the formation of hydrogen chloride by hydrolysis and is therefore preferable.

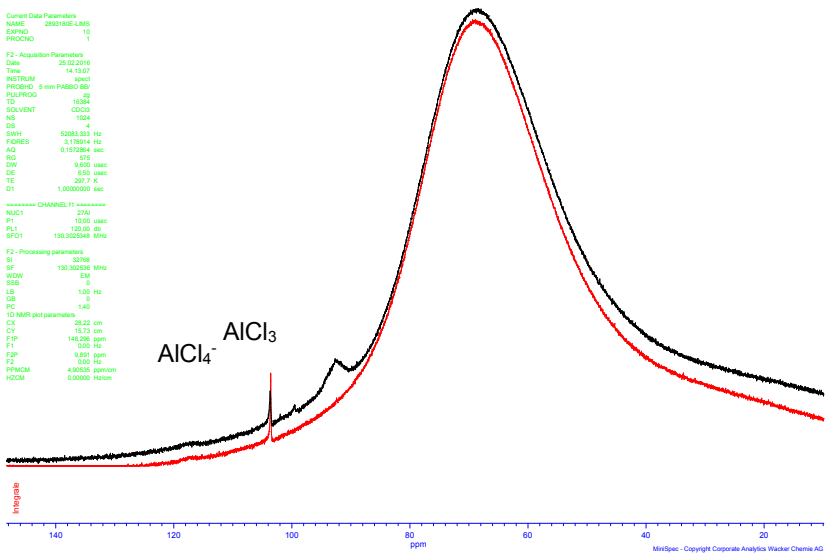

Figure 9: *^{27}Al-NMR of silane mixture before (black) and after treatment with methylimidazolium chloride, broad hump from 20 – 120 ppm caused by probe and cavity of the NMR spectrometer*

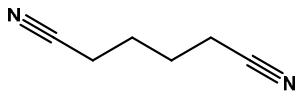

Figure 10: *Adiponitrile*

Summary and Conclusions

It could be shown that aluminum chloride dissolved in the silane product mixture of the Müller-Rochow direct synthesis is the main cause for the formation of solid precipitates clogging filters, pipes and tubing of equipment used in its distillation. The strong Lewis acid reacts with other components of the product mixture to yield tetrachloroaluminate salts which are scarcely soluble in silanes and thus precipitate in several stages of the distillation. This can be prevented by either removing aluminum chloride from the silane mixture or by blocking its Lewis-acidic site with a strong aprotic Lewis base. Removal of aluminum chloride is best achieved by addition of urea or imidazolium chlorides resulting in the formation of ionic liquids which are barely soluble in and can be easily separated from the silane mixture. To block the reactivity of aluminum chloride, strong Lewis bases like adiponitrile can be used. Already a very low concentration of this readily available solvent in the product mixture prevents the formation of solid precipitates without the risk of contaminating the desired product. If filters, pipes and tubing have already started to plug, aprotic high polarity solvents like tertiary amines or nitriles can be used to dissolve the precipitates and clean the equipment.

References

[1] a)E. Müh, H. Rauleder, J. Monkiewicz, DE 10 2009 027 729 A1, **2009**; b)T. N. Kitagawa, Mitsutoshi; Inaba, Chikara, US 20090238748 A1, **2009**; c)F. GAZZARRINI, M. MORICI, V. TRAPANI, DE 2852598 A1, **1978**; d)E. MUEH, H. RAULEDER, J. MONKIEWICZ, H. J. HOENE, R. SONNENSCHEIN, WO 09049944 A1, **2008**.

[2] W. Braun, DE 878647, **1951**.

[3] Y. Zheng, K. Dong, Q. Wang, J. Zhang, X. Lu, *Journal of chemical & engineering data* **2013**, *58*, 32.

[4] *Patent pending*.

[5] A. BOCKHOLT, C. KALTENMARKNER, J. MOHSSENI, K. KAEPPLER, K. MAUTNER, P. NUERNBERG, DE 10 2014 206 874 A1, **2014**.

[6] A. BOCKHOLT, C. KALTENMARKNER, J. MOHSSENI, K. KAEPPLER, K. MAUTNER, P. NUERNBERG, DE 10 2014 206 875 A1, **2014**.

Silicon for the Chemical and Solar Industry XIII
Kristiansand, Norway, June 13 – 16, 2016

Mechanistic Aspects of the Rochow Direct Process

Genqiang Xue, Van V. Green
Dow Corning Corporation, 4770 Highway 42 East, Carrollton, Kentucky 41008, USA

Abstract

The Rochow Direct Process involves reaction of silicon with methyl chloride to synthesize methyl chlorosilanes (MCS), which are used in various silicone products. Understanding fundamental mechanisms of this reaction is critical for improving product selectivity and material efficiency. The first part of this manuscript surveys literature about side-reactions and by-products related to methyl group decomposition. The formation of coke deposition, hydrocarbons, hydrogen gas, and MCS containing a Si-H bond or a Si-CH_2-Si moiety is discussed. The involvement of C-H bond cleavage as a rate-determining-step for methyl group decomposition is also assessed. The second part reports new methods for studying the reaction of silicon with cuprous chloride (CuCl). Silicon tetrachloride ($SiCl_4$) yield from this reaction was measured by a GC method with short cycle-time. The onset temperature was also studied by coupling a chemisorption analyser with a mass spectrometer.

Introduction

The reaction of methyl chloride (CH_3Cl) with silicon to synthesize methyl chlorosilanes (MCS), also known as the Muller-Rochow Synthesis or the Direct Process, is a key pillar for the silicone industry. Dimethyldichlorsilane ($(CH_3)_2SiCl_2$ or simply Me2) is the major product and used to manufacture polydimethylsiloxane fluid or elastomer. Some MCS by-products are valuable for different applications. In a commercial process, a balanced Me2-to-by-product ratio might be more important than a maximized Me2 selectivity for assessing process performance.[1]

Mechanistic study of the direct process is an active research area. Key topics/approaches include: (a) surface chemistry study (see ref. 2 for examples); (b) thermodynamic/kinetic modeling for understanding product selectivity (see ref. 3 for examples); (c) roles played by different promoters (see ref. 4 for examples).

The main reaction of forming MCS, particularly Me2, has been the focus for mechanistic studies. On the other hand, knowledge about methyl group decomposition and associated side-reactions within the direct process is still limited. Reaction of CH_3Cl on pristine surfaces such as Cu, single crystal Si and copper silicide has been extensively studied (see references 5-7 for examples) These studies provided a wealth

of information about interaction of CH_3Cl (or methyl groups from other sources) with these surfaces and subsequent reactions. However, it remains a challenge to connect these results with the observations on actual direct process reaction mass, which is a very complex solid mixture of silicon with Cu catalyst, several promoters, and more than 10 metallic impurities.[1] The required information for making the connection includes (a) which is the key active site causing the majority of methyl group decomposition? And (b) how does that relate to the active site that catalyzes MCS formation?

The first part of this manuscript surveys literature about side-reactions of methyl groups and related by-products. The second part reports new methods for studying the reaction of Si with CuCl, which is a key step for forming the active catalyst of the direct process.

Methyl group decomposition in the direct process

During the direct process reaction, it is desirable to keep the per-pass conversion of CH_3Cl well below 100%. Excess CH_3Cl improves the reaction rate of silicon. The un-converted CH_3Cl is separated from products and recycled back to the process.[1] Of all methyl groups from the converted portion of CH_3Cl, however, only part of them are incorporated into MCS. The other methyl groups go through different side-reactions and generate different by-products. For convenience, they are collectively termed as "unproductive" methyl groups in this manuscript. Unproductive methyl groups reduce material efficiency of the direct process. Some unproductive methyl groups go through C-H bond cleavage (decomposition reaction) to generate coke and hydrogen ligands incorporated into hydrogen (H_2), hydrocarbons and MCS products with a Si-H bond. These side-reactions and by-products, as well as possible reaction mechanisms, are summarized below.

By-products associated with methyl group decomposition

Some unproductive methyl groups lose hydrogen atoms and become carbonaceous residue (coke) deposits on the reaction mass. Coke formed in the direct process is not purely carbon based. Coke with hydrogen-to-carbon molar ratio in the range of 0.5-1.8 has been observed.[8] It was proposed that coke can catalyze formation of more coke or even deactivate the direct process reaction.[8,9] Olakangil systematically studied coke formation in the direct process.[10] The impurities present in chemical grade silicon were found insignificant for coke formation. On the other hand, phosphorus, a promoter used in the direct process, was found to suppress coke formation at higher temperature and pressure. CO_2 profiles obtained from temperature programmed oxidation (TPO) of coke deposition showed two major peaks, which were attributed to coke formed near two different sites. The lower oxidation temperature peak was attributed to coke formed near a site rich in copper and/or chlorine, while the higher temperature one was attributed to coke formed near a site lean in copper and/or chlorine. The assignment was based on observation that copper and chlorine catalyzed oxidation of carbon black and reduced oxidation temperature. However, the possibility of generating two forms of coke was not ruled out.[10] Based on kinetic study, Olakangil proposed coke formation mechanism consists of reactions 1-6 (S as an unoccupied active site consisting of Cu, Si or promoters). The proposed mechanism include key assumptions such as (a) reaction 2 was a rate-determining-step; and (b) reaction intermediates were adsorbed on reaction mass surface.[10]

$CH_3Cl + 2\ S \longrightarrow CH_3(ads) + Cl(ads)$ (1)

$CH_3(ads) + S \longrightarrow CH_2(ads) + H(ads)$ (2)

$CH_3(ads) + H(ads) \longrightarrow CH_4(g) + 2\ S$ (3)

$CH_2(ads) + S \longrightarrow CH(ads) + H(ads)$ (4)

$CH(ads) + S \longrightarrow C(ads) + H(ads)$ (5)

$CH_2(ads) + CH(ads) + C(ads) \longrightarrow Coke + nH(ads)$ (6)

Hydrogen, methane and other hydrocarbons with two to six carbon atoms are commonly observed in the direct process.[11] Muller suggested that methane and hydrogen were generated from reaction of two methyl radicals through reaction 7.[12] Alternately, methane can be generated from reaction of an adsorbed methyl group with an adsorbed hydrogen through reaction 3. Chain growing for formation of other hydrocarbons can occur in a reaction similar to 6.

$2\ CH_3\cdot \longrightarrow CH_4 + H_2 + C$ (7)

Methyl chlorosilanes such as CH_3SiHCl_2 (MeH) and $(CH_3)_2SiHCl$ (Me2H) are formed in the direct process. They are valuable for manufacturing of coupling agents and other functional products.[1] The combined selectivity of these Si-H containing by-products was found highly variable. Numbers in the range of around 1% to greater than 50% have been reported.[1,13] It is reasonable to assume that the hydrogen ligands originate from methyl chloride. However, there is no clear evidence of the direct sources. Some possible sources include methyl groups, partially decomposed fragments such as $-CH_2-$, H_2 generated form reaction 7, or adsorbed hydrogen generated from reactions 2 and 4.

In the direct process, there are by-products with the common $L_3Si\text{-}CH_2\text{-}SiL_3$ formula (where L are ligands such as CH_3-, Cl-, or H-). These by-products are collectively named silmethylenes. They are part of the high-boiling by-products generally known as direct process residue.[14] Silmethylenes were generated with higher yields in the reaction of methylene chloride (CH_2Cl_2) and HCl mixture with silicon.[15] In that reaction, the $-CH_2-$ group should be readily formed after cleavage of the two C-Cl bonds in CH_2Cl_2. In the direct process with CH_3Cl, the $-CH_2-$ must be generated from a methyl group after cleavage of one C-H bond. However, the formation mechanism of silmethylenes is not well understood. We speculate that the reaction mechanism involves reaction of a surface methylene group with two silyl groups (8). The other possible mechanism involves decomposition of the methyl group that is already on an adsorbed MCS molecule to generate a $Si\text{-}CH_2-$ moiety, which combine with another silyl group (9).

$2\ L_3Si\cdot(ads) + \cdot CH_2\cdot(ads) \longrightarrow L_3Si\text{-}CH_2\text{-}SiL_3$ (8)

$$L_3SiCH_3(ads) \xrightarrow{\text{H-acceptor}} L_3SiCH_2\cdot(ads) \xrightarrow{L_3Si\cdot(ads)} L_3SiCH_2SiL_3 \quad (9)$$

The side-reactions involving unproductive methyl groups can be summarized by Scheme 1, at least from the mass balance standpoint. Scheme 1 shows that: (a) some unproductive methyl groups are incorporated into methane and higher hydrocarbons without going through C-H bond cleavage; (b) the remaining unproductive methyl groups cleave different numbers of C-H bonds to generate hydrogen ligands and CH_x (x = 0, 1, 2) fragments; (c) the hydrogen ligands are eventually incorporated into MCS with Si-H bonds, hydrogen gas, or methane; (d) the CH_x fragments are eventually

incorporated into silmethylenes, higher hydrocarbons, and coke. It should be pointed out that this scheme does not represent the actual mechanisms involved these reactions. Indeed, understanding the actual mechanisms of these side reactions is critical for controlling the desired ones or suppress the undesired ones to optimize process performance. Two key questions are: (a) what are the rate-determining-steps (RDS) for these side-reactions? And (b) what are the active-sites that catalyze these side-reactions during the direct process?

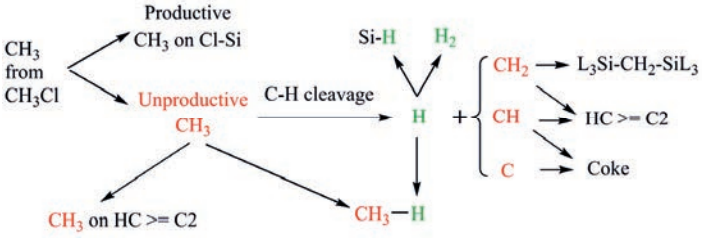

Scheme 1. Summary of side-reactions and by-products related to unproductive methyl groups. HC stands for hydrocarbons.

C-H bond cleavage as a rate-determining-step

Formation of all of the by-products summarized in Scheme 1 requires cleaving C-H bonds. As C-H bonds in a free methyl radical are very strong (~105 kcal/mol),[16] one would expect that C-H bond cleavage is a major component of the rate-determining-step (RDS). One way to test this hypothesis is replacing the proton with a deuterium. If C-H bond cleavage is a major component of the RDS, the reaction rate should be changed (reduced in most cases). This phenomenon is called kinetic isotope effect (KIE).[17] Scheme 2 explains the origin of KIE in C-H bond homolytic cleavage. Changing from a proton to a deuterium doubles its mass and reduces the stretching vibration frequency from 2900 cm^{-1} for a C-H bond to 2100 cm^{-1} for a C-D bond. As vibration frequency reduces, the zero-point-energy (ZPE) also reduces from 4.15 kcal/mol for C-H stretch to 3.00 kcal/mol for C-D stretch, and causes the same difference for homolytic cleavage activation energies ($\Delta G^{\ddagger}$). Based on the Eyring equation, that will reduce the reaction rate by a factor of about 7.[17]

	Frequency (cm^{-1})	ZPE (kcal/mol)	rel. rate
C-H stretch	2900	4.15	~7
C-D stretch	2100	3.00	1

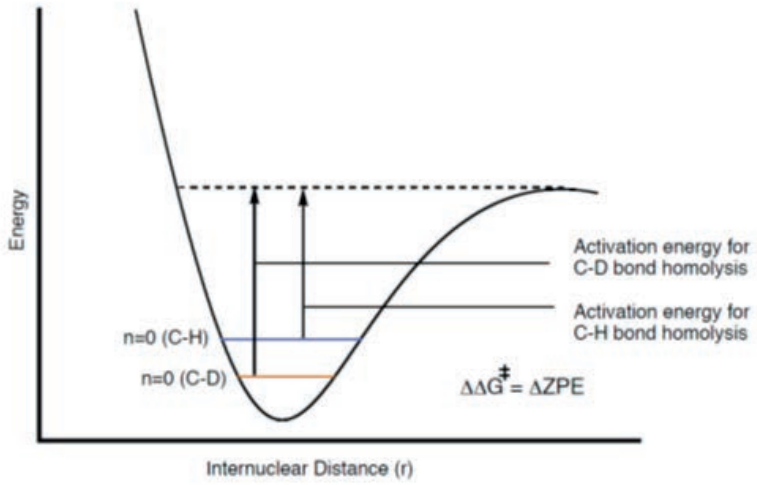

Scheme 2. Illustration of zero point energy (ZPE) and homolytic cleavage activation energy (ΔG‡) differences for C-H and C-D bonds. Adopted from an online publication (https://www.princeton.edu/chemistry/macmillan/group-meetings/RRK-KIE.pdf) with modifications. The values for frequency, ZPA and relative rate are from ref. 17.

Alber studied the direct process with deuterated methyl chloride (CD_3Cl).[13] In that study, the direct process reaction was initiated with CH_3Cl. The feed gas was then switched back-and-forth between CD_3Cl and CH_3Cl. It was observed that switching to CD_3Cl drastically decreased production rate and selectivity of MeH, confirming that its formation involves C-H bond cleavage as the RDS. On the other hand, Me2 production rate and selectivity increased when CD_3Cl was fed. The increase of Me2 was comparable to the loss of MeH.[13] This observation strongly suggests that the hydrogen ligands for Si-H formation are generated from the methyl groups which can also be incorporated into Me2. Therefore, the hydrogen ligand in MeH should be generated on active sites that also form chlorosilane products. Transferring methyl groups into Si to form Me2 and cleaving C-H bond to form MeH are two competing reactions.

On the other hand, feeding CD_3Cl reduced methane formation but increased ethane formation.[13] This observation confirms that C-H bond cleavage is also a key component of the RDS in methane formation. Moreover, methane formation through reaction 3 is competing with ethane formation through combination of two methyl groups.

Reaction of Si with CuCl

CuCl was found to effectively catalyze the direct process reaction and significantly reduce the length of the induction period.[18] Its reaction with silicon is seen as a key reaction and a model for forming catalytically active surface species in the direct process.[19] The thermodynamics and kinetics aspects of the Si and CuCl reaction has been extensively studied. It is proposed that the reaction pathway go through reactions 10 and 11 to generate $SiCl_4$ and copper silicides (Cu_xSi, x = 3, 5, etc., depending on Si and CuCl ratio).[20-22] This manuscript reports new methods for investigating this reaction.

$Si + 4CuCl \longrightarrow 4Cu + SiCl_4$ (10)

$Si + xCu \longrightarrow Cu_xSi$ (x = 3, 5, etc., depending on Si and CuCl ratio) (11)

Experimental details

Reaction mass was loaded into a reactor with a constant flow of N_2 passing through. The reactor was heated up to and maintained at 320 °C. The gas products were separated isothermally by an Agilent 7890 GC instrument with 100 °C column temperature and 3.6 mL/min helium flow. A thermal conductivity detector (TCD) was used. Peak identifications were confirmed by injecting known standards. Based on the N_2 flow rate (45 sccm, 3.4 g/hr) and N_2-to-$SiCl_4$ peak-intensity ratio, $SiCl_4$ formation rate was calculated. The reaction was also performed in a chemisorption analyser (Micromeritics AutoChem II) for better temperature control. The $SiCl_4$ product was monitored by a mass spectrometer (MKS-Cirrus) with cycle-time of 0.1 minute. In these experiments, ~0.5 g reaction mass was used and N_2 flow rate was set at 40 sccm.

Results and discussion

Figure 1 shows a GC chromatogram of the gas product mixture from the reaction of Si with CuCl. The GC method described in the experimental details allowed good separation of all the products exiting the reactor. The GC cycle time was slightly shorter than 2 minutes. We found that increasing the column temperature or flow rate did not significant decrease cycle time. On the other hand, the N_2 and HCl peaks co-eluted at higher temperatures. $SiCl_4$ was found to be the main product, accounting for greater than 95% of the mixture excluding N_2. There were also small amounts of HCl and $HSiCl_3$. We speculate that HCl was generated from reaction of $SiCl_4$ with trace amount of moisture left in the reaction mass. The $HSiCl_3$ could be generated from reaction of HCl gas with Si. Less HCl and $HSiCl_3$ were generated from the reaction mass with longer drying time, confirming that moisture was involved in formation of these by-products. The finding here supports previous proposals that $SiCl_4$ is the main gas phase product from the reaction of Si with CuCl.[20]

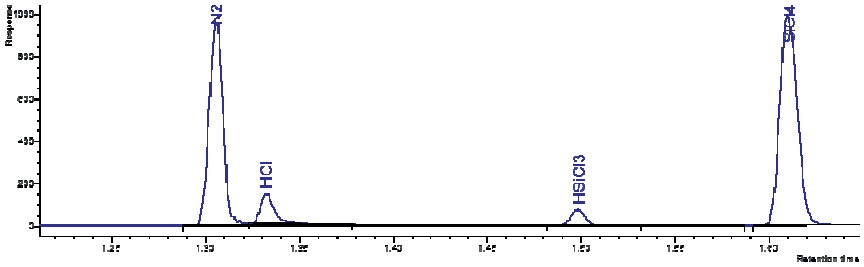

Figure 1. GC chromatogram of the gas product mixture from the reaction of Si with CuCl.

The constant flow of N_2 gas served two functions: as a carrier gas to move products out of the reactor and as an internal standard for quantifying product formation rates. Figure 2 shows $SiCl_4$ formation rate (blue line) and reactor temperature (red line) over the course the reaction. No product was detected below 220 °C. The $SiCl_4$ formation rate drastically increased when reactor temperature reached ~280 °C and dropped near zero about 20 minutes later. Calculation of the area under the blue curve in Figure 2 gave rise to total amount of $SiCl_4$ formed. Four experiments were performed and the average yield of $SiCl_4$ was found to be 107(±4)%.

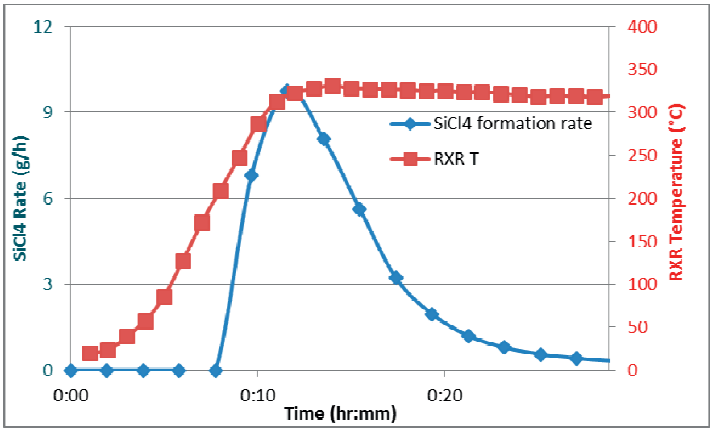

Figure 2. $SiCl_4$ formation rate (blue line with diamonds) and reactor temperature (red line with squares) curves vs time.

Although the above experiments provide accurate quantification of products, the reactor temperature-control and the time-resolution of GC were not ideal for measuring the reaction onset temperature. However, confirmation of $SiCl_4$ as the main product allowed us to monitor its formation with a mass spectrometry (MS) method, and use that as an indicator for reaction rate and progress. The MS method provides significantly higher sensitivity and shorter cycle time (~0.1 minute). The higher sensitivity of the MS method also allows use of less reaction mass (~0.5 g) and use of a chemisorption analyser (CA) to provide better temperature control.

Figure 3 shows the $SiCl_4$ signal intensity vs reactor temperature in a CA-MS experiment. The onset temperature for $SiCl_4$ formation is estimated as ~ 250 °C. This is close to what observed in earlier studies with a differential scanning calorimetric (DSC) method.[22] Upon completion of the reaction within similar timescale as the GC measurement, the MS signal dropped back to baseline level. Although not as good as the GC method for quantifying different products, the MS signal intensity is still a quantitative indicator for $SiCl_4$ formation-rate change (MS signal shows linear response to concentration change of a specific compound within a certain range, although the responses could be very different for different compounds of the same concentration). This reaction has excess Si and the reaction rate should be first-order to CuCl concentration (liming reagent). Based on pseudo-first-order theory, $SiCl_4$ formation rate (MS intensity) is proportional to CuCl concentration.[20] Therefore, the CA-MS method is also applicable for studying reaction kinetics.

Please note that the method here is limited to detecting $SiCl_4$ formation and reduction of CuCl by Si (reaction 10). It does not measure the reaction temperature for copper silicide formation (reaction 11), which may or may not occur at higher temperature as a separate step. Previous study with a DSC method did not suggest a different reaction temperature for silicide formation.[22]

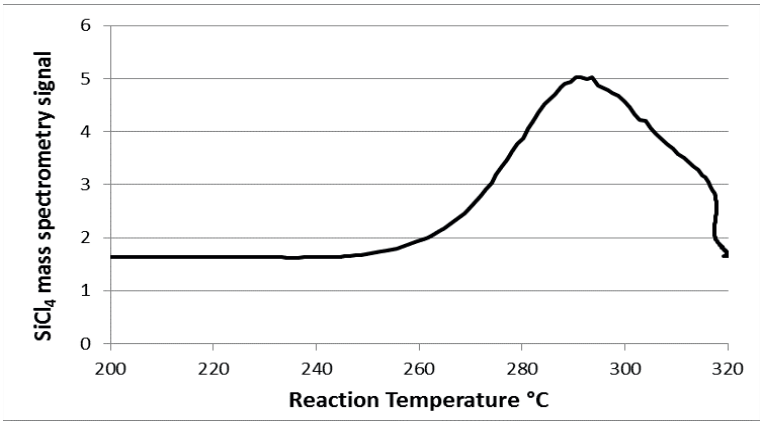

Figure 3. $SiCl_4$ mass spectrometry signal vs reaction temperature curve.

The results from this study conform that $SiCl_4$ is the major product with close to 100% yield in the reaction of Si with CuCl (based on reaction 10). The methods employed here are sensitive and suitable for studying reaction with very high Si/Cu ratio. Preference for Si/Cu molar ratio higher than 40 in the direct process has been reported.[23] Such high Si-Cu ratio could impose challenges for the DCS method commonly employed in previous studies. The heat generated from the reaction of Si with small amount of CuCl could become insignificant compared the heat required for increasing the temperature of the reaction mass. On the other hand, earlier kinetic studies involved hydrolysis of $SiCl_4$ and titration of the resulting HCl to measure CuCl conversion.[20,21] The CA-MS method reported here should provide higher sensitivity and significant shorter cycle time for measuring CuCl conversion, and enable comprehensive studies on the reaction kinetics.

Summary

The recent research results strongly suggest that a major part of methyl group decomposition and related side-reactions occur at or near the active sites which catalyze MCS formation. This is evidenced by the following observations: (a) formation of Si-H and Si-CH_2-Si containing products; (b) the co-relation of MeH suppression and Me2 enhancement when methyl group decomposition is suppressed, (c) formation of coke near Cu and Cl sites. On a single active site, there is competition between transferring activated methyl groups to form MCS and decomposing them. Encouraging methyl group decomposition might increase Si-H containing products. However, the overall material efficiency should decrease, as more methyl groups will likely be converted to hydrocarbon wastes. Fine-tuning the balance to achieve the optimum process performance requires detailed mechanistic information of methyl group decomposition and its related side-reactions. Studying these side-reactions of the direct process face the challenge of separating them from the main reaction of forming MCS. Developing new instrumentation and research methods might be necessary to achieve this goal.

References

(1) Lewis, K. M. In *Catalyzed Direct Reactions of Silicon*; Lewis, K. M., Rethwisch, D. G., Eds.; Elsevier Science Publishers B.V.: Amsterdam, The Netherlands, 1993, p 1.

(2) Lewis, K. M.; McLeod, D.; Kanner, B.; Falconer, J. L.; Frank, T. In *Catalyzed Direct Reaction of Silicon*; Lewis, K. M., Rethwisch, D. G., Eds.; Elsevier Science Publishers B.V.: Amsterdam, The Netherlands, 2003.

(3) Acker, J.; Bohmhammel, K. *J. Organomet. Chem.* **2008**, *693*, 2483.

(4) Gordon, A. D.; Hinch, B. J.; Strongin, D. R. *J. catal.* **2009**, *266*, 291.

(5) Magrini, K. A.; Gebhard, S. C.; Koel, B. E.; Falconer, J. L. *Surf. Sci.* **1991**, *248*, 93.

(6) Samson, Y.; Tardy, B.; Bertolini, J. C.; Laroze, G. *Surf. Sci.* **1995**, *339*, 159.

(7) Okada, M.; Goto, S.; Kasai, T. *J. Am. Chem. Soc* **2007**, *129*, 10052.

(8) Wessel, T. J.; Rethwisch, D. G. *J. catal.* **1996**, *161*, 861.

(9) Voorhoeve, R. J. H. *Organohalosilanes: Precursors to Silicones*; Elsevier, Amsterdam, 1967.

(10) Olakangil, J. F., PhD Thesis, The University of Iowa, 2002.

(11) Hawkins, L. G. In *Catalyzed Direct Reactions of Silicon*; Lewis, K. M., Rethwisch, D. G., Eds.; Elsevier Science Publishers B.V.: Amsterdam, The Netherlands, 1993, p 189.

(12) Muller, R.; Gumbel, H. *ZAAC* **1964**, *327*, 286.

(13) Alber, A., PhD Thesis, The Technical University of Darmstadt, 2010.

(14) Freeburne, S. K.; Jarvis, R. F., Jr. *One step process for converting high-boiling residue from direct process to monosilanes*; Dow Corning Corp., USA . 1997 US5627298A.

(15) Yeon, S.-H.; Han, J. S.; Yoo, B. R.; Jung, I. N. *J. Organomet. Chem.* **1996**, *516*, 91.

(16) Henry, D. J.; Parkinson, C. J.; Mayer, P. M.; Radom, L. *J. Phys. Chem. A* **2001**, *105*, 6750.

(17) Westheimer, F. H. *Chem. Rev.* **1961**, *61*, 265.

(18) Rochow, E. G. *J. Am. Chem. Soc* **1945**, *67*, 963.

(19) Bohmhammel, K.; Roewer, G.; Röver, I.; Acker, J. In *Silicon for the Chemical Industry VII*; Øye, H. A., Holas, A., Nygaard, L., Eds. MS Trollfjord, Trøms-Bergen, Norway, 2004.

(20) Tamhankar, S. S.; Gokarn, A. N.; Doraiswamy, L. K. *Chem. Eng. Sci.* **1981**, *36*, 1365.

(21) Gokarn, A. N.; Doraiswamy, L. K. In *Catalyzed Direct Reactions of Silicon*; Lewis, K. M., Rethwisch, D. G., Eds.; Elsevier Science Publishers B.V.: Amsterdam, The Netherlands, 1993.

(22) Acker, J.; Kother, S.; Lewis, K. M.; Bohmhammel, K. *Silicon Chem.* **2003**, *2*, 195.

(23) Ward, I. W. J.; Lewis, L. N.; Bablin, J. M.; Demoulpied, D. C. *Method for promoting dialkyldihalosilane formation during direct method alkylhalosilane production*; General Electric Company, USA . 2001 US6258970B1.

Silicon for the Chemical and Solar Industry XIII
Kristiansand, Norway, June 13 – 16, 2016

Advanced Modeling of Mueller-Rochow Synthesis

Michael Müller[1)], Stefan Heinrich[2)]
1) Wacker Chemie AG,
2) Hamburg University of Technology

Abstract

The Mueller-Rochow synthesis is a key process in the industrial manufacture of silicone products. Optimizing this process therefore offers high cost-saving potential, with benefits for a wide range of silicone materials. Modern process design and optimization are performed with computer simulation tools. For solids-gas processes, such as MCS synthesis, however, there are no adequate simulation tools available on the market to describe the complex physical and chemical interactions in a fluidized- bed process. Improving and optimizing existing MCS reactors as well as designing new reactors that are optimized as regards selectivity, production and conversion rates, as well as silicon use, require an integrated and holistic simulation tool covering all the influences that are relevant to the MCS process. The simulation model presented in this paper combines the influences of fluid dynamics and design aspects on the chemical reaction, such as the effects of operational parameters, different grain sizes or fluidized-bed internals. To validate the simulation tool, extensive experimental investigations were carried out on different adequate pilot plants in order to adapt the model and to confirm the reliability of the simulation tool.

Introduction

The Mueller-Rochow reaction, first described in 1940 by Mueller and Rochow, still forms the basis of industrial-scale silane chemistry [1, 2]. Almost all of the diverse silicone products known from everyday life are produced via this process. By direct synthesis, metallurgical silicon, together with chloromethane and copper catalyst, is converted into chlorosilane monomers at temperatures between 250 and 350°C. The major silane products from **m**ethyl**c**hloro**s**ilane (MCS) synthesis are shown in simplified form in Equation 1, in which dichlorodimethylsilane is the most desirable component and is usually produced in a yield range of 75-94% [3].

$$Si + CH_3Cl \rightarrow (CH_3)_2SiCl_2 + (CH_3)_m H_n SiCl_{4-m-n} \qquad m = 0-4, n = 0.1 \tag{1}$$

On a large scale, the reaction is carried out in fluidized-bed reactors, in which silicon powder mixed with catalyst is fluidized by the second reactant chloromethane (see

Figure 1). The heat of reaction has to be removed by means of heat-removal internals. The gaseous product flow at the top of the reactor also entrains solid particles. To improve raw-material utilization, the particles are separated out in one or more cyclones, and are returned to the reactor, so that only small amounts of silicon that pass through the cyclone are lost from the process. Subsequently, the crude silane is processed in multiple distillation steps.

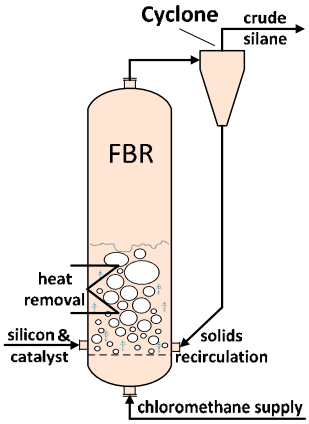

Figure 1: Schematic of a Mueller-Rochow fluidized-bed reactor

Since the Mueller-Rochow reaction is a surface-catalyzed gas-solids reaction, the fluidized-bed apparatus offers optimal conditions for high mass and heat transfer rates. At the same time, the process as a whole is becoming more and more complex. For process optimization and equipment design, an integrated and holistic simulation tool is needed that can cover all the required influences.

Modeling overview

The first step is to identify all the relevant influence parameters to be considered by the model. Basically, the Mueller-Rochow fluidized-bed process can be split into three major modeling subgroups that influence each other. First of all there is the fluid-dynamic behavior of the fluidized bed, which expresses the interaction between the solid particles and the fluid phase. Fluid dynamics plays a very central role here, providing information on gas distribution and on the availability of the gaseous reactant for the chemical reaction, based on gas-bubble behavior.

The chemical reaction is represented in a second modeling subgroup, in which the influences of reactant concentrations and pressure and temperature dependencies are considered. Finally, the influence of plant design parameters and their impact on fluid dynamics, on particle entrainment as well as on the chemical reaction also have to be taken into account (see Figure 2).

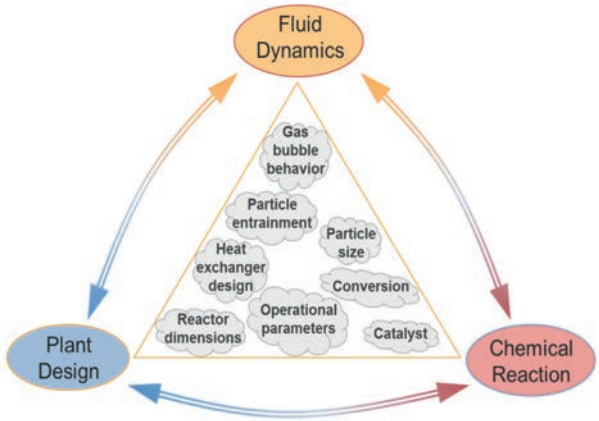

Figure 2: Influence parameters on the Mueller-Rochow reaction

Basically, various commercial process simulation tools (also for solids applications) are available. In the field of flow sheet simulation, ASPEN Plus™, for instance, offers various solids process modeling units that also comprise fluidized-bed reactors. However, at present, it is not possible, using this tool, to fully describe the complexity of the interactions between the different impact factors of the Mueller-Rochow synthesis in detail. On the other hand, there are **c**omputational **f**luid **d**ynamics simulation tools available, which are capable of describing fluid dynamics in great detail. Despite great progress in computing capacities during the last years, it is still not possible to employ this simulation tool for large-scale fluidized-bed reactors due to the enormous computational effort required to simulate huge numbers of particles.
Hence, in order to meet all the complex and individual requirements, an own rate- based model approach for the simulation of the Mueller-Rochow process was developed using the **A**spen **C**ustom **M**odeler™ programming environment. Besides the opportunity to create individual programming code, ACM also offers the advantage of access to ASPEN property data banks, and, furthermore, the possibility of implementing user-defined models in the ASPEN Plus™ environment, which can be connected to further downstream processes in order to optimize the entire MCS process chain.

Experimental validation data from pilot plants

When developing a simulation tool it is crucial to have basic experimental data available to validate the model equations. Therefore pilot plants are needed to provide scalable and transferable data.

Pilot plant for fluid-dynamic investigations

Especially in the case of fluidized-bed pilot plants, certain requirements concerning e.g. minimum diameter have to be considered to achieve significant and reliable data. For investigating the fluid dynamics of the Mueller-Rochow reactor, a fluidized-bed pilot plant was built in cooperation with Hamburg University of Technology (TUHH), with a diameter of one meter and a total height of 5.4 meters, including a cyclone and a solids recirculation system (see Figure 3 on the left). The pilot plant can be equipped with different interchangeable internals. For the experimental investigations, the gas volume flow and therefore the superficial gas velocities as well as the dense bed inventory were

varied within wide ranges. By employing different powders the influence of the grain size distribution was also examined.
To characterize the fluid dynamics in the fluidized-bed pilot plant the gas bubble behavior was measured by means of a capacity measuring probe system at different axial and radial positions throughout the dense bed. This well approved measuring method [4, 5] provides information on the distribution of gas bubbles in the form of data on the fractions, velocities, dimensions and frequencies of bubbles, which are important validation parameters for the fluid-dynamic model.
Beside the bubble behavior, particle entrainment was also measured and investigated by means of the pilot plant under different operational conditions, by mass flow rate and particle size distribution.

Continuous MCS pilot plant

To obtain basic data for the validation of the chemical model, a continuous small-scale Mueller-Rochow pilot plant is used. The mini plant allows operating conditions such as gas flow rate, operating pressure and temperature to be varied. Furthermore, the influence of different particle size distributions and catalyst mixtures, on yield, selectivities and conversion rates can also be observed. From the data gained, the model parameters “reaction constant” and the “order of reaction” were determined.

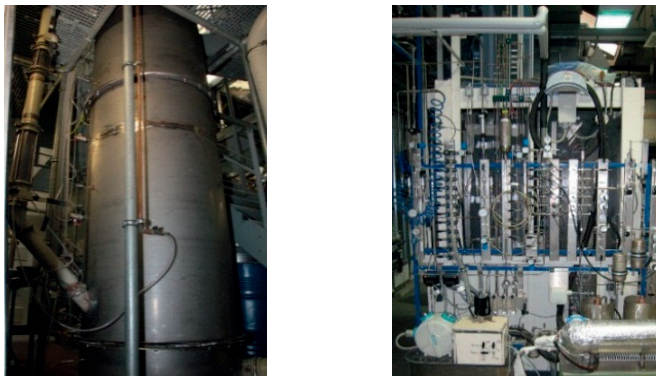

Figure 3: Pilot plants used for the experimental investigations of the fluid dynamics (left) and the chemical reaction (right)

Using the experimental data provided by these two pilot plants, the simulation model was gradually and continuously developed, improved and validated.

Mueller-Rochow fluidized-bed modeling approach

For modeling the Mueller-Rochow fluidized-bed reactor, a well approved and established two phase model approach is used [8, 9]. As shown in Figure 4, the fluidized-bed riser is axially discretized. Each element consists of a well-mixed solid-gas phase, called the “suspension phase” and a solid-free “gas bubble phase”. The solids particle distribution in the dense bed is considered to be ideally mixed, whereas the gas phase rises as plug flow within the fluidized bed. The gas fraction within the “suspension phase” is determined by the minimum fluidization velocity, while the excess gas forms bubbles (“bubble phase”). In the “suspension phase”, where gas and particles are mixed very intensively, the MCS-reaction takes place at the surface of the particles. The gaseous reactant held within the bubbles bypasses the fluidized bed and

is accessible for the chemical reaction only by mass transport from the "bubble phase" into the "suspension phase". The driving force considered for the mass transport is the concentration gradient of the respective components.

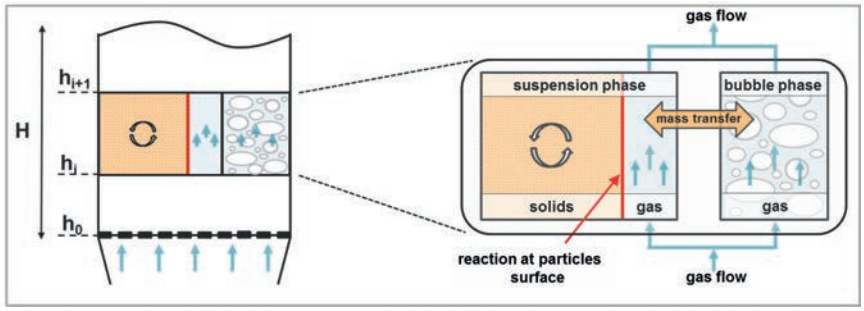

Figure 4: Schematic of the two phase model approach used

The differential gas mass balances for the two phases are formulated as follows:

Bubble phase:

$$\left[u - u_{mf} \cdot (1 - \varepsilon_b)\right] \frac{\partial c_{b,i}}{\partial h} = -k_{G,i} \cdot a_b \left(c_{b,i} - c_{s,i}\right) \tag{2}$$

Suspension phase:

$$u_{mf} (1 - \varepsilon_b) \frac{\partial c_{s,i}}{\partial h} = -k_{G,i} \cdot a_b \left(c_{b,i} - c_{s,i}\right) + (1 - \varepsilon_b) \cdot \varepsilon_{mf} \cdot a_P \cdot k_{r,i} \cdot c_{educt} \tag{3}$$

Where u denotes the superficial gas velocity, and u_{mf} and ε_{mf} are the minimum fluidization velocity and the bed porosity at minimum fluidization respectively. It is recommended to determine both of these parameters experimentally to characterize the powder that is used. Alternatively u_{mf} and ε_{mf} can also be calculated from the equations according to Ergun [10] or Wen and Yu [11] for example. ε_b is the local bubble volume fraction and $c_{b,i}$ the corresponding concentration of each component i within the bubble phase. The mass transport between the two phases caused by the concentration difference in the "bubble phase" ($c_{b,i}$) and the "suspension phase" ($c_{s,i}$) is calculated by means of a mass transfer coefficient $k_{G,i}$, based on a correlation by Sit and Grace [17]. The specific mass transfer area a_b is determined by the overall, local gas-bubble surface areas of each volume element. On the assumption that the heterogeneously catalyzed gas-solid reaction only occurs within the "suspension phase," the chemical reaction is considered by means of a reaction constant approach, where $k_{r,i}$ represents the reaction constant relating to the product component i, a_P is the total specific particle surface area that contributes to the reaction and c_{educt} refers to the availability of the gaseous reactant (chloromethane).

To describe the ideally mixed solid phase an overall mass balance is formulated according to Equation 4 considering the solids inlet flow rate $\dot{m}_{in}$, the particles that are entrained with the gas flow at the reactor's outlet $\dot{m}_{entr}$, the loss of solids due to chemical reaction, $\dot{m}_{reac}$, as well as the particle flow rate that is separated out by the cyclones and recycled to the reactor, $\dot{m}_{recycle}$.

$$\dot{m}_{in} - \dot{m}_{entr} - \dot{m}_{reac} + \dot{m}_{recycle} = 0 \tag{4}$$

To describe the changes of the particle size distribution within the fluidized bed, mass balances for each particle class *i* are also considered in the model according to Equation 5 by means of the particle mass fraction distribution $Q_{3,i}$. Here, the inlet particle size distribution, the shrinking of the particles due to the chemical reaction as well as the changes in the bed's composition due to particle entrainment are considered.

$$\dot{m}_{in} \cdot \Delta Q_{3,in,i} - \dot{m}_{entr} \cdot \Delta Q_{3,entr,i} - \dot{m}_{reac} \cdot \Delta Q_{3,reac,i} + \dot{m}_{recycle} \cdot \Delta Q_{3,recycle,i} = 0 \tag{5}$$

Modeling the chemical reaction of the fluidized-bed reactor

In order to improve selectivity and yield, a lot of research work concerning the chemical reaction was performed in the past, particularly on catalyst systems, on reaction conditions or on the influence of the powders used. Despite the extensive research activities, the reaction mechanism of the Mueller-Rochow reaction is still not fully understood. Thus for modeling the chemical reaction, a reliable and robust reaction constant approach is chosen, according to Equation 6.

$$c_i = c_{MeCl}^{\,n_i} \cdot a_p \cdot k_i \cdot e^{-\frac{E_{A,i}}{RT}} \tag{6}$$

Here, the formation of the different products *i,* such as from Equation 1, depend on the availability of the gaseous reactant chloromethane c_{MeCl} and on the availability of the active centers on the particles surface that is assumed to correspond to the total surface area of the silicon particles a_p. Both parameters are governed by the fluid dynamics of the fluidized bed and so are connected to the fluid-dynamic submodel. The order of reaction n_i, as well as the reaction constants k_i for each product component are determined experimentally by means of the Mueller-Rochow pilot plant. In order to describe the temperature dependency on the reaction constant, the Arrhenius approach is used, whereas activation energies $E_{A,i}$ were validated as well by means of the Mueller-Rochow pilot plant. Furthermore, R represents the gas constant and T the corresponding temperature of reaction.

Modeling the fluid dynamics of the fluidized-bed reactor

As the Equations 2-3 show, fluid-dynamic input data is required, such as the local bubble fraction or the bubbles' overall surface area for mass transport calculations. These parameters are provided by a fluid-dynamic submodel, which describes the bubble growth in the dense bed with height, by means of a volume-equivalent, spherical bubble diameter, d_v, using Equations 7-10 according to Hilligardt and Werther [12]. Besides the bubble growth, the second term in Equation 7 takes the splitting of bubbles on the basis of a mean bubble lifetime λ into account, which becomes relevant especially for Geldart A powders.

$$\frac{d(d_v)}{dh} = \left(\frac{2\varepsilon_b}{9\pi}\right)^{1/3} - \frac{d_v}{3\lambda u_b} \qquad \text{with: } \lambda = 280\frac{u_{mf}}{g} \tag{7}$$

The bubble volume fraction, ε_b which is also a height-dependent input variable for the employed two phase model approach, is calculated from the visible bubble flow $\dot{V}_b$ and the bubble rise velocity u_b. Here, g denotes the acceleration due to gravity. The visible

bubble flow depends on the hydrodynamic parameter φ that has to be experimentally identified (or can be roughly estimated at 0.8).

$$\varepsilon_b = \frac{\dot{V}_b}{u_b} \qquad \text{with: } \dot{V}_b = \varphi \cdot \left(u - u_{mf}\right) \tag{8}$$

According to Equation 9, the bubble rise velocity u_b depends on the visible bubble flow $\dot{V}_b$, on the bubble size d_v and also on the diameter of the fluidized-bed riser, expressed by the geometry parameter ϑ (Eq. 10) [8].

$$u_b = \dot{V}_b + 0.71\vartheta\sqrt{g d_v} \tag{9}$$

$$\vartheta = \begin{cases} 0.63 & d_r < 0.1m \\ 2.0\sqrt{d_r} & 0.1m \le d_r < 1.0m \\ 2.0 & d_r > 1.0m \end{cases} \tag{10}$$

As Equations 9 and 10 illustrate, the bubble velocity increases with increasing bubble size. Furthermore, it can be seen from the geometry parameter ϑ that, for smaller bed diameters, the bubbles rise at a slower rate due to the dominance of wall effects. With increasing bed diameter those wall effects are steadily reduced until they are negligible at diameters greater than one meter. So the model can also be used for lab-scale and pilot-plant fluidized beds with smaller diameters.
Since the distribution of the gaseous phase for each discretized height element, Δh_i, is known from the Equations 7 – 10, the solids volume concentration c_v is accessible so that the bed´s overall pressure drop, Δp_{fb} can be calculated by the summation of the pressure drop of each element according to Equation 11.

$$\Delta p_{fb} = \sum_{i=0}^{N} \left\{ \left(c_{v,i} \cdot \rho_s\right) + \left[\left(1 - c_{v,i}\right) \cdot \rho_{g,i}\right] \right\} \cdot g \cdot \Delta h_i \qquad \text{with: } c_{v,i} = \left(1 - \varepsilon_{b,i}\right) \cdot c_{vd} \tag{11}$$

The first term here represents the pressure drop caused by the solids, and the second one the gas phase. However the gas phase is almost negligible due to the large difference between solids and gas densities, ρ_s and $\rho_{g,i}$. c_{vd} is a correction value, when calculating the solids volume concentration from gas bubble fraction, depending on gas velocities and material properties, taken from [8]. Based on the pressure drop calculations, information on the total height and the overall solids mass content of the dense bed is available. On the other hand, the required bed mass can also be calculated from the model when a certain pressure drop or bed height is desired.

Modeling the influence of internals on the fluid dynamics

As mentioned at the beginning, the Mueller-Rochow synthesis is an exothermic reaction which means that the heat of reaction has to be removed in order to keep the temperature, and therefore yield and selectivity, constant. For this purpose, different types of vertical or horizontal heat-exchange internals, connected to a cooling system, as shown exemplarily in Figure 5, are commonly used [13].

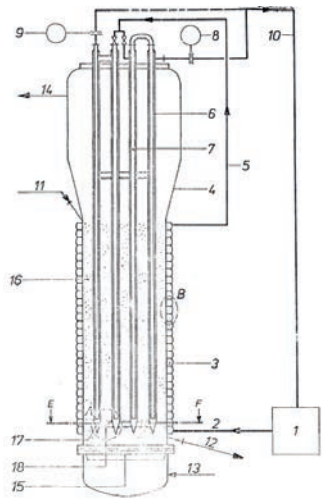

Figure 5: Example of heat removal internals in fluidized-bed reactors [13]

To follow the goal of developing an integrated and holistic model to simulate and optimize MCS synthesis, the influence of the heat removal internals on the fluid dynamics has to be identified and integrated into the simulation tool. Thus the design of the internals can also be considered for optimization work. At first sight the internals reduce the volume of reaction and the free cross-sectional area, which influences gas velocities in the riser. Furthermore, it turned out during the experimental investigations on the TUHH´s pilot plant that the bubble rise velocity in the dense bed decreased with an increased total surface area of the immerged internals. That means that the bubbles are decelerated at the internals surface. At the same time, the lower bubble velocities lead to a higher gas residence time in the dense bed which means a higher availability of the gaseous reactant for the MCS reaction. This example underlines how plant design, fluid dynamics and chemical reaction are closely interconnected. The surface effects of the internals are characterized by the hydraulic plant diameter d_{hyd} in the simulation model. As can be seen from Equation 12 and Figure 6, the hydraulic diameter recalculates an equivalent (reactor) diameter taking all the surfaces of the internals into account. Here, A_{cs} denotes the free cross-sectional area and P_{wet} depicts the wetted perimeter.

$$d_{hyd} = \frac{4 \cdot A_{cs}}{P_{wet}} \tag{12}$$

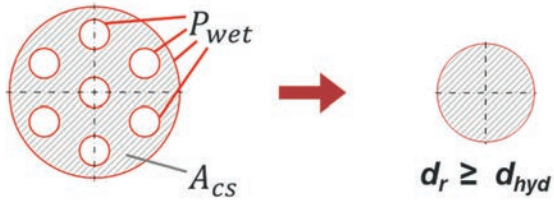

Figure 6: Illustration of the hydraulic diameter

As Equations 9 and 10 from the fluid-dynamic model show, the influence of wall effects on the bubble rise velocity, relating to the reactors diameter, are already considered. By replacing the reactor diameter d_r with the hydraulic diameter d_{hyd} in Equation 10, the effect of the internals surfaces can be applied directly to the existing model equations. In case of a void reactor without internals, the hydraulic diameter corresponds to the reactors diameter.

Fluid-dynamic model validation results

In order to confirm that the model correctly describes the physical interactions, a model validation based on experimental data was carried out. For this purpose, fluid-dynamic data provided from the pilot plant at the TUHH was used. Based on the capacity measuring probe system the height-dependent validation parameters: bubble fraction (ε_b) bubble size (d_v) and bubble rise velocity (u_b) are accessible for wide ranges of operational parameters. Furthermore, discrete pressure-drop measurements along the dense bed's height show the axial powder distribution and the fluidized-bed extension. As an example of the validation results of fluid dynamics, Figure 7 shows a comparison of the measured and simulated bubble diameters (d_v) by means of a parity plot for different internal configurations (A-D) and for two different superficial velocities (u). Here, the bubble diameters are normalized to the maximum bubble size. As the plot shows, the fluid-dynamic model corresponds very well to the measured data even for different internal configurations and gas velocities.

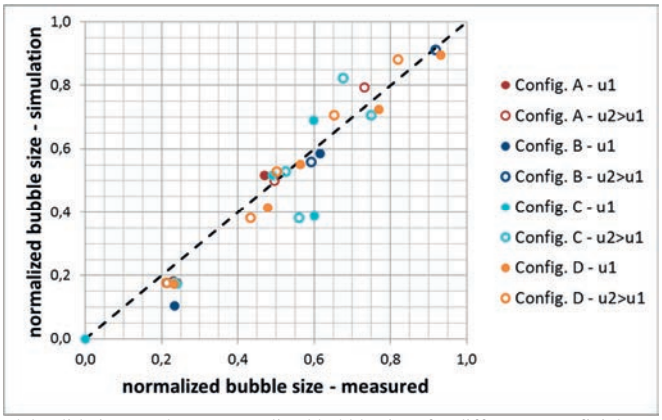

Figure 7: Model validation results on normalized bubble sizes for different superficial gas velocities (u1, u2) and internal configurations (A-D)

Modeling particle entrainment

For the Mueller-Rochow reaction and for fluidized-bed reactors in general, the effect of particle entrainment from the reactor is very significant. The particle entrainment determines the solid mass flow rate that leaves the reactor with the gaseous product flow and that has to be separated from the gas flow and recycled to the reactor. Both the solid separation by means of cyclones and the solids recirculation capacities are limited by practical considerations. Furthermore, depending on the cyclone's separation efficiency, the loss of silicon and therefore the silicon utilization is also affected directly by the particle entrainment.

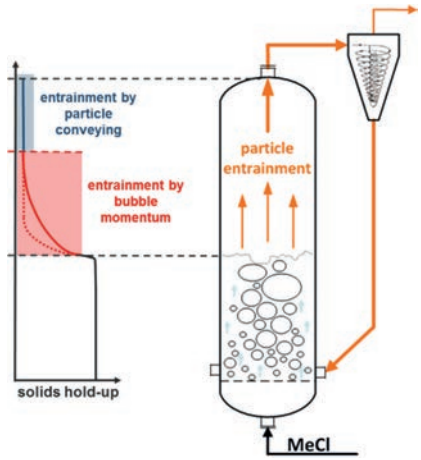

Figure 8: Particle entrainment in fluidized-bed reactors

As is shown in Figure 8, the solids concentration in the fluidized bed is almost constant up to the bed surface. At the bed surface, particles, independent of particle size, are thrown into the freeboard by means of bubble momentum, which mainly depends on the fluid-dynamic parameters bubble size and velocity. On their way up, bigger particles fall back to the fluidized bed, so that the solids concentration decreases with increasing height. At the same time, screening of particles takes place. At a certain distance, at the transport disengagement height [6], the screening process is almost finished, so that the solids concentration remains constant until the outlet is reached. Particle entrainment at this stage mainly takes place by particle conveying only, depending on the superficial gas velocity.

Thus the particle entrainment model has to consider both mechanisms, the height-dependent influences caused by bubble momentum and that caused by particle conveying in order to calculate the particle mass flow rate and the particle size distribution. The applied model Equation 13 comprises both entrainment mechanisms to calculate a resulting mass flow rate for each particle class *i*, related to the free cross-sectional area, A_{cs} [14]. The overall entrained solid mass flow rate then results from the summation of the individual flow rates, and the particle size distribution is calculated from the corresponding mass fractions.

$$\dot{m}_{entr,i} = A_{cs} \cdot \left[\left(E_0 \cdot \Delta Q_{3,i} \cdot \exp(-ah)\right) + \left(k_{\infty,i} \cdot \Delta Q_{3,i}\right)\right] \tag{13}$$

The first term in the Equation 13 represents the height-dependent entrainment flux of the particle class *i*. Here, E_0 is the entrainment flux directly at the fluidized-bed surface, weighted by the mass fraction of the corresponding particle class. The decrease of the entrainment flux with increasing distance from the surface *h* is modeled by means of the dumping coefficient *a,* which is fitted and validated based on experimental pilot plant data. Though it turned out that the dumping coefficient, and therefore the entrainment flux, strongly depend on the configuration of internals. The internals act like precipitators on the particles, reducing the entrainment flux. Here, an exponential dependency between the dumping coefficient *a* and the reactor's hydraulic diameter d_{hyd} was found, which allows the influence of the internals on the particle entrainment by the simulation model to be described.

To calculate the entrainment flux E_0 directly at the bed surface (at h=0) there are different semi-empirical correlations available in the literature such as the approach by Wen and Chen [15] for example, according to Equation 14.

$$E_0 = 3.07 \cdot 10^{-9} \cdot \frac{A_{cs} \cdot d_v \left(u - u_{mf}\right)^{2.5} \cdot \rho_g{}^{3.5} \cdot g^{0.5}}{\eta^{2.5}} \tag{14}$$

As can be seen from Equation 14, E_0 depends on the fluid-dynamic parameters bubble diameter d_v and the superficial gas velocity u, which are both provided again by the fluid-dynamic model, taking the bubble behavior in the dense bed into account. Furthermore, the entrainment flux at the bed surface also depends on the gaseous property data such as the density ρ_g and the dynamic viscosity η_g, as well on the dimensions of the cross-sectional area A_{cs} of the fluidized bed.
The second term in Equation 13 describes the entrainment mechanism that takes over above the transport disengagement height (TDH). Therefore an elutriation rate constant $k_{\infty,i}$ approach relating to different particle classes, is used [6]. To calculate $k_{\infty,i}$, there are several (semi-)empirical equations available in the literature [14] such as the approach according to Geldart et al [16], shown in Equation 15. From this equation it can be seen that particle entrainment above TDH, primarily depends on the superficial velocity u, on the density of the gaseous phase ρ_g and on the terminal velocity of a single particle $u_{t,i}$. Hence, at freeboard heights greater than the TDH, primarily particle sizes with terminal velocities lower than the superficial gas velocity are entrained.

$$k_{\infty,i} = 23.7 \exp\left(-5.4 \frac{u_{t,i}}{u}\right) \rho_g u \tag{15}$$

Thus, using Equation 13, the solids mass flow that leaves the reactor with the gas flow and its particle size distribution can be calculated. Figure 9 shows exemplarily the results of the model validation for the entrainment of different particle classes by means of a parity plot that compares the measured and the simulated data. As can be seen, the simulation results correspond very well to the measured data.

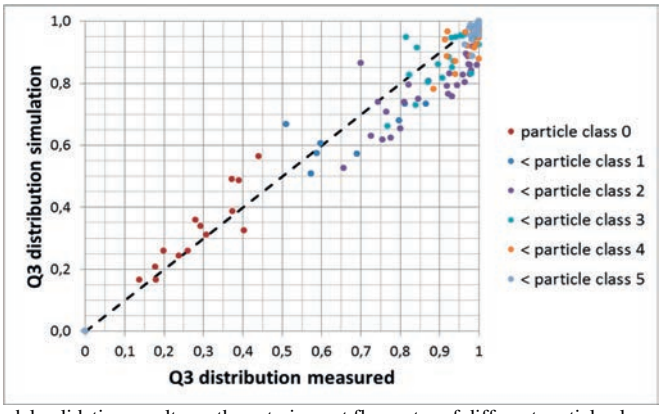

Figure 9: Model validation results on the entrainment flow rates of different particle classes

Conclusion

Although several commercial simulation tools for modeling solids applications are available on the market, it is not possible to describe the highly complex Mueller-Rochow fluidized-bed process sufficiently. So an own, tailored simulation model was created, comprising all the relevant influence parameters. During the modeling work extensive experiments were carried out in order to identify and quantify these influence parameters. For that purpose, a pilot plant was built in cooperation with Hamburg University of Technology to investigate the fluid dynamics of the fluidized-bed process, including the influence of different internal configurations on the gas bubble behavior and on particle entrainment. Furthermore, a second pilot plant was used to investigate the MCS reaction. Based on the know-how and on the basic data provided by the pilot plants, an own integrated and holistic simulation model of the Mueller- Rochow process was gradually developed and validated.

This comprehensive fluidized-bed simulation tool now can be used to optimize yield, selectivity and silicon utilization efficiency of the Mueller-Rochow reactor. The optimization work can concentrate on different aspects of the process such as on operational parameters, such as gas flow rates, temperatures or pressures, but also on the design of the reactor and internals, as well as on different grain sizes, with the aim of achieving operational excellence.

References

1. E.G. Rochow, US Pat. 2 380 995, General Electric, 1941.
2. R. Mueller, Deutsches Patent DD 5 348, VEB Siliconchemie, 1942.
3. B. Pachaly, F. Achenbacher, C. Herzig, K. Mautner: *Silicones*, Wiley-VCH Verlag, 2005.
4. J. Werther, O. Molerus, *The local structure of gas fluidized beds – I. A statistically based measuring system*, Int. J. Multiphase Flow, Vol. 1, pp. 103-122, Pergamon Press, 1973.
5. J. Werther, *Bubbles in gas fluidized beds – Part I*, The transactions of the institution of chemical engineers, Vol. 52, pp. 149-159, 1974.
6. D. Kunii, O. Levenspiel: *Fluidization Engineering*, Butterworth-Heinemann, 1991.
7. J. Werther, O. Molerus, *The local structure of gas fluidized beds – II. The spatial distribution of bubbles*, Int. J. Multiphase Flow, Vol. 1, pp. 103-122, Pergamon Press, 1973.
8. J. Werther, J. Wein, *Expansion behavior of gas fluidized beds in the turbulent regime*, AiChe Symp. Ser. No. 301, Vol. 90, pp. 31-44, 1994
9. J. Werther, E.-U. Hartge, *Modeling of industrial fluidized-bed reactors*, Ind. Eng. Chem. Res., Vol. 43, pp. 5593-5604, 2004
10. S. Ergun, Chem. Eng. Prog., 48,89, 1952

11. C.Y. Wen, Y.H. Yu, AiChE Journal, Vol. 12, pp. 610, 1966
12. K. Hilligardt, J, Werther, *The influence of temperature and solids properties on the size and growth of bubbles in gas fluidized beds*, Chem. Eng. Techn., Vol. 10, pp. 272, 1987
13. J. Muschi, J. Gansauge, H. Freudlsperger, Deutsches Patent, DE2704978, WackerChemie, 1982.
14. C.Y. Wen: *Handbook of fluidization and fluid-particle systems*, Marcel Dekker, Inc., New York, 2003.
15. C.Y. Wen, L.H. Chen, *Fluidized bed freeboard phenomena: entrainment and elutriation*, AIChE journal 28, pp. 117-128, 1982.
16. D. Geldart et al., Trans. Inst. Chem. Eng., pp. 57, 1979.
17. S.P. Sit, J. R. Grace: *Effect of Bubble Interaction on Interphase Mass Transfer in Gas Fluidized Beds*. Chem. Eng. Sci. 1981, 36, 327.

Silicon for the Chemical and Solar Industry XIII
Kristiansand, Norway, June 13 – 16, 2016

Identification and root cause analysis of micro-cracks in a trichlorosilane reactor

Sean Gaal[1)], Bill Larson[2)], John Herman[1)], Eric Davis[1)]
1) Dow Corning Corporation, Midland, MI, USA
2) Hemlock Semi Conductor, Hemlock, MI, USA

Abstract

During a routine inspection cracking was identified in a carbon steel trichlorosilane fluid bed reactor in the weld heat affected zone under a lifting lug. Further investigation using wet fluorescent magnetic particle inspection revealed more extensive cracking. A root cause analysis was performed which identified the mechanism as chloride salt induced stress corrosion cracking. Methods are identified to mitigate the risk.

Introduction

Stress corrosion cracking (SCC) of metals is a form of environmental cracking in which cracks form in the simultaneous presence of a tensile stress (as an applied stress due to live loading or as a residual stress from fabrication) and a corrosive environment. A unique characteristic of SCC is that the metal dissolution component of the corrosion reaction is essentially localised to the site and interior of the cracks, generally this is the primary factor in determining the rate of propagation. This type of localisation is atypical, it is only found in certain combinations of metals and corrosive environments. In corrosion engineering, this has led to the compilation of SCC susceptibility for a given metal by associating it with specific corrosive agents or environments.

Identification

Trichlorosilane reactors are routinely inspected, as part of the maintenance schedule. To accomplish this, they are first emptied and then washed out with water, hydrolysing any residual chlorides. During a routine visual inspection some small cracks were observed on the inside of the reactor, corresponding to the location of a lifting lug which had been welded to the vessel exterior. To better characterise the cracks the inside of the reactor was sand blasted and the cracks were imaged using wet fluorescent magnetic particle (WFMP) analysis (Figure 1). It was quickly discovered that the cracks were significantly more extensive than initially realised, located under the lifting lug near the man way and in several areas of the knuckle radius.

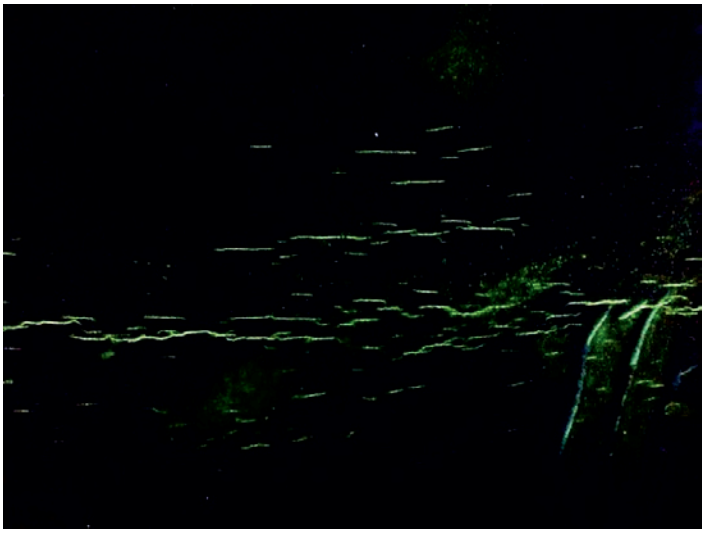

Figure 1: Wet fluorescent magnetic particle image of the cracks inside the reactor.

Even after identifying the cracks with WFMP, most of them were not possible to visually locate under normal light. To further characterise the cracks, two pieces 150-200 mm diameter were identified and cut from the reactor wall. Arrows in Figure 2 indicate the position of some of the cracks that were only possible to identify with WFMP.

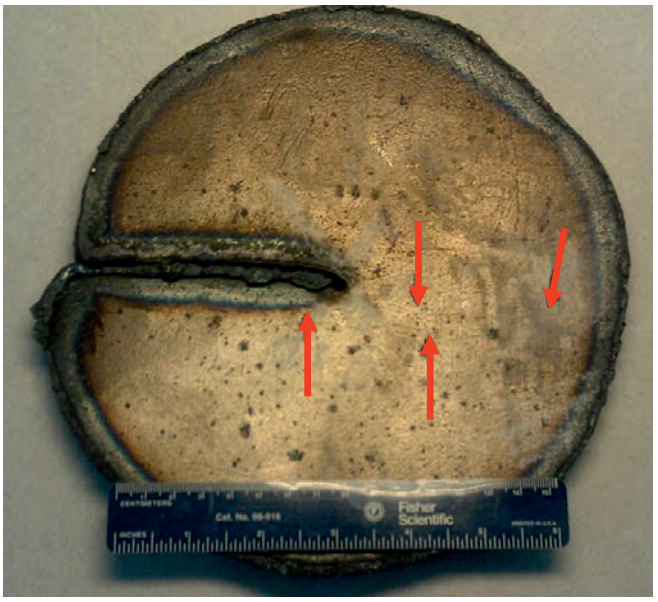

Figure 2: Inside surface of a cut-out. The red arrows indicate the location of cracks identified by visual examination at 10x–20x magnification.

All of the cracks that were identified in the cut-outs were open to the interior surface; interior, non-surface breaking cracks were not found. Figure 3 indicates the cut surface, with cracks indicated by arrows.

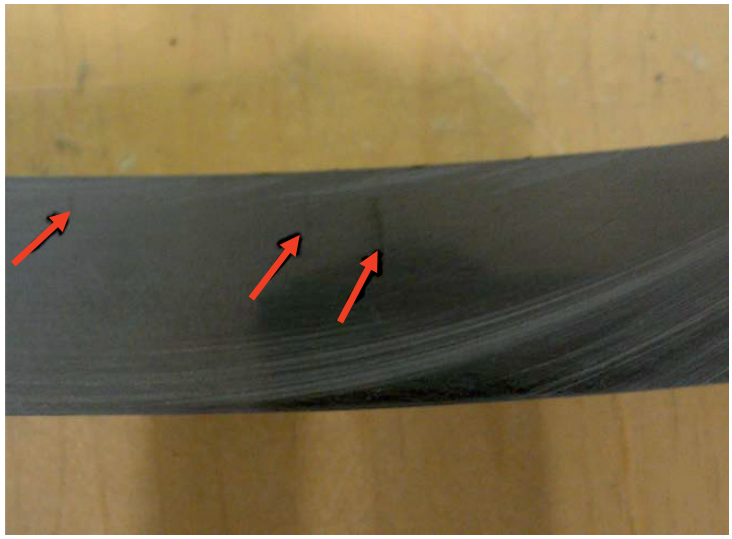

Figure 3: Wall cross section, showing the crack depth and morphology.

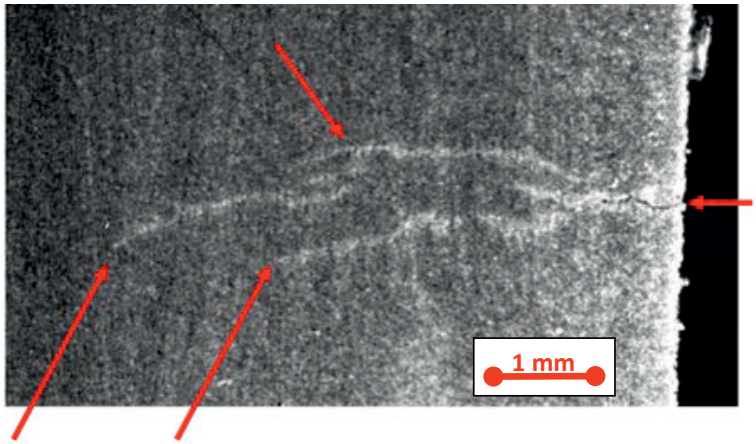

Figure 4: Significant branching of the cracks, with corrosion products. Inside surface of reactor at the right hand side of the image.

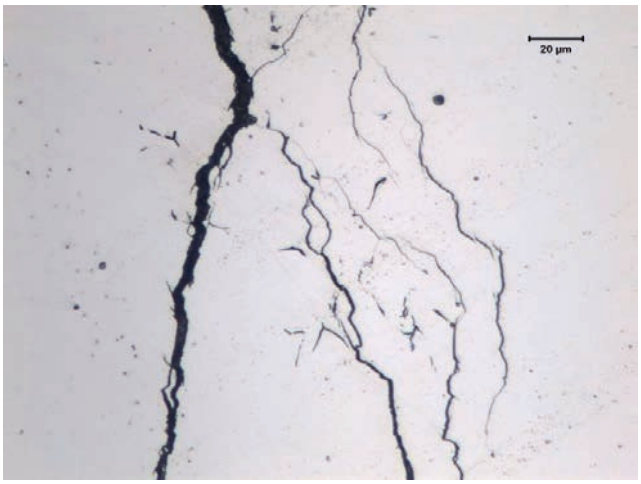

Figure 5: Branching also visible at a microscopic scale.

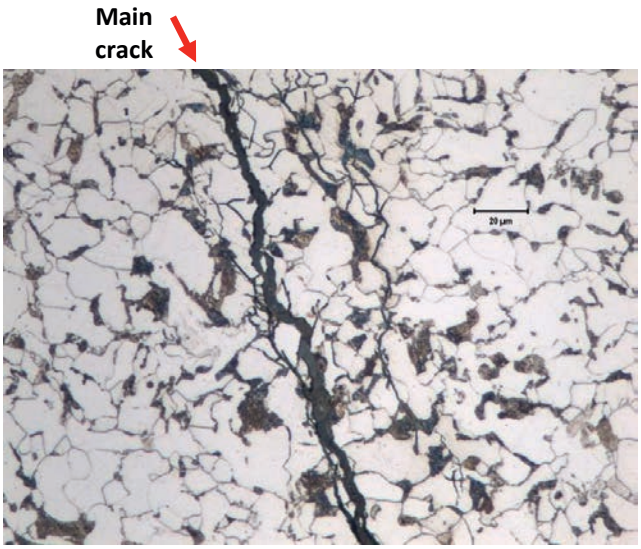

Figure 6: Optical micrograph of etched sample.

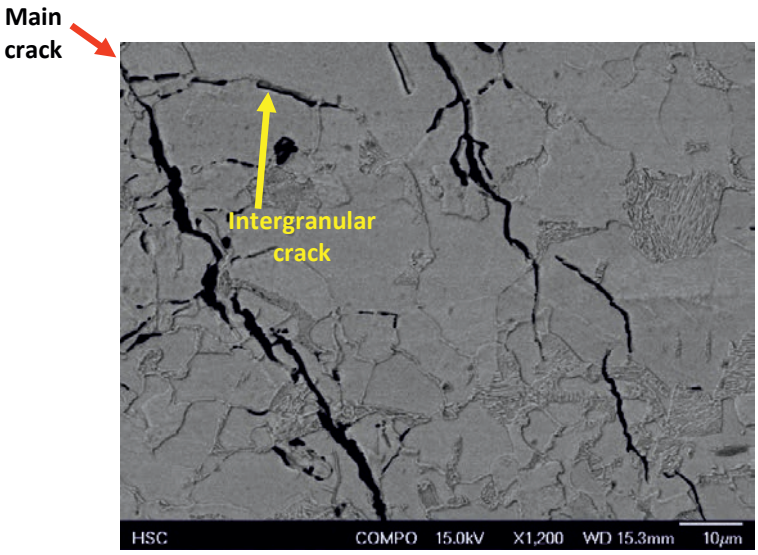

Figure 7: Electron micrograph.

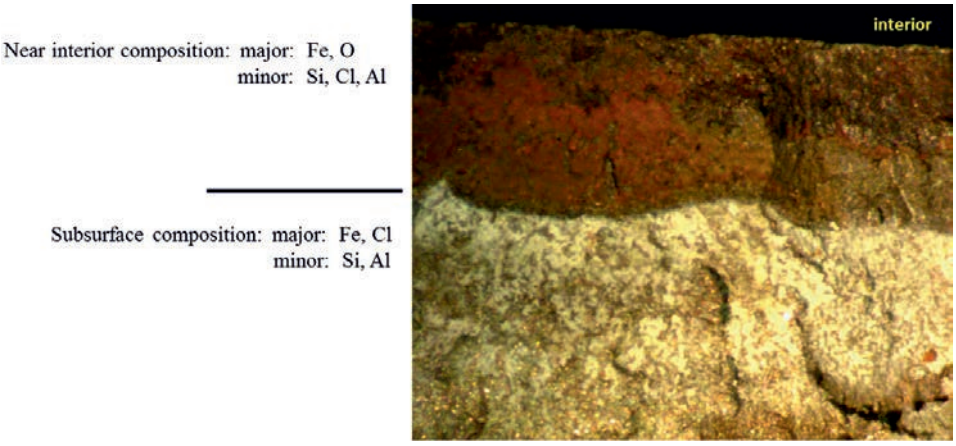

Figure 8: Opened cracks showed two zones, a red corrosion product extending 1-2 mm and a light filmed area beyond this extending to the crack tip.

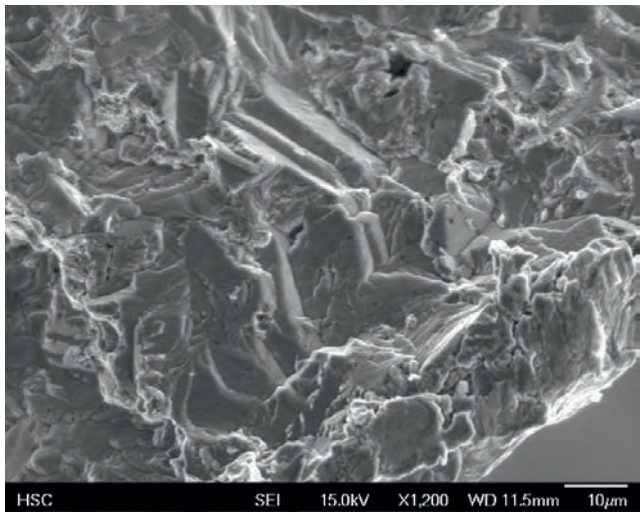

Figure 9: Electron micrograph of fracture surface.

The depth of the cracks investigated was from 5 to 11 mm deep, which is consistent with the expected rate of crack formation for SCC of 1 – 3 mm/year (1). As shown in Figure 4 to Figure 9, the cracks all share several features:

- The apparently simultaneous initiation and propagation of multiple cracks at a given location.
- Crack propagation with the development of extensive branching.
- The presence of corrosion products in the crack indicating a chloride salt.
- A trans-granular cleavage-type fracture surface morphology.
- Cracks only located in some areas of high internal stress due to forming or welding

While individually none of these uniquely identify a specific failure mechanism, taken together they are consistent with stress corrosion cracking as the damage mechanism or failure mode.

Root Cause

Stress corrosion cracking requires the simultaneous presence of three factors: a susceptible material (in this case carbon steel), a specific corrosive environment or agent, and a tensile stress above a certain threshold. Generally, three basic mechanisms have been identified for stress corrosion cracking (1).

1. Active path dissolution, where the bulk of the material is passive, but segregation of impurities at the grain boundary results in a susceptible material. This process can occur in the absence of stress.
2. Hydrogen embrittlement, which occurs where hydrogen is drawn to areas of stress in the matrix, generally at the grain boundary. In general the reactor temperature is too low for this mechanism.
3. Film induced cleavage, when a normally ductile material becomes coated with a brittle film formed by a corrosion process. The ductile surface blunts the crack, where the brittle film is reformed, progressively expanding to form a trans-granular fracture.

In this investigation the fractures are only located at areas where high stress might be present; at lifting lugs and at the knuckle radius where extensive forming has occurred. Carbon steel is generally considered immune to chloride stress corrosion cracking, but chlorides were the main component in the crack.

A search of literature uncovered two chloride based agents identified as causing stress corrosion cracking of carbon steel, by $HCl+AlCl_3$ (2) and $FeCl_3$ (3). Although the conditions are not identical, literature does establish a precedent for chloride stress corrosion cracking in carbon steel under the correct conditions.

In the trichlorosilane reactor, the feed materials are hydrogen chloride and metallurgical silicon. The major metallic impurities in the metallurgical silicon are iron and aluminium, which will react with hydrogen chloride to form salts. It is feasible that the salts and hydrogen chloride are then able to react with the surface of the carbon steel to form a very thin but brittle iron (II) chloride layer. The tensile stress within the steel is then able to crack this brittle chloride layer, forming further corrosion products and resulting in the slow propagation of a crack.

Mitigation

Stress corrosion cracking requires several conditions to co-exist, in this case a susceptible material, a corrosive medium and residual tensile stress. This can be illustrated with a triangle, similar to a fire triangle. If one of the conditions is eliminated, then the SCC will not occur.

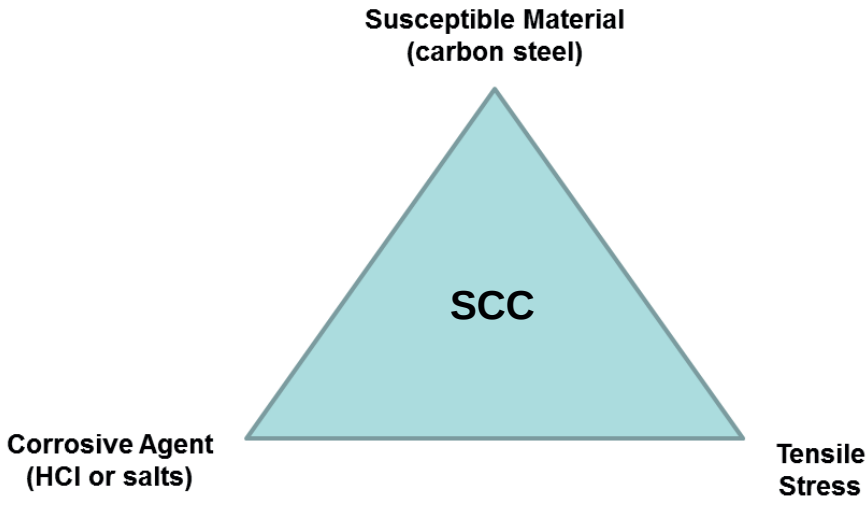

Figure 10: Required conditions for stress corrosion cracking.

Susceptible Material

The material of construction is carbon steel, which is susceptible to chlorination resulting in iron (II) chloride. Although it is feasible to use a different alloy, this would be an expensive solution.

Corrosive Agent

The process consists of hydrogen chloride and some chloride salts formed from the impurities present in metallurgical silicon. Due to the nature of the reactor, it is not possible to eliminate the chlorination sources.

Tensile Stress

The cracks in the reactor were only present in isolated areas, where the lifting lug was welded and some areas of the knuckle radius, where the steel plate was formed to make a dished shape. However, the knuckle was not uniformly covered in cracks, they were only located in isolated areas, indicating that the required stress was only located in specific areas. This indicates that the post-weld heat treatment was inadequate in these specific locations

Solution

Although there were several areas with stress corrosion cracking, it was only found in areas where high stress was present during construction (bending or welding) and it was not uniformly distributed around the knuckle. It is difficult to determine the residual stress in the reactor without destructive testing, but the distribution of SCC indicates that it is possible to use carbon steel in the environment if the stress is correctly relieved through heat treatment.

Records indicate that the conditions specified for post-weld heat treatment exceeded pressure vessel design code minimum requirements, but were not ideal. Due to placement of thermocouples, it is highly probable that the area where the SCC occurred was not heated to a sufficient temperature. The implemented solution is to install several thermocouples, controlling the heating rate and temperature gradient across the entire section to ensure that all parts, especially the thickest sections and the most highly stressed areas, have uniformly attained sufficient temperature.

Conclusion

It was found that carbon steel is susceptible to stress corrosion cracking in a trichlorosilane reactor. The combination of carbon steel in a chlorinating environment with residual tensile stress allowed cracks to slowly propagate up to 11 mm into reactor wall. The solution is to place more focus on a stringent heat treatment regime, effectively relieving the residual tensile stress and eliminating a pre-requisite for stress corrosion cracking.

References

1. Cottis RA. Guides to Good Practice in Corrosion Control - Stress Corrosion Cracking http://www.npl.co.uk/upload/pdf/stress.pdf.
2. Treseder RS, Wachter A. Corrosion. 1949;5: 383-91.
3. Strauss MB, Bloom MC. Corrosion. 1960;16: 109-12.

Acknowledgements

We would like to thank Dow Corning Corporation for permission to publish this work.

Explosion and Fire at Yokkaichi Plant – Explanation, Consequences and Action Items from the Incident that had Five Fatalities

Matt Wilson, President, Mitsubishi Polycrystalline Silicon America Corporation

Abstract

On January 9, 2014 an explosion and fire occurred at Mitsubishi Materials Polysilicon Plant in Yokkaichi, Japan. This incident occurred during what would have been considered a routine maintenance task, cleaning a fouled heat exchanger. There were five fatalities and thirteen injuries. An external Accident Investigation Committee was formed utilizing academic experts and specialists with relevant knowledge and experience as well as internal investigations. The facility suspended operations for over 6 months. In addition to specific corrective actions directly relevant to the incident, safety systems and safety culture were examined throughout the Yokkaichi Plant and with the parent company Mitsubishi Materials as a whole.
It is our objective to reach out to the polysilicon and industrial communities to present the information surrounding the incident, from specific findings to general information, so that this type of tragedy will never happen again.

Introduction

The Yokkaichi facility has been producing high purity polycrystalline silicon for the semiconductor industry since 1967. There are two plants, #1 and #2. The incident occurred in the #1 plant. Below is an outline of the plant and the location of the incident within the plant.

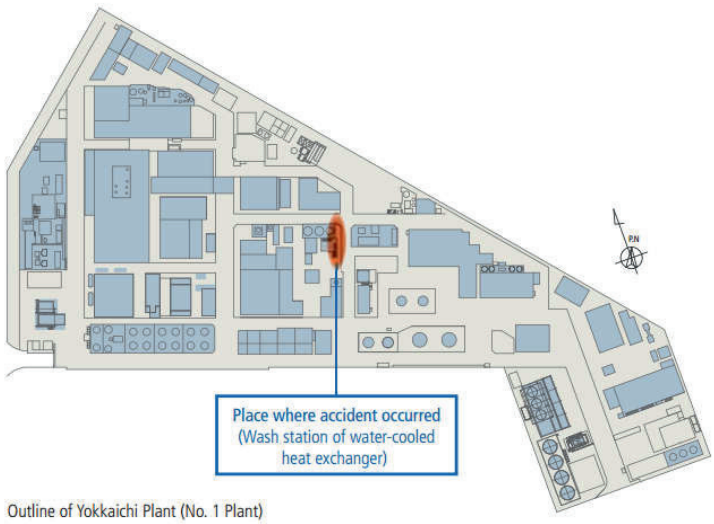

Outline of Yokkaichi Plant (No. 1 Plant)

The manufacturing process is carried out by reacting metallurgical silicon with hydrogen chloride to produce trichlorosilane, purifying the trichlorosilane through distillation, and performing further reactions including thermal decomposition and reduction to produce the silicon as shown below.
The water cooled heat exchanger involved in the incident was installed in the hydrogen recycling facility. Its process purpose is to cool the vent gas from the reactors. It is a one pass shell and tube heat exchanger as shown.

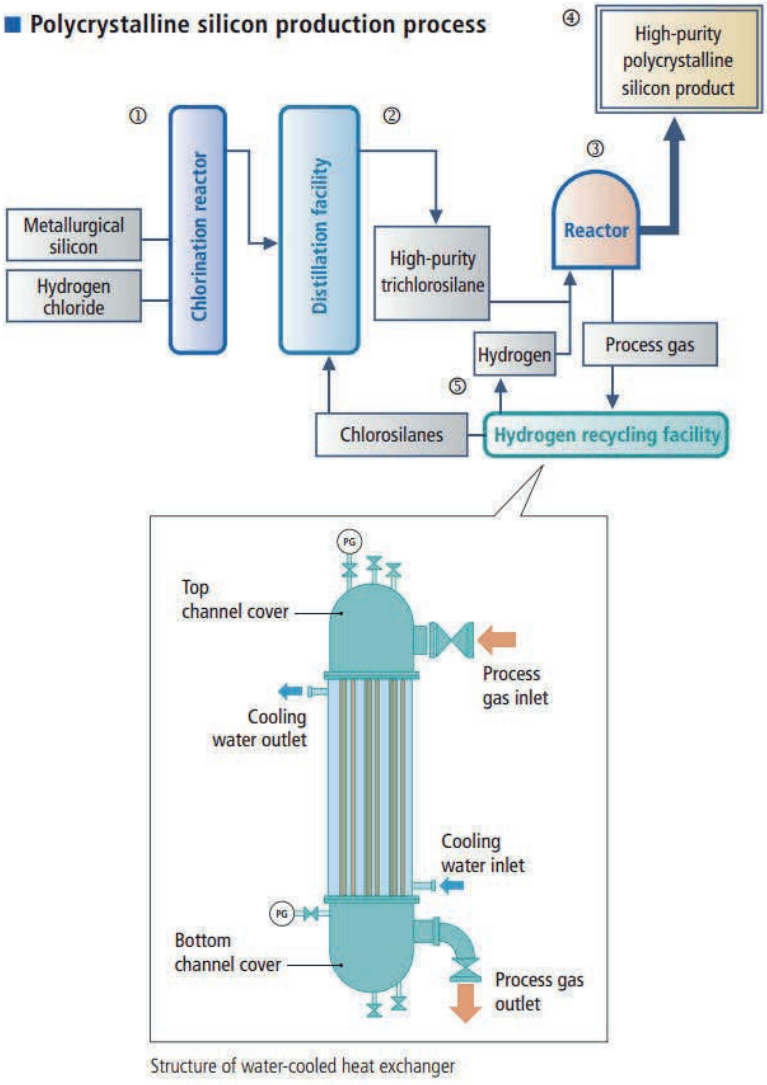

Structure of water-cooled heat exchanger

The incident occurred at 14:05 on Thursday, January 9, 2014. The weather was clear, 8°C, 60% humidity, wind at 4m/sec from the NNW. The activity was a joint effort between Yokkaichi operators and maintenance contractors. All were experienced. Three of the fatalities were Yokkaichi employees, two were contract employees. Ten

of the injured were Yokkaichi employees, three were contract employees. There was structural damage to the facility including structural steel, buildings, and broken windows. There was no significant impact to the environment.

Prior to the Incident

November 27, 2013 – The heat exchanger was removed from the process unit and placed in a designated storage area for preparation prior to opening.

November 28 – Dec 2, 2013 – A dry nitrogen purge was performed for 3 days.

December 3 – December 27, 2013 – A humidified nitrogen purge was performed for 20 days.

January 6 – January 8 – A dry nitrogen purge was performed for 3 days.

January 9, 2014 – The heat exchanger was transported to the wash area inside the plant and a dry nitrogen purge was performed. At around 11:00, the bottom head was removed and cleaned. At around 13:40, the procedures for removing the top head were started.

Explosion, Fire and Response

14:05 – Blast inside plant was heard and white smoke was confirmed

14:07 – Explosion and fire was recognized

– 119 (Emergency Services) called to give notification of explosion

14:08 – 119 called to request ambulances

14:10 – 119 called to confirm injured and that fire was under control

14:19 – Neighborhood community associations contacted

14:21 – Fire was extinguished

14:21 - Ambulances arrive

Suspension of dichlorosilane distillation facility ordered by Yokkaichi City Fire Department

14:31 – Yokkaichi Labor Standards Inspection office contacted

14:34 – Yokkaichi Police – Community Safety Division contacted

15:05 – Showa Yokkaichi Cooperative Disaster Prevention Force, Local industries contacted, multiple other governmental agencies notified through chain of communications

Post Incident

Immediately after the accident, Yokkaichi Plant set up a Disaster Task force to take charge of the injured and notification of relevant authorities. Mitsubishi Materials

Corporation (MMC) headquarters also set up an Accident Task Force headed by the President to take charge of responding to relevant parties and to disseminate information to those both inside and outside the company.

Operations at the facility were suspended the day after the incident to confirm safety, but were resumed on June 30, 2014, after implementing an inspection of production facilities and other measures in accordance with the guidance of relevant authorities and the recommendations of the Accident Investigation Committee.

MMC set up the Accident Investigation Committee on January 17, inviting external academic experts and specialists with appropriate knowledge and experience. Their charter was to clarify the cause of the fire and explosion and to formulate measures to prevent reoccurrence. Through a series of seven meetings held over five months, the Accident Investigation Committee analyzed the causes of the accident and made recommendations for measures.

Accident Investigation Committee Findings

Based on interviews of external experts, evaluation by external specialized agencies and experiments by MMC, analysis was conducted for the following items:

(1) Investigation of explosion energy from analysis of explosion phenomena.

The explosion energy was estimated from two separate phenomena at the accident site.

(2) Considerations on materials causing explosion and fire.

The chemical structure and ignition and explosion properties were analyzed for the hydrolyzed products of chlorosilane polymers inside the heat exchanger. The estimated explosion energy was almost equivalent to the explosion energy from the above (1). Therefore, it is inferred that the hydrolyzed products of chlorosilane polymers were the materials that caused the explosion. It is thought that the chlorosilane polymers scattered by the explosion and also decomposed to generate combustible materials which then erupted into the atmosphere and burned.

(3) Process of explosion and fire.

The hydrolyzed products of chlorosilane polymers were ignited and exploded due to impact occurred at the flange surface where the upper channel cover was fastened to the body of the heat exchanger →The top channel cover was sent flying. →The blast shattered glass windows at the nearby building. Chlorosilane polymers remaining inside the heat exchanger were then sent flying. →Combustible materials from chlorosilane polymers erupted into the atmosphere, burned and created a fireball.

The following items were identified as direct causes of the explosion and fire accident at the heat exchanger:

(1) Low-temperature hydrolysis of chlorosilane polymers generated materials with high ignition and explosion sensitivity, and large explosion energy.

(2) Dry conditions induced an increase in the ignition and explosion sensitivity and the explosion energy of the hydrolyzed products of chlorosilane polymers. The ignition and explosion was caused by an unidentified impact which acted as an ignition source when the top channel cover of the water-cooled heat exchanger was opened.

(3) Lack of sufficient and accurate public scientific information regarding the risks of ignition and explosion for the hydrolyzed products of chlorosilane polymers, their generation process, and appropriate humidified processing conditions for chlorosilane polymers, led to insufficient consideration of the appropriate safety measures.

Furthermore, direct causes of casualty in personnel were the top channel cover being blown by the ignition and explosion, the blast, and the ensuing fire. The presence of nearby workers resulted in a greater amount of personal injury.

The following items were identified as causes other than direct causes, i.e. indirect causes:

(1) Risk assessment - Due to a lack of knowledge regarding the ignition and explosive properties of the hydrolyzed products of chlorosilane polymers which was a direct cause of the accident, as a management issue, there were insufficient risk assessments for handling of chlorosilane polymers.

(2) Safety management for heat exchanger - It was confirmed that the process gas flow through the heat exchanger involved in the accident was not blocked by an accumulation of chlorosilane polymers. Therefore, while no correlation was found between the accident and safety management for the heat exchanger, it is recommended to establish the management methods of the heat exchanger.

(3) Standard Operating Procedures - As the result of insufficient knowledge regarding the ignition and explosion properties of the materials which were a direct cause of the accident, their risks were not reflected sufficiently into standard operating procedures. Also, some contents of those procedures lacked objectiveness and specificity, and relied on workers' experiences.

(4) Training, etc. - As the result of insufficient knowledge regarding their properties, the risks were not reflected sufficiently into training. Also, there existed insufficient confirmation methods to properly evaluate the workers for the training efficiency and their compliance to the rules.

Accident Investigation Committee Recommendations

The following are recommendations on preventative measures for heat exchanger maintenance:

(1) Improvements for methods for opening and cleaning heat exchangers

- The amount of chlorosilane polymers is measured. The hydrolysis process time and amount of generated gas is calculated. During transportation to the maintenance area, a safe condition should be created using inert gas enclosure. At the maintenance area, required pipes, etc. are connected.
- Hydrolysis should be conducted while keeping the inside of the heat exchanger full of water. After filling the exchanger with water, a water temperature of approximately 40 degrees Celsius is maintained during hydrolysis. Appropriate data are measured and monitored. The ending point for hydrolysis is determined from pH and hydrogen concentration.
- The channel cover is opened by remote control.
- High-pressure water is used to wash away chlorosilane polymers and the hydrolysis products of chlorosilane polymers from inside the heat exchanger. Wastewater is discharged into a sump pit under moist conditions.
- In the sump pit of the existing wastewater treatment facilities is used to neutralize the top clear layer of discharged water and dispose of externally. Residue is then crushed, ground, neutralized and disposed of as industrial waste under the safe conditions.

(2) New dedicated facilities for opening/washing heat exchangers in order to ensure safety during activities. Minimum requirements should include:

- Installation of protective walls against the explosion.
- Enable opening of the channel cover using remote control.
- Enable safe processing of exhaust gas.
- Enable temperature control and monitoring of hydrolysis.

The following are recommendations for strengthening safety management:

(1) Reduction of risk via hazard extraction and risk assessment.
   - FTA (Fault tree analysis) is used to create a hazard checklist and implement countermeasures. For all hazards identified through FTA, a checklist is created which shows specific countermeasures to be implemented, implementation schedule and progress status. It is confirmed that appropriate measures are formulated.
   - Risk assessment is conducted for materials, facilities and operations. Risk assessment is conducted if new knowledge is obtained regarding materials or if there is a change in facilities. It is reflected as necessary to ensure safe operations. Also, it is important to cooperate with subcontractor companies on conducting risk assessment.

- Residual risk associated with handling of similar hazardous materials is decreased. Case histories and near-misses are analyzed. Processes are extracted for the handling of chlorosilane polymers. Risk assessment is conducted again based on new knowledge gained during this accident investigation. It is necessary to continually implement measures to decrease risk in the future. Also, it was confirmed that in the manufacturing line there were no processes with the same handling conditions of the materials which was a direct cause of the accident.

(2) Systemization of safety and health manuals, reformation of standard operating procedures
- Required contents for standard operating procedures. In order to improve the standard operating procedures with vague judgment criteria and operators' experience, it is necessary to establish new rules which define the required contents and caution points etc. for standard operating procedures.
- Classification of standard operating procedures according to degree of danger (size of effect) and revision of risk assessment procedures. For operations with a high degree of danger (size of effect), it is important to perform risk assessment again even if those operations were judged as having a low priority in risk response and to reconfirm safety from the perspectives of current facilities, operation and management. Specifically, it is necessary to classify standard operating procedures according to the degree of danger (size of effect), and based on that classification, to assign priority to staff with inspection and approval authority.
- Comprehensive inspection of standard operating procedures. Starting from items with a high degree of danger (size of effect), it is important to perform sequential and comprehensive inspection of standard operating procedures, to conduct training for employees and to ensure thorough compliance. Also, it is necessary to receive validation from a third party when revising operation standards and to revise again as necessary.
- Assigned duties of safety administrators. It is necessary to clarify the duties, the date of election and dismissal, and the responsibilities of safety administrators in relation to hazardous operations.
- Follow-up for near-misses. It is important to promote increased reporting activities for near-misses. Also, in addition to reporting near-miss cases to the Safety and Health Committee, follow-up should be conducted for the status of countermeasure implementations.
- Follow-up system for corrective actions. In the future, it is necessary to conduct systematic follow-up for the status of corrective actions etc. in relation to major accidents and disasters.

(3) Retraining. In order to raise awareness for safety management measures and to ensure reliable implementation of safe operation, it is necessary to conduct periodic safety training for MMC employees and employees of subcontractor companies.

(4) Utilize PDCA cycle to continuously strengthen safety management. As shown below, it is important to construct a safety and health management system with active involvement from MMC headquarters and to conduct continual improvement by executing the PDCA cycle.

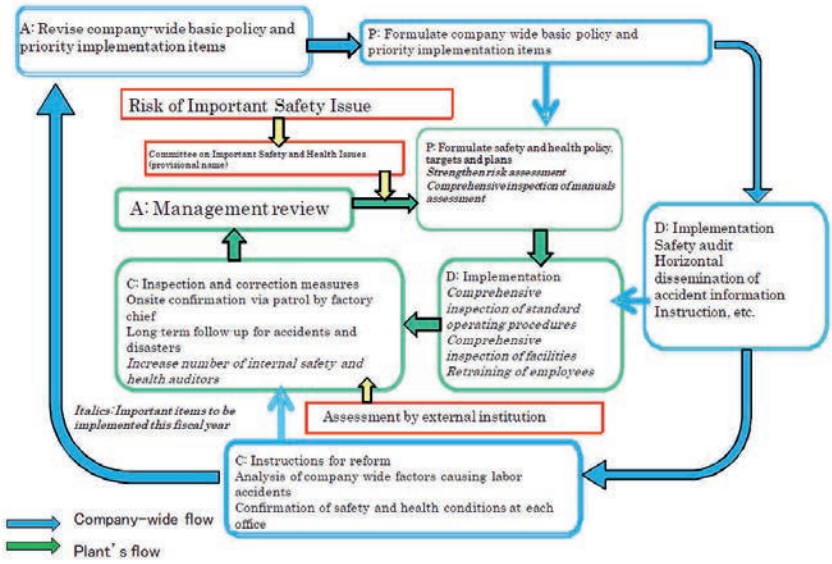

(5) Strengthening the safety management of MMC. Regarding safety activities of MMC, in addition to the contents of company-wide labor safety and health activities, the Committee confirmed the following responses by headquarters following the accident: implementation of emergency safety patrols, inspection of hazardous procedures and standard operating procedures, establishment of a Safety Declaration Day (January 9), strengthening of organizations related to safety and health, starting a New Zero-Accident Project, and strengthening of safety auditing.

The following is a review of background factors and suggested improvements to foster a positive safety culture:

(1) Background factors found as a result of discussion with plant personnel by an external organization.
- Insufficient systematic training on safety infrastructure
- Insufficient transfer of technology for safety infrastructure
- Low sensitivity to danger
- Insulation from outside information / events.

(2) Recommendations for long term improvements as countermeasures for background factors:
- Develop systematic training methods and curriculum including chemical knowledge, process, operations standards, etc.…

- Training of personnel based on accident case histories, transfer of experience from skilled workers, emergency response scenarios.
- Strengthen safety infrastructure through establishment of a dedicated process technology department, cooperation between headquarters and the plant, and cooperation with external institutions.
- Improve safety management functions through revision of plant organizations.

(3) Establish system of continuous reform, construct a system for incorporating external assessments and information, “Yokkaichi Plant Safety Culture Rebuilding Project”

Ending

Safety Declaration Monument at Yokkaichi

References

Much of this paper is from the Abridged Version (English) of the final report of the Accident Investigation Committee, June 12, 2014.

Acknowledgements

Masayuki Tebakari, MMC, for presentation materials.

Yuko Jordan, Mitsubishi Polycrystalline Silicon America Corporation for translations.

Quantum chemical approach toward the identification of hydrolyzed chlorosilane oligomer

Takako Kudo[1)], Yasuhiro Hanaue[2)], and Norikazu Komada[3)]

1) Division of Pure and Applied Science, Graduate School of Science and Technology, Gunma University.

2) Process Technology Department, Yokkaichi Plant, Mitsubishi Materials Corporation.

3) Electronic Materials and Components Company, Mitsubishi Materials Corporation.

Abstract

Seven candidates were proposed for the structural model of the unidentified explosive molecule which caused the fatal accident at Yokkaichi Plant, Mitsubishi Materials Corporation in 2014. Those models were optimized by means of ab initio molecular orbital calculations including electron correlation effects at the level of MP2/6-31G*, and compared with the available data in order to choose a model which is most consistent with them for the further study. The chemical formula of the chosen model (Model A) is $Si_8H_{10}O_{14}$. Its structure is described as a partial hexahedron composed of four Si-Si bonds, seven Si-O-Si bonds and one open ring. Three H atoms and seven OH groups are attached to eight Si atoms. There is a hydrogen bond formed in the area of the open ring.

Possible intramolecular reaction path was explored and one candidate path was found. The reaction along the path is significantly exothermic and includes oxidation of a Si-Si bond and formation of a H_2 molecule, which is qualitatively consistent with the observation. The reaction products are a closed hexahedral $Si_8H_8O_{14}$ and a H_2 molecule. The $Si_8H_8O_{14}$ molecule has three Si-Si and nine Si-O-Si bonds. The path consists of three transition states and two metastable intermediates, each of which is interleaved between the transition states, in serial sequence. H_2 molecule is formed in the path from the 2nd transition state to the 2nd metastable intermediate counting from the reactant. The reaction may be interpreted as the initial ignition stage of the explosion.

Background

There was an explosion and fire during opening/cleaning work of a heat exchanger in Yokkaichi Plant on January 9, 2014. Five employees were killed and 13 employees were injured by the accident. A committee was organized to investigate the cause of the accident and to provide recommendations for preventive measures. The chemical analysis, infrared absorption spectroscopy and several other measurements were

performed on the substances taken from the site of the accident. The results of the investigation and the proposals were made public on June 12, 2014 and the plant operation was resumed soon after that. The cause of the accident identified by the committee was the explosive chemical reaction of chlorosilane polymers remained in the heat exchanger and hydrolyzed in situ at low ambient temperatures. Some basic chemistry of explosive substance, however, remained unidentified or unquantified. It included the mechanism of the chemical reaction, the thermodynamic and the kinetic properties related to the explosion, though hypothetical explosion processes have been proposed elsewhere [1, 2].

Ab initio molecular orbital calculations

For preliminary calculations, a tool of molecular mechanical (MM) calculations, Avogadro (Version 1.0.3) [3], which includes empirical parameters was used to get approximate molecular structures. The set of the obtained atomic coordinates was served as the initial condition for the further structural optimization.

Based on the geometries obtained by MM, more sophisticated ab initio molecular orbital calculations were carried out by Gaussian 09 [4]. The geometries of the models and some stationary points on the potential energy surface of the reaction path were fully optimized at the restricted Hartree-Fock (RHF) level of theory using the 6-31G* basis set [5] which is one of the split-valence type basis functions with a set of d-type polarization functions on the heavy atoms. In addition, the geometries were refined using second-order Møller-Plesset perturbation theory (MP2) [6].

Then, all optimized molecules were characterized as minima or transition states by normal mode (vibrational) analysis.

Structural modeling

Possible molecular skeletons

The chemical composition and the infrared spectra obtained in the investigation of the cause of the accident were used for structural modeling of the chlorosilane polymers hydrolyzed at low temperatures. Several pieces of information found in the literature were also utilized in the modeling. One is the existence of Si-SiOH group [7] in the substance. Another one is decrease in the stability of the compound as increase in the number of directly linked Si atoms in it [8, 9]. And the other is that the so-called "silicooxalic acid" which can be synthesized by hydrolysis of Si_2Cl_6 cooled by ice [10] has two directly linked Si atoms [11].

On the basis of the above observed and literature information the molecular formula of $Si_8H_{10}O_{14}$ with four Si-Si bonds was chosen as a basis for the modeling. Also the same molecular formula with smaller number of Si-Si bonds was considered.

There are six possible molecular skeletons or possible stereoisomers with four Si-Si bonds. The schematic diagrams of those models are shown in Figure 1. They are divided into two groups. Models A, B and C are all featured by partial hexahedral cage structure with one open ring. Models D, E and F have twisted cage with one diagonal Si-O-Si bond. All four Si-Si bonds are arranged almost in parallel for Models A and D. A set of two parallel Si-Si bonds is in orthogonal arrangement to the other two parallel Si-Si bonds for the other models. It should be noted that those concept of "parallel" or "orthogonal" is applicable only for idealized schematic diagram in Figure 1 and not for actual structure.

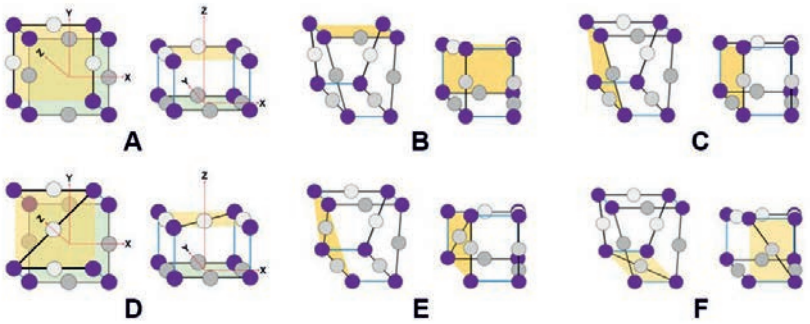

Figure 1: Diagram of possible skeletons of $Si_8H_{10}O_{14}$ molecule with 4 Si-Si bonds.

Structural optimization of the models

The all six models were found to have its equilibrium structure, which means that all those stereoisomers theoretically exist. The all six models are stable or metastable in a sense that they are located in the bottom of local potential well. The optimized molecular structures of Model A ~ F are presented in Figures 2. The dashed lines in the figure indicates the hydrogen bond.

The results of the MP2/6-31G* and RHF/6-31G* level calculations were compared and the agreement between the both levels of calculations are satisfactory for the all models. Therefore, the effect of electron correlation is not important as far as for the geometry of the present models.

The data based on MP2/6-31G* level calculations were employed for the further study.

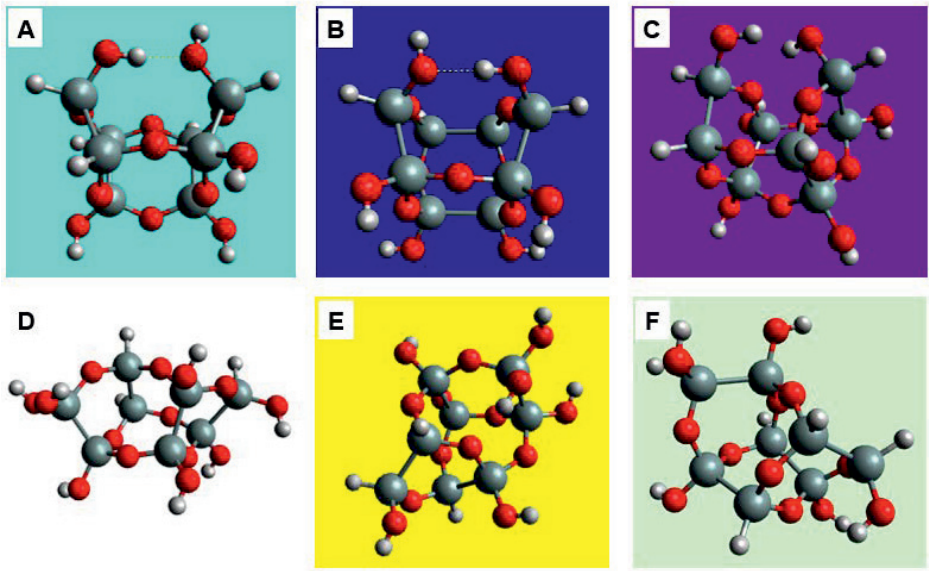

Figure 2: Structures of six $Si_8H_{10}O_{14}$ molecule models with 4 Si-Si bonds optimized at MP2/6-31G* level.

Figure 3 compares the total electronic energies plus nuclear repulsive energies, in other words, the stabilities of the optimized Model A ~ F molecules. The condition at the reference point for zero energy is that all component atoms are stationary or motionless

and isolated each other so that there is no interaction between them. A larger negative value, therefore, indicates that the electrons and atomic nuclei are more stabilized by mutual interaction including formation of chemical bond.

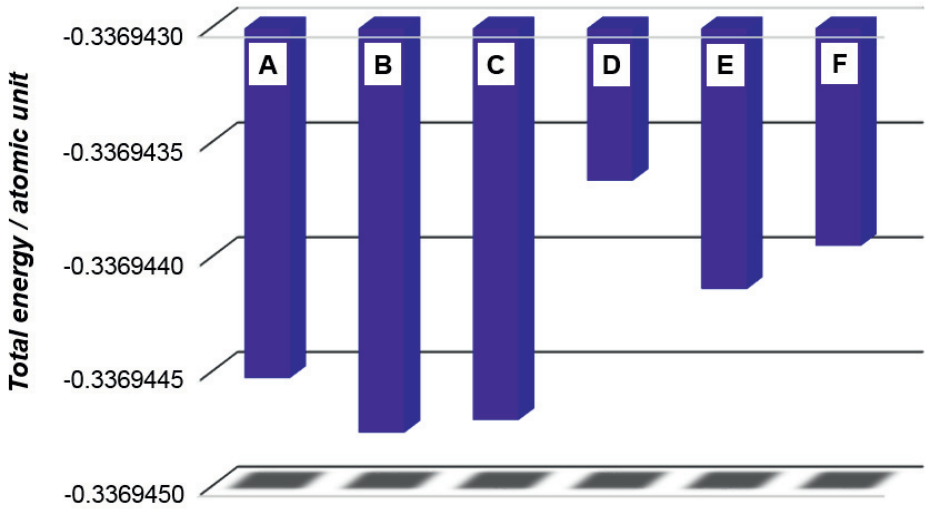

Figure 3: Total electronic energy plus nuclear repulsive energies between the six models.

The partial cage structure of Models A ~ C is apparently more stable than the twisted cage of Model D ~ F. The schematically parallel configuration of four Si-Si bonds of Model A is less stable than the other two orthogonal configurations of Models B and C in the partial cage group as illustrated in Figure 1. The similar relationship is found between Model D and Models E and F in the twisted cage group. Model B is the most stable among the six models and the other models are metastable in the common potential energy surface.

They may be interpreted in terms of internal structural strain. The structural flexibility of Si-O-Si bond more or less relaxes the strain and allows the theoretical existence of all those stereoisomers.

H/OH replacement on the ends of open ring

Two OH groups which terminate both ends (Si atoms) of the open ring of Model A can be replaced one by one with H atom which is bound to the other Si atom. These replacements are expected to affect stability of the models, and therefore the structures of those isomers of Model A were optimized by the same method described in the previous section and the total electronic energies plus nuclear repulsive energies were evaluated.

The structures optimized at MP2/6-31G* level are depicted in Figure 4.

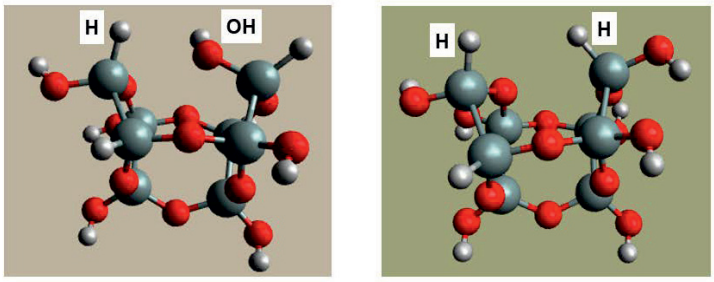

Figure 4: Optimized structures of two isomers of Model A with different arrangement of OH/H on the ends of open ring. The optimization level is MP2/6-31G*.

The obtained total electronic energies plus nuclear repulsive energies are compared in Figure 5 for three combinations of OH/OH, H/OH and H/H on the end of the open ring of Model A.

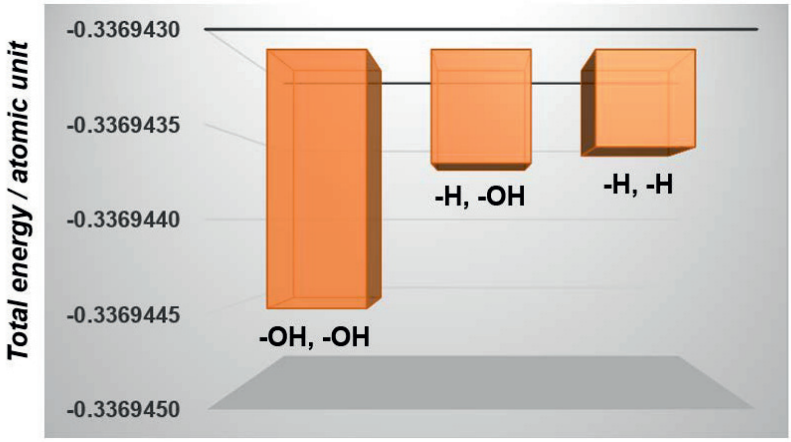

Figure 5: Impact of H/OH replacement on the end of Model A open ring on the total electronic energy plus nuclear repulsive energies.

As Figure 5 shows, the combination of two OH groups on the ends of the open ring gives the lowest energy among the three isomers. This notable stabilization is attained by hydrogen bonding between the two OH groups facing each other across the open ring as indicated by the dashed line for Model A in Figure 2. In comparison the difference is significantly small between the other two combinations of H/OH and H/H.

Number of Si-Si bonds per molecule

The impact of the number of Si-Si bonds on total electronic energy plus nuclear repulsive energies was examined. Structural models based on the partial cage were prepared for three Si-Si bonds and two S-Si bonds. They were optimized again by the same method. The results of the optimization are given in Figure 6. The hydrogen bond is formed between the two OH groups on the end of the open ring for both three and two S-Si bond models as indicated by the dashed line. The position of the hydrogen bond in those isomers is configurationally equivalent to the one in Model A.
The model of three Si-Si bonds, a stereoisomer of the models with four Si-Si bonds, is named Model G for the further study.

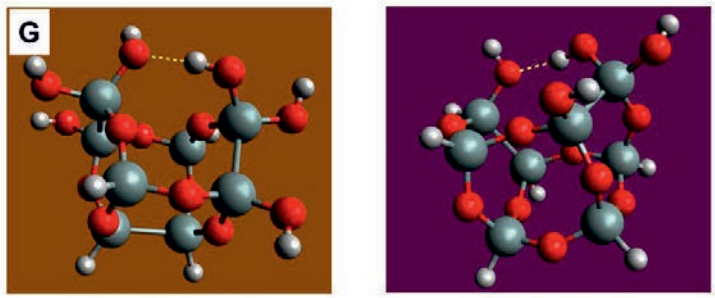

Figure 6: Optimized partial cage structures modified by reducing the number of Si-Si bonds. The optimization level is MP2/6-31G*.

Figure 7 shows the dependency of total electronic energy plus nuclear repulsion on the number of Si-Si bonds. Model A is used to represent the four Si-Si bond model in the figure.
The least stability for the four Si-Si bond model may suggest the largest energy release by their oxidation.

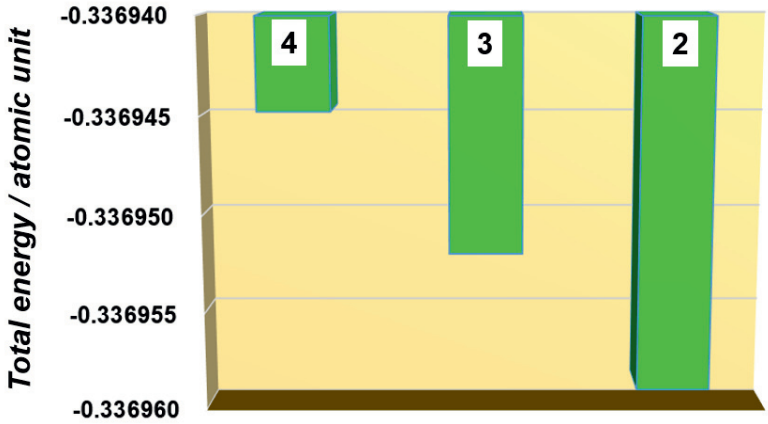

Figure 7: Impact of the number of the Si-Si bonds on the total electronic energy plus nuclear repulsive energies. The number of the Si-Si bonds is indicated in each bar.

Vibrational analysis

The vibrational analysis was conducted for the seven models of A ~ G under harmonic oscillator approximation. This approximation has been widely used as a reliable and reasonably accurate representation of actual molecular vibrations except highly excited conditions.
The anharmonic relaxation effect was corrected by multiplying scale factor to the calculated frequency values. The scaling factor of 0.9427 obtained for MP2/6-31G* level calculation [12] was chosen for this study.
Each model molecule consisting of 32 atoms has 96 degrees of freedom and 90 of them correspond to molecular deformation. The vibrational modes are orthogonal each other. The remaining six degrees of freedom are allocated to three translational modes and the other three rotational modes. Those six modes were not evaluated in this study.

The molar absorptivity or infrared intensity was also calculated for each vibrational mode.
The scaled molecular vibrational spectra are shown for Models A ~ C with partial hexahedral cage in Figure 8, and Models D ~ F with twisted cage with one diagonal Si-O-Si bond in Figure 9.
Seven modes of O-H stretching vibration are observed above 3000 cm^{-1} for the models of A ~ F. One of those seven modes for each of Models A and B indicates significantly lower wave number which is affected by the hydrogen bonding. The influence of hydrogen bond on the O-H vibration is reported by Chojnowski et al. [13] According to them the vibrational frequency or the wave number is lowered in the range of 100 ~ 400 cm^{-1} depending on the type of hydrogen bond complex.
There are three modes of Si-H stretching vibration in 2000 ~ 2500 cm^{-1} range common for the spectra of Models A ~ F.
The strong infrared intensities around 1000 cm^{-1} are related to Si-O vibrations.
It is difficult to describe the other infrared absorption peaks in the fingerprint region by particular motion of component atoms. It should be noted that a peak around 875 cm^{-1} was consistently observed in FTIR spectra of the actual explosive substances.

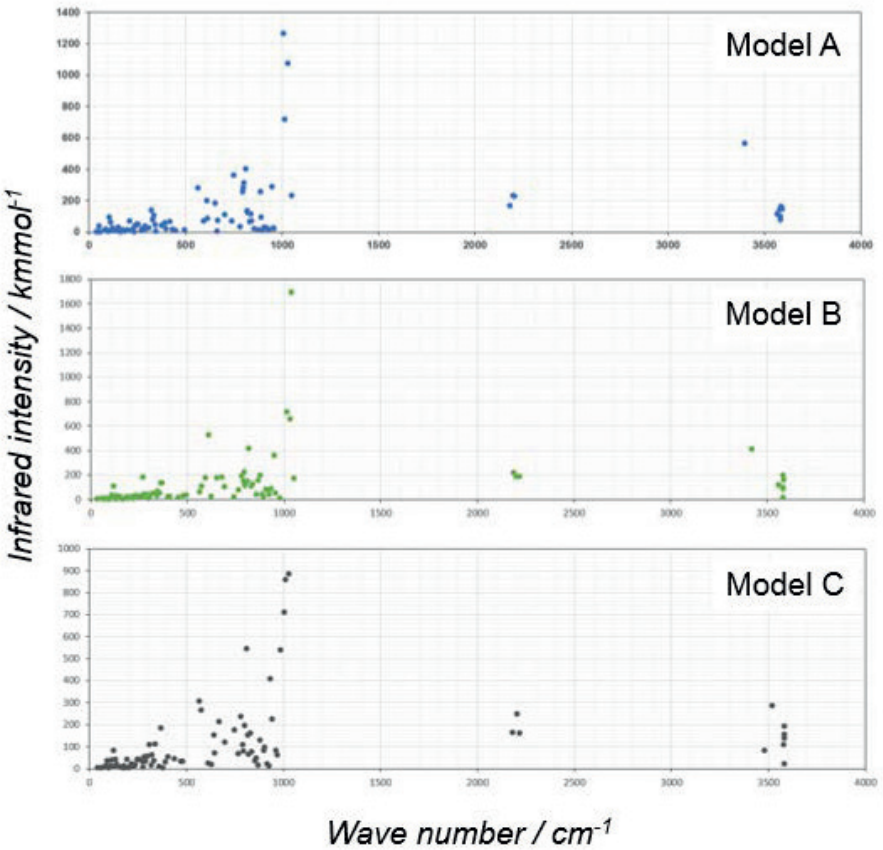

Figure 8: Scaled molecular vibrational spectra for Models A ~ C with partial hexahedral cage including four Si-Si bonds.

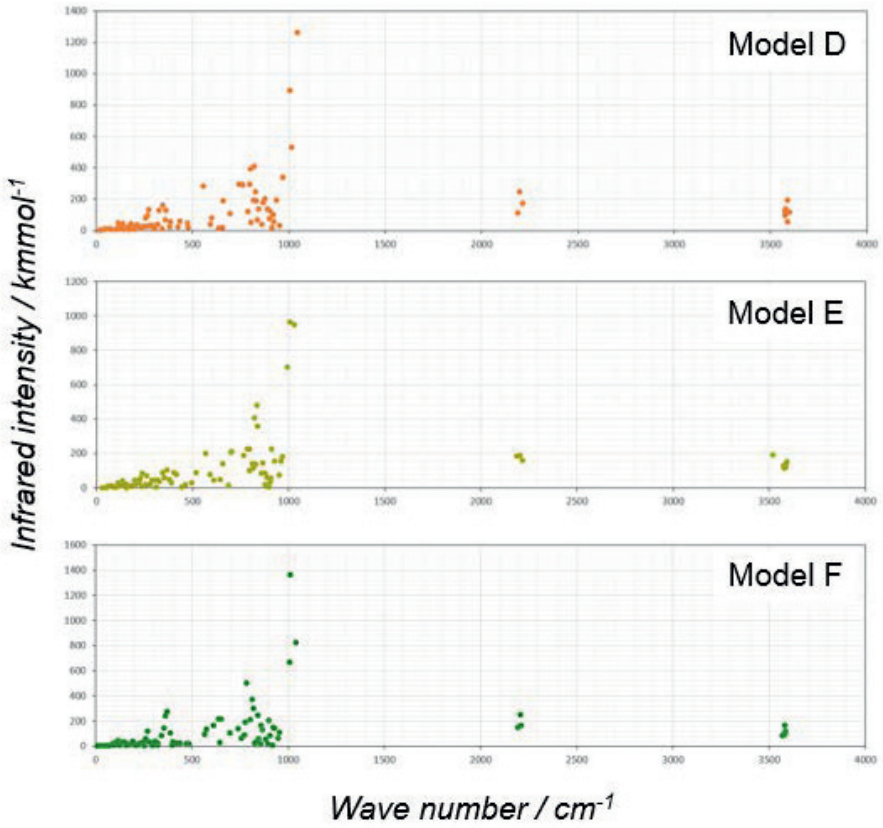

Figure 9: Scaled molecular vibrational spectra for Models D ~ F with twisted cage including one diagonal Si-O-Si bond and four Si-Si bonds.

The scaled molecular vibrational spectrum is given for Model G with three Si-Si bonds in Figure 10. There are four distinctive Si-H stretching and six O-H stretching modes in Model G.

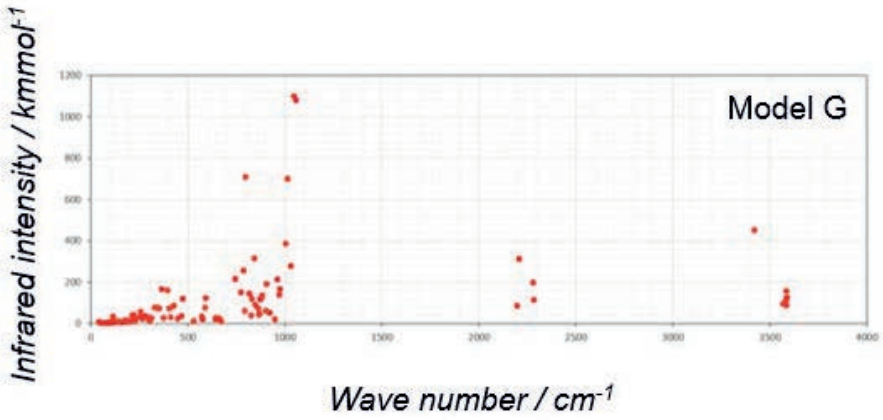

Figure 10: Scaled molecular vibrational spectrum for Model G with partial cage including three Si-Si bonds.

The seven scaled spectra for Models of A through G were compared with the observed spectra, and Modal A was selected based on the agreement between the calculated and observed spectra for the further study. The visual comparison is shown in Figure 11 for the selected Model A. A small but independent peak is seen at 892 cm^{-1} in the calculated spectrum. It may be related to the observed 875 cm^{-1} peak.

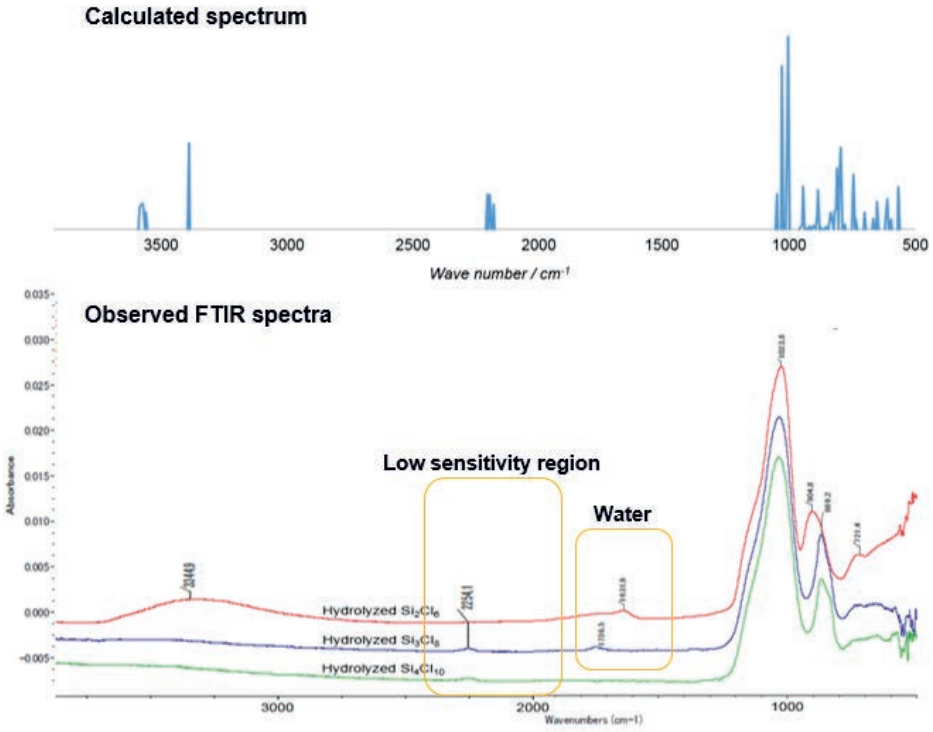

Figure 11: Calculated absorption spectrum for Model A and FTIR spectra for hydrolysed Si_2Cl_6, Si_3Cl_8 and Si_4Cl_{10}.

Reaction mechanism for the internal oxidation

The reaction mechanism for the internal oxidation with H_2 formation is explored by using Model A. The liberation of H_2 accompanying the explosive reaction was actually observed. The internal oxidation with H_2 formation has been suggested by Britton [1] and Timms [2].

The internal oxidation can be divided into two categories, that is, intramolecular and intermolecular reactions. The former possibility was explored in this study.

One reaction path for the intramolecular oxidation was thus found. The schematic potential energy surface along the path is shown in Figure 12. The path is composed of three transition states (saddle point structures) and two metastable states (equilibrium structures) in between as well as the reactant (Model A) and the products. The energy barrier of each step is evaluated from the difference of the total electronic energy plus nuclear repulsive energies between the transition state and the stable/metastable state. The zero-point energy associated with the vibrational motion was corrected for those energy values. The corrected energies for the five states relative to Model A are shown in square brackets.

The first step starting from Model A molecule includes 1,2-transfer of OH group and dissociation of Si-Si bond. Elimination of a H_2 molecule occurs in the second step. The third and the last step consists of 1,2-transfer of H atom and closure of the open ring.

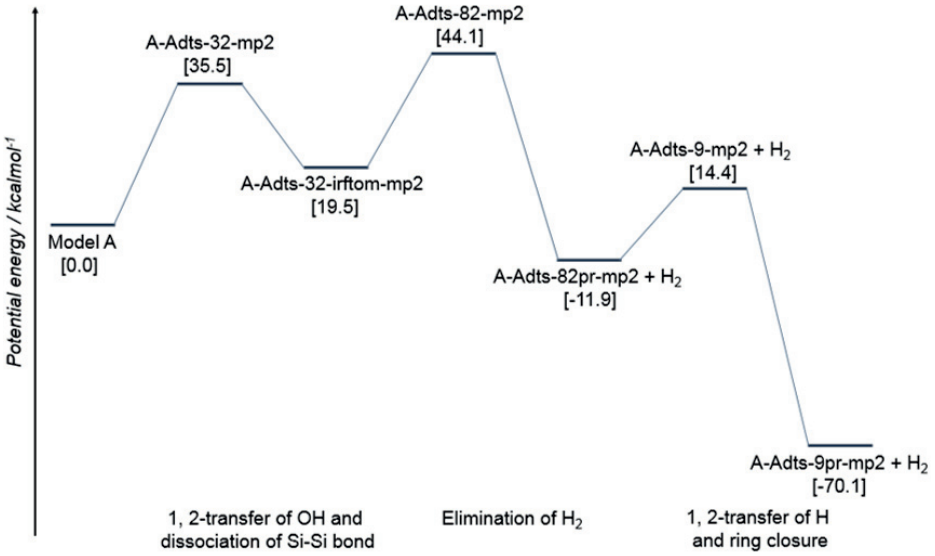

Figure 12: Schematic presentation of the potential energy surface for the intramolecular oxidation process in Model A calculated at the MP2/6-31G* level. The potential energy values given in [ ] are corrected for zero-point energy.

The three steps or elementary reactions are illustrated in Figures 13, 14 and 15 respectively.
The overall chemical reaction is represented as

$$Si_8H_{10}O_{14} \rightarrow Si_8H_8O_{14} + H_2 \qquad (1)$$

The number of Si-Si bonds per molecule decreases from four to three according to the reaction, which is found to be significantly exothermic.
This is possibly the initial ignition stage or the trigger of the explosion since the overall explosion reaction is thought to be still more exothermic.

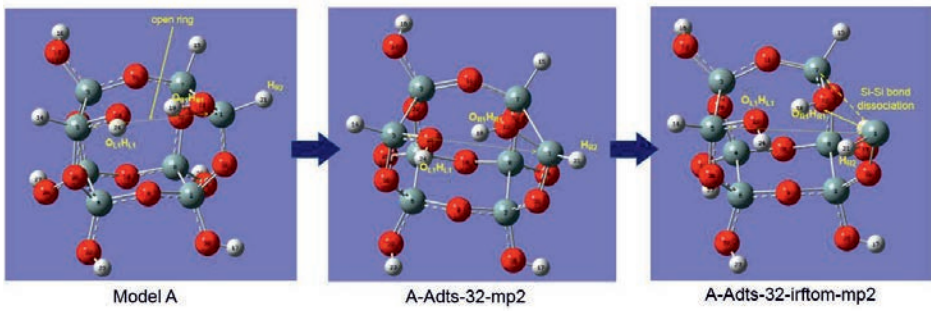

Figure 13: 1,2-transfer of OH group and dissociation of Si-Si bond the via the transition state "A-Adts-32-mp2".

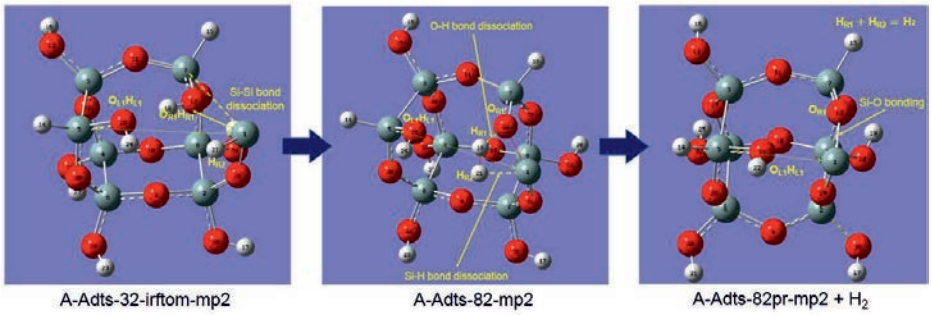

Figure 14: Elimination of a H_2 molecule via the transition state "A-Adts-82-mp2".

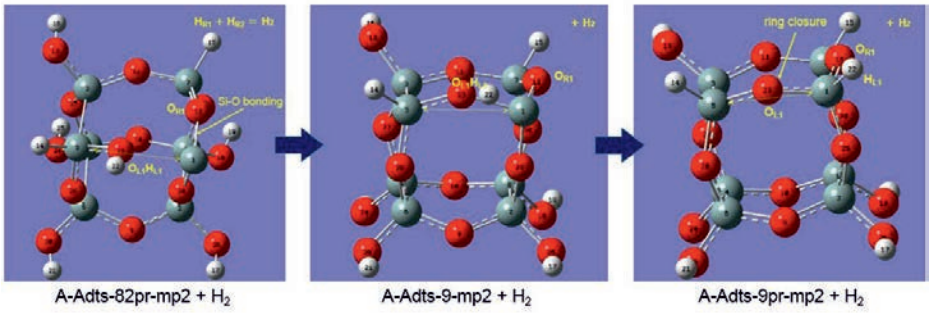

Figure 15: 1,2-transfer of H atom and ring closure via the transition state "A-Adts-9-mp2".

Conclusion

The ab initio molecular orbital calculations were successfully applied to the modeling of the explosive molecule, which was based on the available information obtained in the investigation of the cause of the accident and found in the literature.

The optimized structure of the model is described as a partial hexahedral cage composed of four Si-Si bonds, seven Si-O-Si bonds and one open ring. Four Si-Si bonds are schematically in parallel configuration. Three H atoms and seven OH groups are attached to eight Si atoms on each corner of the hexahedron. There is a hydrogen bond in the area of the open ring.

A possible intramolecular reaction path was found. The reaction path is composed of three serial steps with three transition states and two metastable states in between. The reaction is significantly exothermic and includes oxidation of a Si-Si bond and formation of a H_2 molecule, which is qualitatively consistent with the observation. The reaction may be interpreted as the initial ignition stage of the explosion.

The intermolecular reaction path for the internal oxidation will be explored in the next step. Finally we will consider the explosion mechanism on the basis of the results obtained so far and in the next step.

Acknowledgements

The authors would like to express their special thanks to Mr. Rikito Sato, Yokkaichi Plant, Mitsubishi Materials Corporation, for his invaluable input and persistent support.

References

1. L.G. Britton, Plant/Operations Progress, **9**, 1990, p16.
2. P.L. Timms, Journal of the Chemical Society, Dalton Transactions, No.6, 1999, p815.
3. M.D. Hanwell, D.E. Curtis, D.C. Lonie, T. Vandermeersch, E. Zurek and G.R. Hutchison, Journal of Cheminformatics, **4**, 2012, No.17.
4. M.J. Frisch, G.W. Trucks, H.B. Schlegel, G.E. Scuseria, M.A. Robb, J.R. Cheseman, G. Scalmani, V. Barone, B. Mennucci, G.A. Petersson, H. Nakatsuji, M. Caricato, X. Li, H.P. Hratchian, A.F. Izmaylov, J. Bloino, G. Zheng, J.L. Sonnenberg, M. Hada, M. Ehara, K. Toyota, R. Fukuda, J. Hasegawa, M. Ishida, T. Nakajima, Y. Honda, O. Kitao, H. Nakai, T. Vreven, J.A. Montgomery, J.E. Peralta, Jr., F. Ogliaro, M. Bearpark, J.J. Heyd, E. Brothers, K.N. Kudin, V.N. Staroverov, R. Kobayashi, J. Normand, K. Raghavachari, A. Rendell, J.C. Burant, S.S. Iyengar, J. Tomasi, M. Cossi, N. Rega, J.M. Millam, M. Klene, J.E. Knox, J.B. Cross, V. Bakken, C. Adamo, J. Jaramillo, R. Gomperts, R.E. Stratmann, O. Yazyev, A.J. Austin, R. Cammi, C. Pomelli, J.W. Ochterski, R.L. Martin, K. Morokuma, V.G. Zakrzewski, G.A. Voth, P. Salvador, J.J. Dannenberg, S. Dapprich, A.D. Daniels, O. Farkas, J.B. Foresman, J.V. Ortiz, J. Cioslowski, and D.J. Fox, Gaussian 09, Gaussian, Inc., Wallingford, CT, USA, 2009.
5. M.M. Francl, W.J. Pietro, W.J. Hehre, J.S. Binkley, M.S. Gordon, D.J. DeFrees and J.A. Pople, Journal of Chemical Physics, **77**, 1982, p3654.
6. J.A. Pople, K. Raghavachari, H.B. Schlegel and J.S. Binkley, International Journal of Quantum Chemistry, **16**, Issue S13, 1979, p225.
7. H. Kautsky and H. Thiele, Zeitschrift fuer Anorganische und Allgemeine Chemie, **173**, 1928, p115.
8. G. Martin, Journal of the Chemical Society, Transactions, **107**, 1915, p319.
9. A. Stock and K. Somieski, Berichte der Deutschen Chemischen Gesellschaft, **53B**, 1920, p759.
10. L. Gattermann and K. Weinlig, Berichte der Deutschen Chemischen Gesellschaft, **27**, 1894, p1943.
11. R.M. Hagenmayer, B. Friede and M. Jansen, Journal of Non-crystalline Solids, **226**, 1998, p225.
12. J.A. Pople, A.P. Scott, M.W. Wong and L. Radom, Israel Journal of Chemistry, **33**, 1993, p345.
13. J. Chojnowski, S. Rubinsztajn and L. Wilczek, Macromolecules, **20**, 1987, p2345.

Cost saving of using a metallurgical grade silicon with higher trichlorosilane yield in the hydrochlorination based polysilicon process

Alan Crawford, Alan Crawford Consulting LLC, Bozeman, Montana, USA
Independent Engineering Consultant

Abstract

Synthesis of trichlorosilane (TCS) by hydrochlorination (HC; $Si + H_2 + SiCl_4$) has become a favored commercial source of TCS for TCS-Siemens based stand alone polysilicon plants. TCS from the HC unit can also be converted to silane (SiH_4). Silane can be sold or converted to polysilicon via silane-Siemens or silane-fluid bed reactor (FBR). Solar-grade polysilicon has become a highly specialized low-margin commodity material. Commercial HC plant operators need to place high emphasis on all methods to reduce plant operating costs.

Decreasing TCS yield from the HC fluid bed reactor results in higher energy input costs for a plant producing a fixed amount of polysilicon. Laboratory HC reactor results show that metallurgical grade silicon composition can have a strong influence on TCS yield. This paper provides information about chemistry, process design, commercial process operation, energy input and parameters that influence overall TCS yield of the HC process. The discussions are applicable for a commercial HC process unit used to produce polysilicon-grade TCS or silane (SiH_4).

Not discussed in this paper are additional areas of commercial HC plant operation that impact operating costs. These areas focus on plant reliability. Reliability is achieved through optimization of process design, operating strategy and operating experience. Poor plant reliability can result in higher differential operating costs than differential costs resulting from low TCS yield.

Hydrochlorination Chemistry and Basic Information

The process to produce trichlorosilane (TCS) by reaction of ground metallurgical grade silicon (MGS), hydrogen and silicon tetrachloride (STC) has been given several names. Hydrochlorination (HC) has become the most widely used name and is used in this paper. The HC reaction is comprised of parallel reaction steps. The overall equilibrium reaction is written:

$$Si\ (s) + 2H_2\ (g) + 3SiCl_4\ (g) = 4HSiCl_3\ (g) \qquad (1)$$

The original name used by Union Carbide was STC hydrogenation, which was later shortened to hydrogenation. In recent years the terms "cold hydrogenation" and "cold conversion" have been used in China. The adjective "cold" refers to the much lower operating temperature for this process (~535° C) compared to the present high temperature STC hydrogenation process (~ 1200° C). This paper does not go into detail about the other commercial TCS routes:

$Si\ (s) + 3HCl\ (g) \rightarrow HSiCl_3\ (g) + H_2\ (g)$ (Direct chlorination) (2)

$SiCl_4\ (g) + H_2\ (g) = HSiCl_3 (g) + HCl\ (g)$ (hydrogenation; STC hydrogenation) (3)

$H_2SiCl_2\ (l) + SiCl_4\ (l) = 2HSiCl_3\ (l)$ (Redistribution) (4)

Reaction

Union Carbide researchers [1] discovered the HC reaction (Reaction 1) in 1948 as part of research for an alternate route to produce TCS instead of direct chlorination (Reaction 2). Work on HC was abandoned around 1950 and not restarted until early 1976 when the Jet Propulsion Laboratory (JPL) Low Cost Solar Array project started. Through the JPL project, Union Carbide developed a viable commercial route to produce silane (SiH_4). The first commercial plant was built in Moses Lake, Washington, USA. Union Carbide produced polysilicon rods from silane in Moses Lake using modified Siemens technology developed by Komatsu (Japan).

The HC reaction is an equilibrium reaction that has a maximum TCS yield determined by operating conditions. The reaction is typically run in a fluid bed reactor (FBR) and is slightly endothermic assuming there is no anhydrous HCl co-feed. Reaction temperature is normally controlled by superheating feed streams of hydrogen and STC. An acceptable reactor operating temperature is 520 – 550° C and typical operating pressures are 10 – 34.5 barg (150 – 500 psig). Reactor conditions, MGS composition, MGS particle size distribution (PSD) and the use of externally supplied catalyst can facilitate pushing the reaction closer to equilibrium TCS yield. Detailed discussions of HC reaction chemistry can be found in several references [2, 3, 4, 5, 6, 7].

Dichlorosilane (DCS; H_2SiCl_2) is the main HC reaction by-product. DCS yield is typically 20-30 times lower than TCS. HC reaction selectivity to DCS is proportional to TCS. DCS is produced in the following reactions. Reaction 6 is catalyzed by aluminum chloride ($AlCl_3$). $AlCl_3$ is produced from reactive aluminum present in the MGS fed to the HC reactor.

$HSiCl_3\ (g) + H_2\ (g) = H_2SiCl_2\ (g) + HCl\ (g)$ (5)

$2HSiCl_3\ (g) = H_2SiCl_2\ (g) + SiCl_4\ (g)$ (6)

DCS is a desired by-product if the HC unit is part of a silane plant as DCS is a desired intermediate in the conversion of TCS to silane. DCS can be a desirable and / or undesirable by-product if the HC unit is part of a TCS-based polysilicon plant. Some DCS can be co-fed with TCS to the TCS Siemens polysilicon reactors. High pure DCS can also be sold to semiconductor producers. Excess DCS can be redistributed with STC to produce TCS (Reaction 4). Reacting DCS with STC represents incremental capital and operating costs.

Impurities

Some important impurities are produced in the HC reaction. Removal of these impurities is a significant focus of the remainder of the HC process and the downstream plant sections designed to produce polysilicon-grade TCS or silane. Optimum design of a purification system requires knowledge about the specific chemical form of the impurities.

Impurities of interest with regards to polysilicon purity include hydrocarbons (methane through heptane), boron trichloride (BCl_3), phosphorus trichloride (PCl_3) and phosphorus oxychloride ($POCl_3$). Phosphine (PH_3) is not formed. While most report PCl_3 as the main volatile form of phosphorus present in TCS, dichlorophosphine (DCP; $PHCl_2$) and monochlorophosphine (MCP; PH_2Cl) are believed to also be present.

DCP is the most troublesome volatile phosphorus impurity formed for a HC plant integrated with a TCS-based polysilicon plant due to suspected strong binary interactions between DCP and TCS [8]. The normal boiling point (NBP) of TCS is 31.9ºC and NBP of DCP is 45ºC. The strong binary interactions result in DCP being present in TCS and difficult to remove. MCP production in HC is rare but possible if higher than normal amounts of PCl_3 are inadvertently fed to the HC reactor with STC. Higher than desired amounts of PCl_3 can be present in STC if the plant is operated with aggressive STC recovery and recycle from slurry generated in the HC process scrubber.

Most reactive boron, carbon and phosphorus enters the HC reactor with MGS. Carbon can be present as organic carbon impurities in the MGS and as external contamination resulting from lump and ground MGS shipment methods. Carbon and phosphorus also enter the plant through make-up chlorine sources (STC or hydrogen chloride). Carbon can also be introduced through lubricating greases and oils.

MGS always contains aluminum, calcium, iron, titanium and lower amounts of other metallic impurities. These impurities are present as intermetallic phases located at silicon crystal grain boundaries. Some amount of Al, Ca, Fe, Ti (and other impurities) are converted to $AlCl_3$, $CaCl_2$, Fe_xSi_y and $TiCl_4$. $FeCl_2$ may also be produced but $FeCl_3$ is not produced in the HC reaction (unlike direct chlorination; Reaction 2). Arsenic trichloride ($AsCl_3$) is produced from reactive arsenic present in the MGS, but has a sufficiently high boiling point to normally not present problems with TCS or silane purification.

Polychlorosilanes (such as hexachlorodisilane; Si_2Cl_6; HCDS) are not produced in the HC reaction, unlike the direct chlorination TCS synthesis reaction (Reaction 2). Polychlorosilanes are cracked in the HC reaction due to the severe reaction conditions.

HCl Co-feed

Introduction of anhydrous hydrogen chloride (HCl) as part of the HC FBR feed introduces some interesting chemistry [9, 10]. Anhydrous HCl is now part of the normal HC FBR feed for a TCS-based polysilicon plant. HCl produced in the TCS Siemens reactors is recovered and recycled to the HC FBR. HCl could also be fed to a HC FBR that is part of a silane-based polysilicon plant as an alternative source of make-up chlorine (instead of STC).

Three possible anhydrous HCl reactions are provided below. Recent published work on the net impact of HCl co-feed on final TCS yield from the HC reactor has not been reported and represents potential future work.

$Si\ (s) + 3HCl\ (g) \rightarrow HSiCl_3\ (g) + H_2\ (g)$ (Reaction 2; direct chlorination) (7)

$HSiCl_3\ (g) + HCl\ (g) \rightarrow SiCl_4\ (g) + H_2\ (g)$ (8)

$H_2SiCl_2\ (g) + HCl\ (g) \rightarrow HSiCl_3\ (g) + H_2\ (g)$ (9)

Catalysis

The HC reaction can be run with a separately added external catalyst. The external catalyst helps drive the HC reaction closer to equilibrium and higher TCS yield. Copper is the preferred externally added catalyst and can be added to the HC FBR in the same forms used in the Rochow-Müller direct process (reaction of MGS and methyl chloride to produce methylchlorosilanes used for silicones production): copper oxide, metallic copper or copper chloride. Eta phase (Cu_3Si) is believed to be the catalytically active form of copper in the HC reaction, as is the case for the Rochow-Müller direct process. Proof of eta phase as the catalytically active form of copper in the HC reaction has not been published. There is no reported evidence to suggest that the direct process promoters (P, Sn, Zn) benefit the HC reaction.

Unlike the Rochow-Müller direct process reaction, the HC reaction can be run successfully without use of external catalyst; the only result is lower TCS yield. MGS impurities, such as Al and Fe, always provide in-situ catalysis for the HC reaction. Optimization of MGS composition represents an opportunity to improve commercial HC TCS yield regardless of external catalyst use.

Process Description

Hydrochlorination (HC) produces TCS by continuous reaction of ground MGS, hydrogen and STC. Optionally, anhydrous HCl can be co-fed. Figure 1 provides a flowsheet of a typical commercial HC process unit. A HC unit can be used to support TCS or silane-based polysilicon production. The location of the HC unit in a TCS-based polysilicon plant (batch Siemens rods) is shown in Figure 2. The location of the HC unit in a silane-based polysilicon plant (batch Siemens rods and / or semi-continuous granular FBR) is shown in Figure 3 [11, 12, 13].

Hydrochlorination Process

The HC reaction is normally conducted in a fluid bed reactor (FBR) which can include a cyclone. Ground MGS and, optionally, external catalyst is fed to the FBR. Superheated hydrogen and STC are combined and fed to the bottom of the FBR. Optionally, anhydrous HCl can be fed along with hydrogen and STC. Anhydrous HCl is usually fed when the HC process is integrated with TCS-based polysilicon production. Gas and entrained solids from the reaction mass (fluidized solids inside the FBR) enter the cyclone where a portion of the entrained solids are separated and returned to the reaction mass. Finer particles exit the cyclone with the overall gas stream.

A single line exits the top of the FBR-cyclone. The exit stream leaves the FBR-cyclone at about 520 – 540° C and contains a mixture of gas / vapor and fine particle size solids. The gas / vapor portion of the exit stream contains TCS product, DCS by-product, unreacted STC, unreacted

hydrogen, traces of HCl, sublimed aluminum chloride ($AlCl_3$) and volatile impurities (arsenic, boron, carbon, phosphorus-based) described previously. Solids include unreacted MGS, MGS impurities (intermetallic phases), externally added catalyst (if used), solid metal chlorides ($CaCl_2$ for example) and iron silicide. The exit stream can flow through two cross exchangers before entering the scrubber.

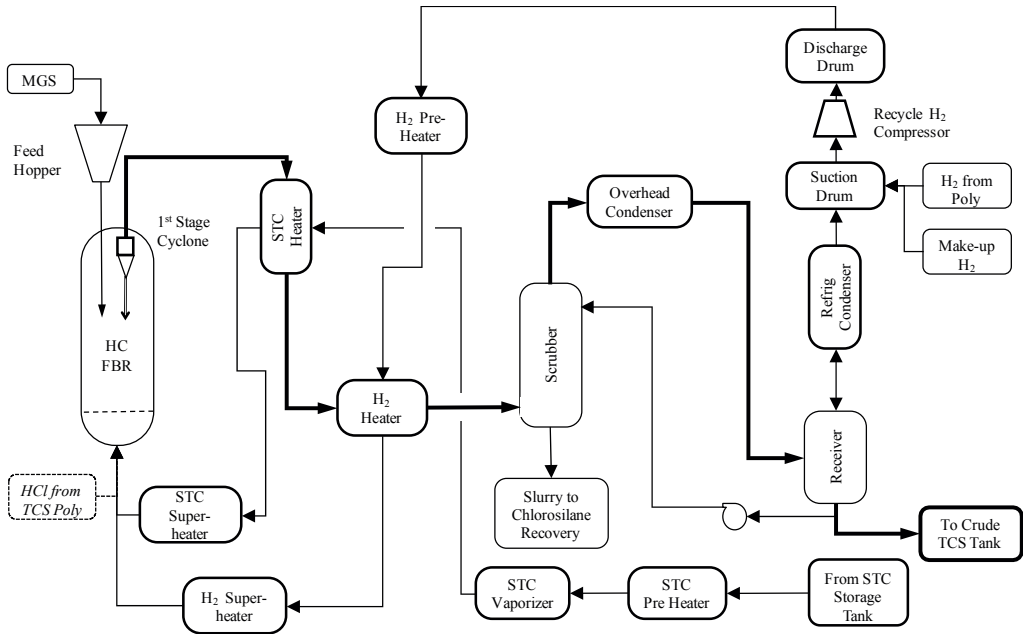

Figure 1: General commercial hydrochlorination flow sheet. HCl feed to the HC FBR is present with TCS-based polysilicon plants; HCl feed is normally not present with silane-based polysilicon plants. External catalyst feed is optional.

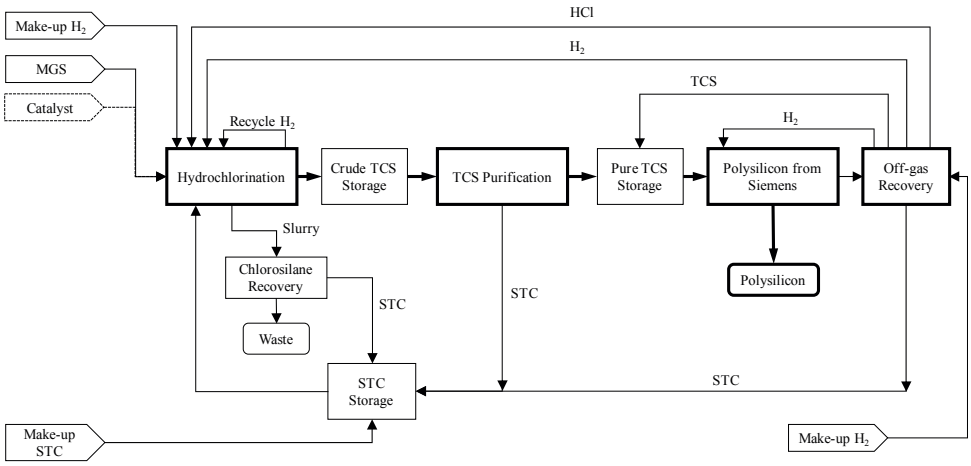

Figure 2: TCS based polysilicon plant with hydrochlorination.

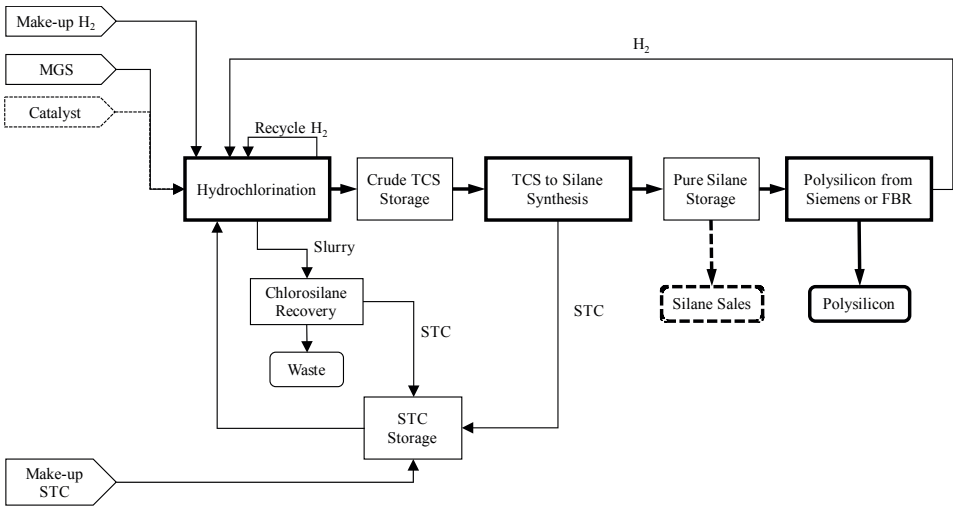

Figure 3: Silane based polysilicon plant with hydrochlorination.

The cross exchangers are designed to transfer heat to STC and hydrogen FBR feed streams and are an integral part of the overall STC and hydrogen heat addition system. Design of the cross exchangers is critical to prevent solids fouling caused by accumulation of sticky metal chlorides.

The scrubber is designed to 1) provide a first stage of chlorosilane (DCS, TCS, STC) condensation; 2) remove entrained solids and 3) de-sublime $AlCl_3$ vapor. The scrubber is refluxed with condensed chlorosilanes in a variety of arrangements. Figure 1 shows one simple reflux arrangement. Recovered solids and de-sublimed $AlCl_3$ are periodically discharged from the bottom of the scrubber as a slurry.

The slurry is transferred to a process unit designed to recover and recycle some amount of the chlorosilane fraction. The slurry is comprised mostly of STC with trace amounts of TCS and polychlorosilanes (such as HCDS), arsenic trichloride ($AsCl_3$), PCl_3, $AlCl_3$ (high solubility in hot chlorosilanes) and the solids previously listed. Chlorosilane recovery efficiency is an important variable that must be balanced between minimization of polysilicon quality and chlorine loss. Excessive chlorosilane recovery can result in recycle of excessive PCl_3 to the HC process, which places a higher load on overall plant phosphorus removal systems.

Off-gas exits the top of the scrubber and enters the final part of the HC process. The scrubber off-gas stream should be solids-free and contain only traces of $AlCl_3$. The scrubber off-gas passes through a series of heat exchangers. One or more of the heat exchangers may be a cross exchanger that is designed to preheat hydrogen and liquid STC feed streams. The specific location of these cross exchangers is not provided in Figure 1. The exchangers are designed to separate chlorosilanes from unreacted hydrogen. The initial exchangers can use air and water; the final requires refrigeration.

Condensed chlorosilanes are accumulated downstream from the refrigerated condenser. This stream is usually referred to as crude TCS. Crude TCS contains TCS, by-product DCS, unreacted STC along with volatile carbon, boron and phosphorus compounds, traces of hydrogen, HCl and $AlCl_3$. Crude TCS is transferred from the HC process unit to one or more storage tanks. The storage tanks supply crude TCS to the TCS purification train (for TCS-based polysilicon plant) or to the silane plant (for silane-based polysilicon plant). Some crude TCS can be used as scrubber reflux.

Unreacted hydrogen is recovered as a gas stream from the refrigerated condenser. Hydrogen enters a compressor and is recycled back to the HC FBR. Make-up hydrogen (from the polysilicon area and / or external supplier) is added to the process. Figure 1 shows make-up hydrogen addition on the low pressure side of the hydrogen recycle compressor.

Hydrogen discharged from the compressor can pass through two cross exchangers. The second hydrogen cross exchanger is located on the FBR exit stream. Heated hydrogen from the second cross exchanger enters a superheater for heating to the final desired feed temperature. Superheated hydrogen is combined with STC downstream from the superheater and fed to the FBR.

Liquid STC is pumped from a storage tank, through a STC pre-heater (cross exchange with higher temperature process stream) and into the STC vaporizer. Liquid STC enters the storage tank from four sources: 1) Unreacted STC separated from TCS crude; 2) Recovered chlorosilanes from scrubber slurry; 3) STC by-product from conversion of TCS to polysilicon or from conversion of TCS to silane and 4) purchased STC (makeup chlorine source)

While STC is not produced in the HC reaction, STC is an important by-product from both TCS Siemens polysilicon production and TCS to silane conversion. The ability to recycle by-product STC back to the HC reactor presents one of the strong advantages of HC for stand-alone polysilicon synthesis. High temperature hydrogenation reactors (Reaction 3) are not required for HC-based polysilicon plant.

STC is produced as a significant by-product in the production of polysilicon from TCS. The chemical reactions in a TCS-Siemens reactor are extremely complex [14] and are not presented in this paper. STC is produced as the only by-product production of silane from TCS by weak-base ion exchange resin catalyzed disproportionation / redistribution reactions. The overall TCS to silane reaction is written as:

$$4HSiCl_3\ (l) = SiH_4\ (g) + 3SiCl_4\ (l) \qquad (10)$$

Saturated STC vapor exits the vaporizer and passes through a cross exchanger located on the FBR-cyclone exit stream. Heated STC vapor exits the cross exchanger and enters the STC superheater for heating to the final desired feed temperature. Superheated STC is combined with hydrogen downstream from the superheater and fed to the FBR.

Some producers may combine hydrogen and STC vapor streams prior to entry into the final superheater as a way to reduce superheater capital costs. This practice requires special consideration to accommodate formation of anhydrous HCl produced from the reaction of hydrogen and STC at superheater temperatures (Reaction 3). One concern is high temperature HCl corrosion of the heater internals.

The only significant process difference between a HC unit supporting TCS-based polysilicon compared to silane-based polysilicon is anhydrous HCl co-feed to the HC FBR with hydrogen and STC. Anhydrous HCl is generated when polysilicon is produced from TCS. HCl co-feed has the chance to introduce temperature related corrosion problems to the HC FBR vessel depending on the amount and physical HCl feed location. HCl co-feed to a HC unit supporting silane production is possible.

TCS Hydrochlorination Yield

A primary metric of commercial HC process operation is the amount of TCS produced in the HC reaction. The metric is called “TCS yield”, “TCS conversion” and / or “TCS Selectivity”. TCS yield is used in this paper. Lower TCS yield results in higher energy cost for constant TCS production. Laboratory reactor TCS yields have been reported [2] to range from 15-35 mole percent (12-30 weight percent) depending on reaction conditions. Commercial TCS yield can be assumed to be similar although the upper end is lower. TCS yield is controlled through HC plant design, raw material selection and active process control.

TCS Yield Design Basis

Each commercial HC plant is designed to produce a specific amount of polysilicon at an assumed annual uptime for a specific TCS yield. There is no correct value for TCS yield design basis but conservative engineering practices dictate selection of the lowest possible value for TCS yield that does not result in excessive capital costs. If the TCS yield design basis is too high, chances are

high that the plant may not reliably produce sufficient TCS to enable production of desired polysilicon. If the TCS yield deign basis is too low, capital cost is wasted on excessively large HC unit equipment.

The amount of TCS present in the crude chlorosilane stream can be reported as mole percent or weight percent. DCS content of crude TCS is about 0.2 – 0.8 mole percent based on laboratory reactor results [2]. TCS yield is reported on a hydrogen and HCl-free basis and is normally measured in the liquid stream entering the TCS crude storage tanks. The amount of DCS in the TCS crude is rarely reported and sometimes included with the TCS.

TCS yield = 100 * TCS in TCS crude / (total TCS crude [DCS, TCS, STC]) (11)

Raw Material TCS Yield Control

Several raw material inputs can be adjusted to change TCS yield.

MGS Composition

The global Rochow-Müller direct process operators began to quantify the relationship between MGS composition and economic operation of the methylchlorosilane FBR's in the late 1980's [15]. The global silicone producers have invested considerable time and money to optimize MGS composition specifications.

Knowledge and experience about the impact of MGS composition on HC reaction TCS yield has been slow to translate from the global silicone industry. There is no reason that MGS composition specifications, optimized to enable maximum TCS yield, would not exist for HC operation.

Union Carbide JPL researchers [2] considered MGS composition relationship on TCS yield but their work did not result in reporting an optimized MGS composition specification. German researchers [4, 5, 6, 7] identified iron as an important MGS impurity based on laboratory results. Elkem laboratory reactor results show that use of MGS containing greater than 50 ppmw manganese result in lower TCS yield [16]. Confirmation of the Elkem laboratory results for optimum Mn levels in a commercial HC unit has not been published.

As with the Rochow-Müller direct process, it is hypothesized that some MGS impurities (Mn for example based on the Elkem patent) which accumulate in the HC FBR reaction mass have a negative impact on TCS yield. TCS yield may slowly decline during the duration of a commercial HC FBR reactor run.

Externally Supplied Catalyst

Use of separate externally fed catalyst increases TCS yield. Copper (oxide, metallic, chloride) is the preferred external catalyst. Feeding the correct amount of external catalyst can result in statistically higher TCS yield. Physical size of the copper catalyst is an important parameter. TCS yield can be reduced if the wrong size copper catalyst is used. If the particle size is too fine, excessive amounts of the fresh catalyst are lost from the HC FBR. If the particle size is too coarse, conversion of the catalyst to the catalytically active form is too low.

Ground MGS Particle Size Distribution

The influence of ground MGS particle size distribution (PSD) on TCS yield is not well understood. Every unique ground MGS PSD has different fluidization properties and requires optimized FBR and cyclone designs. There is no single optimum ground MGS PSD for commercial HC FBR's.

Active Process Control

Several process parameters can be adjusted during plant operation to influence TCS yield. These parameters can be adjusted, within boundary limits established by the overall HC process design, on a day to day basis by plant engineers and operators.

FBR operating temperature

The normal HC FBR operating temperature is 520 – 550^{o} C. All other parameters being held constant, higher temperature translates to higher TCS yield. Higher temperatures drive the reaction faster towards equilibrium. Limitations to maintaining maximum temperatures are the thermal design, reliability and materials of construction of the hydrogen and STC heating systems and the ability to minimize radiant heat loss from the FBR and associated equipment.

Residence time

Reactant gas residence time in the FBR reaction mass (fluidized bed of MGS) is controlled by a combination of hydrogen and STC feed rates to the FBR and reaction mass level. TCS yield is proportional to reactant gas residence time. Residence time is inversely proportional to gas feed rate assuming FBR bed level is constant. Reaction mass level is controlled by the feed rate of ground MGS to the FBR. Maximum safe reaction mass level is determined by the physical design of the FBR and specification of ground MGS particle size distribution.

Hydrogen to STC feed molar ratio

The molar ratio of hydrogen to STC is proportional to TCS yield. The molar ratio is controlled by overall plant design. Overall plant design includes all aspects of the hydrogen and STC feed systems: available supply, compressor design, pump design and heat input design. A typical hydrogen to STC molar ratio is 2:1.

FBR operating pressure

Operating pressure of a commercial HC FBR is defined during initial plant design. Commercial HC units can be designed to operate from 10 – 34.5 barg (150 – 500 psig). There is no "correct" answer to the question of "what is the optimum operating pressure". Operating pressure selection requires consideration of local chemical plant design standards and economic analysis of total equipment costs of the commercial HC unit. Once a HC unit has been designed, built and started, operating pressure changes are minor and have no measureable impact on TCS yield.

As the operating pressure increases, the maximum achievable TCS yield increases, the required diameter of the FBR decreases and the required wall thickness of the FBR increases. Commercial HC FBR are normally constructed of Incoloy 800H [17, 18]. There are physical limitations on FBR diameter based on the mechanical properties of Incoloy 800H and the appropriate pressure vessel mechanical design standards.

Hydrochlorination Plant Operations

The purpose of this section is to provide information about commercial HC plant operation. This information describes important process design and operating parameters that influence total operating costs. Operating costs are a function of TCS yield, energy consumption, silicon utilization, chlorine utilization and plant design. The impact of TCS yield on energy consumption is the focus of this paper. These discussions are applicable for HC operations that produce polysilicon-grade TCS or silane.

Process metrics

A primary metric of commercial HC process operation is TCS yield Some producers may also use other metrics such as STC, hydrogen and / or MGS conversion. Each HC plant is designed to produce sufficient TCS equivalent to the final desired polysilicon capacity at a specific TCS yield. The HC plant can operate at TCS yields lower than design TCS yield. If this is the case, *higher* feed rates of hydrogen and STC are required to produce the required amount of TCS. The HC plant can also be operated at TCS yields higher than design TCS yield. In this case, hydrogen and STC feed rates are *lower*.

Energy Consumption

Published information about polysilicon plants focus on the energy required to convert TCS or silane to polysilicon, which is the largest source of polysilicon plant energy consumption. Energy required to operate the HC plant is equally important but usually neglected in published reports. Discussion of HC plant energy consumption assumes a fixed amount of TCS is produced. Figure 1 shows one possible configuration of the heat input system and is used in the present analysis of energy costs as a function of TCS yield.

As TCS yield from the HC FBR decreases, the total energy costs required to heat hydrogen and STC feed streams increase. Energy costs increase because the required flow rates of hydrogen and STC to the HC FBR increase with decreasing TCS yield. Higher gas flow rates result in higher heater energy consumption. The selection of heater design and heating energy source is a function of geographic plant location and capability of each specific commercial operator. Geographic location of the plant can be very important with regards to selection of the most optimum energy source.

Process Heat Input

Energy requirements for the HC FBR feed hydrogen and STC heat input system can be calculated with a heat and material balance. Energy costs are calculated from the calculated energy requirements. Comments are provided about the specific heat exchangers shown in Figure 1.

STC Vaporizer

The STC vaporizer is assumed to receive a preheated liquid stream of STC. Hot heat transfer oil (HTO) is assumed to be the energy source to vaporize STC. The HTO can be heated with a direct fired natural gas furnace or a radiant electric heater. Energy loss in the STC vaporizer is assumed to be negligible assuming proper insulation is provided and there is no solids deposition on the STC side of the vaporizer.

STC and Hydrogen Superheaters

Superheaters are used to raise the temperature of hydrogen and STC vapor to the final desired temperature for feed to the FBR. Commercial hydrogen and STC superheater designs are normally indirect radiant box or direct immersion electric. The indirect radiant box can be heated with natural gas or electricity.

A direct immersion heater uses electrical heating elements placed in direct contact with the hydrogen and / or STC streams. Indirect radiant heater design involves flowing hydrogen or STC through a pipe coil that is installed inside a large insulated vessel. Electrical heating elements or natural gas burners are provided inside the vessel. Heat transfer from the energy source to the pipe coil is by radiation.

Process-to-Process Heat Exchangers

STC fed to the STC vaporizer and hydrogen fed to the hydrogen superheater are pre-heated by process-to-process heat exchangers. These exchangers are indicated on Figure 1. These exchangers are recovering heat from hotter process streams to increase the temperature of hydrogen and STC streams. A plant can be designed without process to process exchangers but energy costs are considerably higher.

Maintenance Costs

Maintenance costs are an important metric of commercial HC. Annual maintenance costs for a HC plant represent a significant portion of total plant maintenance costs. Maintenance costs are highly dependent on plant design, equipment technology, operating experience, geographic location and application of preventative maintenance programs, regardless of TCS yield or overall plant polysilicon capacity. The maintenance costs for a basic technology HC plant can be considerably higher than for a best available technology HC plant of the same TCS capacity. Maintenance costs can be related to HC reactor TCS yield for production of a fixed amount of TCS. Higher hydrogen and STC feed rates results in higher maintenance costs due to higher wear on compressors, pumps and load on the heat input system. Higher hydrogen and STC feed rates are normally associated with lower TCS yield. Increasing TCS yield through use of optimized MGS composition, and the subsequent reduction in hydrogen and STC flow rates, can reduce HC plant maintenance costs.

It is difficult to quantify the impact of HC maintenance cost since some equipment is maintained on a predetermined basis and some equipment is replaced due to wear. Commercial HC operators usually do not publish maintenance costs. The impact of increased maintenance cost due to higher hydrogen and STC flow rates can be substantial. It is suggested that each producer evaluate the TCS yield influence on maintenance cost.

Laboratory HC Reactor MGS Composition Influence on TCS Yield

Recent laboratory work shows a relationship between MGS composition and TCS yield. Two MGS samples of different composition but identical PSD were evaluated in a well established continuous HC laboratory reactor. The lab reactor has a history of TCS yield results that are believed to be consistent with overall commercial HC results.

Operating conditions of the lab reactor were held constant when the two MGS samples were evaluated: 550^{o} C, 10 barg and 1 weight % copper as CuCl. TCS yield as a function of reaction

time is provided in Figure 4. The data clearly show an advantage of MGS sample A compared with MGS sample B. The lab results have not yet been commercially validated.

Lab Reactor Validation

Commercial experience with HC and Rochow-Müller direct process operations indicate the risk of well-planned commercial HC MGS composition and catalysis experiments on overall polysilicon plant operations (safety, quality, economics) to be low. Similar commercial trials on Rochow-Müller direct process FBR's can result in serious plant upsets [19]. Due to the low risk, commercial HC operators should not be afraid to run well-planned MGS trials based on promising laboratory reactor results.

Translation of HC lab reactor MGS composition results to commercial operations requires cooperation between the commercial HC operator, lab reactor operator and a technically capable MGS smelter. The HC operator and MGS smelter can develop an overall commercial trial plan starting with how to modify the existing MGS composition specification of the HC operator, how to produce the desired trial MGS, how much trial MGS to produce and how to conduct the commercial trial on the HC FBR. The trial plan includes procedures and protocols to measure results of the commercial HC FBR trial to determine if the desired increased TCS yield was achieved without causing downstream problems. Multiple commercial trials can be anticipated.

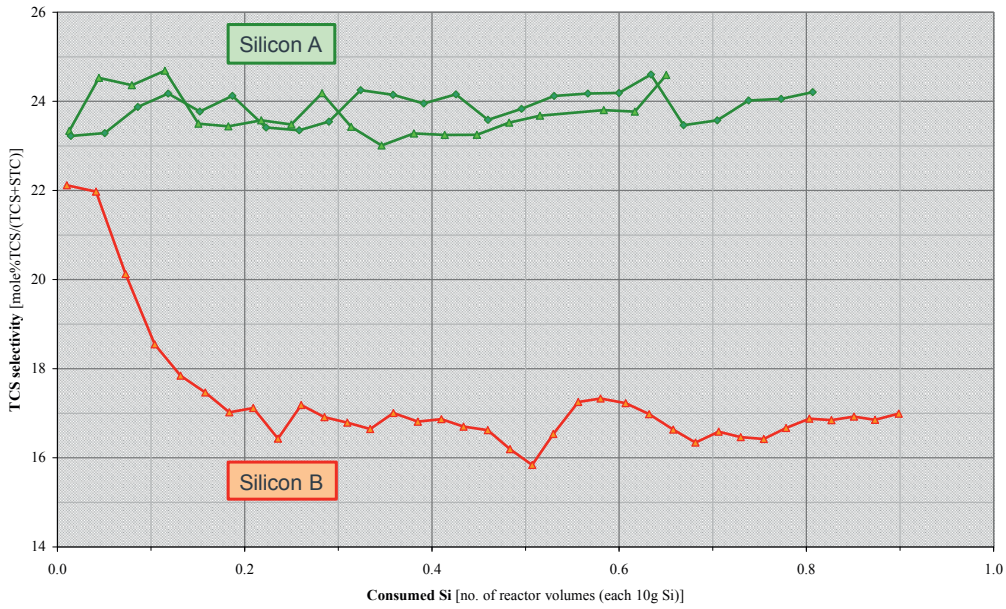

Figure 4: Laboratory data for MGS-A and MGS-B showing TCS yield (mole %) as a function of consumed MGS (reaction time).

Hydrochlorination Energy Cost versus TCS Yield

Lower TCS yield results in higher energy costs to produce a constant amount of TCS. Background information about the HC reaction, process design and process operation have been provided. Parameters that influence TCS yield have been discussed. One relatively unexplored area to influence TCS yield in commercial HC operations is changes to MGS composition.

Overall Plant Capacity

Each polysilicon plant is designed to produce a specific amount of polysilicon at a specified annual uptime. Actual operations can range from 100% capacity utilization to a value well below 100% depending on market conditions.

When polysilicon demand is strong, capacity utilization is 100%. Extra revenue from incremental polysilicon production (over and above design capacity) is possible if plant operation can be modified without significant capital cost. Incremental polysilicon production requires incremental TCS production and extra TCS Siemens reactor capacity. Incremental TCS production requires higher HC unit TCS yield and extra TCS purification capacity. If other sections of the plant do not enable production of incremental polysilicon, operation of the HC unit with higher TCS yield but original 100% capacity utilization TCS production rates still enables energy cost savings.

In times of soft polysilicon demand, the entire plant is run at less than 100% capacity utilization. Soft market conditions do not offer the chance to produce and sell incremental polysilicon. There are turn-down limits, especially in the HC unit due to the necessity to maintain proper fluidization and cyclone operations. Lower TCS yields in the HC unit still results in higher energy costs. Operation of the HC unit at higher TCS yield can result in lower energy costs provided the lower total gas flow rates to the FBR enable operation within the overall design ranges. Any energy savings are immediately lost if TCS production is increased to the point that storage tanks are full and the HC plant must be shutdown. HC plants cannot be idled in analogous fashion to distillation.

Example

Some calculations were made for a HC-based polysilicon plant. The calculations show an increase in energy costs as the TCS yield decreases. The following variables were held constant for the calculations: 1) 10,000 TPY polysilicon capacity; 2) HC plant TCS production; 3) 520^{o} C FBR exit temperature; 4) 28 barg HC FBR operating pressure and 5) 2:1 molar feed ratio of hydrogen to STC. The method to increase TCS yield was not specified but could include changes to MGS composition, MGS PSD, use of external catalyst and / or alteration of reactant gas residence time.

Energy consumption calculations are based on the heat exchanger arrangement provided in Figure 1. The STC vaporizer is assumed to be heated with heat transfer oil that is heated by a direct-fired natural gas furnace having 80% energy efficiency. Hydrogen and STC superheaters are assumed to be radiant box design that use electricity as the energy source with 85% energy efficiency. The natural gas price used is average 2015 USA Henry's Hub price of $2.63 per million BTU and electricity price was assumed to be $0.060 / kW-hr.

A summary of total energy input costs as a function of HC FBR TCS yield is provided in Figure 5. The assumed TCS yield range is 20 – 35 mole percent (16.6 – 30.0 weight percent) while TCS production rate was held constant. Potential energy savings resulting from an increase of TCS

yield from 25 mole % to 28 mole % is about $400,000 per year. Incremental 3 mole % increase was selected as a practical commercial example. If the higher TCS yield can be achieved through optimization of MGS composition, the reported savings can be achieved with zero capital investment.

An example of the benefit of process to process heat exchange (cross exchangers) is provided for the 30 mole percent TCS yield case. The energy cost for a HC process that uses the cross exchangers indicated in Figure 1 is about $3,100,000 per year. The energy cost for a HC process that does not use the Figure 1 cross exchangers is about $6,200,000 per year.

Conclusion and Recommendation

1) HC process energy costs are inversely proportional to TCS yield for fixed TCS production rate.

2) Laboratory reactor data show that MGS composition has a significant impact on TCS yield from the HC reaction. Increasing TCS yield through changes to MGS specification represents a way for a commercial HC operator to reduce operating costs with zero capital spending.

3) Well-planned commercial HC MGS trials offer low risk to overall polysilicon plant operations.

4) Collaboration between commercial HC operator, HC lab reactor operator and MGS smelter is required to enable the best chance to translate positive MGS composition lab results to plant operations.

5) There is a relationship between TCS yield and HC plant maintenance costs.

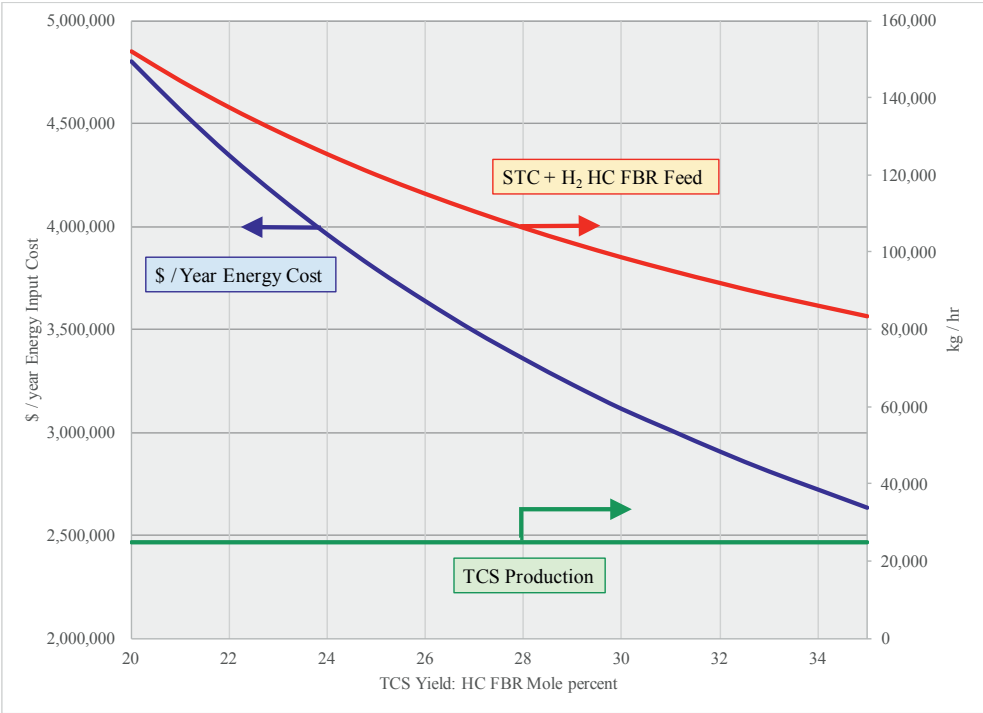

Figure 5: Hydrochlorination (HC) unit hydrogen and STC energy input costs as a function of HC FBR TCS yield for a 10,000 TPY polysilicon plant. TCS production is held constant for each case.

Acknowledgements

The author would like to acknowledge the contribution from Elkem A/S towards this paper. Elkem A/S provided access to laboratory HC reactor data that were used to show the influence of MGS composition on HC reaction TCS yield.

References

1. G. F. Wagner, C. E. Erickson, *Hydrogenation of Halosilanes*, U.S. Patent 2,595,620, 1952.
2. J. Y. P. Mui, D. Seyferth, *Final Report: Investigation of the Hydrochlorination of STC*, JPL Contract 955382, 1981. http://ntrs.nasa.gov/archive/nasa/casi.ntrs.nasa.gov/19810019076.pdf
3. W. M. Ingle, M. S. Peffley, *Kinetics of the Hydrogenation of Silicon Tetrachloride*, J. Electrochem. Soc, **132(5)**, 1985, pp. 1236-1240.
4. P. Cygon, *Technical Reaction Studies of the Hydrochlorination of Silicon in a Laboratory Fluidized Bed Reactor*, Diploma Thesis, University of Köln, 1999.
5. T. Sill, *Hydrochlorination Study of Silicon for the Trichlorosilane Synthesis in a Fluidized Bed Reactor*, PhD Thesis, Ruhr-University Bochum, 2001.

6. R. J. Lehnen, *Studies Concerning the Catalytic Hydrochlorination of Metallurgic Silicon with Silicon Tetrachloride and Hydrogen in a Laboratory Fixed Bed Reactor*, PhD Thesis, Ruhr-University Bochum, 2002.
7. F. Becker, Modeling and Simulations of the Hydrochlorination of Silicon to Trichlorosilane for the Development of a Technical Fluidized Bed Reactor, Doctor - Engineer Thesis, Rheinisch-Westfälischen Technischen Hochschule Aachen, 2005.
8. L. M. Coleman, private communication, 2016.
9. W. M. Ingle, M. S. Peffley, H. S. Setty, *Trichlorosilane Production Process*, U. S. Patent 4,526,769, 1985.
10. T. Noda, E. Nakayama, *Manufacture of Trichlorosilane*, Japanese Laid-open Patent application S56-73617, 1981.
11. L. M. Coleman, *Process for the Production of Ultrahigh Purity Silane with Recycle from Separation Columns*, U.S. Patent 4,340,574, 1982
12. W. C. Breneman, *High Purity Silane and Silicon Production*, U.S. Patent 4,676,967, 1987.
13. S. Müller, *SiTec's Innovative, Advanced Silane Process* (poster), Silicon for the Chemical and Solar Industry XII, H.A. Øye, H. Brekken, L. Nygaard, H. M. Rong, M. Tangstad, H. Tviet Eds., (Trondheim, Norway), 2014.
14. M. T. Swihart, R. W. Carr, *On the mechanism of homogeneous decomposition of chlorinated silanes*, J. Phys. Chem. A, 1998 (102), pp. 1542-1549.
15. A. Ritzer, G. E. Tabit, *Strategic Alliance: Silicon Metal for Silicone Manufacturing*, Silicon for the Chemical Industry I, H.A. Øye. H. M. Rong Eds., (Geiranger, Norway), 1992, pp. 133-144.
16. G. J. Andersen, J. O. Hoel, H. M. Rong, T. Røe, *Method for Production of Trichlorosilane and Silicon for use in the Production of Trichlorosilane*, World Patent 2007/035108-A1, 2007.
17. J. Y. P. Mui, *Corrosion Mechanism of Metals and Alloys in the Silicon-Hydrogen-Chlorosilane System at 500 Deg C*, Corrosion, **41(2)**, 1985, pp. 63-69.
18. Verolme Special Equipment b.v., www.vmij.nl/products/polysilicon-equipment/
19. J. M. Bablin, A. C. Crawford, D. C. DeMoulpied, L. N. Lewis, *Effect of low aluminum silicon on the direct process*, Ind. Eng. Chem. Res., 2003, 42, pp. 3555-3565.

Optimize Your Chlorosilane Distillation Columns

Larry Coleman, Engineering Consultant, Buffalo, New York, USA
Independent Engineering Consultant

Abstract

Physical property parameters are given for chlorosilanes and all major impurities to allow distillation columns to be optimized using process simulators. Included are a reduced-form thermodynamically consistent vapor pressure equation, critical properties, recommendations for Equation of State, and a method for estimating VLE relationships. Data gaps are filled for many trace impurities that have process significance.

Background

Sophisticated computer process simulation packages are available from several sources (for example ASPEN, ChemCad and VMGsim), which can be used to optimize chlorosilane distillation column performance and allow evaluation of alternative distillation schemes. The benefits of using these simulators include reduced energy consumption, improved product through-put, and maintaining on-specification of impurities. In conjunction with a well-planned analytical program, process impurities can be speciated and tracked through the system in an operating polysilicon plant. This allows correlating the raw material specifications to product quality, and to energy use. Such distillation improvement is applicable for hydrochlorination (HC), direct chlorination (DC) synthesis, and off-gas processing from several polysilicon process unit operations.

Advances have been made in modelling hydrocarbons' vapor-liquid equilibria (VLE) over the last few decades in the oil and gas industry – but there is a lack of advancement in slightly polar compounds like chlorosilanes. In recent years, the ability of analytics to track chlorosilane impurities has out-stripped the ability of process simulators to provide optimization feedback, particularly at higher pressures. The following work gives the culmination of a multi-year effort to fill in that technology gap, for use in process simulators. Included in this paper are:

1. a thermodynamically consistent vapor pressure equation, in reduced form
2. the critical properties table needed to use it (including the acentric factor)
3. above items 1 and 2 are given for chlorosilanes and all major chlorosilane process impurities
4. recommendations and "work-arounds" on Equations of State, to allow evaluation of fugacity coefficients
5. a method to estimate liquid-phase activity coefficients, to allow VLE calculations

Space limitations in this paper preclude going into VP equation derivation, iterative solution method and details on estimating properties for trace impurities (for which experimental data may be poor or missing). A full disclosure of this detail is in an e-published monograph[1], which will also allow addition of other fluids of interest.
Examples of poor/missing data, key to chlorosilane purification are:

- Dichlorophosphine (major phosphorus impurity in TCS)
- Iso-pentane VLE with TCS (a primary cause of carbon in TCS)
- Phosphine VLE with silane (major impurity in silane-produced polysilicon)
- The various methyl chlorosilane fluids that are close-boiling to TCS and DCS

The improvement potential on OPEX of existing plants is easily targeted at 10% of column reboiler and condenser energy, and somewhat lower on CAPEX for new plants. The ability to reduce off-spec product, by better rejection of impurity species, is hard to quantify, but very real.

The modified Thek-Stiel vapor pressure equation

Developed in 1965, this relationship was recommended by Reid and Prausnitz[2] as the best choice for polar compounds. The work was abandoned in the mid-1980's as requiring too much computing power and an iterative solution method, but no replacement has been offered. Using modern computing power, software, and global access to vapor pressure data, I have taken this work to its logical completion for chlorosilanes and the similar fluids that comprise the process impurities. For definition of parameters, see the last section of this paper.
Existing process simulation packages offer VP equations for the chlorosilane family and some impurity compounds; however they are not thermodynamically consistent and offer poor property correlation at high pressure. These "extended Antoine" relationships frequently are inconsistent with database values for NBP, the critical point, and at T_r =0.7 (where the acentric factor is evaluated). That can cause problems when used with any Equation of State more advanced than van der Waals.
Thek-Stiel[3] starts with the Clapeyron relationship, $\frac{-d(LnP_r)}{d(1/T_r)} = \frac{\Delta H_v}{\Delta ZRT_c} = \psi$ as taught in all chemistry and chemical engineering university courses. They proposed a two term equation form that allows integration of this relationship, and included the two Riedel consistency conditions. By iterative solution, the Riedel "α_c" parameter is solved at the normal boiling point (NBP = T_b). The Watson exponent "q" is iteratively solved by the Pfizer acentric factor "ω". After modification, the resulting Thek-Stiel reduced vapor pressure equation is:

$$Ln(P_r) = A[B_0 - T_r^{-1} - B_1 LnT_r + B_2 T_r - (1/2)B_3 T_r^2] + c[\frac{(T_r^{n-1} - 1)}{n-1} + k(T_r^{-1} - 1)]$$

$$A = \frac{\Delta H'_{vb}}{RT_c(1-T_{br})^q} \qquad \mathbf{q = 0.37028 + 0.065404\omega}$$

$$B_0 = 1 - B_2 + B_3/2 \qquad B_1 = q$$

$$B_2 = q(q-1)/2! = q(q-1)/2$$

$$B_3 = q(q-1)(q-2)/3! = q(q-1)(q-2)/6$$

$$c = \frac{\alpha_c - A(1 - B_1 + B_2 - B_3)}{(1-k)} \qquad n = (1-k) + \frac{A}{c}(1 - B_2 + 2B_3)$$

Of the two remaining parameters, "k" is found to be a function of the degree of hydrogen bonding and $\Delta H'_{vb}$ is valued as best-fit to the vapor pressure data. Note that while $\Delta H'_{vb}$ is closely related to the NBP latent heat (ΔH_{vb}), it is slightly displaced by the effect of ΔZ.

After iterative solution using a stand-alone BASIC program, Table 1 gives the parameter values for the chlorosilanes and most major impurities. Table 2 gives the critical property values for those same fluids, to allow the reduced temperature and pressure to be related to conventional temperature & pressure units (i.e., °K and bar absolute). The acentric factor is a needed parameter in the Equation of State. Critical molar volumes are important to assessing binary interactions. Critical compressibility is related to the sphericity of the compound's molecule, for mildly polar fluids like chlorosilanes.

An example of the use of this technology is a comparison plot between the chlorosilanes and chlorophosphines, Figure 1.

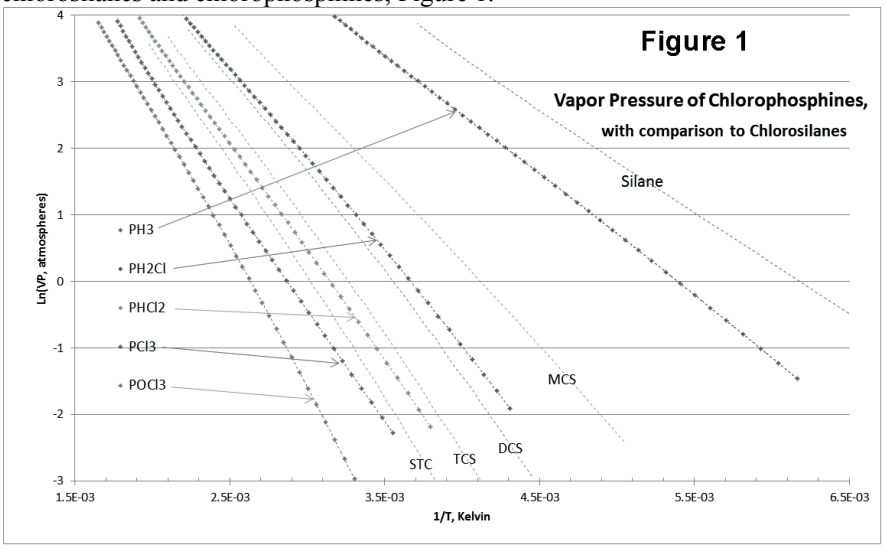

On below Tables 1 and 2, note that Group III fluids are sometimes better organized as their dimers (as noted by ǂ), featuring either hydrogen or chlorine bridge-bonding. N-pentane and iso-pentane are included because of their process significance and frequent occurrence as impurities.

These two tables include entries for impurities where experimental data is either missing or of poor quality, such as dichlorophosphine. This is accomplished by means of the modified Lyderson methods for interpolation. In the case of methyl chlorosilanes, an additional neural network estimation technique is used. Both methods are fully detailed in the e-published monograph[1].

Note that some fluids are not included in the tables, such as aluminum hydride, di-gallane, trichloro-diborane and the hydrochlorides of arsine and stannane. This is purposeful, since these fluids are unstable at normal process conditions. Some, like aluminum hydride, have shown stability in the near-cryogenic solid state, under laboratory conditions.

Table 1, VP solutions, by Group and Homologue

Compound	MW	A	B_0	B_1	B_2	B_3	c	n	k
Group III(A)									
B_2H_6	27.670	8.9910	1.1494	0.37848	-0.11762	0.063573	2.8701	4.7796	0.1197
B_2H_5Cl	62.119ǂ	8.1915	1.1494	0.37867	-0.11764	0.063578	3.4560	3.8431	0.1073
BH_2Cl as monomer	42.284	8.3872	1.1495	0.37888	-0.11766	0.063583	3.2767	4.0925	0.0938
$BHCl_2$ as monomer	82.722	8.9910	1.1495	0.37937	-0.11772	0.063596	2.7577	4.9953	0.0636
BCl_3 as monomer	117.169	9.5652	1.1496	0.37988	-0.11779	0.063609	2.2357	6.2975	0.0291
$AlCl_3$ as monomer	133.341	11.9183	1.1512	0.39300	-0.11928	0.063892	2.2700	7.5185	0.0291
$Ga_2H_4Cl_2$ as dimer	214.383ǂ	7.0714	1.1506	0.38810	-0.11874	0.063799	5.3346	2.5583	0.0938
$Ga_2H_2Cl_4$ as dimer	283.273ǂ	10.8499	1.1513	0.39333	-0.11931	0.063898	3.3656	4.9567	0.0636
Ga_2Cl_6 as dimer	352.162ǂ	11.1760	1.1520	0.39974	0.11997	0.063996	3.8566	4.5874	0.0291
Group IV(A)									
SiH_4	32.117	7.4652	1.1492	0.37673	-0.11740	0.063525	3.6247	3.4716	0.0914
SiH_3Cl	66.562	8.8830	1.1494	0.37847	-0.11761	0.063572	2.7614	4.9286	0.0756
SiH_2Cl_2	101.007	9.9221	1.1497	0.38068	-0.11788	0.063629	2.1589	6.6627	0.0598
$SiHCl_3$	135.452	9.9796	1.1501	0.38395	-0.11827	0.063708	2.5687	5.7950	0.0446
$SiCl_4$	169.896	10.0240	1.1504	0.38651	-0.11856	0.063765	2.8465	5.3590	0.0291
$SiH_3(CH_3)$	46.144	9.0535	1.1494	0.37855	-0.11762	0.063574	2.6380	5.1963	0.0758
$SiH_2Cl(CH_3)$	80.589	10.1402	1.1499	0.38201	-0.11804	0.063662	2.1796	6.7338	0.0600
$SiHCl_2(CH_3)$	115.034	9.1805	1.1503	0.38512	-0.11840	0.063735	3.3346	4.3854	0.0446
$SiCl_3(CH_3)$	149.479	10.1187	1.1506	0.38512	-0.11840	0.063789	2.9357	5.2665	0.0291
$SiH_2(CH_3)_2$	60.169	8.2747	1.1497	0.38077	-0.11789	0.063631	3.4554	3.9214	0.0603
$SiHCl(CH_3)_2$	94.615	9.1914	1.1503	0.38509	-0.11840	0.063734	3.3232	4.4012	0.0447
$SiCl_2(CH_3)_2$	129.061	10.1007	1.1507	0.38820	-0.11875	0.063801	3.0279	5.1285	0.0291
GeH_4	76.642	8.1986	1.1494	0.37858	-0.11763	0.063575	3.3615	3.9445	0.0914
GeH_3Cl	111.087	8.6130	1.1496	0.37993	-0.11779	0.063610	3.1743	4.3025	0.0756
GeH_2Cl_2	145.532	8.8966	1.1498	0.38154	-0.11798	0.063650	3.1184	4.4929	0.0598
$GeHCl_3$	179.976	9.1230	1.1501	0.38344	-0.11821	0.063696	3.1490	4.5641	0.0446
$GeCl_4$	214.421	9.4041	1.1503	0.38554	-0.11845	0.063744	3.1654	4.6724	0.0291

Table 1, continued

Compound	MW	A	B_0	B_1	B_2	B_3	c	n	k
SnH_4	122.742	9.0298	1.1497	0.38087	-0.11790	0.063634	3.0671	4.5745	0.0914
$SnCl_4$	260.521	10.1994	1.1506	0.38745	-0.11867	0.063744	2.8471	5.4354	0.0291
Group V(A)									
PH_3	33.998	7.8041	1.1485	0.37228	-0.11684	0.063396	2.8050	4.3644	0.1009
PH_2Cl	68.443	8.6412	1.1490	0.37518	-0.11721	0.063482	2.4920	5.2267	0.0766
$PHCl_2$	102.888	8.5412	1.1495	0.37919	-0.11770	0.063591	3.0719	4.3813	0.0527
PCl_3	137.333	7.2366	1.1501	0.38413	-0.11829	0.063712	4.4289	2.9789	0.0291
$POCl_3$	153.331	9.7746	1.1500	0.38331	-0.11819	0.063693	2.4586	5.9576	0.0000
AsH3	77.945	7.4208	1.1484	0.37116	-0.11670	0.063362	2.9474	4.0298	0.1009
AsH2Cl	112.390	8.5242	1.1488	0.37403	-0.11707	0.063448	2.3972	5.3468	0.0766
AsHCl2	146.835	9.3548	1.1493	0.37782	-0.11754	0.063555	2.1821	6.2831	0.0527
AsCl3	181.281	10.0281	1.1499	0.38254	-0.11810	0.063675	2.2519	6.5171	0.0291
SbH3	124.781	8.5409	1.1484	0.37136	-0.11673	0.063368	2.0491	6.0821	0.1009
SbCl3	228.115	7.1200	1.1511	0.39192	-0.11916	0.063873	5.3455	2.6317	0.0291
Pentanes									
N-pentane	72.149	10.0508	1.1504	0.38593	-0.11849	0.063753	2.6269	5.7673	0
Iso-pentane	72.149	9.9797	1.1502	0.38432	-0.11831	0.063717	2.4514	6.0715	0

Table 2, Critical Properties, by Group and Homologue

Compound	MW	T_b	T_c	P_c	V_c	Z_c	ω
Group III(A)							
B_2H_6	27.670	180.54	289.70	39.58	173.10	0.2882	0.1254
B_2H_5Cl	62.119‡	216.37	346.33	37.13	189.92	0.2481	0.1283
BH_2Cl as monomer	42.284	237.72	379.56	37.10	206.73	0.2463	0.1315
$BHCl_2$ as monomer	82.722	266.07	422.71	37.63	240.37	0.2608	0.1389
B_2HCl_5 hypothetic	199.893‡	276.67	438.47	37.92	257.18	0.2711	0.1433
BCl_3 as monomer	117.169	285.88	451.95	38.20	274.00	0.2822	0.1468
$AlCl_3$ as monomer	133.341	466.86*	625.70	26.00	261.80	0.1326	0.3474
$Ga_2H_4Cl_2$ as dimer	214.383‡	350.86	545.93	40.94	231.9	0.2120	0.2726
$Ga_2H_2Cl_4$ as dimer	283.273‡	421.79	639.69	41.02	247.5	0.1943	0.3525
Ga_2Cl_6 as dimer	352.162‡	473.49	694.00	37.70	263.0	0.1741	0.4504

Table 2, continued

Compound	MW	T_b	T_c	P_c	V_c	Z_c	ω
Group IV(A)							
SiH_4	32.117	161.75	269.65	47.99	130.07	0.2821	0.09860
SiH_3Cl	66.562	242.75	396.65	47.82	169.32	0.2488	0.1252
SiH_2Cl_2	101.007	281.45	449.45	44.83	215.05	0.2614	0.1589
$SiHCl_3$	135.452	306.15	479.15	41.15	267.28	0.2797	0.2090
$SiCl_4$	169.896	330.72	506.95	36.50	326.00	0.2860	0.2482
$SiH_3(CH_3)$	46.144	216.48	348.35	41.53	185.20	0.2691	0.1264
$SiH_2Cl(CH_3)$	80.589	278.82	439.11	41.16	233.90	0.2672	0.1793
$SiHCl_2(CH_3)$	115.034	314.17	489.18	39.25	287.81	0.2814	0.2269
$SiCl_3(CH_3)$	149.479	339.72	517.61	35.86	345.70	0.2919	0.2655
Compound	MW	T_b	T_c	P_c	V_c	Z_c	ω
$SiH_2(CH_3)_2$	60.169	252.86	399.17	36.05	245.84	0.2706	0.1604
$SiHCl(CH_3)_2$	94.615	305.30	471.35	35.94	300.32	0.2791	0.2264
$SiCl_2(CH_3)_2$	129.061	342.89	519.21	34.26	358.20	0.2880	0.2740
GeH4	76.642	184.93	307.98	54.77	128.28	0.2780	0.1270
GeH3Cl	111.087	302.91	495.10	49.95	180.17	0.2215	0.1476
GeH2Cl2	145.532	334.60	536.93	45.36	236.71	0.2437	0.1721
GeHCl3	179.976	343.54	541.41	41.42	283.96	0.2647	0.2012
GeCl4	214.421	357.28	553.16	38.10	335.86	0.2819	0.2334
SnH4	122.742	221.07	360.20	51.70	152.90	0.2674	0.1619
SnCl4	260.521	387.21	591.85	36.95	351.20	0.2672	0.2625
Group V(A)							
PH3	33.998	185.41	324.75	64.51	113.33	0.2743	0.03052
PH2Cl	68.443	273.09	463.73	62.29	153.63	0.2515	0.0750
Compound	MW	T_b	T_c	P_c	V_c	Z_c	ω
Group V(A), cont'd							
PHCl2	102.888	318.44	524.74	55.82	202.52	0.2625	0.1362
PCl3	137.333	349.25	558.95	50.00	260.00	0.2834	0.2117
POCl3	153.331	379.00	605.21	47.59	276.00	0.2645	0.1993
AsH3	77.945	210.73	373.00	65.12	132.50	0.2819	0.01341
AsH2Cl	112.390	300.41	515.99	64.33	174.85	0.2657	0.0573
AsHCl2	146.835	359.66	600.00	61.57	218.29	0.2730	0.1153
AsCl3	181.281	403.30	654.00	58.35	259.56	0.2822	0.1875
SbH3	124.781	256.09	446.20	66.61	157.20	0.2860	0.01659
SbCl3	228.115	794.05	794.05	68.85	268.00	0.2832	0.3309
N-pentane	72.149	309.16	470.05	32.86	310.0	0.2641	0.2393
Iso-pentane	72.149	300.82	460.56	33.17	307.1	0.2695	0.2147

The Thek-Stiel vapor pressure relationship is best used between the NBP and 95% of critical. The Thek-Stiel relationship is known to poorly predict vapor pressures at absolute pressures well below 0.5 atmospheres. This should not be a problem for commercial plant design or operation.

Equation of State Recommendations

There is no known Equation of State that accurately represents the chlorosilanes and their impurities across all temperatures and pressures. For pressures above atmospheric and below P_r 0.90, and for determination of compressibility (Z), the Peng-Robinson Equation of State [4] gives reasonable values. Knowing the

temperature-pressure relationship, the saturation vapor and liquid density can be back-calculated from Z.

Peng-Robinson should not be used for any derivative properties, partial molar properties, or in calculations that involve calculus functions. Since the valuation of fugacity coefficients involves such, the following "work-arounds" are recommended.

For saturated liquid/vapor, use the Thek-Stiel relationship to determine the VP for a given temperature (or vice versa iteratively, T from VP). Then set up the Peng-Robinson cubic equation for Z. The largest root is Z_{vapor}; the smallest root is Z_{liquid}; and the remaining root is false. Rather than using a cumbersome Newton-Raphson iterative solution, a direct solution is possible using a trigonometric method [5].

As given in modern chemical engineering texts, the valuation of the vapor-phase fugacity coefficient requires integration of Z-functions. Peng-Robinson will not hold up to this test, other than near-atmospheric. Instead, a "work-around" is recommended that takes advantage of the near-linear relationship between reduced pressure and Z_{vapor}, below $P_r = 0.4$. The approximation for vapor fugacity coefficient:

$\phi^V = \mathrm{EXP}(Z^V_{T,P} - Z^V_{sat})$ results from that, where $Z^v_{T,P}$ *and* Z^v_{sat} are respectively: the Z_{vapor} value for the actual temperature & pressure; and Z_{vapor} at the saturated condition. To estimate ϕ^Vat reduced pressures above 0.3, use the following equation that results from fitting a cubic polynomial to P_r vs Z_{vapor}:

$Ln(\phi^v) = a_3(P_{r2}^3 - P_{r1}^3) + a_2(P_{r2}^2 - P_{r1}^2) + a_1(P_{r2} - P_{r1}) + a_0[Ln(P_{r2}) - Ln(P_{r1})]$, with a_3 through a_0 being valued at -0.175248; 0.393866; -0.887714; -0.0141409, respectively.

Likewise the valuation of the liquid-phase fugacity coefficient requires a "work-around. Near the saturation line, the liquid density is almost unaffected by small pressure changes. The approximation for liquid fugacity coefficient:

$\phi^L = EXP[Z^L \times (P - VP)/VP]$ results from that, also with the limitation that P_r<0.9.

Liquid Activity Coefficients

The vapor and liquid-phase fugacity coefficients cover expected non-idealities of VLE, resulting from the minority components being either super-heated or sub-cooled (relative to their pure component saturation state). While generally insignificant at atmospheric conditions, such departures from Dalton's and Raoult's Laws become important as column operating pressures increase to 5-10 atmospheres, and higher. In addition to fugacity coefficients, there are additional non-idealities for each binary pair, resulting from liquid-liquid mixing. These effects are termed the Liquid Activity Coefficients, and can add 10-30% to the non-ideality, and thus have an impact on distillation column simulation.

Unfortunately, there is limited data on this topic for chlorosilanes, and what lab data exist can be flawed as a result of disproportionation. In commercial-scale columns, especially in chlorosilane purification, this non-ideality tends to be addressed by massive over-design of tray count and/or very high reflux. To assist in estimating liquid activity coefficients, I have used the approach of Lin and Daubert [6] but with a modification of their parameters. This modification is needed because of the mildly polar nature of chlorosilanes, as opposed to hydrocarbons.

Lin and Daubert use a two-term relationship, resulting in a set of Van Laar [7] parameters which model liquid activity coefficients as a function of composition. Van Laar parameters are easily converted to the Wilson model, by evaluating at the extrema of mole fractions. Their first term is evaluated based on binary component differences in acentric factor, critical temperature and critical pressure. For

chlorosilanes (and their impurities) I recommend that the dimensionless "c" parameter be $= 0.00762 \times \Delta^{-1.6458}$, where Δ is the absolute difference between the components' acentric factors. For the second term, the binary interaction is evaluated using the differences in critical molar volumes per their equation 25, with a multiplier of 112.1.

Van Laar model for Liquid Activity Coefficient:

$$Ln(\Upsilon_1) = A_1 \times [1 + (A_1 \times X_1)/(A_2 \times X_2)]^{-2}$$

$$Ln(\Upsilon_2) = A_2 \times [1 + (A_2 \times X_2)/(A_1 \times X_1)]^{-2}$$

$A_i = c \times F_i + 112.1 \times k_{ij} \times G_i$ (Lin & Daubert Equation 25)

$$F_i = \frac{T_{ci}}{P_{ci}T}[(1 + M(\omega_i)(1 - T_{ri}^{0.5}))^{1/2}(1 + M(\omega_j))^{1/2}P_{ci}^{1/2} - (1 + M(\omega_j)(1 - T_{rj}^{0.5}))^{1/2}(1 + M(\omega_j))^{1/2}P_{cj}^{1/2}]^2$$

$$G_i = \frac{T_{ci}P_{cj}^{1/2}}{TP_{ci}^{1/2}}[(1 + M(\omega_i)(1 - T_{ri}^{0.5}))^{1/2}(1 + M(\omega_i))^{1/2} \times (1 + M(\omega_j)(1 - T_{rj}^{0.5}))^{1/2}(1 + M(\omega_j))^{1/2}]]$$

$$k_{ij} = 1 - 2 \times \left[V_{ci}^{1/3} \times V_{cj}^{1/3}\right]^{0.5} / \left[V_{ci}^{1/3} + V_{cj}^{1/3}\right]$$

$$M(\omega_i) = 0.480 + 1.574\omega_i - 0.176\omega_i^2$$

$c = 0.0694 \times \{ |\omega_1 - \omega_2| \}^{-1.6458}$

The method seems to reasonably reproduce known moderate impurity interactions, such as between dichlorophosphine and TCS; also phosphine and diborane with silane. More quality data is needed (i.e., data that is devoid of disproportionation effects and analytical error). This suggests a developmental program for specific impurity interactions, in order to make the best use of this method and improve the accuracy of these predictive methods.

Equation Notation Used

Notation	Usage	Units		Notation	Usage	Units
NBP	Normal boiling point	°K		k_{ij}	binary interaction coeff	-
P, VP	Pressure, Vapor Pressure	atmos.		q	Watson exponent	-
P_c	Critical Press	atmos.		ΔH_{vb}	Latent heat @ NBP	Cal/g-mol
P_r	Reduced Press	-		$\Delta H'_{vb}$	T-S parameter	Cal/g-mol
R	Gas constant	Cal/g-mol°K		Z	compressibility	-
T	Temperature	°K		α	Riedel derivative	-
T_c	Critical Temp	°K		α_c	α @ critical	-
T_r	Reduced Temp	-		ψ	V.P. derivative	-
T_{br}	Reduced NBP			ø	fugacity coeff	-
V_c	Critical Volume	cc/g-mol		Υ	activity coeff	-
k	H bonding parameter	-		ω	acentric factor	-

References

1. “Distilling Chlorosilanes”; Larry M. Coleman; e-publication in progress
2.” The Properties of Gases and Liquids”, 3rd Edition; Reid, Prausnitz and Sherwood, page 191; McGraw-Hill
3.”A New Reduced Vapor Pressure Equation”; Richard E. Thek and Leonard I. Stiel; A.I.Ch.E. Journal, Vol. 12, No. 3, May 1966, pp 599-602
4.”A New Two-Constant Equation of State”; D.Y.Peng and D.B.Robinson; Ind & Eng’g Chem. Fundamentals, Vol. 15, 1976, pp 59-64
5.https://en.wikipedia.org/wiki/Cubic_function#Trigonometric_method_for_three_real_roots
6.”New Correlation for the Prediction of Activity Coefficients for Binary Nonpolar Hydrocarbon Mixtures”; Chung-Ton Lin and Thomas E. Daubert; Ind. Eng.Chem.Process Des. Dev., Vol.20, No.4 1981, pp652-658
7. https://en.wikipedia.org/wiki/Van_Laar_equation

"An overview of recent EU regulatory developments in industrial emissions having a direct impact on Silicon production in Europe".

Nadia Vinck [1)]

1) Director EHS & Scientific Issues at Euroalliages, Association of European ferro-alloy producers

Abstract

The Industrial Emissions Directive or IED (Directive 2010/75/EU of the European Parliament and the Council on industrial emissions is the main EU instrument regulating pollutant emissions from industrial installations and hence operating permits. The Best Available Techniques (BAT) conclusions are adopted according to the IED process by the Commission and are the legal reference for setting Industry permit conditions. Following the publication the BAT conclusions in the Official Journal of the EU, Member States have a maximum of 4 years to implement them through an update of the operating permits. The BAT conclusions of the NFM BREF covering e.g. the production of Silicon (and ferro-alloys) have been adopted in December 2015 and shall be published before summer 2016. The purpose of this paper is to give an overview of the relevant best available techniques (BAT) and the BAT-associated emission levels for the production of ferro-alloys, and in particular, for the production of silicon. Other EU environmental regulations having a direct or indirect influence on the operating permits are briefly addressed in the comments section. The BAT Conclusions for the Silicon (and ferro-alloys) industry and the related emissions limits values are very strict, in particular for dust emissions often in the range of 2-5 mg/Nm^3, as for other industrials sectors. The Industry is calling for a robust and transparent methodology to set the limit values based on representative data. The present and future high environmental ambition levels could lead to additional requirements going beyond what is technically feasible and have detrimental effects for EU industry's competitiveness and EU jobs.

1. Introduction

The Industrial Emissions Directive or IED (Directive 2010/75/EU of the European Parliament and the Council on industrial emissions is the main EU instrument regulating pollutant emissions from industrial installations and hence operating permits.

The IED adopted in November 2010 was recasting 7 previously existing directives, and in particular the IPPC Directive (Integrated Pollution Prevention and Control Directive). The IED entered into force on 6 January 2011 and had to be transposed by Member States by 7 January 2013. The IED aims to achieve "a high level of protection of human health and the environment taken as a whole by reducing harmful industrial emissions across the EU", in particular through better application of Best Available Techniques (BAT). Around 50,000 installations undertaking the industrial activities listed in Annex I of the IED are required to operate in accordance with a permit granted by the authorities in the Member States. This permit should contain conditions set in accordance with the principles and provisions of the Directive. The IED regulatory process results in BAT Reference Documents (Best available techniques Reference document or BREFs), the BAT conclusions contained are adopted by the Commission as Implementing Decisions and are the legal reference for setting permit conditions.

IED gives a particular role to the BAT-associated emission levels (BAT-AELs) set out in the BAT conclusions. It requires the emissions of the installations concerned not to exceed the BAT-AELs, except in specific cases where the conditions are fulfilled to allow a derogation by the competent authority. Such derogation needs to be justified on the basis of an assessment demonstrating the disproportionality of the costs of meeting the BAT-AELs against the environmental benefits. Following the publication of a Decision on BAT conclusions in the Official Journal of the EU, Member States have a maximum of 4 years to implement the BAT conclusions through an update of the permits concerned.

The original best available techniques (BAT) reference document (BREF) on Non-ferrous metals covering the production of Silicon (and ferro-alloys) was adopted by the European Commission in 2001 under the former IPPC regulation. A review of this BREF commenced in 2007 and has been achieved by the adoption of the decision on BAT conclusions in December 2015 [1]. The publication is foreseen in the coming weeks (in principle before summer 2016).

The BAT reference document for the Non-ferrous metals industries (NFM BREF) is the outcome of an exchange of information between nominated technical experts from EU Member States, the industries concerned, non-governmental organisations promoting environmental protection and the European Commission within a formal Technical Working Group (TWG).

The production of Silicon and ferro-alloys is one 8 industrials sectors covered by the NFM BREF.

The BAT conclusions of the NFM BREF have been established through an iterative process involving the following steps:

- identification of the key environmental issues for the relevant industrial sector;
- examination of the techniques most relevant to address these key issues;
- identification of the best environmental performance levels, on the basis of the available data in the European Union and worldwide;
- examination of the conditions under which these environmental performance levels were achieved, such as costs, cross-media effects, and the main driving forces involved in the implementation of the techniques;
- Selection of the best available techniques (BAT), their associated emission levels (and other environmental performance levels) and the associated monitoring for this sector.

Expert judgement by the European Commission (IPPC Bureau) and the TWG has played a key role in each of these steps and the related outcome.

BAT is a dynamic concept and so the review of BREFs is a continuing process related to the development of science and technologies. The BREF and the related BAT conclusions will be periodically reviewed and, if necessary, updated accordingly.

The publication of the BAT conclusions is of key importance for the Silicon producers on the European territory as new requirements related to industrial emissions will be set in the operating permits of the plants. The purpose of this paper is to give an overview of the relevant best available techniques (BAT) and the BAT-associated emission levels for the productions of ferro-alloys, and in particular, for the production of Silicon. Other EU environmental regulations having a direct or indirect influence on the operating permits are briefly addressed in the comments section.

2. BAT Conclusions for Silicon (and Ferro-Alloys) Industry [1].

1. BAT on diffuse emissions from raw materials

A series of best available technologies are listed to cover the storage, the handling and transport of raw materials as outlined in table 1 here below. BAT is to use a combination of the techniques given.

Table 1: Example of BAT for the storage, the handling and transport of raw materials in case of diffuse emissions

BAT 7. Use a combination of the techniques given below for <u>storage</u> of raw materials - Enclosed buildings or silos/bins - Use of water sprays and fog sprays with or without additives such as latex - Dust/gas extraction devices placed at the transfer and tipping points - Certified pressure vessels for chlorine gas or mixtures that contain chlorine * - Construction materials for the tanks resistant to the contained materials * - Use of inert gases blanketing for the storage of materials that react with air *…
BAT 8 Use a combination of the techniques given below for <u>the handling and transport</u> of raw materials - Enclosed conveyors or pneumatic systems to transfer and handle dust-forming concentrates and fluxes and fine grained material * - Covered conveyors to handle non-dust-forming solid materials * - Closed bags or drums to handle materials with dispersible or water soluble components * … * Generally applicable

BAT 9 is related to the reduction of diffuse emissions from metal production by optimising the efficiency of off-gas collection and treatment with the use of a combination of the techniques given in table 2 below. What is of concern for the silicon producers is that only closed furnace is indicated, with an applicability only restricted by safety constraints; semi-open furnaces commonly used for the production of silicon is not recognized.

Table 2: Example of BAT for the storage, the handling and transport of raw materials in case of diffuse emissions

	Technique	**Applicability**
a	Thermal or mechanical pretreatment of secondary raw material to minimise organic contamination of the furnace feed	Generally applicable
b	Use a closed furnace with a properly designed dedusting system or seal the furnace and other process units with an adequate vent system	The applicability may be restricted by safety constraints (e.g. type/design of the furnace, risk of explosion)
c	Use a secondary hood for furnace operations such as charging and tapping	The applicability may be restricted by safety constraints (e.g. type/design of the furnace, risk of explosion)
d	Dust or fume collection where dusty material transfers take place (e.g. furnace charging and tapping points, covered launders)	Generally applicable
e	Optimise the design and operation of hooding and ductwork to capture fumes arising from the feed port and from hot metal, matte or slag tapping and transfers in covered launders	For existing plants, the applicability may be limited by space and plant configuration restrictions

f	Furnace/reactor enclosures such as 'house-in-house' or 'doghouse' for tapping and charging operations	For existing plants, the applicability may be limited by space and plant configuration restrictions
g	Optimise the off-gas flow from the furnace through computerised fluid dynamics studies and tracers	Generally applicable
h	Charging systems for semi-closed furnaces to add raw materials in small amounts	Generally applicable
i	Treat the collected emissions in an adequate abatement system	Generally applicable

2. Monitoring of emissions to air

BAT 10 is to monitor the stack emissions to air with at least the frequency given below and in accordance with EN standards. If EN standards are not available, BAT is to use ISO, national or other international standards that ensure the provision of data of an equivalent scientific quality.

Table 3: Parameters to be monitored for air emission in the Silicon and ferro-alloys production

Parameter	**Monitoring associated with**	**Minimum monitoring frequency**	**Standard(s)**
Dust (2)	**Silicon & Ferro-alloys:** BAT 155, BAT 156, BAT 157, BAT 158 Crushing, …; SAF* (semi) open; SAF Closed	Continuous (1)	EN 13284-2
	Silicon & Ferro-alloys: BAT 154, BAT 155, BAT 156, BAT 157, BAT 158 Storage, …; Crushing, …; SAF (semi) open; SAF Closed	Once per year (1)	EN 13284-1
Cadmium and its compounds, expressed as Cd	**Silicon & Ferro-alloys:** BAT 156 SAF (semi) open	Once per year	EN 14385
Chromium (VI)	**Silicon & Ferro-alloys:** BAT 156 SAF (semi) open	Once per year	No EN standard available
Lead and its compounds, expressed as Pb	**Silicon & Ferro-alloys:** BAT 156 SAF (semi) open	Once per year	EN 14385
Thallium and its compounds, expressed as Tl	**Silicon & Ferro-alloys:** BAT 156 SAF (semi) open	Once per year	EN 14385

Parameter	Monitoring associated with	Minimum monitoring frequency	Standard(s)
Other metals, if relevant [3]	**Silicon & Ferro-alloys:** BAT 154, BAT 155, BAT 156, BAT 157, BAT 158 Storage, …; Crushing, …; SAF (semi) open; SAF Closed	Once per year	EN 14385
Mercury and its compounds, expressed as Hg	**Ferro-alloys** BAT 11 Pyrometallurgical processes	Continuous or once per year [1]	EN 14884 EN 13211
NO_X, expressed as NO_2	**FeSi, Si** BAT 13 Pyrometallurgical processes	Continuous or once per year [1]	EN 1492
TVOC	**Ferro-alloys:** BAT 160 Rotary kilns	Once per year	EN 12619
PCDD/F	**Ferro-alloys:** BAT 159 Pyrometallurgical processes	Once per year	EN 1948 parts 1, 2 and 3
Benzo-[*a*]-pyrene	**Ferro-alloys:** BAT 160 Rotary kilns	Once per year	ISO 11338–1 ISO 11338–2

[1] For sources of high emissions, BAT is continuous measurement or, where continuous measurement is not applicable, more frequent periodic monitoring.
[2] For small sources (< 10 000 Nm^3/h) of dust emissions from the storage and handling of raw materials, monitoring could be based on the measurement of surrogate parameters (such as the pressure drop).
[3] The metals to be monitored depend on the composition of the raw materials used.

* SAF means Submerged Electric Arc Furnace

3. Mercury emissions

BAT 11 is to reduce mercury emissions to air from a pyrometallurgical process by using one or both of the following techniques: 1) Use of raw materials with a low mercury content or 2) Use of adsorbents (e.g. activated carbon, selenium) in combination with dust filtration.

The associated emission limit values are outlined in table 4 (BAT-AEL).

Table 4: Associated emission limit values to mercury emissions in the Silicon and ferro-alloys production

Parameter	**BAT-AEL (**mg/Nm^3) [(1) (2)]
Mercury and its compounds, expressed as Hg	0.01 – 0.05
[(1)] As a daily average or as an average over the sampling period. [(2)] The lower end of the range is associated with the use of adsorbents (e.g. activated carbon, selenium) in combination with dust filtration, except for processes using Waelz kilns.	

4. NO_X emissions

BAT 13 is to prevent NO_X emissions to air from a pyrometallurgical process by using one of the techniques given in table 5.

Table 5: BAT to prevent NOX emissions to air from a pyrometallurgical process

	Technique ([1])	**Applicability**
a	Low-NO_X burners	Generally applicable
b	Oxy-fuel burners	
c	Flue-gas recirculation back through the burner to reduce the temperature of the flame	Applicable for oxy-fuel firing burners

In the "Concluding remarks and recommendations for future work" of the BREF document (not published) a chapter is added on the need to gather plant-specific data on NOX emissions both as loads and concentrations, including other relevant contextual information.

5. Channeled dust emissions

BAT 154 is to prevent channeled dust and metal emissions from storage, handling and transport of solid materials, pretreatment operations such as metering, mixing, blending and degreasing, and from tapping, casting and packaging by using a bag filter. The associated emission limit values are outlined in table 6.

Table 6: Associated emission limit values to channeled dust and metal emissions from storage, handling and transport of solid materials and pretreatment operations in the Silicon and ferro-alloys production

Parameter	**Unit**	**BAT-AEL ([1])**
Dust	mg/Nm^3	2 – 5
(1) As a daily average or as an average over the sampling period.		

BAT 155 is to prevent channeled dust and metal emissions from crushing, briquetting, pelletising and sintering by using a bag filter or a bag filter in combination with other techniques. The applicability of a bag filter may be limited in case of low ambient temperatures (-20 – -40°C) and high humidity of the off-gases, as well as for the crushing of CaSi due to safety concerns (i.e. explosivity). The associated emission limit values are outlined in table 7.

Table 7: Associated emission limit values to channeled dust and metal emissions from crushing, briquetting, pelletising and sintering operations in the Silicon and ferro-alloys production

Parameter	**Unit**	**BAT-AEL ([1]) ([2])**
Dust	mg/Nm^3	2 – 5
([1]) As a daily average or as an average over the sampling period. ([2]) The upper end of the BAT-AEL range can be up to 10 mg/Nm^3 for cases where a bag filter cannot be used.		

BAT 156 is to prevent channeled dust emission and metal emissions from an open or a semi-closed submerged arc furnace by using a bag filter. The associated emission limit values are outlined in table 8.

Table 8: Associated emission limit values to an open or a semi-closed submerged arc furnace in the Silicon and ferro-alloys production

Parameter	**Unit**	**BAT-AEL (1) (2) (3)**
Dust	mg/Nm^3	2 - 5
(1) As a daily average or as an average over the sampling period. (2) The upper end of the range may be up to 15 mg/Nm^3 for the production of FeMn, SiMn, CaSi due to the sticky nature of the dust (caused e.g. by its hygroscopic capacity or chemical characteristics) affecting the efficiency of the bag filter (3) Dust emissions are expected to be towards the lower end of the range when e.g. emissions of cadmium, chromium, thallium and lead are above the following values: 1 mg/Nm^3 for Pb and 0.05 mg/Nm^3 for Cd, CrVI, Tl.		

BAT 157 is to prevent channeled dust emission and metal emissions from a closed submerged arc furnace (or a closed plasma dust process), by using one of the techniques given in table 9. The associated emission limit values are outlined in table 10.

Table 9: BAT to prevent channeled dust emission from a closed submerged arc furnace in the ferro-alloys production

	Technique ([1])	**Applicability**
a	Wet scrubber in combination with an ESP	Generally applicable
b	Bag filter	Generally applicable unless safety concerns exist related to the CO and H_2 content in the off-gases

Table 10: Associated emission limit values to a closed submerged arc furnace in the ferro-alloys production

Parameter	**Unit**	**BAT-AEL ([1])**
Dust	mg/Nm^3	2 – 5
([1]) As a daily average or as an average over the sampling period.		

A note is added in the "Concluding remarks and recommendations for future work" of the BREF document (not published about the need to collect information on the economic viability of the use of a bag filter and on the use of a wet scrubber in combination with an ESP. In addition, the decision to set 5 mg/Nm^3 as the higher end of the range for dust emissions is not supported by Spain and Euroalliages.

6. Water emissions

BAT 16 is to use ISO 5667 for water sampling and to monitor the emissions to water at the point where the emission leaves the installation at least once per month[1] **(1)** and in accordance with EN standards. If EN standards are not available, BAT is to use ISO, national or other international standards that ensure the provision of data of an equivalent scientific quality.

The parameters to be monitored are outlined in table 11.

[1] The monitoring frequency may be adapted if the data series clearly demonstrate sufficient stability of the emissions.

Table 11: Parameters on emissions to water to be monitored in the Silicon and ferro-alloys production

Parameter	Standard(s)	Parameter	Standard(s)
Mercury (Hg)	EN ISO 17852, EN ISO 12846	Iron (Fe) Arsenic (As) Cadmium (Cd) Copper (Cu) Nickel (Ni) Lead (Pb) Zinc (Zn) Chromium total (Cr)	EN ISO 11885 EN ISO 15585 EN ISO 17294-2
Chromium(VI) (Cr(VI))	EN ISO 10304-3 EN ISO 23913		
Other metals, if relevant (2)			

The BAT-AELs for emissions to water are outlined in table 12. There are neither BAT-AELs expressed in kg/yr or in kg/t metal nor distinction based on the type of receiving water body (e.g. sea or river). BAT-AELs apply to direct emissions to a receiving water body from the production.

Table 12: Associated emission limit values to water emissions in the Silicon and ferro-alloys production

BAT-AEL (mg/l) ([1])						
Sector Parameter	**Copper**	**Lead and Tin**	**Zinc and Cadmium**	**Precious metals**	**Nickel and Cobalt**	**Ferro-alloys**
Ag	NR	NR	NR	≤ 0.6	NR	NR
As	≤ 0.1 ([2])	≤ 0.1	≤ 0.1	≤ 0.1	≤ 0.3	≤ 0.1
Cd	0.02 - 0.1	≤ 0.1	≤ 0.1	≤ 0.05	≤ 0.1	≤ 0.05
Co	NR	≤ 0.1	NR	NR	0.1 - 0.5	NR
Cr total	NR	NR	NR	NR	NR	**≤ 0.2**
Cr (VI)	NR	NR	NR	NR	NR	≤ 0.05
Cu	0.05 - 0.5	≤ 0.2	≤ 0.1	≤ 0.3	≤ 0.5	≤ 0.5
Hg	0.005 - 0.02	≤ 0.05	≤ 0.05	≤ 0.05	≤ 0.05	≤ 0.05
Ni	≤ 0.5	≤ 0.5	≤ 0.1	≤ 0.5	≤ 2	≤ 2
Pb	≤ 0.5	≤ 0.5	≤ 0.2	≤ 0.5	≤ 0.5	≤ 0.2
Zn	≤ 1	≤ 1	≤ 1	≤ 0.4	≤ 1	≤ 1

NR: Not relevant
([1]) As a daily average.
([2]) In case of high arsenic content in the total input of the plant, the BAT-AEL may be up to 0.2 mg/l

3. Comments of the impact on operating permits

1. Emission limit values

The BAT Conclusions for the Silicon and ferro-alloys industry and the related emissions limits values are very strict, in particular for dust emissions, as for other industrials sectors covered by the Non-Ferrous Metals BAT conclusions. Euroalliages and the other industrial representative associations have expressed concerns about the way these emissions limits values are set. The Industry is calling for a robust and transparent methodology to set the limit values based on representative data. In principle, the upper end value of a BAT-AEL should be set on the basis of the maximum observed emissions of the plants applying BAT for the pollutant at stake, while the lower end should be set above the lowest maximum observed emissions of the plants applying BAT, after discarding all performances that only occur under specific circumstances. Indeed, the legal obligation for permitting authorities to set the emission limit value for a given pollutant at a level that ensures that, under normal operating conditions, emissions do not exceed the BAT-AEL, has far-reaching consequences.

2. Impact of other legislations

In addition, site permit conditions also take into account individual Member State targets for ambient air, surface waters and waste:

- For water, the environmental quality standards (EQS) of EU water framework directive on Priority (Hazardous) Substances like Pb, Ni, Hg, flouranthene, naphthalene, PAHs; B(a)P) with the ongoing second review of the Priority Substances list ;
- For air, the National Emissions Ceilings directive and its ongoing revision for more ambitious national caps for sulphur dioxide (SO2), nitrogen oxides (NOx), non-methane volatile organic compounds (NMVOC), ammonia (NH3), and fine particulates (PM, less than 2.5 micrometers), to be achieved by 2020 and 2030 [2].;
- For waste, the circular economy package, comprising the revision of existing regulations like the waste framework directing or the landfill directive, but also an EU Action Plan with measures covering the whole cycle: from production and consumption to waste management and the market for secondary raw materials [3].

Other policy areas impacting the operating requirements of the Silicon and ferro-alloys Industry include e.g.**:**

- Climate and Energy policy: e.g. since 2013, Silicon and ferro-alloys producers fall under the EU's Emission Trading Scheme (ETS) which incentivises companies to lower their CO2 emissions, ;

- All installations are directly or indirectly concerned by the provisions of chemicals legislations, such as the REACH and the Classification and Labelling (CLP) Regulations;

- Depending on the range of individual materials produced and their related hazard classification(s), some installations may fall under the scope of the Seveso Directive, which seeks to prevent major accidents involving dangerous substances. In this respect, the current contested classification of high temperature coal tar pitch (HT CTP) as Aquatic Acute 1 (H400) and Aquatic Chronic 1 (H410) used in electrode pastes for the submerged electric arc furnaces as well as in e.g. tapping, lining and other repairs pastes for the production of Silicon and ferro-alloys trigger in principle Seveso status for these operating plants;

- The Carcinogens at work Directive (CMD): a first proposal of amendment planned by June 2016 will include respirable crystalline silica generated by processes with a Binding Limit Value of 0.1 mg/m³.

3. Conclusions

The Industrial Emission Directive places a duty on industry to use the "best available technology" in order to reduce emissions to air, water and land in order to improve public health and to protect the environment. Best available technology is the path to follow, however the word "available" seems to be often by-passed in the assessment methods and the related decisions taken. More stringent emissions requirements are or will be soon imposed in operating permits, probably complemented by additional provisions from other major regulations currently under revision. As a result, the proposed high environmental ambition levels are at significant risk of being unattainable which would consequently lead to additional requirements going beyond what is economically or even technically feasible and have detrimental effects for EU industry's competitiveness and EU jobs.

References

1. BAT conclusions for the non-ferrous metals industries, final version for translation, working document, Comitology Register, January 2016.
2. Council of the European Union, Proposal for a Directive of the European Parliament and of the Council on the reduction of national emissions of certain atmospheric pollutants and amending Directive 2003/35/EC, document n°15401/15, 16 December 2015
3. European Commission, Communication from the Commission to the European Parliament, the Council, the European Economic and Social Committee and the Committee of the Regions: Closing the loop - An EU action plan for the Circular Economy, JOC COM(2015) 614 final of 2 December 2015

A New Method to Improve *Siemens* Chemical Vapor Deposition Operations

Larry Coleman, Consultant on Demand, Buffalo, New York, USA
Independent Engineering Consultant

Abstract

Research is presented on a process to improve the off-gas recovery from a trichlorosilane(TCS) Siemens Chemical Vapor Deposition (CVD) Reactor, reducing the energy employed as well as solving the problem of carbon-bed contamination. The catalytic reaction simplifies the CVD off-gas process and can be retro-fit to existing operations. The same development has alternative applications in polysilicon production.

Background

In a Siemens CVD reactor, hydrogen is fed along with TCS, to epitaxially grow a polysilicon rod plus co-produce a variable composition off-gas. Several parallel reactions occur near the many growing silicon rods in the CVD reactor, but none of them come to equilibrium before the gas exits to a collection manifold. During a reactor's batch cycle, the temperature and flowrate are varied to optimize the polysilicon growth rate, frequently with dichlorosilane (DCS) added to the TCS. In a poly plant many CVD reactors are operating in parallel, each at a different point in its multi-day growth cycle. However there can be still be some variation in the collection manifold's gas composition.

The currently operated technology of CVD off-gas recovery (OGR) separates the three chlorosilanes (DCS, TCS, and silicon tetrachloride/STC) into high purity liquid streams, as well as separating the hydrogen and HCl gases (see Figure 3 at the end of the paper). The TCS and hydrogen are recycled back to the CVD; the DCS can either be recycled back to the CVD or used elsewhere; and the STC recycled to a different part of the process. The hydrogen and HCl are separated, with the typical specification for HCl in the recycle hydrogen being <50 ppm (v/v). This separation is achieved in a two-step process: (1) absorption in cold STC; (2) adsorption of remaining HCl onto activated carbon. The regeneration of these processes consumes significant energy, but more importantly can cause the activated carbon to form powder in the recycled hydrogen. The powdered carbon causes purity problems with the CVD-grown polysilicon rods.

The concerns are the same over carbon contamination and HCl in the recycle hydrogen, whether the TCS is synthesized by either direct chlorination (DC) or hydrochlorination (HC).

Research Summary

To eliminate the separation of HCl from hydrogen, and therefore the potential for carbon contamination, a new method was developed and tested in a laboratory environment. Laboratory experiments showed that the new process worked according to predictions. The new process can be retrofit into an existing operation and has the side advantage of slightly boosting TCS utilization.

By reacting away the HCl (to a <10 ppm level), the problems and energy consumption are eliminated of the STC absorber/desorber and carbon bed. The HCl destruction is accomplished in a gas-phase reactor using the same chlorosilane disproportionation reviewed in a 2014 conference paper [1]. That 2014 paper showed the mechanism of hydrogen-adducted amines, in swapping Si-H and Si-Cl bonds.

The development and use of amine resins like AMBERLYST™ A21 DRY Resin (The Dow Chemical Company), activated as either hydrogen-adducted or chlorine-adducted, goes back over 50 years with patents filed by Don Bailey[2], Carl Backay[3], and Carl Litteral [4] and as well as others. As confirmed by testing under JPL/NASA contract [5], HCl interferes with the hydrogen-adducted reaction of TCS to DCS; DCS to MCS; and MCS to silane. Work done at the Union Carbide labs in the late 1970's under JPL/NASA funding inferred that the HCl reaction is not directly with MCS, DCS or TCS; but rather with the hydrogen-adducts formed with the amine catalyst by those chlorosilanes.

Both hydrogen-adducted and chlorine-adducted weak-based amine resins drive important processes, and are seemingly mirror-image in their action. Both forms must be completely moisture deficient to work, and have the same bulk properties. H-adducted resin will swap Si-H and Si-Cl bonds, but does not appear to cause the interchange of Si-Cl and $SiCH_3$ bonds. Cl-adducted resin will swap of Si-Cl and $SiCH_3$ bonds, but does not appear to allow the swap of Si-H and Si-Cl bonds. The selection of which amine resin to use, and its activation are critical, since the activated resin must possess ability for adduct duality.

After the topic of retro-fitting, a schematic is given in Figure 3 that summarizes the new technology.

Process Detail and Mechanism

Making an extrapolation from that technology basis, I tested if the two adduct mechanisms could co-exist, using TCS-activated AMBERLYST™ A21 DRY Resin:

(1) HCl reacting with amine-hydrochlorosilane hydrogen-adducts to form H_2 + chlorine-adducts

(2) Hydrochlorosilanes (e.g., DCS and TCS) reacting with chlorine-adducts to form hydrogen-adducts plus a more chlorinated chlorosilane

Using DCS as the hydrochlorosilane, the net reaction is:

$$DCS + HCl \rightarrow TCS + H_2$$

In Figure 1 below, the two-step reaction mechanism is shown.

In step 1, the HCl attacks the Si-H-N bond area, with a chlorine atom breaking the Si-H bond and adducting itself to the N, so as to make a TCS Cl-adduct. The H atom left

from the HCl, and the H atom left from the cleaved DCS H-adduct then combine to make a molecule of hydrogen gas.

In step 2, a molecule of DCS converts the TCS Cl-adduct back to a DCS H-adduct, and forming a molecule of TCS.

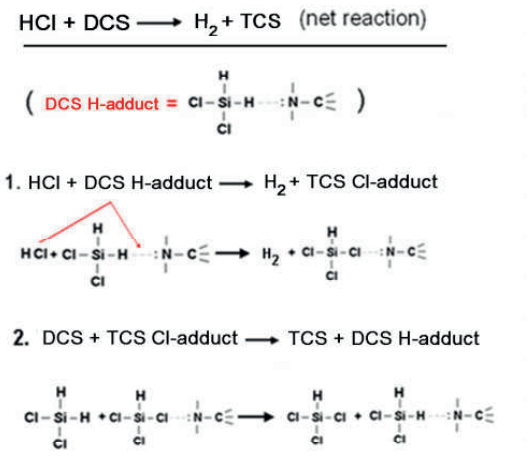

Figure 1: Mechanism of HCl-DCS Reaction

If TCS were instead chosen as the hydrochlorosilane, then the reaction would net out as:

$HCl + TCS \rightarrow H_2 + STC$, again going through a set of H-adducts and Cl-adducts.

From prior work, the distribution of hydrochlorosilane adducts ($R\text{-}H\text{-}SiCl_3$, $R\text{-}H\text{-}SiHCl_2$, and $R\text{-}H\text{-}SiH_2Cl$) closely tracks the atomic bulk Cl/Si ratio. (STC has a Cl/Si ratio of 4, TCS has a Cl/Si ratio of 3, etc).

Said differently, the presence of DCS converts some $R\text{-}H\text{-}SiCl_3$ adducts to $R\text{-}H\text{-}SiHCl_2$ adducts. This gives the familiar equilibrium plot of mole fractions (STC through silane), such that the overall Gibbs Free Energy of the continuous phase is minimized [6]. See Figure 2, below. Figure 2 can be downloaded in color and enlarged directly from my website[6].

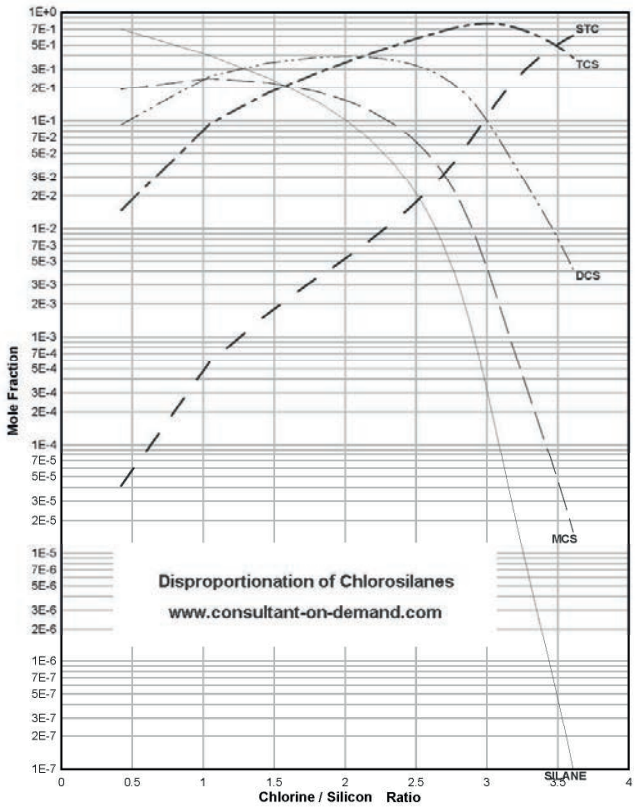

Figure 2: Chlorosilane Disproportionation Equilibrium

I hypothesized that if more molar TCS + DCS than HCl was in the gas phase (i.e. a surplus of hydrogen-adducted bonds on the amine), then the rate of H-adduct formation and H-adduct destruction would be nominally equal. There could be essentially no chlorosilane disproportionation, since the H-adducts were all engaged. Once all the HCl is consumed, the population of H-adducts would then return to normal, and disproportionation would resume. In fact, that is what is seen experimentally; although the kinetics seem so fast that I could not tell whether the rebuilding of H-adducts is gradual or a sharp peak.

Extending the mechanism analogy, if the HCl concentration was greater than the combined TCS+DCS, then all of the adducting would be chlorine-based, and the exit gas should just be a mixture of H_2, residual HCl and STC. Generally that happens experimentally, but there seems to be consistent side reaction occurring as well. Some of the TCS ends up converting to H_2 plus Si_2Cl_6 (and perhaps even a small amount of Si_3Cl_8). I have no explanation for why that side-reaction happens. With CVD off-gas, there is always more chlorosilane (DCS+TCS) than HCl, so this side reaction is greatly suppressed, and of not much concern.

Obviously there is more research needed to identify/quantify the set of reactions and their relative kinetics.

Laboratory Set-Up

In the lab set-up, the catalyst resin was loaded into a pair of 25 mm outer diameter stainless tubing lengths, with resin depths up of 0.5 and 1.25 meters, and each bed constrained by 5 micron Swagelok filters. Both the inlet gas and each laboratory reactor were electric heat-traced to provide a constant 60C temperature. After the reactors were both loaded with resin and dried using nitrogen, they were TCS conditioned per standard procedure: a small amount of TCS vapor was added to nitrogen gas, and the mixture was flowed through the resin bed until the formation of DCS was seen. This indicated that the resin was TCS activated (i.e., H-adducts had formed). A 1% HCl in hydrogen gas mixture was combined with a DCS/TCS/STC flash-evaporated liquid mixture to simulate 60°C CVD off-gas, with a nominal 100cc/minute gas flowrate at slightly above atmospheric pressure. The superficial vapor velocity calculated to 0.2 m/sec, indicating a hold-up time of 1.5 - 4 seconds, depending on which of the two lab reactors was used.

In multiple runs of up to 15 minutes each in duration, no HCl was found with either reactor, using a TCD Gas Chromatograph with a Thermal Conductivity Detector, which has a nominal 10 ppm limit of detection. With the shorter reactor, the HCl destruct was total, but there was no disproportionation. With the longer hold-up time (4 seconds), there was a definite indication that conventional disproportionation was re-starting after all HCl was reacted. That indicated that H-adducts were reforming. Using a set of Thermophysical Tables, the heats of reaction were calculated and applied to the total gas flow. A theoretical 30°C temperature rise was predicted. The lab equipment was noted to have an unquantified exotherm, but not nearly enough to soften the resin.

The runs were terminated after proof of concept, due to a lack of funding and the lab's running into financial problems. Given the positive results it is suggested that this new process be further developed. At least one CVD operator is considering such development, but others may want to try it as well. To date, a pilot reactor has not been tried on a commercial level.

Retro-Fitting to an Existing Plant

The application would retro-fit into the existing process in this way:

(1) The last water-cooled condenser would stop the CVD off-gas condensation at about 50°C, where some of the STC liquid is starting to condense, but the majority of the off-gas stream is still vapor. Accounting for the exotherm, higher than 60°C off-gas temperature could lead to a softening of the resin catalyst at the bed exit, or require that the resin reactor be cooled. Both condensate and vapor fractions would feed the new reactor. (Note that the heat of reaction is going to elevate the temperature, so the feed stream will not be two-phase for long).

(2) The reactor is preferentially flowed upward, at a nominal 0.2 m/sec (or less) superficial velocity, so as to not fluidize the resin beads. Depending on whether DCS is desirable or not in the product, the reactor hold-up time could vary from 2 to 5 seconds. A micronic depth filter would be used on the reactor outlet, to insure that none of the resin beads ever escaped. An online GC would be used to verify that HCl destruct was complete (or if not, a small amount of DCS or TCS vapor would added to the reactor inlet, to boost the H-adduct formation rate, and thereby accelerate HCl destruct). The expected reactor exit temperature would be about 80°C.

(3) The reactor's outlet gas would be fed to the existing final condenser train (including the last refrigerated condenser). The liquid condensate (DCS/TCS/STC)

would flow to the existing set of columns. But the STC bottoms product would bypass all of the HCl absorption/desorption equipment (since there is no longer any HCl in the gas stream).
(4) The final condenser's hydrogen stream (devoid of HCl) would be warmed and compressed back to CVD recycle.
(5) Since there is no HCl captured by the STC, the STC absorber/desorber/heat exchangers/pumps would be re-purposed. Likewise the carbon beds could be re-purposed (actually they would be great to clean up the process make-up HCl from any organics, thus reducing incoming reactive carbon).
(6) There is likely no reason for a duplicate HCl destruct resin bed, since the main degradation causes of amine resin do not exist here: no siloxane colloids, no $AlCl_3$ vapor, and only sub-ppb amounts of boron or phosphorus compounds. Over several years, the resin would collect some boron and phosphorus compounds and slowly de-activate, but such as degradation would take many years and be very gradual.
To illustrate how the gas composition might change across the amine resin bed, the lab results are projected for two typical CVD off-gas compositions, along with the expected exit gas composition.

	100 g-mols inlet gas from CVD					100 g-mols outlet gas from amine reactor				
Case	H_2	HCl	DCS	TCS	STC	H_2	HCl	DCS	TCS	STC
1	78.33	1.25	1.16	13.40	5.86	79.58	0.00	0.16	14.15	6.11
2	79.63	0.95	1.40	11.00	7.02	80.58	0.00	0.64	11.57	7.21

Case 1 = moderate growth with some DCS enhancement, average composition over the cycle
Case 2 = higher growth with significant DCS enhancement, average composition over the cycle

(7) Many modern CVD operations recycle the DCS in the outlet gas, for increased growth rate. While the new method does simplify the OGR and remove a quality problem, the reduction of DCS in the outlet gas might seem sufficiently disadvantageous; that the new method may not seem applicable to such modern CVD operations. It must be pointed out that some of this concern is counter-balanced by the increase in TCS in the outlet gas, as shown in the above two cases. Furthermore, it is easy to increase the DCS in the CVD inlet gas just by diverting some TCS vapor to the new amine reactor and making the amine reactor with a longer contact time (such as 6-8 seconds instead of 4 seconds). Using such a design, the DCS in the CVD inlet can be varied, as desired for increased production, and yet enjoy the cost benefit of easily removing HCl from the OGR. See Figure 3 below.

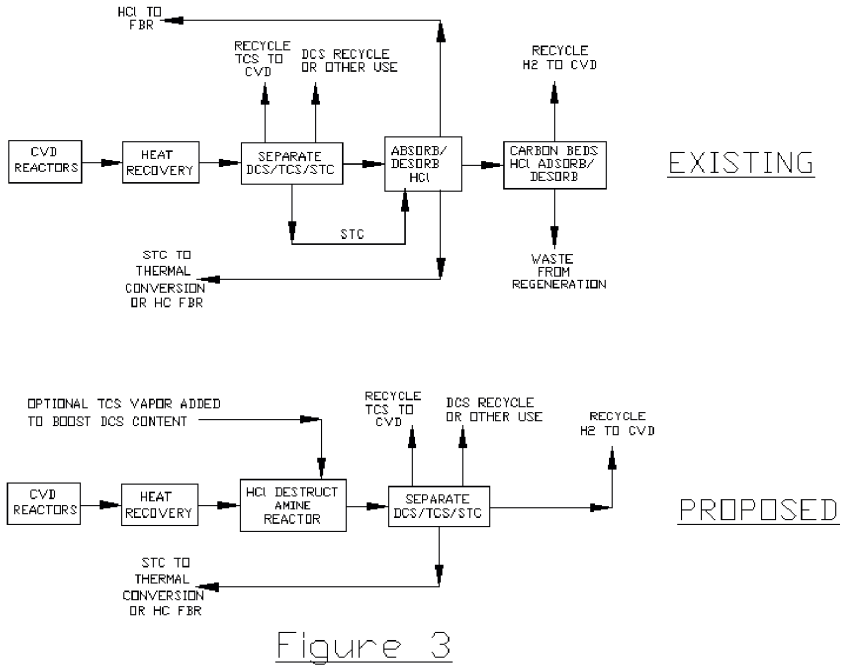

Figure 3

Other Applications

It should be noted that this chemistry also has utility in other parts of a polysilicon plant (but perhaps not as highly valued as improving CVD off-gas systems). (1) In either TCS synthesis process, there is some unreacted HCl that is present, along with a greater amount of DCS. In the condenser train, adding an "HCl destruct" reactor would slightly improve the TCS production. (2) In the TCS purification process, the removal of "TCS light impurities" causes a process loss of up to 10% of the TCS made, with resulting load on waste treatment and adding to the "chlorine make-up".

By reacting HCl gas with the DCS (and some TCS content) of the "TCS lights", the hydrochlorosilanes are converted to STC, and the BCl_3 and isopentane impurities easily distilled away from the STC. The STC bottoms would be recycled back to the appropriate place (depending on whether the process is DC or HC). This off-loads waste treatment and reduces "chlorine make-up". (3) In vent gas systems, HCl could be added to light chlorosilanes, to convert them back to TCS and recover them. (4) There might be other places in the plant where DCS is less desirable than TCS, and so HCl conversion is a cost-effective option.

Lastly it is noted that the reaction of a TCS/STC vapor stream with HCl over an amine resin bed will produce about a 5-10% mole fraction content of Si_2Cl_6 (HCDS) in the condensate. HCDS is now a highly valued fluid, used in substrate etching operations. While a self-standing process using the amine catalyst is not a cost-effective synthesis process, such an "add-on" can produce nice revenue.

Catalyst Specification

All experimentation has been done using TCS-activated AMBERLYST™ A21 DRY Resin. This resin has a known (and constant) pore size, tight particle size distribution, a reasonably high softening point, and a moderate amine loading. As with chlorosilane disproportionation, substituting for other amine resins with different properties and amine loading can lead to different results. The properties of this specific catalyst allow it to both exhibit hydrogen-adducting and chlorine-adducting, which is key to this innovative process.
For more information about AMBERLYST™ A21 DRY Resin, contact Dr. Klaus-Dieter Topp at KTopp@dow.com. Alternately you can contact one of the Dow Chemical Company representatives for non-aqueous amine catalysts.

Conclusions/Recommendations

While enough lab work has been done to show this approach conceptually works, more data should be collected with longer duration, to properly size the contact time for all HCl to be destructed and to understand side-reactions (such as the capture of B and P compounds). A pilot test is then suggested on a CVD line to determine how long the resin lasts in a real-world application.

There are various ways to use this chemistry to reduce costs in a polysilicon plant, and these should be considered as a part of any process improvement studies.

References

[1] “Catalyzed Disproportionation of Chlorosilanes”, L. Coleman and Pellney, Silicon for the Chemical and Solar Industry XII, Trondheim, Norway, pages 141-148
[2} US patent 2,834,648, Don Bailey et al
[3] US patents 3,928,542 and 3,968, 199, Carl Backay
[4] US patent 4,113,845, Carl Litteral
[5] Low-Cost Solar Array Project, JPL contact #954334, NASA # 162172, 1979 Union Carbide Corp. Final Report; JPL contract #955533-83/7, NASA #173957, 1982 Hemlock Semiconductor Corp. Final Report
[6] Download from website http://consultant-on-demand.net/Redistribution.htm

Emissions from MG-Si/FeSi production – a summary

Ida Kero[1], Svend Grådahl[1] and Gabriella Tranell[2]
1) SINTEF Materials and Chemistry, Alfred Getz vei 2, NO-7465 Trondheim, Norway
2) Norwegian University of Science and Technology, Alfred Getz vei 2, NO-7491 Trondheim, Norway

Abstract

As part of the research activities related to emissions and energy recovery in SFI Metal Production[1], a thorough review of published and unpublished work on emissions from- and emission measurements in the production of MG-Si and FeSi alloys, has been carried out. This work has been submitted as a review article for publication in the Journal of Environmental Science and Technology by the authors of this article. The present work aims to summarise highlights of this extensive work.

Introduction

Most of the emissions related to the MG-Si/FeSi production are generated in the smelting furnace (SAF) itself and includes Green House Gases (GHG), particulate matter (PM), heavy metals, NO_x, SO_x, and PAH/Dioxins[1]. The majority of emissions from the furnace are captured through the furnace off-gas cleaning system. "Fugitive" plant emissions are emissions which do not pass through a stack, chimney, vent, duct or other functionally equivalent opening. Typical fugitive emissions in the Si/FeSi industry are gases and particulate matter leaking into the working atmosphere from processes where the hoods are not capable of capturing 100% of the emissions. These processes include furnaces, metal tapping, casting and refining operations, as well as crushing, handling and transport of raw materials and solidified products. The transport and handling of raw materials, reductants and products at ambient conditions generates particulate matter through mechanical impact. Hot processes on the other hand, such as tapping, refining and casting, are sources of thermally generated fumes. Major emissions from a Si/FeSi plant are summarised in Table 1.

Table 1: Emission types and their origins in the plant

Type	Primary Origin	Emission Point
GHG	Reductants, Electrodes	SAF
NO_X	Reductants & SiO	SAF, Tapping

[1] SFI Metal production is a centre for research-based innovation hosted by NTNU and funded from 2015-2023 by the Research Council of Norway, Norwegian metal producers, NTNU, SINTEF and Teknova

	Combustion	
SO_2	Reductants	SAF
Dioxin	Combustion, Reductants	SAF
PAH	Reductants, Electrodes, Carbon paste	SAF, Tapping
Heavy metals	All raw materials	SAF, Refining
Mechanically generated PM	Solid material handling	Conveyor belts, Mills, Sieves, Etc.
Thermally generated PM	Liquid alloy in contact with air	Tapping, Refining, Casting

In Europe, emission and waste associated with the production of silicon and ferrosilicon is regulated and reported both at national and EU levels and there are similar divisions between state/territorial and federal legislations in the U.S.A., Canada and Australia. Some of the national environmental agencies offer guidelines and recommendations, published to complement and detail the legal requirements of this industrial branch[2-6]. In some countries, emission data (typically per ton alloy produced) are made publically available through annual publication in open databases such as the European Pollutant Releases and Transfer Register (E-PRTR)[7], the national Norwegian PRTR[8], the Australian National Pollutant Inventory (NPI)[9] and the Canadian National Pollutant Release Inventory (NPRI)[10].

For the fresh industry professional and even for experienced engineers and researchers in the field, it is difficult to get a collective overview of types and amounts of emissions from the industry, as measured data is often scarce, incomplete and scattered. Much progress in emission abatement has been achieved in the industry itself over the last decades but such work is rarely published. At best, it may be partially presented at industry-specific conferences or in confidential reports, producing little or no documentation available through data base search engines. With this in mind, the review article to be published, from which this article is an excerpt, attempts to be a first entry point into the diverse topic of Si/FeSi production emissions.

Gaseous Emissions

Major Greenhouse Gases

In the production of both MG-Si and FeSi alloys, greenhouse gases are mainly created through the overall oxide reduction reaction[1]:

$$SiO_2 + 2C \rightarrow Si + 2CO \quad (1)$$

The CO gas will oxidise to CO_2 at the furnace charge top in an open or semi-open furnace. In addition to CO generated through the silicon producing reactions, methane (CH_4) and volatile hydrocarbons are generated in the combustion of the carbonaceous materials and electrodes (pre-baked for MG-Si production and Søderberg type for FeSi production). Typically, most production emissions are reported on the basis of raw material type/use and production tonnage. Based on typical raw material- and production-based emissions, generic (average), total emission factors for different high Si alloys are summarised in Table 2. Note that CH_4 emissions based on semi-

open furnaces with the sprinkle charging and off gas temperatures > 750ºC are included as default in these factors.

Table 2. Generic CO_2 emission factors for Si and FeSi alloys (ton CO_2/ton tapped metal)

Type of Alloy	Generic Emission Factor
Ferrosilicon 45% Si	2.5
Ferrosilicon 65% Si	3.6
Ferrosilicon 75% Si	4.0
Ferrosilicon 90% Si	4.8
MG-Si (>98% Si)	5.0

All hydrocarbon emissions are highly dependent on both alloy type and furnace operation which in turn lead to high variations and uncertainties of reported data. Lindstad et al. [11] estimated typical CH_4 emissions for different alloys and furnace operations in the 1990's. Comparing these estimations to the reported CH_4 emission values from Norwegian Si and FeSi smelters (available at norskeutslipp.no [8] for the period 2002 to 2014), the discrepancy is in the order of a factor 10. With such large divergences of data there is undoubtedly room for improvement. Although these emissions represent a small part of total GHG emissions, a comprehensive study into the levels- and variations of hydrocarbon emissions could improve the accuracy of industrially relevant GHG emission factors.

Nitrogen Oxides, NO_x

Nitrogen oxide formation (NO and NO_2; often referred to as NO_X) in Si/FeSi production is attributed to several different reaction mechanisms. So called "fuel NO_X" is formed by oxidation of the nitrogen components present in the solid fuel while "thermal NO_X" is formed by direct oxidation of nitrogen (from the air) at temperatures above 1400ºC. Such temperatures are frequently observed in the furnace hood[12-14]. Emission of NO_x always reports as NO_2, because NO is unstable and will react to NO_2. The basic chemical equations for NO_X formation are:

$$N + \frac{1}{2}O_2 \rightarrow NO \qquad (2)$$

$$NO + \frac{1}{2}O_2 \rightarrow NO_2 \qquad (3)$$

Combustion of gaseous SiO above the charge surface and in the tap-hole may locally increase the temperature. The amount of SiO(g) released from the charge will therefore also influence NO_X formation. The Norwegian Ferroalloy Association (FFF), SINTEF and the Norwegian University of Science and Technology (NTNU) have worked together on NO_X reducing strategies for nearly 20 years. The collaboration and joint efforts have resulted in many industrial initiatives and investments which, in turn, have given positive NO_X reduction results[14, 15-16]. The NO_X production is inversely proportional to the silicon yield, at least up to a certain level of silica fume formation. As described by Slizovsky et al. [26] and Brede [27], the NO_X formation is also correlated to the moisture content of the furnace gas. Moisture is introduced through the raw materials and hence, will vary throughout the materials charging cycle. NO_X also forms during tapping, when an oxygen lance is used to open up the tapping channel to increase the metal flow out of the furnace [13,17-18]. Efforts to understand the

NO_X formation have shown that furnace design and furnace operating procedures, such as stoking and charging, heavily influence NO_X emissions [19-25]. Reported NO_X emission values vary greatly with typical values ranging from 500 to 1500 ton per site and year.

Dioxins, SO_2 and other gases

A great number of gases may be present in the flue gases from a submerged arc furnace (SAF), some of which are regularly measured and some are more occasionally detected and documented. Examples of such gases include sulphur oxides (SO_X) and other -compounds such as H_2S and various volatile organic compounds (VOC) [1, 29]. SO_2 emissions are often mentioned as a type of gaseous emissions which occurs in the silicon alloy industry, but very few authors seem to have studied these emissions specifically. Grådahl et al. [12] showed the correlation of SO_2 and CO gas emissions to certain furnace events called "avalanches"; the occurrence of which could be reduced by use of semi-continous charging procedures. The reported SO_2 emissions from silicon alloy production are typically in the same order of magnitude as the NO_X emissions [1, 8]. The origin of SO_2 gas is the sulphur content of the raw materials and the reported emissions levels are typically calculated based on material balances.

Dioxins are a class of persistant organic pollutants (POP) which are highly toxic to human health. Like polycyclic aromatic hydrocarbons (PAH), dioxins may be both gaseous and particle-bound, depending on temperature. The generation of dioxins in combustion and metallurgical processes is, in a general sense, quite well established [30-31,12]. The presence and generation of dioxins in the silicon alloy industry is, however, not well documented or understood. Nonetheless, there is some information on the management of dioxins in silicon alloy furnace off gases to be found. The destruction of dioxins and organic compounds, such as furans and PAH's, at high temperatures allows for efficient reduction or even elimination in modern, semi-open SAF's. Furnace design and operation are keys and must be optimized for close control of the flue gas temperature

Particle-bound gas compounds

Polycyclic aromatic hydrocarbons, PAH

Polycyclic Aromatic Hydrocarbons (PAH) are a group of more than 100 different chemical compounds consisting of organic structures having more than two joined aromatic (benzene) rings. The lighter compounds, with few aromatic rings, are gaseous at room temperature whereas the larger molecular compounds are liquid or solid and commonly adsorbed on particles, for example soot. Anthropogenic PAHs are typically formed by incomplete combustion of organic materials and the main sources of PAH in the high silicon alloy production is the combustion of reductants in the furnace and the baking of electrodes. As for so many other airborne emission types, emission factors are used to estimate PAH emissions from industrial sites [32-37]. Tveit et al.[28] reports that the formation of PAH is linked to soot formation which in turn is influenced by furnace design and operation. As PAHs are destructed at high temperatures, Grådahl et al.[12] could show that the PAH emissions from ferrosilicon furnaces were significantly reduced when off gas temperatures were increased.

Heavy Metals

Heavy metals are carried into the production process as trace elements in the raw materials and the electrodes. During the production process steps, the heavy metals are redistributed to metal, slag, dust and gas. This redistribution and the final concentrations in the product and by-products depends heavily on the type of ferroalloy produced and the temperatures of the processes. The heavy metal emissions can be gaseous, particle-bound or oxidized. At process temperatures of 1600°C or higher, volatile metals go into the gas phase and may escape as metal vapour. When the off gas temperature drops, the metal vapours are condensed and therefore often collected with the dust. Myrhaug and Tveit [38-39] showed that a boiling point model can be used to predict whether an element is most likely to escape the SAF as gas, condensed silica fume or remain in the tapped metal. Næss et al. [40] showed that the boiling point model also is applicable to the fume of the oxygen-blown refining ladle, with some modifications due to the oxidation of elements.

The reported emissions of the trace elements from a Si/FeSi plant are most often based on material balances and may vary greatly between plants but an example of how trace elements may be distributed from a silicon plant is shown in Table 3[28]. Emission estimations to air through the filter systems must cover both gaseous and particle-bound heavy metals. A major challenge in the estimation of heavy metal emissions is their low concentrations in the material flows. Mercury typically has detection limits (DL) given in units of parts per billion (ppb) whereas the other heavy metals have DL in the order of magnitude of parts per million (ppm). This means that very significant measurement uncertainties are introduced when the detected concentrations are below DL and it is often impossible to "close" the material balance for individual elements. The total uncertainty for elements such as Co, Hg and Mo is often around or above 100%. Such uncertainties may be lowered by continuous, on-line measurements in off-gases after the filter systems but such measurements are often practically challenging.

Table 3: Estimated distribution of heavy metals for a plant producing 10 kilo tonnes silicon annually. Calculations by Tveit et al. [28,39]. All numbers in kg per year.

	As	Cd	Cr	Cu	Hg	Pb	Zn
To Air	6	0	0	0	0.10	0	0
In Si product	6	1	600	160	0.00	5	10
In Microsilica	100	9	60	40	0.05	95	190
Total	112	10	660	200	0.15	100	200

Particulate Emissions

Airborne particulate matter (PM), originating from various sources in the metallurgical industry are a concern in terms of working environment and potential adverse health effects. Furthermore, the PM is an important constituent in the diffuse emissions escaping the plants and may affect the air quality of the local, urban communities as well as the environment at large. Almost all processes involved in silicon and high-silicon alloy production produces PM in some form. Table 4 provides an overview of the PM sources and a rough estimate of their relative importance to indoor air PM concentration and to PM emissions out of the plant[4,13].

Table 4: Estimated relative importance of dust sources in silicon production facilities [25,13]

Activity	Share of emissions to outer environment (%)	Share of indoor air pollution (%)
Raw material transport pre-storage	0-5	0
Raw material handling, post-storage	0-5	5-10
Semi-closed furnace process	10-20	5-20
Tapping	20-40	30-50
Casting and liquid alloy handling	20-40	15-25
Solid alloy product handling	5-15	5-15
Microsilica packing and handling	0-5	5-10
Off-gas system	5-10	0-5

While very few quantitative measurements of thermal or mechanical PM have been published, Næss[45] studied the amount of dust typically formed over a refining ladle producing MG-Si. Depending on the refining gas flowrate, typical measured dust amounts were between 0.8 – 1.7 kg SiO_2 per tonne Si produced

The dust which is generated during handling and transport of solid materials, such as the product and the raw materials, is fundamentally different from the dust generated by the active oxidation process. The dust from the solid materials typically generates coarser PM with physical and chemical properties which depends on the material from which it was generated. Raw material handling and transport can, for example, produce airborne crystalline alpha-quartz which is a health hazard in its own right. No literature on the generation, collection and reduction of the mechanically generated PM in high-Si alloy smelters has been found.

Emission Measurements

The concentration of a given pollutant in a gas stream as a function of time can be determined with *in-situ*, *direct-reading* or *in-line* instruments. They operate in real-time and are often equipped with data logging. *Indirect* instruments are samplers which collect the pollutant over a certain time interval with subsequent laboratory analysis. This is sometimes referred to as *ex-situ* analysis. *Active* or *extractive* sampling refers to the use of a pump to draw the polluted air into the instrument whereas *passive* methods operate without alteration of air flow [6, 41-42].

In addition to in-situ and extractive measurements, the materials balance (process- or site specific mass flow calculations) is often carried out to estimate the emission of, for example, heavy metals and CO_2.

To report the correct emission of the different components, representative flow measurement in the off gas channel is an essential complement to correct gas measurements. Different measuring principles are used, like pitot tubes, annubars, orifice plates, ultrasonic flowmeters and thermal mass flow meters. Extractive measurement techniques applied to off-gas ducts and pipes often call for isokinetic sampling and/or dilution, which can be extremely challenging in terms of practical

operation. Both procedures will also, inevitably, introduce additional error sources and increase uncertainty, especially under the non-ideal conditions of industrial operations [42-44].

Conclusions

Current knowledge on emissions relevant to the Si and FeSi producing industry, has been summarized in a critical review article by Kero, Grådahl and Tranell, from which the current article is an excerpt.

Most gaseous emissions are reported and monitored by use of emission factors. The overall GHG emissions from FeSi and MG-Si production are reasonably well understood and quantified, with the exception of hydrocarbons. The extent of GHG emission is highly dependent on the carbon and electricity consumption (which in turn depends on the type of Si/FeSi alloy), the carbonaceous material mix, charging methods and furnace operation. NO_X emissions are heavily influenced by the furnace design, flue gas management and furnace operating procedures - such as stoking and charging. Measurements show strong correlations between PM and NO_X formation above the furnace charge. Localized temperature control can only be achieved by limiting the extent of silica fume production through SiO(g) combustion.

Close flue gas temperature control is extremely important for several reasons. One reason is the delicate trade-off between PAH and NO_X management. PAHs are destructed at high temperatures and PAH emissions can be significantly reduced when off gas temperatures are kept above 800°C.

PAH and heavy metals are simultaneously present as gases and particulate forms, and their distribution is highly temperature dependent. The particle-bound compounds are often collected in the particulate control devices (e.g., fabric filter or wet scrubber). The more volatile compounds however, will risk to be emitted to the atmosphere if no further gas treatment is applied

Round-the-clock gas measurements of emissions are desirable, but may be difficult to achieve in high-temperature dusty gas streams. Smelters flue gas ducts present an extremely harsh environment where sampling is very challenging and the available instruments must be selected based on their ability to operate under such conditions. Dilution and isokinetic sampling requirements may present additional difficulties and typically increases uncertainty values. PM measurement principles often remain to be validated for the specific types of dust encountered in Si and FeSi smelters. Hence, site-specific calibrations are recommended to ensure reasonable accuracy of the measurements.

Acknowledgements

This article was enabled through funding from the Research Council of Norway through the center for research-driven innovation (SFI) Metal Production. The authors wish to thank Dr. Edin Myrhaug and Dr. Nils Eivind Kamfjord at Elkem AS for comments and discussions

References

1. Schei, A., et al., Production of High Silicon Alloys. 1st ed.; TAPIR forlag: Trondheim, Norway, 1998.
2. Environmental Code of Practice for Base Metals Smelters and Refineries. Environment & Climate Change Canada: Environment, D. o. t., Quebec, Canada, 1999.
3. National Pollutant Inventory (NPI) Guide. Department of the Environment: Government of Australia: Canberra, Australia, 2015. ISBN 8 642 54690 8
4. Best Available Techniques (BAT) Reference Document for the Non-Ferrous Metals Industries. Integrated Pollution Prevention and Control (IPPC): European Commission: 2014.
5. Emission Estimation Technique Manual for Non-Ferrous Metal Manufacture. National Pollutant Inventory (NPI): Commonwealth of Australia: Environment, D. o. t., Canberra, Australia, 2001.
6. Reference Document on the General Principles of Monitoring (BREF MON). Integrated Pollution Prevention and Control (IPPC): European Commission: 2003.
7. The European Environment Agency (EEA) European Pollutant Release and Transfer Register (E-PRTR). http://prtr.ec.europa.eu/#/home (accessed March 29, 2016).
8. The Norwegian Environment Agency Total emissions to air in Norway - The Norwegian PRTR. http://www.norskeutslipp.no/en/Frontpage/?SectorID=90 (accessed February 1, 2016).
9. The Australian Government, Department of the Environment National Pollutant Inventory (NPI). http://www.npi.gov.au/ (accessed March 29, 2016).
10. Government of Canada, Department of Environment and Climate Change National Pollutant Release Inventory (NPRI) - Tracking Pollution in Canada. http://www.ec.gc.ca/inrp-npri/ (accessed March 29, 2016).
11. Lindstad, T., et al., Industrial Processes. In IPCC Guidelines for National Greenhouse Gas Inventories.
12. Grådahl, S., et al. Reduction of Emissions from Ferroalloy furnaces, In INFACON XI, New Delhi, India, MacMillan: New Delhi, India, 2007; pp 479-488. 10:0230-63069-3
13. Kamfjord, N. E. Mass and Energy Balances of the Silicon Process - Improved Emission Standards. Ph.D. Thesis, The Norwegian University of Science and Technology, Trondheim, Norway, 2012. ISBN (print): 978-82-471-3613-3 ISBN (el): 978-82-471-3614-0 ISSN: 1503-8181 (NTNU 2012:162)
14. Myrhaug, E. H., et al. NOx Emissions from Silicon Production, In Silicon for the Chemical and Solar Industry XI, Bergen-Ulvik, Norway, June 25-29; Øye, H. A., et al., Eds. Fagtrykk AS/ The Norwegian University of Science and Technology: Bergen-Ulvik, Norway, 2012; pp 95-106. 978-82-997357-7-7
15. Nikolaisen, P. I., Slik kuttet Elkem utslipp tilsvarende 150.000 dieselbiler på rekordtid. Teknisk Ukeblad February 13, 2014.
16. Tveit, H.; Wittgens, B., Grønnere Metallproduksjon. Dagens Næringsliv March 14, 2014.
17. Olsen, J. E., et al., Status on NOx-Related Studies for the Norwegian Ferroalloy Industry. SINTEF: Trondheim, Norway, 2012.
18. Kadkhodabeigi, M. Modeling of Tapping Processes in Submerged Arc Furnaces. Ph.D. Thesis, Norwegian University of Science and Technology, Trondheim, Norway, 2011. ISBN (print): 978-82-471-2841-1 ISBN (el): 978-82-471-2843-5 ISSN: 1503-8181 (NTNU 2011:149)
19. Ravary, B.; Johansen, S. T. 2D modeling of the combustion and NOx formation in furnaces producing FeSi, In 2nd International Conference on CFD in the Minerals and Process Industries, Melbourne, Australia, CSIRO: Melbourne, Australia, 1999; pp 6-8.
20. Kamfjord, N. E., et al. Pilot Scale Measurements of NOx Emissions from the Silicon Process, In 3rd International Symposium on High-Temperature Metallurgical Processing, Orlando, FL, U.S.A., Tao Jiang, et al., Eds. Wiley Online Library; John Wiley & Sons, Inc., Hoboken, NJ, USA: Orlando, FL, U.S.A., 2012; pp 411-418. 1118364988
21. Solheim, I., et al., Equipment for Pilot Scale Experiments of NOx-Emissions from the Silicon Process. In 3rd International Symposium on High-Temperature Metallurgical Processing, Tao Jiang, et

al., Eds. Wiley Online Library; John Wiley & Sons, Inc., Hoboken, NJ, USA: Orlando, Florida, USA, 2012.
22. Ravary, B., et al. Modelling Combustion and Thermal NO_X Formation in Electric Arc Furnaces for the Production of Ferrosilicon and Silicon Metal, In INFACON XI, New Delhi, India, MacMillan: New Delhi, India, 2007. 10:0230-63069-3
23. Panjwani, B., et al. Effect of Combustion on NOx Emissions, In 8the International Conference on CFD in the Oil & Gas, Metallurgical and Process Industries, Trondheim, Norway, SINTEF: Trondheim, Norway, 2011.
24. Solheim, I.; Kamfjord, N. E. NOx-emissions from the silicon process: Comparing wet and dry raw materials pilot scale experiment, In INFACON XIII, Almaty, Kazakhstan, Almaty, Kazakhstan, 2013. 9965-729-34-4
25. Skreiberg, Ø., Evaluation of detailed gas-phase chemical kinetics mechanisms for NOx modelling in biomass- and MSW combustion applications. SINTEF: Trondheim, Norway, 2002.
26. Slizovskiy, D., et al. The Industrial Scale Study of the Effect of Charge Frequency and H2O Behaviour in the Off-gases on NOx emissions in Si Furnace, In Silicon for the Chemical and Solar Industry XII, Trondheim, Norway, June 23-26; Øye, H. A., et al., Eds. Fagtrykk Trondheim AS/ The Norwegian University of Science and Technology: Trondheim, Norway, 2014; pp 207-218. 978-82-997357-8-0
27. Brede, I., Parameters Contributing to the Formation of NOx in the Silicon Furnace: The effect of the charging frequency and raw material composition on the formation of NO. The Norwegian University of Science and Technology: Trondheim, Norway, 2013.
28. Tveit, H., et al. The Silicon Process - Improved Environmental Standards, In Siliconn for the Chemical Industry VII, MS Trollfjord Tromsø-Bergen, Norway, Øye, H. A., et al., Eds. The Norwegian University of Science and Technology: MS Trollfjord Tromsø-Bergen, Norway, 2004; pp 55-66. 82-902265-25-5
29. Tveit, H.; Eikeland, I. J. Environmental Aspects of the Silicon Industry, In Silicon for the Chemical Industry IV, Geiranger, Norway, Øye, H. A., et al., Eds. The Norwegian University of Science and Technology: Geiranger, Norway, 1998; pp 365-376. 82-905265-20-4
30. Buekens, A., et al., Dioxins from thermal and metallurgical processes: recent studies for the iron and steel industry. Chemosphere 2001, 42 (5), 729-735.
31. Yu, B.-W., et al., Emission of PCDD/Fs and dioxin-like PCBs from metallurgy industries in S. Korea. Chemosphere 2006, 62 (3), 494-501.
32. Bandeira, G. C.; Meneses, H. E., Handbook of Polycyclic Aromatic Hydrocarbons - Chemistry, Occurrence and Health Issues. Nova Science Publishers. Inc.: New York, U.S.A., 2013. 978-1-62257-473-5
33. Zhang, Y.; Tao, S., Global atmospheric emission inventory of polycyclic aromatic hydrocarbons (PAHs) for 2004. Atmos. Environ. 2009, 43 (4), 812-819.
34. Boffetta, P., et al., Cancer risk from occupational and environmental exposure to polycyclic aromatic hydrocarbons. Cancer Causes & Control 1997, 8 (3), 444-472.
35. Yang, H.-H., et al., PAH emission from various industrial stacks. J. Hazard. Mater. 1998, 60 (2), 159-174. DOI: http://dx.doi.org/10.1016/S0304-3894(98)00089-2
36. Yang, H.-H., et al., Profiles of PAH emission from steel and iron industries. Chemosphere 2002, 48 (10), 1061-1074. DOI: http://dx.doi.org/10.1016/S0045-6535(02)00175-3
37. Ravindra, K., et al., Atmospheric polycyclic aromatic hydrocarbons: source attribtion, emission factors and regulation. Atmos. Environ. 2008, 42 (13), 2895-2921.
38. Myrhaug, E. H.; Tveit, H., Material balances of trace elements in the ferrosilicon and silicon processes. In 58th Electric Furnace Conference and 17th Process Technology Conference Proceedings, Iron & Steel Society: Warrendale, PA, USA, 2000; Vol. 17, pp 591-604.
39. Tveit, H.; Myrhaug, E. Important sub-processes in the silicon process. The behavior of trace elements, In Silicon for the chemical industry, 5th, Tromsø, Norway, Tromsø, Norway, Øye, H. A., et al., Eds. The Norwegian University of Science and Technology: Tromsø, Norway, 2000; pp 23-30. 82-90265-22-0
40. Naess, M. K., et al., Element distribution in silicon refining – Thermodynamic model and industrial measurements. JOM 2014, 66 (11), 2343-2354. DOI: 10.1007/s11837-013-0797-7
41. Hinds, W. C., Aerosol technology: properties, behavior, and measurement of airborne particles. Wiley-Interscience: New York, USA 1982; Vol. 1.
42. Kulkarni, P., Aerosol Measurement - Principles, Techniques and Applications. John Wiley & Sons, Inc.: Hoboken, U.S.A., 2011. 978-0-470-38741-2

43. Gaertner, H. Characteristics of particulate emissions from aluminium electrolysis cells. Ph.D. Thesis, Norwegian University of Science and Technology, Trondheim, Norway, 2013. ISBN (print): 978-82-471-4763-4 ISBN (el): 978-82-471-4764-1 ISSN: 1503-8181 (NTNU 2013:314)
44. Vincent, J. H., Aerosol Sampling - Science, Standards, Instrumentation and Applications. John Wiley & Sons Ltd.: Chichester, U.K., 2007. 978-0-470-02725-7
45. Næss, M.K, Mechanisms and Kinetics of Liquid Silicon Oxidation. Ph.D. Thesis Norwegian University of Science and Technology, Trondheim, Norway, 2013. ISBN (print): 978-82-471-4394-0 ISBN (el): 978-82-471-4396-4 (NTNU 2013:145)

Use of agglomerated raw materials in Si production

Fei Li, Merete Tangstad

Department of Material Science and Engineering, Norwegian University of Science and Technology, Trondheim, Norway

Abstract

The use of agglomerates in the Si-furnace is believed to decrease the top temperature of the furnace and increase the Si-yield. This paper will both describe the results done by modelling the energy distribution in the furnace, but also show experimental results of using agglomerates. The heat balance shows that increased amount of agglomerates will increase the Si-yield. Meanwhile the energy consumption per ton Si and energy content in the off gas lost to environment will decrease. According to the experimental results, $SiO_2(s) + 3\ C(s) = SiC(s) + 2\ CO\ (g)$ happens in agglomerate. No SiO gas loss from agglomerate in SiC-producing step. Higher temperature and lower CO concentration are positive to the reaction.

I. INTRODUCTION

In the silicon production process, the carbon materials reduce the quartz in the three-phase submerged arc furnace. Quartz and carbon sources (coke, coal, charcoal or woodchips) are added as lumps at the top of a submerged arc furnace. As the carbon materials are descending in the furnace they are simultaneously heated and transformed to SiC. The SiC is then reacting with SiO gas to produce silicon. The produced silicon is tapped at the bottom and gas leaves at the top of the furnace. Generally, the carbothermic process could be described simply as equation 1. However, a series of sub-reactions occur in the furnace [1-3].

$$SiO_2 + 2\ C = Si + 2\ CO \qquad (1)$$

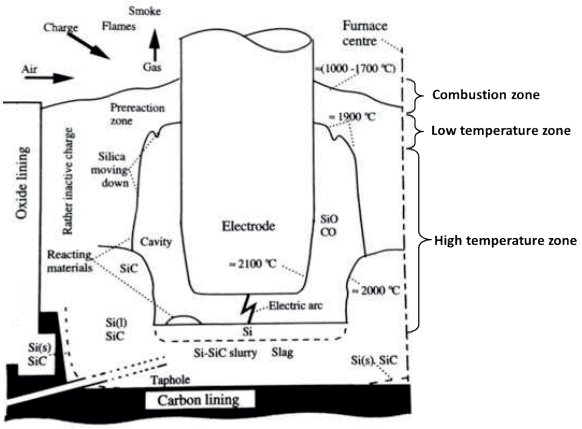

Figure 1: Inner structure of a submerged arc furnace for silicon production [1]

Figure 1 shows the inner structure of the arc furnace. The furnace can be divided into three parts, the combustion zone, the low temperature zone and the high temperature zone. Generally, the longer distance from the electrode tip position, the lower temperature it is.

The combustion zone is where the raw materials are charged, and is open to the air. The charge will be heated and some of the carbon materials in the charge will burn. In the combustion zone SiO gas and CO gas from the charge will enter and be oxidized by the air (reaction 2 and 3). The formed $SiO_2(s)$ and CO_2 will then leave the furnace with the off gas [4-5].

$$SiO(g) + 0.5O_2 = SiO_2(s,l) \qquad \Delta H°_{25°C} = -220 \text{Wh/mol} \qquad (2)$$

$$CO + 0.5\ O_2 = CO_2 \qquad \Delta H°_{25°C} = -78.7 \text{Wh/mol} \qquad (3)$$

When the charge materials descend to the low temperature zone (in this model defined as 1400-1800 °C), quartz and carbon materials will meet the SiO and CO gas produced in the inner zone. Reaction 4 to 7 is occurring in this zone. Carbon materials will react with some of the SiO gas and produce SiC according to reaction 4. Reaction 4 is the most important reaction in the low temperature because it captures SiO gas and produces the intermediate product SiC, which is the key reactant for silicon forming reactions in the inner part of the furnace.

$$SiO(g) + 2\ C(s) = SiC(s) + CO(g) \qquad \Delta H°_{1500°C} = -20.8 \text{ Wh/mol} \qquad (4)$$

$$2SiO = Si(l) + SiO_2(l) \qquad \Delta H°_{1500°C} = -169 \text{ Wh/mol} \qquad (5)$$

$$3\ SiO(g) + CO(g) = 2\ SiO_2\ (s,l) + SiC(s) \qquad \Delta H°_{1500°C} = -390 \text{ Wh/mol} \qquad (6)$$

When the temperature is above 1700-1900℃, the materials arrive at the high temperature zone of furnace, which is the cavity zone in Figure 1. In this zone SiC and SiO_2 reacts. Liquid silicon, SiO gas and CO gas are produced from this step according to reaction 7, 8 and 9.

$$2SiO_2(s,l) + SiC(s) = 3\ SiO(g) + CO(g) \qquad \Delta H°_{1900°C} = 384 \text{ Wh/mol} \qquad (7)$$

$$SiC(s) + SiO\ (g) = 2\ Si(l) + CO(g) \qquad \Delta H°_{1900°C} = 47.5 \text{ Wh/mol} \qquad (8)$$

$$SiO_2(s,l) + Si(l) = 2\ SiO(g) \qquad \Delta H°_{1900°C} = 165 \text{ Wh/mol} \qquad (9)$$

In this paper, the behavior of different quartz and carbon agglomerate for silicon production process will be studied, and the heat balance of an industrial furnace will be included to signify the use of agglomerates on the Si-yield.
For the general cases, when lumpy material is used, the contact area between quartz and carbon is very limited. There will hence be no reaction between the quartz and the carbon material in the low temperature zone. However if agglomerates are used, quartz and carbon have a large contact area. Around 1500℃, the following solid-solid reaction may occur, according to Schei. et al [1] :

$$SiO_2(s,l) + 3\ C(s) = SiC(g) + 2\ CO(g) \qquad \Delta H°_{1500°C} = 163.8 \text{ Wh/mol} \qquad (10)$$

Reaction 10 is an endothermic reaction. This indicates that this reaction will absorb energy in the low temperature zone. This will decrease the temperature. As the temperature decreases, the extent of the condensation reactions (reaction 5 and 6) will increase, and less SiO gas will be lost. This will contribute to a higher Si-yield and thus, lower energy consumption.

II. Theoretical heat balance when modeling a silicon furnace

As shown in Figure 2. The Si furnace can be divided in three zones: The high temperature zone (HTZ) where most of the Si and SiO-gas production is taking place. The low temperature zone (LTZ) where the C reacts with SiO to SiC, SiC forms in the agglomerates and SiO gas condensates. The last zone is the combustion zone (CZ) where CO and SiO gas are combusted with air to CO_2 and SiO_2. In order to simplify the reactions, reactions in Figure 2 are the selected as the main reactions in each zone.

Based on this 3 zone model, a heat and mass balance is calculated for each zone. The output from one zone is equal to the input in the next zone and hence, the variables are total input masses of SiO_2, C and air in the combustion zone. The temperatures for the raw materials in are set as 25 ºC, the air in as 25 ºC and the tapped liquid silicon is set as 1600 ºC. The relative temperature of off-gas from the CZ is 1200 ºC, however the energy relative to this temperature is calculated. The solid from LTZ to HTZ and gas from HTZ to LTZ are set to 1720ºC and 1900ºC [6-7].

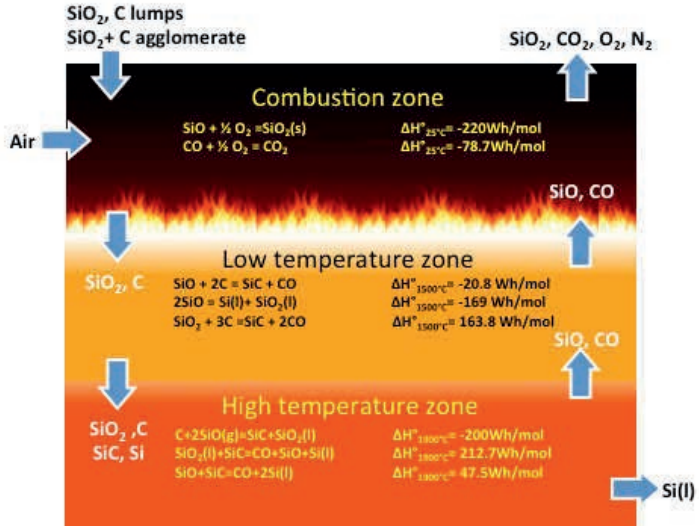

Figure 2: Model of silicon furnace

Assumptions in the three zones are listed below:

- All the electrical energy is provided to the high temperature zone (HTZ) and the temperature in high temperature zone (HTZ) is constant and 1900 ºC.
- The low temperature zone (LTZ) should be adiabatic, that is no extra energy in or out except solid and gas in and out. There are no thermal losses that are no radiation and convection losses as well as no loss of energy to cooling water.
- Raw materials including the quartz and carbon materials are 100% pure. Neglecting limestone, moisture, volatiles and ash in the raw material. 1 mole of quartz and 2 mole of carbon are charged in the furnace. 5% of carbon lump and 3% of carbon in agglomerate are burnt. Carbon in agglomerate has 100% SiO reactivity. The mole ratio between SiO_2 and C in agglomerate is 1:3. The proportion of carbon in the pellets in the proportion of total amount of carbon increased from 0% to 5%, 10%, 20% and 30%.

- SiO_2 + 3C = SiC + 2CO is only occurring in the agglomerates. The reaction between SiO_2 and SiC in the low temperature zone (LTZ) is neglected. There is also no SiO production in agglomerates.
- The product from the tapping hole is 100% liquid silicon.
- In the high temperature zone, the total pressure is 1 atm, and hence p(SiO)+p(CO)=1atm. The SiO pressure as a function of temperature can then be given by $p(SiO)= 2.427-9.6\cdot10^{-4}\cdot T(°C)$ according to thermodynamic data (HSC). The relationship between SiO content and temperature of off-gas from LTZ for the industry is not in thermodynamic equilibrium and is hence not known. Mole SiO in low temperature zone: $Mole(SiO) = 2E\text{-}11e^{0.0144T}$ (°C) from HSC is used in this modeling. Although there is the difference between the theoretical SiO pressure and the industrial one, the trend of changes when agglomerate used in the furnace will be demonstrated.
- The case when no agglomerate is used in the charge is used as the reference case. When the mass and heat were balanced, the Si yield is 72%, the temperature of off-gas from LTZ is 1595.5ºC and SiO loss is 19%. The energy consumption in CZ and HTZ are -56.57kWh and 219 kWh respectively. The energy consumption per ton Si is 10862kWh. The temperature in the solid from CZ to LTZ is 881ºC.

Theoretical heat balance modeling results are shown in Figure 3 and 4. According to Figure 3, when the contents of agglomerate is increased to 30%, the temperature of off-gas from LTZ decreased to 1540ºC, SiO loss decreased to 8.5% and energy consumption per ton Si decreased to 8372kWh, while the Si yield increased 91.8%.

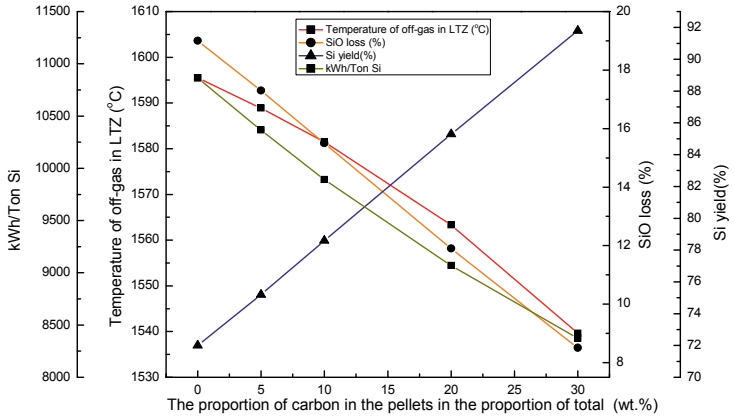

Figure 3: The proportion of carbon in the pellets in the proportion of total effects on off-gas temperature of LTZ, SiO loss, Si yield and energy consumption per ton Si

Figure 4 a) shows the relative energy content in the off gas and the energy consumption in HTZ. As the amount of agglomerate increase the temperature will decrease in the LTZ due to the endothermic reaction where SiO_2 and C react to SiC in the agglomerates. This will lead to a higher condensation of the SiO gas and hence a higher Si yield. With high amounts of agglomerates the energy in the off gas will be lower, both due to less oxidation of SiO as well as a lower gas temperature from the LTZ. Figure 4 b) shows the amount of SiC deposit decreased in HTZ decreased from 0.09 kmoles to -0.003 kmoles from when carbon in

agglomerate increased to 30%. This is helpful to extend life of furnace, but will also make the furnace narrower.

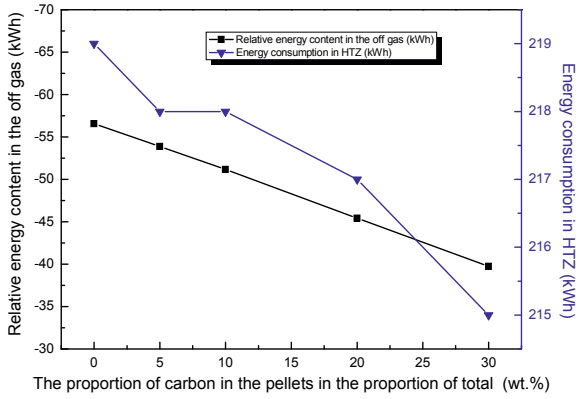

a)

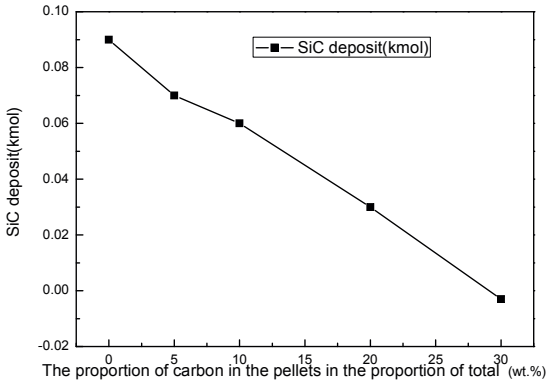

b)

Figure 4: The proportion of agglomerates of total effects on a) relative energy content inn off-gas and energy consumption of HTZ, b) SiC deposit.

III. Summary of experimental results

In order to investigate the reaction mechanism of agglomerates at elevated temperature, quartz and carbon black pellets are studied experimentally. Carbon black is used to see if natural gas can be a good carbon source in the silicon production. Two different types of pellets have been studied, the mixed pellet and the carbon deposited pellet. For the mixed pellet, the spherical carbon black particles adhere to the surface of the non-uniform polyhedron shaped quartz lump. In the carbon deposited pellet, carbon cracked from methane formed a coating which envelopes the quartz lumps. It will be reported how the temperature, the CO gas concentration, the carbon content affect the rate of SiC formation.

A. The effects on the holding temperature[8]

The heating experiments of mixed quartz and carbon black pellets (15 *w*t.%) in temperature range from 1600℃ to 1675℃ were conducted in CO gas. The weight loss (%) versus time at different holding temperature is shown in Figure 5.

The whole reaction process can be divided into two stages according to the reaction rate, the fast stage, which lasts several minutes and the slow stage, after fast stage to the end of experiment. The fast stage is represented by the reaction $SiO_2 + 3C = SiC + 2CO$, that is the SiC formation.

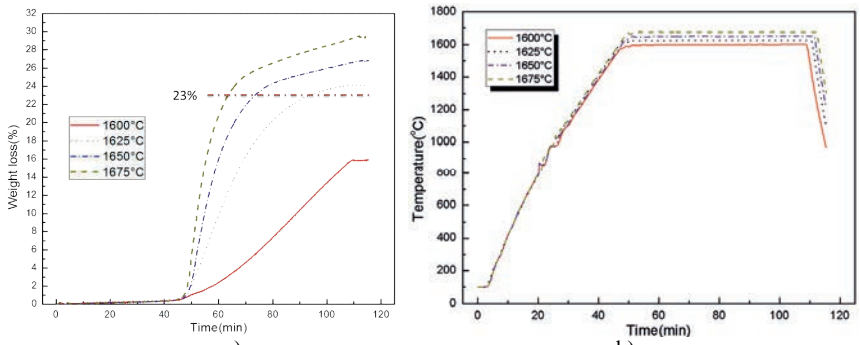

Figure 5: Effect of holding temperature from 1600℃ to 1675℃ in CO gas atmosphere
a) Weight loss (%) versus time b) temperature profile

As shown in figure 5a, the final weight loss of each experiment increased as the holding temperature increased from 1600℃ to 1675℃. The reaction between quartz and carbon black in this investigation starts around 1550℃. The conjunction part from fast stage and slow stage for these two experiments are all 2-3% higher than 23%. The value of 23% is the theoretical weight loss when all the carbon was reacted according to reaction 10, the SiC transformation, at carbon content of 15%. It is hence reasonable to believe that the main reaction during fast stage is the reaction between SiO_2 and 3C (reaction 10). During fast stage, SiC is produced. Though this reaction has to go through a gas phase, it seems like there is no loss of SiO gas during the first stage, as the turning point of the graph is close to 23%, the theoretical weight loss of CO. It is believed that in the slow stage, the main reaction is the solid-solid reaction between SiO_2 and SiC(reaction 6) which is provided from the fast stage. For better distinguish this two reaction steps, the fast step will be named as SiC-producing stage (reaction 7) while the slow stage will be named as SiO-producing step (reaction 5) in the following part of this paper.

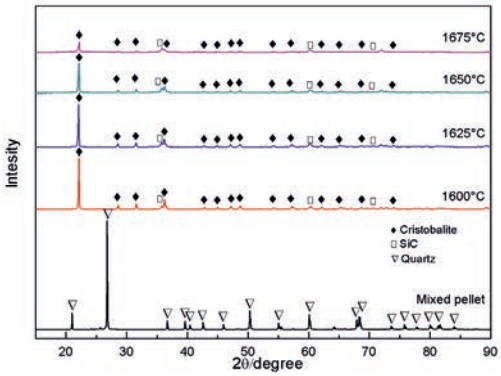

Figure 6: X-ray diffractometer patterns for different holding temperature from 1600℃ to 1675℃ in CO gas atmosphere and mixed quartz and carbon black pellets (before heating)

Figure 6 presents the phase changes of XRD patterns for four different pellets after heated in different temperatures and the pellets before heating. Carbon black is

difficult to detect in pellets before heating because it is amorphous, and after heating its' content is too low to detect. When comparing the pellet before heating with the pellet after heating, quartz is transferred to cristobalite in heated samples. The intensity of main peaks for cristobalite is fading while the intensity of SiC increasing when holding temperature increased from 1600℃ to 1675℃. This indicates a higher consumption of SiO_2 at higher temperature.

B. The effects of CO gas concentration

CO gas concentration is affected either by partial pressure of CO in atmosphere or gas transfer rate.

Experiments for different partial pressure of CO were conducted at 1650℃. The atmosphere is pure CO, pure Ar or 50% of CO and 50% of Ar. The mixed quartz and carbon black pellets with the carbon content of 15 wt.% is used in these experiments. The final weight loss of experiments in argon is obviously higher than experiments in CO. As shown in Figure 7, the starting point of reaction in argon is earlier than CO. The reaction rate in the only Ar gas is the highest one, followed by the 50% of CO and the CO only. This indicates that CO gas in the ambience depresses the reaction in both fast stage and slow stage as should be expected in CO producing reactions.

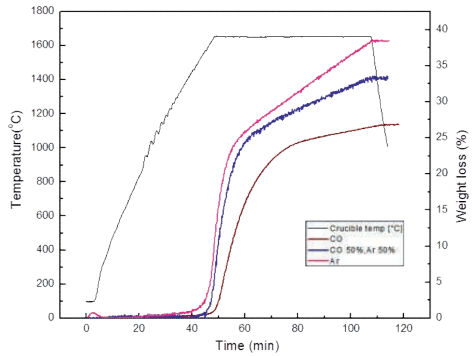

Figure 7: Effect on atmosphere of CO partial pressure showing weight loss (%) versus time.

According to figure 8[10], the opening area of sample holder that affects the gas transfer rate in and out of the crucible has significant impact on the reaction process. Four different sample holders with the varying opening area were used. The total opening area of the four types of sample holder are $7mm^2$, $10mm^2$, $86mm^2$ and $321mm^2$. All the four experiments started at the same time, while the reaction speed of SiC-producing step, the final weight loss and the reaction speed of SiO-producing increased when the opening area is bigger. The higher reduction rate is because, bigger holes on the sample holder provides more convenient pathway for mass transfer of gas products e.g. SiO and CO. The more timely removal of SiO and CO speeds up the reaction rate. For the SiC-producing step, faster mass transfer caused more SiO loss and lower CO partial pressure inside crucible, which caused the position of turning area of each experiment higher. For SiO-producing step, lower gas partial pressure makes reaction 6 happens faster.

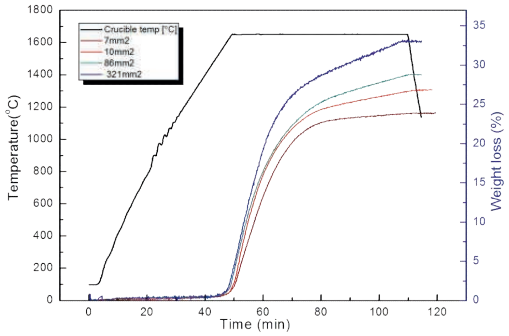

Figure 8: Effect of opening area for sample holder showing weight loss (%) versus time.

C. Influence of carbon content[9,10]

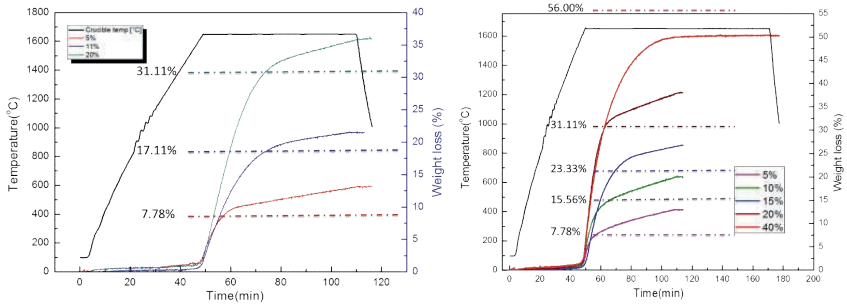

a) b)

Figure 9: Effect of carbon content in mixed pellets and carbon deposited pellets
a) Weight loss (%) versus time for mixed pellets
b) Weight loss (%) versus time for carbon deposited pellets

Figure 9 shows the influence of carbon content in mixed pellets and carbon deposited pellets. All the experiments can also be divided into SiC-producing step and SiO-producing step as described in the previous study. The theoretical weight loss of all carbon going to SiC for the pellet with the carbon content of 5 wt.%, 10 wt.%, 11 wt.%, 15 wt.%, 20 wt. % and 40 wt. % are 7.78 wt.%, 15.56 wt.%, 17.11 wt.%, 23.33 wt.%, 31.11 wt.% and 56 wt.% respectively.

As shown in Figure 9 a) and b), the weight loss curves bend over at the theoretical value of weight loss of reaction 7 except for the sample of mixed pellet with a carbon content of 40 wt.%. This indicates two things: 1) The SiO gas loss is still very low in most of the experiments during the SiC production; 2) The commercial carbon black and carbon obtained from methane cracking reaction reacts in a similar manner. The reason for the weight loss of mixed pellet with carbon content of 40 wt.% is ca.6 wt.% lower than the theoretical calculation is attributed to insufficient carbon contact area to react with SiO gas, because reaction rate between quartz and carbon black increased dramatically. The reaction rate increased according to the increase of carbon content.

D. Influence of pellet structure[10]

In this section, carbon content at 5 wt.%, 10 wt.% and 20 wt.% of mixed pellets and carbon content at 5 wt.%, 11 wt.% and 20 wt.% of mixed pellets were used for

comparison. Figure 10 were draw by thermo-gravimetric data extracted from Figure 8 to compare the difference of reaction process for mixed pellet and carbon deposited pellet. It is shown that carbon deposited pellets and mixed pellets have about the same reaction rate. As shown in Figure 10, all the weight loss curves started to rise at almost at same time. For the carbon content of 5wt.%, the weight loss curves almost overlap all the time except the position of turning area of carbon deposited pellets is higher than mixed pellet. This implies more SiO gas loss in carbon deposited pellet when carbon content is 5 wt.%. For the comparison for 10 wt.% of mixed pellet and 11 wt.% of carbon deposited pellet. Due to the 1 wt.% of carbon content difference, the weight loss curves are somewhat different. When carbon content is 20 wt.%, the weight loss curve is parallel at the SiO-producing step.

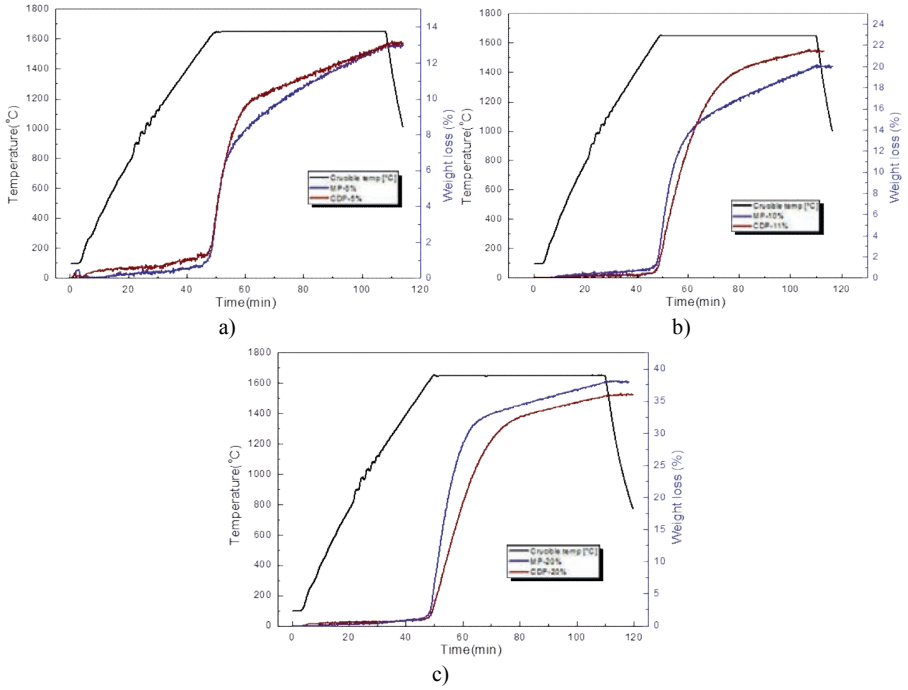

Figure 10: Comparison of weight loss (%) versus time for mixed pellets and carbon deposited pellets of carbon content. a) 5 wt% of carbon content for both types of pellets b) 10 wt % of mixed pellets and 11 wt % of carbon deposited pellets c) 20 wt% of carbon content for both types of pellets

IV. Conclusions

When the raw materials in silicon production process are charged in the form of agglomerate, the reactions in the furnace especially in the low temperature zone will be changed.

According to the theoretical heat balance, when the amount of agglomerate in the charge material increased, the temperature in the low temperature zone is decreased, end thence the SiO loss will be decreased. The energy consumption per ton Si decreased will decrease, while the Si yield will increase. Energy content in the off gas lost to environment or recovered in an energy recovery system will also decrease.

According to the experimental results, the reaction between quartz and carbon agglomerate can be divided into two stages, the SiC-producing step and SiO-producing step. At SiC-producing step, SiO_2 and C is reacting according to the reaction: $SiO_2(s) + 3\ C(s) = SiC(s) + 2\ CO(g)$. The reaction rate at SiO-producing step is quite slow and has a constant reaction rate. Higher temperature and lower CO concentration is positive parameters for SiC formation. The increase of carbon content in the pellet increased the reaction rate quite proportionally. By comparing the two different pellet structure, thicker carbon coating in carbon deposited pellet hinders reaction rate.

V. Acknowledgments

The authors acknowledge Elkem and the Research Council of Norway for the financial support through the project "235123 Silicon Production with use of Natural Gas". Also Halvor Dalaker from SINTEF and master student Henrik Lindgaard are acknowledged for helping with the carbon deposited pellets preparation.

References

1. Schei, A., Tuset, J. K. and Tveit, H: Production of High Silicon Alloys, Tapir, Trondheim, Norway 1998, pp. 25-72
2. V. Myrvågnes. Ph.D. Dissertation, "Analyses and characterization of fossil carbonaceous material for silicon production". Norwegian University of Science and Technology, Trondheim, Norway, 2008.
3. E. H. Myrhaug. Ph.D. Dissertation, "Non-fossil reduction materials in the silicon process-properties and behavior". Norwegian University of Science and Technology, Trondheim, Norway, 2003.
4. M. Tangstad, "Metal Production in Norway", Trondheim: Akademika Forlag, 2013.
5. W. Kjell. Ph.D. Dissertation, "Kinetics of reactions between silica and carbon". Norwegian University of Science and Technology, Trondheim, Norway, 1990.
6. Merete Tangstad. "Staged heat and mass balance of the Si process". Sintef report. Trondheim, Norway, 2012.
7. M. Takla a, N.E. Kamfjord, Halvard Tveit and S. Kjelstrup. "Energy and exergy analysis of the silicon production process". Energy, 58 (2013), pp. 138–146.
8. F. Li, M. Tangstad and I. Solheim, Quartz and carbon black pellets for silicon production. In The Fourteenth International Ferroalloys Congress (Infacon XIV) Energy efficiency and environmental friendliness are the future of the global Ferroalloy industry, (Kiev, Ukraine, 2015).
9. F. Li and M. Tangstad, Behaviour of quartz and carbon black pellets at elevated temperatures. In 2016 Annual Meeting of the Minerals, Metals & Materials Society, (John Wiley & Sons, Inc.: Nashville, USA, 2016).
10. F. Li and M. Tangstad, Carbothermal reduction of quartz with carbon from natural gas. Metallurgical and Materials Transactions B (2016, under review).

Phase transformations in quartz and it's effect on furnace operation

Eli Ringdalen[1)], Merete Tangstad[2)]
1) Sintef, Norway,
2) NTNU, Norway

Abstract

Quartz (SiO_2) is the main silicon source for production of metallurgical grade silicon in submerged arc furnaces. During heating in the furnace, quartz will first transform to other SiO_2 polymorphs, then soften and melt. These changes may affect furnace operation. This can be either by increased fines generation, by melting that reduces gas permeability or by affecting rates for SiO generating reactions. Formation of cristobalite from β-quartz goes through an amorphous phase. Its amount depends on temperature and quartz source. Reaction rate for SiO-forming reaction and melting properties are both believed to be affected by amount of amorphous silica. Phase transformation in silica may through this affect both temperature distribution and mass flow in sub-merged arc Si-furnaces.

Introduction

Silicon is produced in submerged arc furnaces, as illustrated by the sketch in Figure 1. The main raw materials, quartz and reductants are added to the top of the furnace.
Energy, around 11-13 MWh/ton alloy for Si production, is another important input factor. The electrical energy is supplied through electrodes. An electric arc is generated between the electric tip and carbon containing crater walls or liquid silicon bath. This generates a high temperature zone in the crater where silicon is produced at approximately 2000ºC. Liquid metal, at approximately 1500ºC, is tapped at the bottom of the furnace.

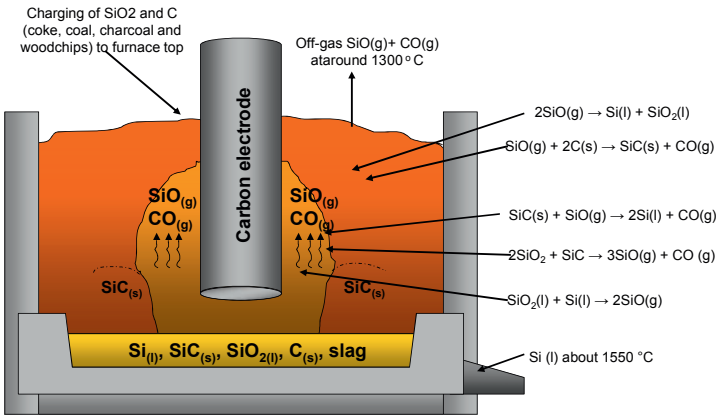

Figure 1: Sketch of Si furnace with critical reactions. Revised after[1].

The reduction of silica to Si takes place by the overall reaction (1).

$$SiO_2 + 2C = Si + 2CO \qquad H^o_{2000^oC} = 687 \text{ kJ/mol} \quad (1)$$

In industrial furnaces, the reactions take place in several steps as described by Schei et al. [2]. These are described more in detail and discussed in the next chapter.

Both a high silicon yield and a stable furnace operation are needed to achieve good results and low energy consumption. To obtain a high silicon yield, the off gas must have a low SiO-content. To obtain a good furnace performance, there must be an even gas flow and a good charge permeability in the furnace.

Reactions and material flow in silicon furnaces

The charge mixture consisting of carbon and quartz are fed to the top of the charge mixture. In the upper part of the furnace, material flow and contact and reaction area between quartz and other phases depend on its percentage of the total volume of raw materials In a furnace operation with 100 % carbon coverage 2 mol of carbon as fix C is added for each mol of quartz. Various carbon sources as coal, coke and charcoal are used. Wood chips are normally added to obtain a more porous charge mixture. Quartz has highest density, around 2,65 kg/m^3 and its volume % will be lower than its weight % while this is opposite for wood chips. A typical charge mixture may contain around 25-volume % of quartz. Particle size of the quartz is usually larger than for the other raw materials, often around 50 mm and more than 10 times large than carbon particles. In a charge mixture where the wood chips are still intact and the quartz has not disintegrated, quartz will have little effect on the permeability of the charge. Its surface area which are of importance for the reaction rate is also low. This will change when the temperature increase and silica properties may then affect both gas permeability and rate for SiO- forming reactions.

The temperature at the top of charge mixture is around 800-1300 °C [3]. When the raw materials descend further down, they are heated at different rates varying both with operation and with distance from the electrodes. For Si furnaces, a heating rate of 5.5 ºC/min is estimated [4]. It will then take around 3 hours to heat the charge from 25ºC to 1000 ºC and additional 3 hours for further heating to 2000 ºC. These are average values and material flow and temperature distribution will vary both vertically and horizontally. It is affected by extent of the exothermic reactions. There is as discussed by Ksiazek [5] be a temperature gradient inside the quartz particles and time needed to heat the centre of a silica particle vary with its size.

In the upper part of the furnace, descending raw materials, fed to the top of the furnace, meet ascending SiO and CO gas. Here carbon react to SiC by reaction (2) and the ascending SiO gas react to "condensates" according to reaction (3) and (4). In the lower part of the furnace, where the temperatures reach more than 2000 °C, Si is produced by reaction (5). SiO gas required for this reaction and for SiC production in the upper part of the furnace is produced from SiO_2 by reactions (6) and (7). Dominant reactions and their stability depend strongly on the partial pressures of SiO and CO.

$$2C(s) + SiO(g) = SiC(s) + CO(g) \qquad H^o_{1800^oC} = -78 \text{ kJ/mol} \quad (2)$$

$$2SiO(g) = SiO_2(s,l) + Si(l) \qquad H^o_{1800^oC} = -606 \text{ kJ/mol} \quad (3)$$

$3SiO(g) + CO(g) = 2SiO_2(s,l) + SiC(s)$ $\Delta H^o_{1500^oC} = -1380$ kJ/mol (4)

$SiC(s) + SiO(g) = 2Si(l) + CO(g)$ $\Delta H^o_{2000^oC} = 167$ kJ/mol (5)

$SiO_2(l) + Si(l) = 2SiO(g)$ $\Delta H^o_{2000^oC} = 599$ kJ/mol (6)

$2SiO_2(s,l) + SiC(s) = 3SiO(g) + CO(g)$ $\Delta H^o_{2000^oC} = 1364$ kJ/mol (7)

The final product: Silicon is produced by reaction (5) at temperatures above 1811^0C. The gas in the Si-furnace is a mixture of CO and SiO at 1 atm. pressure. To produce Si at 1811 ^{0}C by reaction (5), partial pressure of SiO must be higher than 0.67 [2]. To achieve a high Silicon yield, SiO-gas should preferably be produced at temperatures above 1811^{o}C. For reactions with quartz, reaction (6) and (7) a slow reaction rate at low temperatures is thus preferable.

SiO produced at lower temperatures than 1811 ^{o}C, e.g. higher up in the furnace may either react with carbon to SiC by reaction (2), be captured in the furnace by reaction (3) and (4) or leave the furnace with the off-gas. Reaction (3) and (4) are highly exothermic. A surplus of SiO produced in the lower part of the furnace that condenses in the upper part will thus transport energy to increase the temperature in the upper part of the furnace.

To achieve a high silicon yield, the SiO gas must not leave the furnace with the off-gas, but react according to reactions (2), (3) or (4). The reaction products from (3) and (4), the "condensates" are sticky, will glue the charge materials together and hinder material and gas flow in the furnace. Gas flow and permeability in Si-furnaces are believed to be more affected by condensates than by amount of fines and size distribution. At 1726 ^{o}C. SiO_2 melts to viscous fluid that will also affect material and gas flow as well as reaction rates. Softening of SiO_2 particles giving a semi--molten surface that start before they reach the melting temperature will also reduce gas permeability and reaction rates.

Phase transformation in quartz

When quartz is heated, its structure will change to different SiO_2 polymorphs as shown in the phase diagram in Figure 2 [6].

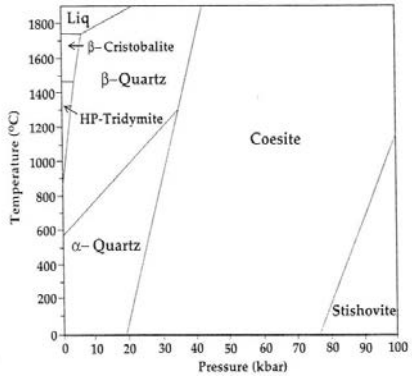

Figure 2. SiO_2 phase diagram [6]

When heated in air at 1 atm α-quartz is transformed to β quartz at 573 °C. This transformation is fast and will be reversed during cooling. It will lead to an increase in volume of around 0.4% According to the phase diagram tridymite will be formed at 873°C. It is debated if this phase change really will take place or if β quartz alternatively will be transformed directly to β cristobalite at a temperature somewhere between the temperature for tridymite formation from the phase diagram and the melting temperature for SiO_2 at 1711 °C. During this transformation, the volume will increase with around 17%. When it is cooled, β cristobalite is transformed to α-cristobalite and not back to the stable phase, α-quartz. The large increase in volume by the phase transformations will give a lower density and a higher specific surface area after heating. Cracking as a result of the volume change will contribute to the higher surface area. The transformation from α-quartz to β-cristobalite is slow and in experiment by Wiik [7], the quartz was heat treated at 1400 °C for 5 days in order to achieve complete transformation to cristobalite. The rate for the phase transformation from α-quartz to β-cristobalite has as illustrated in Figure 3 been shown to vary considerably between different quartz sources [8,9]. With further heating, the quartz will soften and melt. The melting temperature is 1726 °C. During heating the quartz will first start to soften, normally at a temperature lower than 1726 °C, and not be completely molten until the temperature is considerably higher than 1726 °C. Melting properties vary as shown in Figure 3 between quartz sources and depend on heating rate. [8,10].

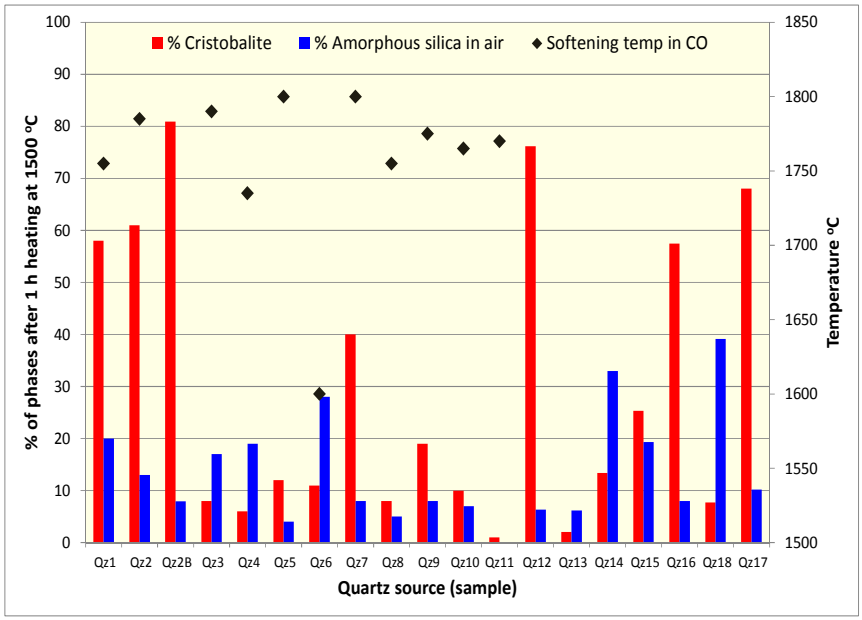

Figure 3 Amount of cristobalite and amorphous silica in different quartz samples after heating for 1 hour at 1500 °C. Softening temperatures for sample Qz 1-11 are also included.[8]

Amount of cristobalite has earlier been proposed [8, 11] to be of importance for reaction rate. Ongoing unpublished research has so far not given any conclusive results regarding this. The α-quartz – β cristobalite transformation is as described by Wiik [7] assumed to go through an amorphous phase. The amorphous phase is

expected to be more reactive than the crystalline phases and might as indicated by Doris [11] also affect the melting properties, possibly giving a lower softening temperature. Amount of amorphous phases may thus be of importance for reactions and performance in Si-furnaces. Appearance of the amorphous phase has in addition to earlier investigations [8] recently been investigated as summer and student project by Kjelstadli [12,13]. Results from these and earlier investigations are here summarised and discussed.

Formation of cristobalite and amorphous phase were investigated by heating of quartz in air in a rapid heating furnace by the method described by Ringdalen [8]. The amounts of different phases in the samples were measured by quantitative XRD. (Bruker D8 advance with the software Diffrac Plus Topaz). The amount of amorphous silica was determined by the method described in detail by Kjelstadli [13]. The main principle is to add a known amount of a crystalline phase, and to calculate amount of amorphous silica based on this known amount and the XRD measurements. The bias in the measured results is calculated to ± 2 weight % (absolute %).

Amount of cristobalite and amorphous silica after a certain heating time were in earlier investigations [8] found as illustrated in Figure 3 to vary considerably between different quartz sources. It was also as shown in Figure 4 found that amount of amorphous phase first increased up to a level and the decreased again while amount of cristobalite increased. The rate of formation of amorphous silica and its maximum values also varied between different quartz sources. The described trend in amount of amorphous phase is taken as a strong support to the theory [11] that cristobalite formation goes through an amorphous phase.

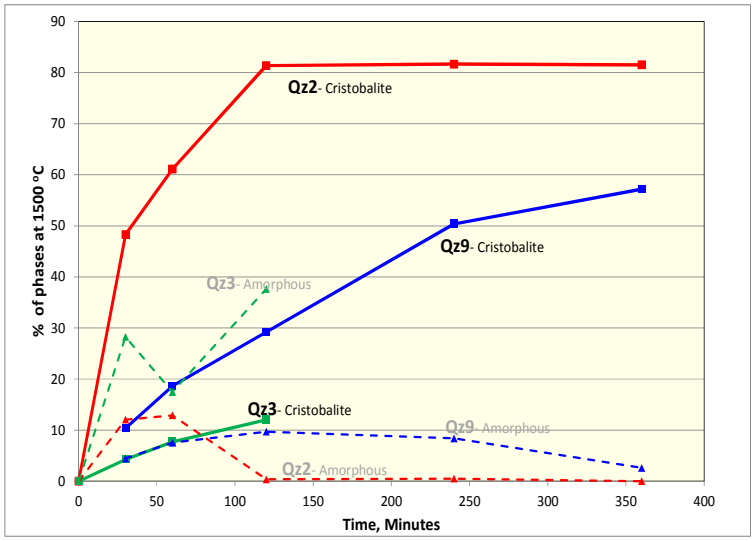

Figure 4 Effect of time on formation of cristobalite and amorphous silica when different quartz sources are heated in air at 1500 °C [8].

At 1500 °C, transformation to cristobalite is relatively slow. In order to evaluate its effect of reactions with silica, it will be important to know if the intermediate amorphous phase is formed also when the transformation takes place at higher

temperatures. Cristobalite formation in one of the quartz sources, Qz 9 was therefore investigated at higher temperatures by KjelstadliKjelstadli [12, 13]. The data from the different investigations of Qz 9 are combined in Figure 5.

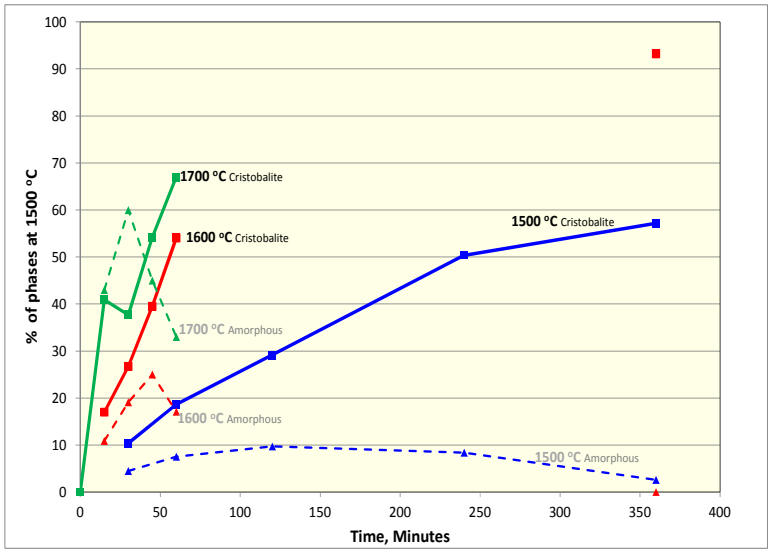

Figure 5 Effect of temperature and time for formation of cristobalite and amorphous silica for one quartz source, Qz 9, heated in air. Investigations at 1500 °C and at 1600 °C after 6 hours by Ringdalen [8] and the remaining investigations from Kjelstadli [12, 13]

When quartz Qz 9 is heated to 1600 °C and 1700 °C, amount of amorphous silica will act similarly as when it is heated to 1500 °C, first increase and then decrease again, while amount of cristobalite increase continuously. Transformation from β-quartz to cristobalite thus seems to go through an amorphous phase at temperatures from 1500 ^{0}C and higher. Maximum amount of amorphous silica and rate of formation of cristobalite and amorphous silica increase with increasing temperature. Even at temperatures as high 1700 °C, it takes more than 1 hour before the investigated quartz, Qz 9 is completely converted to cristobalite. After 30 minutes, the sample contains 60 % amorphous silica. It is hence likely that quartz at its melting temperature of 1726 °C will contain some amorphous silica that may effect the melting properties of the quartz.

The results in Figure 5 are based on quartz particles in the size 1-2.8 mm with an average size of 1.9 mm. The effect of size was investigated by Kjelstadli [13] in the same apparatus by using larger pieces, average sizes 33 mm and 42 mm. An intermediate amorphous phase was as shown in Figure 6 also present during cristobalite formation in these larger particles. In these investigations, only one particle was used. The weight of one 33 mm particle is 50 gram, the same as the weight used in the investigations of 1-2.8mm particles. One 42 mm particle weighs 100 gram, twice the mass used in the other investigations. Only one sample has been tested for each of the conditions. Statistical data for the samples are thus not known and the results are only indicative. Amorphous content in the 33 mm sample heated for 20 minutes is contradictory to other results and in further discussions regarded as an outlier.

To see if observed variation between different quartz sources after 1-hour at 1500 ºC also could be found at conditions more similar to those in industrial furnaces, larger particles, 42 mm and 33 mm were heated to 1600 ºC for shorter times. The results for amorphous silica are shown in Figure 7. Amount of cristobalite was below 10 % and mostly below 5 % in all the samples

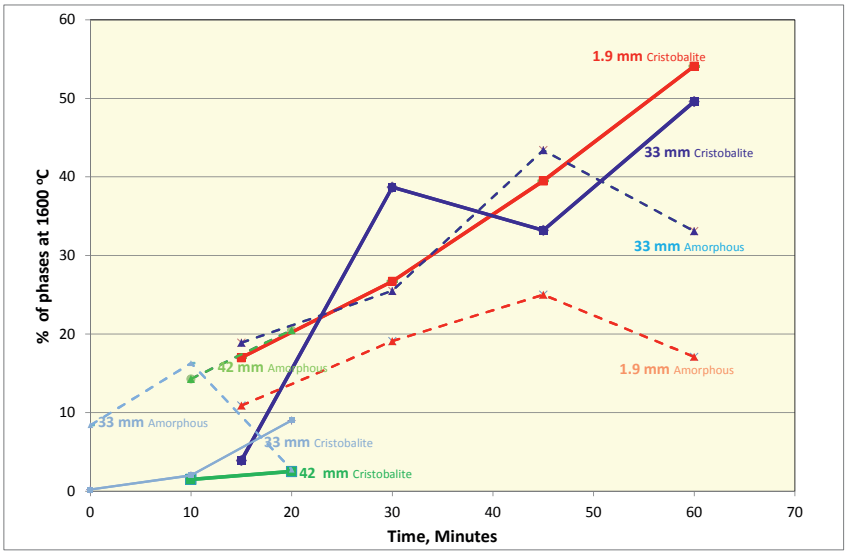

Figure 6 Effect of particle size on amount of cristobalite and amorphous silica for quartz source, Qz 9, heated for different times in air at 1600 ºC. From Kjelstadli [12, 13]

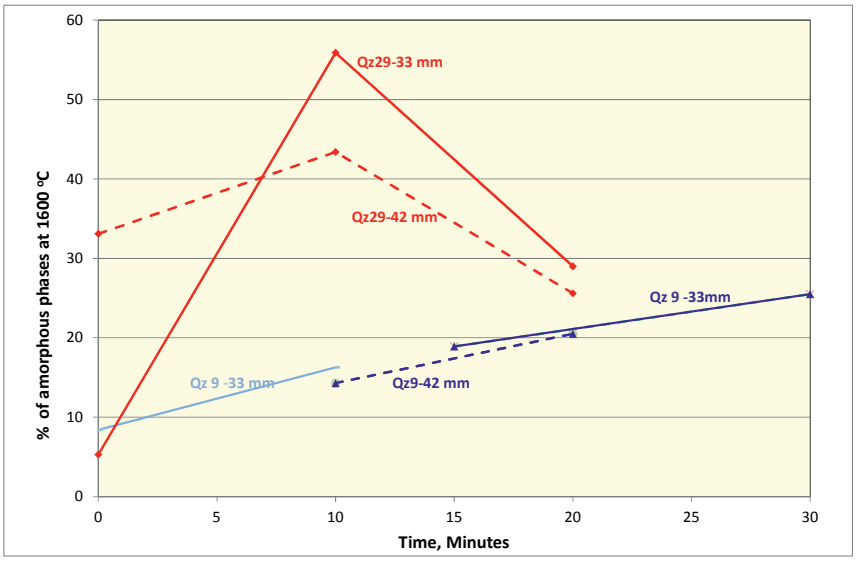

Figure 7 Effect of quartz source and particle size on amount of amorphous silica formed after different heating times.

For all investigated cases both different quartz sources and different sizes, amount of amorphous phase first increases and then decreases again supporting the theory that formation of cristobalite goes through an amorphous phase.

Cristobalite formation might either propagate from the surface of the particle and inwards, topochemical or simultaneously throughput the whole grain by nucleation. The rate-determining step either may be transformation from quartz to amorphous phase, transformation from amorphous phase to cristobalite, heating of the particle, or may be most likely a mixture of these. More investigations is needed to clarify both the mechanism for transformation and the rate determining step, but the achieved data gives valuable information about quartz properties.

Stevens [14] proposed that cristobalite formation takes place by nucleation which is supported by observation of particles by Kjelstadli [12, 13]. The nearly similar values for amount of cristobalite formed after different times for 50 gram of 1.9 mm and 33 mm particles support this. The amount formed in the 42 mm particle is considerably lower, but this is a larger mass, 100 gram and only heated for a shorter time so it might not be completely heated to target temperature. The data obtained so far shows that maximum amount of amorphous phase increases with increasing temperature and increasing particle size. At higher temperatures, shorter time is needed to obtain the maximum amount of cristobalite. Maximum amount vary with quartz source. High amount of amorphous phase is found after 30 minutes at 1700 ^{o}C.

Effect on Silicon furnaces of phase transformation in quartz

Phase transformation in quartz may affect performance of silicon furnaces in different ways:

Increased amount of fines and reduced gas permeability

Volume expansion during transformation from quartz to cristobalite may give cracking and fines generation. Earlier investigations [9] did not show any correlation between amount of fines and cristobalite. Fines generation and variation in amount of fines are believed to be caused by other mechanisms than phase transformation. Only around 25% of the total charge volume is quartz so a large amount of fines must be formed before it will have a pronounced effect on gas flow Sticky condensate and molten quartz are both in addition believed to have important effect on gas permeability. The relative effect of different parameters is not known.

Reduced gas permeability and reduced material flow due to melting of quartz

Softening of quartz and further melting to a viscous fluid will glue the charge mixture together and reduce gas permeability. This is a consequence of the melting and not a result of the solid-state phase transformation. Earlier investigations [8] illustrated in Figure 3 have shown that melting properties vary between different quartz sources. With lower softening and melting temperatures, silica will start to melt higher up in the furnace. More of the furnace volume will then contain molten quartz and the charge may have a lower permeability. High melting temperatures are thus regarded as most favourable. Existence of amorphous phase is proposed to enhance melting [11]. As shown in Figure 5 quartz heated to 1700 ^{o}C, which is close to the melting temperature, may contain high amount of amorphous phase, which will possibly

affect melting properties. Similarly as for fines generation, the relative effect on gas permeability of molten phases versus effect of condensates is not known.

Increased formation of SiO-gas in the upper part of the furnace

SiO-gas is formed with reaction (6) and (7) both involving quartz. Rate for these reactions are assumed [3] to be affected by type of silica polymorph, and to change when silica melts to liquid phase. SiO should preferably be produced in the lower parts of the furnace and at temperatures above 1811 ^{o}C. A low reaction rate in solid state and in liquid state up to 1811 ^{o}C is thus preferred. A liquid phase will generally have higher contact area with other phases and increased reaction rate. Melting at higher temperatures are then favourable. Both cristobalite and amorphous silica have been proposed to increase reaction rates [8]. Amount of both of these vary between quartz sources. Amount of cristobalite increases with increasing temperature and holding time while amount of amorphous phase will be more dependent on heating rates. Since low reaction rates are preferable, low amounts of cristobalite and amorphous phase is also preferred.

Conclusions

Investigations of phase transformations in industrial quartz sources have shown that when quartz is transformed to cristobalite, an intermediate amorphous phase is formed. This is seen for particle sizes from 1-44 mm and for different quartz sources. Maximum amount of amorphous silica and rate of formation of both cristobalite and amorphous silica increases with increasing temperature. High amount of amorphous silica is formed at 1700 ^{o}C and this might affect softening and melting properties.

Phase transformation in quartz may affect furnace performance in various ways. Volume expansion during phase transformation may contribute to cracking, fines formation and reduced gas permeability. Amorphous silica may reduce softening temperature and contribute to more sticky material and reduced gas permeability. Higher reactivity of cristobalite and amorphous phase relative to quartz may increase formation of SiO-gas in the upper parts of the furnace and contribute to higher losses of SiO gas or more condensate formation. Relative importance between these effects and towards other parameters are not known. For furnace operation, it is s regarded as most favourable that the quartz has low maximum amount of amorphous silica, low rate for formation of amorphous silica and cristobalite, high softening temperature, and low amount of amorphous silica at high temperatures.

Acknowledgements

This work is based on results generated in the research projects ESiP funded by Elkem and the Research Council of Norway (RCN) and in the project SFI Metal Production funded by RCN and Norwegian metal industry. They are all acknowledged.

References

1 Kvande R: Trial Lecture, PHD dissertation, Trondhein, Norway 2008

2 A Schei A., J K Tuset J.K., and H. Tveit, Production of High Silicon Alloys, Tapir forlag, Trondheim, Norway, 1998, ISBN: 82-519-1317-9.

3 Ringdalen, E. and Tangstad, M: Reaction Mechanisms in Carbothermic Production of Silicon, Study of Selected Reactions, Proceedings of International Smelting Technology Symposium

(Incorporating the 6th advances in sulphide smelting) held during TMS 2012, Editors: Jerome P Downey, Thomas P Battle, Jesse F White p. 195 – 204. ISBN 978-1-11829-116-0

4 Tveit Halvard, Elkem: Personal communication 2015

5 Ksiazek M: The thermophysical properties of raw materials for ferromanganese production; PhD thesis, NTNU Trondheim 2012, ISBN 978-82-471-3360-6, ISSN 1503-8181

6 Kurt Aasly: Properties and behaviour of quartz for the silicon process. PhD thesis 2008:236, NTNU Trondheim, Norway 2008, ISBN 978-82-471-1163-5

7 Kjell Wiik, Kinetics of reactions between silica and carbon. PhD thesis 1990-60, NTNU Trondheim ,Norway 1990; ISBN: 82-7119-170-5

8 Ringdalen E: Changes in quartz during heating and the possible effects on Si production; JOM (The Journal of the Minerals, Metals&Materials society (TMS) October 2014, ISSN 1047 -4838, DOI 10.1007/11837-014-1149-y

9 Ringdalen E: Quartz properties in the silicon production: Silicon for the Chemical and Solar Industry XII, Trondheim, Norway 2024, Proceedings page 7-18. ISBN 978-82-997357

10 Ringdalen E, Tangstad M: Softening and melting of SiO2, an important parameter for reactions with quartz in Si-production: Molten Slags and fluxes. Seattle, USA 2016, To be published

11 Doris Kuhlman_Wilsdorf: Theory of Melting, Physical Review Letters, Volume 140, A1599 November 1965 DOI:http://dx.doi.org/10.1103/PhysRev.140.A1599

12 Kjelstadli, M, E: Kinetics and Mechanism of Phase Transformations from Quartz to Cristobalite; Summer work, NTNU, Norway, 03.08. 2015.

13 KjelstadliKjelstadli, M, E: Kinetics and Mechanism of Phase Transformations from Quartz to Cristobalite; Specialization Project, NTNU, Norway, Fall 2015.

14 S. J. Stevens, R. J. Hand, and J. H. Sharp. The polymorphism of silica. Journal of

Materials Science, 32:2929{35, 1997..

Assessment of production performance of quartz in the Si-furnace

Kurt Aasly[1)], Vishu Dosaj[2)]

1) NTNU, Norwegian University of Science and Technology, Department of Geology and Mineral Resources Engineering, NO-7491 Trondheim, Norway; kurt.aasly@ntnu.no

2) Dow Corning Corporation, 2200 Salzburg Road, Midland, Mi. 48686-0994, USA Vishu.dosaj@dowcorning.com

Abstract

This paper has attempted to correlate furnace performance to thermal and chemical properties of quartz. Eleven different types of quartz samples used for commercial silicon production were tested for furnace performance. They represent quartz of different origin ranging from vein quartz to gravel quartz. These quartz raw materials are all used in Dow Corning´s furnaces in Brazil and the USA. The shock heating tests to determine the decrepetation of quartz samples was carried out in an induction furnace at 1300 °C for 10 minutes and cooling at ambient temperature. The resulting samples after heating were screened for grain size distribution and further analyzed by XRD to evaluate the quartz to cristobalite conversion. The samples were also analyzed for chemical impurities. The amount of quartz to cristobalite phase transformations and the fines generation were a good predictors of the performance of these quartz deposits in commercial production of silicon.

Introduction

Dow Corning produces silicon in electric reduction furnaces at two plants in Brazil and one in the US. Each plant uses quartz that is mainly mined locally. The quality of the quartz in terms of chemistry and mechanical and thermal strength varies from deposit to deposit. The thermal strength and chemistry of quartz are key considerations for efficient production of silicon. This paper discusses the results of shock heating experiments and cristobalite generation using eleven quartz samples that were obtained from Dow Corning's manufacturing sites. These results are seen in relation to furnace experience for all eleven samples.

Silicon is typically produced in a three-electrode, AC submerged electric arc furnace by the carbothermic reduction of crystalline silicon dioxide (quartz) with carbonaceous reducing agents. The reductants consist of a mixture of coal, charcoal, petroleum coke, and wood chips. The overall reaction for the production of silicon is expressed as shown in (1).

$$SiO_2 + 2C \rightarrow Si + 2CO \quad (1)$$

The production of silicon takes place via two key intermediates, silicon monoxide (SiO), and silicon carbide (SiC). In the high temperature zone of the furnace below and around the electrode, SiC reacts with SiO_2 to produce silicon, SiO, and carbon monoxide. As the gaseous SiO and CO ascend through the charge bed, the SiO reacts

with the carbon reductants to produce silicon carbide. The silicon carbide, produced in the upper and middle zone of the furnace, reacts with SiO_2 to produce silicon. The silicon produced is periodically or continuously tapped. Rising SiO reacts with the carbon in the bed and is converted to SiC and the process repeats itself. Carbothermic production of silicon is thoroughly described by [1]. The quality of the silicon is controlled by careful selection of the raw materials. This is especially true for impurities such as Fe and Ti and P, which are more difficult to remove by refining.

Previous Work

The methods used for the investigations presented in this paper are based on earlier work on thermo-mechanical properties of quartz by [2] and [3]. In the work presented by [2] and [3], six different quartz samples were tested using several approaches to characterise thermo-mechanical properties of quartz. As described by [4], the industry uses different methods for assessing the thermal properties of the quartz raw material. The results are all used as indications of these properties and may indicate variations within deposits and shipments, depending on the mode of sampling. Their work presented results from shock heating of quartz in induction furnace to 1300 °C and 1500 °C and indicated that polymorphic properties of quartz are important factors for the thermo mechanical properties of metallurgical quartz. The authors utilized many techniques showing that several inherent properties in quartz such as the content of fluid inclusions in the quartz grains and the amount of impurity minerals, especially mica minerals influence thermo-mechanical properties of different quartz raw materials. Additional work by [3] showed that micro textures and the polymorphism of different types of quartz influences the thermal properties of quartz.

Research work on quartz has been followed up in recent yeas by e.g. [5, 6]. Their work has focused on cristobalite formation in quartz and is considered important for understanding as to how quartz will respond to shock heating and the reactions in the furnace for production of silicon [3] and [5].

Impact of quartz quality on Furnace Performance

There are three main considerations in selecting quartz for producing silicon [1]:

- Chemical analysis (Fe, Ti, Al and P, Tot Si >99.5%)
- Mechanical strength
- Thermo-mechanical strength

Depending on the impurity content of the quartz, it may be used to produce silicon for either Aluminum or Chemical industry. Primary Aluminum grade silicon requires low iron content whereas the silicon used to produce methyl chlorosilane requires low titanium content. The iron, titanium and phosphorus contents in quartz are important since these impurities cannot be economically refined from molten silicon. Aluminum and calcium levels in quartz can be flexible as they can be refined by treating molten silicon with oxygen containing gases.

Mechanical strength of quartz is important for mining, transportation and handling of quartz from mine to the plant and eventually to the furnace. Generation of fines due to mechanical properties of quartz can result in feeding excessive fines to the furnace.

A quartz with adequate thermo-mechanical strength is desirable for good furnace operation. Poor quality quartz results in generation of fines in the furnace as a result of thermal shock as the quartz is charged in the furnace. The temperature on top of the furnace can vary between 300 – 1000 deg. C. Poor quality quartz breaks down generating fines due to thermal shock and also during stoking of the furnace. These

fines result in reducing the porosity of the bed. The gas pressure in the furnace also becomes high. Reduced bed porosity can result in blowhole around the electrodes and on top of the furnace. On the charge top, there may be problems with gas blows throwing charge material from the charge top on to the stoking deck. In extreme cases the SiO escapes the furnace through the tap hole in form of a strong flame. Breakdown of quartz due to poor thermal strength can also be observed by the presence of small quartz pieces on the stoking floor of the furnace. Cracking sound produced when quartz breaks due to thermal shock in the furnace bed is also an indicator of quartz thermal strength. On the other hand good quality quartz or quartz mixes result in minimal gas blows, higher silicon yield and better process performance [1, 3, 7].
In order to qualify new quartz deposits, raw materials have to be systematically tested and the test should be capable of giving reproducible results. Getting representative samples is very important. Effort should be made to obtain samples away from the blast areas [8]. As a final test of the quartz deposit, the quartz should be evaluated in a commercial furnace for a period of approximately two weeks.

Materials and Methods

Materials

In total 11 samples were studied by shock heating and resulting cristobalite generation by holding the samples in the induction furnace for a period of ten minutes at 1300 ºC. Similar experiments have been performed by [9] and also reported in [3]. The quartz samples were obtained from the stock piles at three of Dow Corning's production units namely Dow Corning Para and Dow Corning Minas in Brazil and Dow Corning Alabama in USA. Five samples came from the Para site, four from the Minas site and two from the Alabama site.
In manufacturing operations, technical information regarding the quartz deposits is mainly related to metallurgical nomenclature i.e. (rock or gravel, quartz or quartzite), impurity content, thermo mechanical properties and furnaceability. Thus, there is a lack of knowledge about history and geological origin of some of the quartz raw materials discussed in this paper. A "qualified guess" as to the history and geological origin of the quartz deposits is provided based on information received and the appearance of the quartz fragments.
Table 1 contains description of the origin, type and typical appearance of each of the 11 samples investigated in this research. Typical industrial sources for quartz are quartzite, hydrothermal veins and pegmatite. Both the former types are represented in this set of samples. The pegmatite on the other hand may be difficult to distinguish from the hydrothermal vein quartz, without further geological descriptions of the deposit.
The "gravels" typically represent river gravels with various source rocks. As the size of the river gravels used as quartz raw materials need to fulfill size requirements of the silicon process combined with requirements to chemical purity, the source rocks for produced river gravels must also here be quartzite, hydrothermal veins or pegmatite. Although, large pieces of pure quartz deposited as river gravels, also may represent pockets or areas with high quartz content in the source rocks. In the latter case, the quartz is the most resistant mineral to weathering and would normally survive erosion processes longer than other rock forming minerals in e.g. granites.
Most samples appeared grey to white in color with hints of yellow, red or purple. These weak color shadings probably indicate low degree of impurity, especially for iron. Apart from color shading, few signs of impurity is visible, except from in Sample H where clay minerals frequently appear, as filling materials, in cavities.
From a mechanical-strength point of view, some of the samples may show visual indications of brittleness that may affect its mechanical strength. In such samples fines

could be generated during transport and handling. Sample I appears more brittle and is likely to generate more fines during handling processes compared to most gravels and Sample F. Mechanical strength was not tested by any of the methods used in this project.

Table 1: Specific sample descriptions including deposit type and origin of the sample

Sample	Deposit	Origin	Comments
Sample A	Rock	Brazil	Relatively coarse grained, yellowish-brown quartz. Appears more or less massive, but with some preferred orientation or cleavage that may be weaker to mechanical interaction. No visible impurities. Most likely representing a vein quarts.
Sample B	Gravel	Brazil	Rounded boulders of quartz from river gravels. Weak color variation from grey to grey with hint of purple. Semitransparent in places. No visible impurities. Grain size of boulders typically 2-4 cm.
Sample C	Gravel	Brazil	Whitish grey massive quartz boulders, typically 4-6 cm. No visible impurities. Corners of fragment is well rounded but main shape still intact.
Sample D	Gravel	Brazil	Whitish grey to week brown quartz boulders. Relatively well rounded with some spots showing traces of iron-hydroxides (reddish-brown). Typically 4-8 cm. Tested sample was grey.
Sample E	Gravel	Brazil	Whitish grey massive quartz. Semi rounded with no trace of impurities. Typically 6 cm.
Sample F	Rock	Brazil	Greyish to white-grey, fine grained quartz. Appears massive and probably represent recrystallized quartz?
Sample G	Rock	Brazil	White coarse grained quartz with no visual impurities. Quartz appearance suggests a vein type quartz.
Sample H	Rock	Brazil	Coarse grained, clear to weak purple quartz. Appears brittle and with frequent cavities that are sometimes filled with impurity minerals like kaolin and other clay minerals. Some rusty – red spots of oxidized iron minerals?
Sample I	Rock	Brazil	Clear – white quartz Appears coarse grained with brittle texture. Fractures leave sharp edges of quartz.
Sample J	Gravel	USA	River gravels with three main appearances: Yellowish white, greyish white and beige white quartz. All are massive and would be difficult to distinguish without comparison. Probably a quartzite source rock. The variant tested was greyish white.
Sample K	Gravel	USA	River gravel with mainly three appearances: White-grey quartz, yellowish with purple spots and clear brownish quartz. All appear massive. Source rocks for the two first types are probably meta-sandstone/quartzite whereas the clear brownish quartz may be of vein type origin. Purple spots are probably due to iron? The variant tested was white-grey.

Methods

Sample preparation for shock heating of quartz lumps

Quartz samples were mainly prepared by hammering of larger pieces to suitable size. Some samples were originally of suitable size to be used directly. Requirements set for the samples to be tested were:

- Should be approximately 190 g (+/-)
- Preferably one piece of lump

X-Ray Fluorescence (XRF)

XRF analyses were performed at NTNU, Department of Geology and Mineral Resource Engineering, using a Bruker XRF S8 Tiger unit and the data were analyzed with Spectra Plus software. Major element analyses were performed on fused glass pills and trace element analyses was performed on pressed powder tablets. LOI of the bulk sample was determined gravimetrically after ignition at 1000°C. The LOI was calculated in as part of the total analyses.

X-Ray Diffraction (XRD)

XRD data were collected at NTNU, Department of Geology and Mineral Resource Engineering, on a Bruker X-ray Diffractor D8 Advance using 40 kV, 40 mA, and CuK_ radiation. The results from the X-ray diffraction were interpreted using the Bruker EVA® software to find a predefined crystal structure suited mineralogy (ICDD database) fitting the 2θ-intensity data. Then the mineralogy found was imported to the software Topas Rietveld XRD and a structural refinement was performed.

Shock heating

Shock heating of quartz samples was performed according to the procedures established by [3]. A lab scale induction furnace type IF75 with graphite crucible was preheated to 1300 °C. As the temperature reached the target temperature, one quartz sample was carefully inserted in to the graphite crucible and the thermocouple was placed on top of, or immediately next to the sample for temperature monitoring. Few minutes after placing the sample, the internal of the crucible reached the target temperature as shown in Figure 1. Because of the nature of the furnace control, the temperature exceeded the target temperatures slightly before dropping back to the target temperature. After holding the sample inside the furnace for 10 minutes at the target temperature, it was carefully removed and cooled to ambient temperature.

Particle size analyses

As result of shock heating some quartz samples break down in to smaller fragments. The entire sample is subjected to particle size analysis carried out on a set of screens, according to standard industry procedures as described e.g. by [e.g. 10, 11] and Aasly [3]. The three indicators for characterizing the thermal strength of quartz are:

- Dust Index (DI): Defined as the percentage of sample less than 2 mm
- Fines Index (FI): Defined as the percentage of sample less than 10 mm
- Thermal Strength Index (TSI): Calculated according to equation 2.

$$TSI = \frac{(\%>20\ mm)+(\%>10\ mm)+(\%>4\ mm)+(\%>2mm)}{4} \quad (2)$$

In the original equation described by e.g. [10, 11], the ranges are all below 25 mm, as the starting grain size in their work was <25 mm. In this research all samples are >25 mm and thus some samples contains fragments >25 mm even after heating.

Results

Chemical analyses by XRF

The eleven quartz samples evaluated for thermal shock resistance were also analyzed for chemical impurities. Major and trace element contents are summarized in Table 2 and Table 3.

Table 2: Major element analyses of quartz samples by XRF. *=LOI at 1000 ºC; P_2O_5, Na_2O, MgO and MnO had all results <det. limit.

Sample	Fe_2O_3 (%)	TiO_2 (%)	CaO (%)	K_2O (%)	SiO_2 (%)	Al_2O_3 (%)	LOI (%)*	Sum (%)
Quartz A	0,09	0,00	0,04	0,01	98,66	0,09	0,11	99,00
Quartz B	0,06	0,02	0,03	0,01	97,44	0,09	0,11	97,75
Quartz C	0,07	0,01	0,04	0,01	98,22	0,14	0,09	98,58
Quartz D	0,07	0,00	0,03	0,01	98,40	0,09	0,09	98,69
Quartz E	0,08	0,01	0,03	0,01	98,00	0,29	0,13	98,55
Quartz K	0,07	0,01	0,03	0,01	98,48	0,12	0,09	98,82
Quartz F	0,08	0,00	0,05	0,03	98,45	0,17	0,09	98,87
Quartz I	0,05	0,02	0,03	0,01	96,82	0,08	0,09	97,09
Quartz G	0,07	0,02	0,03	0,01	98,70	0,10	0,11	99,04
Quartz J	0,08	0,03	0,03	0,01	95,43	0,12	0,1	95,79
Quartz H	0,08	0,01	0,04	0,02	98,18	0,14	0,07	98,54

Table 3: Trace element analyses of quartz samples by XRF. Blank fields = analyses below det. limit.

Sample	TiO_2 (%)	V (PPM)	Co (PPM)	Ni (PPM)	Cu (PPM)	Zn (PPM)	Ga (PPM)	As (PPM)	Rb (PPM)	Sr (PPM)
Quartz A	0,003	2	177	2	1	62	1	36		8
Quartz B	0,007	3	213	1	4	14	2	49		8
Quartz C	0,005	3	162	2	1	7	2	34		8
Quartz D	0,005	2	124	2	2	6	1	26		7
Quartz E	0,005	3	136	2		5	1	28		9
Quartz K	0,005	5	138	1	4	5	2	28		7
Quartz F	0,004	3	156	2	1	20	1	33	1	7
Quartz I	0,003	2	183	2		6	2	39		7
Quartz G	0,009	4	139	1	3	9	2	28		7
Quartz J	0,024	3	148	4	1	6	1	28		9
Quartz H	0,005	2	223	1		7	2	44		8

Sample	Y (PPM)	Zr (PPM)	Nb (PPM)	Mo (PPM)	Sn (PPM)	Sb (PPM)	Ba (PPM)	Ce (PPM)	Pb (PPM)

Quartz A	2	11	2	1		6	5	19	1
Quartz B	2	12	2			6	2	24	1
Quartz C	2	12	2	1		5	3	20	2
Quartz D	2	11	2		1	6	7	13	1
Quartz E	2	15	2	1		6	5	14	2
Quartz K	2	12	2	1		4	19	20	1
Quartz F	2	11	2			6	4	13	2
Quartz I	2	11	1			5	5	16	2
Quartz G	2	11	2	1		6	1	13	1
Quartz J	7	37	3	1		5	11	22	3
Quartz H	2	11	2	1	1	6	1	26	2

Shock heating

Shock heating tests were performed in an induction furnace, one sample at a time. In Figure 1 the temperature profiles for all 11 shock heating tests can be seen. A highly similar profile was observed for all 11 samples. The profile shows the temperature profile during heating cycle. First the temperature is raised to target temperature before the insulation lid is removed and a sample carefully inserted leading to a small drop in temperature, typically about 50 – 80 °C. Upon attaining target temperature the sample is retained in the furnace for 10 minutes. Further, upon removing the sample the crucible temperature drops by 300 -400 °C and the furnace is heated back up to the target temperature and the furnace is once again ready for a new samples. Eight samples were tested during a given day and the remaining 3 samples were tested on the following day.

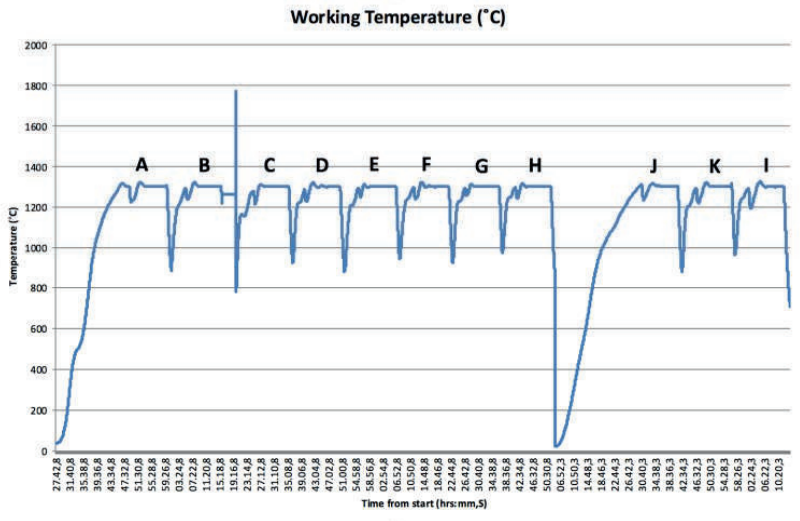

Figure 1: Temperature profile showing the temperature changes in different phases of testing. Testing order: Samples A, B, C, D, E, F, G, and H on the first day. Last three samples J, K & I were tested on a following day. The different phases in the profile includes: Bringing the furnace to target temperature, inserting the sample (T-drop), stabilizing at target temperature, keeping the temperature stable at target and removing sample (abrupt T drop).

After shock heating, for most of the samples the appearance of the quartz was significantly modified, providing a visual observation as to the expected metallurgical performance of the quartz in the furnace. Figure 2 shows two extreme examples of quartz before and after heating. Sample A had violent reaction to shock heating whereas sample C remained unchanged. The first two minutes after insertion of the sample, the most violent reactions to the shock heating appeared. Different observations were made during these two minutes, showing that different quartz samples responded differently to shock heating (Table 4).

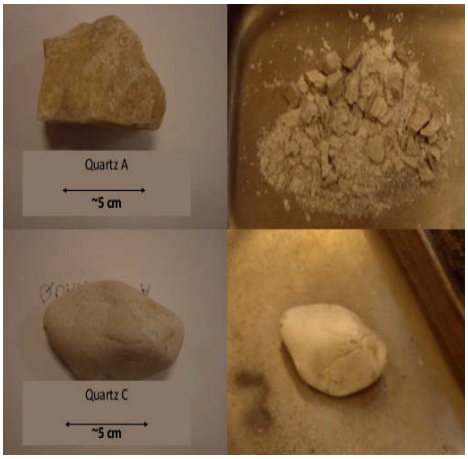

Figure 2: Examples of quartz before and after shock heating tests. Sample Quartz A shows high degree of decrepitation and generated vast amounts of fines. Sample Quartz C, on the other hand, has apparently not reacted to the shock heating and remained in one piece.

Table 4: Visual observations made during and after shock heating of quartz samples

Sample	Observations
Sample A	Violent response to shock heating. Lot of cracking noise and small pieces of quartz were flying out of the crucible.
Sample B	Violent response to shock heating. Lot of cracking noise and small pieces of quartz were flying out of the crucible. Fair amount of fines but less than with sample A.
Sample C	The quartz sample by weight at 288 g was much bigger than others. Typical sample weight was 200 g. This was the only sample that did not break up.
Sample D	This quartz broke to larger fragments with very little fines. The black fines were from erosion of the graphite crucible and not from quartz.
Sample E	This quartz broke into few larger fragments with no fines. The color of the quartz changed from yellowish to white.
Sample F	This sample broke in to large fragments with small amount of fines
Sample G	This quartz had coarse grained crystalline appearance on the surface. The quartz broke in to mostly large and small pieces with small amount of fines.
Sample H	This quartz had impurity inclusions of clay minerals. The quartz broke to large number of fragments with significant amount of fines. Evidence of clay minerals in the fragmented sample was observed.
Sample I	The quartz broke to mostly large pieces which were uniformly sized with very little fines.
Sample K	The quartz broke into four large fragments with very little fines. The black fines were from erosion of the graphite crucible and not from quartz. The quartz had red/yellowish color before heating which could be due to oxidation of Fe compounds.
Sample L	The quartz broke in to several fragments with some evidence of fines. The fracture planes for this quartz were rather unique. The black fines were from erosion of the graphite crucible and not from quartz.

Particle size analyses and performance indicators

All samples from the shock heating experiment was screened carefully on screens 2 mm, 4 mm, 10 mm, 20 mm and 25 mm. Particle size distribution for the shock heated sample products can be seen in Figure 3. Sample C was not reduced by size at all and Sample J was only partly reduced by size. Sample A on the other hand shows a relatively flat particle size distribution between 20 and 4 mm. These are the two extremes when it comes to the particle size. Sample A generating highest fines content, whereas Samples J and C generating literally no fines.

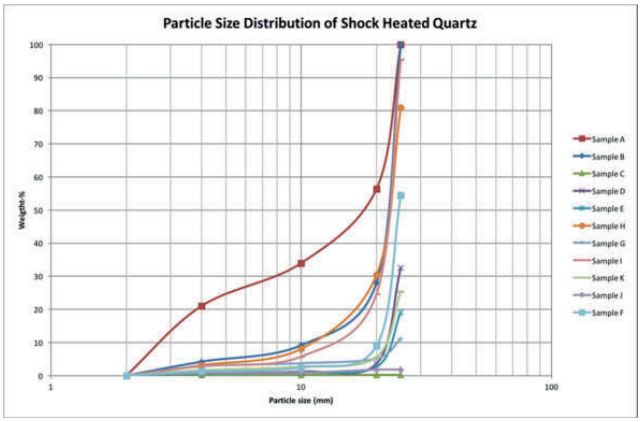

Figure 3 shows particle size distribution of products from shock heated quartz samples. Largest screen size used was 25 mm, hence few samples reached 100 % cumulative weight through 25 mm screen. Sample C remained intact and did not break down in size by thermal shock. Sample J resulted in four fragments, three of them larger than25 mm

Table 5 shows results of the different Index calculations using Equation 2. TSI, HI and DI values reflect the different measures of effects from shock heating. Sample A stands out with low indexes for TSI and FI and high index for DI. Sample C and J gave high indexes for TSI and very low FI and DI index.

Table 5: Combined results from thermal strength analyses (TSI, FI and DI) and XRD analyses (Quartz % and Cristobalite (%) from shock heated quartz. "Quartz Performance" numbers represent subjective smelting performance in the furnace indicative of thermal properties of quartz. The performance is rated on a scale of 1 to 10 with 1 being poor and 10 as excellent

Quartz Sample	Thermal Strength Index (TSI)	Fines Index (FI)	Dust Index (DI)	Quartz (%)	Cristobalite (%)	Furnace Performance
Sample A	47.16	56,42	21.00	98.55	1.45	1
Sample B	64.65	28,06	4.18	99.96	0.04	5
Sample C	99.79	0,21	0.21	99.97	0.03	6
Sample D	90.43	3,65	0.78	99.98	0.02	7
Sample E	94.17	2,72	0.59	99.98	0.02	6
Sample F	83.21	30,42	1.20	99.98	0.02	8.5

Sample G	94.31	9,00	2.80	99.98	0.02	5
Sample H	69.35	5,15	3.11	98.87	1.13	1
Sample I	67.82	24,73	2.83	99.48	0.52	4.5
Sample J	98.72	5,61	0.70	99.82	0.18	9
Sample K	91.16	1,78	1.59	97.91	2.09	7

X-ray diffraction

Results from XRD analyses are shown in Table 5. All samples showed minimum trace levels of cristobalite. Sample K showed the highest amount of cristobalite, 2.09 wt. % after subjecting to heating for 10 minutes at 1300 ºC. No other minerals than quartz and cristobalite were found by XRD.

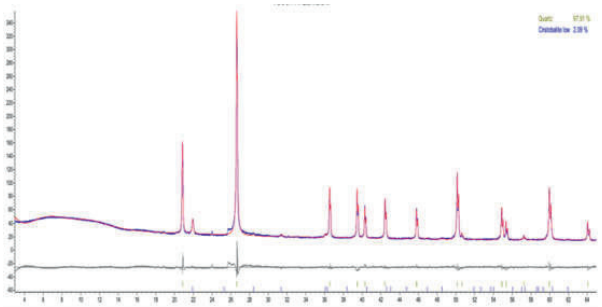

Figure 4: Example spectra from XRD analyses. Sample K contained 97.9 % Quartz and 2.1 % cristobalite after 10 minutes at 1300 ºC

Furnace operations

All the quartz samples that were evaluated have been used for production of silicon at one of the Dow Corning owned manufacturing sites. Each quartz has its unique characteristics. Some quartz have lower impurity levels but poor thermal strength. Other quartz have good thermal strength but contain higher level of impurities. Very few quartz sources have the desired properties for use as a single source. In order to meet the chemical specifications and maximize the furnace performance, a blend of quartz types is commonly used. The smelting performance of quartz on commercial operations is summarized in Table 6. It should be noted that ”Furnace Performance” numbers represent subjective smelting performance in the furnace indicative of thermal properties of quartz. The performance is rated on a scale of 1 to 10 with 1 being poor and 10 as excellent

Based on data in Table 5, several correlations plots were created. Figure 5 shows the correlation between furnace performance and thermal strength index (TSI). Based on limited number of samples and subjective furnace performance data, this correlation is considered to be significant.

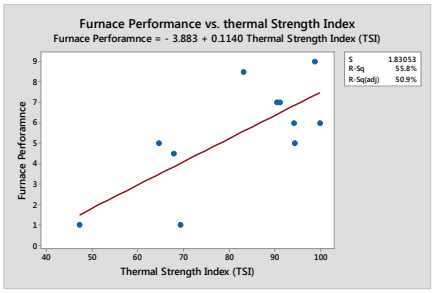

Figure 5: Furnace performance as a function of thermal strength index.

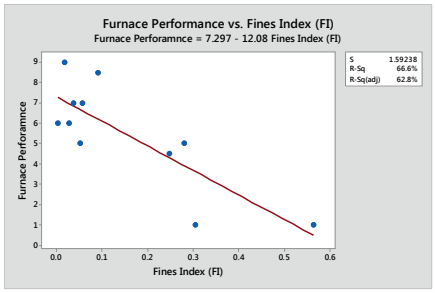

Figure 6: Performance in the furnace as a function of fines Index (FI).

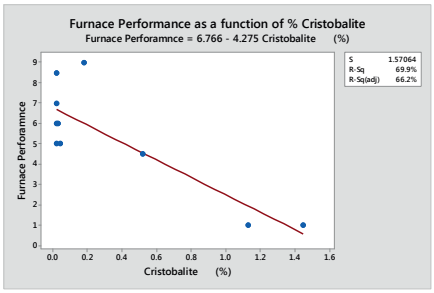

Figure 7: Performance in the furnace as a function of percent cristobalite in the shock heated quartz sample

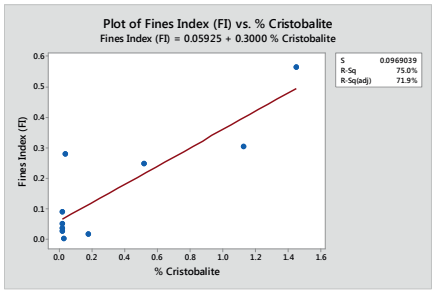

Figure 8: Plot of Fines Index (FI) as a function of percent crystobalite in the shock heated quartz sample

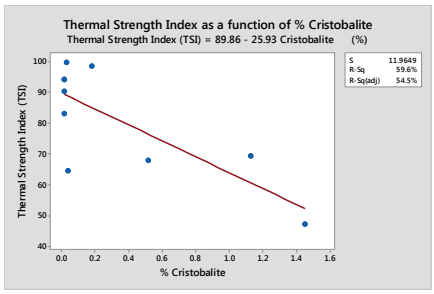

Figure 9: Thermal strength index as a function of percent crystobalite in the shock heated quartz sample

Figure 6 shows the furnace performance as a function of the fines index (FI) i.e. the total quartz fraction < 10 mm. The rationale for choosing <10 mm fraction is based on the hypothesis that as the quartz breaks down in the furnace resulting in higher weight fraction <10 mm in size, it would pack the bed reducing the bed porosity. A packed bed would would result in blow holes leading to loss of SiO and reduced silicon recovery. The corelation in Figure 6 supports this hypothesis.

Figures 7 shows the performance of quartz in the furnace as a function of cristobalite content. At low cristobalite levels the data are scattered as the reported values are close to the analytical detection limit. Figure 8 shows the correlation between quartz fines less than 10 mm and percent cristobalite in the shock heated sample. Figure 9 shows the correlation between thermal strength index and percent cristobalite in the shock heated sample.

Table 6: Performance of Quartz on Industrial Scale Furnace

Sample	Comments
Sample A	This quartz has poor thermal strength as characterized by the quartz heating tests. The performance of this quartz in the furnace is poor as well. Due to its poor thermal strength it cannot be used as a single source to produce silicon. Since this quartz is lower in chemical impurities and meets the chemical specification to produce desired grades of silicon, a small percentage of this quartz can be used in the quartz mix.
Sample B	This gravel quartz has average thermal strength as characterized by the quartz heating tests. The performance of this quartz in the furnace is considered average as well. This gravel quartz can be used as a sole source as it meets both the chemical and thermal strength requirements.
Sample C	This gravel quartz has excellent thermal strength as characterized by the heating tests. This was the only sample that did not breakdown to smaller pieces when subjected to heating test at 1300 C. Due to presence of high level of impurities such as aluminum, titanium and phosphorus, etc. its percentage in blend with other quartz is very limited. Since it has been used in very small amounts its behavior in the furnace cannot be properly characterized. Its performance in the furnace from smelting standpoint is expected to be good.
Sample D	This gravel quartz has average thermal strength as characterized by the heating tests. As this quartz is high in aluminum and titanium its use in the quartz blend is limited. The performance of this quartz in the furnace is considered to be good as well.
Sample E	This gravel quartz has good thermal strength but is limited in use due to very high titanium content. The performance of this quartz in the furnace is considered to be good as well.
Sample F	This rock quartzite has good thermal strength and performance in the furnace is considered to be excellent. It contain high levels of alumina restricting its use as a sole source of quartz.
Sample G	Based on thermal shock heating tests this rock quartz was characterized to have good thermal strength. The performance of this quartz in the furnace is considered to be average. When used in excess of 65% in blend with other quartz, the furnace begins to show indications of increased gas blows both from the furnace top as well as the tap hole.
Sample H	This quartz has very poor thermal strength. The performance of quartz in the furnace verifies this finding.
Sample I	This quartz has average thermal strength and performance in the furnace is average as well. Due to the geological nature of this deposit the impurities can vary over a wide range especially for aluminum.
Sample J	This quartz has excellent thermal strength as characterized by the thermal shock test. The performance of this quartz in the furnace is considered to be very good as well.
Sample K	The thermal test results predicted below average performance of this quartz in the furnace. However the performance of this quartz in the furnace has been quite good. Since the thermal test results are based on evaluating a single rock, more samples need to be evaluated to verify the findings.

Discussion

All samples were analysed for major and trace elements before subjecting to shock heating. The chemical analyses shows that the main elements of interest with relation to silicon production are fairly stable between the samples (Table 2 and Table 3). Sample E contained relatively high content of Al_2O_3 (0.29 %). Apart from that, five samples show levels above 0.100 %. For the other elements only small variations in concentration occur, Fe_2O_3 0.05-0.09 %. The TiO_2 was below 0.03. The colours of quartz varied, ranging from pure white to more brownish and reddish. The colour does not influence the chemistry and should not be used as an indicator of quartz quality. Of more importance to thermal and mechanical properties of quartz is the texture of the quartz [3]. For mechanical properties, typically coarse grained and angular quartz boulders of vein type quartz deposits shows more fines and dust generation than do

massive, medium to fine grained quartzes from river gravels, ancient or more recent deposits.

As the shock heating tests were logged with respect to temperature development, it is clearly shown in Figure 1 that all samples were tested under similar conditions. Samples were inserted into the furnace at target temperature. When the sample had been inserted, the temperature dropped about 50 – 100 ºC before the insulation was reattached and the temperature was brought back to target. Because of the accuracy of the settings on the IF75 furnace, the temperature exceeded the target temperature by a few tens of degrees before stabilizing at the target. Although these temperature deviations are slightly different between runs they are not expected to significantly affect the results of the shock heating experiments.

As reported in Table 4, shock heating of quartz may result in violent reactions in the quartz lumps as seen during the test sequence. Especially, the two first samples, Sample A and B, reported small fragments flying out of the furnace top. Similar happenings are reported from similar tests on other quartz raw material [3]. It is also reported from the experience with certain quartz types in industrial furnaces that they react violently to the shock heating (Table 6).

After shock heating, the products from the heating tests appeared different depending on the outcome of the shock heating test. Figure 2 shows the most extreme examples of resulting products from shock heating tests. Sample A and Sample C have both undergone the same test regime but the final products deviate significantly. Sample A is extremely fractured and produces a large amount of very fine quartz powder as well as some nice larger cm scale fragments. Sample C on the other hand shows no sign of fragments, only the same lump quartz as inserted before the heating cycle. Some slight colour change and some more exaggerated fractures that still has some cohesion, are the only visible effect of the shock heating treatment of that sample.

Table 5 shows the amount of cristobalite formed in the different samples after the shock heating. Based on experience from previous work, [3] no significant formation of cristobalite was expected. The sample with the highest cristobalite content at 2.09 % is not considered too high, based on heating the sample to 1300 ºC for 10 minutes. This result shows that there is a potential for high transformation rates for conversion of quartz to cristobalite. Figure 8 shows the correlation between amount of fines -10 mm and cristobalite content. As the cristobalite content increased the fraction below 10 mm also increased. This is consistent with the hypothesis that stresses created by the volume increase upon conversion from quartz to cristobalite on heating to 1300 ºC and holding for 10 minutes would result in stress within the sample leading to higher generation of fines. A strong correlation with R-sq. value of 75% was obtained based on 10 data points. One sample result was not considered as an outlier since the data was based on single measurement. A good correlation was also observed between furnace performance and percent cristobalite in the quartz as shown in figure 7. Figure 9 shows the correlation between thermal strength index and percent cristobalite. Once again all the data points were not considered and more work is needed with multiple measurements to obtain meaningful results.

The correlation between furnace performance and thermal strength index (Figure 5) as well as the fines fraction less than 10 mm (Figure 6) was quite good. It should be noted that ”Furnace Performance” numbers represent subjective smelting performance in the furnace indicative of thermal properties of quartz. The rationale for this analysis considers that the quartz that is uniform in size as it breaks in the furnace upon thermal shock, would give higher bed porosity which is desirable. The fraction below 10 mm would reduce bed porosity due to packing of the bed, resulting in blow holes leading to loss of SiO and reduced silicon recovery. The plot in Figure 6 supports this hypothesis.

Sample F is one of the top performing quartz on industrial scale with a performance rating of 8.5. The thermal strength index for this quartz was measured at 83.2 which is not considered to be very high. One other factor that needs to be considered is the size of the quartz fractions upon shock heating. When the quartz breaks in to equally sized fraction it would give higher bed porosity which is desirable. Once again repeated sample measurements are recommended to improve the confidence of the results.

Conclusion

Shock heating of quartz to 1300 °C for 10 minutes, followed by measuring the conversion of quartz to cristobalite is a reliable method to predict its performance in the furnace for production of silicon. Significant differences were observed in the behavior of quartz in response to shock heating. Couple of samples responded violently to shock heating with hearable cracking and fragments of quartz flying out of the crucible. Other samples behaved normally. The temperature profiles from shock heating tests show similar development through each sample. Deviation in mass/volume was insignificant for the samples. Most of the samples had good thermal strength index (TSI) except samples A and H. These two samples also had high fines index (FI). Both samples A and H had relatively high cristobalite content. Sample H also had evidence of clay minerals in the fragmented sample.

The performance of quartz in the furnace support thermal test findings showing good correlation with thermal strength index (TSI), the percentage of cristobalite in the shock heated sample and the fines index (FI). The correlation between cristobalite and fines index (FI) as well as the thermal strength index (TSI) was quite good. The correlation between thermal strength index and percent cristobalite was also considered to be good. The results from these tests support the finding from previous work reported in the literature.

Finally there are two aspects to quartz characterization for new deposits. In case of currently operating plants, thermal shock test at 1300 ºC as the first step followed by evaluation of quartz on commercial scale is recommended. For new projects where a commercial furnace may not be available, it is recommended that thermal shock test at 1300 ºC should be followed by X-Ray Diffraction (XRD) to determine the conversion of quart to cristobalite.

Acknowledgement

Dow Corning is acknowledged for the financial contribution for performing analytical experiments. Torill Sørløkk and Laurentius Tijhuise (NTNU-IGB) are acknowledged for performing XRF and XRD analyses respectively. Delphine Leroy (NTNU-IMT) is acknowledged for running the shock heating experiments on the induction furnace.

References

1. Schei, A., J.K. Tuset, and H. Tveit, *Production of High Silicon Alloys*. 1998, Trondheim: Tapir Forlag.
2. Aasly, K., T. Malvik, and E. Myrhaug, *A review of previous work on important properties of quartz for FeSi and Si metal production*, in *Innovation in the Ferro Alloy Industry (INFACON XI)*. 2007, MacMillan: New Dehli, India. p. 393-401.
3. Aasly, K., *Properties and behavior of quartz for the silicon process*, in *Geology and Mineral Resources Engineering*. 2008, NTNU: Trondheim. p. 206.

4. Aasly, K., T. Malvik, and E. Myrhaug. *Advanced methods to characterize thermal properties of quartz*. in *INFACON XI*. 2007. New Dehli, India: MacMillan.
5. Ringdalen, E., *Changes in Quartz During Heating and the Possible Effects on Si Production.* Jom, 2015. **67**(2): p. 484-492.
6. Ringdalen, E., *Quartz Cristobalite transformation and its Effect on Reactions in Si Production: Initial Studies*, in *Celebrating the Megascale: Proceedings of the Extraction and Processing Divission Symposium on Pyrometallurgy in Honor of David C.G. Robertson* P.J. Mackey, et al., Editors. 2014, TMS (The Minerals, Metals and Materials Society).
7. Pujjatt, A., et al., *Furnace capacity increase and the approach to a better performance of the silicon metal process*, in *Silicon for the Chemical Industry VIII*, Ø.H. A, et al., Editors. 2006, Department of Materials Science and Engineering: NTNU, Trondheim, Norway.
8. Brenden-Veisal, T. *Application of quartz in the Ferro-Silicon and Silicon Metal Industry*. in *33rd International Geological Congress*. 2008. Oslo.
9. Aasly, K., T. Malvik, and E. Myrhaug. *Quartz for carbothermic production of silicon - effect of the process steps, handling and transport from mine to furnace*. in *Silicon for the Chemical Industry VIII*. 2006. Trondheim, Norway: Norwegian University of Science and Technology.
10. Alnæs, L.I., *A geological and mineralogical investigation of the Mårnes quartzite in Gildeskål, Nordland (in Norwegian)*. 1986, Unpublished Thesis, NTH: Trondheim.
11. Johannesen, U., *A geological and mineralogical investigation of the quartzite deposit at Tananeset, Finnmark (in Norwegian)*. 1998, Unpublished Thesis, NTNU: Trondheim, Norway.

New Monosilane Decomposition Technology

Mark Dassel, Executive Vice President for Polysilicon Technology
Seattle Center for Applied Research and Product Development, SiTec GmbH

Abstract

SiTec is developing a novel vibrationally fluidized bed reactor (V-FBR) that can significantly lower overall costs compared to current practice, using undiluted monosilane to produce polysilicon granules for solar use. This FBR is compact, self-seeding, operates at high pressure, and demonstrates very low dust levels at high conversion efficiencies. A commercially prototypic pilot reactor is in the early stages of scale-up testing, with good results.

Summary

SiTec technology will reduce monosilane fluid-bed reactor (FBR) capital and operating costs by approximately 45% each, compared to legacy FBR decomposition processes. Called "Genesis™," SiTec's technology fluidizes the granular reaction bed by mechanically induced vibration as opposed to gas induced (a.k.a., "hydraulic") fluidization used by legacy processes. SiTec calls its development "vibrationally fluidized bed reaction" or V-FBR. Legacy FBR processes fluidize reaction beds by blowing a mixture of monosilane gas (diluted to 5% to 20% concentration in hydrogen recycle) up through a bed of small silicon particles. The feed gases lift and fluidize the bed. Decomposition and particle growth occur when monosilane gas contacts hot granules in the bed. Resultant epitaxial growth increases particle size until sufficiently large to be harvested. Attempts to increase hydraulic fluid bed reactor productivity by operating at high pressure and high monosilane feed concentration result in high rates of dust formation and low yield. In marked contrast, SiTec's Genesis™ process operates with 100% monosilane feed – no hydrogen dilution, and at high pressure, with less than 2% dust formation. SiTec recently started up a commercially prototypic pilot reactor at its Seattle Center for Applied Research and Product Development. The pilot plant is being used to perfect its mechanically fluidized beds, prove commercial design and product quality, and verify the fast reaction rates, *in situ* self-seeding, and high yields demonstrated in earlier lab test work.

Background

A. A Historical Overview of Monosilane Fluidized Bed Reaction

There are currently two main process routes to polysilicon (a.k.a., "legacy" processes):

1. The conversion of metallurgic silicon to refined trichlorosilane, followed by decomposition to rod form polysilicon in a Siemens type reactor, and
2. The conversion of metallurgic silicon to refined monosilane, followed by decomposition to granular form polysilicon in a fluidized bed reactor, where

fluidization is due to gases rising through the bed – referred to herein as hydraulically fluidized beds or H-FBR.

In addition to these main routes, monosilane is converted to very high quality rod form in Siemens reactors (commercial), and TCS is decomposed to granular form factor in a fluidized bed reactor (believed to be pre-commercial).

Work on the granular process began in earnest in the 1970's by Union Carbide, at its Washougal, Washington State, U.S.A. laboratory and semi-works facility, and by Albemarle Corporation at its plant site in Pasadena, Texas. Albemarle Corporation subsequently sold its granular process technology and the Pasadena facility to MEMC, and this plant was successfully operated until recent times. The monosilane source for the Pasadena plant was unique in that it was based on a silicon tetrafluoride process. The Pasadena plant used lined reactor technology to mitigate the migration of metal ions from the reactor walls into the granular product.

Union Carbide stopped its granular process development in favor of monosilane decomposition in Siemens reactors. This approach was successfully practiced at both its Washington State and Montana U.S.A. plant sites. Union Carbide subsequently sold its technology and plant facilities to Komatsu, and Komatsu to REC Inc. (now operated as REC Silicon). Between 2000 and 2015, REC Silicon resurrected Union Carbide's early efforts to convert monosilane to granular polysilicon in an H-FBR, based on perceived economic advantages. REC Silicon subsequently installed significant monosilane H-FBR capacity at its Washington State, U.S.A. plant site. Its plants use unlined reactor technology. Instead a barrier of polysilicon is formed on interior reactor surfaces. This *in situ* barrier is at least partially successful in preventing the migration of metal ions into the granular product. REC's monosilane process – as was Union Carbide's original – is based on redistribution of crude TCS. REC Silicon recently developed a lined H-FBR process and, in conjunction with Shaanxi Non-Ferrous Tian Hong New Energy Company, is building a plant based on this technology in China.

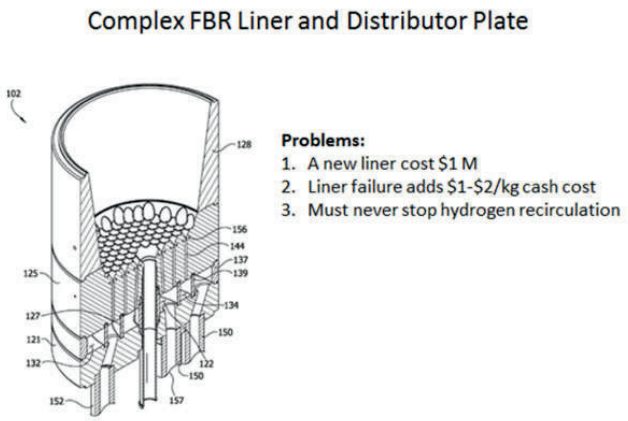

Figure 1: A conceptual drawing of a lined reactor.
Liners typically comprise graphite and silicon carbide.

B. Key Issues with Legacy Monosilane H-FBR Decomposition Processes

Issues include:

- Excessive monosilane yield loss to dust,
- Requirement to make seed *ex situ* (i.e., outside the H-FBR),
- Thermal heat load is increased as much as 10X due to hydrogen diluent,
- Heat transfer limits reactor size and efficiency,
- Relatively high FBR system capital cost, and
- Problematic product quality.

The common factor in these issues is the use of reactant and diluent feed gases to fluidize the reaction bed.

Fluidization is essential to uniformly distribute monosilane to hot granular surfaces where heterogeneous decomposition occurs, and to prevent the formation of agglomerates which can plug the bed.

Legacy H-FBR processes fluidize the granule bed with feed gases consisting of monosilane and hydrogen diluent. Hydrogen diluent is added to:

1. Help fluidize the bed, and
2. Minimize the conversion of monosilane feed gas to dust (also known as "poly-powder").

A 1:5 to 1:20 monosilane to hydrogen feed gas ratio is used. Thus the dominant fluidization gas is hydrogen. Pure monosilane feed is avoided in H-FBRs because it results in very high dust formation rates (e.g., > 25% of monosilane to dust) and because, without hydrogen diluent, there is insufficient hydraulic flow to lift and fluidize the bed.

Even with hydrogen dilution 15 ±5 % of the monosilane feed is converted to dust. The gas rate required for fluidization blows this dust out of the reactor. The gas also blows seed out of the reactor – to the extent it is made *in situ*. Typically all material made in the FBR smaller than approximately 85 microns in size is lost as dust in the off-gas filters. As a result, on-purpose seed is made *ex situ*. Seed is required to replace harvested granular product. *Ex situ* manufacture requires product classification, size reduction, and seed recycle. These *ex situ* steps are capital and cost intensive, and introduce impurities into the H-FBR.

Hydrogen gas has an inherently high heat capacity, thus hydrogen dilution significantly increases H-FBR heat load. The addition of heat to an H-FBR is difficult because the heat is added to the non-process side of the liner system on the circumference of the reactor. Heat exchangers in the fluidized bed itself would be more efficient but would increase metal contamination, so this is not practiced. Scale-up to larger diameter reactors is difficult because the surface area for heat transfer increases only by the diameter whereas the internal reaction volume – and concomitant heat load – goes up by the square of the diameter. As a result, legacy H-FBR reactors are usually ≤ 1 meter in diameter and limited to around 500 to 1,000 metric annual tons (MTA).

H-FBRs are typically tall vessels with a large height to diameter ratio (e.g., 10:1). Extra reactor volume, in the form of additional height, is added to increase heat transfer from the heated wall to the granules in contact with the wall, and for granule de-entrainment. Consequently, much of the reactor volume – as much as 2/3^{rds} – is relatively non-reactive.

Legacy H-FBRs run near atmospheric pressure. Theory, however, suggests reactor productivity (as production per unit volume per unit time) increases with increasing

pressure. Attempts to increase hydraulic fluid bed reactor productivity by operating at higher pressure have reportedly resulted in high rates of dust formation and low yield. Notwithstanding, efforts to increase reaction pressure by an order of magnitude continue, and one major producer has announced plans to start up a high pressure reactor in hopes of increasing reactor productivity.

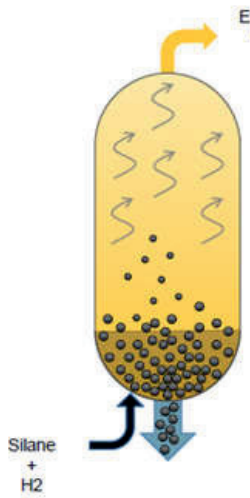

Problems:

1. Complex product size separation system
2. Significant granular recycle system is required
3. Smaller seeds are blown out of the reactor by high gas rate
4. High gas rate is required to fluidize the bed and dilute the monosilane
5. Effluent gas must be cooled, filtered to remove dust, recompressed, re-circulated to the reactor, and reheated
6. Heat transfer limits reactor size and efficiency

Figure 2: A conceptual drawing of an H-FBR.

C. Factors Affecting Dust Formation in an H-FBR System

Monosilane decomposition chemistry proceeds in two regimes:

1. Heterogeneous
2. Homogeneous

Heterogeneous decomposition is desired and produces granules. Seed-stock is required for this to occur. This decomposition reaction occurs at temperatures above 500 C, and typically in the 600 C to 700 C temperature range.

Homogeneous decomposition produces dust, also known as "poly powder." Poor contact with hot granular surfaces is a necessary condition for homogeneous decomposition. Further, the following conditions promote homogeneous decomposition:

- High temperature (e.g., >600 C), and/ or
- High monosilane molar density.

Large gas bubbles formed in H-FBRs contribute to dust formation. Their formation is inherent in the physical process as is well documented in the literature.

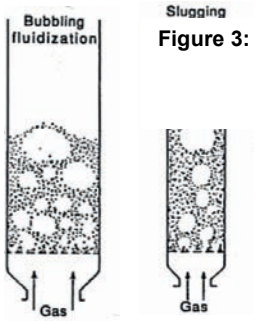

Figure 3: Bubble formation in legacy style H-FBRs.

Bubble size approaches the inner diameter of the fluidized bed. Poor resultant contact with hot granular surfaces combined with high bubble temperature and unreacted monosilane gas produce excessive amounts of dust.

D. Factors Affecting Product Quality in an H-FBR System

Considerable effort is devoted to improving granular product quality. Unlined systems produce granules with relatively high metals content. Current generation lined systems are better, but fall short of high electronic grade quality. Factors impacting quality include:

1. Granule contact with metal surfaces,
2. Granule contact with impure gases, and
3. Impurities introduced as a result of *ex situ* seed generation.

Impurity content due to metal contact is proportional to surface area, and a function of temperature. Legacy systems operate at 600 C to 700 C. At these temperatures metal ions migrate from metal to granules by surface-to-surface contact. The addition of extra reactor height to promote heat transfer increases metal transport.

Liners are used to manage metal contamination. In one system, silicon carbide is applied to the process side (i.e., inside) of a graphite liner. This mitigates metal transport but introduces carbon – also an impurity – into the reaction zone. As a result, carbon content in granular product is orders of magnitude greater than that in rod form polysilicon produced from monosilane.

The carbon impurity may be sourced by carbon migration through the graphite/ silicon carbide composite liner and/or by hydrogen gas introduced into the pressurized plenum surrounding the liner system. Hydrogen purge gas introduced into the plenum may transport carbon from the non-process side (i.e., the outside) of the liner into the process side of the reactor.

However, the greatest potential source of metal impurity in granular product is the granule product classification and *ex situ* seed generation system. Product removed from the H-FBR is processed to separate particles smaller than 400 microns and larger than 3,000 microns. The large particles are size reduced to create reactor seed-stock, combined with the small particles, and this combination is recycled back to the reaction zone. Elimination of these requirements would significantly improve granule product quality; however, the inherent physics controlling hydraulic fluidization (i.e., high required gas rates) have so far precluded the achievement of this goal.

SiTec's New Monosilane Decomposition Technology

A. Vibrationally Induced Fluidization

SiTec is developing a novel silane decomposition process that will produce solar and electronic-grade polysilicon. The new process is called Genesis™. Genesis™ fluidizes a granular reaction bed by mechanically induced vibration as opposed to the gas induced (a.k.a., "hydraulic") fluidization used in legacy processes.

Production cost of the new technology is forecast to be lower than that of legacy H-FBR technology and that of refined TCS/Siemens CVD.

Advantages include high reactor productivity, self-seeding, in-situ particle size classification, <2 % yield loss to dust formation, and lower CapEx.

Genesis™ is being developed at lab and pilot-reactor scale at SiTec's Seattle Center for Applied Research and Product Development (Seattle Center). Genesis™ reactors run at 10 to 20 BARG operational pressure and with 100% silane feed gas. Hydrogen diluent is not used. Ninety-nine percent conversion-per-pass is achieved in pilot-plant demonstrations. Micro-photographs show scavenging contributes to improved silane yield and reactor productivity, and that seeds – formed *in-situ* – are tight clusters of micron-sized polysilicon spheres. Liquid-like motion is achieved in the operating reactors – completely decoupled from gas velocity in and through the bed.

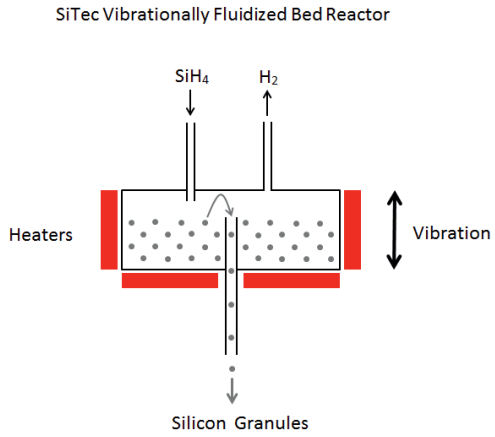

Figure 4: Simplified sketch of the Genesis™ reactor.

Vibrational rates and amplitudes (mid-point to peak) comprise 1,800 to 2,200 cycles per minute, and 0.75 to 1.25 mm.

B. Purpose of Development, Approach, Innovation, and Scientific Relevance

The purpose is to develop a new production means for lower cost, high quality solar-grade polysilicon granules. Genesis™ reactor technology is positioned to dramatically reduce the cost of converting silane gas to polysilicon granules, compared to existing processes. SiTec forecasts that polysilicon plant operating costs will be greatly reduced and achieve savings that will strengthen the entire solar energy value chain.

SiTec's technological approach is to fluidize the granular reaction bed by mechanically induced vibration. SiTec calls its development "vibrationally fluidized bed reaction" or V-FBR. This novel approach to fluidization has been demonstrated in bench tests and at pilot scale to greatly improve reactor throughput and yield, while simplifying reactor operation.

Figure 5: Commercially prototypic pilot reactor operated at the Seattle Center for Applied Research and Product Development

Legacy H-FBR processes fluidize reaction beds by blowing a mixture of hydrogen and monosilane gas up through a bed of small silicon particles ranging in size from 85 to 3,000 microns. The feed gases lift and fluidize the bed. Decomposition and particle growth occur when monosilane gas contacts hot granules in the bed. Resultant epitaxial growth increases particle size until sufficiently large to be harvested. Large particles sink to the bottom of the H-FBR reactor where they are removed batch-wise. In contrast, in a V-FBR the large particles move to the top of the bed where they are removed in a continuous, self-regulating, overflow process.

Legacy H-FBR processes typically run close to atmospheric pressure with 5:1 to 20:1 hydrogen dilution. Yield loss to dust – a waste product – typically runs 10% to 20%. This dust is called "poly-powder" in the industry and:

- Is micron and sub-micron in size,
- Sticks to surfaces,
- Has low density (in the 0.1 to 0.2 grams per cc range), and
- Bridges instead of pouring.

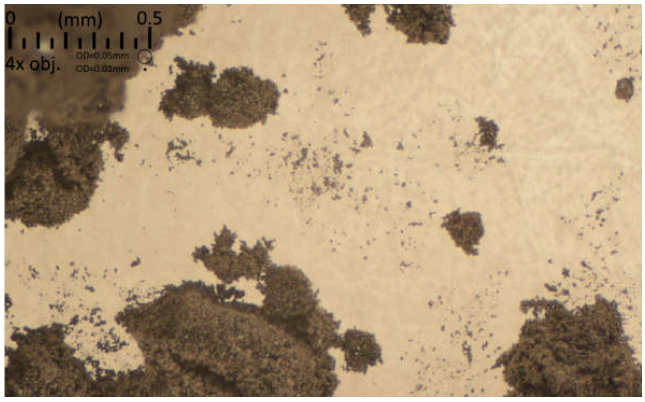

Figure 6:
Microphotograph of poly-powder. The scale is in the upper left hand corner. The large clumps are filter cake removed from the reactor off-gas filters. The filter cake is comprised of individual, separable fine particles measuring under a few microns in size.

In marked contrast, the V-FBR process operates with 100% monosilane feed, no hydrogen dilution, and at high pressure (e.g., 10 BARG) with low dust formation. Seeds formed *in situ* range from 5 microns to 50 microns in size, are dense, and have a compact, spherical morphology. They are free-flowing and do not stick to surfaces or bridge.

Test work on the new fluidization technology is being performed in a commercially prototypic pilot reactor at SiTec's Seattle Center. The pilot reactor is being used to perfect the vibrationally fluidized bed, prove commercial design and product quality, and to further study the fast reaction rates, self-seeding, and high yields demonstrated in test work at the Seattle Center.

SiTec's V-FBR reactor is designed to run at temperatures up to 700 C and high pressure (up to 20 BARG) with 100% monosilane in reactor feed gas. These conditions make for high conversion rate and economical, efficient, small-sized reactors. SiTec believes these same conditions, if attempted in a legacy H-FBR process, would convert around one-half of silane feedstock to dust.

Dust formation in SiTec's reactor is <2% and is minimized by keeping the reactant gas in close contact with hot granules at all times. The film thickness between monosilane reactant molecules and hot granules is less than 400 microns because, with vibrational fluidization, there are no gas bubbles. By way of contrast, as a first approximation, the separation distance in a conventional hydraulic bed can be as much as 250X to 1,000X as great due to the formation of large-sized gas bubbles.

Seeds formed in the V-FBR reactor tend to stay in the bed because exit gas velocity is relatively low – only $1/50^{th}$ to $1/100^{th}$ as high as in a legacy H-FBR. Exit gas velocity is low because the V-FBR is operated at high pressure and because silane feedstock is not diluted with hydrogen. In comparison, the high exit gas velocity in a legacy H-FBR blows a substantial fraction of seed particles smaller than 85 microns out of the bed, necessitating the installation of costly *ex situ* seed generation and recycle facilities.

C. Product Morphology and Size Range

Figures 7 and 8 show material produced in the pilot reactor. Figure 8 compares Genesis™ product morphology with commercial polysilicon granules sold by legacy producers.

Figure 7: Material produced in the Genesis™ pilot reactor.

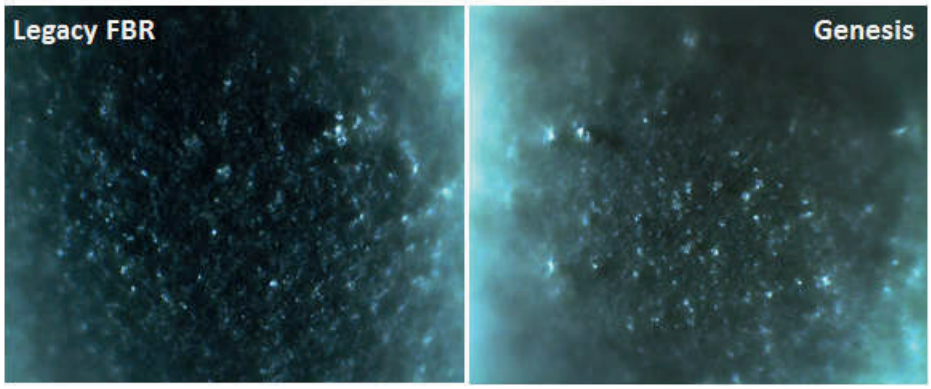

Figure 8: Genesis™ product has the same surface morphology as legacy granules. This photograph is of a single granule (about 2 mm in diameter). The surface texture is believed to be a result of concurrent epitaxial deposition and scavenging of small micron-sized particles produced *in situ*.

D. In Situ Seed Formation

Genesis™ is unique among all fluid bed reaction processes in that it makes and retains seed, in the reaction mass, sufficient for on-going operations (i.e., does not require supplemental *ex situ* seed manufacture). Figures 9 and 10 are photographs of seed made in the Genesis™ pilot-reactor.

The seeds measure 10 to 30 microns in diameter, are spherical in shape, free-flowing, and non-sticky. Each seed is comprised of an aggregate of smaller particles measuring a few microns in size.

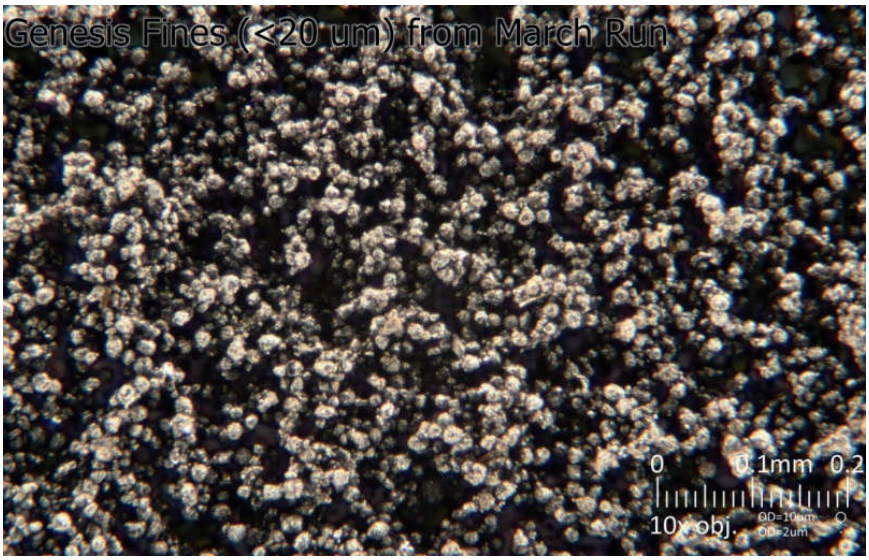

Figure 9: Microphotograph of seed made in the Genesis™ pilot-reactor.

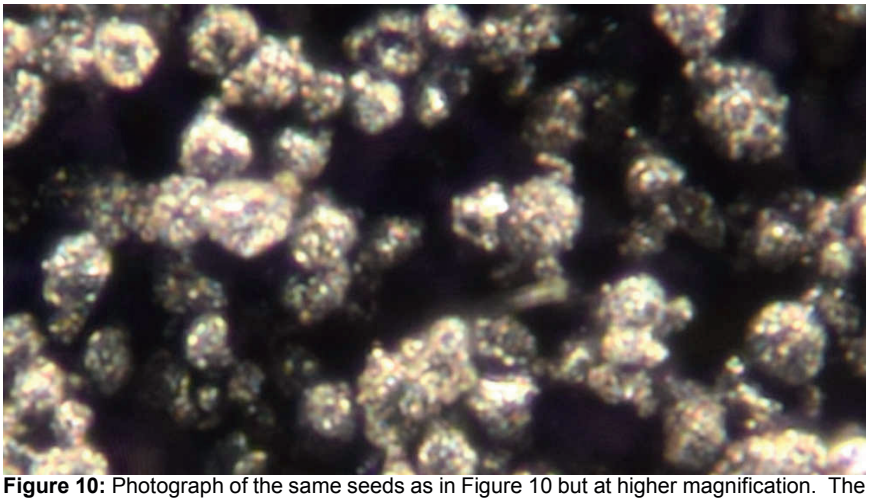

Figure 10: Photograph of the same seeds as in Figure 10 but at higher magnification. The 1 to 2 micron size particles making up the individual seeds are clearly visible.

E. Product Withdrawal System

The Genesis™ reaction system employs a unique product withdrawal system. In legacy FBRs, product is withdrawn from the bottom as underflow. In Genesis™, product is withdrawn from the top surface of the reaction bed in an overflow standpipe. Overflow

works well in a V-FBR because the top surface of the bed, while highly fluidized, is relatively flat and not prone to the surging flow seen in H-FBRs. Further, and critically, large particles move to the surface in a vibrationally fluidized bed. The Genesis™ product withdrawal system is designed in a way that particles sized smaller than 400 microns stay in the reaction bed, while large particles are preferentially removed.

F. Reaction Kinetics

A reaction rate model, see Figure 11, has been fitted to Genesis™ laboratory data collected at temperatures ranging from 500 C to 650 C, and pressures ranging from 2 BARG to 12 BARG. While the activation energy for the reaction rate constant is similar to that reported by others (200 KJ/mole), the overall kinetics are faster for a given temperature. This is attributed to greater space time from operation at higher pressure. Further, the yield to product is higher because the amount of dust (a.k.a., poly-powder) made is much lower.

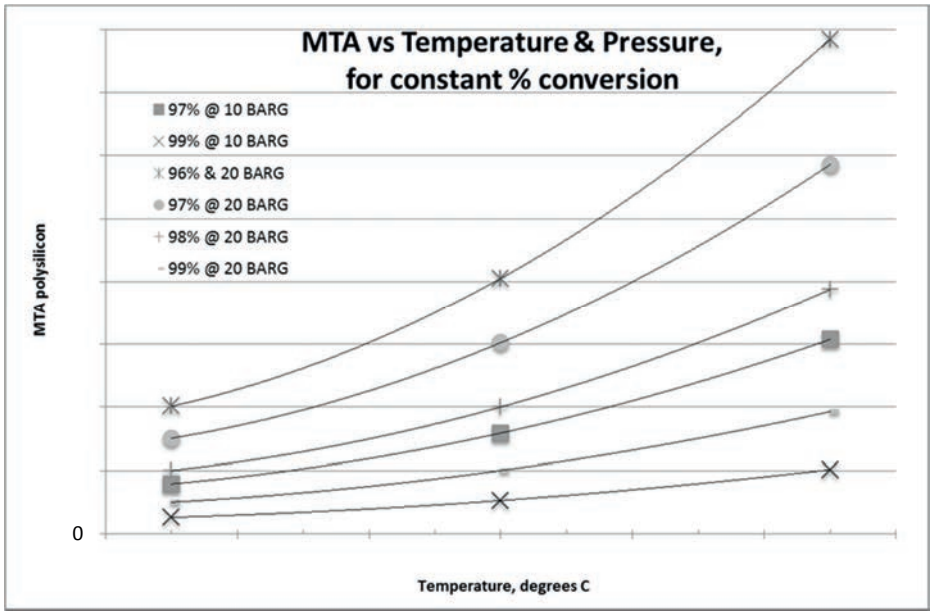

Figure 11: Relative effects of temperature and pressure on reactor productivity. For example, in the operating ranges studied, doubling the pressure roughly doubles productivity for a given size reaction mass.

Photographic evidence indicates that Genesis™ runs with a high degree of scavenging – i.e., dust is incorporated into product granules.

Figure 12: The particle shown is around 2.5 mm in size. Scavenged particles appear as bumps on its surface.

G. Conclusions and Path Forward

V-FBR technology brings the following advantages compared to conventional hydraulic fluidization (H-FBR):

1. Fluidization is decoupled from gas flow meaning hydrogen dilution is not required
2. Reactor heat load is reduced because hydrogen dilution is not required
3. Lower reactor heat load enables an 80% savings in decompositional electrical demand
4. Capital cost is lower because reactors are more efficient and small in size, expensive hydrogen recycle equipment is eliminated, and off-gas cooling and filtration loads are reduced in size by an order of magnitude
5. Yield is improved by up to 15% (e.g., from 85% to 99%) because <2 % of monosilane feed is converted to poly-powder
6. The monosilane plant is 15% smaller for a given polysilicon production rate due to improved yield
7. The technology is self-seeding; *ex situ* seed generation facilities are not required
8. Superior quality
9. Easy "on-off" operation

SiTec's innovative approach to fluid-bed silane decomposition should significantly lower silicon feedstock cost and, at the same time, break the quality barrier long associated with legacy H-FBR product.

Total polysilicon plant investment and energy consumption, including the monosilane feedstock plant, will be reduced by approximately 35% each compared to legacy H-FBR processes. Cash cost in China will be reduced to only $7.25/kg polysilicon*, compared to $9.50/kg cash cost for legacy monosilane/FBR polysilicon plants, and compared to $14/kg for legacy refined TCS/Siemens plants.

**Based on 8.5 cents per KwHr electricity price, $10/million BTU natural gas price, $2.25 per kg metallurgic silicon price, $43/kg total CapEx for a 10,000 MTA plant (including monosilane mfg.), and 2% maintenance cost factor.*

Extra steps to eliminate metal contamination are economical because SiTec's reactor is small in size and highly productive. SiTec's goal is quality solar-grade feedstock containing low metals content <10 ppbw. Quality will be inherently superior compared to legacy H-FBR because *ex situ* seed generation and recycle is not necessary.

Because V-FBR fluidizes by simple mechanical means, fluidization is "on-off". The complicated startup and shutdown protocols of legacy FBR processes are eliminated. Time to steady-state reaction from a cold start is a few hours, compared to legacy FBR

processes which may require days. Heating is simple electrical resistance applied with direct conduction or radiation. Scale-up is easier with SiTec's V-FBR reactor because heat load is low. Electrical requirements are forecast to be 1 kwhr/kg polysilicon in commercial reactors.

Vibrational silane decomposition is an important new technology. When commercialized it will be a substantial improvement over legacy H-FBR processes.

References

1. Daleffe, R.V., Ferreira, M.C., and Freire, J.T., *Effects of binary particle size distribution on the fluid dynamic behavior of fluidized, vibrated and vibrofluidized beds*, Brazilian Journal of Chemical Engineering, **25**, No. 1, January – March 2008, p83-94
2. Laroche, C., Douady, S., and Fauve, S., *Convective flow of granular masses under vertical vibrations*, Le Journal de Physique, **50**, April 1989, p699-706
3. Ford, Kenneth J., Gilchrist, James F., and Caram, Hugo S., *Transitions to vibro-fluidization in a deep granular bed*, Powder Technology, **192**, 2009, p33-39
4. Wassgren, C.R., Brennen, C.E., and Hunt, M.L., *Vertical vibration of a deep bed of granular material in a container,* Journal of Applied Mechanics, **63**, September 1996, p713-719
5. Clement, E., Labous, L., and Vanel, L., *Granular Packing Under Vibration*, Europhysics News, May/June 1998, p107-111

On the road to industrialisation of a new centrifuge CVD reactor for polysilicon

Werner Filtvedt[1,2], Sverre Sørensen[1], Hallgeir Klette[2], Josef Filtvedt[1]
1) Dynatec Engineering Rakkestadvn. 1814 Askim
2) Institute For Energy technology Instituttvn. 2027, Kjeller Norway

Abstract

In order for polysilicon producers to achieve good economy, they need to produce a high quality material for as low cost as possible. In terms of quality both the quality of the largest part of the production needs to be high and the fraction of lower qualities needs to be low. Today, the fluidized bed is the most cost effective method for production of polysilicon. However, fluidized bed material on the market is primarily sold as second grade material and in addition a substantial part of the silicon production becomes fines that is sold at a price below the production cost. In order to improve this situation both the bulk quality of the material needs to be increased and the fines fraction needs to be reduced. Both these mechanisms are successfully addressed with the Dynatec Centrifuge Reactor technology. This is the first reactor in the world capable of converting up to 95% of the inserted monosilane into high quality dense crystalline silicon with a fines production below 0,5%. The technology has been proven successfully through a prototype reactor and an up scaled reactor. The current project is to test the technology in industrial scale. The project is started and is presently in the engineering phase.

Introduction

Historically only two reactor designs have been developed and commercialized for production of high purity silicon feedstock to electronics and solar cell applications. These are the Siemens Bell Jar reactor and the Fluidized Bed reactor, first proposed by H.W. Ling of E.I. du Pont [1, 2]. Both designs was proposed in the late 1950s, and traditionally the Siemens reactor has facilitated high quality at the expense of a high cost while the fluidized bed has given lower cost at the expense of lower quality. The quality challenges of the FBR have both included purity, fines, porosity and crystallinity [3]. The motivation for proposing a new design has been to combine the benefits of the Siemens reactor with the cost structure of the FBR.
The concept has been through two stages. A prototype reactor Dynatec 1.0 and later the upscaled Dynatec 2.0 has been and successfully tested. In this article the team discloses some of the principles being used in the industrial pilot reactor. Dynatec 3.0 which is an industrial demonstration unit.

Theory

Decomposition of silane

In the early days of silicon CVD, several gases were explored for the purpose, but in today's reactors monosilane SiH4 (silane) and trichlorosilane SiHCl3 (TCS) are the ones frequently used. Upon being heated to the decomposition temperature, the gases undergo the following reactions:

$$\mathbf{SiH4 \rightarrow Si + 2H2} \qquad \mathbf{(1)}$$

The silane decomposition sequence initiation is about 420°C.
However at this temperature, pressure and the present hydrogen concentration, the silicon will form amorphous structures with dispersed hydrogen. One needs temperatures of about 700°C to avoid this problem or even higher depending on the design of the process [4 - 6].

Silicon growth

When the monosilane molecule decomposes, a chain reaction is initiated [6]. The chain reaction involves a large number of intermediate reactions and species and will depend on silane concentration, temperature, pressure, temperature of confining surfaces and the gradient of these variables.
In general the decomposition process involves the development of higher order silanes moving through silicon hydrogen complexes into a silicon-hydride structure that gradually desorbs the hydrogen moving into crystalline silicon [5 - 9]. There has historically been a discussion on whether the growth rate is limited by the transport of gaseous species to the surface or the surface chemistry that forms the incoming silicon into a crystalline structure.
In the earlier proposed designs the transport of gaseous species to the surface has been depending on gas diffusion and concentration gradients. The limiting factor controlling the surface chemistry seems to be connected directly to the rate of hydrogen desorption from the surface, which is inversely dependent of the hydrogen partial pressure outside the surface. High hydrogen partial pressure outside the surface seems to limit the hydrogen desorption rate and thus the surface silicon growth.

Influence of reactor layout

Since there are a number of stages in silane decomposition and silicon growth, the history of the gas flow in terms of concentrations, temperature, pressure and time will all contribute to the probability of competing events and products.

In general there are two competing macro mechanisms, gas phase nucleation and growth and surface initiated growth. To complicate this picture the produced silicon particles may be scavenged by the growing surface, thus also contributing to the bulk growth [3, 5, 6].

The more developed the intermediate species are in terms of complete dehydrogenated particles, the more complicated it will be to fully incorporate them into a lattice without defects. It is therefore crucial to capture and incorporate the species as early as possible in their development.

When optimizing a silane decomposition reactor the key factor is control of the reaction sequence and ultimately the growth.

Centrifuge CVD

Fundamentally there are two challenges in terms of bulk growth that needs to be addressed to increase the growth speed, limit the fines production, obtain complete silane utilization and grow a dense high quality material.

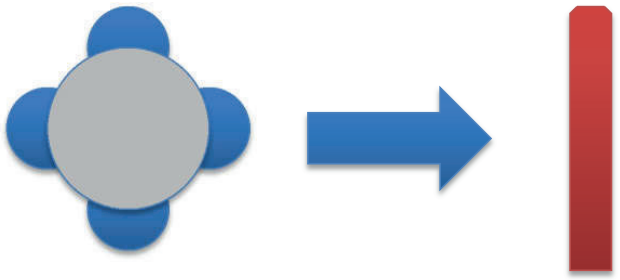

Figure 1: Effective transport of all silicon containing species to the growth surface

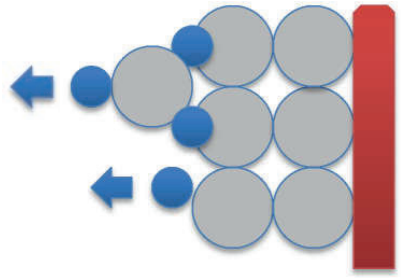

Figure 2: Low hydrogen partial pressure at the growth surface to increase hydrogen desorption and thus increase the silicon lattice incorporation efficiency

These two fundamental mechanisms controlling the silicon growth are both addressed when designing the whole reactor as a centrifuge, see figure 1 and 2. The silane and all other higher order species, complexes and particles will experience a force that actively moves them to the deposition surface. At the same time the hydrogen will experience the opposite effect and be actively moved towards the centre of reactor. This effect will be the same as when releasing hydrogen into air and that it then moves directly upwards. In a centrifuge up is toward the centre and the g force is substantially higher than earth gravity. At the growth surface the hydrogen will be released faster as the hydrogen partial pressure outside the surface is reduced due to this effective transport of hydrogen away from the surface. This release will both directly supply more vacant bonds and increase the capture of incoming silicon atoms, but also indirectly enhance the hydrogen transport to the surface from the bulk material since the amount of hydrogen inn the close to surface lattice is reduced. The team has been able to grow over 250 micron pr minute with the method which is substantially faster than all presently used commercial methods.

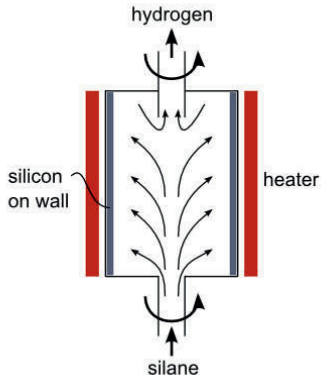

Figure 3: Centrifuge CVD reactor (CCVD), heavy silane is forced to the wall and decomposes, light hydrogen goes to the center and out

Figure 4: The Dynatec reactor 2.0

The material

The material produced in the Dynatec reactor is a dense crystalline material of high purity. The nature of the material is polycrystalline, but differs in appearance from other polysilicon sources in that there is very high homogeny in the structure of the material. The material consist of very similar crystalline columns growing out from the seed layer on the wall towards the centre of the reactor.

Figure 5: Material produced in the Dynatec reactor

The material has been tested by several institutions among them Evans Aanalytical Group (EAG) in the United States. The result of this investigation is presented in table 1. The team see that we are able to produce according to SEMI PV17 1st grade and that it may be possible to go beyond this quality with minor modifications to the reactor and if the gas feed, environment and product handling is dealt with appropriately.

Silicon product quality PPB			
Purity	Max.	Min.	Average
B	34	29	30
P	14	14	14
Ti	14	13	13
Fe	< 0,4	< 0,4	< 0,4
Al	12	11	11
Cr	< 0,2	< 0,2	< 0,2
Mn	< 0,1	< 0,1	< 0,1
Zn	4,6	2	3

Table 1. Purity of the material from Dynatec 2.0

We encourage the reader who is interested in further details to read the corresponding article in this volume [10].

The industrial reactor

The industrial reactor will also be a semi continuous reactor where harvest and seeding is done automatically hot without cooling down and heating the reactor.

Conclusions

The Dynatec reactor is the world's first method for production of high quality bulk polysilicon at a cost lower than fluidized bed. The gas utilization, low energy consumption, high degree of automation and low fines production makes the cost to price ratio very beneficial and the CCVD method is likely to play a major role in the polysilicon market of tomorrow.

Hot harvest is demonstrated and the Dynatec reactor is the world's first reactor to demonstrate harvest of bulk polysilicon and initialization without cooling down the reactor between runs. This is crucial to make use of the high growth rate of the method, which is demonstrated at over 250 micron pr minute.

The upscaling of the reactor to version 3.0 is in the engineering phase and the reactor is planned to be finalized in 2017.

Acknowledgements

The authors would like to thank the Norwegian Research Council and the EnergiX program.

References

[1] H. Gutsche Attn. Siemens-Schuckertwerke, Method for production of highest-purity silicon for electronic semiconductor devices US Pat 3.042.494

[2] Harry W. Ling Attn. E. I. du Pont de Nemours and Co. Production of Silicon, US Pat 3.012.861

[3] W. O. Filtvedt, M. Javidi, A. Holt, M. C. Melaaen, E. Marstein, H. Tathgar, P. A. Ramachandran, Development of fluidized bed reactors for silicon production, Solar Energy Materials & Solar Cells 94 (2010) 1980 – 1995.

[4] Robert H. Allen, James E. Boone, Process for preparing polysilicon with diminished hydrogen content by using a fluidized bed with a two-step heating process, Assigned to Ethyl Corporation, US Pat 5.242.671. (1993)

[5] J. O. Odden, P. K. Egeberg, A. Kjekshus, From monosilane to crystalline silicon. Part III. Characterization of amorphous, hydrogen containing silicon products, Journal of Non-Crystalline Solids 351 (2005) 1317–1327.

[6] W.O. Filtvedt, A. Holt, P.A. Ramachandran, M.C. Melaaen, Chemical Vapor Deposition of Silicon from Silane: Review of Growth mechanisms and Modeling/Scaleup of Fluidized Bed Reactors, Solar Energy Materials and Solar Cells 107, 188–200 (2012)

[7] A. A. Onischuk, V. P. Strunin, M. A. Ushakova, V. N. Panfilov, On the path ways of aerosol formation by thermal decomposition of silane, Journal of Aerosol Science 28 (2) (1997) 207–222.

[8] S. P. Walch, C. E. Dateo, Thermal decomposition pathways and rates for silane, chlorosilane, dichlorosilane and trichlorosilane, Journal of Physical Chemistry 105 2015–2022 (2001)

[9] C. S. Herrick, D. W. Woodruff, The Homogeneous Nucleation of Condensed Silicon in the Gaseous Si-H-Cl System, J. Electrochem. Soc.: Solid-state Science and Technology, 2417-2422, (1984)

[10] T. Mongstad, H. Klette, Ø. Nordseth, T. J. Preston, G. M. Wyller, W. O. Filtvedt New technologies for silicon production from monosilane; Pilot testing and on-line process monitoring aiding the development. Silicon for the Chemical and Solar industry XIII

New technologies for silicon production from monosilane; Pilot testing and on-line process monitoring aiding the development

Trygve Mongstad, Hallgeir Klette, Ørnulf Nordseth, Thomas J. Preston, Guro M. Wyller, Werner O. Filtvedt
Institute for Energy Technology (IFE), Box 40, 2027, Kjeller Norway

Abstract

Production of high-purity silicon for solar cells and electronics can be done through several routes. Although the trichlorosilane-based Siemens process is dominating the industry today there is reason to believe that monosilane-based processes and upgraded metallurgical silicon will take over in the long run.

This paper will give a short description of the status on research and development on monosilane-based polysilicon production technologies. Furthermore we will summarize some of our experiences as an independent research facility for silicon production and demonstrate some results on how pilot reactor testing, on-line monitoring and process control improves silicon production technologies.

Introduction

High-purity silicon, or polysilicon, is a feedstock for crystalline silicon wafers used in electronics and silicon solar cells. The demand for polysilicon has increased ten-fold over the last decade, driven by the sustained growth in the market for solar panels – a year on year growth of average 44% in the period from 2000 to 2014 [1]. The demand for polysilicon is expected to reach 325 000 MT/year in 2016 [2]. From 2008 to 2010, the prices collapsed from almost 500 USD/kg to around 50 USD/kg. After that, the prices have continued going down, and they are currently hovering between 10 and 15 USD/kg. This price collapse has been a challenge for the industry, being forced to reduced cost with little capital to invest in development of technology and innovation.

Since the rise of silicon-based electronics in the 1950's and 1960's, the so-called Siemens process has dominated polysilicon production. The principle of the process has been the same, but new Siemens reactors are more energy efficient. However, the process is still very energy intensive, and new Siemens reactors consume 40-50 kWh of electrical energy per kg polysilicon for the thermal decomposition step [3], which is about 1/3 of the overall energy use of for Siemens polysilicon purification of about 130 kWh/kg [4].

Siemens capacity still accounts for around 90% of the market, but it is expected that monosilane-based fluidized bed reactors (FBR), upgraded metallurgical grade (UMG) silicon, and other technologies for polysilicon production will take market shares of

more than 50% in only ten years from now [5]. Bye and Ceccaroli argue in a 2014 paper that the technology roadmaps for PV modules put a constraint on long-term polysilicon prices of 20 USD/kg, while it seems unlikely that traditional Siemens technology can deliver sustainably below 22.5 USD/kg [4].

Monosilane-based FBR production of polysilicon had been considered a high-cost and low quality method until REC Silicon started up production with their FBR plant in Moses Lake in 2009 [6]. REC Silicon demonstrated that monosilane-based FBR production yielded good quality at low cost. FBR silicon products have several advantages, among them that the product is easy to handle and process further. The energy consumption of the thermal decomposition step is about 80-90% lower than that of the Siemens process, and overall energy consumption about 60% lower [4].

While Siemens and FBR processes are based on chemical purification through distillation of gas-phase products, the UMG route deals with purification of silicon in the liquid state. An up-to-date description of this method is given by Safarian et al. [7]. Elkem Solar in Norway has since 2013 been running at full capacity of about 6000 MT/year using this method. Several initiatives on UMG and other silicon purification routes are described by Braga et al. in a review from 2008 [8]. UMG proves very promising for the future. The material is less pure than Siemens material, but use of UMG silicon in PV cells have given very promising results, even for high efficiency (>20%) solar cells [9]. The most important advantages are, however, the potential low cost (down to 11 USD/kg cash cost [4]) and the low overall energy consumption (down to around 20 kWh/kg [4]).

Chemical purification of silicon via the monosilane route

This article focusses on developments within monosilane-based technologies. Monosilane can be produced from trichlorosilane ($SiHCl_3$, abbreviated TCS) through the so-called redistribution process [10]. While TCS can be used directly in Siemens reactors, the monosilane route is an alternative which will become increasingly important in the future polysilicon industry [4].

Production of polysilicon from monosilane has several benefits: Silane has a very low boiling point (-112°C), which makes it easy to distill and very high purity can be achieved. Furthermore, the highly corrosive by-products from TCS are avoided, which simplifies the decomposition technology and the corresponding choice of materials. Monosilane also has a substantially lower decomposition temperature than TCS, which lowers the energy use and further simplifies the decomposition reactor setup.

There are, however, also challenges with monosilane. The gas is extremely reactive in air, and can self-ignite or explode under certain conditions. Therefore, the safety of experimental setups and industrial facilities is of high priority. This is, however, not only an issue for monosilane; TCS gas and its by-products also come with a safety hazard, maybe more severe than for monosilane.

Another practical challenge with monosilane is that there currently are very few producers of the gas, and any large-scale industrial facility based on monosilane would require a monosilane source co-located with the silicon production facility. Such monosilane production technology has only recently become commercially available [11].

New monosilane-based technologies

Fluidized bed reactor technology

Most of the non-Siemens polysilicon capacity to be added over the next few years is based on FBR technology. Currently there are three large FBR plants with capacities of several thousand tons/year in the pipeline; GCL-Poly (China), REC Silicon and Youser Group joint venture (China), and SunEdison Semiconductor (South Korea). Even though the principles of FBR polysilicon production was developed in the 1960's, there is substantial room for variation in the practical implementation [12]. Most of the recent development has taken place in-house in the various companies. There is therefore little information available on the projects that are currently under construction, but there is reason to believe that all the three main current projects are substantially different [6].

Recently the German-American company SiTec claims to have developed a concept based on decomposition of monosilane in a vibrating FBR, which they intend to offer as a third-party equipment provider [13]. Vibration contributes to the fluidization of the bed and makes the reactor able to run with low gas flow velocities and no dilution gas.

Centrifugal chemical vapor deposition

Dynatec Engineering has since 2011 tested two pilot-scale reactors based on a completely new principle within silicon production, in what they call a centrifuge chemical vapor deposition (C-CVD) reactor [14], [15]. The principle is to inject monosilane gas in a rotating reactor volume. The centrifuge effectively separates heavier gas molecules and fines from the light hydrogen gas. The pilot reactors have proven very promising; yields reach well above 95%, growth rates are 40 times higher compared to the Siemens reactor, and the reactor operates in semi-continuous mode [15]. The material from the C-CVD reactor is granular and can therefore be handled similar to FBR granules. More information about Dynatec's progress is available in the current conference proceedings [16]. Some results from the C-CVD reactor are also presented in this article as a demonstration of how the silicon production lab platform at Institute for Energy Technology (IFE) can be used for testing pilot technologies.

Free space reactors

The simplest of all monosilane decomposition technologies might be the hot wall, or so-called free-space reactor (FSR), where flowing silane gas is subjected to heating and converted to hydrogen and solid silicon. Several players, including Union Carbide and Joint Solar Silicon, have attempted to develop FSR technology for polysilicon production [17]. To the best of our knowledge, none of these technologies are currently being pursued.

However, free space silicon products may find other applications. Beyond the electronics and solar cells, there is a promising future application for silicon as a battery material. Silicon in the anode of Li-ion batteries is capable of storing up to ten times more Li ions than the current carbon anode [18]. For this purpose, silicon particles with size distributions in the sub-micron range are desired, and production methods are therefore different from those for polysilicon grains and chunks. Mangolini et al. have provided a thorough review of research-scale production methods for silicon powders and their applications [19]. Technology based on the use of lasers, or low-pressure plasmas give high level of control with the reaction zone and high quality products, but yield low production throughput. We believe that thermal decomposition in atmospheric or higher pressure CVD chambers is the most industrially relevant method. At IFE, we have developed a pilot FSR capable of producing silicon powder at a rate

in the range of 100 g/h. The FSR setup can also tailor crystallinity [20], doping and size distribution [21] of the products.

As will be demonstrated in the following, an FSR is also very useful for exploring the parameter space and chemistry of monosilane decomposition technologies. That is because its simple geometry yields good control with the actual reactor conditions instead of other technologies where the local conditions vary substantially over the reactor volume. Conditions can also be changed quickly, so the large parameter space (e.g. flow rates, gas mixtures, residence times, temperature ranges) can be mapped out in a continuous manner.

The silicon production pilot platform at IFE

The silicon production research group at IFE has over the last ten years developed an independent platform for testing monosilane-based reactor technology. Currently, two free space reactors, one fluidized bed reactor and one centrifugal CVD reactor are installed in the lab. Pilot projects and contract research have been carried out for close to ten industrial customers within the silane and silicon production industry.

A principle sketch of the IFE pilot platform lab for silicon production is displayed in Figure 1. The lab space and infrastructure is designed to easily install and test pilot reactors for silane decomposition, and entails common gas delivery system, control room, process monitoring tools and an exhaust handling system for hazardous gases.

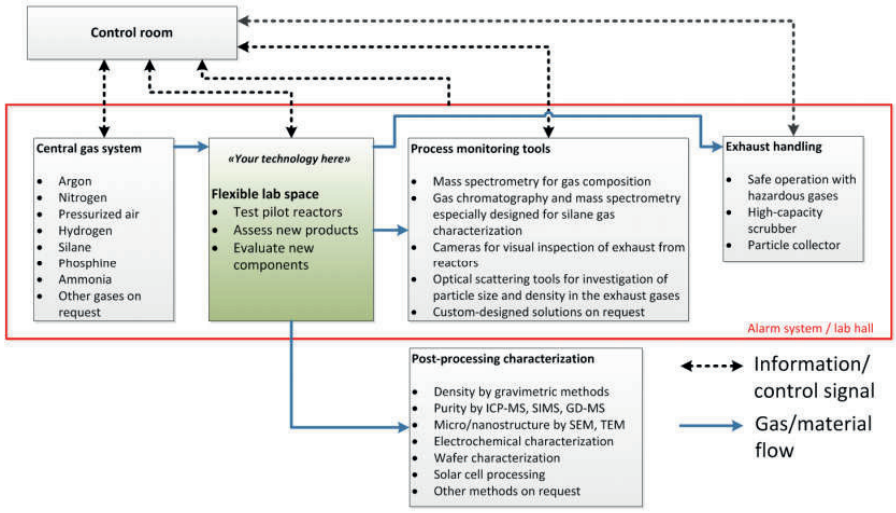

Figure 1: An outline of the silicon production pilot lab at Institute for Energy Technology.

The main lab is a hall with 200 m^2 ground floor and a 45 m^2 mezzanine. There is a wide garage door and a roof-mounted crane in the hall for easy installation of pilot reactors and parts.

The hall is designed for a controlled collapse in case of explosion and all reactors are run from a safe control room with concrete walls and bulletproof windows. The lab space is monitored by gas detectors, fire sensors, smoke detectors and video cameras in strategic locations and the detectors feed in to a central alarm system for IFE which also notifies the fire brigade directly in case of any incident. A photo of the lab hall and the control room can be seen in Figure 2.

Figure 2: The silicon production laboratory at IFE. Inset: The control room from which all pilot reactors are controlled remotely to ensure the safety of the operators.

Process monitoring tools

The process monitoring tools are designed to understand exactly how the reactor conditions affect the silicon production and the chemical events that take place at any time. There are several on-line tools for chemical monitoring and particle detection, in addition to the direct monitoring of temperature, pressure and other conditions in the reactor subject to testing.

For gas characterization, a Vision 1000-C Mass Spectrometer (MS) from MKS Instruments is connected to the outlet stream of the reactors. The MS has a fast response rate and high sensitivity to changes in the outlet gas, related to quantification and detection of gases in the exhaust stream. There is also a Gas Chromatography - Mass Spectrometer (GCMS) from Agilent, that is specially designed for detection of silanes. The GCMS is a suitable tool for quantification of SiH_4, Si_2H_6, and Si_3H_8, and for detection and qualitative concentration comparison of even higher order silanes, as demonstrated on the next page of this article. The presence of higher order silanes is an important indicator of the state of the decomposition process and the local chemical environments in the decomposition reactors. Such sensitive instruments can help identify optimization points and aid the design of reactor technology.

Particles (fines) can be detected in an optical detector based on scattering of light from a broad-spectrum UV to near-IR light source. Scattered light is collected at different scattering angles by video cameras and an optical spectrometer, and gives valuable on-line information on the amount and nature of the particles generated in the reactors. The generation of fines is one of the prime challenges for monosilane-based FBR technology [6]. Knowing under what conditions fines formation occur is crucial to design efficient industrial FBR's.

Testing of monosilane-based reactor technology at IFE

IFE has over the last ten years run tests on three different free-space reactor designs, one FBR and two C-CVD reactors. In the next section we demonstrate some results and how our experiments help understand these technologies.

Free-space reactor experiments

Recently, we have been using an FSR quite intensively for understanding the chemistry of monosilane decomposition and how parameters such as temperature, pressure, residence time, dilution gas and concentration affect the process and the produced

material. The FSR shows to be a very useful tool for increasing the fundamental understanding of silicon production. We achieve high control with parameters, and we can change the experimental conditions very fast. In contrast, in FBRs the local conditions vary a lot over the extension of the bed, and there is a large thermal mass that makes it slow to change temperatures. The FSR can *simulate* the local conditions in the FBR or other reactor technologies and in that way provide information that is impossible to obtain directly.

A large set of data for temperature, pressure, mass flows and chemistry in different locations is collected from the FSR during experiments. Figure 3 shows how the correlation of three of these parameters (temperature, silane concentration and particle generation) can be used to find the particle nucleation onset (also called the homogenous nucleation point). More details on the experiment and the further interpretation and analysis are available elsewhere [22].

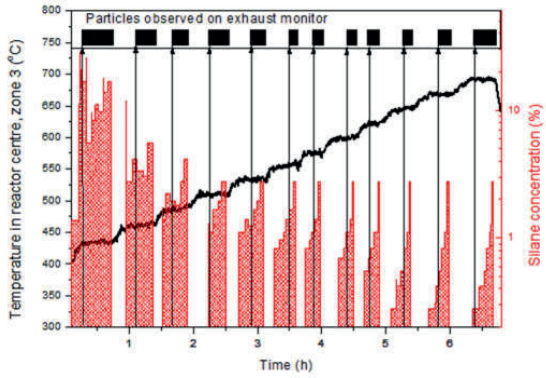

Figure 3: Detection of the homogenous particle nucleation onset for monosilane in hydrogen. The data are presented as a function of time in the experiment, while reactor temperature and silane concentration are varied. For more details, see ref. [22].

At the same time we can measure the concentration of different gases and chemical species in the reactor exhaust with the MS and GC-MS. Figure 4 shows an example of how the population of higher order silanes develops as a function of temperature. An analysis of this will be subject of a future publication.

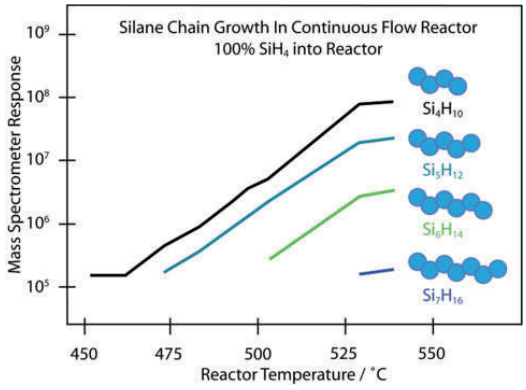

Figure 4: Development of concentration of higher order silanes as a function of temperature, as measured by the GC-MS on the exhaust flow from our pilot FSR reactor.

FBR experiments

In a series of experiments from 2010 to 2013, we explored how different parameters in an FBR affect the processing and the properties of the polysilicon granules. We found that both the chemistry of the fluidization gas and the processing temperature play an

important role in the deposition of material on the surface, and thus the material quality. Figure 5 shows that two different growth regimes were identified, whereof we believe one is more preferable to pursue for industrial purposes than the other. We also observed two regimes for fines formation, which may provide a key to what is believed to be one of the main challenges with FBR production of polysilicon. More details are available elsewhere [23].

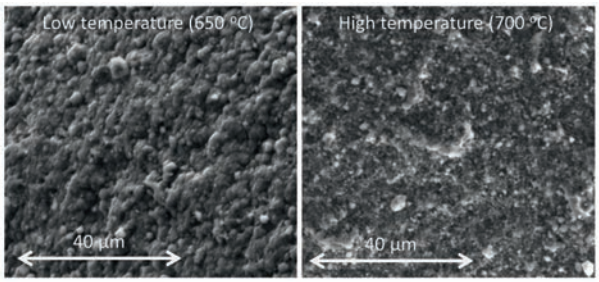

Figure 5: Scanning electron microscopy image demonstrating two different regimes of silicon growth on FBR granules: Here, low temperature promotes a more uniform growth with less fines formation. For more details, see ref. [23].

C-CVD reactor experiments

Since 2011, IFE has been testing pilot reactors based on the new C-CVD principle with Dynatec Engineering. This is a completely new technology for polysilicon production that, as described in the start of this article, promises high yields, simplicity of operation and good material quality. The reactor technology has been developed by Dynatec Engineering, while IFE has been responsible for providing the necessary support infrastructure, process monitoring, planning and running production experiments and for the silicon product characterization.

As mentioned before, the process can achieve yields of 95% and above. Figure 6 displays a sample of a measurement where adjustments of reactor conditions changes the yield from around 85% to above 95%. By adjustments of processing conditions combined with on-line monitoring of chemistry and particle generation, we can quickly reach ideal production conditions. The on-the-fly yield is calculated based on flow rates of silane into the reactor and calibrated MS measurements of the silane concentration in the exhaust. The overall yield for the experiment is found by post-processing measurement of the mass of the silicon product compared to the total silane use. We encourage the reader who is interested in further details to read the corresponding article in this volume [16].

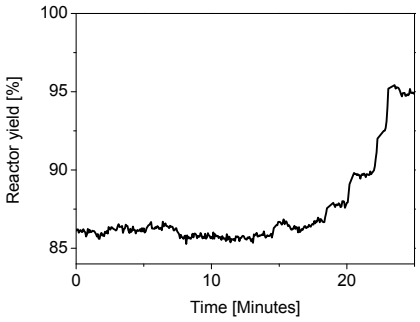

Figure 6: Development of reactor yield (conversion of monosilane to solid silicon) as a function of time when adjusting parameters in a pilot C-CVD polysilicon production reactor.

Figure 7 shows examples of data from the optical exhaust monitoring setup, which guides us in understanding the reactor conditions. A collimated light beam is passing from top to bottom in the images, and we see how the beam intercepts the particle flow.

In this case we see optical scattering on smaller particles (parameter set 1) and larger particles (parameter set 2). In the case of no particle generation, no optical scattering is observed, and with very high particle flow rates the scattered light will also be low due to high absorption of light in the particles. The optical exhaust monitoring is a close to instant feedback tool that helps the operator to quickly find the optimum working conditions for the desired product.

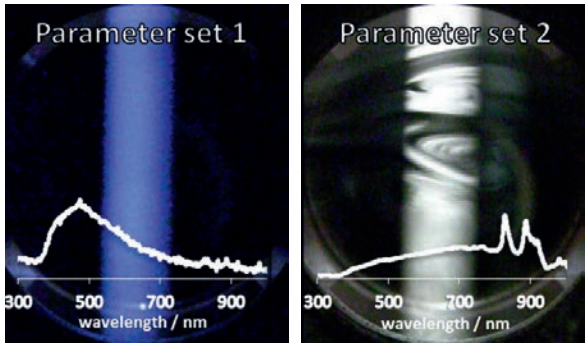

Figure 7: Optical scattering on particles in the exhaust gas from a pilot C-CVD reactor under different reactor operation parameters. The overlay displays optical scattering intensity as a function of wavelength, measured by an optical spectrometer.

Conclusions

The polysilicon industry will over the coming decade experience continued pressure on price. To lower the cost it will be necessary to move to monosilane-based production and UMG processes. These technologies are, however, not yet fully mature and only to a limited extent available for polysilicon producers through third party suppliers. Substantial technological development is to be expected. We have here seen some examples of how our tools have been applied to optimize FBR and C-CVD silicon production technologies, and we are poised to accelerate the development of many future and maybe unheard-of silicon production technologies.

Acknowledgements

The work has been performed in The Norwegian Research Centre for Solar Cell Technology (NFR project no. 193829/E20), with funding from the Norwegian Research Council and the centre partners (see http://www.solarunited.no/partners/).

References

1. B. Burger, *Fraunhofer ISE: Photovoltaics report 2015*, November. 2015.
2. J. Chase, *Bloomberg New Energy Finance: PV Market Outlook,* in INTPOW SOLAR DAY 2016, Oslo 10 February 2016.
3. S. K. Chunduri, *Innovations in inertia - Market survey on Siemens-type CVD reactors*, Phot. Int., no. April, pp. 114–126, 2013.
4. G. Bye and B. Ceccaroli, *Solar grade silicon: Technology status and industrial trends*, Sol. Energy Mater. Sol. Cells, **130**, pp. 634–646, 2014.
5. *International Technology Roadmap for Photovoltaic (ITRPV),* 2015.
6. C. Roselund, *The slow grind of FBR polysilicon*, PV Mag., vol. 09, pp. 88–91, 2015.
7. J. Safarian, G. Tranell, and M. Tangstad, *Processes for upgrading metallurgical grade silicon to solar grade silicon*, Energy Procedia, **20**, no. 1876, pp. 88–97, 2012.

8. A. F. B. Braga, S. P. Moreira, P. R. Zampieri, J. M. G. Bacchin, and P. R. Mei, *New processes for the production of solar-grade polycrystalline silicon: A review*, Sol. Energy Mater. Sol. Cells, **92**, no. 4, pp. 418–424, 2008.
9. P. Zheng, F. E. Rougieux, C. Samundsett, X. Yang, and Y. Wan, *Simulation of 20.96 % efficiency n-type Czochralski UMG silicon solar cell*, Energy Procedia (submitted), 2016.
10. V. Petrova-Koch, R. Hezel, and A. Goetzberger, *High-Efficient Low-Cost Photovoltaics*. Springer, 2009.
11. GT-AT, *Silane Production*. Available online: http://www.gtat.com/Collateral/Documents/English-US/Polysilicon/SilaneProductionOriginal_Data Sheet_low.pdf. [Accessed: 06-Apr-2016].
12. W. O. Filtvedt, M. Javidi, a. Holt, M. C. Melaaen, E. Marstein, H. Tathgar, and P. A. Ramachandran, *Development of fluidized bed reactors for silicon production*, Sol. Energy Mater. Sol. Cells, **94**, no. 12, pp. 1980–1995, Dec. 2010.
13. *SiTec GmbH Announces New Monosilane Decomposition Technology*, SiTec Press release, 2015. [Online]. Available: http://centrotherm-sitec.de/fileadmin/Pressemitteilungen/2015/News_SiTec_Genesis_201509_Final.pdf. [Accessed: 22-Mar-2016].
14. W. O. Filtvedt, T. Mongstad, H. Klette, A. Holt, S. Sørensen, and J. Filtvedt, "*A Novel Centrifuge CVD Reactor Yielding High Quality Polysilicon By Low-Energy Silane Pyrolysis*, in 28th European Photovoltaic Solar Energy Conference, 2013.
15. W. O. Filtvedt, H. Klette, S. Sørensen, and J. Filtvedt, *Low cost/high quality silicon production by centrifuge CVD upscaled and hot harvest*, in EU PVSEC, 2015.
16. S. Sørensen, W. O. Filtvedt, and J. Filtvedt, *On the road to industrialisation of a new centrifuge CVD reactor for polysilicon*, (submitted) in Silicon for the Chemical and Solar Industry XIII, 2016.
17. B. Ceccaroli and S. Pizzini, *Processes*, in *Advanced Silicon Materials for Photovoltaic Applications*, John Wiley and Sons, 2012, pp. 21–78.
18. D. Larcher, S. Beattie, M. Morcrette, K. Edström, J.-C. Jumas, and J.-M. Tarascon, *Recent findings and prospects in the field of pure metals as negative electrodes for Li-ion batteries*, J. Mater. Chem., **17**, no. 36, p. 3759, 2007.
19. L. Mangolini, *Synthesis, properties, and applications of silicon nanocrystals*, J. Vac. Sci. Technol. B, **31**, no. 2, p. 020801, 2013.
20. B. S. Holsclaw, M. J. Molnar, W. Herron, J. P. McDonald, M. A. Gave, and J. J. Host, *Controlled Crystallinity of Silicon Powders*, in Silicon for the Chemical and Solar Industry XII, 2014, pp. 167–176.
21. H. F. Andersen, W. O. Filtvedt, J. P. Mæhlen, T. Mongstad, M. Kirkengen, and A. Holt, *Production of Silicon Particles for High-Capacity Anode Material, Yielding Outstanding Production Capacity*, ECS Trans., **62**, no. 1, pp. 97–105, 2014.
22. G. M. Wyller, T. J. Preston, H. Klette, Ø. Nordseth, T. T. Mongstad, W. O. Filtvedt, and E. S. Marstein, *Critical Nucleation Concentration for Monosilane as Function of Temperature Observed in a Free Space Reactor*, Energy Procedia (submitted), 2016.
23. W. O. Filtvedt, T. Mongstad, A. Holt, M. Melaaen, and H. Klette, *Production of Silicon from SiH4 in a Fluidized Bed , Operation and Results*, Int. J. Chem. React. Eng., **11**, no. 1, pp. 1–12, 2013.

Property control of mc-Si containing P and B using Al co-doping method

Yuliu You, Kazuki Morita
Department of Materials Engineering, The University of Tokyo, Japan

Abstract

In the present work, an Al co-doping method was employed to improve the electrical properties of mc-Si containing P and B. The method is based on the compensation theory and on the different segregation coefficients of Al (k_{Al}=2.8×10^{-3}), B (k_B=0.8), and P (k_P=0.35) in Si during solidification. The resistivity and minority carrier lifetime throughout the height of the Si ingots with and without co-doping of Al were measured. The results show that a relatively high resistivity and minority carrier lifetime can be achieved by adding a controlled amount of Al. In addition, the effect of the grain boundary on the electrical properties was studied.

1. Introduction

A promising path to reduce the cost of solar energy is the use of low-cost Si feedstock, or upgraded-metallurgical-grade Si (UMG-Si), obtained by simplified purification processes. A distinctive characteristic of UMG-Si is that it contains both acceptor (B) and donor (P) atoms in a relatively large amount, which can be considered an inevitable issue. Owing to compensation defined as the presence of donor and acceptor species in comparable amounts, it is possible to tolerate high concentrations of P and B that are frequently difficult to remove completely by means of metallurgical refining methods. In compensated Si of this sort, the electrical properties differ from those of simply B-doped Si. Previous results [1] have shown the minority carrier lifetime to be higher and thus solar cells to be more efficient at high compensation levels (C_l), i.e., low net doping, N_A-N_D. Further, a high C_l seems to have a positive effect on the so-called light-induced degradation observed in B-doped and O-contaminated Si. However, because of the lower segregation coefficient of P (0.35) compared to that of B (0.8), the net doping is not uniform along the ingot height and inversion of Si polarity, from p- to n-type, may occur during crystallization. This reduces the material yield for industrial solar cell fabrication. To overcome this issue, controlled amounts of Al were added to P-B-compensated Si. The triple doping of Al, B, and P relies on the low segregation coefficient of Al (2.8×10^{-3}), which enables the increased P concentration (relative to that of B) to be counterbalanced during crystal growth. In this study, we explore the influence of Al co-doping on a multi-crystalline Si (mc-Si) ingot, grown with high-purity solar-grade Si (SOG-Si) to

which known concentrations of B, P, and Al were added. The study focuses on the dependence of electrical properties, such as the minority carrier lifetime and resistivity, on the concentration of doping impurities. Finally, the effect of grain boundaries on the electrical properties is characterized.

2. Calculation

The vertical distribution of dopants concentration along cast crystalline mc-Si ingots follows the Scheil equation:

$$C_I \quad C_{I,0} \bullet k_I \bullet (1-f_S)^{k_I-1} \qquad (1)$$

where C_I is the concentration of dopant I at a given solidified fraction fs, $C_{I,0}$ is its initial content in molten Si before solidification, and k_I is its segregation coefficient in Si.

Based on equation (1), the distribution of the net doping concentration was calculated along the ingot height, under the different initial conditions listed in Table1.

Table 1: Dopant contents in the molten Si before solidification.

Dopant	$C_{B,0}$(cm^{-3})	$C_{P,0}$(cm^{-3})	$C_{Al,0}$(cm^{-3})
SOG	0	0	0
P	0	2×10^{17}	0
Al	0	0	1×10^{19}
B	1×10^{17}	0	0
Al+B+P	1×10^{17}	2×10^{17}	1×10^{19}

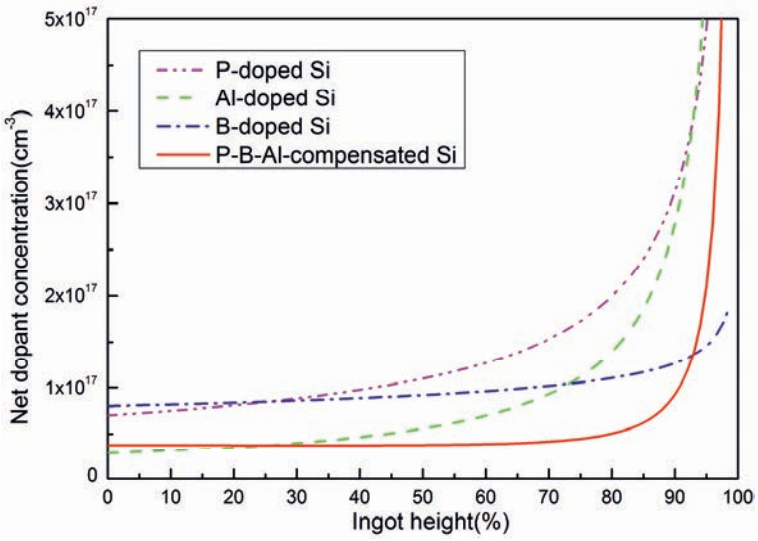

Figure 1: Calculated net doping distribution profiles under different conditions.

The calculation results are shown in Figure 1. For the Si doped with only one kind of dopant, each distribution profile shows a different trend. Owing to the different segregation coefficients, the distribution is not uniform throughout the ingot height. Furthermore, we can also see an intersection between B-doped Si and P-doped Si indicating an inversion of the polarity type in Si ingot co-doped with B and P. This

would certainly reduce the material yield. As a comparison, the ingot co-doped with Al, B, and P shows a quite narrow variation of net dopant concentration along the ingot. This calculation indicates that it is possible to obtain a very uniform net doping and hence uniform electrical properties over a large fraction of the ingot by adding a specific amount of Al.

3. Experiment

For this study, an mc-Si ingot with a diameter of ~ 20mm was grown using the directional solidification method. High-purity solar-grade single crystal Si feedstock was used, to which known concentrations of B, P, and Al were added (Table 1). The concentrations of B and P correspond to those of UMG-Si. The added Al concentration was calculated using Scheil's law in order to obtain a fully p-type ingot, with a relatively low net doping concentration. B and P were introduced through highly doped Si wafers, for which the doping impurity concentration was evaluated by means of four-point probe resistivity measurements correlated to the Irvin curves. Al was introduced in the form of high-purity Al powder. All the dopant sources were accurately weighed, and then placed in the crucible together with the Si feedstock before melting. The Si ingot was grown with an average lowering rate of v=0.2 mm/min and a temperature gradient of 1.2 °C/mm under Ar gas protection. The experimental apparatus is shown in Figure 2.

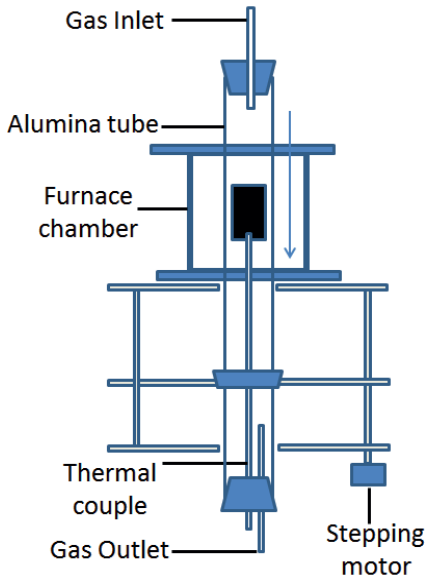

Figure 2: Apparatus for directional solidification.

The resulting ingot was then sliced into 4-mm-thick wafers along the ingot height. After mechanical polishing, four-point probe resistivity measurement was performed on the wafers to determine the electrical activation of dopants. After surface passivation by 0.01 mol/L Quinhydrone/Methanol solution for 1 h in the dark, the minority carrier lifetime was measured using the μ-PCD method. Then, after etching using 200 g/L NaOH solution for 10 min, the average grain size was measured.

4. Results and Discussion

4.1 Resistivity profiles

Figure 3 shows the resistivity measured at various points along the ingot height. We can see that the measured resistivity of P-B-Al-compensated Si is p-type along the entire ingot height, ranging from 0.9 to 2.7 Ω•cm, a proper range for the fabrication of high-performance solar cells. In addition, the resistivity of the compensated sample is comparable with that of SOG-Si and much higher than those of other uncompensated samples. It is well known that for uncompensated Si, the resistivity is given by:

$$\rho = 1/\mu n_0 e \qquad (2)$$

where μ is the carrier mobility and n_0 is the net dopant concentration. Therefore, by measuring the resistivity, we can determine the net dopant concentration n_0, which determines most of the electrical properties of Si and the overall performance of solar cells. Nevertheless, because of the presence of dopants of both types, there is no unambiguous relation between the resistivity and the net dopant concentration in compensated Si.

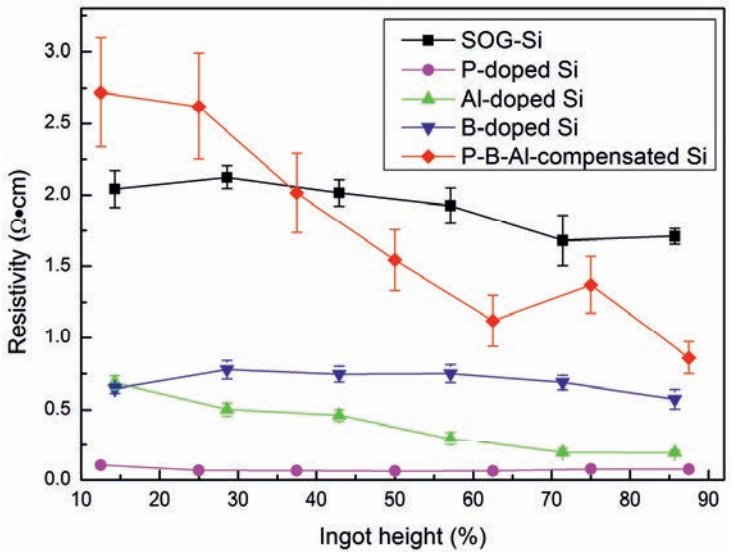

Figure 3: Resistivity along the ingot height under different conditions.

According to the available experimental evidence and the widely accepted model of Klaassen [2], the net dopant mobility is lower in compensated Si than in uncompensated Si with the same net doping. At equal net dopant density n_0, the resistivity will generally be higher in compensated Si than in uncompensated Si [3]. As a result, the resistivity specifications defined for uncompensated SOG-Si are not sufficient to determine the suitability of the compensated Si material. We also need to measure the most important property, which is the minority carrier lifetime of Si for solar cells.

Furthermore, there is a drastic decreasing trend of the resistivity along the ingot height in Al-doped Si and P-B-Al-compensated Si. Table 2 quantitatively shows the

decrease of the resistivity from bottom to top. This phenomenon can be explained by the segregation of Al at grain boundaries. The Al prefers to segregate at the grain boundaries. When the concentration of Al at grain boundaries increases to a given extent, the insulating grain boundaries will become electrically active, resulting in the decrease of the resistivity.

Table 2: Decrease of the resistivity from bottom to top.

	Bottom (Ω•m)	Top (Ω•m)	Decrease
SOG	2.045	1.711	16.3%
P	0.105	0.076	27.2%
Al	0.690	0.193	**72.0%**
B	0.647	0.575	11.1%
Al+B+P	2.719	0.862	**68.3%**

4.2 Minority carrier life time

Figure 4 shows that for the compensated samples, the measured lifetime lies in the range 70-130 μs along the entire ingot. This value is much higher than those for uncompensated samples (the minority carrier lifetime of P-doped Si is too low to be detected) and even higher than that of SOG-Si at most parts of the ingot. These results highlight the possibility of fabricating high-performance solar cells with Si feedstock containing high concentrations of B and P.

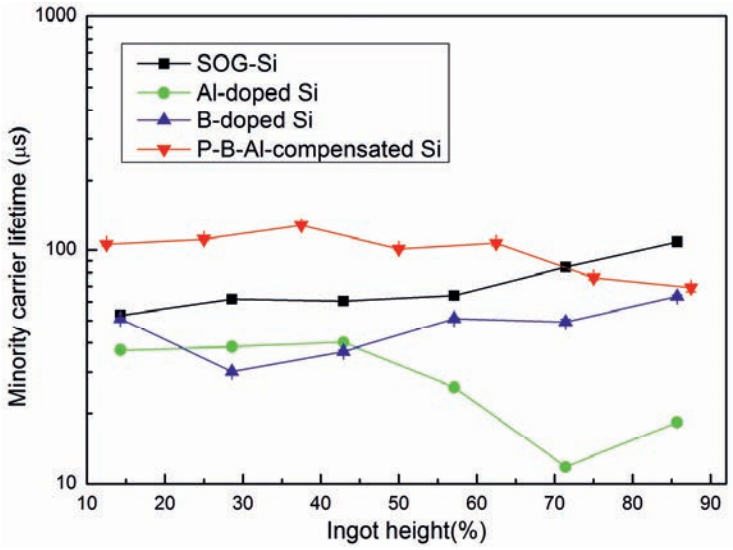

Figure 4: Minority carrier lifetime along ingot height under different conditions.

The high minority carrier lifetime of compensated samples can be explained by a recombination mechanism. There are three main recombination mechanisms in semiconductors: radiative recombination, Auger recombination, and recombination through defects. Radiative and Auger recombination are intrinsic recombination mechanisms. The recombination rate for p-type Si is given by:

$$R_{intrinsic}=n\times p\times (6\times10^{-25}\times p_0+3\bullet10^{-27}\Delta p^{0.8}+9.5\times10^{-15}) \quad (3)$$

$$\tau_{intrinsic}=\Delta p/ R_{intrinsic} \quad (4)$$

where p_0 stands for the net doping and Δp is the excess carrier density [4]. Therefore, with a lower net doping, higher Auger and radiative lifetimes are expected to be obtained in both compensated and non-compensated Si. Regarding the recombination through defect, the main defect in mc-Si is grain boundaries. Thus, the grain boundary length and the electrical properties of the grain boundaries have significant effect on the minority carrier lifetime.

4.3 Effect of grain boundaries on the minority carrier lifetime

On a linear scale, we can see the trend of the minority carrier lifetime of SOG-Si and compensated Si clearly (Figure 5). As a comparison, the trend of the grain size along the ingot is shown in Figure 6.

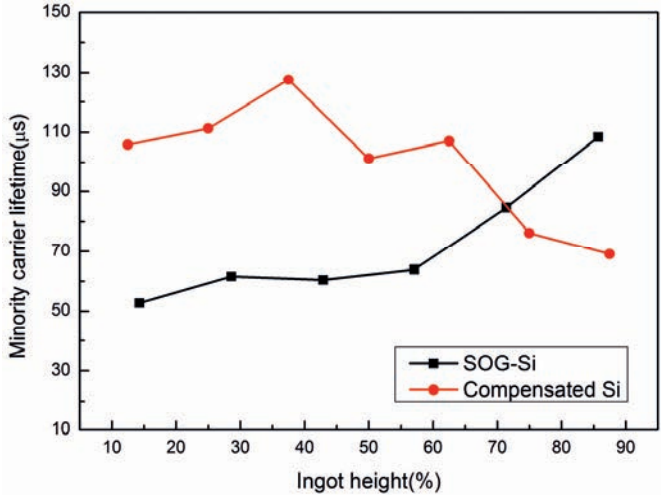

Figure 5: Minority carrier lifetime of SOG-Si and compensated Si on a linear scale.

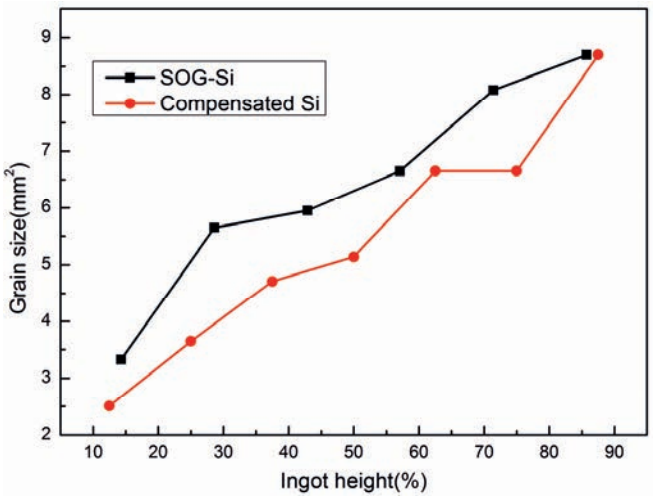

Figure 6: Grain size trend of SOG-Si and compensated Si along the ingot height.

In Figure 5, we can see that the minority carrier lifetime of SOG-Si increases with the grain size. This is expected, as a larger grain size leads to a shorter grain boundary length and hence, fewer recombination centers. However, the minority carrier lifetime of the compensated Si increases first and then decreases as the grain size increases continuously. This phenomenon can also be explained by Al segregation at the grain boundaries. The Al segregation at the grain boundaries to a certain extent makes the grain boundaries electrically active. These kinds of grain boundaries can act as strong recombination centers. The increase of the grain size and the increase of the Al concentration at the grain boundaries have opposite effects on the minority carrier lifetime resulting in the trend inversion.

5. Conclusions

An Al co-doping method for controlling the properties of mc-Si containing both P and B has been proposed, based on the compensation theory and Scheil's law. After calculation, the amount of Al added to the P-B-containing Si was determined. The electrical properties such as resistivity and minority carrier lifetime were determined to verify this method. The conclusions are as follows:

(1) The net dopant concentration of P-B-Al-compensated Si ingot remains uniform along the entire ingot height compared with that of uncompensated Si.

(2) The electrical properties of compensated Si are better than those of uncompensated Si, and are comparable to those of SOG-Si after the same directional solidification procedure.

(3) The Al co-doping method effectively eliminates some of the adverse effects of B and P in Si. Thus, it may be used to increase the B and P concentration limits allowed in UMG-Si to produce high-quality solar cells.

(4) The grain boundary has a significant effect on the electrical properties and further studies are recommended.

References

1. S. Dubois et al., Applied Physics Letters, **93**, 2008, 032114
2. D.B.M. Klaassen, Solid State Electronics, **35**, 1992, p953

3. M.Foster et al., Solar Energy Materials & Solar Cells, **111**, 2013, p146
4. M. J. Kerr et al., Journal of Applied Physics, **91**, 2002, p2473

Removal of phosphorus and boron from silicon via solvent refining with ferrosilicon alloys

Leili Tafaghodi[1)], Mansoor Barati[2)]
1) Department of Materials Engineering, University of British Columbia
2) Department of Materials Science and Engineering, University of Toronto

Abstract

Distribution of phosphorus and boron between solid silicon and silicon-iron alloy melt was studied to investigate the extent of phosphorus and boron removal from silicon by solvent refining with ferrosilicon alloys. Distribution coefficient values for phosphorus obtained at different temperatures are as follows: 0.22 (1583K (1310°C)), 0.29 (1533K (1260°C)) and 0.33 (1483K (1210°C)). The corresponding removal percentages of phosphorus were: 86% (1583K (1310°C)), 75% (1533K (1260°C)), and 67% (1483K (1210°C)). The average phosphorus content of the purified silicon in the proposed solvent refining process would be over two times less than that of the conventional directional solidification. In the case of boron, solvent refining at lower temperatures results in smaller distribution coefficients. For the lowest boron concentration examined in this study, the distribution coefficient values are: 0.51 (1583K (1310°C)), 0.45 (1533K (1260°C)) and 0.33 (1483K (1210°C)). The boron removal percentages associated with the same samples are 70, 65, and 65% respectively. The average boron content of the refined silicon in the proposed process is 2-3 times less than that of the conventional directional solidification refining.

Introduction

Producing silicon with acceptable purity level for solar applications through a cost efficient process is a major challenge in solar silicon industry. Producing low-cost solar grade silicon by metallurgical refining techniques is one of the approaches that have attracted wide research interests. Since metallurgical processes are selective in removing impurities, a combination of various purification processes can be applied to decrease the impurity level in silicon. Each refining step is responsible for lowering specific impurities due to different thermodynamic characteristics of impurities. Recrystallization of silicon from an alloy, also known as solvent refining is one of the metallurgical steps that has been employed for producing solar grade silicon from metallurgical grade silicon.

Phosphorus and boron removal with solidification refining processes is problematic due to their high distribution coefficient between solid and liquid silicon. Various metallic elements including, Al [1-10], Cu [11-13], Ni [14], Sb [15], Sn [16] and Fe [17-20] have been used as the getter. One of the main advantages of iron is its high density in comparison with silicon. This allows employing a liquid heavy media in order to separate Si and Si-Fe alloy phases after the solvent refining stage [17-18]. Moreover iron is potentially a suitable candidate since it is considerably less expensive and its solid solubility in silicon is significantly lower than aluminum, copper, nickel [21-22]. This will result in lower costs and less residual iron in the purified silicon. The by-product of the process, ferrosilicon, can be used in the steel industry. In the view of the above iron has been employed as the alloying element for purification of silicon [17-20].

Aside from the properties mentioned above, one of the primary requirements of the alloying agent in solvent refining of silicon is the affinity of the solvent for phosphorus and boron; this influences the efficiency of phosphorus removal. Thus it is essential to study the distribution of phosphorus and boron in solid silicon and in silicon-iron melt in order to optimize their removal from silicon.

Materials and Methods

The experimental procedure starts with preparing an alloy of silicon, iron and either phosphorus or boron as the impurity of interest. As the presence of elements other than these can influence the thermodynamic properties of the impurity, it is critical to avoid the introduction of other impurities from the possible sources. Therefore, electrolytic iron and high purity silicon (99.998%) were used as the starting materials. Also, the experiments were carried out in ultra pure quartz crucibles to avoid contamination from the crucible.

According to the silicon-iron phase diagram (Figure 1), the alloy should contain more than 58.2wt% silicon to allow formation of silicon crystals at the equilibrium condition above the eutectic temperature. The solvent refining process involves melting and controlled solidification of a silicon iron-phosphorus (or boron) alloy (80 wt% Si- ~20 wt% Fe).

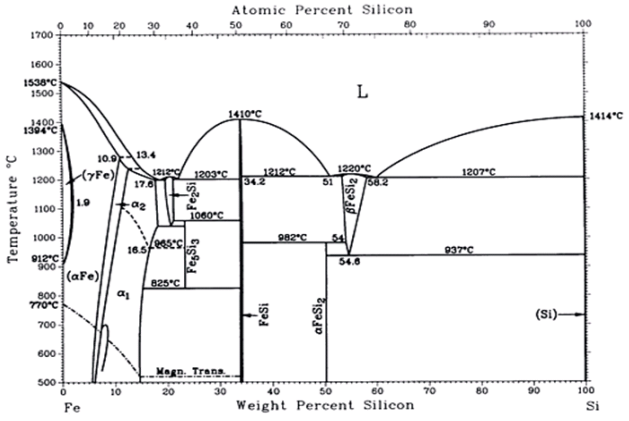

Figure 1: Si-Fe phase diagram [23].

The samples were heated up to 1600 C (1873K) in a vertical tube furnace. The samples were kept at 1600 C for 3 hours and then slowly cooled down to 1310 C (1583K) at the rate of 0.5 C/min. The first series of samples were kept at 1310 C for 1 hour and finally quenched in water. Trying to investigate the effect of temperature on impurity removal, quenching from 1260 C (1533K) and 1210 C (1483K) was also examined. The heating/cooling profiles with different quenching temperatures are shown in Figure 2.

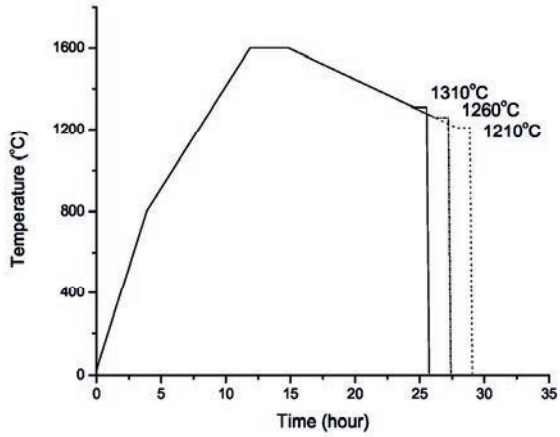

Figure 2: Temperature profile of the furnace for different quenching temperatures.

The solidified sample is removed from the crucible and ground to -37 μm (Mesh No. 400). The next stage involves separation of silicon and alloy particles by leaching in a HF solution. Leaching solution includes 10 vol% HF, 20 vol% acetic acid and 70 vol% deionized water. Iron-silicon alloy dissolves in HF while silicon particles remain intact. The silicon product is then digested for ICP-AES analysis.

Results and discussion

The concentration of phosphorus (and boron) in the whole sample and in solid silicon phase was measured using ICP-AES. Using the two values, the phosphorus (and boron) content of the alloy melt was calculated based on mass balance. The mass fraction of the alloy melt that was calculated based on iron-silicon phase diagram is as follows: 0.49 (1483K), 0.57 (1533K) and 0.64 (1583K). For each sample, the average of 3 replicates was used for reporting the phosphorus concentration.

Distribution coefficient

Concentration of phosphorus (or boron) in silicon and alloy phase were employed to calculate distribution coefficient of impurity i between silicon and the alloy phase using Eq. 1 . According to the k values presented in **Error! Reference source not found.**, distribution coefficient of phosphorus does not depend on the phosphorus concentration. The distribution coefficient at each temperature was calculated by averaging 5 values for various concentrations at that temperature. The values obtained for phosphorus distribution coefficient are as follows: 0.22±0.02 (1583K), 0.29±0.02 (1533K) and 0.33±0.02 (1483K). It is clear that smaller distribution coefficients were obtained at higher temperatures.

$$k_i = \frac{X_{i\ in\ solid\ Si}}{X_{i\ in\ Si-Fe\ alloy}} \quad (1)$$

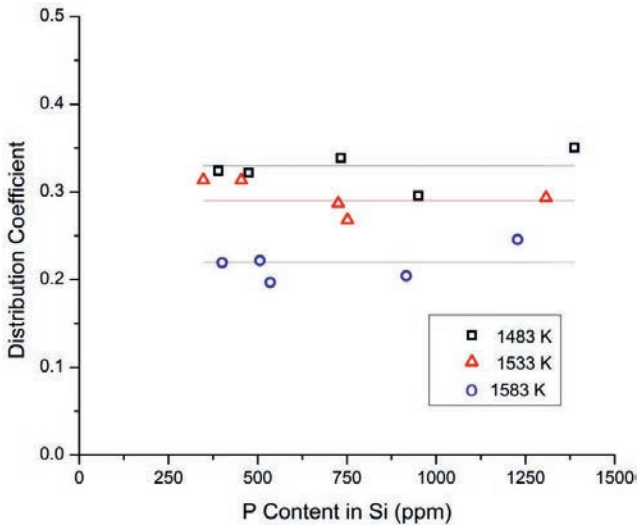

Figure 3: Distribution coefficient of phosphorus between solid silicon and iron-silicon melt at different temperatures and concentrations.

According to the data obtained in this study, the distribution coefficient of boron is not only a function of temperature but also a function of boron concentration (Figure 4). It is evident that the distribution coefficient increases with increasing boron content. Furthermore, unlike the case of phosphorus, boron distribution coefficient increases with temperature.

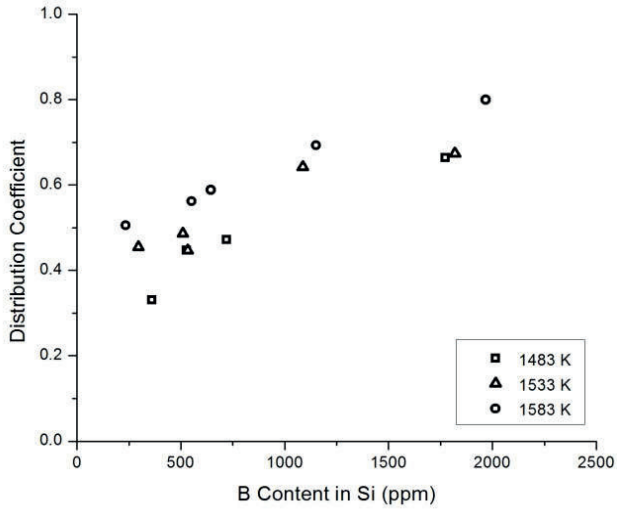

Figure 4: Distribution coefficient of boron between solid silicon and iron-silicon melt at different temperatures and concentrations [19].

Silicon yield and impurity removal

According to the results explained above, smaller distribution coefficients for phosphorus can be achieved at higher temperatures, while boron distribution coefficient is larger at higher temperatures. Regardless of the distribution coefficient values obtained for phosphorus and boron, higher temperature indicates less silicon yield for a given alloy mass. The percentage of impurity removal from silicon at each temperature is calculated based on mass balance of that impurity. The theoretical yield of silicon at each temperature is calculated from Fe-Si phase diagram using lever rule. The removal percentage of each impurity is calculated using the following equation:

$$\boldsymbol{Impurity\ removal}\ (\%) = \mathbf{100}\left(\mathbf{1} - \frac{X_{Si(purified)} \times X_{i\ in\ solid\ Si}}{X_{Si\ (initial)} \times X_{i\ (initial)}}\right) \qquad (2)$$

Figure 5 shows phosphorus removal and theoretical yield of silicon at different temperatures. It can be seen that higher phosphorus removal can be achieved at the expense of lower silicon yield.

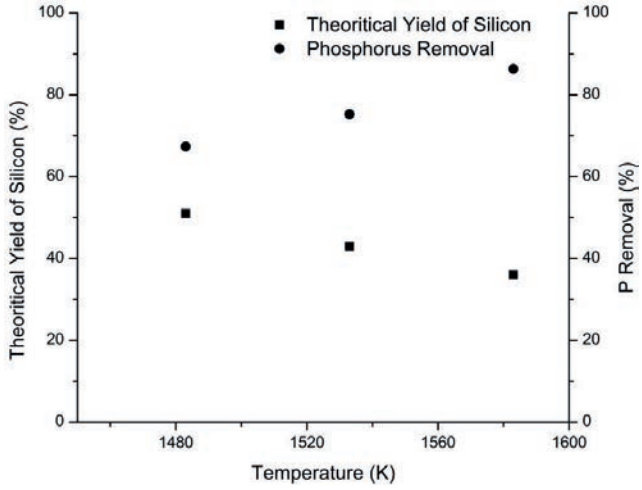

Figure 5: Dependence of phosphorus removal and silicon yield on temperature.

The variations of boron removal percentage and theoretical silicon yield with temperature are presented in Figure 6. Although the distribution coefficient of boron increases with temperature, the boron removal percentage showed a small rise with temperature. This was obtained due to the decrease in silicon yield at higher temperatures. In other words, although the initial Si content is constant, the fraction of the purified Si varies because of different quenching temperatures.

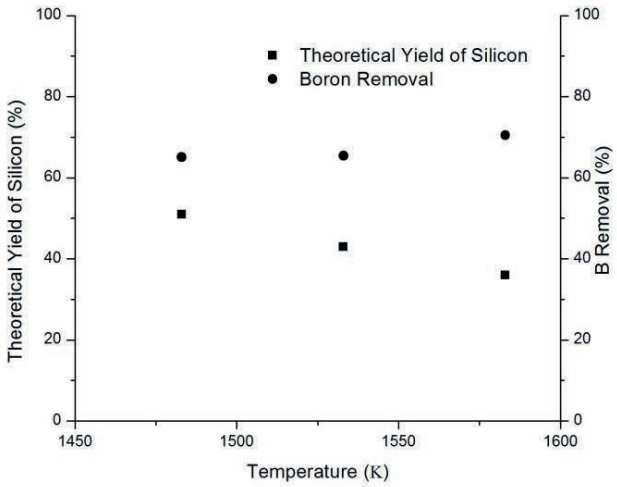

Figure 6: Dependence of boron removal and silicon yield on temperature [19].

Effective impurity removal and comparison with directional solidification

When comparing impurity removal in solvent refining with that of directional solidification, it should be noted that a significant amount of the alloying element (iron) is added in the case of solvent refining and subsequently the yield of silicon is different. Therefore in order to have a legitimate comparison, the distribution coefficient of each impurity for these two methods should be compared at equal yields of silicon.

The concentration profile of phosphorus for the solidified sample in directional solidification process based on Scheil equation (Eq. 3) [24] is presented in Figure 7.

$$C_s = kC_0(1 \quad f)^{(k-1)} \qquad (3)$$

k is the distribution coefficient and C_0 is the initial concentration of the impurity and f is the solidified fraction in directional solidification process. For a certain fraction of the ingot, the average concentration of an impurity is determined by integrating Eq. 3 and dividing the result by the solidified fraction. In order to determine the effective phosphorus removal in directional solidification and compare it with the current process, equal yield of silicon should be considered for conventional directional solidification and the proposed solvent refining process. In the current solvent refining process at 1310 C (1583K), where maximum phosphorus removal occurs, the solidified silicon is 36 wt% of the whole sample. Considering the initial silicon content, 80wt%, the yield of silicon is 0.36/0.80 = 0.45. Considering the same yield for directional solidification, i.e. 0.45 and K_P = 0.35, the average phosphorus content is calculated as $0.42C_0$ which is more than two times larger than what was obtained in the current solvent refining process (1 - 0.86 = 0.14).

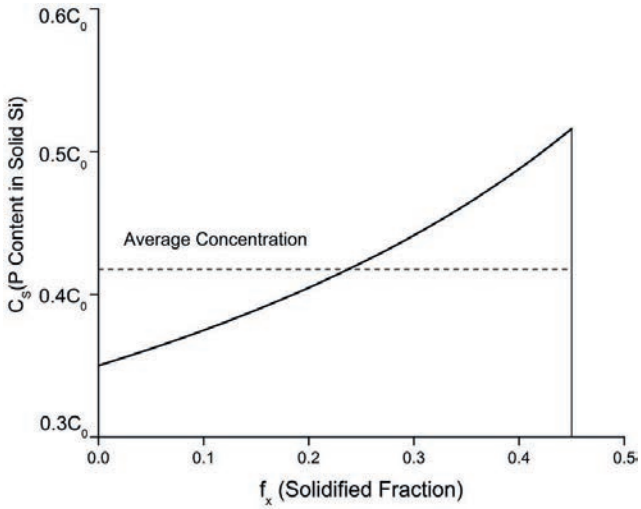

Figure 7: Phosphorus concentration profile of solidified sample with 45% silicon yield based on Scheil equation.

The concentration of B vs. the solidified fraction of silicon is shown in Figure 8.
In the case of boron removal at 1210 C (1483K) where the smallest distribution coefficient was obtained, the theoretical yield of silicon is 0.51. The initial concentration of Si in the alloy is 80 wt%, the actual yield is =0.51/0.8 = 0.64. Considering the equal yield for directional solidification and K_B = 0.8, the average boron content of the refined ingot is calculated as $0.87C_0$ [19]. This is 2-3 times more than the boron content of silicon produced in the proposed solvent refining process (1-0.65=0.35).

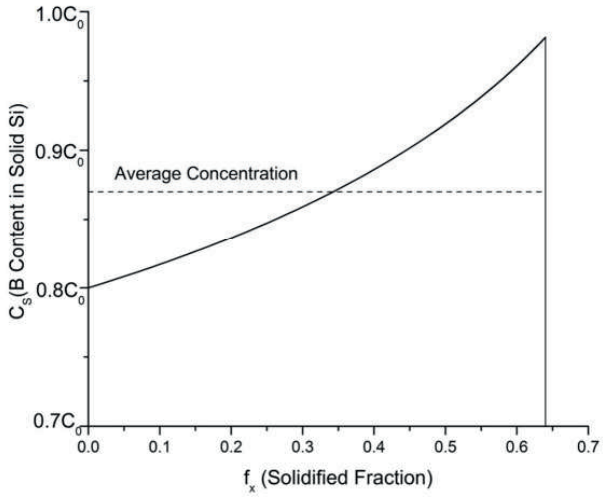

Figure 8: Boron concentration profile for a sample with 64wt% silicon yield based on Scheil equation [19].

Conclusions

The distribution coefficient of phosphorus between solid silicon and the silicon-iron liquid alloy decreases with temperature implying favorable conditions for phosphorus removal at higher temperatures. In contrary, the distribution coefficient of boron between solid silicon and the alloy melt increases with temperature.

While no significant correlation was observed between the phosphorus distribution coefficient and the phosphorus content of the solid silicon, the distribution coefficient of boron between solid silicon and the iron-silicon alloy melt increases with boron content.

The removal percentage of phosphorus obtained based on the distribution coefficient values are as follow: 86% (1310 C), 75% (1260 C), 67% (1210 C), those values for boron are: 70%, 65%, and 65% respectively. Considering the same yield for directional solidification, the average phosphorus and boron content would be over two times larger than what was obtained in the current solvent refining process.

References

1. T. Yoshikawa and K. Morita, *Removal of phosphorus by solidification refining with Si-Al melts*. Science and Technology of Advanced Materials, **4**, 2003, p531.
2. T. Yoshikawa and K. Morita, *Removal of B from Si by solidification refining with Si-Al melts*. Metallurgical and Materials Transaction B, **36**, 2005, p731.
3. T. Yoshikawa and K. Morita. *Thermodynamics on the Solidification refining of Silicon with Si- Al Melts*. in *EPD Congress*. 2005. TMS(The Minerals, Metals and Maerials Sociey).
4. T. Yoshikawa and K. Morita, *Refining of silicon during its solidification from a Si-Al melt*. Journal of Crystal Growth, **311,** 2009, p776.
5. T. Yoshikawa and K. Morita, *An Evolving Method for Solar-Grade Silicon Production: Solvent Refining*. JOM Journal of the Minerals, Metals and Materials Society, **64**(8), 2012, p946.
6. K. Morita and T. Yoshikawa, *Thermodynamic Evaluation of New Metallurgical Refining Processes for SoG-Silicon Production*. Transactions of Nonferrous Metals Society of China, **21**(3), 2011, p685.
7. B. Bathey and M.C. Cretella, *Review: Solar- grade silicon*. Journal of Materials Science, **17**, 1982, p.3077.
8. I. Obinata and N. Komatsu, *A study on purification of metallurgical grade silicon by Si-Al alloy*. Sci. Rep. RITU, **A-9**, 1957, p118.
9. J.L. Gumaste, et al., *Solvent Refining of Metallurgical Grade Silicon*. Solar Energy Materials and Solar cells, **16,** 1987, p289.
10. K. Morita and T. Miki, *Thermodynamics of Solar-Grade-Silicon Refining*. Intermetallics, **11**, 2003, p1111.
11. J. Juneja and T. Mukherjee, *A study of the purification of metallurgical grade silicon*. Hydrometallurgy, **16**(1), 1986, p69.
12. A.M. Mitrainovic and T.A. Utigard, *Refining silicon for solar cell application by copper alloying*. Silicon, **1**(4), 2009, p239.
13. A.M. Mitrainovic and T.A. Utigard, *Copper removal from hypereutectic Cu-Si alloys by heavy liquid media separation*. Metallurgical and Materials Transactions B, **43**(2), 2012, p379.
14. Z. Yin, et al., *Solvent refining of silicon using nickel as impurity getter*. Canadian Metallurgical Quarterly, **50**(2), 2011, p166.

15. E. Bonnier, H. Pastor, and J. Driole, *Sur une preparation de silicum de haute purets*. Metallurgie, **7**, 1965-66, p299.
16. J. Driole and E. Bonnier, *Herstellung yon silizium mit hohem reinheitsgrad*. Metallwiss, **25**, 1971, p2.
17. S. Esfahani and M. Barati, *Purification of MG-Si using iron as impurity getter, Part 1: Growth and separation of silicon*. Metals and Materials International, **17**(5), 2011, p823.
18. S. Esfahani and M. Barati, *Purification of MG-Si using iron as impurity getter, Part II: Extent of silicon purification*. Metals and Materials International, **17**(6), 2011, p1009.
19. L. Tafaghodi Khajavi and M. Barati, *Removal of boron from silicon by solvent refining using ferrosilicon alloys*, Metallurgical and Materials Transactions B, **46**, 2015, p615.
20. L. Tafaghodi Khajavi and M. Barati, *Thermodynamics of boron distribution in solvent refining of silicon using ferrosilicon alloys*, Journal of Alloys and Compounds, **619**, 2015, p634.
21. S. Fischler, *Correlation between maximum solid solubility and distribution coefficient for impurities in Ge and Si*, Journal of applied physics, **33**, 1962, p1615.
22. R. Jaccodine and C. Pearce, *Defects in silicon*, in *Proceedings - The Electrochemical Society* (W. Bullis and L. Kimmerling, eds.), 1983. p115, Electrochemical Society Incorporation.
23. T. Massalski, H. Okamoto, P. Subramanian, and L. Kacprzak, *Binary Alloy Phase Diagrams*. ASM International, 1990.
24. H. Fredriksson and U. Akerlind: *Solidification and Crystallization Processing in Metals and Alloys*: John Wiley and Sons, 2012.

Metallurgical route to produce solar grade silicon

Tiago Ramos Ribeiro[1)], Moysés Leite de Lima[1)], João Batista Ferreira Neto[1)], John Bernardo Vilca Neira[2)] and André Alexandrino Lotto[3)]

1) Laboratory of Metallurgical Processes, Center for Metallurgical and Materials Technology, Institute for Technological Research – IPT, Sao Paulo, Brazil. tiagorr@ipt.br

2) Former with IPT, now with the Federal University of the South and Southeast of Pará, Marabá, Brazil.

3) Former with IPT

Abstract

Aiming at the development of a metallurgical route to produce solar grade silicon, a project was conducted at IPT to investigate the purification of metallurgical-grade silicon. Injection of gases on melted silicon was used for boron removal and vacuum treatment for phosphorous removal. Additionally, controlled directional solidification was performed in order to remove metallic elements (Fe, Al, Mn, Mg, etc.) and carbon. The results showed good reproducibility among many different trials of each treatment. By running all these treatments sequentially it was possible to produce a material with final purity higher than 99.9998% which shows that this refined silicon has potential to be used for photovoltaic applications.

Introduction

The use of photovoltaic energy has grown at an average rate of 49% per year[(1)] from 2003 to 2013. The demand for solar panels and solar cells has risen accordingly, which in turn increases the demand for solar grade silicon. Aiming at the development of a metallurgical route to produce solar grade silicon, a project was conducted at IPT to investigate the purification of metallurgical grade silicon.

The purification treatments were divided by impurity to be removed. Injection of gases on melted silicon was used for boron removal, vacuum treatment for phosphorous and controlled directional solidification for metallic elements (Fe, Al, Mn, Mg, etc.) and carbon.

Boron removal

Boron is less volatile than silicon, their boiling points are 2547ºC (2820 K) and 2267ºC (2540 K), respectively. However, boron can be vaporized from silicon under

oxygen/steam/hydrogen atmosphere. Under these conditions boron will evaporate mainly as BOH compound, as we can observe in Figure 1.

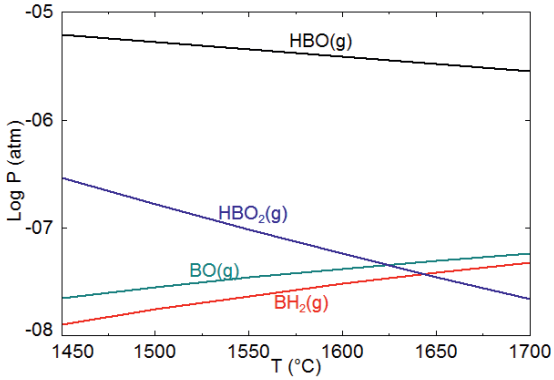

Figure 1. Main boron gaseous species in equilibrium with Silicon (H_2-5% Vol H_2O – Si with 10 ppm B). Calculated using FactSage.

Therefore, boron volatilization requires either a mixture of oxygen or steam with hydrogen. However, the formation of a silica layer at high oxygen/steam flow rate or at high H_2O/H_2 ratio is the main phenomenon limiting volatilization kinetics, since that layer consists in a barrier for BOH volatilization. In addition, a higher H_2O/H_2 ratio will increase the silicon losses as SiO(g), decreasing the yield of the process. Hence that parameter must be controlled precisely in order to promote boron removal and preventing silica layer formation and high Si losses as SiO(g).
Figure 2 shows a thermodynamic evaluation showing the effect of the temperature and the H_2/H_2O ratio on the silica layer at silicon surface during plasma treatment, as well as, silicon losses as SiO(g).

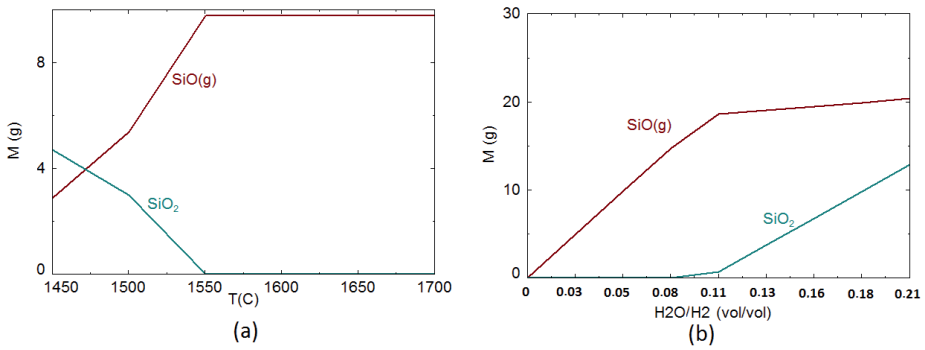

Figure 2. SiO(g) and SiO_2 formation (g/100g Si) during treatment of molten silicon with H_2/H_2O atmosphere. (a) 100 g Si, 100 L of 95%H_2 vol-5%H_2O vol. (b) 100 g Si, 100 L of H_2+H_2O at 1550°C. Calculated using FactSage.

SiO(g) formation is favoured at higher temperatures while SiO_2 and BOH formation are favoured at lower temperatures. Therefore the temperature should be as low as possible but higher than the limit for SiO_2 formation. This leads to a temperature range between 1550°C (1823K) and 1600°C (1873K). Regarding the H_2O/H_2 ratio,

values below 0.08 would prevent SiO_2 formation. On the other hand, BOH is more prone to evaporate for higher H_2O/H_2. Therefore the best value to use is around 0.08 for 1550ºC.
For a gas mixture of 90%H_2-10%H_2O the temperature should be higher than 1610ºC to prevent the SiO_2 formation, but this would cause a higher silicon loss as SiO(g).
Experiments were made using an induction furnace where 3 kg of silicon were melted inside a graphite crucible. After melting, a mixture of argon, hydrogen and steam was injected on top of the bath. The temperature was controlled by a thermocouple inserted in the liquid metal protected by a quartz tube. Samples were taken at different times of treatment and boron content was determined by analysis in an ICP-MS.
The results of a treatment made at 1550ºC with a mixture of Ar-H_2O-H_2 (H_2O/H_2 = 5/95 = 0.05) are showed in Figure 3.

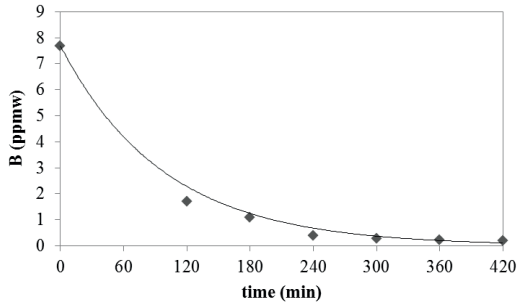

Figure 3. Boron content in molten silicon during refining with H_2-H_2O-Argon gas mixture.

Many trials were made using the same treatment for boron removal, and the results showed a good reproducibility with final boron contents below 1 ppmw as showed in Figure 4.

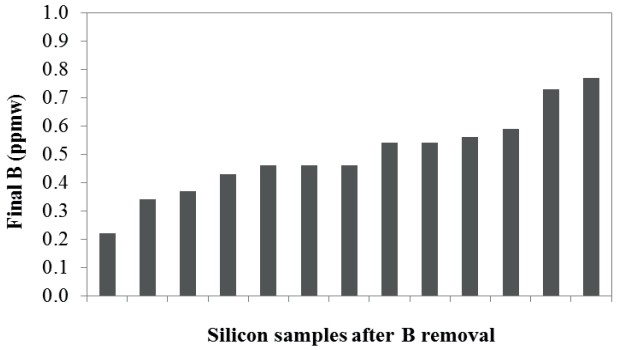

Figure 4. Final boron concentration for different trials of boron removal in silicon by the injection of Ar-H_2-H_2O gas mixtures.

Phosphorous removal

Vacuum removal of phosphorus from silicon is feasible. This is explained by a volatility criterion for silicon refining under vacuum based in the Hertz-Langmuir-Knudsen equation. This criterion can be re-written as:

$$\beta = \gamma^0 \cdot \frac{p_i^{\,0}}{p_{Si}^{\,0}} \cdot \left(\frac{M_{Si}}{M_i} \right)^{\frac{1}{2}} \qquad (1)$$

The β value for monoatomic phosphorus in silicon at 1550°C (1823K) is approximately 485[(2)], showing the possibility for removal.
Monoatomic phosphorus is the dominant specie in the gas equilibrated with silicon below approximately 60 ppmw. Therefore, for silicon refining which contains few ppm of phosphorus, the following equation can represent the thermodynamic of P transferring from molten silicon to the gas phase.

$$\text{P (wt\% in Si)} = \text{P (g)} \qquad \Delta G^o = 387{,}000 - 102.8\ T\ \text{J/mol} \qquad (2)$$

A kinetic model was developed in order to simulate the phosphorus removal by vaporization in an induction furnace. This numerical simulation is based on 3 steps:

- Step 1: Transport across a liquid boundary layer to the melt surface
- Step 2: Vaporization from the free melt surface into the gas phase above the surface
- Step 3: Transport across a gas phase in the chamber

Figure 5 depicts a scheme showing these steps.

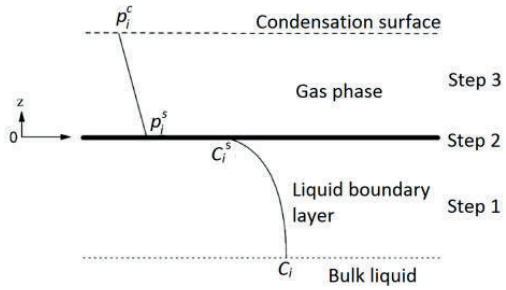

Figure 5. Scheme of the steps considered for phosphorous removal from liquid silicon.

The steps related with the transport of phosphorus dissolved in silicon through the melt to the neighbourhood of the melt surface and the step of condensation on the chamber inner surface or gas removal by pump, are considered too fast to affect the global kinetic of phosphorus removal, since the mixing of the molten silicon in an induction furnace and the presence of cooling parts at the vacuum chamber make those steps much faster than steps 1, 2 and 3.
Therefore, the total mass transfer coefficient (kp) of the process is calculated as a function of the mass transfer coefficient on the liquid boundary layer (k_l), the reaction

velocity coefficient (k_e) and the mass transfer coefficient on the gas phase (k_g), as showed in equation 3.

$$\frac{1}{k_p} = \frac{1}{k_l} + \frac{1}{k_e} + \frac{1}{k_g} \qquad (3)$$

The equations that describe k_l, k_e and k_g are presented elsewhere[3].
Figure 6 shows the values of the three coefficients at different temperatures.
For temperatures lower than 2000K the kinetics of phosphorous removal is controlled by chemical reaction (k_e) while at temperatures above 2500K it is controlled by mass transfer in the liquid boundary layer (k_l). In the range between these values, there is a mixed control.

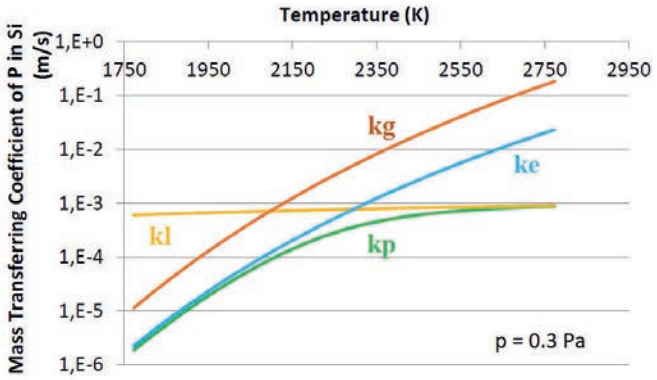

Figure 6. Effect of T(K) on the mass transfer coefficient of P in Si at system pressure of 0.3 Pa.

The temperatures used during trials in the induction furnace are lower than 2000 K and therefore vaporization from the free melt surface into the gas phase above the surface (k_e) is the controlling step, as showed in Figure 6.
For phosphorous as monoatomic specie (P) the kinetic of vaporization can be written as:

$$\ln\left(\frac{\%P_t}{\%P_0}\right) = -k_p \cdot \frac{A}{V} \cdot t \qquad (4)$$

where, $\%P_t$ is the mass concentration of phosphorous at time t, $\%P_0$ is the initial phosphorous concentration, A is the bath surface area in contact with furnace atmosphere, V is the bath volume, t is time and k_p is the total mass transfer coefficient as defined before.
Trials of phosphorus removal from metallurgical grade silicon have been carried out in IPT using a vacuum induction furnace.
The trials in the vacuum induction furnace were performed in two different temperatures, 1650ºC (1923 K) and 1750ºC (2023 K) at pressure of 0.3 Pa. The induction furnace nominal power is 30 kVA and the frequency is 7 kHz. The initial concentration of phosphorous in the silicon was 33 ± 6 ppmw. Samples were taken at

different time of treatment and were analyzed in an ICP-OES. The A/V ratio was also varied by changing the mass of silicon inside the crucible. Two levels were studied 12.6 m^{-1} and 37.7 m^{-1}.
For the higher temperature and lower higher A/V ratio it was not possible to keep the chamber pressure at 0.3 Pa as silicon evaporation was too intense. For this particular case the measured pressure was 2 Pa.
The experimental results are presented in Figure 7 along with the curves obtained from the developed kinetic model.
Results show that a higher A/V ratio (m^{-1}) increases the phosphorus removal from silicon and that after 10800s (3 h) of treatment the phosphorous is lower than 1 ppmw which is necessary for solar applications. The simulation model predicts relatively well the behavior of phosphorus during vacuum treatment of molten silicon, even though the calculated values for A/V = 12.6 m^{-1} were lower than experimental data.

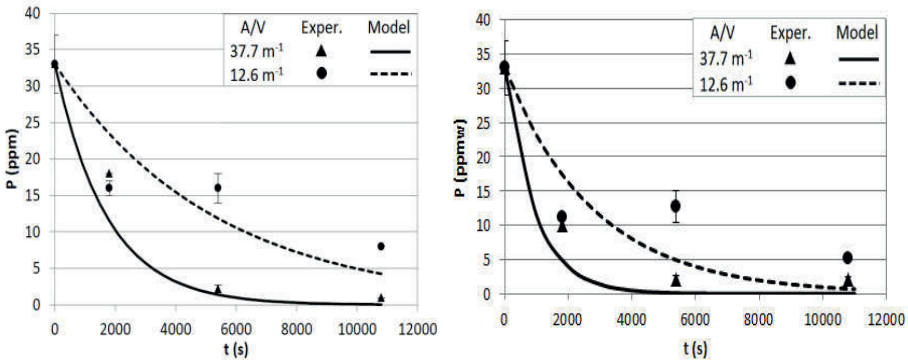

Figure 7. Experimental results and numerical simulation of P removal from silicon. (a) 1650°C and 0.3 Pa, (b) 1750°C and 0.3 Pa for A/V = 37.7 m^{-1} and 2 Pa for A/V = 12.6 m^{-1}).

Based on the experimental and model results it is possible to calculate the total mass transfer coefficient (k_p) that are presented in Table 1. These values are similar to those presented by Safarian and Tangstad[2] that obtained kp = $4.9 \cdot 10^{-6}$ for 1600ºC (1873 K) and 0.5 Pa.

Table 1. Total mass transfer coefficients (k_p – m/s) for phosphorous evaporation in silicon treated in vacuum induction furnace.

Temperature	1650ºC	1750ºC
Experimental	$7.0 \cdot 10^{-6}$	$4.0 \cdot 10^{-6}$
Model	$1.3 \cdot 10^{-5}$	$2.8 \cdot 10^{-5}$

The results showed that vacuum induction furnaces are suitable for phosphorous removal of silicon reaching final P-content lower than 1 ppmw.
Other equipment that could be used for vacuum treatment of silicon is an electron beam furnace. In this furnace the vacuum is higher than in induction furnaces due to the requisites for operating the electron beam gun. Also, the temperatures obtained are higher which enhance the process kinetics.

Many runs for removal of P in electron beam furnace were performed with good reproducibility and final phosphorous concentration below 1 ppmw. These results are shown in Figure 8.

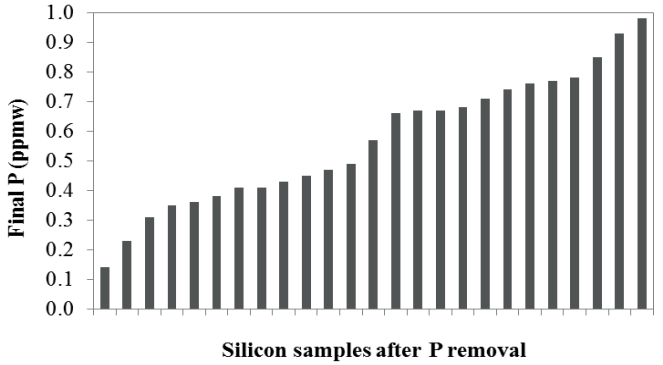

Figure 8. Final P concentration for different trials of phosphorous removal in silicon by vacuum.

Carbon removal

The typical concentration of carbon in MGSi is between 500 and 1000 ppmw, present in a solution with solid/liquid silicon and as silicon carbide (SiC) particles embedded in this solution. Carbon solubility in liquid silicon is 65 ppmw[4] at the melting point 1414ºC (1687 K). Therefore, more than 90 pct of carbon in MGSi is combined in SiC particles. These particles have two deleterious effects for photovoltaic applications: wire breakage during silicon wafering[5] and shunting in solar cells[6]. To avoid these problems, the SEMI PV17-0611[7] standard sets a maximum concentration limit of 43 ppmw (100 ppma) of carbon in the solar grade silicon produced by the metallurgical route. This limit value is higher than for other elements, possibly because the material must be free of SiC particles as dissolved silicon has little effect on the wafer and solar cells properties.

Directional solidification has been reported in the literature to remove carbon from silicon. In general, when particles interact with an advancing solidification front, they can be pushed or engulfed, depending on the critical front velocity for pushing/engulfment transition (PET). At relatively low solidification front velocities, particles of SiC can be pushed ahead and, during directional solidification upward, be transported to the ingot top[8,9].

Experiments of directional solidification upward were carried out in a Bridgman furnace. Silicon with 1200 ± 300 ppmw of carbon was melted inside a 30-mm-diameter cylindrical quartz mold internally coated with silicon nitride. The furnace was heated by an induction coil at a rate of 14.5 C/min up to 1500ºC (1773 K). After a 20 minutes period of stabilization, the mold was pulled from the furnace hot zone down into the cold zone at different velocities, namely, 5, 10, 20, 40, and 80 μm/s.

After solidification and cooling to room temperature, the 30-mm-diameter, 100-mm-height cylindrical ingots were sectioned longitudinally for macro and microstructure examination. Samples were also extracted at different distances from the ingot base, along the ingot axis, for chemical analysis of carbon.

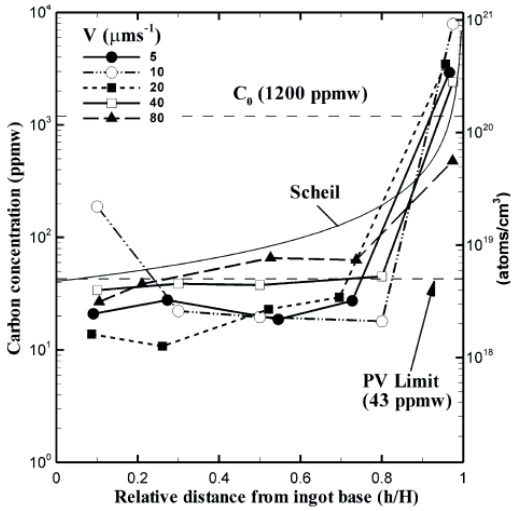

Figure 9. Macrosegregation profiles of the ingots obtained in the directional solidification experiments for different mold velocities (V): carbon concentration as a function of the relative distance (h/H), where h is the distance from the ingot base along the axial direction and H is the ingot length. The concentration profile given by the Scheil equation, the initial carbon concentration (C_0), and the maximum limit for carbon content according to the SEMI PV17-0611 are also presented.

In the ingots obtained in the directional solidification experiments, carbon concentration increases from the ingot bottom to the top regardless of the mold pulling velocity (Figure 9). The concentration at the top of the ingots for velocities between 5 and 40 μm/s is nearly one order of magnitude larger than that for 80 μm/s, displaying a more intense carbon macrosegregation. Moreover, for these lower velocities ($V \leq 40$ μm/s), the carbon content in the refined region ($h/H < 0.8$) is lower than the maximum limit recommended by the SEMI PV17-0611[7].

To investigate the mechanism responsible for the formation of the concentration profiles in Figure 1, a profile calculated by the Scheil equation is included. In this calculation, the relative distance from the ingot base was adopted as the solid fraction, the average carbon concentration was assumed as 1200 ppmw, and a solute partition coefficient of 0.034, which is one of the lowest values reported in the literature[10], was considered. The discrepancy between the measured and calculated profiles is evident. Therefore, it seems possible to conclude that the measured concentration profiles were not caused by simple carbon rejection by the solid into the liquid at a planar solid–liquid interface during the upward solidification.

To investigate if silicon carbide particles could be pushed by the solidification front to the ingot top the macro and microstructures of the obtained ingots are shown in Figure 10 and Figure 11, respectively.

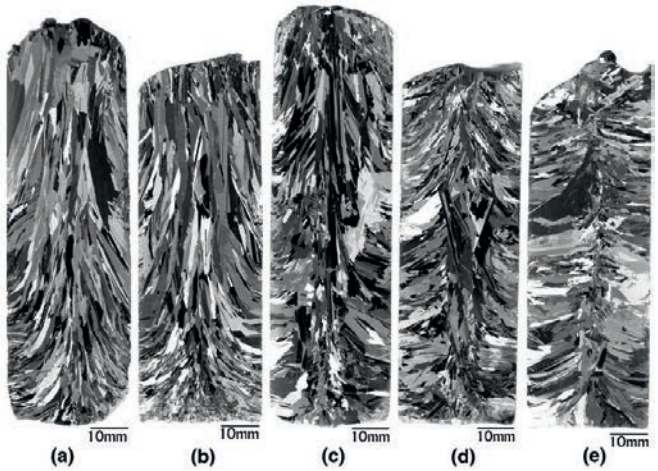

Figure 10. Macrostructures of the ingots obtained in the directional solidification experiments at different mold velocities: (a) 5 μm/s; (b) 10 μm/s; (c) 20 μm/s; (d) 40 μm/s; (e) 80 μm/s.

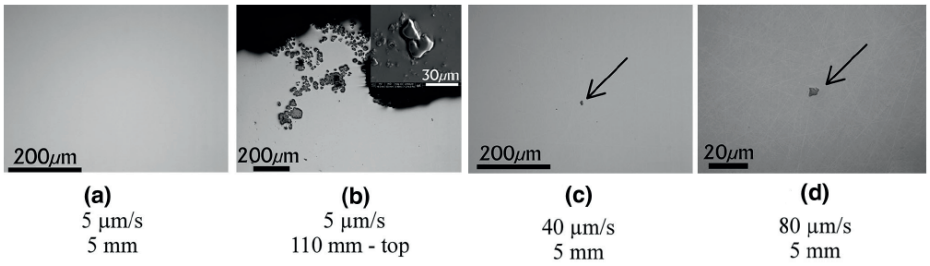

Figure 11. Microstructures observed in the optical microscope of samples extracted at different distances from the base of the ingots obtained in the solidification experiments at different mold velocities. Arrows indicate SiC particles.

For the lowest mold velocities, namely 5, 10, and 20 μm/s, a planar solid–liquid interface is expected, as described by Martorano et al.[11]. The structure of columnar grains aligned in the axial direction observed for these velocities (Fiures 10(a) through (c)) is consistent with a planar solid–liquid interface growing upward, pushing the SiC particles to the ingot top and causing the larger carbon concentration in this region (Figure 9). An accumulation of precipitated particles was confirmed at the ingot top for these experiments, as seen in Figure 11(b). The bottom and middle part of these three ingots (V = 5, 10, and 20 μm/s) were free of particles, as seen in Figure 11(a) for the 5 μm/s pulling velocity.

When the pulling velocity increases to 40 or 80 μm/s, SiC particles exist throughout the ingot, as shown in Figure 11(c) and (d), indicating that the pushing of particles to the ingot top by the solid–liquid interface was less effective. For these larger pulling velocities, a nonplanar solid–liquid interface is more likely, which is not as efficient as the planar interface to push particles.

These results show it is possible to produce silicon with carbon content less than the required limit (< 43 ppmw) by direct solidification. Moreover, the best condition is

that the solidification velocity is lower than 20μm/s which is consistent with a planar solid–liquid interface moving to the ingot top and pushing the SiC particles.

Metallic elements removal

Directional solidification has been adopted to eliminate a large number of important impurities from silicon. These impurities segregate to the last portion of the ingot to solidify, leaving a purer solid material. The intensity of this segregation is strongly related to the solute partition coefficient, also known as the equilibrium segregation coefficient (k).Values of k for several of important impurities in Si are given in Table 2 . As a result of segregation to the melt, all impurities other than B, P and O experience severe macrosegregation in the solid during solidification, since $k << 1$.

Table 2. Equilibrium partition coefficient of important impurities in silicon[11].

Element	Fe	Al	Ti	V	Mn	B	P
k_0	$8 \cdot 10^{-6}$	$2 \cdot 10^{-3}$	$3.6 \cdot 10^{-6}$	$4 \cdot 10^{-6}$	$1 \cdot 10^{-5}$	0.716-0.8	0.35

Metalurgicall grade silicon of about 99% purity (Fe = 1363 ppmw, Al = 445 ppmw, Ti = 117 ppmw, Mn = 216 ppmw) was used in a directional solidification experiment. An induction furnace with a graphite susceptor was used. To contain the silicon, a graphite crucible was placed on top of a water cooled base. After melting and homogenization at 1550°C, the furnace was cooled at a controlled rate of 0.5°C/min down to 1000°C and turned off. The obtained ingot was cut in its longitudinal section for macro and microstructure examination. Samples were also extracted from different positions along the ingot axis for chemical analysis.
The macro and typical microstructures of the longitudinal section of the ingot obtained are presented in Figure 12.

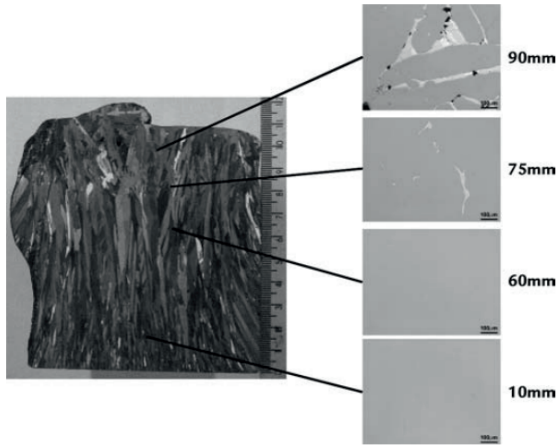

Figure 12. Macrostructure of the ingot longitudinal section and typical microstructures at different distances (indicated on the right) from the ingot bottom.

From the ingot base up to 70 mm, there are columnar grains aligned in the vertical direction, which is a typical macrostructure of unidirectional solidification. At 70 mm, these columnar grains lost their common alignment, but still remained elongated. Intermetallic particles were found only in the upper part of the ingot, where grains

were not completely aligned. The lower part of the ingot, however, was free from these particles (Figure 12), suggesting a macrosegregation of impurities from the ingot bottom to the top. Similar results were obtained by Martorano et. al[11]. The transition region, at which intermetallic compounds were first seen, occurred at 75 mm from the ingot bottom.

The relative concentration profile for the main metallic impurities measured by ICP-OES is shown in Figure 13, indicating a macrosegregation of Fe, Mn, Ti, and Al to the ingot top, in agreement with the microstructures. The concentrations of metallic impurities are lower than that in the metallurgical silicon (raw material) along 70 mm from the ingot base, in which no intermetallic compound was observed.

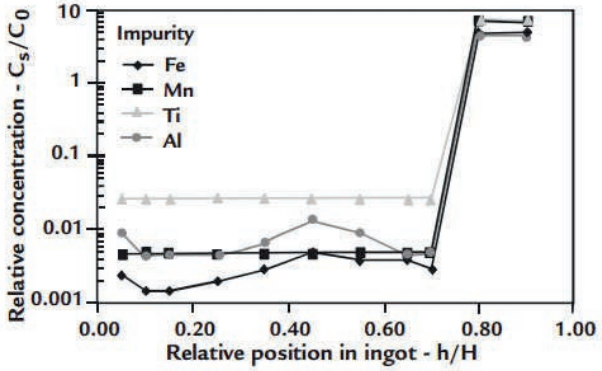

Figure 13. Relative concentration of Fe, Mn, Ti, and Al obtained by by ICP-OES as a function of the relative distance from the ingot base, where C_S and C_0 are the local and initial impurity concentration, respectively, h is the distance from the ingot base and H is the ingot length.

Integration of the refining treatments

The challenge of setting-up a metallurgical route to refine silicon is not only the development of each treatment, but the integration of them in a way that avoid re-contamination. I.e., silicon must not be contaminated during one of the refining treatments with the impurity removed in a previous step. Additionally, all used materials such as crucibles, refractories, sensors, etc., must be correctly selected to prevent silicon contamination.

In that sense, the presented refining treatments were integrated in a route. By running this route in a laboratory scale, refined silicon was produced and its final chemical composition measured in an ICP-OES is showed in Table 3.

Table 3. Chemical composition of refined silicon in lab scale at IPT. Values are in ppmw.

B	P	Fe	Al	Ni	Cu	Ti	Co
0.62	0.49	0.28	0.27	0.12	< 0.1	< 0.1	< 0.1
Cr	**Mn**	**Zn**	**Mg**	**Ba**	**Zr**	**V**	**Total**
< 0.1	< 0.1	< 0.1	< 0.1	< 0.1	< 0.1	< 0.1	**< 2**

The chemical analysis shows that the silicon produced after the refining treatments has purity higher than 99.9998%. Previous chemical analysis performed with GDMS on samples refined by direct solidification showed that the contents of all metallic elements were around or below 0.01 ppm. Sample preparation for ICP-OES may lead to some contamination and that would explain the higher values obtained. Therefore it is expected the contents of Fe, Al and Ni to be lower and the silicon to be purer than showed in Table 3.

This refined silicon shows potential to be used as a material for the production of solar cells for photovoltaic applications.

Silicon ingots will be produced for wafer and solar cells characterization with 100% refined silicon and also with 50% refined silicon mixed with 50% of polysilicon.

Acknowledgements

The authors acknowledge the financial support of Cia Ferroligas Minas Gerais-MINASLIGAS and BNDES (The Brazilian Development Bank) for the execution of this project.

References

1. International Energy Association, *Technology Roadmap – Solar Photovoltaic Energy*, 2014.
2. J. Safarian and M. Tangstad, Metall. Mater. Trans. B, **43**, 2012, n.6, p.1427-1445.
3. A.A. Lotto, J.B. Ferreira Neto, M.B. Mourão, *Silicon Refining by Vacuum Treatment* (in Portuguese), Tecnol. Metal. Mater. Miner., **11**, 2014, n.4, p.304-310.
4. H. Dalaker and M. Tangstad, Mater. Trans., **50**, 2009, n .5, pp. 1152–56.
5. G. Du, L. Zhou, P. Rossetto, and Y. Wan: Sol. Energy Mater. Sol. Cells, **91**, 2007, n.18, pp. 1743–48.
6. A. Lotnyk, J. Bauer, O. Breitenstein, and H. Blumtritt: Sol. Energy Mater. Sol. Cells, **92**, 2008, n. 10, pp. 1236–40.
7. Semiconductor Equipment and Materials International: SEMI PV17-0611: Specification for Virgin Silicon Feedstock Materials for Photovoltaic Applications, 2011.
8. A.K. Soiland: Ph.D. Thesis, Norwegian University of Science and Technology, Trondheim, 2004.
9. D.M. Stefanescu, R.V. Phalnikar, H. Pang, S. Ahuja, and B.K. Dhindaw: ISIJ Int., **35**, 1995, n.6, pp. 700–07
10. T. Narushima, A. Yamashita, C. Ouchi, and Y. Iguchi: Mater. Trans., **48**, 2002, n. 8, pp. 2120–24.
11. M.A. Martorano, J.B. Ferreira Neto, T.S. Oliveira and T.O. Tsubaki, Metall. Mater. Trans. A, **42**, 2011, n. 7, pp. 1870-1886.

Silicon to Silicone – We help make things work better

Dr. Pierre Germain[1)] and Ralf Maecker[2)]
1) CES Secretary General, CEFIC
2) Director Government and Industry Relations, Momentive Performance Materials

Abstract

CES – Silicones Europe is a non-profit organisation representing the six major producers of silicones in Europe.

Committed to promoting information on silicones from a health and environmental perspective, CES has commissioned several studies, to look at the impact of their use and production. The carbon balance study on silicones shows that CO_2 reductions enabled by using silicones, siloxanes and silanes are 9 times greater than the greenhouse gas emissions from production and end of life treatment of these products, and that the use of silicone products in Europe, North America and Japan yields greenhouse gas emissions reductions equivalent to about 54 million tons of CO_2. Silicone manufacturing also directly employs 30,000 people – indirectly up to 14 million people. The industry generates 11 billion USD in sales. The benefits were also measured for the solar industry in particular.

CES works with other stakeholders to communicate relevant information to downstream users, policy makers and regulators.

About CES – Silicones Europe

CES – Silicones Europe is a non-profit organisation and a sector group of CEFIC (the European Chemical Industry Council). CES represents the 6 major producers of silicones in Europe:

- Bluestar Silicones
- Evonik
- Dow Corning
- Momentive Performance Materials
- Shin-Etsu
- Wacker Chemie A.G.

The primary mission of CES is to raise awareness of silicones and their many uses as well as to promote their safety from a health, safety and environmental perspective – through the following activities:

- Commission, co-ordinate and guide scientific research on questions of health, safety and the environment.
- Interpret and evaluate data.
- Provide information and perspective to European and international regulators.
- Co-ordinate input from the silicone industry on issues affecting the overall chemical sector.
- Monitor and assess topics relevant to the silicone industry.
- Liaise with sister organisations.
- Provide information on the benefits of silicones in everyday life.

CES, SEHSC (the Silicones Environmental, Health and Safety Council of North America) and SIAJ (Silicone Industry Association of Japan) are all regional associations of the GSC, the Global Silicones Council. The objective of the GSC is to promote the safe use and stewardship of silicones globally. To accomplish its mission, the GSC undertakes the following activities:

- Monitor the environmental, health, and safety activities of the three Regional Silicones Industry Associations (RSIAs) and coordinate such activities on a global basis.
- Proactively promote industry communication with regulatory bodies around the world and with international environmental, health, and safety organizations.
- Through the RSIAs, identify and anticipate opportunities to enhance environmental, health, and safety research relating to silicones and engage in global projects to communicate the industry's product stewardship commitment.
- Through the RSIAs, sponsor projects to improve the public's understanding of the benefits and safety of silicones.

Benefits of silicones

Silicones can take many forms – from liquids to solids – that allow engineers, scientists, inventors and companies to use them as a vital component in thousands of consumer and industrial applications. Whether as fluids, rubber, gels, resins or mixtures, it is their versatility that makes silicones a key ingredient in products that make our lives better every day. From baking moulds and cars to computers and precision engineered spacecraft, silicones can be found in a myriad of applications. Silicone can be used to make everything from wind turbines to solar panels, LEDs to green tires.

Put simply, silicones make things work better.

Benefits of silicones in renewable energy

A relatively modest quantity of silicone can be sufficient to obtain a large increase in the efficiency of processes, energy consumption and use of materials. Silicones have helped cut energy demand for decades, while simultaneously playing an important role in clean energy supply. In one way or another, the performance and reliability of millions of modern products depend on silicones.

Within the renewable energy sector in particular, silicones have several major benefits compared to other materials.

Silicones are in fact used in 90% of solar panels which reach up to 150 ºC [1]. They are also used in other renewable energy applications such as wind turbines.

Silicone improves the efficiency, durability, and performance of solar panels and electricity-generating devices, making them more cost-effective. While solar cells are made of silicon, silicones are used during module assembly and installation as encapsulants, coatings, adhesives, and sealants. Because they can withstand the sun's unrelenting rays year after year, silicones are ideal materials for solar panel and other solar power-generating applications.

For solar grade silicone, chlorosilanes are used. Silicones have various uses in solar panels, including but not limited to:

- Sealants and adhesives for bonding for conventional (wafer cell) panels
- Electrically conductive adhesives
- Part of thin semiconductors for the «new» generation of solar panels
- Solar cell encapsulate providing protection against corrosion
- With thermally conductive fillers – as diode temperature controllers in solar panels. [1, p. 25]

In 2015, 180 Gigawatt of solar photovoltaic (PV) capacity has been installed globally – up from 1.2 GW in 2000. This contributes 0.7% of the total electricity production in the world. The largest share of global capacity is in Europe (59%) [1].

Environmental benefits of silicones

The Global Silicones Council commissioned Denkstatt, an expert consultancy for sustainability, environment, energy, waste and resource management, to carry out a study of the carbon balance of silicones [2]. The purpose of the report was to better understand the sustainability of silicone chemistry products, and is the first study of its kind for silicones. Overall, the study found that the use of silicones provides more efficient transport and processes, saves electricity and heating energy.

The study was carried out following the Denkstatt guidelines, which are based on ISO 14040/44. The study aimed for a conservative approach, and was peer reviewed by Professor Adisa Azapagic of the University of Manchester.

Consisting of 26 case studies, the aim was to uncover measurable effects on greenhouse gas emissions. That is, ways in which silicone products replace or protect other materials and the ways in which use of silicone products is linked to greenhouse gas abatement effects.

Results extrapolated from the case studies show that the greenhouse gas benefits realised by silicones, siloxanes and silanes are 9 times greater than the greenhouse gas emissions from production and end of life treatment of these products.

The use of silicone products in Europe, North America and Japan yields greenhouse gas emissions reductions equivalent to about 54 million tons of CO_2.

Solar-related energy applications
One of the major benefits identified by the study is that silicones help in the production of photovoltaic electricity. **Solar-energy related applications** in fact provide the largest contributions to net reductions in GHG emissions. Chlorosilanes for Solar Grade Silicon alone constitute savings of 360.1 tons of CO_2 per year in the three markets considered.

The benefit/impact ratio of chlorosilanes for solar grade silicon (benefits realised by the silicone product divided by the GHG emissions from production and end-of-life) is 7.5 and the absolute net GHG benefits, representing the "GHG benefit realised by the silicone product decreased by the GHG emissions from the production and end-oflife phases of the silicone product" are more than 9000 tons CO_2 equivalent. [2, p. 29]

Socio-economic contributions of silicones

The Global Silicones Council commissioned Amec Foster Wheeler to carry out a socio-economic evaluation of the global silicones industry [1].

In general, silicones were found to aid durability and functionality, providing durable bonds and seals alongside electrical insulation. Silicones provide a combination of properties at low cost, significantly contributing to the unit cost reductions witnessed in the sector alongside the energy efficiency and durability.

Key markets for silicones are found in most sectors and include: transportation, construction materials, electronics, energy, healthcare, industrial processes, personal care and consumer products as well as special systems (such as paper and textile coatings).

Sales of around 2 million tonnes of formulated silicone products in 2013 have made the industry of silicones worth nearly 10 billion EUR globally, 3 billion of which was generated in Europe. R&D related to silicone product lines in 2013 made up around 4% of turnover, or 419 million EUR.
In terms of employment in Europe, silicone manufacturing directly employs around 10,000 people. Indirectly, up to around 14 million employees globally and 1.7 million in Europe could be involved in economic activities related to silicone products.

Activities related to solar PV technology account for around **2.5 million jobs globally.** In Europe, sales of 14,000 tonnes of silicones brought around 76 million EUR in sales. Current global investments in solar PV technologies are above 100 billion EUR per year, around 15 times more than ten years ago.

Collaborating with authorities, value chain and stakeholders

CES collaborates with regulators and other stakeholders to communicate the value of silicones.

EU regulatory collaboration

The use of silanes and siloxanes is registered Under the EU Chemicals legislation for Registration, Evaluation, Authorisation and Restriction of Chemicals (REACH).

Registration of silicones under REACH is carried out by Reconsile, a consortium that brings together the interests of producers, importers and data holders of a large number of silicone substances. Downstream users and other data holders are invited to submit to the consortium any relevant information that can support the registration dossiers.

CES, SIAJ and SEHSC also carry out voluntary monitoring initiatives to generate additional data to better understand the behaviour of cyclic siloxanes in the environment and propose actions to minimise or reduce the possibility of release to the aquatic environment.

Together with Reconsile, CES submits information to on-going REACH consultations and interested policy makers.

References

1. Amec Foster Wheeler and GSC, *Socio-economic evaluation of the global silicones industry*, Amec Foster Wheeler Environment & Infrastructure UK Limited, 2015
2. Denkstatt and GSC, *Silicon-Chemistry Carbon Balance – an assessment of greenhouse gas emissions and reductions*, Denkstatt and GSC, 2012

Between Oversupply and Shortage – Where Will the Polysilicon Market Head?

Johannes Bernreuter[1)]
1) Bernreuter Research

Abstract

The rise of the photovoltaic industry has thoroughly changed the dynamics of supply and demand on the polysilicon market. In the next few years, overcapacity will continue to drag the price down.

Demand structure: A complete reversal

From the late 1950s, when the Siemens process was commercialized, until the late 1990s, highly pure polysilicon was produced for just one application: semiconductors. Although the photovoltaic (PV) industry made its first steps as early as 1974, when Japan launched the Sunshine program, the industry's polysilicon demand was so low that it was able to live on scrap silicon from the semiconductor sector until 1998. Between 1995 and 2014, however, the ratio between the two main consumers of polysilicon completely reversed: During those twenty years, the PV industry's share of polysilicon demand increased from only 10% to 90% (see Figure 1).

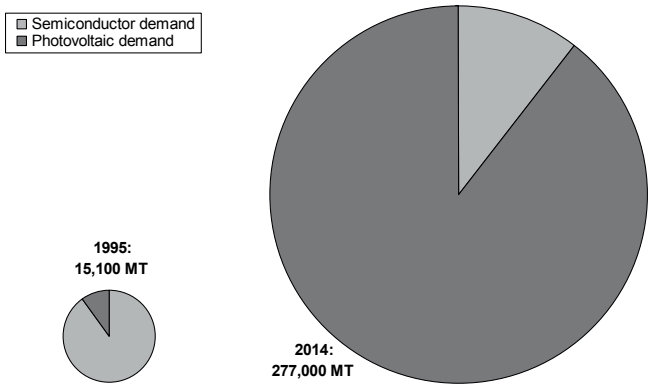

Figure 1: Shift of polysilicon demand (in metric tons = MT) from the semiconductor to the PV industry between 1995 (left) and 2014 (right)

Supply-demand dynamics: Changes in the pork cycle

Between 1980 and 2004, the polysilicon contract price showed a remarkably uniform pattern: The intervals between price trough (corresponding to oversupply) and price peak (shortage), and vice versa, regularly lasted seven to eight years (see Figure 2). Since the engineering, construction and ramping-up of a new polysilicon plant can easily take three years, supply will always lag behind demand, thus creating a typical pork cycle.

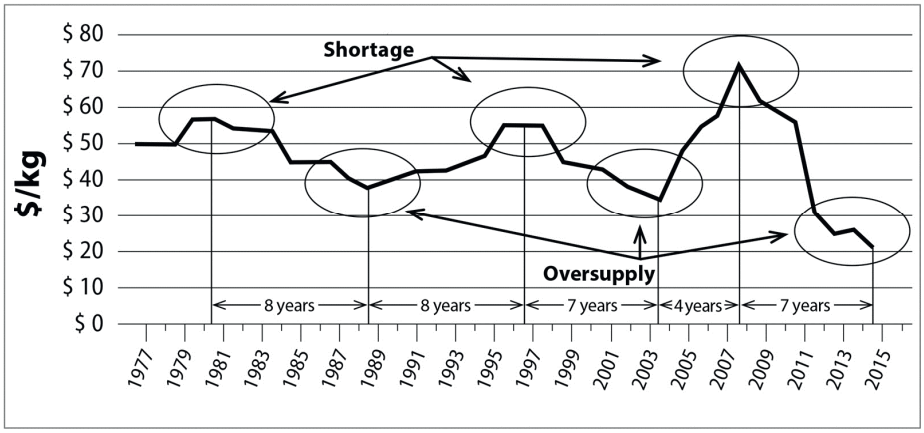

Figure 2: Pork cycle of the polysilicon industry with intervals between contract price peaks and troughs from 1980 to 2015 (Sources: GT Advanced Technologies, PVinsights)

The polysilicon industry is like a super tanker with a long brake path: When a falling price signals that one should stop investing in additional capacity, construction of new plants is already underway and can hardly be stopped without a considerable financial loss. The logical result is overcapacity, which accelerates the drop in price. On the other hand, as long as the price decreases, there will be no incentive for investing in new polysilicon capacity. Only when the price goes up again will it indicate that supply is running short and attract more investments. Manufacturers can try to anticipate the market development, but this is only possible to a limited degree.

After polysilicon demand from the PV industry – and, following it, the spot price – shot up in 2004, however, it took only four years until 2008 when the next price peak was reached. Obviously, the price increased so rapidly that the incentive was high enough for strong investment in new polysilicon production capacity, in particular in China. The way down to the next trough of the contract price in 2013 was also shorter than in the past – only five years. The curve of the spot price was even more extreme: As rapidly as it had risen to a peak of US$500/kg in 2008, so steeply did it slump to a new low of US$15.35/kg in December 2012. Those new entrants who had solely relied on a high spot price – mostly Chinese – were swept out of the market. [1]

Market distortion: The Chinese factor

However, the price trough in 2012/2013 was only of interim nature. At that point in time, the intervention of the Chinese Ministry of Commerce (Mofcom) came into play. The impact was twofold: First, Mofcom's promulgation of preliminary duties on polysilicon imports from the United States and South Korea in July 2013 encouraged several Chinese manufacturers to resume production. Second, when Mofcom

announced in August 2014 that the loophole offered by processing trade, which had avoided any duties, would be closed, a couple of large and mid-sized Chinese producers expanded capacity (see Table 1).

Table 1: Capacity expansion of major Chinese polysilicon manufacturers between 2014 and 2015 (effective end-of-year capacities in metric tons)

Company	2014	2015	Expansion
GCL-Poly	70,000	76,000	+ 6,000
Xinte (TBEA)	22,000	25,000	+ 3,000
China Silicon	11,000	15,000	+ 4,000
Daqo	7,200	14,200	+ 7,000
Asia Silicon	5,000	12,000	+ 7,000
Sichuan Yongxiang	4,000	15,000	+ 11,000
Total	119,200	157,200	+ 38,000

Consequently, oversupply grew again; according to market researcher *PVinsights*, the international spot price average tumbled to a record low of $12.93/kg in January 2016 before it began to recover. [2] In effect, the Chinese market intervention has prolonged the interval between the last price peak and trough from five to seven years.

Outlook: Where the market will head

The spring rally that started on the spot market in February 2016 might lead one to the conclusion that the polysilicon market has entered a new upward cycle. However, our analysis of the industry cost curve and corresponding demand scenarios point to the opposite direction: Continuing overcapacity will again drag the spot price down below US$14/kg. This surprising result will become more evident when one takes a look at the past and projected future growth rates of global PV installations as shown in Figure 3:

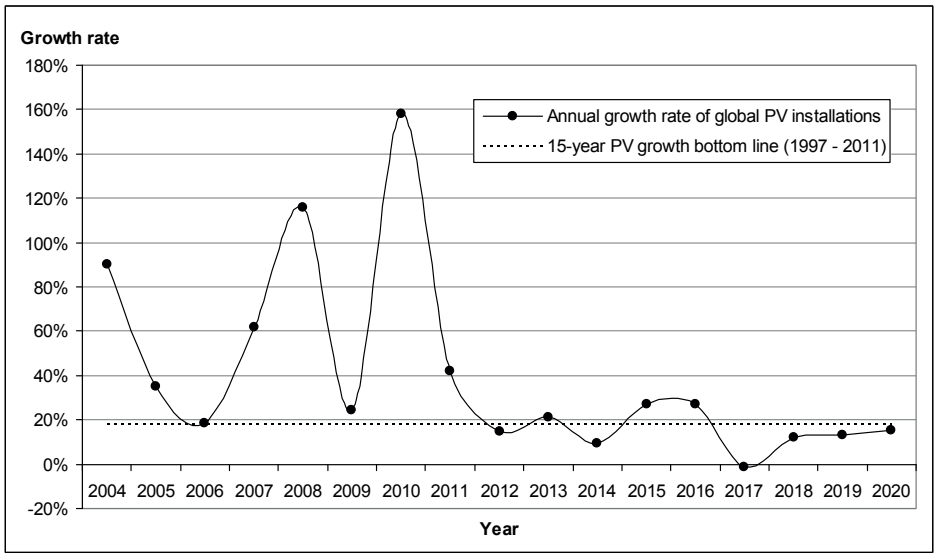

Figure 3: Annual growth rates of global PV installations between 2004 and 2020

After infant PV market grew wildly from 2004 through 2011, the year 2012 became a turning point: The growth rate of global installations broke through the long-term bottom line of 18%, signalling the onset of a new phase in the development of the global PV market. In our scenario, 18% will be the new ceiling for growth rates between 2017 and 2020.

This trend will still be amplified by increasing solar cell efficiencies. They will further reduce the specific silicon consumption (g/W) and thus additionally slow down the growth of polysilicon demand from the PV industry. While we project a combined PV and semiconductor demand on the order of 420,000 metric tons (MT) in 2020, global production capacity is already close to 500,000 MT today. [3] Hence, further market correction will be inevitable.

References

1. Johannes Bernreuter, *The 2014 Who's Who of Solar Silicon Production*, Bernreuter Research, 2014, pp 10-11, 102, 104-106
2. http://pvinsights.com, PV Poly Silicon Weekly Spot Price, retrieved in January 2016
3. Johannes Bernreuter, *The Polysilicon Market Outlook 2020*, Bernreuter Research, 2016

How are supply-side changes affecting the silicon market?

Jorn P. de Linde [1)]
1) Senior Vice President, CRU

Abstract

China will continue to account for a majority of global silicon output for the foreseeable future, underpinned by an expanding local market. However, as the growth in net capacity additions in China slows, other countries will gradually meet a higher proportion of global silicon demand. Production gains outside China will be supported by the completion of new silicon plants in the US, parts of Europe and, conceivably, the Middle East.

The difference between production costs in China and those in other countries has narrowed substantially over the past two years. At the same time, there has been a significant downward shift in the cost of producing silicon due to a combination of exchange rate movements and falling input prices.

Introduction

Silicon supply is inherently driven by demand. The distribution of supply in individual markets, as well as world-wide, depends on available production capacity, cost competitiveness and barriers to trade. Fuelled by rapid gains in chemical-related consumption, global silicon production has more than doubled since 2000, reaching an all-time high of more than 2.54 Mt in 2015. This growth has been facilitated by a rapid expansion of production capacity, principally in China.

China has increased its share of global silicon production from less than 30% in 2000 to almost 65% in 2015. Silicon output has also risen in Europe, Australia and in some other parts of Asia where comparatively inexpensive electricity was available at the time. However, these production gains are insignificant in relation to the massive expansion of Chinese silicon supply.

Of the total advance in Chinese silicon production of nearly 1.29 Mt since 2000, almost 60% has been absorbed by the domestic market, reflecting rapidly growing local demand. The balance has been exported, meeting virtually all of the net increase in non-Chinese silicon demand over the past 15 years.

In spite of the dominant position of China, the last few years have also seen the emergence of a significant pipeline of silicon projects in other countries. In fact, total silicon supply has continued to advance in spite of slowing demand and plunging prices. After highlighting some of the key characteristics of silicon supply, the

subsequent discussion focuses on how supply-side changes are affecting the silicon market globally.

Key characteristics of silicon supply

Electric power is typically the single largest cost component in the manufacture of silicon, and access to low-cost electricity is an important consideration in determining the location of silicon plants, especially in the case of export-oriented operations. Electric power is normally priced in local currency, and exchange rate movements can have a significant impact on silicon production costs expressed in US Dollars and, by extension, on international cost competitiveness.

In many areas of the world, the availability of affordable power is closely linked to hydroelectric generation. Thus, depending on the characteristics of the power system, hydrological conditions can also have a significant influence on the level of silicon production in specific locations.

Although it is an important element, electric power is not the only consideration that enters into site selection, and other factors such as the quality and cost of raw materials, process efficiencies and market access, are also crucial in determining the overall cost competitiveness of individual plants and locations.

Operations in a small number of countries have been responsible for the vast majority of silicon production outside China. Five countries have consistently accounted for 70-75% of non-Chinese silicon supply. Three of these countries, Brazil, France and Norway, also rank as large silicon exporters, although their combined exports are much smaller than the amount of internationally-traded silicon originating in China.

A number of different options are available in order to increase the supply of silicon. These include furnace rehabilitations, furnace conversions, additions of new furnaces at existing plants and the construction of greenfield silicon smelters. Moreover, the output that can be derived from existing production units tends to increase over time due to furnace upgrades and “capacity creep” associated with process improvements and equipment modifications.

Since 2000, furnace conversions have been the largest source of additional production capacity outside China and the CIS, accounting for more than 31% of the total growth in capacity, ahead of capacity creep (26%) and new plants (24%). The vast majority of greenfield capacity has been added since the beginning of this decade, while most of growth associated with furnace conversions and capacity creep occurred before 2010.

Greenfield investment has driven the expansion of silicon supply in China and the CIS. Some years back, two new plants were constructed in Kazakhstan. Meanwhile, the massive expansion of local production capacity in China has coincided with a westward migration of the industry in search of less expensive electricity. Although the overall impact has been modest relative to the output obtained from new plants in China, capacity creep and furnace conversions have played a significant role in augmenting silicon supply in some provinces.

From shortage to surplus

Shifts in the gap between global silicon demand and supply provide an indication of the size and direction of inventory movements. Because of seasonal capacity closures, most prevalent in China, total silicon demand tends to exceed supply by a significant amount in the first quarter of every year. This deficit is typically covered by stocks that were accumulated during the previous six months.

Adjusting for seasonal variations, silicon supply fell short of demand during 2013 and this situation persisted well into 2014 until supply eventually caught up with demand towards the end of the year. The tightening of the global supply/demand balance was accompanied by a steady rise in silicon prices. In spite of a fall-back during the final months of 2014, most pronounced in Asia, spot prices for standard secondary aluminium (5.5.3) grade silicon in the US and the EU ended the year significantly higher than they were at the beginning of 2014. The biggest y/y gain occurred in the US, where prices rose by nearly 16%. Spot prices for 5.5.3 silicon in the EU advanced by nearly as much in local currency terms but, due to the depreciation of the Euro during 2014, prices increased by only moderately expressed in US Dollars.

Since 2015 Q1, supply has consistently surpassed demand, fuelling a downward spiral in silicon prices. For the year as a whole, spot prices in the US declined by more than 25%, as did Chinese export prices for 5.5.3 grade silicon. The corresponding fall of US Dollar-equivalent spot prices for 5.5.3 grade material in the EU was of a similar magnitude, although prices declined considerably less in local currency terms, reflecting a significant further weakening of the Euro.

Except for a recent rally in Chinese prices caused by a short-term tightening of local supply, the downward trajectory of silicon prices has continued in 2016. This erosion can be attributed to deteriorating market fundamentals and a strong US Dollar. Amplified by destocking, silicon demand slowed considerably in all of the major markets during 2015. Meanwhile, supply continued to escalate.

The increase in total output in 2015 was principally attributable to China, reflecting the completion of substantial new production capacity, mostly in Xinjiang, but also in Sichuan and other provinces where comparatively low-cost power is available. Greenfield silicon plants, adding upwards of 55,000 t/y of capacity, were commissioned in the US, Bosnia and Thailand last year, although these facilities did not have a perceptible impact on supply until the fourth quarter. More recently, a dramatic decrease of electricity prices in Minas Gerais has sparked a big jump in Brazilian silicon production.

An extended period of elevated electricity prices caused by a lingering drought had resulted in the loss of more than 100,000 t of Brazilian silicon production between 2012 and 2015. Much, if not all, of this decline will be reversed in 2016, as most of the previously idled production capacity in Minas Gerais has been restarted. Reflecting recent and pending completions of new production capacity, silicon production is also expected to advance y/y in Europe and the US.

The increase in US output this year would have been much larger were it not for the early 2016 shutdown of Ferroglobe's Selma, Alabama plant. In addition to extensive closures in China, silicon production has also been suspended at plants elsewhere in Asia that together provided about 30,000 t of silicon last year. Still, adding up likely production gains in other countries, the potential rise in total silicon production in 2016 is much bigger than the expected increase in global demand.

Compounding the challenge of balancing the silicon market in the near-term, substantial declines in US Dollar-based production costs, in large part linked to currency depreciation, have make it easier for operations in Australia, Canada, Kazakhstan, Norway, Russia and South Africa to maintain current production levels in spite of the low level of prices. Although some of the previous losses have been reversed this year, except for the Chinese RMB, the currencies of the major silicon exporters have depreciated sharply against the US Dollar since the beginning of 2014.

At least 70-80% of the cost of producing silicon in these countries is incurred in local currencies, highlighting the importance of exchange rates as a determinant of international cost competitiveness. Falling prices of carbon-based raw materials have added to the decline in production costs over the past several years, as have recent declines in market-based power prices, most notably in Brazil. As a result of these changes, there has been a downward shift in silicon production costs. At the same time, the gap between production costs in China and those in other countries has narrowed substantially.

A drawn-out recovery

The global supply overhang will diminish in 2017, as capacity additions outside China will slow significantly y/y, while the growth in silicon demand accelerates. Fuelled by double-digit gains in solar-related silicon consumption, total demand is expected to advance at more than 6%/y between 2018 and 2020, reaching more than 3.26 Mt by the end of this decade. This implies a corresponding increase in global silicon production of more than 150,000 t/y on average between 2015 and 2020.

Supply from existing production units and new furnaces scheduled to enter production by 2018 will be sufficient to meet projected demand through 2019. Substantial additional silicon capacity will be needed in 2020, most of which can be provided by projects that have been announced but have yet to be confirmed. Larger-than-expected exports from China would reduce the amount of new capacity called for, as would lower-than-projected growth in total silicon demand, most notably should the growth in solar-related silicon consumption falter. However, there is also a distinct possibility that a significant amount of existing production capacity outside China could be permanently closed, most likely for power-related reasons.

The main impediment to greenfield plants is the comparatively high cost of amortising the required investment, but new silicon operations will play an increasing role in meeting future demand as other capacity options become less attractive due to rising operating costs in established locations. More than 260,000 t of new silicon production capacity could conceivably be added in Iceland and the Middle East by the end of 2020. In view of the recent plunge in prices, not all of these projects are expected to proceed according to previously announced timelines, and the actual increase in capacity will likely be much smaller. Still, rising prices will support greenfield investment going forward.

Trade flows

A majority of the silicon produced around the world is traded internationally. Trade flows are influenced not only by shifts in demand and changes in local production but are also impacted directly and indirectly by trade restrictions. Trade restrictions are currently in effect in markets that together account for more than 35% of global silicon demand. Led by Germany and the UK, the EU is by far the world's largest importer of silicon, followed by Japan, the US, South Korea and Thailand. China is the dominant exporter of silicon, ahead of Norway, Brazil, and France.

The future status of trade restrictions aside, a key question is whether the steady increase in Chinese silicon exports can be sustained. In the short-term, China will face increased competition from Brazil in many markets, while the sharp drop in silicon prices will slow the rate of investment in new production capacity.

Looking further into the future, domestic silicon demand is expected to expand rapidly, consistent with government policies to encourage value-added manufacturing. Moreover, the Chinese economy in all likelihood will continue to advance at a clip

that is more than double the rate expected for the world economy as a whole. Meanwhile, we expect that the growth in local silicon production will slow as China gradually moves to curb investment in basic, power-intensive and polluting industries such as silicon.

Recent developments in China suggest that this transition will take longer than previously anticipated and that the peak in Chinese silicon exports will occur further into the future, but an eventual decline in silicon exports from China implies that a growing share of non-Chinese silicon demand will be supplied by other sources. Still, China will remain by far the largest exporter and will retain a key role in balancing the global silicon market.

Over time, new production hubs for silicon in Iceland and the Middle East will have a significant impact on established trade flows. The Middle East, which is currently entirely dependent on imports, will move towards self-sufficiency. Icelandic plants would not produce enough silicon to turn Europe into a net exporter by 2020, but would substantially reduce the need for non-European supply. The US will also remain a net importer, in spite of a gradual expansion of local silicon production.

AUTHOR INDEX

PARTICIPANTS 1992-2016

Argentine

Carmona, José Luis 1998

Australia

Breit, Wolf 1998, 2000, 2002
Brosnan, James Gerard 2014, 2016
Brosnan, Jim 2000
Bultitude-Paull, John 1994
Ferraro, Mike 1998
Harris, Leighton Drew 2016
Lund, Chris 2000
Matisons, Janis 2002, 2004
Miles, David 1998, 2000, 2004, 2006
Miyashita, Masaru 2000
Naude, Christiaan Petrus 2016
Ryabova, Elena 2000, 2002
Simpson, Andrew Vincent 1994, 2002
Snow, Brad 2006
Spratt, Michael 2002
Spratt, Mike 1994, 1996
White, George 1998

Austria

Grogger, Christa 2004
Schlosser, Viktor 2010
Stueger, Harald 2004

Bahrain

Jahnke, Uwe H. 1998, 2000

Belgium

Blümlein, Otto K. 1996, 1998, 2000, 2002, 2004, 2006
De Poortere, Michel 2006
Fiat, Michel 1996
Germain, Pierre 2016
Seys, Freddy 2000
Verniers, Francois 1992, 1996, 1998, 2000, 2002
Zijlema, Tjakko 2006

Brazil

Amaral, Luciano 1998, 2000
Augusto, Thales Xavier 1998, 2000, 2002, 2004, 2006, 2008, 2010, 2012, 2014, 2016
Azvedo Cysne, Marcos J. de 1996
Barbosa Vilaboim, Luiz F. 2004
Bolzer, Walter 2002, 2004
Borges, Cezar 2006
Caracas, Ronaldo Winter 1994, 1996, 2000
Daher, Nelson 1996
Eulálio de Souza 2004
Fernandes, José G. 2002, 2004, 2006
Fialho, Paulo Cezar 1998, 2002
Flavio Lúcio 2004
Fonseca, Roberto G. Da 1994
Freitas Nogueira, Paulo de 1998
Fudaba, Masayuki 2002, 2004, 2006
Gomes, Gabriel Mousinho 1998
Hugo Mitsuo 2010
Jordao, Marco 1998, 2004
Keller, Peter 1998

Lage, Braulio 2006

Ledic, Marco Luz 2010

Nacif, Mario Odiniz 1998

Neto, David dos Santos 2002, 2004, 2006, 2008
Neto, Joao Batista Ferreira 1996, 1998
Parreiras, Bruno dos Santos 1994, 1996, 2002, 2004, 2006, 2008`, 2012, 2014
Patrus, Marcos Caram 1996, 1998, 2000, 2002, 2004, 2006, 2008, 2010, 2012, 2014, 2016
Pecora, Luis A. 1994, 1996
Pereira, Guilherme Antunes 2016
Pujatti, Arquimedes 2006
Ramos Ribeiro, Tiago 2016
Rodrigues, Átila Benito P. 2010, 2014
Rodrigues, Daniel 2000
Santos, Everaldo E. dos 1998, 2000, 2002
Schmidt, Jorg 2002, 2004, 2006
Senna, Marco 2000
Spinola, José Carlos 2002, 2004, 2006
Tsukamoto Goto 2010
Versiani dos Anjos, Fernando 1998, 2000
Vicintin, Bruno Bello 2004
Vicintin, Ricardo 1996, 1998, 2000, 2002, 2004
Zica, Felipe Simões 2006, 2008, 2010, 2012, 2016
Zica, Henrique Simões 1998. 2000, 2002, 2004, 2006, 2008, 2010, 2012, 2014, 2016

Canada

Barati, Mansoor 2010, 2014
Boisvert, Rene 1996, 1998, 2000, 2002, 2004, 2006, 2008 2010
Choo, Roland 2010
Dold, Peter 2008
Haertel, Lutz 2004
Ksinsik, Dieter W. 1994, 1996, 1998, 2000, 2002, 2004, 2006
Lalancette, Michel 1996, 1998, 2000
Leblanc, Dominic 2008, 2010
Nichol, Scott 2008
Sagan, Nicholas 2006, 2008, 2010, 2012
Tafaghodi, Leili 2016
Utigard, Torstein 2010

Chile

Camino, Nicolas 2002
Pena, Roberto J. 2016

China

Cao, Jizhuang 2012
Jun, Fan 2010
Liu, Alanzo 2006, 2008
Liu, Tao 2002
Marsilio, Matteo 2008
Su, Zhiyi 2014
Tao, Wei 2010
Xiaodan, Hu 2008
Xijin, Zhang 2008
Xue, Jilai 2006
Yang, Wang 2008
Yuegang, Shao 2004, 2006, 2010

Cyprus

Vinogradov, Andrey 2004

Denmark

Hadsbjerg, Casper 2012

Egypt

ElSabee, Karim Maher 2012, 2014, 2016

FINLAND

Palo, Juha 2016

France

Apostolou, Georges 1994
Bandelier, Pascal 1996,1998, 2000
Baud, Luc 1994, 1996, 1998
Bertolini, Jean-Claude 1996, 1998, 2000, 2006
Borel, Jean-Marc 1996, 1998, 2000
Bricou, Alain 1998
Brown, Michael 2000
Bucher, Jean Philippe 1994, 1996, 1998, 2000
Bulteau, Thierry 1998, 2000
Caillod, Lisa 2004
Casulli, Stephane 1994
Chaal, Mohammed 2012, 2014, 2016
Choulet, Jean-Claude 1994
Colin, Pascale 1996, 1998, 2000, 2002, 2004
Decourtive, Bernard 1992, 1994, 1996
Degoulange, Julien 2014
Doguet, Loic 1996
Dubois-Quilbeuf, Isabella 2002
Floquet, Nicole 1992
Garcia-Escomel, Cristina 2006
Garcin, Eric 2006
Gautier, Pascal 2002
Glasson, Thomas 1996, 1998
Guerin, Pascal 2002
HUET, Michel Henri 2016
Humbert, Gilles 2012, 2014, 2016
Jenck, Jean-Francois 1992
Jugnet, Yvette 2000
Kewes, Eloi 2014
Laroze, Gilles 1992, 1994, 1996
Lecordix, Jean-Pascal 2008, 2012, 2014
Linglois, Alain 2008
Margaria, Thomas 1994, 1996, 1998, 2000, 2008, 2010, 2012
Martinon, Jean 1996, 1998, 2000
Morin, Nathalie 2008
Muratet, Jean-Claude 1996
Neulat, Laurent 2000, 2002, 2004
Nilssen, Benedicte Eikeland 2016
Pelletier 2012
Plagne, Jean-Louis 1992, 1994
Portal, Jerome 2012, 2014, 2016
Ramé, Frédéric 2002, 2004
Roche, Christian 1998
Rogier, Jean-Baptiste 1998
Rondeau, Jacques 1992, 1994
Roques, Yves 2002
Rosier, Cécile 2006, 2008, 2012, 2014, 2016
Rouvière, Philippe 2010
Ruckebusch, Alain 1996, 1998, 2000, 2002
Saillant, Bruno 1998
Traversaz, Frank 1996
Troude, Pierre 2000, 2002, 2004

Germany

Acker, Jörg 1998, 2000, 2002, 2004, 2012, 2014, 2016
Ackermann, J. 1998
Alber, Anne 2008, 2010
Antel, Detlef 1994, 1998
Antel, Hans-Detlef 2000, 2006, 2008, 2012, 2014, 2016
Armbrust, Ralph 1998
Auner, Norbert 2000, 2004, 2006, 2008, 2010, 20122014
Bade, Heinz 1994, 1996
Bauer, Stefan 2012, 2014, 2016
Becker, Robert Karl 2016
Berendes, Eckart 2010, 2012
Berg, Gerd 2010, 2012
Bernreuter, Johannes 2016
Bidlingmaier, Thomas 2010
Block, Hans-Dieter 2000
Bockholt, Andreas 2016
Boersting, Alfred 1994
Bramsiepe, Friedhelm 1994, 1998, 2000, 2006, 2008, 2012
Brantl, Stefan 1998, 2000
Braun, Rudolf 2008
Brenske, Michael 2012
Brumme, Johannes 1992, 1994, 1996
Candussio, Anton 2004
Conrad, Jürgen 2002
Damiotti, Dario 2008, 2010
Degel, Rolf 2014
Dembek, Joerg 2012, 2014
Deusser, Hans 1996, 1998
Diedrigkeit, Klaus 2012
Domingos, Valdiney 2014, 2016
Rimböck, Karl-Heinz 2016
Ehrich, Heike 1996, 1998
Fabry, Laszlo 2016
Fischer, Bernd 1992
Frey, Volker 1992
Frings, Albert 2000
Fritz, G. 1994
Froehling, Christian 2014
Gamon, Norbert 1996, 1998, 2002
Garcia-Alonso, Nuria 2006
Gebauer, Klaus 1998, 2000
Goetze, Brigitte 2006, 2010, 2012, 2014, 2016
Goetze, Ulrich 1994
Gomon, Dmytro 2008, 2010
Gottschalk-Gaudig, Torsten 2016
Gross, Jochen 2000
Groth, Thomas 2008, 2012
Gruenleitner, Walter 2002, 2004, 2008, 2010, 2006
Hackl, Michaela 2016
Hager, Rudolf 1996
Harrmann, Martin 2000
Hecker, Erik 2014
Heinrichs, Arne 2002
Heitmann, Claus 2000
Hennecke, Dieter 2010
Hesse, Karl 1994, 2000, 2004, 2008
Heuer, Matthias 2014, 2016
Heyen, Erk Thorsten 2012, 2014, 2016
Hock, Sebastian 2006, 2010
Höcker, Harald 1998, 2000, 2006, 2008
Hoffmann, Volker 2006, 2008
Höfler, Andreas 2012, 2014, 2016
Holl, Sven 2002, 2004
Horn, Guido 2008
Horns, Udo 1994, 1996, 1998, 2000
Hübner, Dieter 2010
Ilies, Dinu Mihai 2016
Immenkeppel, Michael 2000
Kai, Petter 2008
Kalchauer, Wilfried 1994, 1998, 2000, 2002, 2004, 2006, 2008
Kammergruber, Konrad 2004

Hong Kong

Alary, Thierry	2004

Iceland

Bjorn, Helgi	2014
Björnsson, Hákon	2014
Dembek, Jörg	2016
Fenger, John	2014
Gardarsson, Magnus	2014
Gargarsson, Magnus	2012
Gudnason, Edvard G	2012
Gunnarsson, Jökull	2016
Jonsdottir, Stella Marta	2012
Saadieh, Raghed	2016
Thorhallsson, Helgi	2016
Viktorsson, Hafsteinn	2016
Wenzel, Peter	2016

India

Bachal, Sanjiv	1998
Badani, Manish	2002
Chandola, Pankij	1998
Padubidri, Sushama	1994, 1996, 1998, 2000, 2004, 2008
Paman, Ajeet S.	2000
Paulmer, Robert	1998
Samala, Murali	1998

Italy

Angelis, Daniele de'	2000
Broggi, Andrea	2016
Cerofolini, Gianfranco	1996
Damiotti, Dario	2002
Foglia, Foglia Gianmichele	2012
Marangoni, Giovanni	2006
Osvaldo, Brioni	2012
Pasolli, Claudio	2008, 2010
Scandola, Pietro	2008
Smagghe, Alain	2012

Japan

Abe, Mitsuo	1996, 1998
Arai, Fumio	1998
Araki, Isamu	2002
Aramata, Mikio	1998, 2000, 2002, 2004, 2006, 2008, 2010
Arita, Yoji	2010
Bolzer, Walter	1996, 1998, 2000
E, Piljoon	2012
Grandum, Svein	2008
Gunji, Toru	1996
Hanaoka, Hiroaki	1998
Harada, Katsuyoshi	2002, 2008, 2010
Hasegawa, Takao	1994
Iida, Katsunori	2010
Ikeda, Tatsuya	2004
Inoue, Yuji	2000
Kambara, Makoto	2010, 2012
Kato, Yoshiei	2016
Kirii, Seiichi	1992
Kishimoto, Hiroyuki	2002, 2004,
Kohno, Hiroshi	1994
Komada, Norikazu	2016
Kondo, Katsumi	1998
Kusama, Shin-ichi	2002
MA, Xiaodong	2012
Miyata, Masahiro	1992, 1994, 1996
Morita, Kazuki	2008, 2010, 2012, 2014, 2016
Muraida, Akio	2004
Murakami, Kazushiro	1996
Nakanishi, Tetsuo	1996
Nakano, Mamoru	2004
Nakayasu, Akio	2016
Nishikawa, Mitsuhiro	1996, 1998
Ochiai, Mitsuji	1992
Oda, Hiroyuki	1992
Ohtani, Jiroh	1998, 2000, 2002
Okamoto, Masaki	1996
Ono, Yoshio	1994, 1998
Otani, Eiichi	2000
Sakaguchi, Hiroki	2014
Sakai, Sho	1998
Sakai, Tetsuo	2014
Samori, Hirosi	1996
Sandberg, Bjorn	2008
Sato, Yuzuro	2006, 2008, 2010
Shimada, Shiro	2006
Shimizu, Hiroshi	1992, 1994, 1996, 1998, 2000, 2002
Sugiura, Kengu	2004
Takahashi, Takashi	2000
Tanaka, Shoichi	1992
Terada, Ikuhiro	1998
Tsumura, Hiroshi	1994
Uesugi, Nobuyuki	2004
Umehara, Mitsuiro	1994
Wakamatsu, Satoru	1998
Wang, Ye	2014
Yamashita, Toru	1996
Yoshizawa, Hironori	2012, 2014
You, Yuliu	2016

Kazakhstan

Zhandayev, Nurlan Makataevich	2014

Mexico

Aguilera, Alberto F.	1992, 1994, 2000, 2002, 2004, 2010, 2012
Cervantes, Jorge	1992, 1994, 1996, 1998, 2000, 2002, 2004, 2010
Plascencia, Gabriel Plascencia	2010

New Zealand

Harris, Graeme	2004
Matheson, Andy	2002
Simpson, Andrew Vincent	2004

Norway

Aabakken, Skjalg	2014
Aasly, Kurt	2006, 2016
Abrahamsen, Thorstein	2010
Andersen, Geir	2000, 2002, 2004, 2012
Andersen, Vegar	2012
Andresen, Birger	1996, 1998, 2000, 2002, 2004, 2006, 2008, 2010, 2012, 2014, 2016
Backström Iversen, Cecilie	2010
Bakke, Per	2008
Berget, Kjell Håkon	2012, 2014
Bergkvist, Anders	2002, 2004
Bjørseth, Alf	1998, 2006
Breidenthal, Mark	2010